LEABHARLANN CHOLÁISTE NA TRÍONÓIDE, BAILE ÁTHA CLIATH | TRINITY COLLEGE LIBRARY DUBLIN
Ollscoil Átha Cliath | The University of Dublin

Terms and Conditions of Use of Digitised Theses from Trinity College Library Dublin

Copyright statement

All material supplied by Trinity College Library is protected by copyright (under the Copyright and Related Rights Act, 2000 as amended) and other relevant Intellectual Property Rights. By accessing and using a Digitised Thesis from Trinity College Library you acknowledge that all Intellectual Property Rights in any Works supplied are the sole and exclusive property of the copyright and/or other IPR holder. Specific copyright holders may not be explicitly identified. Use of materials from other sources within a thesis should not be construed as a claim over them.

A non-exclusive, non-transferable licence is hereby granted to those using or reproducing, in whole or in part, the material for valid purposes, providing the copyright owners are acknowledged using the normal conventions. Where specific permission to use material is required, this is identified and such permission must be sought from the copyright holder or agency cited.

Liability statement

By using a Digitised Thesis, I accept that Trinity College Dublin bears no legal responsibility for the accuracy, legality or comprehensiveness of materials contained within the thesis, and that Trinity College Dublin accepts no liability for indirect, consequential, or incidental, damages or losses arising from use of the thesis for whatever reason. Information located in a thesis may be subject to specific use constraints, details of which may not be explicitly described. It is the responsibility of potential and actual users to be aware of such constraints and to abide by them. By making use of material from a digitised thesis, you accept these copyright and disclaimer provisions. Where it is brought to the attention of Trinity College Library that there may be a breach of copyright or other restraint, it is the policy to withdraw or take down access to a thesis while the issue is being resolved.

Access Agreement

By using a Digitised Thesis from Trinity College Library you are bound by the following Terms & Conditions. Please read them carefully.

I have read and I understand the following statement: All material supplied via a Digitised Thesis from Trinity College Library is protected by copyright and other intellectual property rights, and duplication or sale of all or part of any of a thesis is not permitted, except that material may be duplicated by you for your research use or for educational purposes in electronic or print form providing the copyright owners are acknowledged using the normal conventions. You must obtain permission for any other use. Electronic or print copies may not be offered, whether for sale or otherwise to anyone. This copy has been supplied on the understanding that it is copyright material and that no quotation from the thesis may be published without proper acknowledgement.

Application of Colloidal Quantum Dots to a Range of Photovoltaic Designs

Finn Purcell-Milton

A thesis submitted to the University of Dublin, Trinity College for the degree of doctor of Philosophy

School of Chemistry and CRANN

Trinity College Dublin

Dublin 2

Ireland

February 2015

TRINITY COLLEGE DUBLIN
10 JUN 2015
ACADEMIC REGISTRY

PhD in Che

50555786
50555786

THESIS
10661

TRINITY COLLEGE
2 9 JUL 2015
LIBRARY DUBLIN
Thesis 10661

Declaration

The thesis is submitted by the undersigned to the University of Dublin, Trinity College for the examination of Doctorate of Philosophy. It has not been submitted as an exercise for a degree to this or any other university. Except as stated otherwise, the author carried out the work described herein alone. The author agrees that the University Library may lend or copy the thesis upon request. This permission covers only single copies made for study purposes, subject to Irish Copyright Legislation and Trinity College Library conditions of acknowledgement.

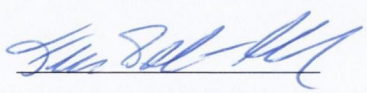

Finn Purcell-Milton

Summary

This project explores the use of quantumly confined materials as photon absorbers, with the aim to produce nanomaterials that we believe will increase efficiency in reported quantum dot based photovoltaic designs. The structure of the thesis is as follows.

Chapter 1 is a literature review of topics important to this research and a general introduction into semiconductors, nanomaterials and photovoltaics. The aims and objectives of the work are also detailed in this chapter.

Chapter 2 describes all of the experimental details relating to the work presented in the thesis and has been labelled with experimental specifics concerning each result chapter. Also included is a brief explanation of instrumentation and the range of characterisation methods used throughout the thesis work.

Chapter 3 is dedicated to the development and optimisation of the hot injection synthesis of a range of semiconductor nanomaterials for use in photovoltaic devices, with materials chosen to explore the effect of band gap size and band gap structure when incorporated in QD based solar cells. We also describe the application of gold nanoparticles to these produced structures and the effects of oleylamine based halide treatments upon the resulting luminescent, with the aim of improving surface passivation and so making the synthesised structures more effective as sensitizers in a photovoltaic design.

Chapter 4 investigates the use of electrophoretic deposition as a tool to produce thin films of CQDs upon porous TiO_2 electrodes, with the resulting photosensitisation examined. We have also studied a number of post treatments as a means to increase the resulting photocurrent through bulk semiconductor deposition and ligand exchange. Included in this work is a brief examination of cation exchange also as means to alter the absorption and stability of a QD sensitised TiO_2 electrode.

Chapter 5 describes the fabrication of two alternative types of QD based photovoltaic devices, quantum dot sensitised solar cells and depleted heterojunction solar cells. This study also explores discotic liquid crystal quantum dot composites, as possible materials for photon harvesting. Overall, the chapter covers the material fabrication of these devices; examine their properties, followed by analysis of the resulting devices produced.

Chapter 6 provides a conclusion to this body of work and outlines the main achievements of our research. This chapter also includes a number of suggestion for research to carry out based on our finds, which we believe will be fruitful and interesting.

Finally, we strongly believe that this project will contribute to further development of quantum dot based materials and their uses in a range of important photovoltaic devices.

Acknowledgements

Many people have played an important part in making this work possible, but first and foremost I would like to thank Prof Yurii Gun'ko, my supervisor. He has been an immense help in all aspects of my research at Trinity College Dublin and a constant source of knowledge and ideas. His style of supervision I found especially refreshing and conducive to a constructive and enjoyable work environment, allowing me to pursue my own interests while always being at hand to advise and direct me, especially when I found myself at a loss of what step to take next.

Next, I need to thank everybody in the Yurii Gun'ko group, past and present, for your constant support and advice throughout the past 4 years. It has been an absolute pleasure working with you all and you have made every day insightful, challenging and enjoyable. A number of the group's members I worked with especially closely and I would like to thank them individually. Firstly, I need to thank Lorcan Brennan who I worked with closely throughout many of the most challenging aspects of solar cell fabrication and testing procedure. His optimistic attitude and perseverance made possible the design and testing of many of the quantum dot based solar cell designs, and without his help, it would have been impossible to achieve. Secondly, I would like to thank Cormac Hanley, for initially training and introducing me to quantum dot synthesis, and as the project evolved, being an important colleague for discussing synthetic strategies and troubleshooting complicated synthetic procedures. Thirdly, I would like to thank Shane Gallagher, who was always at hand to discuss papers across the discipline, with enthusiasm. Lastly, I would like to thank Valeria Gerard, who aside from many other things, demonstrated to me, day in day out, that working efficiently was much more effective than just putting hours in.

My work also enormously benefited from the many other extra hands I had, due to the six undergraduate students that participated in my project over the four-year period. I found the experience very much a two way street of learning in which I would initially train the students in their specific project, but by the end I was inevitably learning as much as I was teaching. I would like to especially thank two students who were outstanding in their effort, enthusiasm and ability, Aude Buffard and Antton Curutchet, both of which I have no doubt will be become exceptional researchers in their own right.

The process of producing this PhD thesis was remarkably enjoyable at stretches, while other times I found it incredibly difficult and challenging. During these periods, I found my enthusiasm waned and I was lucky enough to have an exceptional support structure to lift my spirits, in the

form of my family and friends, all of which have been super positive about this undertaking from day one. Always giving words of encouragement and I would assume feigning interest at times just to let me express my own frustrations or challenges. Paramount in this role was my long-term partner Eva Dowling, who has been supporting me from the beginning. She has been a saint to put up with my obsession with the PhD and my near complete lack of engagement with life outside it during the last six months of the process. She was always present to cheer me up and remind me of the end goal, I have no doubt in my mind that I would not have achieved this milestone, not too this standard, without her by side.

As a final point, I would like to thank the school of Chemistry for funding my research and Trinity College for facilitating my work and all the support staff who helped in a million a one ways across the School of Chemistry, the Centre for Research on Adaptive Nanostructures and Nanodevices, and the Advanced Microscopy Laboratory.

Abbreviations

AM- Air Mass

BOS - Balance of Systems

BG - Band Gap

CBD - Chemical Bath Deposition

CB - Conduction Band

CE - Counter Electrode

CQD - Colloidal Quantum Dot

DCM - Dichloromethane

DHCQD - Depleted Heterojunction Colloidal Quantum Dot

DI - Deionized Water

DC- Direct Current

DLC - Discotic Liquid Crystal

DSE - Donor Supply Electrode

DSSC - Dye Sensitised Solar Cell

E_g - Band Gap Energy

EPD - electrophoretic deposition

EDX - Energy dispersive X-ray spectroscopy

FF - Fill factor

FWHM - Full width half maximum

FTO - Fluorine Doped Tin Oxide

H6TP- 2,3,6,7,10,11,Hexahexyloxy-triphenylene

HEL - Hole Extraction Layer

HPA - Hexadecylphosphonic acid

HRTEM - High Resolution Transmission Electron Microscopy

HTAC-Hexadecyltrimethylammonium chloride)

I_{sc} - Short Circuit Current

IV- Current-Voltage

ITO - Indium Doped Tin Oxide

LC - Liquid Crystal

LACO - Linear Combination of Atomic Orbitals

MEG - Multiple Exciton Generation

MO - Molecular Orbital

MPA - Mercaptopropionic acid

MOCVD - Metalorganic Chemical Vapour Deposition

NIR - Near infrared

NR - Nanorods

NC - Nanocrystal

NP- Nanoparticle

OA - Oleic acid

ODE - Octadecene

ODA - Octadecylamine

ODPA - Octadecylphosphonic acid

OLY - Oleylamine

P_{max} - Maximum Power

P_t - Theoretical Power

PBDT - 1,4-phenylenedicarbamodithioate

PDI - soluble perylene diamide, (N,N9-bis(1-ethylpropyl)-3,4,9,10-perylenebis

PL - Photoluminescence

PCE - Power conversion efficiency

POM - Polarized optical microscopy

PVB - Polyvinyl butyral

SEM - Scanning electron microscopy

QD - Quantum Dots

QDDSSC- Quantum Dot Sensitised Solar Cell

QR - Quantum Rod

QY - Quantum Yield

RE - Reference Electrode

R_s - Series Resistance

R_{sh} - Shunt Resistance

RTAQ - 1,5-dihydroxy-2,3,6,7-tetrakis(3,7-dimethyloctyloxy)-9,10-anthraquinone

SB - Schottky Barrier

SEM - Scanning Electron Microscope

SPD - Spray Pyrolysis Deposition

SILAR - Successive Ion Layer Adsorption and Reaction

STEM - Scanning Transmission Electron Microscopy

TBP - Tributylphosphine

TDPA - Tetradecylphosphonic acid

TEM - Transmission electron microscopy

TOP - Trioctylphosphine

TOPO - Trioctylphosphine oxide

TMS - Bis (trimethylsilyl) sulfide

WE - Working Electrode

UV- Ultraviolet

VB - Valence Band

V_{oc} - Open Circuit Voltage

Vis - Visible

XRD - X-ray crystal diffraction

Table of Contents

Chapter 1 Introduction....1

1.1 Semiconducting materials....1

1.1.1 Band Theory....1

1.1.2 Semiconductor Types and Properties....3

1.1.3 P-N Junction....5

1.1.4 Schottky Junction....6

1.1.5 Quantum Size Effects and Quantum Dots....7

1.1.6 Optical Properties of Quantum Dots....8

1.1.7 Colloidal Quantum Dots (CQD)....9

1.1.8 Core-Shell QD Heterostructures....11

1.1.8.i Type I....11

1.1.8.ii Reverse Type I....11

1.1.8.iii Type II....11

1.1.9 Multiple shelled QDs....11

1.1.10 Lattice Mismatch and Strain....12

1.1.11 Bulk Modulus and crystal defects....12

1.1.12 Synthesis of core-shell quantum dot structures....13

1.1.13 Cation exchange in nanostructures....14

1.1.14 CQD films....15

1.1.15 Doping of QD films....16

1.2 Photovoltaic Cells....17

1.2.1 Main concepts and definitions....17

1.2.2 Blackbody radiation....18

1.2.2.i Recombination....18

1.2.2.ii Spectrum loss....19

1.2.3 Dye Sensitized Solar Cell (DSSC) 20
1.2.4 TiO_2 material 21
1.2.5 Colloidal Quantum Dot Based Photovoltaic 22
1.2.6 Manufacturing Cost 22
1.2.7 Tuneable and Broad Absorption 22
1.2.8 MEG (Multiple Exciton Generation) 23
1.2.9 The effect of quantum dot size polydispersity 23
1.2.10 Quantum Dot cell designs 23
1.2.11 CQD Schottky Cell 24
1.2.12 Quantum Junction Solar Cells 25
1.2.13 Depleted Heterojunction Colloidal Quantum Dot Solar Cell 25
1.2.14 Hole Extraction Layer 26
1.2.15 Anion passivation 26
1.2.16 Donor Supply Electrode 27
1.2.17 Durability 27
1.2.18 New Cell Architecture 28
1.2.19 Quantum Dot Sensitised Solar Cell (QDSSC) 28
1.2.20 Linker Approach to CQD Deposition 30
1.2.21 Electrophoretic Deposition of CQDs 30
1.3 Liquid Crystals 31
1.3.1 Discotic Liquid Crystals 32
1.3.2 Discotic Liquid Crystal Devices 33
1.3.3 Liquid Crystal QD Composites 33
1.4 Aims and Objectives of Project 33
Chapter 2 Experimental 50
2.1 Materials 50

2.1.1 Materials supplied by Sigma – Aldrich 50

2.1.2 Solvents supplied by Trinity College Solvent Stores 50

2.1.3 Other suppliers 50

2.2 Experimental Details of Chapter 3 51

2.2.1 Preparation of oleic acid capped CdS Quantum Dots 51

2.2.1.i Preparation of 0.05 M sulphur stock solution 51

2.2.1.ii CdS QD synthesis 51

2.2.2 Preparation of oleic acid capped CdSe 51

2.2.2.i Se-TBP solution preparation 51

2.2.2.ii CdSe Synthesis 51

2.2.3 *Preparation of ODPA capped CdSe QDs* 52

2.2.3.i Preparation of Se 0.75 M stock solution 52

2.2.3.ii Synthesis of CdSe QDs 52

2.2.4 Preparation of Octadecylamine capped -CdSe QDs 52

2.2.4.i Preparation of 1.5 M Se stock solution 52

2.2.4.ii Preparation of 0.5 M Cd stock solution 52

2.2.4.iii SILAR stock solutions of Cd and Se 52

2.2.4.iv Synthesis of CdSe QDs 53

2.2.5 Preparation of PbS Quantum Dots 53

2.2.5.i Preparation of 0.1 M TMS stock solution 53

2.2.5.ii Oleic acid capped PbS QD synthesis 53

2.2.6 Preparation of CdS/CdSe Quantum Dot 53

2.2.6.i Preparation of 0.5 M sulphur stock solution 54

2.2.6.ii Preparation of 0.4 M Se stock solution 54

2.2.6.iii Preparation of 0.4 M Cd $(oleate)_2$ stock solution 54

2.2.6.iv CdS/CdSe QD synthesis 54

2.2.7 Preparation of CdSe/CdS Core-Shell Quantum Dots 54

2.2.7.i Preparation of 0.1 M S stock solution 55

2.2.7.ii Preparation of 0.1 M Cd stock solution 55

2.2.7.iii Synthesis of CdSe/CdS QDs 55

2.2.8 Preparation of CdSe/CdS Core-Shell Heterostructured Quantum Rods 55

2.2.8.i Preparation of 2.5 M S - TOP and CdSe QD stock solution 55
2.2.8.ii Synthesis of CdSe/CdS core-shell quantum rods 55
2.2.9 Preparation of CdTe/CdSe Type II Core-Shell Quantum Dots 56
2.2.9.i 0.08 M Te Stock solution 56
2.2.9.ii 0.09 M Se Stock solution 56
2.2.9.iii 0.1 M Cd Stock solution 56
2.2.9.iv Synthesis of CdTe/CdSe Quantum Dots 56
2.2.10 Preparation of PbS/CdS core-shell quantum dots 57
2.2.10.i 0.25 M Cd Stock solution 57
2.2.10.ii Synthesis of PbS/CdS Quantum Dots 57
2.2.11 Cation exchange of CdX quantum to Cu_2X quantum dots 57
2.2.11.i 0.03 mM Tetrakis(acetonitrile)copper(I) hexafluorophosphate solution 57
2.2.11.ii Preparation of Cu_2X quantum dots 57
2.2.12 Cation exchange of Cu_2X quantum dots to PbX quantum dots (X= Se or S) 58
2.2.12.i Preparation of 0.15 M solution of Pb^{2+} solution 58
2.2.12.ii Preparation of PbX using cation exchange (X= Se or S) 58
2.2.13 CdSe/CdS/Au quantum rods 58
2.2.14 Halide Oleylamine treatment 59
2.2.14.i Stock solution 59
2.2.14.ii Halide oleylamine solution treatment 59
2.3 Experimental Details of Chapter 4 59
2.3.1 Synthesis of Disodium 1,4-phenylenedicarbamodithioate (PBDT) 59
2.3.2 Electrophoretic Quantum Dot Deposition 60
2.3.2.i Electrophoretic Deposition Method A 60
2.3.2.ii Electrophoretic Deposition Method B 60
2.3.3 ZnS Coating of TiO_2 electrode 60
2.3.4 CdS Coating of TiO_2 electrode 61
2.3.5 HTAC ligand exchange of TiO_2 electrode 61
2.3.6 MPA ligand exchange of TiO_2 electrode 61

2.3.7 Cation exchange of PbS QDs to PbS/CdS upon the surface of a porous TiO_2 electrode 61

2.3.7.i 0.025 M $CdCl_2$ solution 61

2.3.7.ii Preparation of PbS/CdS sensitized TiO_2 electrode 61

2.3.8 Cation exchange of CdX QDs to Cu_2X upon the surface of a porous TiO_2 electrode (X= S or Se) 62

2.3.8.i 03 mM Tetrakis(acetonitrile)copper(I) hexafluorophosphate solution 62

2.3.8.ii Preparation of Cu_2X sensitized TiO_2 electrode (X= S or Se) 62

2.3.9 Cation exchange of Cu_2X QDs to PbX QDs upon the surface of a porous TiO_2 electrode (X= S or Se) 62

2.3.9.i Preparation of 0.075 M solution of Pb^{2+} solution 62

2.3.9.ii Preparation of PbX using cation exchange (X= S or Se) 62

2.4 Experimental Details of Chapter 5 62

2.4.1 Quantum dot Sensitised Solar Cell Fabrication 62

2.4.1.i Cu_2S Counter Electrode Preparation 62

2.4.1.ii PbS Counter Electrode Preparation 63

2.4.1.iii Pt electrode 63

2.4.1.iv Electrode Cleaning 63

2.4.1.v Bulk TiO_2 layer deposition upon working electrode 63

2.4.1.vi Porous nanoparticulate TiO_2 layer deposition upon working electrode 64

2.4.1.vii Device Fabrication 64

2.4.2 DHCQD cell Fabrication 65

2.4.2.i FTO Etch 65

2.4.2.ii TiO_2 deposition and sintering 65

2.4.2.iii Dip coating of Colloidal Quantum Dots 66

2.4.2.iv Metal Evaporation of Au back electrode 66

2.4.3 Discotic Liquid Crystal Testing and Solar Cell Fabrication 67

2.4.3.i Liquid Crystal Electrical conductivity Device Fabrication 67

2.4.3.ii Alignment of Discotic Liquid Crystals 67

2.4.3.iii Spin Coating of diluted TiO_2 paste 67

2.4.3.iv Metal evaporation of Ag or Al back electrode 68

2.5 Instrumentation 68

2.5.1 Microscopy 68

2.5.1.i Transmission Electron Microscopy (TEM) 68

2.5.1.ii High Resolution Transmission Electron Microscopy (HRTEM) / Scanning Transmission Electron Microscopy (STEM) 68

2.5.1.iii Scanning Electron Microscopy (SEM) 69

2.5.1.iv Incident Polarized Optical Microscopy (POM) 69

2.5.2 Spectroscopy 70

2.5.2.i Ultra violet- visible –infrared (UV-Vis-NIR) absorption spectroscopy 70

2.5.2.ii Photoluminescence (PL) Spectroscopy 71

2.5.2.iii Raman spectroscopy 72

2.5.2.iv Energy dispersive X-ray spectroscopy (EDX/EDS) 72

2.5.2.v Photoluminescence lifetime spectroscopy 72

2.5.2.vi Spectrograph 72

2.5.3 Diffraction 72

2.5.3.i X-ray powder diffraction (XRD) 72

2.6 Electrical measurements 72

2.6.1 Cyclic voltammetry 72

2.6.2 DC conductivity testing 73

2.6.3 Photocurrent Action Response Measurement 73

2.6.3.i Solar PCE Measurements 75

2.6.3.ii External Quantum Efficiency (EQE) spectrum 76

2.6.4 Current-Voltage (IV) Curve 78

2.6.4.i Power In (P_{in}) 79

2.6.4.ii Short Circuit Current (I_{sc}) 79

2.6.4.iii Open Circuit Voltage (V_{oc}) 79

2.6.4.iv Maximum Power Point (MPP), Maximum Power (P_{max}) and Theoretical power (P_t) 79

2.6.4.v Fill Factor (FF) 80

2.6.4.vi Series Resistance (R_s) and Shunt Resistance (R_{sh}) 80

2.6.4.vii Power Conversion Efficiency (PCE) 81

Chapter 3 Hot Injection Quantum Dot Synthesis: Characterisation and Studies of the Effects of Cation and Anion Solutions 84

3.1 Introduction 84

3.2 Aim 86

3.3 Hot injection synthesis and characterisation of quantum nanostructures 88

3.3.1 Octadecylphosphonic acid capped CdSe Quantum Dots: Synthesis and Characterisation 88

3.3.1.i Optical analysis of ODPA capped CdSe QDs 89

3.3.1.ii Electron Microscopy analysis of ODPA capped CdSe QDs 91

3.3.2 Octadecylamine capped CdSe Quantum Dots: Synthesis and Characterisation 92

3.3.2.i Optical Characterisation 93

3.3.3 Oleic Acid Capped CdSe Quantum Dots: Synthesis and Characterisation 94

3.3.3.i Optical characterisation of oleic acid capped CdSe 95

3.3.3.ii Microscopic Analysis of oleic acid capped CdSe QDs 96

3.3.4 CdS Quantum Dots: Synthesis and Characterisation 96

3.3.4.i Optical characterisation 97

3.3.4.ii Electron Microscopy Analysis 99

3.3.5 PbS Quantum Dots: Synthesis and Characterisation 100

3.3.5.i Optical measurements 101

3.3.5.ii Electron Microscopy Analysis 102

3.3.6 CdSe/CdS QD Synthesis 105

3.3.6.i Optical Characterisation 106

3.3.6.ii Electron Microscopy Analysis 107

3.3.7 CdS/CdSe Quantum Dots: Synthesis and Characterisation 108

3.3.7.i Optical characterisation 109

3.3.7.ii Electron Microscopic Analysis 111

3.3.8 CdTe/CdSe QD: Synthesis and Characterisation 111

3.3.8.i Optical Characterisation 112

3.3.8.ii Electron Microscopy Analysis 115

3.3.9 CdSe/CdS Quantum Rods: Synthesis and Characterisation 116

3.3.9.i Optical analysis QRs 117

3.3.9.ii Electron Microscopy Analysis 119

3.3.10 CdSe/CdS/Au nanocomposites Synthesis and Characterisation 121

3.3.10.i Optical Characterisation 122

3.3.10.ii Electron Microscopy Analysis 123

3.4 Cation exchange 124

3.4.1 Cation exchange: PbS QDs to PbS/CdS QDs 124

3.4.1.i Optical characterisation 125

3.4.1.ii Electron Microscopy Analysis 126

3.4.2 Cation exchange of CdSe to $Cu_{2-x}Se$ 126

3.4.2.i Optical spectroscopy 127

3.4.3 Transformation of CdSe/CdS to $Cu_{2-x}Se$/$Cu_{2-x}CdS$ to PbSe/PbS 128

3.4.3.i Optical Characterisation 128

3.5 Halide Oleylamine Treatment 129

3.5.1 Halide Oleylamine Treatment: Oleic acid capped CdSe QDs 130

3.5.2 Halide Oleylamine Treatment: ODPA capped CdSe QDs 133

3.5.3 Halide Oleylamine Treatment: ODA capped CdSe QDs 133

3.5.4 Halide Oleylamine Treatment: CdS QDs 134

3.5.5 Halide Oleylamine Treatment: CdSe/CdS QDs 135

3.6 Conclusions 136

Chapter 4 Electrophoretic Deposition of CQDs to Increase Photosensitisation of TiO_2 films 141

4.1 Introduction 141

4.2 Aim 143

4.3 EPD of CdSe QDs upon TiO_2 photoelectrode 144

4.3.1 Quantum dots electrophoretic deposition: method A 144

4.3.2 Quantum dot Electrophoretic Deposition: Method B 147

4.3.2.i Solvent effect 147
4.3.2.ii Time of deposition 149
4.3.2.iii Effect of potential 149
4.3.2.iv Origin of charge and current 150
4.3.2.v Repeatability 150
4.3.2.vi Adherence and comparison to controls 151
4.3.2.vii Microscopic analysis 152
4.3.2.viii EDX 153
4.3.2.ix Photocurrent Action Spectra 155
4.3.3 Octadecylamine capped CdSe QDs 156
4.3.4 Octadecylphosphonic acid capped CdSe QDs 157
4.4 Post EPD treatments of Electrodes 158
4.4.1 SILAR Deposition: ZnS coating effect 158
4.4.2 SILAR Deposition: CdS coating effect 160
4.4.3 Ligand exchange: HTAC 162
4.4.4 Ligand Exchange: MPA Ligand treatment 162
4.4.5 EPD of CdS QDs 163
4.4.6 EPD of PbS QDs 166
4.4.7 EPD of CdSe/CdS core-shell QDs 168
4.4.8 EPD of CdS/CdSe core/shell QDs 169
4.4.9 EPD of CdTe/CdSe core/shell QDs 169
4.4.10 EPD of CdSe/CdS heterostructured quantum rods 170
4.5 Cation Exchange of EPD QDs upon TiO_2 electrodes 173
4.5.1 Cation exchange of PbS QDs to PbS/CdS QDs on TiO_2 173
4.5.2 Cation exchange of CdSe to Cu_2Se to PbSe QDs on TiO_2 176
4.6 Conclusions 179
Chapter 5 Quantum Dot Solar Cell Fabrication and Testing 184
5.1 Introduction 184

5.2 Aim 188

5.3 QDSSC Cells 189

5.3.1 Counter Electrodes 189

5.3.1.i PbS counter electrode 189

5.3.1.ii Cu_2S counter electrode 190

5.3.1.iii Platinum counter electrode 193

5.3.1.iv Cyclic Voltammetry of counter electrodes 194

5.3.2 Photoaniode: TiO_2 Electrode 194

5.3.2.i Bulk TiO_2 Layer 195

5.3.2.i Porous 20 nm TiO_2 layer 196

5.3.2.ii TiO_2 Scatter Layer 198

5.3.2.iii Post treatment 199

5.3.3 IV Testing of QDSSC Solar Cells 200

5.3.3.i IV testing of Closed QDSSC Cells 200

5.3.3.ii Open Cell 201

5.4 DH-CQD cell 203

5.4.1 FTO Etch 204

5.4.2 TiO_2 Electrode 204

5.4.3 PbS Deposition 209

5.4.4 Back electrode deposition 212

5.4.5 IV testing of DHCQD cells 213

5.5 Discotic Liquid Crystal Solar Cells 214

5.5.1 Discotic Liquid Crystal Characterisation 214

5.5.1.i H6TP: Solution 214

5.5.1.ii H6TP: Solid State 215

5.5.1.iii H6TP/ QD solution 216

5.5.1.iv RTAQ : Solution 216

5.5.2 Discotic Liquid Crystal / Quantum Dot Composite Characterisation 217

5.5.2.i Electrical DC Conductivity of DLC-QD composites 217

5.5.2.ii Polarised Optical Microscopy of DLC-QD composites 220

5.5.3 DLC Cell fabrication 227

5.5.3.i Spincoating 227

5.5.3.ii Device results 229

5.6 Conclusions 230

Chapter 6 Conclusions and Future Work 236

6.1 Conclusions 236

6.2 Future Work 239

Chapter 7 Appendix I

7.1 Appendix A: Equations I

7.1.1 Exciton Bohr radius I

7.1.2 Schottky Barrier Height I

7.1.3 The Marcus equation I

7.1.4 The Brus Equation I

7.1.5 Energy balance underlying Heterostructures formation II

7.1.6 Electrophoretic deposition II

7.2 Appendix B: Tables of Material Properties III

7.3 Appendix C: Extra Experimental Results of Chapter 3 VIII

7.4 Appendix D: Extra Experimental Results of Chapter 4 XV

7.5 Appendix E: Extra Experimental Results of Chapter 5 XVI

Table of Figures

Figure 1.1 Showing the three molecular orbitals created between three atoms each with one atomic orbital 1

Figure 1.2 Band structure formed from LCAOs, where N is the number of atoms 2

Figure 1.3 Band diagram of a metal, semiconductor and Insulator 3

Figure 1.4 Formation of an exciton in a semiconductor due to absorption of a photon 4

Figure 1.5 Diagram showing the structure of a p-n junction formed between a n-doped and p-doped semiconductor, graphing charge, electric field and voltage 6

Figure 1.6 Diagram showing the effect of exciton confinement. The effect of reduction of size of a semiconductor nanocrystal below the Bohr radius produces this quantum confinement of the exciton. This in turn increase the band gap as size reduces further and the nanocrystal can now be described as a quantum dot. 7

Figure 1.7 A collodial quantum semiconductor with organic ligand covering the surface 9

Figure 1.8 This shows the nucleation and growth process of collodial quantum dots using the hot injection method 10

Figure 1.9 Different band alignments of core-shell quantum dots, dependent upon the band gap, valance band and conduction bands of shell and core semiconductor materials. 12

Figure 1.10 This shows the process of cation exchange taking place in a nanocrystal, in which one cation is replaced by another in solution over time, while maintaining the anion framework. 14

Figure 1.11 The diagram shows the movement of electrons between CQD, ... 16

Figure 1.12. The Solar Irradiation at AM 0 and AM 1.5G and 1.5 D compared to a blackbody radiator at 5800K reproduced from ref [147] 18

Figure 1.13 The Shockley-Queisser limit of a single junction cell under AM 1.5G solar illumination 19

Figure 1.14 CQD Schottky cell, showing the basic structure of the cell 24

Figure 1.15 This shows one of the most common designs used in a quantum dot depleted heterojunction solar cell (right) and the basic movement of electrons and holes in this device (left). 26

Figure 1.16 This a common design for a quantum dot sensitised solar cell (right) and the flow of electrons across the device (left) 28

Figure 1.17. Diagram showing the difference in order on the molecular scale between the solid crystalline phase, the liquid crystal phase and the liquid phase 32

Figure 1.18 The change from cooling from the liquid phase to the self-organised columnar liquid crystal phase 32

Figure 2.1 Electrophoretic deposition setup to deposit quantum dots upon electrodes 60

Figure 2.2 TiO_2 electrode thermal treatment cycle using a tube furnace in air 64

Figure 2.3 Diagram showing the FTO glass etch carried out enabling multiple DHCQD cells be produced upon the same glass 65

Figure 2.4 This shows the basic process used to deposit collodial quantum dots upon the TiO_2 elctrode 66

Figure 2.5 Diagram of devices fabricated to test the conductivity of DLC/QD composites 67

Figure 2.6 Diagram showing the basic structure of a TEM microscope. 68

Figure 2.7 Diagram of scanning electron microscope showing the basic setup of the device. The image was reproduced from ref 288. 69

Figure 2.8 Diagram of the operation of a dual beam UV-Vis absorption spectrometer. Image reproduced from ref 290. 70

Figure 2.9 This diagram explains the operation of ta photoluminescent spectrometer. Image reproduced from ref 291. 71

Figure 2.10 This is the experimental design used to take photocurrent action response measurements; the photoaniode illuminated is carried out using a white light LED ring. 74

Figure 2.11 This shows the ideal current response of a photoaniode when cycled between illumination/darkness as a function of time. 74

Figure 2.12 Emission spectra of white light LED used to approximate sunlight illumination for photocurrent spectra measurements 75

Figure 2.13 The emission spectra of the Xenon arc discharge lamp used for solar simulation. 75

Figure 2.14 This shows the setup of the EQE device designed in house. 77

Figure 2.15 IPCE measurement of a silicon solar cell 78

Figure 2.16. I-V curve of a solar cell under illumination and darkness, reproduced from ref 147. 79

Figure 2.17.I-V curves showing P_{max} , I_{mpp} , V_{mpp} on left, I_{sc} , V_{oc} P_t,in middle and FF on right, reproduced from ref 147. 80

Figure 3.1 This is the basic experimental setup for hot injection colloidal quantum dot synthesis, ... 84

Figure 3.2 UV-Vis absorption (A) and photoluminescent emission (B) for ODPA capped CdSe quantum dots, ... 90

Figure 3.3 UV-Vis Absorption pattern of a number of samples of CdSe quantum dots capped with ODPA..... 91

Figure 3.4 TEM analysis (A and B) of ODPA capped CdSe QDs., (sample CdSe IV) 92

Figure 3.5 Photograph of amine capped CdSe quantum dots under visible light (A) and under UV illumination (B). 93

Figure 3.6 UV-Vis absorption spectroscopy (A) and photoluminescent spectroscopy (B) of Octadecylamine capped CdSe QDs 94

Figure 3.7 Photograph of oleic acid capped CdSe quantum dots under visible light (top) and under UV illumination (bottom). 95

Figure 3.8 UV-Vis absorption (A) and photoluminescent emission (B) of oleic acid capped CdSe quantum dots 95

Figure 3.9 TEM of oleic acid capped CdSe QDs synthesised using a growth time of 40 seconds and an injection temperature of 260 ˚C.. 96

Figure 3.10 Photograph of oleic acid capped CdS QDs in toluene under visible light illumination and UV light illumination, sample C. 97

Figure 3.11 CdS QD UV-Vis absorption spectroscopy (A) and photoluminescent spectroscopy (B and C) of sample CdS B. 98

Figure 3.12 HRTEM analysis (A and B) of CdS QDs (B) with the resulting size distribution shown (C)..... 100

Figure 3.13 The UV-Vis absorption spectra (A and C) and photoluminescent spectra (B) of PbS QDs. 102

Figure 3.14 TEM images of PbS QDs. 103

Figure 3.15 STEM (A) and EDX (B) spectra of PbS QDs (sample PbS VI). 104

Figure 3.16 Powder x-ray crystal diffraction of PbS QDs sample, confirming the PbS rock salt crystal structure from the peak positions. 104

Figure 3.17 Photograph of CdSe/CdS quantum dot under visible light (A) and under UV illumination (B). 106

Figure 3.18 UV-Vis absorption spectroscopy (A) and photoluminescent spectroscopy (B) of CdSe/CdS core /shell quantum dots. 106

Figure 3.19 HRTEM images of CdSe/CdS QD (A and B) produced from a three shell coating of CdS upon a CdSe core QD of 3.4 nm 108

Figure 3.20 Uv-Vis absorption spectroscopy and phtoluminescent spectroscopy of CdS/CdSe QDs. 109

Figure 3.21 Photograph of CdS/CdSe quantum dot under visible light (A) and under UV illumination (B) 110

Figure 3.22. TEM and the resulting size distributions of CdS/CdSe core/shell quantum dots. 111

Figure 3.23 UV-Vis absorption spectra and PI spectra chartering the growth of CdTe core quantum dots relative to time 113

Figure 3.24 Photograph of CdTe/CdSe core/shell quantum dots under visible light (A) and under UV illumination (B) 113

Figure 3.25 The changes in A) UV-Vis absorption spectra and B) the photoluminescence spectra of the CdTe QDs, as a shell of CdSe QDs is grown upon the surface of the QDs 114

Figure 3.27 TEM analysis of CdTe/CdSe core/shell QDs 115

Figure 3.27 HRTEM images of CdTe QDs, showing excellent crystallinity evident by the presence of lattice fringes in image A. 115

Figure 3.28 Normalised UV-Vis absorption and emission of CdSe/CdS heterostructured rods 118

Figure 3.29 TEM of CdSe/CdS heterostructred quantum rods (sample CdSe/CdS 2A) and size distribution of the length and width of these particles 119

Figure 3.30 Scanning transmission electron microscopy images of CdSe/CdS core/shel heterostrucured quantum rod 120

Figure 3.31 STEM and EDX analysis of CdSe/CdS rods with the sample showing the presence of Cd, S and Se as is to be expected in this QR structure 120

Figure 3.32 Schematic presentation of the two step process to producing a CdSe/CdS/Au nanorods, from CdSe QDs..... 121

Figure 3.33 This shows the UV-Vis absorption (A) and PL emission (B and C) of CdSe/CdS/Au heterstructred nanorods.(sample CdSe/CdS/Au II)..... 123

Figure 3.34 TEM images and the resulting histograms of Au NPs diameters, produced in the formation of CdSe/CdS/Au heterostructured QRs (sample CdSe/CdS/Au II)..... 124

Figure 3.35 UV-Vis absorption spectra of PbS/CdS 125

Figure 3.36 Histogram of the diameters of PbS QDs measured from TEM images before (A) and after (B) partial Cd-cation exchange,..... 126

Figure 3.37 STEM (A) and EDX (B) are used to analysis a sample of PbS/CdS QD, produced through partial cation exchange..... 127

Figure 3.38 UV-Vis absorption of CdSe QD of 4.0 nm in diameter (red line) and the resulting spectra of $Cu_{2-x}Se$ QDs (black line) produced using a Cu^{+1} cation exchange. 128

Figure 3.39 UV-Vis absorption of CdSe/CdS heterostructured nanorods (blue line) firstly converted to $Cu_{2-x}Se/Cu_{2-x}S$ (red line), followed by conversion to PbSe/PbS (black line)..... 129

Figure 3.40 Normalised photoluminescent spectra to calculated QYs of anion treated oleic acid capped immediately following dilution. 131

Figure.3.41 Normalised photoluminescent spectra to QYs of anion treated oleic acid capped CdSe QDs after one day of dilution. 132

Figure 3.42 Normalised photoluminescent spectra to QYs of ODPA capped CdSe QDs (A) and the resulting luminescent QY are shown in graph B using concentration 2 133

Figure.3.43 Photograph showing the effect of oleylamine/$CdCl_2$ solution treatment upon samples of CdSe capped with ODPA, OLA or OA. 133

Figure.3.44 Normalised photoluminescent spectra to QYs of CdS (A) and the resulting luminescent QY are shown in graph B using concentration 2. 134

Figure.3.45 Normalised photoluminescent spectra to QYs of ODA capped CdSe QDs (A) and the resulting luminescent QY are shown in B using concentration 2. 134

Figure.3.46 Normalised photoluminescent spectra to QYs of core/shell CdSe/CdS QDs (A) and the resulting luminescent QY are shown in graph B using concentration 2 135

Figure 4.1 UV-Vis absorption spectrum monitoring the electrophoretic deposition of CdSe QDs upon a TiO_2 electrode using method A..... 145

Figure 4.2 SEM of EPD CdSe quantum dots on TiO_2 using method A 146

Figure 4.3 UV-Vis absorption spectroscopy was used to measure the deposition of 4.4 nm CdSe quantum dots upon a 16-μm TiO_2 electrode..... 148

Figure 4.4 UV-Vis Absorption spectra showing the change in absorption of oleic acid capped CdSe QDs (3.3 nm) over time into a TiO_2 electrode, showing the negative electrode (A) and the positive electrode (B)..... 149

Figure 4.5 UV-Vis absorption spectrum of TiO_2 electrode after being soaked in four different solutions of oleic acid capped CdSe QDs 151

Figure 4.6 SEM of CdSe QD sensitised TiO_2 nanoparticles electrode. 152

Figure 4.7 STEM images (A and B) of 3.2 nm CdSe QDs upon the surface of a 20 nm TiO_2 nanoparticles produced using electrophoretic depostion. C) and D) show the TiO_2 sensitised with 2.9 nm CdSe QDs upon the surface of 20 nm TiO_2 particles sensitised using electrophortic depostion. 153

Figure 4.8 SEM and EDX of CdSe sensitised TiO_2 electrode through electrophoretic deposition. 154

Figure 4.9 Photocurrent action response (A) of a oleic acid capped CdSe QD sensitized TiO_2 electrode using MeoH (red line) or 0.1 mol aqeouse solution of Na_2S (black line) as an electrolyte. Photocurrent response (B) of TIO_2 electrode without QD sensitization, which produced only a minimal current of 0.0031 mA/cm^2 under illumination. 155

Figure 4.10 This shows the photocurrent response produced from three different TiO_2 electrodes that were sensitised using oleic acid capped CdSe QDs 156

Figure 4.11 Photocurrent action response of ODA capped CdSe QDs showing a peak current of 0.25mA/cm^2 from 4.2 nm CdSe QDs 157

Figure 4.12 UV-Vis absorption spectroscopy (A) and the resulting photocurrent action response (B) of ODPA capped CdSe QDs (5.2 nm) EPD deposited upon a TiO_2 electrode. 157

Figure 4.13 UV-Vis absorption spectroscopy, comparing the change in absorption of TiO_2 electrode (A) or a oleic acid capped CdSe QD (3.4 nm) sensitised TIO_2 electrode (B) due to ZnS coating or CdS coating (only graph A). 158

Figure 4.14 UV-Vis absorption spectroscopy (A) and the resulting photocurrent action response (B) of ODPA capped CdSe (5.2nm) sensitised TiO_2 electrode, showing the change due to SILAR deposition of CdS. 159

Figure 4.15 Photocurrent action response of oleic acid capped (3.4 nm) CdSe QD sensitised TiO_2 electrode, showing the change in response due to ZnS coating. 160

Figure 4.16 SEM (A) and EDX (B and C) of TiO_2 electrode after 3 cycles of SILAR CdS treatment. 161

Figure 4.17 UV-Vis absorption spectroscopy and the resulting photocurrent action response of ODPA capped CdSe QDs sensitised TiO_2 electrode, showing the change due to HTAC treatment. 162

Figure 4.18 Photocurrent action response of ODPA CdSe sensitised TiO_2 electrodes showing the original electrode (A) and the resulting electrode (B) after a 1 minute treatment with 2.5% MPA MeOH solution 163

Figure 4.19 This shows the UV-vis absorption and the resulting photocurrent action response of a TiO_2-FTO electrode sensitized with 3 nm CdS QDs. 164

Figure 4.20 SEM and EDX of a CdS QD sensitised nanoporous 4 μm TiO_2 electrode with 3 nm CdS QDs. 165

Figure 4.21 UV-Vis absorption spectra (A) and resulting photocurrent response (B) of PbS QD sensitised TiO_2 electrode. 166

Figure 4.22 This shows the sensitisation of a nanoporous ~ 17-μm TiO_2 electrode with 2.7 nm PbS QDs 167

Figure 4.23 UV-Vis absorption spectra (A) and photocurrent response (B) of CdSe/CdS sensitised TiO_2 electrode. The total photocurrent produced was 0.05 mA/cm^2. 168

Figure 4.24 UV-Vis absorption spectra (A) and photocurrent response (A) of CdS/CdSe sensitized TiO_2 electrode showing the change in absorption before and after testing, 0.57mA/cm^2 and 0.515mA/cm^2. 169

Figure 4.25 UV-Vis absorption spectra (A) of CdTe/CdSe QD sensitised TiO_2 electrode and photocurrent response (B) of the resulting electrode measured under illumination producing a current of 0.316 mA/cm^2 170

Figure 4.26 UV-Vis absorption spectra of CdSe/CdS sensitised TiO_2 electrode after a 15 min electrophoretic deposition. 171

Figure 4.27 STEM and EDX of a sample of TiO_2 sensitized electrode sensitised with CdSe/CdS heterostructured nanorods. 171

Figure 4.28 This shows the sensitisation of a nanoporous ~ 4-μm thick TiO_2 electrode with 20 nm CdSe/CdS heterogeneous nanorods QDs. 172

Figure 4.29 UV-Vis absorption spectroscopy of a partial cation exchange of PbS QD (6.1 nm) sensitised TiO_2 electrode to PbS/CdS 173

Figure 4.30 UV-Vis absorption spectroscopy (A) and photocurrent action spectra (B) of PbS/CdS QD sensitised TiO_2 electrode. 174

Figure 4.31 SEM and EDX study of PbS/CdS sensitised TiO_2 electrode of ~14 μm thick TiO_2 electrode 175

Figure 4.32 Graph of UV-Vis absorption of CdSe sensitized TiO_2 electrode 176

Figure 4.33 SEM and EDX of Cu_2Se QD sensitized nanoporous TiO_2 electrode. 177

Figure 4.34 SEM and EDX of PbSe QD sensitised TiO_2 electrode distribution in a 7.3 μm nanoporous TiO_2 electrode 178

Figure 5.1 The two liquid crystals utilised in this study were RTAQ (1,5-dihydroxy-2,3,6,7-tetrakis(3,7-dimethyloctyloxy)-9,10-anthraquinone (image A), and H6TP (hexahexyloxy-triphenylene)(image B). 187

Figure 5.2 Photos of the original Pb Foil and the PbS counter electrode produced from this. 189

Figure 5.3 Photos of original brass foil and the produced Cu_2S coated foil produced from this. 190

Figure 5.4 SEM images of the three stages in material as the originally purchased Pb foil (image A) is firstly converted to $PbSO_4$ (image B) and then to PbS (image C) 191

Figure 5.5 SEM images of brass foil before and after treatment to produce the Cu_2S electrode. 192

Figure 5.6 Photos showing the original FTO glass and the Pt coated FTO glass counter electrode 193

Figure 5.7 SEM of Pt coated FTO glass 193

Figure 5.8 Cyclic voltammetry of three different electrodes fabricated for QDSSC cells, Cu_2S, PbS and Pt electrode. 194

Figure 5.9 Diagram of TiO_2 electrode produced for QDSSC cells 194

Figure 5.10 SEM of TiO_2 bulk layer deposited upon FTO glass 195

Figure 5.11 SEM images of nanoparticulate TiO_2 surface on FTO glass. 196

Figure 5.12 This UV-Vis absorption spectra of a FTO coated glass with a differing number of porouse TiO_2 layer deposted upon its surface. 197

Figure 5.13 TEM images of the 20 nm TiO_2 nanoparticulate after sintering 197

Figure 5.14 Photos of transparent TiO_2 electrode (A) produced from 4 layers of screen printed 90T Dyesol 20 nm TiO_2 paste, and the same electrode (B) incorporating a 5th light scattering layer consisting of sintered 200nm TiO_2 particles. 198

Figure 5.15 SEM image (A) of side profile of a TiO_2 electrode 198

Figure 5.16 Image A shows the UV-Vis absorption spectra of TIO_2 electrode with scatter layer, demonstrating the large absorption of these electrodes 199

Figure 5.17 IV curves of the QDSSC cells 201

Figure 5.18 IV-curve of open cell measurement of QDSSC, using oleic acid capped, 4.3 nm, CdSe QDs, treated with 7 dip cycle of CdS following electrophoretic deposition. The open cell measurements were made using two different counter electrodes, composed of either a Cu_2S electrode on brass foil or a PbS electrode on Pb foil. 202

Figure 5.19 Photo of etched FTO enabling the fabrication of multiple cells upon the same glass surface 204

Figure 5.20 SEM images of fluorine doped tin oxide showing the change in surface structure due to the acid etch 204

Figure 5.21 UV-Vis absorption spectra (A) of TiO_2 pastes deposited on FTO glass and SEM of the resulting diluted TiO_2 electrode (B). 205

Figure 5.22 SEM images of nanoparticulate TiO_2 coating upon FTO glass for DHCQD cell. 206

Figure 5.23. Profilometery data of Dyesol 90T TiO_2 film sintered on FTO glass, the histogram on the right shows the colour coding of the 3D image. 208

Figure 5.24 Raman (A) and FTIR (B) spectroscopy of TiO_2 sintered Dyesol diluted and ordinal pastes. 209

Figure 5.25 SEM images showing PbS QD deposition on TiO_2 coated FTO glass using dip coating. 210

Figure.5.26 SEM of MPA-capped CdSe QDs deposited upon TiO_2 coated FTO using method 1. 210

Figure 5.27 PbS QD deposition (A) upon glass and CdSe QD deposition (B) upon FTO coated glass using dip coating using deposition method 1. 211

Figure 5.28 UV-Vis absorption of the deposition of CdSe QDs (A) and PbS QDs (B) upon FTO coated glass showing the increase in absorption as the number of cycles of deposition increases 212

Figure 5.29 SEM cross section of completed DHCQD cell 212

Figure 5.30 IV curve of PbS QD based DHCQD cell.Showing the change in response of the cell under illumination 1 sun AM 1.5 illumination source (light) and its reponse under darkness (dark) 213

Figure 5.31 UV-Vis absorption spectra (A) and photoluminescence Emission spectra (B) of H6TP solution in hexane 214

Figure 5.32 Solid-state UV-Vis absorption (A) and photoluminescence spectra (B) of H6TP liquid crystal in the solid state 215

Figure 5.33 UV-Vis absorption (A) and Pl emission (B) of oleic acid capped CdSe QDS and H6TP in hexane. 216

Figure 5.34 UV –Vis absorption of RTAQ liquid crystal in hexane (A) and in solid state (B) at room temperature 216

Figure 5.35 Polarused optical microscopy images of non-doped RTAQ DLC, under a 10 x zoom at room temperature showing the DLC phase. 220

Figure 5.36 Polarused optical microscopy of RTAQ DLC composite , using a 10 x zoom, mixed with 10:1, w/w, ODA (Image A), ODPA (Image B) and OA (Image C) 221

Figure 5.37 Polarused optical microscopy images of RTAQ /CdSe QD composite, using a 10 x zoom, consising of oleic acid capped CdSe (image A), octadeylphophoinc acid capped CdSe QDs (image B) and octadecylamine capped CdSe (C) added in a ratio of 1:10 , RTAQ/CdSe w/w.222

Figure 5.38 Polarised optical microscopy of RTAQ /CdSe QD composite , using a 10 x zoom, consising of oleic acid capped CdSe (3.77nm in rdiameter) added in a ratio of 1:100 (image A), 1:10 (Image B), 1:5(Image C) and 1:1 (Image D) w/w.....223

Figure 5.39 Polarised optical microscopy images of RTAQ /CdS QD composite, using a 10 x zoom, consising of oleic acid capped CdS (2.2 nm)added in a ratio of 1:100 (image A), 1:10 (Image B) and 1:1(Image C) w/w.....224

Figure 5.40 Polarused optical microscopy of RTAQ /PbS QD composite , using a 10 x zoom, consising of oleic acid capped PbS (3.47 nm in diameter) added in a ratio of 1:100 (image A), 1:50 (Image B) and 1:10(Image C) w/w. 225

Figure 5.41 Polarused optical microscopy of RTAQ:Se composite , using a 10 x zoom, composed of 1:10 Se /RTAQ w/w 226

Figure 5.42 Polarused optical microscopy images of RTAQ:PDI composite , using a 10 x zoom, composed of 1:10 PDI /RTAQ w/w. 226

Figure.5.43. Diagram of proposed designs of DLC/QD photovoltaic cell. 227

Figure 5.44 SEM images of RTAQ, spincoated on FTO, A 30 mg/ml, B 40 mg/ml, and C 50 mg/ml producing a thickness of 250 nm, 300 nm and 400 nm. 228

Figure 5.45 UV-Vis absorption of spincoated film of 1-1, PDI +RTAQ containing 1-10 PbS QD ,w/w, spincoated from a 40 mg per ml solution , on FTO glass 229

Figure 6.1 Photograph showing the effect of oleylamine/$CdCl_2$ solution treatment upon core shell QDs of CdS/CdSe and CdTe/CdSe.....239

Figure 6.2 Diagram of two alternative DLC cell designs that have been reported in literature and have shown a level of success. 241

Figure 7.1 This graph shows the valence band, conduction band and band gap of a range of common elemental and binary semiconductors in eV,.....VII

Figure 7.2 UV-Vis absorption spectroscopy and photoluminescence spectroscopy of ODPA capped CdSe QDs that have undergone excessive growth at 350 °C for 4 minutes. VIII

Figure 7.4 TEM of CdSe/CdS QDs (A), the resulting size distribution (B), and UV-Vis absorption spectra (C) showing the evolution of the absorption spectra of as the shell was grown. IX

Figure 7.4 TEM (A) and the resulting size distribution (B) of a sample of CdSe/CdS core/shell quantum dot. IX

Figure 7.5 This is shows a number of other TEM images of CdSe/CdS heterostructured QRs. ... X

Figure 7.6 This is shows TEM images of CdSe/CdS heterostructured QRs formed from 3.2 nm ODPA capped CdSe QDs XI

Figure 7.7 This shows the results of CdSe/CdS/Au structures showing results obtained from other sample under a range of conditions. XII

Figure 7.8 Photoluminescent spectra showing the shift in luminescence of a PbS QD as a cation exchange is carried XIII

Figure 7.9 TEM of Au NP (A) and the size distribution of the resulting NPs (B) XIII

Figure 7.10 UV-Vis absorption spectra of a range of QDs treated with a variety of oleylamine based solutions. XIV

Figure 7.11 UV-Vis absorption spectroscopy of oleic acid capped CdSe (3.5 nm) sensitised TiO_2 electrode XV

Figure 7.12 UV-Vis absorption spectroscopy of oleic acid capped CdSe (3.8 nm) in DCM showing the change in solution concentration due to deposition XV

Figure 7.13 SEM of cracked bulk TiO_2 surface produced from dropcasting a solution of 10 mM $TiCl_4$ aqueous solution upon FTO glass. XVI

Figure 7.14 SEM images of a TiO_2 upon FTO glass that showed wide spread cracking in the surface XVI

Figure 7.15 ^{1}H (Image A) and ^{13}C NMR (Image B) of Disodium 1,4-phenylenedicarbamodithioate (PBDT) (Image C). XVII

Figure 7.16 ^{1}H (Image A) and ^{13}C (Image B) NMR spectra of RTAQ (1,5-dihydroxy-2,3,6,7-tetrakis(3,7-dimethyloctyloxy)-9,10-anthraquinone) (image C). XVIII

Figure 7.17 ^{1}H- NMR spectra (Image A) of High temperature liquid crystal, H6TP , (hexahexyloxy-triphenylene) (Image B). XIX

Figure 7.18 UV-Vis absorption CdSe QD doped film of H6TP. XX

Figure 7.19 SEM image of 1:50 shown image A and PbS: RTAQ, SEM of 1:10 PbS: RTAQ is shown in image B. XX

Table of Tables

Chapter 1 Introduction 1

Chapter 2 Experimental 50

Chapter 3 Hot Injection Quantum Dot Synthesis: Characterisation and Studies of the Effects of Cation and Anion Solutions 84

Table 3.1 This shows the range of phosphonic acid capped CdSe quantum dots synthesised during the experiment. Diameters displayed are calculated from the first exciton peak position and quantum yields were determined relative to an appropriate standard Rhodamine 6G in ethanol (QY 95%[292]). 89

Table 3.2 This shows the range of oleic acid capped CdS quantum dots synthesised during the experiment. 97

Table 3.3 This shows the range of oleic acid capped PbS quantum dots synthesised during the experiment. 101

Table 3.4 This shows the change in spectra as a shell of CdS is grown upon a CdSe core QD producing a CdSe/CdS core/shell quantum dot. 105

Table 3.5 This shows the change in spectra as a shell of CdSe is grown upon a CdS core QD producing a CdS/CdSe core/shell quantum dot. 109

Table 3.6 This shows the change in spectra as a shell of CdSe is grown upon a CdTe core QD producing a CdTe/CdSe core/shell quantum dot. 112

Table 3.7 A collection of properties of CdSe/CdS QRs synthesised.The size of CdSe cores was determine using the first exciton position of the samples in UV-Vis absorption spectra. Length and width of the resulting QRs was determined using TEM. Quantum yields were determined using a Rhodamine 6G in ethanol (QY 95%[292]). 117

Table 3.8 This shows a selection of CdSe/CdS/Au NRs, synthesised under varying experimental heating parameters producing samples of differing condition. All sample produced utilised a CdSe/CdS QR measuring 35.2 nm in length and 4.7 nm in width and was formed from a 3.4 nm core CdSe QD. 122

Chapter 4 Electrophoretic Deposition of CQDs to Increase Photosensitisation of TiO_2 films.. 141

Chapter 5 Quantum Dot Solar Cell Fabrication and Testing 184

Table 5.1 This shows the result of QDSSC cell testing under AM 1.5, 1 sun illumination, showing the resulting characteristics of the cells determined by measuring the IV response of the produced cells 200

Table 5.2 This shows the result of open QDSSC cell testing under AM 1.5, 1 sun illumination, showing the resulting characteristics of the cells determined by measuring the IV response of the produced cells 202

Table 5.3 This shows the result of DHCQD cell testing under AM 1.5, 1 sun illumination, showing the resulting characteristics of the cells determined by measuring the IV response of the produced cells 213

Table 5.4 This table describes the conductivity measurements made on a number of H6TP composites 218

Table 5.5. This table describes the conductivity measurements made on a number of RTAQ composites each reported value comes from an average of 4-6 measurements, on 2-3 devices. Note σ is the electrical conductivity measured from - 0.5 to 0.5 V. 219

Table 5.6 Optimisation of spin coating for DLC cell fabrication showing the results obtained from a range of solutes and solvents. All spincoating was carried out at 1000 RPM, with a 200 rpm/sec ramp rate. 229

Chapter 6 Conclusions and Future Work 236

Chapter 7 Appendix I

Table 7.1 Bulk modulus values for common binary semiconductors , reproduced from reference [104]. III

Table 7.2 Lattice mismatch of shell on core calculated from bulk material lattice constants of the zinc blende crystal structures of a number of common binary semiconductors. IV

Table 7.3 Lattice mismatch of shell on core calculated from bulk material lattice constants of the a and c axes of the wurtzite crystal structures of a number of common binary semiconductors. V

Table 7.4 Lattice mismatch of shell on core calculated from bulk material lattice constants of the Rock salt structure of a number of common binary semiconductors. VI

Table 7.5 This shows the results of cells tested to date of DLC solar cells. XXI

Table of Equations

Chapter 1 Introduction 1

Equation 1.1 This describes the processes involved in cation exchanges, with (1) describing the overall reaction while (2-5) describes the steps involved in the process. Note M represents a foreign cation, while C the original host material cation and A the original materials anion, prior to carrying out of the cation exchange 15

Chapter 2 Experimental 50

Equation 2.1 Used to calculate relative quantum yield of a sample. Where ϕ= quantum yield, A= absorbance, F= Integrated fluorescence, n= solvent refractive index and the subscript s is for standard and x is for sample being tested 71

Equation 2.2 This relates the power density of the illumination source to the current reading from a calibrated photodiode, and takes in to account the responsivity and area of the sensor for a given wavelength. 77

Equation 2.3 This equation is used to determine the external quantum efficiency of a photovoltaic cell for a given wavelength of illumination. 77

Equation 2.4 Fill factor for a cell can be calculated by relating the measured power maximum measured to the theoretical power maximum. 80

Equation 2.5. This relates the power conversion efficiency (PCE) to the open circuit voltage (V_{oc}), short circuit current (I_{sc}) , fill factor (FF) divided by the actual power in 81

Chapter 3 Hot Injection Quantum Dot Synthesis: Characterisation and Studies of the Effects of Cation and Anion Solutions 84

Chapter 4 Electrophoretic Deposition of CQDs to Increase Photosensitisation of TiO_2 films.. 141

Chapter 5 Quantum Dot Solar Cell Fabrication and Testing 184

Chapter 6 Conclusions and Future Work 236

Chapter 7 Appendix I

Equation 7.1 Where a_{ex}= is the exciton radius, a_H is the Bohr radius of the hydrogen atom, ε is the permittivity of the material, m_o is the electron mass, m_e^* is the electron effective mass and m_h^* is the hole effective mass I

Equation 7.2 This describes how to calculate the Schottky barrier height for a Schottky junction formed between an n-type semiconductor (i) or a p-type conductor (ii) and a metal, where ϕ_m is the workfunction of the metal, E_g is the band gap of the semiconductor and χ_s is the electron affinity of the semiconductor. I

Equation 7.3 Where k_{et} is the rate of electron transfer, $| H_{AB} |$ is the electronic coupling between the initial and final states, λ is the reorganization energy (both inner and outer-sphere), and ΔG is the total Gibbs free energy change for an electron transfer reaction , k_b is the Boltzmann constant , T is temperature in Kelvin, and $\hbar$ is planks constant divided by 2π. I

Equation 7.4 Where E is the new band gap energy due to quantum confinement, E_g is the bulk band gap energy, R is the radius of the sample, , m_e^* is the electron effective mass and m_h^* is the hole effective mass, ε_0 is the permittivity of a vacuum and ε_α is the high frequency dielectric constant. I

Equation 7.5 This represents the Gibbs free energy surface change (ΔG_s),og a heterogeneous deposition process, while γ_1 and γ_2 represent the surface energies of the respective materials and $\gamma_{1,2}$ is the solid/solid interface energy. [298] II

Equation 7.6 Where deposit yield (w), the electric field strength (E), the surface area of the electrode (S), ϕ_s and ϕ_d are the volumetric concentration of particles in suspension and deposit, respectively, C_d is the mass concentration of particles in the deposit, t is time and μ is the electrophoretic mobility and is given by II

Equation 7.7 This describes the factors that affect the electrophoretic mobility of particles in solution, in which ε is the permittivity, ξ is the zeta potential and η is the viscosity of the solution. II

Chapter 1 Introduction

The rapid growth of fossil fuel prices and greater danger of global warming due to increased carbon dioxide emission (greenhouse effect) dictate an urgent need for alternative energy sources. Sunlight is the largest of all available carbon-neutral energy sources, therefore solar energy harvesting based technologies are of extreme importance. The focus of our work is to develop new semiconducting nanomaterials and investigate their potential in solar energy harvesting devices. In this introduction, we will overview the main fundamental aspects related to semiconducting materials and nanomaterials, their properties and applications in solar energy harvesting.

1.1 Semiconducting materials

1.1.1 Band Theory

Electron density in atoms is described by atomic orbitals, giving a probability map in space of electron position relative to the nucleus. For a molecule, a linear combination of atomic orbitals (LCAOs) can be used to describe the electron density across a number of atoms present and is called a molecular orbital (MO). Dependent upon the net interaction of the LCAOs these molecular orbitals can then be assigned a label of bonding, due to in-phase electron wave interaction, anti-bonding, due to out of phase electron wave interaction or non-bonding orbitals, in which the net in phase and out of phase interaction add to zero.

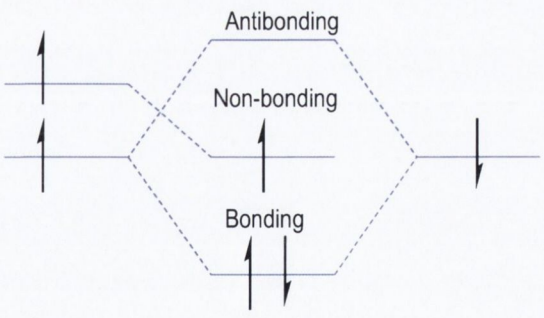

Figure 1.1 Showing the three molecular orbitals created between three atoms each with one atomic orbital

A bonding orbital is a MO of lower energy (Figure 1.1) than the atomic orbitals that have interacted to produce it, generating an electron density map for σ-bonds in which electron(s) present in the orbital have a higher probability of being present between the nuclei. An anti-bonding orbital is a MO, which is of higher energy than its constituent atomic orbitals and produces an electron density map for σ-bonds in which probability of electrons being between the nuclei is low. A non-bonding orbital is a MO of the same energy as one of its constituent

atomic orbital. These three different LCAOs have the effect of producing a number of different energy levels that electrons may occupy in a molecule.

When referring to extended solids, LCAOs can be further applied to explain the band structure

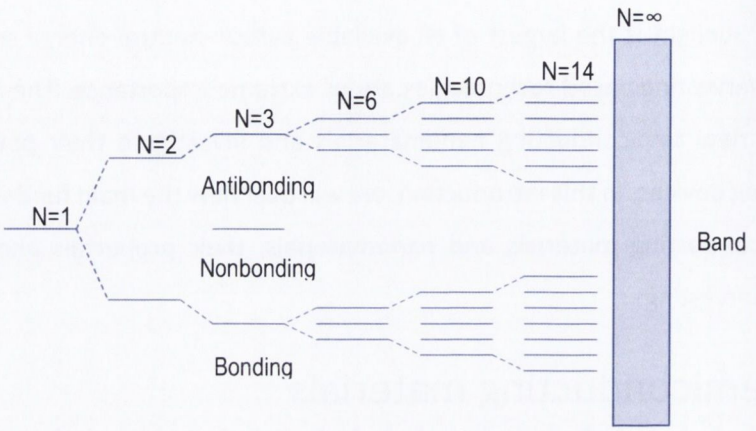

Figure 1.2 Band structure formed from LCAOs, where N is the number of atoms

found in solids[1] (Figure 1.2), this is due to the near infinitely fine energy levels possible due to the sheer number of atoms present, producing bands of allowed energy levels and areas of disallowed energy levels called a band gap (BG). These allowed bands can be further divided into two categories called a valence band (VB) or a conduction band (CB). The VB is the highest energy states that electrons occupy in a material at absolute zero while the CB is the lowest unoccupied state. Electrons in the VBs are considered to be localized upon each atom/molecule, while electrons present in the CB are considered to be delocalized across the solid. Above the conduction band at a given energy lies the vacuum energy, the energy level at which an electron becomes a free electron. Another important term is the energy difference between the conduction band and the vacuum called the electron affinity.

The Pauli Exclusion Principle states that no two electrons may occupy the same electronic state and determines the filling of energy levels with electrons; this therefore gives rise to Fermi-Dirac statistics, which is used to describe the filling of energy levels with single-particles, which are identical and governed by the Pauli Exclusion Principle. These statistics gives rise to the concept of the Fermi-level, which is energy level at which there is a 50% chance of electron occupancy, with energy levels above this being nearly empty and energy levels below this being nearly full. At absolute zero, this correlates to the very top of the VB and is given the term Fermi energy. For temperatures above 0K, the Fermi-level moves up towards the CB, because as electrons gain thermal energy, they can be excited into the CB.

Depending on the LCAO of a chemical, when examined as an extended solid, three distinct band structures are produced giving rise to three distinct classes of materials (Figure 1.3), a semiconductor, an insulator or a metal. Metals are materials that have an overlap between the VB and the CB, placing the Fermi-level in the middle of the band. This gives electrons in metals a huge number of available energy states accessible by a tiny energy input, which produces the many well-known properties of metals, including its excellent electrical and thermal conductivity, and the strong reflectivity of a newly polished metal surface.

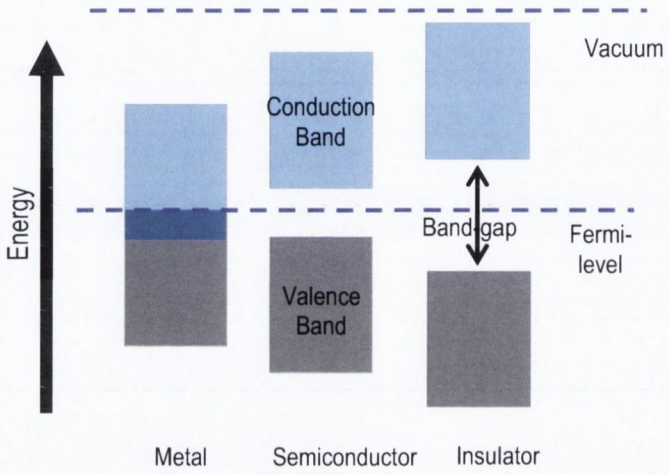

Figure 1.3 Band diagram of a metal, semiconductor and Insulator

In contrast to this, semiconductors and insulators have a BG that separates the VB and the CB, with band gap energy (Eg) being larger in insulators (roughly above 4 eV) and smaller in semiconductors. For semiconductors at absolute zero the Fermi-level lies in the middle of Eg, between the full VB and empty CB at a forbidden energy level if the density of states is equal in the valence and CB. For temperatures above this, some electrons will gain access to the CB due to thermal energy and so the Fermi-level is shifted towards the CB.[2]

1.1.2 Semiconductor Types and Properties

Semiconductor properties are strongly defined by the band gap energy (Eg), corresponding to the ease at which electrons can be excited from the VB to the CB. Electrons excited into the CB can contribute to the electrical conductivity of a material; therefore, as the Eg becomes larger, the conductivity of a material decreases. When an electron is excited into the CB, an unoccupied state is left in the VB, termed an electron hole; these are also responsible for electrical conductivity found in semiconductors. The hole in fact does not move, but electrons in the neighbouring lattice move into the unoccupied position, the hole, which has the net result that the hole appears to move in the opposite direction of electron movement.

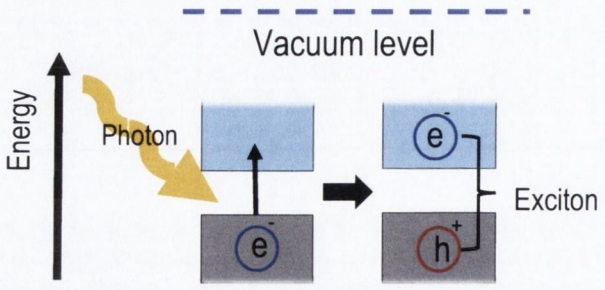

Figure 1.4 Formation of an exciton in a semiconductor due to absorption of a photon

When an electron –hole pair are generated due to photon absorption, they can be described as an exciton, a quasi-particle, held together by the coulomb attraction of the two opposing charges (Figure 1.4). The distance between the electron-hole pair is termed the exciton Bohr radius. The radius is a function of the bond strength, which is determined by the dielectric constant of the material and the effective masses of the excited electron and hole (Appendix A) with the average size lying in the nanometre range (2.9 nm for CdS, 11.3 nm for InP, 46 nm for PbSe). In bulk semiconductors excitons only exist at low temperatures, due to the weak binding energy holding the pair together (27 meV for CdS, 15 meV for CdSe, 5.1 meV for InP)[3] above which temperature, the electron and hole have enough thermal energy to overcome this bound state and act independently.

An excited electron in a semiconductor after a period will decay from its excited state in the CB back to the VB and recombine with an electron hole in what is called recombination. This recombination results in the release of energy either in the form of a photon, termed radiative recombination or in the form of heat, termed non-radiative recombination.

A pure semiconducting material is called an intrinsic semiconductor and has an equal proportion of electron holes to free electrons when stoichiometric, the population of which increases relative to temperature. Intrinsic semiconductors normally have low conductivity values unless heated to high temperatures or possess a small Eg. This low conductivity can be greatly increased through the introduction of dopants creating crystal defects that introduce energy levels within Eg. These crystal defects are categorised with respect to their origins either as extrinsic, due to impurities or intrinsic due to the crystal structure itself.

Extrinsic crystal defects due to aliovalent substitution are termed extrinsic doping. While intrinsic defects produce intrinsic doping due to the pure substance being non-stoichiometric. Both types of dopants can produce an excess of either holes termed p-type or free electrons termed n-type, which dominate the conductivity behaviour. For example, n-type Si can be produced by aliovalent substitution through the introduction of group-15 elements (P, As, Sb)

resulting in excess electrons in a lattice position due to it possessing one electron more in its valence shell than Si. These excess electrons will introduce a donor level in the Eg, near the CB and allow electrons to be easily excited into the CB and so shifting the Femi level towards the CB. The same n-type behaviour is produced by non-stoichiometry in intrinsic ZnO, where Zn is in excess and occupies interstitial sites in the lattice, producing an excess of electron charge carrier in the lattice.[4]

P-type Si can be produced by aliovalent substitution through the introduction of group-13 elements (B, Al, Ga) resulting in hole production in the lattice due to it possessing one electron less in its valence shell than Si. These holes will introduce an acceptor level in Eg just above the VB, which allows electrons to be excited into these levels from the VB, producing holes in the VB, and causing the Fermi-level to shift towards the VB. Therefore, in p-type-semiconductors the majority charge carrier are electron holes and electrons are the minority carrier. The same p-type behaviour is produced by non-stoichiometry in CuO_2, since CuO_2 is intrinsically Cu deficient, this results in Cu vacancies in the crystal structure, resulting in hole production.[5]

1.1.3 P-N Junction

P-N junctions are the basis for semiconductors fundamental role in integrated circuit technology, finding applications in diodes, transistors, photovoltaic cells, lasers and light emitting diodes (LEDs). The simplest device, the diode, allows current flow in one direction more readily than the other direction (rectification) and can be made using a p-n junction. A p-n junction is formed at the point of contact between an n-type and p-type semiconductor (shown in Figure 1.5) and is described as a p-n homojunction when both semiconductors utilised are the same or a p-n heterojunction when two different semiconductors are used. When these two materials are brought together electrons flow from the n-type to the p-type semiconductor and holes flow from the p-type to the n-type. These charge carriers then undergo recombination with majority carriers in the respective materials leaving behind in both materials charged ions. This charge transfer therefore leaves a net positive charge on the n-type material and a net negative charge on the p-type material and so setups an electric field across the p-n junction in the order of 0.6 to 0.7 V for Si. This charging pushes down the n-type band levels and pushes up the p-type band levels until the Fermi-levels of the two materials are equal. The area in which

charge carrier transfer has taken place is called the space charge layer or depletion zone, due to lack of charge carriers in this region and the presence of an electric field.

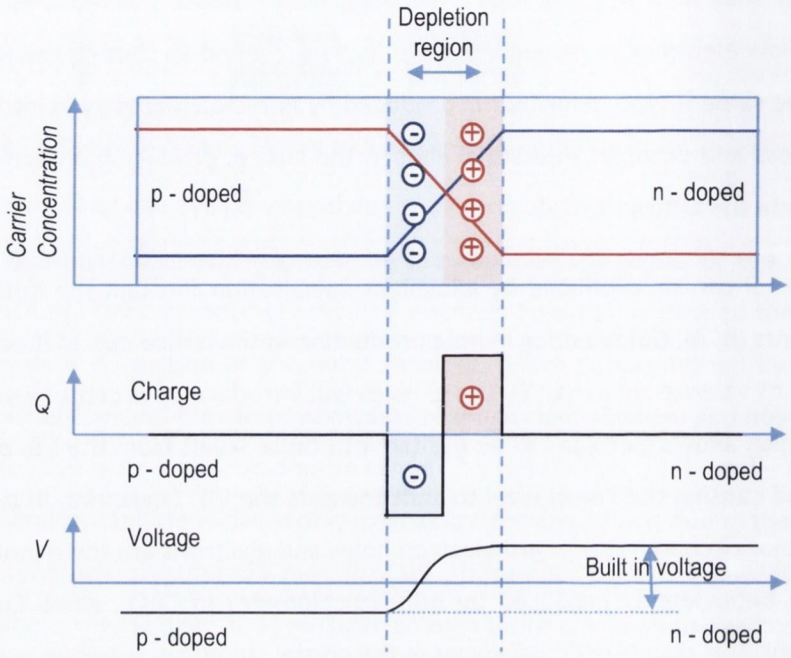

Figure 1.5 Diagram showing the structure of a p-n junction formed between a n-doped and p-doped semiconductor, graphing charge, electric field and voltage

1.1.4 Schottky Junction

Another important type of diode is the one based on Schottky junction, a junction created between a metal and a semiconductor. The semiconductor used can be either n-doped or p-doped and any metal can be used. When the metal is brought into contact with the semiconductor, its majority charge carriers near the junction are injected into the metal, creating a depletion region in the semiconductor called a Schottky Barrier (SB). A simple model for calculating the height of the SB is given by Schottky–Mott theory for n-type and p-type semiconductors (Equation 7.2) (Appendix A). This is an overly simplified model, since this does not take in to account that the work function and electron affinity both contain surface dipole term dependencies. These surface dipoles are a function of electron distribution and so therefore will be effected by the surface condition, i.e. quality, surface states and the particular crystal plane exposed. This therefore means that unfortunately the barrier cannot be accurately predicted using this equation. A number of models have been devised to take better account of the resulting barrier, including the effects of electronegativity, but as of yet no reliably predictive model has been developed.[6-8]

1.1.5 Quantum Size Effects and Quantum Dots

As discussed above the continuum of bands found in a bulk material owes their origins to the huge number of LCAOs in an extended solid. When a material's size is reduced to the nanometre range, creating a nanocrystal (NC), the number of atoms is vastly reduced; so much so that this picture of a continuous band no longer holds, and in fact is better described as finitely spaced discrete energy levels that make up the VB and CB. This new electronic structure due to size is termed the quantum size effect and has a number of consequences for the properties of the material, creating a material that possesses properties intermediate between the bulk and discrete molecules.

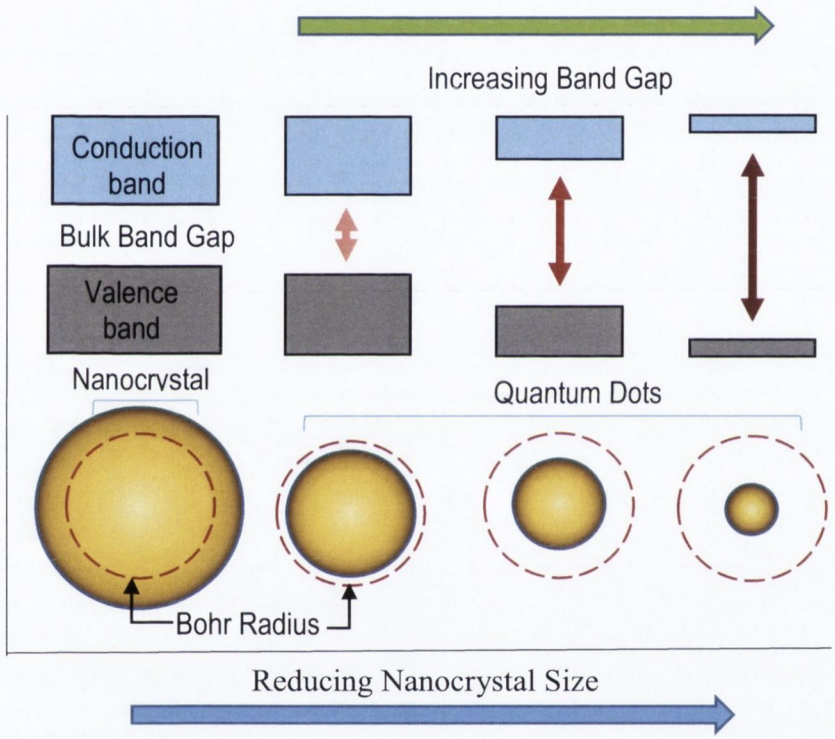

Figure 1.6 Diagram showing the effect of exciton confinement. The effect of reduction of size of a semiconductor nanocrystal below the Bohr radius produces this quantum confinement of the exciton. This in turn increase the band gap as size reduces further and the nanocrystal can now be described as a quantum dot.

When speaking specifically of a semiconductor, the quantum size effect is termed quantum confinement. This takes place when the size of the semiconductor nanocrystal approaches dimensions of the Bohr radius of the exciton (termed intermediate confinement) or below the Bohr radius (termed strong confinement), as shown in Figure 1.6. Quantum confinement of the exciton greatly increases its bonding energy and so excitons are found to exist at room temperature in semiconductor NCs.[3] As the transition is made from bulk to quantumly confined material, the band position alters, resulting in widening of Eg relative to size and can be estimated using the Brus equation (Appendix A).[9, 10] Interestingly, this widening does not push both the VB and CB in opposite directions equally. This effect is dependent upon the actual

effective masses (m*) of the hole and the electron[11, 12], so for example in CdSe, which has a m_e*= 0.13 while m_h*=1.14, the majority of the increase in Eg is seen through the CB of CdSe shifting towards higher energies. When the exciton is confined in one, two, or three dimensions of a semiconductor NC, the structure is called a, quantum well, quantum rod or quantum dot (QD) respectively. Quantum Dots can be composed of any quantum confined semiconducting material, but most commonly used QDs are based on binary semiconductors. These include QDs of group II-VI materials such as CdSe,[13-15] CdS,[16, 17] ZnS,[18-20] ZnSe,[21-23] III-V materials such as InP,[24-27] InAs,[28] and InSb[29] and IV-V materials such as PbS,[30, 31] PbSe,[32-35] PbTe,[36, 37] SnS,[38] SnSe[39] more rarely II-V such as Cd_3P_2[40] and Cd_3As_2.[41] In recent years, QDs based on tertiary semiconductors such $CdSe_xS_{1-x}$,[42, 43] $PbSe_xS_{1-x}$,[44] $CuInS_2$,[45] $CuInSe_2$,[46] and quaternary semiconductors such as ,$Cd_xZn_{x-1}S_ySe_{y-1}$[47] and $CuZnInS_3$[48] have been developed.

1.1.6 Optical Properties of Quantum Dots

Since E_g can be tuned by varying the quantum confinement of the exciton, from the bulk value to much-increased values, the resulting absorption and emission of these QDs can be tuned across a range. QD's absorption profile exhibits a characteristic first peak, which is indicative of the exciton binding energy in the quantum confined semiconductor material. The absorption spectrum after the first exciton, displays rising absorption strength with decreasing wavelength, meaning a QD can absorb light over a broad range of wavelengths. In addition, QDs with a direct bandgap show a large absorption coefficients ranging from 1×10^5 to 1×10^6 M^{-1} cm^{-1}, which is also size dependent.[30, 49-52]

It has also been shown that the absorption pattern of a single QD displays a fine structure not found in the bulk relating to the discrete energy levels in the VB and CB.[11, 53, 54] This fine structure is blurred and hidden as the distribution of QD size increases, termed inhomogeneous line broadening.

Also due to exciton confinement, photoluminescence (PL) becomes strongly pronounced for direct BG QDs. The shape of this luminescence is normally fit using a single Lorentzian peak, with its FWHM dependent upon the temperature and matrix due to homogeneous line broadening[55,56] and the size distribution of QDS (inhomogeneous line broadening). The luminescence may also sometimes have peaks related to trap states, which produce a broad, strongly red shifted luminescence. This type of emission is commonly found in magic sized quantum dots due to their large surface area.

The efficiency of the PL is measured using Quantum Yield (QY), which gives a percentage value corresponding to the number of photons emitted divided by the total photons absorbed. The

QY of a QD is strongly dependent upon the rate of non-radiative relaxation and therefore the existence of inter-bandgap states. These states can be formed due to surface defects, impurities or crystal defects and strongly decrease QYs.

The Stokes shift, the difference between. This value has also been tied to the size of the quantum dot, with decreasing size increasing the observed Stokes shift. This has been explained to be due to the presence of dark and bright exciton states in the valence band, the energy between which increases with decreasing quantum dot radius.[15, 57]

1.1.7 Colloidal Quantum Dots (CQD)

Discrete nanoparticles can be synthesised by a range of different methods[58] including sol-gel,[59] spray pyrolysis,[60] metalorganic chemical vapour deposition (MOCVD),[61-63] molecular beam epitaxy (MBE),[64-67] chemical bath deposition (CBD)[68] and even recently demonstrated biosynthesis [69, 70,] but the most widely used technique today for QD synthesis is a wet chemistry colloidal approach. This route uses chemical precursors that are treated in a solution (using heat or other means), resulting in decomposition and production of monomers that then nucleate and grow to form the NC. The rate of growth is controlled using ligands, which bind to the surface of the NCs forming a colloidal shell around the particle (see Figure 1.7). A huge range of ligand have been used including, alkyl thiols,[71-73] phosphines, phosphine oxides, phosphates, amides, amines, carboxylic acid[74] and nitrogen containing aromatics.[75] The type of ligand chosen will dictate the solubility of the quantum to a range of solvent and so allows a huge range of flexibility when creating CQD solutions. The binding strength of the ligand and its physical size, will dictate the stability of the solution, preventing aggregation of QDs and oxidation of the QD surface.

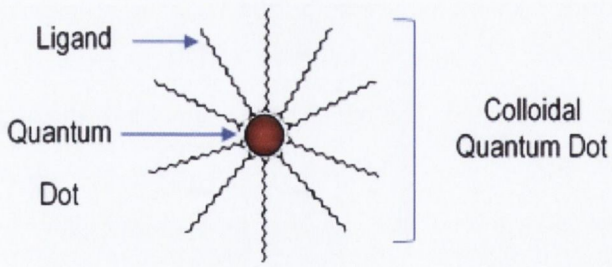

Figure 1.7 A collodial quantum semiconductor with organic ligand covering the surface

Apart from the quantum confinement effect, it is also important to consider that a large portion of the atoms composing a QD is situated on its surface and so the entire QD electronic state is strongly influenced by surface interactions. This can be quickly estimated to equal 24 % of atoms for a 6 nm CdSe QD are upon the QD surface which rises to 35 % for a 4 nm CdSe QD, and further to 60 % for a 2 nm CdSe QD. Due to this, the absorption and emission wavelength of a CQD can

be blue shifted or red shifted by surface ligand interactions and matrix effects. In addition, QDs can be very vulnerable to surface oxidation due to the large surface energies, resulting in surface trap formation. This process is particularly pronounced especially when under illumination, and is termed photobleaching.

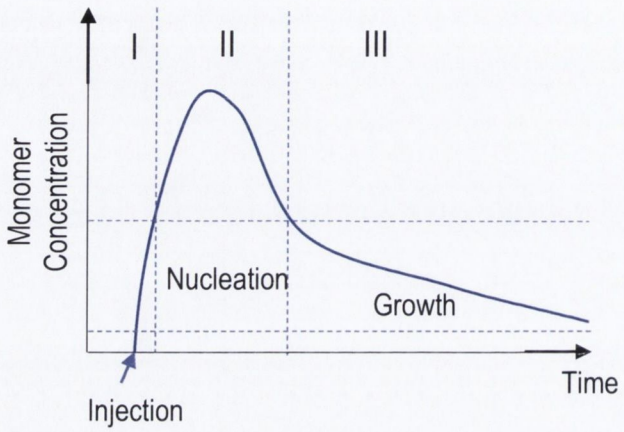

Figure 1.8 This shows the nucleation and growth process of collodial quantum dots using the hot injection method

Colloidal synthesis can be achieved using a range of approaches including solvothermal,[76-78] microwave synthesis,[79, 80] and electron beam irradiation.[81-84] However, the most common approach to produce colloidal quantum dots do date is hot injection first proposed in 1993.[85] This synthesis relies upon the heating of a reaction vessel containing, solvent, ligand and one of the quantum dot precursors to a specific chosen temperature. After reaching this point, a syringe is then used to quickly introduce a volume of the second precursor in the absence of oxygen, quickly increasing the concentration of monomer in solution (as shown in Figure 1.8 . Several factors are used to control the synthesis, including precursor concentrations, temperature and solvent. This initial step produces homogeneous nucleation of monomer into QD seeds in solution, which then immediately begins to grow in size due to heterogeneous nucleation of monomer. Therefore to achieve a small size distribution in QD size it is very important to separate the growth step and the nucleation step, by making the nucleation step of the reaction take place over a short period of time . Following this, seeds are allowed to grow to a set point in time after which the quantum dots solution is cooled. This is done before the monomer concentration reduces to the point at which Ostwald ripening begins. Ostwald ripening is a process that takes place in an inhomogeneous sol, by which smaller crystallites dissolve into solution and redeposit upon the larger crystals. This is a thermodynamically favoured process and so takes place spontaneously due to the increased energy of surface atoms relative to interior atoms. If left unchecked Ostwald ripening has the undesirable effect of increasing size polydispersity in a QD sample.

1.1.8 Core-Shell QD Heterostructures

Quantum dot properties can be further manipulated by coating one semiconductor in a shell of another semiconductor, which is termed a core-shell structure and have been extensively studied.[86] Three distinct types of band alignments can occur between the semiconductors of core-shell QDs and is dependent upon the band gap, work function and electron affinity of the core and shell semiconductors (as shown in Figure 1.9). The following types of QDs are known.

1.1.8.i Type I

Type I involves coating the core material in a semiconductor with a larger E_g with the aim of restricting environmental interaction with the optically active core material. Due to the band gap arrangement, the exciton of the QD is confined to the core material and therefore is less sensitive to surface states, including surface defects. The net effect is an increase in the quantum yield of the core-shell QD and much greater stability against photobleaching. As the shell thickness increases due to the lattice strain, a red shifting in absorption occurs. Examples include CdSe/CdS,[87-90] CdS/ZnS,[91] ZnSe/ZnS,[92] PbS/CdS [93] and InP/ZnS.[94]

1.1.8.ii Reverse Type I

Reverse type I core/shell QDs are formed through the coating of a core QD with a shell of smaller band gap semiconductor. This type results in partial exciton delocalisation in the shell resulting in red shifting of the absorption and emission, increasing with shell thickness. This due to exciton delocalization to the surface of the smaller E_g of the shell and also has the effect of generally lower PL QYs relative to the Type I QD due to the exciton being more exposed to surface trap states and solvent interaction. Examples include CdS/CdSe[95] and ZnSe/CdSe.[96]

1.1.8.iii Type II

Type II core/shell QDs results in the shell material having its CB or its VB in the BG of the core material, producing a staggered band alignment, and results in exciton separation over the two materials, with the hole residing in one material and the electron in the other. This has the end effect of producing a QD with a band gap smaller than either the shell or core material and results in a strongly red shifted absorption and emission for the QD, which is strongly dependent upon shell thickness. Examples include CdSe/CdTe[97, 98] and ZnSe/ZnTe.[99]

1.1.9 Multiple shelled QDs

Apart from binary core-shell QDs it is also possible to produce multi shelled QDs, which consist of a core coated in a multiple of shells of different semiconductors. This enables ever more complex structures to be formed and a range of interactions to take place between the shells ,

examples include CdSe/CdS/ZnS[100] and CdTe/CdS/ZnS.[101] However, the study of these multiple shelled QDs is outside the scope of this project.

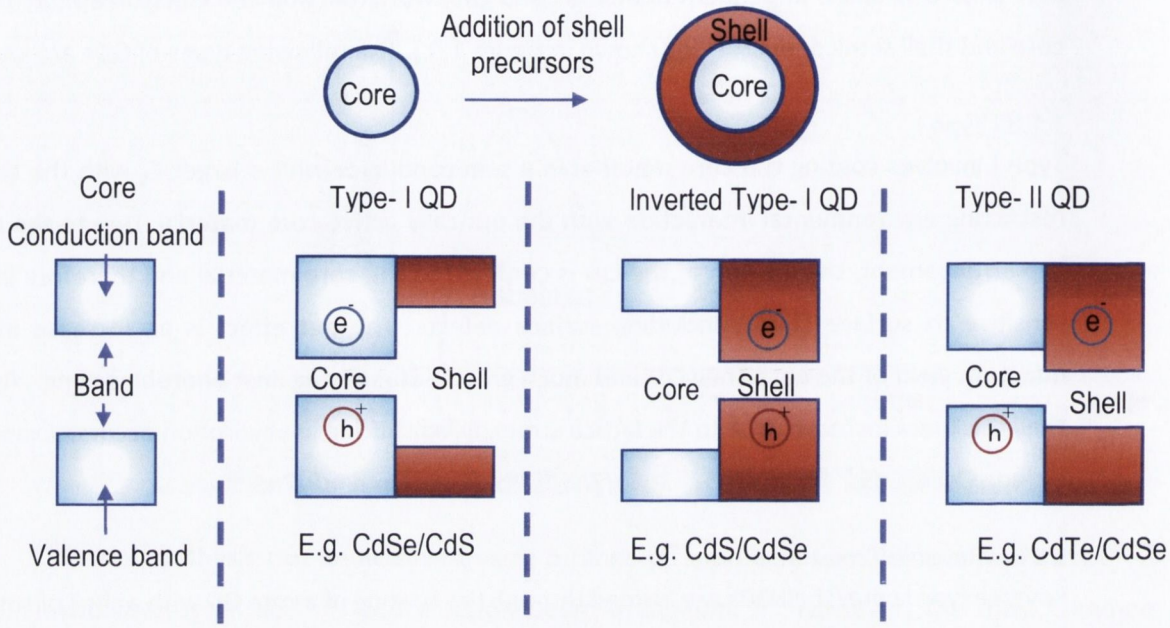

Figure 1.9 Different band alignments of core-shell quantum dots, dependent upon the band gap, valance band and conduction bands of shell and core semiconductor materials.

1.1.10 Lattice Mismatch and Strain

To grow one semiconductor upon another it is important to consider the crystal structure of the two materials, since if the two materials do not share the same crystal phase, epitaxial growth of a shell becomes impossible due to the mismatch between crystal types. Even when crystal structures are shared between materials, lattice parameters may differ, inducing lattice strain upon the resulting structure. The amount of strain induced by a shell is a function of shell thickness and the percentage difference in lattice constants termed lattice mismatch[102] (Appendix A). The effects of strain include crystal defect formation and band shifting of the core-shell energy levels.[103]

1.1.11 Bulk Modulus and crystal defects

The bulk modulus expresses a substance's resistance to compressibility. Therefore, as the value decreases the material will more easily elastically deform and so sustain a larger value of strain before relaxing through formation of crystal defects. This is an important factor when choosing an appropriate core-shell semiconductor combination and shell thickness due to the range in values across common QD core/shell materials (Appendix B).[104]

1.1.12 Synthesis of core-shell quantum dot structures

Again a wide range of synthetic approaches exist to produce core-shell quantum dots nanoparticles,[61, 78, 105] but as with core quantum dots, the most common approach is through the use of a hot injection colloidal synthesise. When applying hot injection to core-shell CQD synthesis, the injection of precursor is carried out under alternative conditions so as to promote heterogeneous nucleation of the shell material while discouraging homogeneous nucleation. To achieve this shell precursor injection takes place at lower temperatures and is introduced at a slower rate (drop wise usually). In addition successive ion layer adsorption and reaction (SILAR) approach can also be applied to control shell thickness. SILAR was firstly applied to the deposition of thin films[106, 107] but as of late has found wide application in CQD core-shell synthesis.[108] This method uses an alternating cycle of injections, each containing just one of the shell precursors, either the anion or cation and therefore produces a half of a monolayer upon the QD per injection. The quantity of each injection is calculated relative to the size and concentration of QDs to add the exact concentration to produce the half monolayer, therefore eliminating the risk of homogeneous nucleation of shell monomers. In addition, the quantity of each injection is increased as the size of the QD increases due to the shell deposition, allowing precise control of the resulting shell thickness.

A range of other morphological core-shell nano heterostructures have also been produced using semiconductor nanocrystal. Some of the most fascinating structures involve the growth a shell of a semiconductor upon a quantum dot that is quantumly confined in two or one direction. In the case of a two dimensionally quantumly-confined shell, the particular structure formed is dependent upon the crystal structure of the core quantum dot. If the core QD is present in a hexagonal structure, shell growth can be preferential upon the terminals of the core, producing a dot in rod structure overall. While if the crystal structure of the core quantum dot is cubic, growth will be preferential upon four faces of the QD, producing a dot in tetrapod structure. The most well-known example of this is demonstrated in CdSe-CdS core- shell heterostructures, CdS will adopt the hexagonal crystal structure of wurtzite while the CdSe can adopt either a cubic structure of zinc blende or the wurtzite structure dependent upon synthetic conditions. Therefore, by coating a CdSe QD of zinc blende structure with CdS, a dot in tetrapod structure is formed while by using a wurtzite CdSe QD core, a dot in rod can be grown.[88, 109] The synthesis of these anisotropic colloidal nanostructures is possible due to the high affinity that phosphonic acid ligands display for crystal faces perpendicular to the crystal c axis in wurtzite. This produces an important difference in growth kinetics between the c axis and the perpendicular directions, producing anisotropic growth in the CdS shell, producing the rod shape of the CdS and either

overall tetrapod or the rod shape of the shell CdS shell also.[110] It has also been shown that through cationic exchange it is possible to produce Cu_2Se/CuS, PbSe/PbS[111, 112] and PbS/CdS[113] dot in tetrapod or dot in rod heterostructures. Also interestingly it was recently reported the synthesis of a dot in platelet heterostructures formed from CdSe/CdS in which the shell is only quantumly confined in a single direction.[110]

1.1.13 Cation exchange in nanostructures

Cation exchange is a process by which the cations of an ionic solid can be exchanged with other foreign cations, usually in solution (Figure 1.11). Though this effect has been known for decades,[114] its specific application to the field of nanocrystal is relatively recent, and is particularly interesting due to the remarkable rate increase of cation exchange in comparison to bulk. This is mostly attributed to the larger surface area of the nanocrystal and lower activation energy to diffusions of ions. This is a relatively new synthetic approach in regards to nanocrystal synthesis, with the first review covering the topic being published in 2007.[115] This method has the advantage of reliability and ease of access to a range of nano structures, which maybe inaccessible through more well-known direct nanocrystal synthetic approaches.[116]

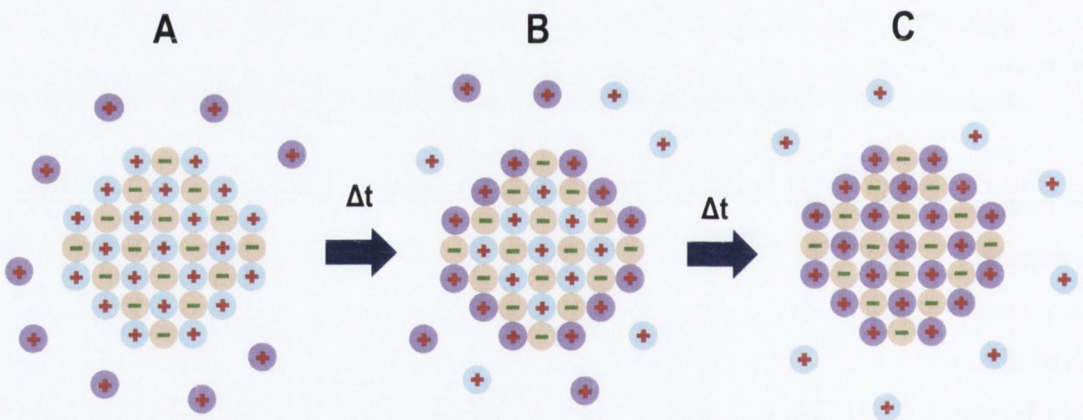

Figure 1.10 This shows the process of cation exchange taking place in a nanocrystal, in which one cation is replaced by another in solution over time, while maintaining the anion framework.

Though the technique can be relatively straightforward, in practice the exact result of the exchange is dependent upon a number of subtle thermodynamic properties and kinetic effects which must be carefully controlled to produce the desired cation exchange.[115] The overall reaction of a cation exchange is described in Equation 1.1 part (1) while the steps involved in this overall process are detailed in part (2-5) of the equation . The dissociation and association processes described in part 2 and 4 are concerned with the lattice energy and the surface energy of a crystal, with strain and dislocation energies also influencing the thermodynamics and kinetics of these processes. The desolvation and solvation processes described in part 3 and 5 are dictated by the relative solubilities of the two ions in the particular solvent used. Therefore,

for a cation exchange to take place readily, the outgoing cation should be more soluble in the solvent used then the foreign cation, while the lattice energy should remain the same or be minimised in the exchanged form.

$$M^{n+}(liquid) + C - A\ (crystal) \rightarrow C^{n+}(liquid) + M - A\ (crystal) \quad (1)$$

$$C - A \rightarrow C + A \text{ (Dissociation) (+ΔG)} \quad (2)$$

$$M^{n+} \rightarrow M \text{ (Desolvation) (+ΔG)} \quad (3)$$

$$M + A \rightarrow M - A \text{ (Association) (-ΔG)} \quad (4)$$

$$C \rightarrow C^{n+} \text{ (Solvation) (-ΔG)} \quad (5)$$

Equation 1.1 This describes the processes involved in cation exchanges, with (1) describing the overall reaction while (2-5) describes the steps involved in the process. Note M represents a foreign cation, while C the original host material cation and A the original materials anion, prior to carrying out of the cation exchange.

By using these controls, it is possible to produce a partially exchanged heterostructure[113, 117] or a completely exchanged structure. Cation exchange can also conserve the original shape of the nanocrystal, retaining the anionic framework under specific conditions.[111, 118] This process can also take place between ions of the same valence or of differing valency giving even greater flexibility in the approach. A range of different cation exchanges have been demonstrated in nanocrystals to date including PbX to CdX (X= Se or S),[93, 113, 117, 119-121] CdX to ZnX,[122, 123] CdX to PtX/PdX,[124] CdX to HgX,[125, 126] InP to GaP,[127] Cd_2X_3 to InX or GaX[128] and ZnTe to MnTe.[129]

1.1.14 CQD films

A number of CQD PV cells include films of CQD as a conducting and absorbing layer. An efficient film of CQD for PV applications needs to be stable and possess a long diffusion length so to allow charge carrier collection. Diffusion length of charge carriers in bulk semiconductors are defined by the crystal defects that scatter charge carriers. In QD films, diffusion lengths strongly depend upon the ability of charge carriers to move from one QD to another (Figure 1.12). Therefore, it shows a strong dependency upon the monodispersity of QD size, so to ensure resonant electronic states between the QDs.

In addition, charge movement between quantum dots is very strongly influenced by the existing distances between neighbouring quantum dots, with shorter spacing ensuring more effective quantum-mechanical overlap. This space is characterised by the ligand present upon the surface of the CQDs, with long chain molecules producing larger distances and therefore insulating films, while short chain ligands give rise to shorter distances and hence conductive films.[130] It has also been demonstrated that replacement of ligands with halide anions produce highly conductive films.[131, 132] Another approach that has been examined is the complete removal of ligands through the application of annealment[133] or specific solvents like dimethylformamide.[135] This produces films of QDs quantumly confined, but packed surface to surface forming a superlattice or supercrystal, and therefore display a vastly improved charge mobility.[135]

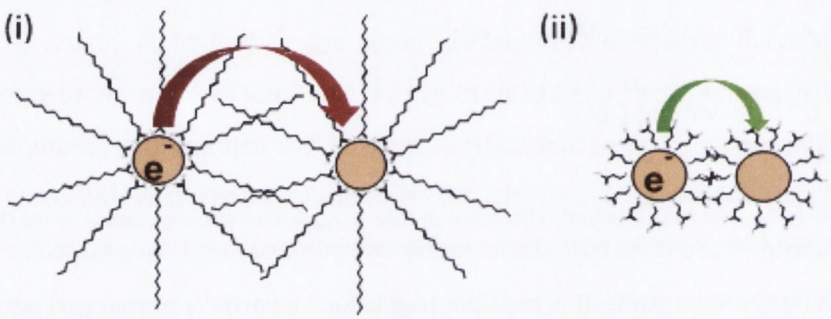

Figure 1.11 The diagram shows the movement of electrons between CQD, in (i) the electron must hop between a two CQDs capped in long fatty acid ligands (oleic acid), leading to high resistance, while in (ii) the electron transfers between two CQDs coated in short chain ligand such as MPA

Quantum mechanical overlap is also dependent upon how strongly the exciton is confined in the QD, and so is a function of the Bohr exciton radius relative to the QD size. Consequently, QDs with large Bohr exciton radiuses are most suitable for conductive film formation. Other factors relevant to QD conduction include a high density of states and high dielectric constants.[129] Interestingly, colloidal Pb chalcogenides films (PbS, PbSe and PbTe) have seen the greatest amount of research relative to other CQDs, due to their large Bohr exciton radiuses, large dielectric constants and high density of states relative to other commonly synthesised QDs.

1.1.15 Doping of QD films

Another important factor for application of QDs in solar energy harvesting is the need to produce films that are appropriately doped, enabling the formation of a p-n junction and/or Schottky junction. Doping of CQDs using impurities has proven to be difficult due to number of factors including stochastic variations of dopant levels in QDs , shifting of dopants energy levels due to quantum confinement[136] and self-purification of dopants.[137] One possible approach is by introducing non-stoichiometry in a QDs resulting in intrinsic doping by changing the surface termination groups. [138-140]

The most successful route to date for producing doped films of CQD is via ligand exchange. This involves firstly depositing a CQD film using spincoating, dip coating or drop casting. The deposited film consists of QDs with long insulating ligands, such as oleic acid. These films then undergo ligand exchange with a short chain ligand of much larger binding energy, replacing the ligand shell of the QDs and in effect shrinking the film. Multiple coatings are undertaken to produce a continuous film, which is electrically conductive and shows either p or n-type conductivity.

CQD films produced for PV applications to date include, hydrazine producing n-type PbSe,[141] short chain carboxylic acids producing p-type PbS and PbSe films,[142] 3-mercaptoproponic acid (MPA) producing p-type PbS,[143] 1,3-benzenedithiol producing p-type PbS_x Se_{1-x}[144] and p-type PbSe,[145] ethanedithiol producing p-type PbS.[146]

1.2 Photovoltaic Cells

1.2.1 Main concepts and definitions

The solar irradiance on Earth's surface is function of a number of factors. Firstly, the solar irradiance of the sun can be modelled closely as a blackbody radiator of 5800 K (see Figure 1.12). When this energy reaches the earth, a number of chemicals in the Earth's atmosphere have an attenuation effect upon the radiation, absorbing some of it before it reaches the surface. In addition, Rayleigh scattering also plays a role in solar irradiance attenuation, scattering high-energy photons more readily than low. The magnitude of both effects is proportional to the amount of atmosphere the radiation passes through, and is described by the term Air Mass (AM). Solar irradiance at the top of the atmosphere is termed AM 0 with a resulting irradiance of 1366.1 W/m^2. The AM at the equator is termed AM 1, with light travelling the shortest distance to reach the surface and is described to have a 0° angle relative to the earth's surface normal, called the zenith angle. The majority of the earth's population in fact lives in the temperate zone, which due to the earth's curvature, means that light reaching this area of the earth travels through a thicker amount of atmosphere and is designated a AM of AM 1.5 with a zenith angle of 48.2°, and a corresponding reduction in irradiance. AM 1.5 can be divided into two sub-categories AM 1.5 G (global) which includes diffuse light while AM 1.5 D (direct) does not, therefore AM 1.5 G corresponds to an irradiance of 1000 W/m^2 while AM 1.5 D corresponds to a reduced irradiance of 900 W/m^2.

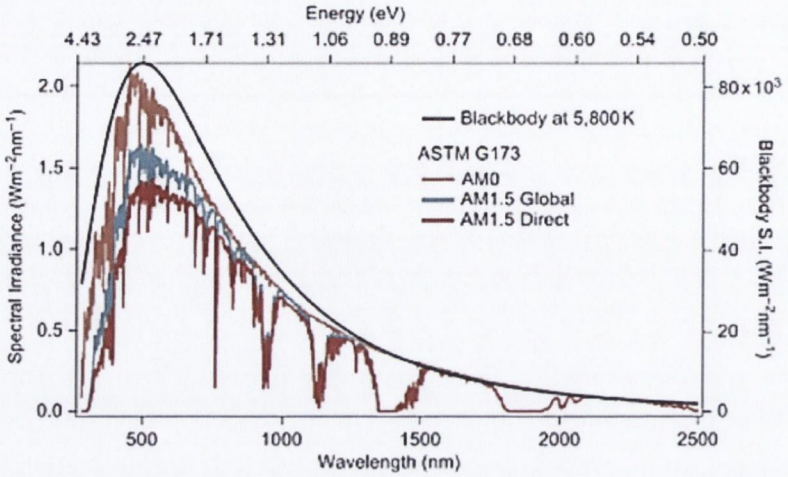

Figure 1.12. The Solar Irradiation at AM 0 and AM 1.5G and 1.5 D compared to a blackbody radiator at 5800K reproduced from ref [147]

A photovoltaic (PV) cell is a photoelectronic device which using the photovoltaic effect allows photons of light to be converted directly into electricity. For this to occur efficiently three processes must take place, firstly a material must be present to absorb incident photons and generate charge carriers, secondly separation of the charge carriers must occur and thirdly the charge carriers need to make their way to the terminals of the device.

For effective absorption of light using semiconductors, two properties must be considered. Firstly, E_g should be chosen to collect the maximum amount of energy from the solar spectrum. This exact problem has been tackled using the Shockley–Queisser limit. [148] The Shockley–Queisser limit describes the highest possible PCE (power conversion efficiency) for a solar cell based on a p-n junction of a specific BG relative to the solar irradiation.[148, 149] The factors that determine this limit upon efficiency are listed below:

1.2.2 Blackbody radiation

A body at a given temperature radiates heat in the form of radiation, with this radiation's energy increasing as temperatures increase. Therefore, a solar cell at 300 K radiates a baseline of energy, which cannot be captured by the cell, which equates to 7 % of the solar irradiation total loss.

1.2.2.i Recombination

This takes into account that a rate of recombination of charge carriers is always present and therefore always will reduce the overall V_{oc} (open circuit voltage) of a cell below the value of the BG of the material.

1.2.2.ii Spectrum loss

When a photon is absorbed which is larger than the E_g of the semiconductor, it produces an electron which is excited into the higher energy levels of the CB of the material, which then relaxes to the band edge of the material through loss of this excess energy in the form of heat. This excess energy is therefore not available to be converted to electrical energy and so to minimize the loss the E_g should be close to the energy of photons being absorbed. This strategy must be balanced with the fact that any photons of energy below E_g will not be able to produce an exciton. Therefore these two factors of loss must be minimised as effectively as possible by choosing a material with an E_g large enough to minimize losses of energy from high-energy photons (UV, visible), but small enough so to enable low energy photon absorption (infrared).

The Shockley–Queisser limit dictates that for maximum efficiency under AM 1.5 G sun illumination the band gap of a single p-n junction based solar cell should lie between 1 eV and 1.5 eV, with the maximum attainable solar energy conversion efficiency possible of 33.7% using an E_g of 1.1 eV (see Figure 1.13). This limit can be surpassed through the use of solar concentration technology and/or with the application of a tandem solar cell design, though both routes carry their own set of specific issues. [149]

Secondly, the semiconductor should be an efficient absorber and hence should have a high absorption coefficient. Therefore, a semiconductor with a direct BG is preferable; meaning the highest point in the VB and the lowest point in the CB should lie in the same k- vector. If this not true the material is described as an indirect semiconductor and has the effect of making photon absorption less likely and so a thicker layer of absorber must be used.

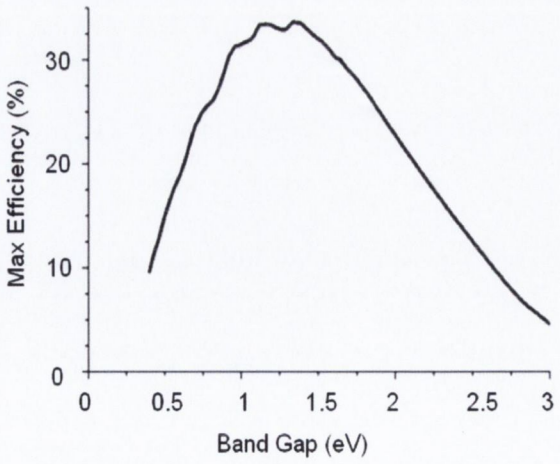

Figure 1.13 The Shockley-Queisser limit of a single junction cell under AM 1.5G solar illumination

Another important factor to consider is that charge carriers must be able to reach the membrane effectively. To achieve this, absorber layer thickness should be less than the

diffusion length of the charge carriers. Consequentially this must be managed relative to the absorption coefficient of the absorber layer.

Effective charge separation of the photogenerated electron hole is needed for efficient solar cell performance to avoid recombination of the charge carriers. This is achieved in solar cell design by using a semi-permeable membrane at either side of the absorption layer, which are more permeable to one charge carrier than the other. This is achieved by using materials which have a higher conductivity to one charge carrier than the other, like an n-type material which shows higher conductivity to electrons than holes.

Another method to realise this membrane approach is to use a band alignment, termed a staggered alignment, which supports charge separation by placing an energy barrier, which boosts one charge carrier injection while discouraging the other. Electron charge injection rates can be increased by having the CB of the absorber in a higher energy position than the CB of the electron permeable membrane and is given by the Marcus equation (Appendix A).[150] Complementary to this is that hole injection rates can be retarded through the use of electron permeable membrane which have a VB of lower energy than the VB of the absorber. This also applies to a hole permeable membrane, which becomes more effective by using a material that has a VB higher than the VB of the absorber and a CB that is of lower energy than the CB of the absorber.

To best bring about these band alignments a semiconductor with a larger E_g than the absorber is used as one or both of the semipermable membranes so as to avoid the membranes absorbing incoming light intended for the absorption layer. Also importantly, recombination rates are dependent upon minority carrier concentrations since these are the limiting factor to the process, therefore in large Eg semiconductors the population of thermally generated charge carriers is minimal and so the rates of recombination is slow.

1.2.3 Dye Sensitized Solar Cell (DSSC)

The Grätzel Cell, also called the dye sensitized solar cell (DSSC) was originally co-invented by Michael Grätzel and Brian O 'Regan in 1988 and published in 1991.[151] This design has shown the ability to produce power conversion efficiencies (PCE) of up to 12%., using a cheap thin film approach.[152, 153] In this cell design, a dye acts as the absorber layer, which when excited by incident photons, injects its photo-generated electrons into the CB of a wide band gap conductor. In this design, a phase barrier is used to prevent recombination of the electron, which is then transported through the wide band gap semiconductor and is injected in to the TCO. The dye itself is regenerated using a redox couple present in the electrolyte, which donates

an electron. The redox couple in turn is regenerated at the cathode, which also provides the electrical connection between the photoaniode and the cathode, which regenerates the redox couple. The voltage of the cell is defined by the difference in conduction band of the wide band gap semiconductor and the oxidation potential of the redox couple present in solution.

The photoaniode of the cell is composed of a porous layer of wide-band gap semiconductor, generally TiO_2 that is deposited on to the surface of a transparent conductive oxide (TCO), though other semiconductors have also been investigated including ZnO, SnO_2 and $SrTiO_3$. TiO_2 is a transparent to visible light and therefore a dye is used to sensitize the cell to the visible spectrum. Either metal complexes (i.e. Ru, Os, Fe, Pt based) or organic dyes (i.e. coumarin, tetrahydroquinoline, triarylamine, heteroanthracene, perylene, etc.) are used as dyes. These are deposited using soaking, producing a monolayer upon the TiO_2. The dyes generally includes an anchoring group (i.e. -COOH,- PO_3H_2,-SO_3H, etc.) which is used to link the dye to the TiO_2 surface. The TiO_2 layer is deposited using an approach to maximise its surface area, and is generally composed of nanoparticulate layer of 20 -30 nm anatase particles, sintered together into a network. This allows a higher loading of the TiO_2 with dye, maximising the absorption of the cell. The cathode is composed of a metal, with a large work function (important to maximising the voltage of the PV cell) and which is catalytic to the redox couple present. Platinum is the most commonly utilised metal for this function and is deposited in a nanoparticulate form, increasing surface and therefore activity. Both electrodes are connected by an electrolyte solution, containing a redox couple, allowing for an electrical connection between the anode and cathode. The redox couple utilised in the majority of DSSC cells is the I^- / I_3^-, which shows the greatest efficiency and was first proposed in the original 1991 paper. While a range of redox couples have been investigated including Br^-/Br_3^-, $SCN^-/(SCN)_3^-$, and metal complexes of Ni^{+3}/Ni^{+4} [154] or Co^{+2}/Co^{+3},[155] none have produced a more efficient cell to date.

1.2.4 TiO_2 material

TiO_2 occurs in three common crystal forms rutile (tetragonal), anatase (tetragonal) and brookite (orthorhombic). Anatase and brookite are metastable and convert to the rutile structure upon heating. Also worth noting is the existence of five high pressure which have been identified. The band gap of the three most common phases are, ~3.4 eV for anatase,[156] ~3.0 eV for rutile[157] and ~3.3 eV for brookite,[158] which therefore means all are transparent to visible light. TiO_2 demonstrates excellent photocatalytic properties under UV illumination, with a mix of rutile and anatase phase TiO_2 showing the greatest activity.[159]

Also importantly, anatase and rutile- TiO_2 display intrinsic conductivity of n-type, enabling the formation of a p-n heterojunction with p-type semiconductors. This n-type character is due to the presence of sub-stoichiometry, resulting in an excess of Ti atoms and produces two resulting crystal defects in the lattice, O vacancies and Ti interstitials.[160] Oxygen vacancies are the more common defect under oxygen rich conditions, with a slightly larger concentration in the anatase form than rutile.[144] Titanium dioxide due to its high stability, ease of production and appropriate VB and CB position is widely used as an n-type wide band gap semiconductor in photovoltaics, enabling charge injection from a range of absorber layers. The most widely used phase for PV applications is anatase since it has been shown to have higher charge mobility relative to the rutile phase, therefore mediating recombination losses.[161] It is also preferred due to the higher position of the CB relative to the vacuum, which increases the related voltage of the PV cells produced.

1.2.5 Colloidal Quantum Dot Based Photovoltaic

For a solar technology to be widely adapted as a means to generate electricity, it must be efficient and cost effective. This is defined by the cost per watt-peak (€ / Wp). The cost of a PV cell depends upon the material used and the manufacturing approach. In addition to this, is the balance of systems (BOS)[162] associated with complete installation of the PV can be considerable. Therefore it has been deemed that some trade off can take place between efficiency and cost, but due to BOS a lower limit of efficiency does also in fact exist. The following aspects should be considered for colloidal QD based photovoltaic devices.

1.2.6 Manufacturing Cost

The CQD PV cells is a thin film technology resulting in minimal material costs. In addition, designs utilise inexpensive solution phase fabrication techniques, such as dip coating, dropcasting or spincoating. The raw materials cost concerning QD synthesis is minimal when using green chemistry approaches,[163, 164] while the colloidal synthetic approach is well suited to QD mass production,[165, 166] therefore it is potentially possible to produce QDs cost effectively for PV applications.

1.2.7 Tuneable and Broad Absorption

The onset wavelength of absorption in a semiconductor is determined by the bandgap of the material. As discussed earlier, the bandgap of QDs becomes size dependent due to quantum confinement, resulting in the bandgap energy increasing as size is reduced. This allows the absorption pattern to be tuned across the entire solar spectrum by using different semiconductors and sizes (CdS, 350-470 nm) (CdSe, 450-640 nm) (InP, 550-650 nm) and (PbS,

800-3000 nm).[167] Additionally by adding specific impurities (e.g. Mn,[168] Cu[169]) to produce a doping effect in QDs , the absorption profile can be even further controlled due to the alteration of band gap energy. A huge range of core/shell structured QDs[86] can also be prepared allowing further manipulations of absorption spectrum. The absorption spectrum after the first exciton, displays rising absorption strength with decreasing wavelength, meaning a QD can absorb light over a broad range of wavelengths. In addition, QDs with a direct bandgap show a large absorption coefficients ranging from 1×10^5 to 1×10^6 M^{-1} cm^{-1}, which is also size dependent.[30, 49-52]

1.2.8 MEG (Multiple Exciton Generation)

A number of QD cell designs have shown the potential to produce high efficiencies, including the ability to surpass the Shockley–Queisser limit due to multiple photon generation (MEG).[170] This causes the absorption of a single photon in a semiconductor to result in the production of a number of excitons through this non-linear process. For this to take place the photons energy must be at least twice the energy of the semiconductor's BG to produce two excitons, three times the BG to produce three excitons and so on. MEG has been observed in a number of QDs including PbSe and PbS[34] though the exact mechanic for the MEG effect is still under discussion. Solar cells based on QDs that show this MEG effect, have the potential ability to give high efficiencies and even enable them to surpass the Shockley Queisser limit.[171]

1.2.9 The effect of quantum dot size polydispersity

It has been demonstrated that polydispersity in quantum dots used in quantum dot based solar designs is a specifically unique issue, with increased size distributions lowering charge mobility due to imperfect packing of QDs reducing I_{sc} and also due to range of bandgaps being present, a lowering of the resulting V_{oc} of the produced cell can also occur. It has been identified not to posse a large issue at present due to large populations of trap states being present in devices to date, but as these surface passivation issues are resolved through cell design, monodispersity of size will become more of an important issue.[172]

1.2.10 Quantum Dot cell designs

Colloidal Quantum Dots have been tested in a wide variety of Solar cell designs[12,173, 174] including Hybrid CQD Polymer Solar Cells,[175-177] Tandem CQD Cells,[178] and Quantum Funnels.[179] Specifically for this project, four types of CQD designs will be examined in detail, the CQD Schottky Cell, the Quantum Junction solar cell, the Depleted Heterojunction Colloidal Quantum Dot solar cell (DHCQD solar cell) and the Quantum Dot Sensitized Solar Cell (QDSSC).

1.2.11 CQD Schottky Cell

One of the first and simplest designs of a CQD based PV cell, is the CQD Schottky cell (Figure 1.15), which to date has shown a PCE of up to 5.2% under 1.5 AM corresponding to a V_{oc} = 0.46 V, a I_{sc} = 19.3 mA/cm^2, and a fill factor FF = 58%.[180] The cell design consists of a Schottky junction formed between the p-type QDs and a low work function metal (Al,[181] Ca[170] and Mg [145]) which is used as the cathode, creating a depletion region at the junction. As an anode, Indium Doped Tin Oxide (ITO) or Fluorine doped Tin Oxide (FTO) is used, as a transparent conducting electrode (TCO). Charge collection is most efficient in the depletion region of this cell and so QD film thickness is restricted to be in the range of thickness of the depletion zone, which is about 150 nm.[170, 180] Illumination takes place through the TCO with the majority of charge carriers being generated outside the depletion region, which has a negative effect upon efficiency. The maximum possible V_{oc} of this cell is defined as the difference between the cathode work function of the metal cathode and VB of the TCO. Unfortunately due to surface defects between the metal –QD contact which produce pinning of the Fermi-level,[182] the actually realisable V_{oc} can be much lower [183] and only show a weak relationship to the metal work function.[170] Also in some of the most recently published designs, a thin layer (1 nm) of LiF has been included between[180, 184, 185] CQD and the metal back electrode.[176, 180, 181] The function of which is to decrease the dark saturation current of the device through passivation of traps present at the junction between the CQD and metal back contact, reducing non-radiative recombination of excitons and therefore increasing cell efficiency. QDs tested in this design include PbSe,[145, 170] PbS[146, 180, 181, 184-186] and $PbS_x Se_{1-x}$ (x = 0.6 - 0.9).[187, 188]

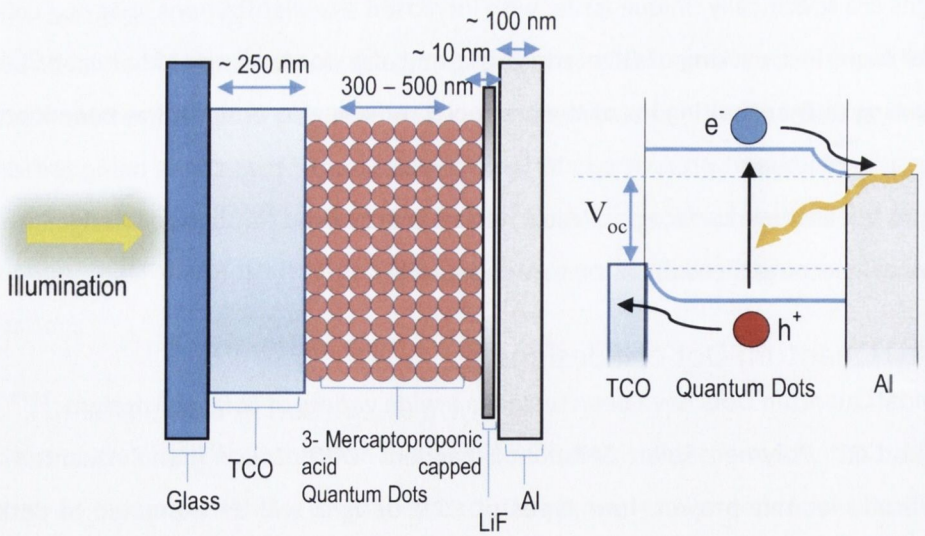

Figure 1.14 CQD Schottky cell, showing the basic structure of the cell is given on the left while the right diagram explains the electron and hole movement in the device, describing the relationship between the materials and the resulting open circuit voltage.

1.2.12 Quantum Junction Solar Cells

This cell is built upon the principle of quantum dots sandwiched between a TCO coated piece of glass and a top electrode normally consisting either a thin layer of LiF and Al or another metal. The difference with this design lies in the formation of a p-n junction between quantum dots. This junction is formed using two different quantum dots, forming a heterojunction or by using two different samples of the same semiconductor forming a homojunctions. Examples of quantum dot homojunction solar cells include n-doped/p-doped PbS CQD,[189] which have PCE of up to 7.4% ,under 1.5 AM corresponding to a V_{oc} of 0.55, a I_{sc} of 24.5 mA / cm^2 and a FF of 55%. Examples of hetero-quantum junctions include p-type PbS/ n-type Bi_2S_2[190] and CdTe/CdSe .[191, 192] PbS will naturally have a p-type doping due to oxidation under air , while n-type character can be produced in PbS using Ag doping [193] and halide soaking.[189, 194, 195]

1.2.13 Depleted Heterojunction Colloidal Quantum Dot Solar Cell

A new cell design, which has emerged recently, is the Depleted Heterojunction Colloidal Quantum Dot solar Cell (DHCQD solar cell) with reported PCEs of up 8.5 %[196] under 1 sun, 1.5 AM illumination and is shown in Figure 1.15. This builds upon the Schottky Cell design by utilising an n-type large Eg semiconductor connected to the film of p-type QDs forming a p-n heterojunction. Therefore, a depletion zone is produced with a built in field, which can be used to enable charge separation of photogenerated charge carriers across the junction. Just as in the Schottky cell the device is designed to use a CQD film thickness of the similar length as the depletion region produced from the p-n junction, which has been determined to be between 200-300 nm in thickness.[196] Also importantly the n-type semiconductor is normally deposited in a nanostructured phase so as to produce a large surface ,allowing excellent contact between it and the CQD layer and so enabling effective charge injection. The cathode is a transparent conducting electrode (TCO) consisting of either Indium Doped Tin Oxide (ITO) or Fluorine Doped Tin Oxide (FTO) and is connected to the n-type semiconductor. As an anode, a large work function metal (gold) is utilised which should be aligned with the VB of the QDs, so as to avoid the creation of a Schottky barrier which would retard hole injection. Illumination takes place through the TCO, with the majority of charge carriers being generated within the depletion zone of the p-n junction enabling charge separation. The maximum V_{oc} is defined by the energy difference between the work function of the anode and the VB of the n-type semiconductor.

CQDs tested in the cell design include PbS,[183, 187, 197-203] PbSe,[187, 204] Sb_2S_3,[205] and $CuInTe_2$[206] while for the n-type wide band gap semiconductors, TiO_2[183, 197, 200-202] and ZnO[187, 199, 203, 204, 207-209] have been investigated.

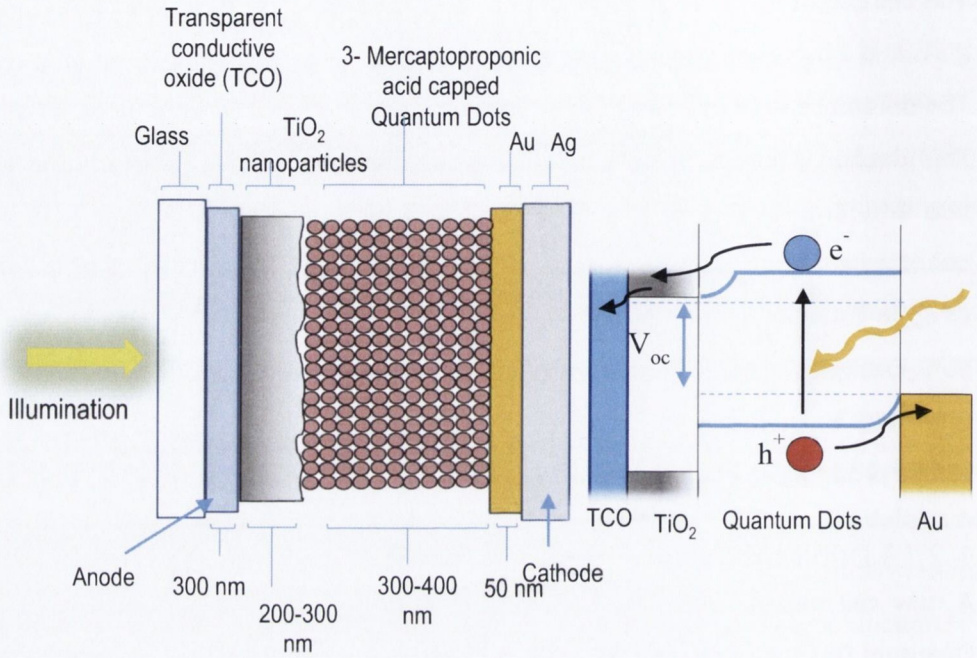

Figure 1.15 This shows one of the most common designs used in a quantum dot depleted heterojunction solar cell (right) and the basic movement of electrons and holes in this device (left).

1.2.14 Hole Extraction Layer

Unfortunately, just as in the Schottky Cell design, V_{oc} has been shown to be reduced due to Fermi-level pinning at the CQD-metal contact creating an unwanted Schottky barrier.[187, 207] Recent developments in this design have included the application of a hole extraction layer (HEL) deposited as a thin layer (1-10 nm) of transition metal oxide upon the CQD layer before deposition of a metal back contact. [199] Examples include MoO_3 [196, 202] or V_2O_5, [199] which when deposited show a n-type behaviour due to the introduction of non-stoichiometry from the thermal evaporation process. These therefore can increase hole extraction at the interface by injecting electrons in to the valence band of the CQDs.

1.2.15 Anion passivation

The CQD layer in a DHCQD cell consists of QDs with a short chain ligands upon the QD surfaces, original designs utilised 3-mercaptoproponic acid[183] or 1,2 ethanedithiol[210] for this purpose. Unfortunately it was determined that these ligands did not give complete surface passivation of the layers, which gave rise to the presence of trap states, decreasing cell efficiency due to recombination losses. These ligands also showed a vulnerability to oxidation and thermal degradation. Therefore a new strategy was proposed in 2011[201] which employed the use of all inorganic ligands to produce halide capped QDs films, which showed a marked increase in

efficiency. This strategy was the combined with a 3-mercaptoproponic acid ligand exchange to produce a hybrid organic-inorganic coating,[163] which has been incorporated into all of the latest highest performing DHCQD cells.[196, 211]

1.2.16 Donor Supply Electrode

The DHCQD cell design has been shown to suffer from a compromise between extraction length of charge carriers and absorption length of incident photons, with thicknesses of CQD layers chosen to compromise between both factors, maximising on photocurrent. If it were possible to extend the depletion zone, this would result in an extension of the extraction length of charge carriers and so enable the use of a thicker film of CQDs to maximise absorption of incident photons, without increasing recombination rates within the CQD film.

In principle, a viable strategy to achieving this would be the use of an n-type material with a higher free carrier density, which would in turn increase the depth of the depletion zone within the CQD layer when the p-n junction is formed. UV radiation has been demonstrated as a viable strategy to increase n-type doping levels in ZnO, displaying an increased depletion zone depth in DHCQD cells.[212] The simplest strategy to achieve this for TiO_2 would be the incorporation of a n-type dopant, unfortunately results to date show that n-type doping of TiO_2 using metal ions affects TiO_2's electron affinity[208] and not its net carrier density as expected. An alternative strategy to achieve this in the DHCQD cell is use of a donor supply electrode (DSE).[196, 209] The principle of a DSE is a material that can readily increase charge density in the n-type material (TiO_2) via charge injection doping. The first DSE was demonstrated in 2011 used a heavily n-doped wide band gap semiconductor (Aluminium doped ZnO) followed by a thin layer of TiO_2 (100 nm) which contacted the CQD layer.[209] This produced a PCE ~ 4% but did not manage to eclipse other DHCQD PCEs reported at the time. The second example published in 2013 holds the current reported record for efficiency for DHCQD cells achieving a PCE of 8.5% corresponding to a V_{oc} = 0.62, I_{sc}= 22.7 mA/cm^2 and a FF = 61%.[196] This used a much shallower work function FTO layer in conjunction with a very thin TiO_2 layer.

1.2.17 Durability

The cells show excellent thermal durability,[183] but unfortunately do not show the ability to tolerate environmental conditions involving oxygen's presence. Therefore, after QD deposition, the cells needed to be stored under an inert atmosphere and PCE and IPCE testing of these cells is also generally carried under these conditions also, to achieve the highest possible efficiency from the cells.[178] [207] While this is reported by several groups, it has also recently been demonstrated that the a PbS/ZnO based DH-CQD cell demonstrated little to no loss in efficiency

over a 1000 hour testing period under one Sun in ambient conditions , which seems to directly contradict other statements concerning stability of DH-CQD cells.[210]

1.2.18 New Cell Architecture

Finally, very recently new designs of DHCQD cells have been published focusing upon the shape and architecture of the cells. A specific design showed that by the incorporation of mirrors and placing the cells at a 45° angle, a 15 % increase in I_{sc} was achieved with a marginal reduction of V_{oc} by 8%.[213] Another example included the use of nanofabrication to produce a periodic structure that enabled a 31% improvement in Isc relative to a planar device with the same volume of absorbing material.[214]

1.2.19 Quantum Dot Sensitised Solar Cell (QDSSC)

It was first demonstrated in by Vogel in 1990 that it was possible to sensitize TiO_2 electrodes to visible light using a CdS Quantum dots,[215] this was further explored by a number of papers which demonstrated sensitisation with a range of other quantum dot materials during the following 12 years.[216-218] In 2006 the first efficient QDSSC cells was demonstrated using CdSe/CdS as sensitizers, producing a PCE of 2.8 % under 1 sun illumination.[219] The QDSSC design is a modified version of the well-known DSSC cell, in which a quantum dot is used to sensitise the TiO_2, instead of a dye. A range of modifications have been incorporated into the QDSSC design to facilitate

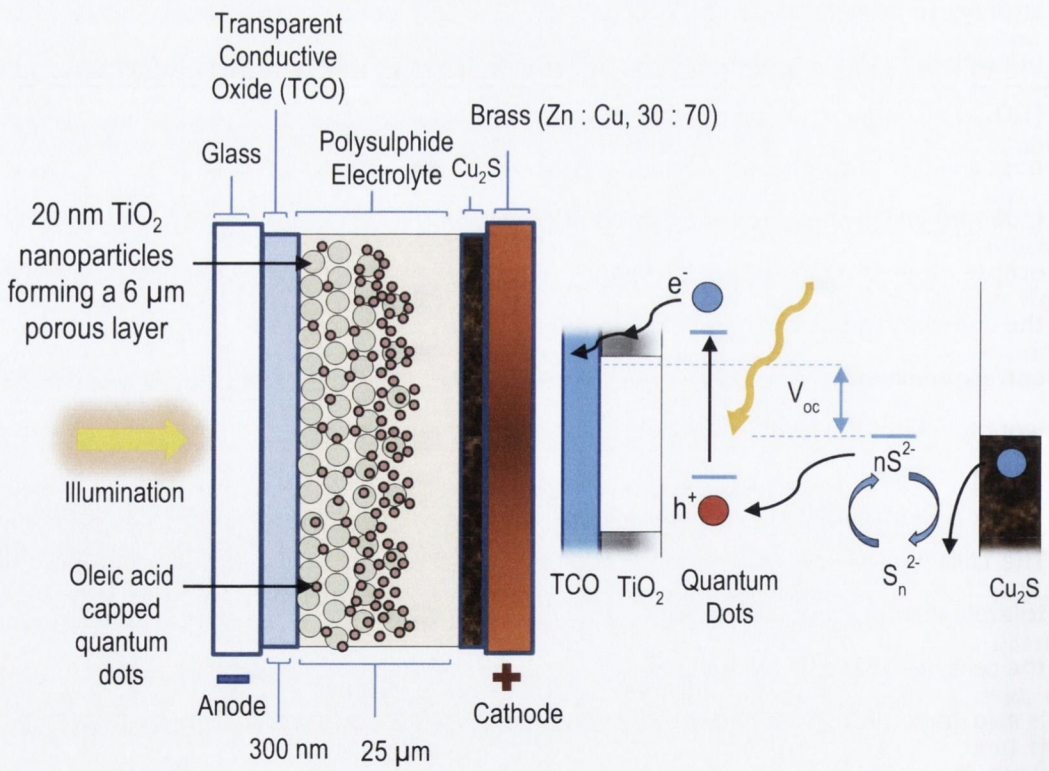

Figure 1.16 This a common design for a quantum dot sensitised solar cell (right) and the flow of electrons across the device (left).

the efficient use of QD particles, these cover changes to the TiO_2 layer, the electrolyte and the counter electrode (Figure 1.16).

An important challenge in utilising QDs as a sensitizer to TiO_2 stems from electrolyte degradation of QDs. It was initially identified that QDs degraded quickly in the presence of the I^-/ I_3^- redox couple, therefore a range of alternative electrolytes have been tested.[220] The highest performing to date are the polysulphide (S_n^{2-}/nS^{2-})[221, 222] based electrolytes, though cobalt metal complexes [Co(1,10-phenanthroline)$_3$] $^{2+/3+}$ [223, 224] based electrolytes couples have also shown impressive efficiencies.

Unfortunately, Pt based counter electrodes, as found in the standard DSSC designs; do not perform effectively in sulphur-based electrolytes due to surface adsorption of sulphur groups, which bind strongly to the metal surface, decreasing Pt surface activity and conductivity. Therefore a range of materials have been investigated to replace it including carbon,[225] Au [226] Cu_2S,[227] CoS,[228] CoS/CuS,[229] NiS[230, 231] and PbS[232] with Cu_2S demonstrating the most efficient cells to date.[233] This counter electrode consists of a Cu_2S layer grown upon a thin sheet of brass, using an acid etch and followed by chemical bath deposition, which produces a large surface area electrode with excellent adherence and conductivity.

A huge range of different QDs have been tested in this design including CdS,[221] CdSe, CdTe, $CdTe_xSe_{1-x}$,[234] CdS/CdSe,[235] $CuInS_2$,[236, 237] PbSe, PbS,[238] InAs[239] and doped QDs such as Hg doping of PbS[233] and Mn doping of CdS.[240] The QDSSC efficiency has hugely increased since there original conception, with PCEs of over 5% reported using a variety of approaches[225, 233, 238, 240, 241] and the record efficiency to date demonstrating a PCE = 6.36 %, FF= 57.5 %, V_{oc} = 0.575 V and I_{sc} = 19.35 mA/cm^2 using $CdTe_xSe_{1-x}$ QDs (x= 0.55).[234] The QDs employed are synthesised and deposited using a range of techniques, these approaches can be broadly categorised into two areas, in situ synthesis or ex situ synthesis.

In situ synthesis has employed a range of processes including chemical bath deposition (CBD) ,[219] successive ion layer adsorption and reaction (SILAR),[242] spray pyrolysis deposition (SPD)[243] and recently electrodeposition[244] to enabling the synthesis and deposition of the desired QDs onto the TiO_2 photoaniodes in a single step. The single step process allows a quick and uncomplicated route to sensitise TiO_2, the approach also ensures excellent contact between deposited QD and the porous photoaniode surface and has been responsible for many of the best performing QDSSC cells recently. Unfortunately, the QDs produced using this range of in situ approaches will inherently have a polydispersity of size and can suffer pure crystallinity. The

in situ approach also does not allow sensitisation of TiO_2 films with more complex QD heterogeneous structures, such as quantum rods or core shell QDs. Therefore, in this project the ex situ synthesis approach has been favoured.

Ex situ synthesis is a relatively new approach to QD sensitization of the photoaniode. This involves firstly the synthesis of QDs using commonly reported colloidal chemistry approaches to produce the desired QDs. Following this, the QDs are then deposited upon the surface of the TiO_2 photoaniode, which is achieved with either a linker molecule or using electrophoretic deposition (EPD). Ex situ synthesis allows for much greater control of the QDs composition and quality since all of the developments in colloidal synthesise can be used to produce near monodisperse samples of QD, with high crystallinity and in a range of complex structures.

1.2.20 Linker Approach to CQD Deposition

The linker approach uses a bifunctional organic ligand to anchor the QDs to the surface of TiO_2 particles using commonly the same groups that are used for dyes in DSSCs (-COOH). The ligands are also chosen to produce the minimal distance between the QD and the TiO_2 surface to enable charge injection from the QD. A wide range of ligands have been tested in this approach [245], 3-mercaptoproponic acid (MPA) has consistently demonstrated the highest efficiencies in QDDSCs. Synthesising high quality MPA capped QDs can be difficult, therefore CQDs are firstly synthesised using bulky organic ligands which is followed by a ligand exchange. Either this ligand exchange can be carried out on the surface of photoaniode, which has already been treated with 3-mercaptoproponic acid, or a separate ligand exchange is done before sensitization of the photoanode, this currently holds the highest PCE record to date of 6.76 % using CdTe/CdSe core/shell QDs.[246]

1.2.21 Electrophoretic Deposition of CQDs

The second ex situ approach is electrophoretic deposition, which was first applied to produce uniform films of CdSe films in 2002, after which the first CQD PV fabricated with this approach was reported in 2008,[247, 248] while the first efficient QDSSC cell was demonstrated in 2010.[249] This approach utilizes an electrical field to drive the deposition of CQDs in a solution upon the surfaces of the TiO_2 electrodes of opposite polarity. The ability to use an electric field to deposit the QDs is due to the presence of a dipole and surface charge in CQDs, whose origin is due to several interactions.

The effects of an electric field have been extensively studied in regards to CQD solutions, leading to the detection of a permanent dipole in CQDs and the origin of which is a matter of debate.[250, 251] Following on from this, the origin of charging in CQDs has been affiliated to a number of

process producing in most solutions a near isoelectric composition of positively and negatively charged CQDs. The reason for this is due to several processes.

Firstly CQDs will generally not be stoichiometric in composition and therefore be rich in either an anion or cation species.[252] Hence, considering CdSe QDs the presence of positively charged CdSe QDs is due to excess Cd while negatively charged CdSe is due to excess Se in the QDs composition. Secondly, the presence or absence of charged ligands or counter ions can also have a marked effect upon the overall charge of a QD. Finally the thermodynamic approach termed thermal charging, a process by which an equilibrium exists between the majority non-charged population of CQDs and a minority of charged CQDs has been used to explain the consistently equal concentrations of negative and positively charged CQDs in solutions in some nonpolar solvents.[253]

The overall effects of these processes allow for the deposition of the charged CQDs upon the TiO_2 electrodes, without the need for a ligand exchange. This avoids issues of QD surface trap formation during the ligand exchange process[71] which leads to an overall reduction in luminesce of ligand exchanged CQDs and also is non-ideal for PV applications. This approach has also demonstrated the advantageous result of better penetration of the porous TiO_2 electrode with the CQD sensitisers, producing a greater loading, and therefore higher incident photon absorption. The CQDs are also deposited close to the TiO_2/TCO junction, reducing efficiency losses affiliated to charge transport in the TiO_2 layer. Other advantages relative to the linker approach is that deposition times can be drastically decreased using electrophoretic deposition.

1.3 Liquid Crystals

The liquid crystal phase is mesophase that has a level of molecular order in between the liquid phase and crystalline solid phase; it shows imperfect molecular ordering, extending to the microscopic but generally not, the macroscopic scale (Figure 1.17). This gives rise to the properties of liquid crystals ,some of which are found in the liquid phase (e. g. fluidity, inability to support shear, formation and coalescence of droplets) and some of which are found in the solid phase (anisotropy in optical, electrical, and magnetic properties, periodic arrangement of molecules in one spatial direction).[254] Liquid crystals adopt three categories of distinct mesophase, the nematic phase, the smectic phases and the columnar. Liquid crystal molecules are generally anisotropic in shape and are categorised upon this as a discotic if plate like in shape or calamitic when rod like in shape. In addition, if the LC phase is found at a temperature

range in between the liquid (isotropic) phase and the crystalline phase, it is termed a thermotropic liquid crystal.

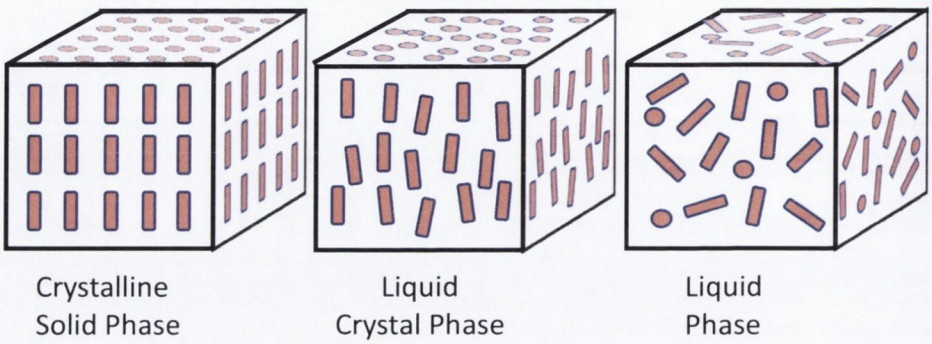

Figure 1.17. Diagram showing the difference in order on the molecular scale between the solid crystalline phase, the liquid crystal phase and the liquid phase

1.3.1 Discotic Liquid Crystals

Discotic Liquid Crystals (DLC) are a class of liquid crystals which are disc shaped, consisting of an aromatic mesogen with a range of long alkyl chain substituents. The mesophases exhibited by these disk-like structures can be classified into three distinct types: columnar (col) (Figure 1.19), discotic-nematic (N d), and discotic-lamellar. A range of different organic molecules have been shown to exhibit a discotic liquid crystal phase including, anthracenes,[255] perylenes,[256] triphenylenes,[257-259] dibenzopyrenes[260] and hexabenzocoronens[261-263] (HBC).

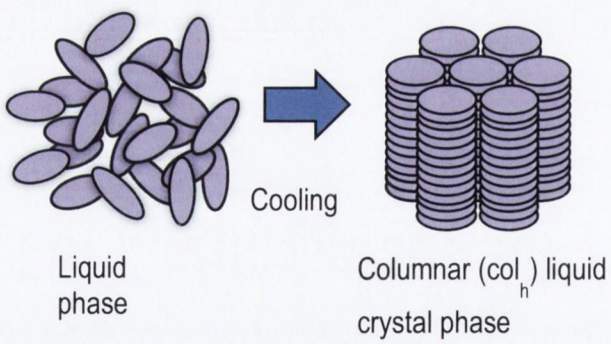

Figure 1.18 The change from cooling from the liquid phase to the self-organised columnar liquid crystal phase

The columnar mesophase is of particular interest due to the self-organisation of the disk molecules into an aligned stack formation. This phase shows unique electrical properties due to the π-overlap of the stacked aromatic systems, which gives rise to an anisotropic conductivity, producing a strong rise in conductivity parallel to the columns, which is due to an increase in charge-carrier mobility through the columns. The particular arrangement of these columns relative to each then gives rise to a subcategories related to the symmetry produced, several variations of which have been identified including a hexagonal lattice (Col $_h$), rectangular lattice (Col $_r$), and an oblique lattice (Col $_{ob}$).

1.3.2 Discotic Liquid Crystal Devices

Several DLCs have been tested in photovoltaic devices to date,[264-270] with the highest reported power conversion efficiency of 2 %.[269] While also interestingly a device demonstrated a PCE of 0.35% for a purely using, a donor-acceptor junction formed from non-DLC HBC.[268] DLCs, specifically triphenylenes , have also shown application as an additive to existing organic solar cell designs and have shown an efficiency boost of up to 35 % achieving a PCE of 3.5 % in a poly(3-hexylthiophene):(6,6)-phenyl-C_{61}-butyric acid methyl ester (P3HT:PC61BM) bulk-heterojunction organic photovoltaic (BHJ OPVs) cell under one sun. [271] While a boost of 31 %, achieving a PCE of 3.97 % under one sun was achieved on another P3HT:PC61BM based BHJ OPV cell. [272]

1.3.3 Liquid Crystal QD Composites

Some work has been published on the properties of quantum dot liquid crystal composites,[273-278] testing the effects upon optoelectronic properties, though only one study carried out by our collaborators ,[273] the exact effects upon discotic liquid crystals. Initial studies carried out by our collaborators have shown that upon the addition of CdSe quantum dots to another DLC triphenylene, H4TP, a large increase in the DC conductivity was measured, of two orders of magnitude when using a 1 % doping of 2.4 nm CdSe QDs. This was explained through the assumption of a donor –acceptor system between the CdSe QDs and the H4TP. Therefore, due to the increase in conductivity these composites were identified as potential photovoltaic materials.

1.4 Aims and Objectives of Project

The main goal of our project is to develop a range of quantum dot based nanomaterials and test them in selected energy harvesting devices such as photoanodes and photovoltaic cells of various designs. This overall goal will be achieved through a number of steps described below:

- Synthesis of a range of high quality quantumly confined nanostructures based on Cd or Pb chalcogenides using a hot injection approach with a range of optical properties, with the aim of tailoring these materials for application as an absorbing layer in a photon harvesting/detecting device.
- Explore the application of cation exchange as a means to access other novel nanostructures which demonstrate novel optical properties, and which are not readily accessible through hot injection using pre-synthesised nanostructures.

- Investigate the application of post synthesis treatments using oleylamine based halide solutions as a means to increase passivation of QD surfaces, which should also decrease recombination losses when incorporated into a PV device.
- Determine and optimise the use of electrophoretic deposition as a means to fabricate a QD sensitised TiO_2 electrode, demonstrating the versatility of the approach by applying a range of different Cd and Pb based QDs to the TiO_2 surface.
- Establish the effects of post-electrophoretic deposition treatments upon CdSe sensitised TiO_2 electrodes, investigating the effects of bulk semiconductor deposition and ligand exchange as a means to increase the determined photocurrent response of the electrodes to illumination.
- Demonstrate the approach of cation exchange as a means to alter QD sensitised TiO_2 electrodes, enabling a novel route to drastically altering the optical properties of QD sensitised electrodes.
- Carry out an in-depth study into QDSSC fabrication, focusing on the optimal TiO_2 electrode, and counter electrode for this device, followed by demonstration of working QDSSC device using these components.
- Investigate a novel technique for DHCQD cell fabrication using more commercially viable techniques, including screen-printing of the TiO_2 electrode and dip coating to deposit the QD films.
- Finally, we investigate the optical and electrical properties of novel QD discotic liquid crystal composites, with the intention of testing a discotic liquid crystal solar cell.

We believe that through these goals, this project will contribute to future development of quantum dots solar energy harvesting technologies.

References

1. Evarestov, R. A., *Quantum Chemistry of Solids: The LCAO First Principles Treatment of Crystals*. Springer: 2007.
2. Solymar, L.; Walsh, D.; Syms, R. R. A., *Electrical Properties of Materials*. OUP Oxford: 2014.
3. Scholes, G. D.; Rumbles, G., Excitons in Nanoscale Systems. *Nature Materials* 2006, 5, 920-920.
4. Zhang, S. B.; Wei, S. H.; Zunger, A., Intrinsic N-Type Versus P-Type Doping Asymmetry and the Defect Physics of Zno. *Phys. Rev. B* 2001, 63.
5. Raebiger, H.; Lany, S.; Zunger, A., Origins of the P-Type Nature and Cation Deficiency in Cu_2o and Related Materials. *Phys. Rev. B* 2007, 76.
6. Tersoff, J., Schottky Barrier Heights and the Continuum of Gap States. *Physical Review Letters* 1984, 52, 465-468.
7. Tung, R. T., Recent Advances in Schottky Barrier Concepts. *Materials Science and Engineering: R: Reports* 2001, 35, 1-138.
8. Tung, R. T., Schottky Barrier Height—Do We Really Understand What We Measure? *Journal of Vacuum Science & Technology B* 1993, 11, 1546-1552.
9. Herron, N.; Calabrese, J. C.; Farneth, W. E.; Wang, Y., Crystal Structure and Optical Properties of $Cd_{32}s_{14}(Sc_6h_5)_{36}$. Dmf4, a Cluster with a 15 Angstrom Cds Core. *Science* 1993, 259, 1426-1428.
10. Brus, L., Electronic Wave Functions in Semiconductor Clusters: Experiment and Theory. *The Journal of Physical Chemistry* 1986, 90, 2555-2560.
11. Norris, D. J.; Bawendi, M. G., Measurement and Assignment of the Size-Dependent Optical Spectrum in Cdse Quantum Dots. *Phys. Rev. B* 1996, 53, 16338-16346.
12. Kamat, P. V., Quantum Dot Solar Cells. Semiconductor Nanocrystals as Light Harvesters. *Journal of Physical Chemistry C* 2008, 112, 18737-18753.
13. Kasuya, A.; Sivamohan, R.; Barnakov, Y. A.; Dmitruk, I. M.; Nirasawa, T.; Romanyuk, V. R.; Kumar, V.; Mamykin, S. V.; Tohji, K.; Jeyadevan, B.; Shinoda, K.; Kudo, T.; Terasaki, O.; Liu, Z.; Belosludov, R. V.; Sundararajan, V.; Kawazoe, Y., Ultra-Stable Nanoparticles of Cdse Revealed from Mass Spectrometry. *Nat. Mater.* 2004, 3, 99-102.
14. Kudera, S.; Zanella, M.; Giannini, C.; Rizzo, A.; Li, Y.; Gigli, G.; Cingolani, R.; Ciccarella, G.; Spahl, W.; Parak, W. J.; Manna, L., Sequential Growth of Magic-Size Cdse Nanocrystals. *Advanced Materials* 2007, 19, 548-552.
15. Nirmal, M.; Norris, D. J.; Kuno, M.; Bawendi, M. G.; Efros, A. L.; Rosen, M., Observation of the "Dark Exciton" in Cdse Quantum Dots. *Physical Review Letters* 1995, 75, 3728-3731.
16. Ouyang, J.; Kuijper, J.; Brot, S.; Kingston, D.; Wu, X.; Leek, D. M.; Hu, M. Z.; Ripmeester, J. A.; Yu, K., Photoluminescent Colloidal Cds Nanocrystals with High Quality Via Noninjection One-Pot Synthesis in 1-Octadecene. *The Journal of Physical Chemistry C* 2009, 113, 7579-7593.
17. Yu, W. W.; Peng, X., Formation of High-Quality Cds and Other Ii–Vi Semiconductor Nanocrystals in Noncoordinating Solvents: Tunable Reactivity of Monomers. *Angewandte Chemie International Edition* 2002, 41, 2368-2371.
18. Wageh, S.; Ling, Z. S.; Xu-Rong, X., Growth and Optical Properties of Colloidal Zns Nanoparticles. *J. Cryst. Growth* 2003, 255, 332-337.
19. Wang, W. Z.; Germanenko, I.; El-Shall, M. S., Room-Temperature Synthesis and Characterization of Nanocrystalline CdS, ZnS, and $Cd_xZn_{1-x}S$. *Chem. Mat.* 2002, 14, 3028-3033.
20. Li, Y. D.; Ding, Y.; Zhang, Y.; Qian, Y. T., Photophysical Properties of Zns Quantum Dots. *J. Phys. Chem. Solids* 1999, 60, 13-15.
21. Chen, H. S.; Lo, B.; Hwang, J. Y.; Chang, G. Y.; Chen, C. M.; Tasi, S. J.; Wang, S. J. J., Colloidal Znse, ZnSe/ZnS, and ZnSe/ZnSes Quantum Dots Synthesized from Zno. *Journal of Physical Chemistry B* 2004, 108, 17119-17123.

22. Hines, M. A.; Guyot-Sionnest, P., Bright UV-Blue Luminescent Colloidal ZnSe Nanocrystals. *Journal of Physical Chemistry B* 1998, 102, 3655-3657.
23. Zheng, Y. G.; Yang, Z. C.; Ying, J. Y., Aqueous Synthesis of Glutathione-Capped ZnSe and $Zn_{1-x}Cd_xSe$ Alloyed Quantum Dots. *Advanced Materials* 2007, 19, 1475-+.
24. Guzelian, A. A.; Katari, J. E. B.; Kadavanich, A. V.; Banin, U.; Hamad, K.; Juban, E.; Alivisatos, A. P.; Wolters, R. H.; Arnold, C. C.; Heath, J. R., Synthesis of Size-Selected, Surface-Passivated Inp Nanocrystals. *Journal of Physical Chemistry* 1996, 100, 7212-7219.
25. Vinokurov, A. A.; Dorofeev, S. G.; Znamenkov, K. O.; Panfilova, A. V.; Kuznetsova, T. A., Synthesis of Inp Quantum Dots in Dodecylamine from Phosphine and Indium(Iii) Chloride. *Mendeleev Communications* 2010, 20, 31-32.
26. Micic, O. I.; Cheong, H. M.; Fu, H.; Zunger, A.; Sprague, J. R.; Mascarenhas, A.; Nozik, A. J., Size-Dependent Spectroscopy of InP Quantum Dots. *Journal of Physical Chemistry B* 1997, 101, 4904-4912.
27. Liu, Z.; Kumbhar, A.; Xu, D.; Zhang, J.; Sun, Z.; Fang, J., Coreduction Colloidal Synthesis of Iii-V Nanocrystals: The Case of InP. *Angewandte Chemie International Edition* 2008, 47, 3540-2.
28. Guzelian, A. A.; Banin, U.; Kadavanich, A. V.; Peng, X.; Alivisatos, A. P., Colloidal Chemical Synthesis and Characterization of InAs Nanocrystal Quantum Dots. *Appl. Phys. Lett.* 1996, 69, 1432-1434.
29. Krier, A.; Huang, X. L.; Hammiche, A., Liquid Phase Epitaxial Growth and Morphology of Insb Quantum Dots. *J. Phys. D-Appl. Phys.* 2001, 34, 874-878.
30. Moreels, I.; Lambert, K.; Smeets, D.; De Muynck, D.; Nollet, T.; Martins, J. C.; Vanhaecke, F.; Vantomme, A.; Delerue, C.; Allan, G.; Hens, Z., Size-Dependent Optical Properties of Colloidal PbS Quantum Dots. *ACS Nano* 2009, 3, 3023-3030.
31. Hines, M. A.; Scholes, G. D., Colloidal Pbs Nanocrystals with Size-Tunable near-Infrared Emission: Observation of Post-Synthesis Self-Narrowing of the Particle Size Distribution. *Advanced Materials* 2003, 15, 1844-1849.
32. Evans, C. M.; Guo, L.; Peterson, J. J.; Maccagnano-Zacher, S.; Krauss, T. D., Ultrabright PbSe Magic-Sized Clusters. *Nano Lett* 2008, 8, 2896-2899.
33. Li, H.; Chen, D.; Li, L.; Tang, F.; Zhang, L.; Ren, J., Size- and Shape-Controlled Synthesis of PbSe and PbS Nanocrystals Via a Facile Method. *CrystEngComm* 2010, 12, 1127.
34. Ellingson, R. J.; Beard, M. C.; Johnson, J. C.; Yu, P. R.; Micic, O. I.; Nozik, A. J.; Shabaev, A.; Efros, A. L., Highly Efficient Multiple Exciton Generation in Colloidal PbSe and PbS Quantum Dots. *Nano Letters* 2005, 5, 865-871.
35. Bae, W. K.; Joo, J.; Padilha, L. A.; Won, J.; Lee, D. C.; Lin, Q.; Koh, W.-k.; Luo, H.; Klimov, V. I.; Pietryga, J. M., Highly Effective Surface Passivation of Pbse Quantum Dots through Reaction with Molecular Chlorine. *Journal of the American Chemical Society* 2012, 134, 20160-20168.
36. Lin, Z.; Wang, M.; Wei, L.; Song, X.; Xue, Y.; Yao, X., PbTe Colloidal Nanocrystals: Synthesis, Mechanism and Infrared Optical Characteristics. *Journal of Alloys and Compounds* 2011, 509, 5047-5049.
37. Murphy, J. E.; Beard, M. C.; Norman, A. G.; Ahrenkiel, S. P.; Johnson, J. C.; Yu, P. R.; Micic, O. I.; Ellingson, R. J.; Nozik, A. J., PbTe Colloidal Nanocrystals: Synthesis, Characterization, and Multiple Exciton Generation. *Journal of the American Chemical Society* 2006, 128, 3241-3247.
38. Xu, Y.; Al-Salim, N.; Bumby, C. W.; Tilley, R. D., Synthesis of SnS Quantum Dots. *Journal of the American Chemical Society* 2009, 131, 15990-+.
39. Li, Z.; Peng, L. W.; Fang, Y. G.; Chen, Z. W.; Pan, D. Y.; Wu, M. H., Synthesis of Colloidal Snse Quantum Dots by Electron Beam Irradiation. *Radiat. Phys. Chem.* 2011, 80, 1333-1336.
40. Xie, R.; Zhang, J.; Zhao, F.; Yang, W.; Peng, X., Synthesis of Monodisperse, Highly Emissive, and Size-Tunable Cd_3P_2 Nanocrystals. *Chem. Mat.* 2010, 22, 3820-3822.

41. Harris, D. K.; Allen, P. M.; Han, H. S.; Walker, B. J.; Lee, J. M.; Bawendi, M. G., Synthesis of Cadmium Arsenide Quantum Dots Luminescent in the Infrared. *Journal of the American Chemical Society* 2011, 133, 4676-4679.

42. Chen, L.-Y.; Yang, P.-A.; Tseng, C.-H.; Hwang, B.-J.; Chen, C.-H., Internal Structure of Tunable Ternary $CdSe_xS_{1-x}$ Quantum Dots Unraveled by X-Ray Absorption Spectroscopy. *Appl. Phys. Lett.* 2012, 100.

43. Wang, B.; Jiang, Y.; Liu, C.; Lan, X.; Liu, X.; Wang, W.; Duan, H.; Zhang, Y.; Li, S.; Zhang, Z., One-Pot Synthesis of Homogeneous $CdSe_xS_{1-x}$ Alloyed Quantum Dots with Tunable Composition in a Green N-Oleoylmorpholine Solvent. *Physica Status Solidi a-Applications and Materials Science* 2012, 209, 306-312.

44. Yu, K.; Ouyang, J.; Zhang, Y.; Tung, H.-T.; Lin, S.; Nagelkerke, R. A. L.; Kingston, D.; Wu, X.; Leek, D. M.; Wilkinson, D.; Li, C.; Chen, I.-G.; Tao, Y., Low-Temperature Noninjection Approach to Homogeneously-Alloyed $PbSe_xS_{1-x}$ Colloidal Nanocrystals for Photovoltaic Applications. *ACS Applied Materials & Interfaces* 2011, 3, 1511-1520.

45. Zhong, H. Z.; Zhou, Y.; Ye, M. F.; He, Y. J.; Ye, J. P.; He, C.; Yang, C. H.; Li, Y. F., Controlled Synthesis and Optical Properties of Colloidal Ternary Chalcogenide $CuInS_2$ Nanocrystals. *Chem. Mat.* 2008, 20, 6434-6443.

46. Allen, P. M.; Bawendi, M. G., Ternary I–Iii–Vi Quantum Dots Luminescent in the Red to near-Infrared. *Journal of the American Chemical Society* 2008, 130, 9240-9241.

47. Deng, Z. T.; Yan, H.; Liu, Y., Band Gap Engineering of Quaternary-Alloyed ZnCdSSe Quantum Dots Via a Facile Phosphine-Free Colloidal Method. *Journal of the American Chemical Society* 2009, 131, 17744-17745.

48. Zhang, J.; Xie, R. G.; Yang, W. S., A Simple Route for Highly Luminescent Quaternary Cu-Zn-in-S Nanocrystal Emitters. *Chem. Mat.* 2011, 23, 3357-3361.

49. Yu, W. W.; Qu, L. H.; Guo, W. Z.; Peng, X. G., Experimental Determination of the Extinction Coefficient of CdTe, CdSe and CdS Nanocrystals. *Chem. Mat.* 2004, 16, 560-560.

50. Jasieniak, J.; Smith, L.; van Embden, J.; Mulvaney, P.; Califano, M., Re-Examination of the Size-Dependent Absorption Properties of CdSe Quantum Dots. *Journal of Physical Chemistry C* 2009, 113, 19468-19474.

51. Dai, Q. Q.; Wang, Y. N.; Li, X. B.; Zhang, Y.; Pellegrino, D. J.; Zhao, M. X.; Zou, B.; Seo, J.; Wang, Y. D.; Yu, W. W., Size-Dependent Composition and Molar Extinction Coefficient of PbSe Semiconductor Nanocrystals. *ACS Nano* 2009, 3, 1518-1524.

52. Cademartiri, L.; Montanari, E.; Calestani, G.; Migliori, A.; Guagliardi, A.; Ozin, G. A., Size-Dependent Extinction Coefficients of PbS Quantum Dots. *Journal of the American Chemical Society* 2006, 128, 10337-10346.

53. Ekimov, A. I.; Hache, F.; Schanneklein, M. C.; Ricard, D.; Flytzanis, C.; Kudryavtsev, I. A.; Yazeva, T. V.; Rodina, A. V.; Efros, A. L., Absorption and Intensity-Dependent Photoluminescence Measurements on CdSe Quantum Dots - Assignments of the First Electronic Transitions. *J. Opt. Soc. Am. B-Opt. Phys.* 1993, 10, 100-107.

54. Du, H.; Chen, C. L.; Krishnan, R.; Krauss, T. D.; Harbold, J. M.; Wise, F. W.; Thomas, M. G.; Silcox, J., Optical Properties of Colloidal PbSe Nanocrystals. *Nano Letters* 2002, 2, 1321-1324.

55. Ikezawa, M.; Masumoto, Y., Ultranarrow Homogeneous Broadening of Confined Excitons in Quantum Dots: Effect of the Surrounding Matrix. *Phys. Rev. B* 2000, 61, 12662-12665.

56. Arzberger, M.; Amann, M. C., Homogeneous Line Broadening in Individual Semiconductor Quantum Dots by Temperature Fluctuations. *Phys. Rev. B* 2000, 62, 11029-11037.

57. Efros, A. L.; Rosen, M.; Kuno, M.; Nirmal, M.; Norris, D. J.; Bawendi, M., Band-Edge Exciton in Quantum Dots of Semiconductors with a Degenerate Valence Band: Dark and Bright Exciton States. *Phys. Rev. B* 1996, 54, 4843-4856.

58. Burda, C.; Chen, X. B.; Narayanan, R.; El-Sayed, M. A., Chemistry and Properties of Nanocrystals of Different Shapes. *Chem. Rev.* 2005, 105, 1025-1102.

59. Lin, K. F.; Cheng, H. M.; Hsu, H. C.; Lin, L. J.; Hsieh, W. F., Band Gap Variation of Size-Controlled Zno Quantum Dots Synthesized by Sol-Gel Method. *Chem. Phys. Lett.* 2005, 409, 208-211.

60. Liu, S.; Zhang, H. W.; Swihart, M. T., Spray Pyrolysis Synthesis of ZnS Nanoparticles from a Single-Source Precursor. *Nanotechnology* 2009, 20, 8.

61. Heinrichsdorff, F.; Mao, M. H.; Kirstaedter, N.; Krost, A.; Bimberg, D.; Kosogov, A. O.; Werner, P., Room-Temperature Continuous-Wave Lasing from Stacked InAs/GaAs Quantum Dots Grown by Metalorganic Chemical Vapor Deposition. *Appl. Phys. Lett.* 1997, 71, 22-24.

62. Tatebayashi, J.; Nishioka, M.; Arakawa, Y., Over 1.5 Mm Light Emission from Inas Quantum Dots Embedded in Ingaas Strain-Reducing Layer Grown by Metalorganic Chemical Vapor Deposition. *Appl. Phys. Lett.* 2001, 78, 3469-3471.

63. Oshinowo, J.; Nishioka, M.; Ishida, S.; Arakawa, Y., Highly Uniform InGaAs/GaAs Quantum Dots (- 15 Nm) by Metalorganic Chemical Vapor Deposition. *Appl. Phys. Lett.* 1994, 65, 1421-1423.

64. Marzin, J. Y.; Gerard, J. M.; Izrael, A.; Barrier, D.; Bastard, G., Photoluminescence of Single Inas Quantum Dots Obtained by Self-Organized Growth on GaAs. *Physical Review Letters* 1994, 73, 716-719.

65. Ustinov, V. M.; Maleev, N. A.; Zhukov, A. E.; Kovsh, A. R.; Egorov, A. Y.; Lunev, A. V.; Volovik, B. V.; Krestnikov, I. L.; Musikhin, Y. G.; Bert, N. A.; Kop'ev, P. S.; Alferov, Z. I.; Ledentsov, N. N.; Bimberg, D., Inas/Ingaas Quantum Dot Structures on GaAs Substrates Emitting at 1.3 μm. *Appl. Phys. Lett.* 1999, 74, 2815-2817.

66. Xin, S. H.; Wang, P. D.; Yin, A.; Kim, C.; Dobrowolska, M.; Merz, J. L.; Furdyna, J. K., Formation of Self-Assembling Cdse Quantum Dots on ZnSe by Molecular Beam Epitaxy. *Appl. Phys. Lett.* 1996, 69, 3884-3886.

67. Mirin, R. P.; Ibbetson, J. P.; Nishi, K.; Gossard, A. C.; Bowers, J. E., 1.3 μm Photoluminescence from Ingaas Quantum Dots on GaAs. *Appl. Phys. Lett.* 1995, 67, 3795-3797.

68. Chang, C. H.; Lee, Y. L., Chemical Bath Deposition of CdS Quantum Dots onto Mesoscopic Tio_2 Films for Application in Quantum-Dot-Sensitized Solar Cells. *Appl. Phys. Lett.* 2007, 91, 3.

69. Sturzenbaum, S. R.; Hockner, M.; Panneerselvam, A.; Levitt, J.; Bouillard, J. S.; Taniguchi, S.; Dailey, L. A.; Khanbeigi, R. A.; Rosca, E. V.; Thanou, M.; Suhling, K.; Zayats, A. V.; Green, M., Biosynthesis of Luminescent Quantum Dots in an Earthworm. *Nature Nanotechnology* 2013, 8, 57-60.

70. Moon, J. W.; Ivanov, I. N.; Duty, C. E.; Love, L. J.; Rondinone, A. J.; Wang, W.; Li, Y. L.; Madden, A. S.; Mosher, J. J.; Hu, M. Z.; Suresh, A. K.; Rawn, C. J.; Jung, H.; Lauf, R. J.; Phelps, T. J., Scalable Economic Extracellular Synthesis of Cds Nanostructured Particles by a Non-Pathogenic Thermophile. *Journal of Industrial Microbiology & Biotechnology* 2013, 40, 1263-1271.

71. Baker, D. R.; Kamat, P. V., Tuning the Emission of CdSe Quantum Dots by Controlled Trap Enhancement. *Langmuir* 2010, 26, 11272-11276.

72. Aldana, J.; Wang, Y. A.; Peng, X., Photochemical Instability of CdSe Nanocrystals Coated by Hydrophilic Thiols. *Journal of the American Chemical Society* 2001, 123, 8844-8850.

73. Liang, Y.; Thorne, J. E.; Parkinson, B. A., Controlling the Electronic Coupling between CdSe Quantum Dots and Thiol Capping Ligands Via Ph and Ligand Selection. *Langmuir* 2012, 28, 11072-11077.

74. Tan, Y.; Jin, S.; Hamers, R. J., Influence of Hole-Sequestering Ligands on the Photostability of CdSe Quantum Dots. *The Journal of Physical Chemistry C* 2012, 117, 313-320.

75. Wang, Y.; Wang, L.; Waldeck, D. H., Electrochemically Guided Photovoltaic Devices: A Photocurrent Study of the Charge Transfer Directionality between CdTe and CdSe Nanoparticles. *The Journal of Physical Chemistry C* 2011, 115, 18136-18141.
76. Byun, H. J.; Lee, J. C.; Yang, H., Solvothermal Synthesis of Inp Quantum Dots and Their Enhanced Luminescent Efficiency by Post-Synthetic Treatments. *J. Colloid Interface Sci.* 2011, 355, 35-41.
77. Li, T. L.; Teng, H. S., Solution Synthesis of High-Quality $CuIns_2$ Quantum Dots as Sensitizers for Tio_2 Photoelectrodes. *J. Mater. Chem.* 2010, 20, 3656-3664.
78. Wang, Q. A.; Pan, D. C.; Jiang, S. C.; Ji, X. L.; An, L. J.; Jiang, B. Z., Luminescent Cdse and CdSe/CdS Core-Shell Nanocrystals Synthesized Via a Combination of Solvothermal and Two-Phase Thermal Routes. *J. Lumines.* 2006, 118, 91-98.
79. Gerbec, J. A.; Magana, D.; Washington, A.; Strouse, G. F., Microwave-Enhanced Reaction Rates for Nanoparticle Synthesis. *Journal of the American Chemical Society* 2005, 127, 15791-15800.
80. Chu, M. Q.; Shen, X. Y.; Liu, G. J., Microwave Irradiation Method for the Synthesis of Water-Soluble CdSe Nanoparticles with Narrow Photoluminescent Emission in Aqueous Solution. *Nanotechnology* 2006, 17, 444-449.
81. Yin, Y. D.; Xu, X. L.; Ge, X. W.; Lu, Y.; Zhang, Z. C., Synthesis and Characterization of ZnS Colloidal Particles Via Gamma-Radiation. *Radiat. Phys. Chem.* 1999, 55, 353-356.
82. Ge, X. W.; Ni, Y. H.; Zhang, Z. C., A Novel Route to Prepare Cadmium Sulfide Nano-Rods. *Radiat. Phys. Chem.* 2002, 64, 223-227.
83. Yang, Q.; Tang, K. B.; Wang, F.; Wang, C. R.; Qian, Y. T., A Gamma-Irradiation Reduction Route to Nanocrystalline Cde (E = Se, Te) at Room Temperature. *Mater. Lett.* 2003, 57, 3508-3512.
84. Ni, Y. H.; Ge, X. W.; Liu, H. R.; Xu, X. L.; Zhang, Z. C., Gamma-Irradiation Preparation of CdS Nano-Particles and Their Formation Mechanism in Non-Water System. *Radiat. Phys. Chem.* 2001, 61, 61-64.
85. Murray, C. B.; Norris, D. J.; Bawendi, M. G., Synthesis and Characterization of Nearly Monodisperse Cde (E = Sulfur, Selenium, Tellurium) Semiconductor Nanocrystallites. *Journal of the American Chemical Society* 1993, 115, 8706-8715.
86. Reiss, P.; Protiere, M.; Li, L., Core/Shell Semiconductor Nanocrystals. *Small* 2009, 5, 154-68.
87. Talapin, D. V.; Koeppe, R.; Gotzinger, S.; Kornowski, A.; Lupton, J. M.; Rogach, A. L.; Benson, O.; Feldmann, J.; Weller, H., Highly Emissive Colloidal CdSe/CdS Heterostructures of Mixed Dimensionality. *Nano Lett* 2003, 3, 1677-1681.
88. Carbone, L.; Nobile, C.; De Giorgi, M.; Sala, F. D.; Morello, G.; Pompa, P.; Hytch, M.; Snoeck, E.; Fiore, A.; Franchini, I. R.; Nadasan, M.; Silvestre, A. F.; Chiodo, L.; Kudera, S.; Cingolani, R.; Krahne, R.; Manna, L., Synthesis and Micrometer-Scale Assembly of Colloidal Cdse/Cds Nanorods Prepared by a Seeded Growth Approach. *Nano Lett* 2007, 7, 2942-2950.
89. Talapin, D. V.; Nelson, J. H.; Shevchenko, E. V.; Aloni, S.; Sadtler, B.; Alivisatos, A. P., Seeded Growth of Highly Luminescent CdSe/CdS Nanoheterostructures with Rod and Tetrapod Morphologies. *Nano Lett* 2007, 7, 2951-2959.
90. Luo, Y.; Wang, L. W., Electronic Structures of the CdSe/CdS Core-Shell Nanorods. *ACS Nano* 2010, 4, 91-98.
91. Reiss, P.; Bleuse, J.; Pron, A., Highly Luminescent CdSe/ZnSe Core/Shell Nanocrystals of Low Size Dispersion. *Nano Lett* 2002, 2, 781-784.
92. Lee, S. H.; Song, K. K., Highly Luminescent (ZnSe)ZnS Core-Shell Quantum Dots: Synthesis and Characterization. *Abstr. Pap. Am. Chem. Soc.* 2000, 219, U825-U825.
93. Neo, M. S.; Venkatram, N.; Li, G. S.; Chin, W. S.; Ji, W., Synthesis of PbS/CdS Core-Shell Qds and Their Nonlinear Optical Properties. *Journal of Physical Chemistry C* 2010, 114, 18037-18044.

94. Haubold, S.; Haase, M.; Kornowski, A.; Weller, H., Strongly Luminescent InP/ZnS Core-Shell Nanoparticles. *ChemPhysChem* 2001, 2, 331-334.
95. Du, F. F.; Zhang, H.; Du, X. L.; Zhu, J.; Zhong, X. H., Controllable Synthesis and Optical Properties of CdS/CdSe Hetero-Nanostructures with Various Dimensionalities. *Mater. Chem. Phys.* 2010, 121, 118-124.
96. Shen, H. B.; Yuan, H.; Niu, J. Z.; Xu, S. S.; Zhou, C. H.; Ma, L.; Li, L. S., Phosphine-Free Synthesis of High-Quality Reverse Type-I Znse/Cdse Core with CdS/$Cd_xZn_{1-x}S$/ZnS Multishell Nanocrystals and Their Application for Detection of Human Hepatitis B Surface Antigen. *Nanotechnology* 2011, 22.
97. Wang, S.; Wang, L.-W., Exciton Dissociation in CdSe/CdTe Heterostructure Nanorods. *The Journal of Physical Chemistry Letters* 2010, 2, 1-6.
98. Lo, S. S.; Khan, Y.; Jones, M.; Scholes, G. D., Temperature and Solvent Dependence of CdSe/CdTe Heterostructure Nanorod Spectra. *J. Chem. Phys.* 2009, 131.
99. Guan, J. Synthesis and Characterisation ZnTe/ZnSe Core-Shell Tunable Quantum Dots.Pdf. MIT, 2008.
100. Talapin, D. V.; Mekis, I.; Gotzinger, S.; Kornowski, A.; Benson, O.; Weller, H., CdSe/CdS/ZnS and CdSe/ZnSe/ZnS Core-Shell-Shell Nanocrystals. *Journal of Physical Chemistry B* 2004, 108, 18826-18831.
101. Green, M.; Williamson, P.; Samalova, M.; Davis, J.; Brovelli, S.; Dobson, P.; Cacialli, F., Synthesis of Type Ii/Type I CdTe/CdS/ZnS Quantum Dots and Their Use in Cellular Imaging. *J. Mater. Chem.* 2009, 19, 8341.
102. Freund, L. B.; Suresh, S., *Thin Film Materials: Stress, Defect Formation, and Surface Evolution*. Cambridge University Press: 2003.
103. Smith, A. M.; Mohs, A. M.; Nie, S., Tuning the Optical and Electronic Properties of Colloidal Nanocrystals by Lattice Strain. *Nature nanotechnology* 2009, 4, 56-63.
104. Al-Douri, Y.; Abid, H.; Aourag, H., Calculation of Bulk Moduli of Semiconductor Compounds. *Physica B: Condensed Matter* 2002, 322, 179-182.
105. Oshinowo, J.; Nishioka, M.; Ishida, S.; Arakawa, Y., Highly Uniform InGaAs/GaAs Quantum Dots (∼15 Nm) by Metalorganic Chemical Vapor Deposition. *Applied Physics Letters* 1994, 65, 1421-1423.
106. Nicolau, Y. F., Solution Deposition of Thin Solid Compound Films by a Successive Ionic-Layer Adsorption and Reaction Process. *Applications of Surface Science* 1985, 22-3, 1061-1074.
107. Park, S.; Clark, B. L.; Keszler, D. A.; Bender, J. P.; Wager, J. F.; Reynolds, T. A.; Herman, G. S., Low-Temperature Thin-Film Deposition and Crystallization. *Science* 2002, 297, 65.
108. Li, J. J.; Wang, Y. A.; Guo, W. Z.; Keay, J. C.; Mishima, T. D.; Johnson, M. B.; Peng, X. G., Large-Scale Synthesis of Nearly Monodisperse CdSe/CdS Core/Shell Nanocrystals Using Air-Stable Reagents Via Successive Ion Layer Adsorption and Reaction. *Journal of the American Chemical Society* 2003, 125, 12567-12575.
109. Talapin, D. V.; Nelson, J. H.; Shevchenko, E. V.; Aloni, S.; Sadtler, B.; Alivisatos, A. P., Seeded Growth of Highly Luminescent CdSe/CdS Nanoheterostructures with Rod and Tetrapod Morphologies. *Nano Letters* 2007, 7, 2951-2959.
110. Cassette, E.; Mahler, B.; Guigner, J.-M.; Patriarche, G.; Dubertret, B.; Pons, T., Colloidal CdSe/CdS Dot-in-Plate Nanocrystals with 2d-Polarized Emission. *ACS Nano* 2012, 6, 6741-6750.
111. Jain, P. K.; Amirav, L.; Aloni, S.; Alivisatos, A. P., Nanoheterostructure Cation Exchange: Anionic Framework Conservation. *Journal of the American Chemical Society* 2010, 132, 9997-9999.
112. Luther, J. M.; Zheng, H. M.; Sadtler, B.; Alivisatos, A. P., Synthesis of PbS Nanorods and Other Ionic Nanocrystals of Complex Morphology by Sequential Cation Exchange Reactions. *Journal of the American Chemical Society* 2009, 131, 16851-16857.

113. Justo, Y.; Goris, B.; Kamal, J. S.; Geiregat, P.; Bals, S.; Hens, Z., Multiple Dot-in-Rod Pbs/Cds Heterostructures with High Photoluminescence Quantum Yield in the near-Infrared. *Journal of the American Chemical Society* 2012, 134, 5484-5487.
114. Jenny, H., Studies on the Mechanism of Ionic Exchange in Colloidal Aluminum Silicates. *The Journal of Physical Chemistry* 1932, 36, 2217-2258
115. Rivest, J. B.; Jain, P. K., Cation Exchange on the Nanoscale: An Emerging Technique for New Material Synthesis, Device Fabrication, and Chemical Sensing. *Chemical Society Reviews* 2013, 42, 89-96.
116. Beberwyck, B. J.; Surendranath, Y.; Alivisatos, A. P., Cation Exchange: A Versatile Tool for Nanomaterials Synthesis. *The Journal of Physical Chemistry C* 2013, 117, 19759-19770.
117. Pietryga, J. M.; Werder, D. J.; Williams, D. J.; Casson, J. L.; Schaller, R. D.; Klimov, V. I.; Hollingsworth, J. A., Utilizing the Lability of Lead Selenide to Produce Heterostructured Nanocrystals with Bright, Stable Infrared Emission. *Journal of the American Chemical Society* 2008, 130, 4879-4885.
118. Bouet, C.; Laufer, D.; Mahler, B.; Nadal, B.; Heuclin, H.; Pedetti, S.; Patriarche, G.; Dubertret, B., Synthesis of Zinc and Lead Chalcogenide Core and Core/Shell Nanoplatelets Using Sequential Cation Exchange Reactions. *Chem. Mat.* 2014.
119. Justo, Y.; Sagar, L. K.; Flamee, S.; Zhao, Q.; Vantomme, A.; Hens, Z., Less Is More. Cation Exchange and the Chemistry of the Nanocrystal Surface. *ACS Nano* 2014.
120. Zhao, H.; Chaker, M.; Wu, N.; Ma, D., Towards Controlled Synthesis and Better Understanding of Highly Luminescent PbS/CdS Core/Shell Quantum Dots. *J. Mater. Chem.* 2011, 21.
121. Zhao, H.; Wang, D.; Zhang, T.; Chaker, M.; Ma, D., Two-Step Synthesis of High-Quality Water-Soluble near-Infrared Emitting Quantum Dots Via Amphiphilic Polymers. *Chemical Communications* 2010, 46.
122. Adel, P.; Wolf, A.; Kodanek, T.; Dorfs, D., Segmented Cdse@Cds/Zns Nanorods Synthesized Via a Partial Ion Exchange Sequence. *Chem. Mat.* 2014, 26, 3121-3127.
123. Groeneveld, E.; Witteman, L.; Lefferts, M.; Ke, X.; Bals, S.; Van Tendeloo, G.; de Mello Donega, C., Tailoring ZnSe–CdSe Colloidal Quantum Dots Via Cation Exchange: From Core/Shell to Alloy Nanocrystals. *ACS Nano* 2013, 7, 7913-7930.
124. Wark, S. E.; Hsia, C.-H.; Son, D. H., Effects of Ion Solvation and Volume Change of Reaction on the Equilibrium and Morphology in Cation-Exchange Reaction of Nanocrystals. *Journal of the American Chemical Society* 2008, 130, 9550-9555.
125. Smith, A. M.; Nie, S., Bright and Compact Alloyed Quantum Dots with Broadly Tunable near-Infrared Absorption and Fluorescence Spectra through Mercury Cation Exchange. *Journal of the American Chemical Society* 2010, 133, 24-26.
126. Gao, D.; Zhang, P.; Jia, J.; Li, M.; Sheng, Z.; Hu, D.; Gong, P.; Wan, Q.; Cai, L., Ultrasmall Paramagnetic near Infrared Quantum Dots as Dual Modal Nanoprobes. *RSC Advances* 2013, 3, 21247-21250.
127. Kim, S.; Kim, T.; Kang, M.; Kwak, S. K.; Yoo, T. W.; Park, L. S.; Yang, I.; Hwang, S.; Lee, J. E.; Kim, S. K.; Kim, S.-W., Highly Luminescent InP/GaP/ZnS Nanocrystals and Their Application to White Light-Emitting Diodes. *Journal of the American Chemical Society* 2012, 134, 3804-3809.
128. Beberwyck, B. J.; Alivisatos, A. P., Ion Exchange Synthesis of III–V Nanocrystals. *Journal of the American Chemical Society* 2012, 134, 19977-19980.
129. Eilers, J.; Groeneveld, E.; de Mello Donegá, C.; Meijerink, A., Optical Properties of Mn-Doped ZnTe Magic Size Nanocrystals. *The Journal of Physical Chemistry Letters* 2012, 3, 1663-1667.
130. Gao, Y. N.; Aerts, M.; Sandeep, C. S. S.; Talgorn, E.; Savenije, T. J.; Kinge, S.; Siebbeles, L. D. A.; Houtepen, A. J., Photoconductivity of PbSe Quantum-Dot Solids: Dependence on Ligand Anchor Group and Length. *ACS Nano* 2012, 6, 9606-9614.

131. Zanella, M.; Maserati, L.; Pernia Leal, M.; Prato, M.; Lavieville, R.; Povia, M.; Krahne, R.; Manna, L., Atomic Ligand Passivation of Colloidal Nanocrystal Films Via Their Reaction with Propyltrichlorosilane. *Chem. Mat.* 2013, 25, 1423-1429.
132. Zhitomirsky, D.; Furukawa, M.; Tang, J.; Stadler, P.; Hoogland, S.; Voznyy, O.; Liu, H.; Sargent, E. H., N-Type Colloidal-Quantum-Dot Solids for Photovoltaics. *Advanced Materials* 2012, 24, 6181-6185.
133. Wills, A. W.; Kang, M. S.; Khare, A.; Gladfelter, W. L.; Norris, D. J., Thermally Degradable Ligands for Nanocrystals. *ACS Nano* 2010, 4, 4523-4530.
134. Talgorn, E.; Abellon, R. D.; Kooyman, P. J.; Piris, J.; Savenije, T. J.; Goossens, A.; Houtepen, A. J.; Siebbeles, L. D. A., Supercrystals of Cdse Quantum Dots with High Charge Mobility and Efficient Electron Transfer to TiO_2. *ACS Nano* 2010, 4, 1723-1731.
135. Baumgardner, W. J.; Whitham, K.; Hanrath, T., Confined-but-Connected Quantum Solids Via Controlled Ligand Displacement. *Nano Letters* 2013, 13, 3225-3231.
136. Talapin, D. V.; Lee, J. S.; Kovalenko, M. V.; Shevchenko, E. V., Prospects of Colloidal Nanocrystals for Electronic and Optoelectronic Applications. *Chem. Rev.* 2010, 110, 389-458.
137. Norris, D. J.; Efros, A. L.; Erwin, S. C., Doped Nanocrystals. *Science* 2008, 319, 1776-1779.
138. Jasieniak, J.; Mulvaney, P., From Cd-Rich to Se-Rich – the Manipulation of Cdse Nanocrystal Surface Stoichiometry. *Journal of the American Chemical Society* 2007, 129, 2841-2848.
139. Voznyy, O.; Zhitomirsky, D.; Stadler, P.; Ning, Z.; Hoogland, S.; Sargent, E. H., A Charge-Orbital Balance Picture of Doping in Colloidal Quantum Dot Solids. *ACS Nano* 2012, 6, 8448-8455.
140. Luther, J. M.; Pietryga, J. M., Stoichiometry Control in Quantum Dots: A Viable Analog to Impurity Doping of Bulk Materials. *ACS Nano* 2013, 7, 1845-1849.
141. Talapin, D. V.; Murray, C. B., Pbse Nanocrystal Solids for N- and P-Channel Thin Film Field-Effect Transistors. *Science* 2005, 310, 86-9.
142. Zarghami, M. H.; Liu, Y.; Gibbs, M.; Gebremichael, E.; Webster, C.; Law, M., P-Type Pbse and Pbs Quantum Dot Solids Prepared with Short-Chain Acids and Diacids. *ACS Nano* 2010, 4, 2475-2485.
143. Jeong, K. S.; Tang, J.; Liu, H.; Kim, J.; Schaefer, A. W.; Kemp, K.; Levina, L.; Wang, X.; Hoogland, S.; Debnath, R.; Brzozowski, L.; Sargent, E. H.; Asbury, J. B., Enhanced Mobility-Lifetime Products in Pbs Colloidal Quantum Dot Photovoltaics. *ACS Nano* 2011.
144. Morgan, B. J.; Watson, G. W., Intrinsic N-Type Defect Formation in Tio2: A Comparison of Rutile and Anatase from Gga Plus U Calculations. *Journal of Physical Chemistry C* 2010, 114, 2321-2328.
145. Koleilat, G. I.; Levina, L.; Shukla, H.; Myrskog, S. H.; Hinds, S.; Pattantyus-Abraham, A. G.; Sargent, E. H., Efficient, Stable Infrared Photovoltaics Based on Solution-Cast Colloidal Quantum Dots. *ACS Nano* 2008, 2, 833-840.
146. Tang, J.; Wang, X. H.; Brzozowski, L.; Barkhouse, D. A. R.; Debnath, R.; Levina, L.; Sargent, E. H., Schottky Quantum Dot Solar Cells Stable in Air under Solar Illumination. *Advanced Materials* 2010, 22, 1398-+.
147. Ginley, D. S.; Cahen, D., *Fundamentals of Materials for Energy and Environmental Sustainability*. Cambridge University Press: 2011.
148. Shockley, W.; Queisser, H. J., Detailed Balance Limit of Efficiency of P-N Junction Solar Cells. *Journal of Applied Physics* 1961, 32, 510-&.
149. Queisser, H. J., Detailed Balance Limit for Solar Cell Efficiency. *Materials Science and Engineering: B* 2009, 159-160, 322-328.
150. Clifford, J. N.; Palomares, E.; Nazeeruddin, M. K.; Grätzel, M.; Nelson, J.; Li, X.; Long, N. J.; Durrant, J. R., Molecular Control of Recombination Dynamics in Dye-Sensitized Nanocrystalline Tio_2 Films: Free Energy Vs Distance Dependence. *Journal of the American Chemical Society* 2004, 126, 5225-5233.

151. Oregan, B.; Gratzel, M., A Low-Cost, High-Efficiency Solar-Cell Based on Dye-Sensitized Colloidal TiO_2 Films. *Nature* 1991, 353, 737-740.
152. Green, M. A.; Emery, K.; Hishikawa, Y.; Warta, W.; Dunlop, E. D., Solar Cell Efficiency Tables (Version 41). *Prog. Photovoltaics* 2013, 21, 1-11.
153. Hagfeldt, A.; Boschloo, G.; Sun, L.; Kloo, L.; Pettersson, H., Dye-Sensitized Solar Cells. *Chem. Rev.* 2010, 110, 6595-6663.
154. Li, T. C.; Spokoyny, A. M.; She, C.; Farha, O. K.; Mirkin, C. A.; Marks, T. J.; Hupp, J. T., Ni(III)/(IV) Bis(Dicarbollide) as a Fast, Noncorrosive Redox Shuttle for Dye-Sensitized Solar Cells. *Journal of the American Chemical Society* 2010, 132, 4580-4582.
155. Yum, J.-H.; Baranoff, E.; Kessler, F.; Moehl, T.; Ahmad, S.; Bessho, T.; Marchioro, A.; Ghadiri, E.; Moser, J.-E.; Yi, C.; Nazeeruddin, M. K.; Grätzel, M., A Cobalt Complex Redox Shuttle for Dye-Sensitized Solar Cells with High Open-Circuit Potentials. *Nature Communications* 2012, 3.
156. Tang, H.; Lévy, F.; Berger, H.; Schmid, P. E., Urbach Tail of Anatase TiO_2. *Physical Review B* 1995, 52, 7771-7774.
157. Amtout, A.; Leonelli, R., Optical Properties of Rutile near Its Fundamental Band Gap. *Phys. Rev. B* 1995, 51, 6842-6851.
158. Landmann, M.; Rauls, E.; Schmidt, W. G., The Electronic Structure and Optical Response of Rutile, Anatase and Brookite TiO_2. *J. Phys.-Condes. Matter* 2012, 24, 6.
159. Hurum, D. C.; Agrios, A. G.; Gray, K. A.; Rajh, T.; Thurnauer, M. C., Explaining the Enhanced Photocatalytic Activity of Degussa P25 Mixed-Phase Tio_2 Using Epr. *The Journal of Physical Chemistry B* 2003, 107, 4545-4549.
160. Morgan, B. J.; Watson, G. W., Intrinsic N-Type Defect Formation in TiO_2: A Comparison of Rutile and Anatase from Gga+U Calculations. *The Journal of Physical Chemistry C* 2010, 114, 2321-2328.
161. Tang, H.; Prasad, K.; Sanjines, R.; Schmid, P. E.; Levy, F., Electrical and Optical-Properties of Tio2 Anatase Thin-Films. *Journal of Applied Physics* 1994, 75, 2042-2047.
162. Green, M. A., *Third Generation Photovoltaics: Advanced Solar Energy Conversion*. Springer: 2006.
163. Dahl, J. A.; Maddux, B. L. S.; Hutchison, J. E., Toward Greener Nanosynthesis. *Chem. Rev.* 2007, 107, 2228-2269.
164. Sun, M.; Yu, H. Z.; Yang, W.; Qi, L.; Yang, F.; Yang, X. R., Shape Evolution of Cdse Nanocrystals in Vegetable Oils: A Synergistic Effect of Selenium Precursor. *Colloid Surf. A-Physicochem. Eng. Asp.* 2009, 350, 91-100.
165. Liu, J. H.; Fan, J. B.; Gu, Z.; Cui, J.; Xu, X. B.; Liang, Z. W.; Luo, S. L.; Zhu, M. Q., Green Chemistry for Large-Scale Synthesis of Semiconductor Quantum Dots. *Langmuir* 2008, 24, 5241-5244.
166. Ayele, D. W.; Chen, H. M.; Su, W. N.; Pan, C. J.; Chen, L. Y.; Chou, H. L.; Cheng, J. H.; Hwang, B. J.; Lee, J. F., Controlled Synthesis of CdSe Quantum Dots by a Microwave-Enhanced Process: A Green Approach for Mass Production. *Chem.-Eur. J.* 2011, 17, 5737-5744.
167. Resch-Genger, U.; Grabolle, M.; Cavaliere-Jaricot, S.; Nitschke, R.; Nann, T., Quantum Dots Versus Organic Dyes as Fluorescent Labels. *Nat. Methods* 2008, 5, 763-775.
168. Chin, P. T. K.; Stouwdam, J. W.; Janssen, R. A. J., Highly Luminescent Ultranarrow Mn Doped ZnSe Nanowires. *Nano Lett* 2009, 9, 745-750.
169. Mocatta, D.; Cohen, G.; Schattner, J.; Millo, O.; Rabani, E.; Banin, U., Heavily Doped Semiconductor Nanocrystal Quantum Dots. *Science* 2011, 332, 77-81.
170. Luther, J. M.; Law, M.; Beard, M. C.; Song, Q.; Reese, M. O.; Ellingson, R. J.; Nozik, A. J., Schottky Solar Cells Based on Colloidal Nanocrystal Films. *Nano Lett* 2008, 8, 3488-3492.
171. Sambur, J. B.; Novet, T.; Parkinson, B. A., Multiple Exciton Collection in a Sensitized Photovoltaic System. *Science* 2010, 330, 63-6.

172. Zhitomirsky, D.; Kramer, I. J.; Labelle, A. J.; Fischer, A.; Debnath, R.; Pan, J.; Bakr, O. M.; Sargent, E. H., Colloidal Quantum Dot Photovoltaics: The Effect of Polydispersity. *Nano Lett* 2012, 12, 1007-1012.
173. Emin, S.; Singh, S. P.; Han, L.; Satoh, N.; Islam, A., Colloidal Quantum Dot Solar Cells. *Solar Energy* 2011, 85, 1264-1282.
174. Kramer, I. J.; Sargent, E. H., Colloidal Quantum Dot Photovoltaics: A Path Forward. *ACS Nano* 2011, 5, 8506-8514.
175. Huynh, W. U.; Dittmer, J. J.; Alivisatos, A. P., Hybrid Nanorod-Polymer Solar Cells. *Science* 2002, 295, 2425-2427.
176. Han, L. L.; Qin, D. H.; Jiang, X.; Liu, Y. S.; Wang, L.; Chen, J. W.; Cao, Y., Synthesis of High Quality Zinc-Blende CdSe Nanocrystals and Their Application in Hybrid Solar Cells. *Nanotechnology* 2006, 17, 4736-4742.
177. Gunes, S.; Fritz, K. P.; Neugebauer, H.; Sariciftci, N. S.; Kumar, S.; Scholes, G. D., Hybrid Solar Cells Using PbS Nanoparticles. *Sol. Energy Mater. Sol. Cells* 2007, 91, 420-423.
178. Wang, X. H.; Koleilat, G. I.; Tang, J.; Liu, H.; Kramer, I. J.; Debnath, R.; Brzozowski, L.; Barkhouse, D. A. R.; Levina, L.; Hoogland, S.; Sargent, E. H., Tandem Colloidal Quantum Dot Solar Cells Employing a Graded Recombination Layer. *Nature Photonics* 2011, 5, 480-484.
179. Kramer, I. J.; Levina, L.; Debnath, R.; Zhitomirsky, D.; Sargent, E. H., Solar Cells Using Quantum Funnels. *Nano Lett* 2011, 11, 3701-3706.
180. Piliego, C.; Protesescu, L.; Bisri, S. Z.; Kovalenko, M. V.; Loi, M. A., 5.2% Efficient PbS Nanocrystal Schottky Solar Cells. *Energy & Environmental Science* 2013, 6, 3054-3059.
181. Johnston, K. W.; Pattantyus-Abraham, A. G.; Clifford, J. P.; Myrskog, S. H.; MacNeil, D. D.; Levina, L.; Sargent, E. H., Schottky-Quantum Dot Photovoltaics for Efficient Infrared Power Conversion. *Appl. Phys. Lett.* 2008, 92.
182. Tung, R. T., Chemical Bonding and Fermi Level Pinning at Metal-Semiconductor Interfaces. *Physical Review Letters* 2000, 84, 6078-6081.
183. Pattantyus-Abraham, A. G.; Kramer, I. J.; Barkhouse, A. R.; Wang, X. H.; Konstantatos, G.; Debnath, R.; Levina, L.; Raabe, I.; Nazeeruddin, M. K.; Grätzel, M.; Sargent, E. H., Depleted-Heterojunction Colloidal Quantum Dot Solar Cells. *ACS Nano* 2010, 4, 3374-3380.
184. Yoon, W.; Boercker, J. E.; Lumb, M. P.; Placencia, D.; Foos, E. E.; Tischler, J. G., Enhanced Open-Circuit Voltage of Pbs Nanocrystal Quantum Dot Solar Cells. *Scientific Reports* 2013, 3.
185. Choi, H.; Kim, J. K.; Song, J. H.; Kim, Y.; Jeong, S., Increased Open-Circuit Voltage in a Schottky Device Using Pbs Quantum Dots with Extreme Confinement. *Appl. Phys. Lett.* 2013, 102.
186. Debnath, R.; Tang, J.; Barkhouse, D. A.; Wang, X. H.; Pattantyus-Abraham, A. G.; Brzozowski, L.; Levina, L.; Sargent, E. H., Ambient-Processed Colloidal Quantum Dot Solar Cells Via Individual Pre-Encapsulation of Nanoparticles. *Journal of the American Chemical Society* 2010, 132, 5952-+.
187. Gao, J.; Luther, J. M.; Semonin, O. E.; Ellingson, R. J.; Nozik, A. J.; Beard, M. C., Quantum Dot Size Dependent J-V Characteristics in Heterojunction ZnO/PbS Quantum Dot Solar Cells. *Nano Lett* 2011, 11, 1002-8.
188. Ma, W.; Luther, J. M.; Zheng, H.; Wu, Y.; Alivisatos, A. P., Photovoltaic Devices Employing Ternary PbS_xSe_{1-x} Nanocrystals. *Nano Letters* 2009, 9, 1699-1703.
189. Ning, Z.; Zhitomirsky, D.; Adinolfi, V.; Sutherland, B.; Xu, J.; Voznyy, O.; Maraghechi, P.; Lan, X.; Hoogland, S.; Ren, Y.; Sargent, E. H., Graded Doping for Enhanced Colloidal Quantum Dot Photovoltaics. *Advanced Materials* 2013, 25, 1719-1723.
190. Rath, A. K.; Bernechea, M.; Martinez, L.; Konstantatos, G., Solution-Processed Heterojunction Solar Cells Based on P-Type PbS Quantum Dots and N-Type Bi_2S_3 Nanocrystals. *Advanced Materials* 2011, 23, 3712-3717.

191. Zillner, E.; Kavalakkatt, J.; Eckhardt, B.; Dittrich, T.; Ennaoui, A.; Lux-Steiner, M., Formation of a Heterojunction by Electrophoretic Deposition of CdTe/CdSe Nanoparticles from an Exhaustible Source. *Thin Solid Films* 2012, 520, 5500-5503.
192. Yaacobi-Gross, N.; Garphunkin, N.; Solomeshch, O.; Vaneski, A.; Susha, A. S.; Rogach, A. L.; Tessler, N., Combining Ligand-Induced Quantum-Confined Stark Effect with Type Ii Heterojunction Bilayer Structure in Cdte and Cdse Nanocrystal-Based Solar Cells. *ACS Nano* 2012, 6, 3128-3133.
193. Liu, H.; Zhitomirsky, D.; Hoogland, S.; Tang, J.; Kramer, I. J.; Ning, Z.; Sargent, E. H., Systematic Optimization of Quantum Junction Colloidal Quantum Dot Solar Cells. *Appl. Phys. Lett.* 2012, 101, 151112.
194. Tang, J.; Liu, H.; Zhitomirsky, D.; Hoogland, S.; Wang, X.; Furukawa, M.; Levina, L.; Sargent, E. H., Quantum Junction Solar Cells. *Nano Letters* 2012, 12, 4889-4894.
195. Ning, Z.; Ren, Y.; Hoogland, S.; Voznyy, O.; Levina, L.; Stadler, P.; Lan, X.; Zhitomirsky, D.; Sargent, E. H., All-Inorganic Colloidal Quantum Dot Photovoltaics Employing Solution-Phase Halide Passivation. *Advanced Materials* 2012, 24, 6295-6299.
196. Maraghechi, P.; Labelle, A. J.; Kirmani, A. R.; Lan, X. Z.; Adachi, M. M.; Thon, S. M.; Hoogland, S.; Lee, A.; Ning, Z. J.; Fischer, A.; Amassian, A.; Sargent, E. H., The Donor-Supply Electrode Enhances Performance in Colloidal Quantum Dot Solar Cells. *ACS Nano* 2013, 7, 6111-6116.
197. Debnath, R.; Greiner, M. T.; Kramer, I. J.; Fischer, A.; Tang, J.; Barkhouse, D. A. R.; Wang, X.; Levina, L.; Lu, Z.-H.; Sargent, E. H., Depleted-Heterojunction Colloidal Quantum Dot Photovoltaics Employing Low-Cost Electrical Contacts. *Appl. Phys. Lett.* 2010, 97, 023109.
198. Brown, P. R.; Lunt, R. R.; Zhao, N.; Osedach, T. P.; Wanger, D. D.; Chang, L. Y.; Bawendi, M. G.; Bulovic, V., Improved Current Extraction from ZnO/PbS Quantum Dot Heterojunction Photovoltaics Using a Moo_3 Interfacial Layer. *Nano Letters* 2011, 11, 2955-61.
199. Gao, J.; Perkins, C. L.; Luther, J. M.; Hanna, M. C.; Chen, H.-Y.; Semonin, O. E.; Nozik, A. J.; Ellingson, R. J.; Beard, M. C., N-Type Transition Metal Oxide as a Hole Extraction Layer in Pbs Quantum Dot Solar Cells. *Nano Lett* 2011, 11, 3263-3266.
200. Ju, T.; Graham, R. L.; Zhai, G.; Rodriguez, Y. W.; Breeze, A. J.; Yang, L.; Alers, G. B.; Carter, S. A., High Efficiency Mesoporous Titanium Oxide PbS Quantum Dot Solar Cells at Low Temperature. *Appl. Phys. Lett.* 2010, 97, 043106.
201. Tang, J.; Kemp, K. W.; Hoogland, S.; Jeong, K. S.; Liu, H.; Levina, L.; Furukawa, M.; Wang, X. H.; Debnath, R.; Cha, D. K.; Chou, K. W.; Fischer, A.; Amassian, A.; Asbury, J. B.; Sargent, E. H., Colloidal-Quantum-Dot Photovoltaics Using Atomic-Ligand Passivation. *Nat Mater* 2011, 10, 765-771.
202. Wang, X. H.; Koleilat, G. I.; Fischer, A.; Tang, J.; Debnath, R.; Levina, L.; Sargent, E. H., Enhanced Open-Circuit Voltage in Visible Quantum Dot Photovoltaics by Engineering of Carrier-Collecting Electrodes. *ACS Appl. Mater. Interfaces* 2011, 3, 3792-3795.
203. Ruhle, S.; Shalom, M.; Zaban, A., Quantum-Dot-Sensitized Solar Cells. *ChemPhysChem* 2010, 11, 2290-304.
204. Leschkies, K. S.; Beatty, T. J.; Kang, M. S.; Norris, D. J.; Aydil, E. S., Solar Cells Based on Junctions between Colloidal PbSe Nanocrystals and Thin ZnO Films. *ACS Nano* 2009, 3, 3638-3648.
205. Lee, D. U.; Woo Pak, S.; Gook Cho, S.; Kyu Kim, E.; Il Seok, S., Defect States in Hybrid Solar Cells Consisting of Sb_2S_3 Quantum Dots and Tio2 Nanoparticles. *Appl. Phys. Lett.* 2013, 103,
206. Kim, S.; Kang, M.; Kim, S.; Heo, J. H.; Noh, J. H.; Im, S. H.; Seok, S. I.; Kim, S. W., Fabrication of $Cuinte_2$ and $CuInTe_{2-x}Se_x$ Ternary Gradient Quantum Dots and Their Application to Solar Cells. *ACS Nano* 2013, 7, 4756-4763.
207. Brown, P. R.; Lunt, R. R.; Zhao, N.; Osedach, T. P.; Wanger, D. D.; Chang, L. Y.; Bawendi, M. G.; Bulovic, V., Improved Current Extraction from Zno/Pbs Quantum Dot Heterojunction Photovoltaics Using a MoO_3 Interfacial Layer. *Nano Lett* 2011, 11, 2955-61.

208. Liu, H.; Tang, J.; Kramer, I. J.; Debnath, R.; Koleilat, G. I.; Wang, X. H.; Fisher, A.; Li, R.; Brzozowski, L.; Levina, L.; Sargent, E. H., Electron Acceptor Materials Engineering in Colloidal Quantum Dot Solar Cells. *Advanced Materials* 2011, 23, 3832-+.

209. Koleilat, G. I.; Wang, X.; Labelle, A. J.; Ip, A. H.; Carey, G. H.; Fischer, A.; Levina, L.; Brzozowski, L.; Sargent, E. H., A Donor-Supply Electrode (Dse) for Colloidal Quantum Dot Photovoltaics. *Nano Lett* 2011, 11, 5173-5178.

210. Luther, J. M.; Gao, J.; Lloyd, M. T.; Semonin, O. E.; Beard, M. C.; Nozik, A. J., Stability Assessment on a 3% Bilayer PbS/ZnO Quantum Dot Heterojunction Solar Cell. *Adv Mater* 2010, 22, 3704-7.

211. Ip, A. H.; Thon, S. M.; Hoogland, S.; Voznyy, O.; Zhitomirsky, D.; Debnath, R.; Levina, L.; Rollny, L. R.; Carey, G. H.; Fischer, A.; Kemp, K. W.; Kramer, I. J.; Ning, Z.; Labelle, A. J.; Chou, K. W.; Amassian, A.; Sargent, E. H., Hybrid Passivated Colloidal Quantum Dot Solids. *Nat Nano* 2012, advance online publication.

212. Nozik, A. J., Quantum Dot Solar Cells. *Physica E* 2002, 14, 115-120.

213. Koleilat, G. I.; Kramer, I. J.; Wong, C. T. O.; Thon, S. M.; Labelle, A. J.; Hoogland, S.; Sargent, E. H., Folded-Light-Path Colloidal Quantum Dot Solar Cells. *Scientific Reports* 2013, 3.

214. Adachi, M. M.; Labelle, A. J.; Thon, S. M.; Lan, X.; Hoogland, S.; Sargent, E. H., Broadband Solar Absorption Enhancement Via Periodic Nanostructuring of Electrodes. *Scientific Reports* 2013, 3, 6.

215. Vogel, R.; Pohl, K.; Weller, H., Sensitization of Highly Porous, Polycrystalline TiO_2 Electrodes by Quantum Sized CdS. *Chem. Phys. Lett.* 1990, 174, 241-246.

216. Liu, D.; Kamat, P. V., Photoelectrochemical Behavior of Thin CdSe and Coupled TiO_2/CdSe Semiconductor Films. *The Journal of Physical Chemistry* 1993, 97, 10769-10773.

217. Vogel, R.; Hoyer, P.; Weller, H., Quantum-Sized PbS, CdS, Ag_2S, Sb_2S_3, and Bi_2S_3 Particles as Sensitizers for Various Nanoporous Wide-Bandgap Semiconductors. *The Journal of Physical Chemistry* 1994, 98, 3183-3188.

218. Fang, J. H.; Wu, J. W.; Lu, X. M.; Shen, Y. C.; Lu, Z. H., Sensitization of Nanocrystalline Tio_2 Electrode with Quantum Sized Cdse and Zntcpc Molecules. *Chem. Phys. Lett.* 1997, 270, 145-151.

219. Niitsoo, O.; Sarkar, S. K.; Pejoux, C.; Rühle, S.; Cahen, D.; Hodes, G., Chemical Bath Deposited CdS/CdSe-Sensitized Porous TiO_2 Solar Cells. *Journal of Photochemistry and Photobiology A: Chemistry* 2006, 181, 306-313.

220. Jun, H. K.; Careem, M. A.; Arof, A. K., Quantum Dot-Sensitized Solar Cells—Perspective and Recent Developments: A Review of Cd Chalcogenide Quantum Dots as Sensitizers. *Renewable and Sustainable Energy Reviews* 2013, 22, 148-167.

221. Lee, Y.-L.; Chang, C.-H., Efficient Polysulfide Electrolyte for Cds Quantum Dot-Sensitized Solar Cells. *Journal of Power Sources* 2008, 185, 584-588.

222. Jun, H. K.; Careem, M. A.; Arof, A. K., A Suitable Polysulfide Electrolyte for CdSe Quantum Dot-Sensitized Solar Cells. *International Journal of Photoenergy* 2013.

223. Lee, H. J.; Chen, P.; Moon, S.-J.; Sauvage, F.; Sivula, K.; Bessho, T.; Gamelin, D. R.; Comte, P.; Zakeeruddin, S. M.; Il Seok, S.; Graetzel, M.; Nazeeruddin, M. K., Regenerative PbS and CdS Quantum Dot Sensitized Solar Cells with a Cobalt Complex as Hole Mediator. *Langmuir* 2009, 25, 7602-7608.

224. Lee, H. J.; Chang, D. W.; Park, S.-M.; Zakeeruddin, S. M.; Graetzel, M.; Nazeeruddin, M. K., Cdse Quantum Dot (Qd) and Molecular Dye Hybrid Sensitizers for TiO_2 Mesoporous Solar Cells: Working Together with a Common Hole Carrier of Cobalt Complexes. *Chemical Communications* 2010, 46, 8788-8790.

225. Fang, B.; Kim, M.; Fan, S.-Q.; Kim, J. H.; Wilkinson, D. P.; Ko, J.; Yu, J.-S., Facile Synthesis of Open Mesoporous Carbon Nanofibers with Tailored Nanostructure as a Highly Efficient Counter Electrode in CdSe Quantum-Dot-Sensitized Solar Cells. *J. Mater. Chem.* 2011, 21, 8742-8748.

226. Lee, Y. L.; Lo, Y. S., Highly Efficient Quantum-Dot-Sensitized Solar Cell Based on Co-Sensitization of CdS/CdSe. *Adv. Funct. Mater.* 2009, 19, 604-609.
227. Shen, Q.; Yamada, A.; Tamura, S.; Toyoda, T., Cdse Quantum Dot-Sensitized Solar Cell Employing Tio_2 Nanotube Working-Electrode and Cu_2S Counter-Electrode. *Appl. Phys. Lett.* 2010, 97, 3.
228. Yang, Z.; Chen, C.-Y.; Liu, C.-W.; Chang, H.-T., Electrocatalytic Sulfur Electrodes for CdS/CdSe Quantum Dot-Sensitized Solar Cells. *Chemical Communications* 2010, 46, 5485-5487.
229. Yang, Z.; Chen, C.-Y.; Liu, C.-W.; Li, C.-L.; Chang, H.-T., Quantum Dot–Sensitized Solar Cells Featuring CuS/CoS Electrodes Provide 4.1% Efficiency. *Advanced Energy Materials* 2011, 1, 259-264.
230. Kim, H. J.; Kim, S. W.; Gopi, C.; Kim, S. K.; Rao, S. S.; Jeong, M. S., Improved Performance of Quantum Dot-Sensitized Solar Cells Adopting a Highly Efficient Cobalt Sulfide/Nickel Sulfide Composite Thin Film Counter Electrode. *Journal of Power Sources* 2014, 268, 163-170.
231. Kim, H.-J.; Kim, D.-J.; Rao, S. S.; Savariraj, A. D.; Soo-Kyoung, K.; Son, M.-K.; Gopi, C. V. V. M.; Prabakar, K., Highly Efficient Solution Processed Nanorice Structured NiS Counter Electrode for Quantum Dot Sensitized Solar Cells. *Electrochimica Acta* 2014, 127, 427-432.
232. Lin, C. Y.; Teng, C. Y.; Li, T. L.; Lee, Y. L.; Teng, H. S., Photoactive P-Type Pbs as a Counter Electrode for Quantum Dot-Sensitized Solar Cells. *Journal of Materials Chemistry A* 2013, 1, 1155-1162.
233. Lee, J.-W.; Son, D.-Y.; Ahn, T. K.; Shin, H.-W.; Kim, I. Y.; Hwang, S.-J.; Ko, M. J.; Sul, S.; Han, H.; Park, N.-G., Quantum-Dot-Sensitized Solar Cell with Unprecedentedly High Photocurrent. *Sci. Rep.* 2013, 3.
234. Pan, Z. X.; Zhao, K.; Wang, J.; Zhang, H.; Feng, Y. Y.; Zhong, X. H., Near Infrared Absorption of $CdSe_xTe_{1-x}$, Alloyed Quantum Dot Sensitized Solar Cells with More Than 6% Efficiency and High Stability. *Acs Nano* 2013, 7, 5215-5222.
235. Pan, Z.; Zhang, H.; Cheng, K.; Hou, Y.; Hua, J.; Zhong, X., Highly Efficient Inverted Type-I CdS/CdSe Core/Shell Structure Qd-Sensitized Solar Cells. *ACS Nano* 2012, 6, 3982-3991.
236. Santra, P. K.; Nair, P. V.; George Thomas, K.; Kamat, P. V., $Cuins_2$-Sensitized Quantum Dot Solar Cell. Electrophoretic Deposition, Excited-State Dynamics, and Photovoltaic Performance. *The Journal of Physical Chemistry Letters* 2013, 4, 722-729.
237. Li, T.-L.; Lee, Y.-L.; Teng, H., High-Performance Quantum Dot-Sensitized Solar Cells Based on Sensitization with $CuInS_2$ Quantum Dots/Cds Heterostructure. *Energy & Environmental Science* 2012, 5, 5315-5324.
238. Sung, S. D.; Lim, I.; Kang, P.; Lee, C.; Lee, W. I., Design and Development of Highly Efficient PbS Quantum Dot-Sensitized Solar Cells Working in an Aqueous Polysulfide Electrolyte. *Chemical Communications* 2013, 49, 6054-6056.
239. Yu, P. R.; Zhu, K.; Norman, A. G.; Ferrere, S.; Frank, A. J.; Nozik, A. J., Nanocrystalline TiO_2 Solar Cells Sensitized with Inas Quantum Dots. *The Journal of Physical Chemistry B* 2006, 110, 25451-25454.
240. Santra, P. K.; Kamat, P. V., Mn-Doped Quantum Dot Sensitized Solar Cells: A Strategy to Boost Efficiency over 5%. *Journal of the American Chemical Society* 2012, 134, 2508-2511.
241. Hossain, M. A.; Jennings, J. R.; Shen, C.; Pan, J. H.; Koh, Z. Y.; Mathews, N.; Wang, Q., CdSe-Sensitized Mesoscopic TiO_2 Solar Cells Exhibiting >5% Efficiency: Redundancy of CdS Buffer Layer. *J. Mater. Chem.* 2012, 22, 16235-16242.
242. Senthamilselvi, V.; Saravanakumar, K.; Begum, N. J.; Anandhi, R.; Ravichandran, A. T.; Sakthivel, B.; Ravichandran, K., Photovoltaic Properties of Nanocrystalline CdS Films Deposited by Silar and Cbd Techniques-a Comparative Study. *J. Mater. Sci.-Mater. Electron.* 2012, 23, 302-308.
243. Zhu, G. A.; Lv, T. A.; Pan, L. K.; Sun, Z.; Sun, C. Q., All Spray Pyrolysis Deposited CdS Sensitized ZnO Films for Quantum Dot-Sensitized Solar Cells. *Journal of Alloys and Compounds* 2011, 509, 362-365.

244. Yu, X.-Y.; Liao, J.-Y.; Qiu, K.-Q.; Kuang, D.-B.; Su, C.-Y., Dynamic Study of Highly Efficient CdS/CdSe Quantum Dot-Sensitized Solar Cells Fabricated by Electrodeposition. *ACS Nano* 2011, 5, 9494-9500.
245. de la Fuente, M. S.; Sánchez, R. S.; González-Pedro, V.; Boix, P. P.; Mhaisalkar, S. G.; Rincón, M. E.; Bisquert, J.; Mora-Seró, I., Effect of Organic and Inorganic Passivation in Quantum-Dot-Sensitized Solar Cells. *The Journal of Physical Chemistry Letters* 2013, 4, 1519-1525.
246. Wang, J.; Mora-Seró, I.; Pan, Z.; Zhao, K.; Zhang, H.; Feng, Y.; Yang, G.; Zhong, X.; Bisquert, J., Core/Shell Colloidal Quantum Dot Exciplex States for the Development of Highly Efficient Quantum-Dot-Sensitized Solar Cells. *Journal of the American Chemical Society* 2013, 135, 15913-15922.
247. Brown, P.; Kamat, P. V., Quantum Dot Solar Cells. Electrophoretic Deposition of CdSe–C_{60} Composite Films and Capture of Photogenerated Electrons with Nc_{60} Cluster Shell. *Journal of the American Chemical Society* 2008, 130, 8890-8891.
248. Smith, N. J.; Emmett, K. J.; Rosenthal, S. J., Photovoltaic Cells Fabricated by Electrophoretic Deposition of Cdse Nanocrystals. *Appl. Phys. Lett.* 2008, 93, 3.
249. Salant, A.; Shalom, M.; Hod, I.; Faust, A.; Zaban, A.; Banin, U., Quantum Dot Sensitized Solar Cells with Improved Efficiency Prepared Using Electrophoretic Deposition. *ACS Nano* 2010, 4, 5962-5968.
250. Blanton, S. A.; Leheny, R. L.; Hines, M. A.; GuyotSionnest, P., Dielectric Dispersion Measurements of CdSe Nanocrystal Colloids: Observation of a Permanent Dipole Moment. *Physical Review Letters* 1997, 79, 865-868.
251. Shim, M.; Guyot-Sionnest, P., Permanent Dipole Moment and Charges in Colloidal Semiconductor Quantum Dots. *J. Chem. Phys.* 1999, 111, 6955-6964.
252. Jia, S.; Banerjee, S.; Herman, I. P., Mechanism of the Electrophoretic Deposition of CdSe Nanocrystal Films: Influence of the Nanocrystal Surface and Charge. *Journal of Physical Chemistry C* 2008, 112, 162-171.
253. Cirillo, M.; Strubbe, F.; Neyts, K.; Hens, Z., Thermal Charging of Colloidal Quantum Dots in Apolar Solvents: A Current Transient Analysis. *ACS Nano* 2011, 5, 1345-1352.
254. Andrienko, D. Introduction to Liquid Crystals 2006, p. 27.
255. Murschell, A. E.; Sutherland, T. C., Anthraquinone-Based Discotic Liquid Crystals. *Langmuir* 2010, 26, 12859-12866.
256. Struijk, C. W.; Sieval, A. B.; Dakhorst, J. E. J.; van Dijk, M.; Kimkes, P.; Koehorst, R. B. M.; Donker, H.; Schaafsma, T. J.; Picken, S. J.; van de Craats, A. M.; Warman, J. M.; Zuilhof, H.; Sudhölter, E. J. R., Liquid Crystalline Perylene Diimides: Architecture and Charge Carrier Mobilities. *Journal of the American Chemical Society* 2000, 122, 11057-11066.
257. Chiang, L. Y.; Safinya, C. R.; Clark, N. A.; Liang, K. S.; Bloch, A. N., Highly Oriented Fibres of Discotic Liquid Crystals. *Journal of the Chemical Society, Chemical Communications* 1985, 695-696.
258. Nakayama, H.; Ozaki, M.; Schmidt, W. F.; Yoshino, K., Measurements of Carrier Mobility and Quantum Yield of Carrier Generation in Discotic Liquid Crystal Hexahexyl-Oxytriphenylene by Time-of-Flight Method. *Jpn. J. Appl. Phys. Part 2 - Lett.* 1999, 38, L1038-L1041.
259. van de Craats, A. M.; Warman, J. M.; de Haas, M. P.; Adam, D.; Simmerer, J.; Haarer, D.; Schuhmacher, P., The Mobility of Charge Carriers in All Four Phases of the Columnar Discotic Material Hexakis(Hexylthio)Triphenylene: Combined Tof and Pr-Trmc Results. *Advanced Materials* 1996, 8, 823-826.
260. Uznanski, P.; Marguet, S.; Markovitsi, D.; Schuhmacher, P.; Ringsdorf, H., Photophysical Properties of Discotic Dibenzopyrenes. *Molecular Crystals and Liquid Crystals Science and Technology Section a-Molecular Crystals and Liquid Crystals* 1997, 293, 123-133.
261. Fechtenkötter, A.; Saalwächter, K.; Harbison, M. A.; Müllen, K.; Spiess, H. W., Highly Ordered Columnar Structures from Hexa-Peri-Hexabenzocoronenes—Synthesis, X-Ray

Diffraction, and Solid-State Heteronuclear Multiple-Quantum Nmr Investigations. *Angewandte Chemie International Edition* 1999, 38, 3039-3042.

262. Brown, S. P.; Schnell, I.; Brand, J. D.; Müllen, K.; Spiess, H. W., An Investigation of Π–Π Packing in a Columnar Hexabenzocoronene by Fast Magic-Angle Spinning and Double-Quantum ^{1}h Solid-State Nmr Spectroscopy. *Journal of the American Chemical Society* 1999, 121, 6712-

263. Craats, A. M. v. d.; Warman, J. M.; Fechtenkötter, A.; Brand, J. D.; Harbison, M. A.; Müllen, K., Record Charge Carrier Mobility in a Room-Temperature Discotic Liquid-Crystalline Derivative of Hexabenzocoronene. *Advanced Materials* 1999, 11, 1469-1472.

264. Grelet, E.; Bock, H.; Brunet, T.; Kelber, J.; Thiebaut, O.; Jolinat, P.; Mirzaei, S.; Destruel, P., Toward Organic Photovoltaic Cells Based on the Self-Assembly of Discotic Columnar Liquid Crystals. *Mol. Cryst. Liquid Cryst.* 2011, 542, 182-189.

265. Hassheider, T.; Benning, S. A.; Lauhof, M. W.; Kitzerow, H. S.; Bock, H.; Watson, M. D.; Mullen, K., Organic Heterojunction Photovoltaic Cells Made of Discotic, Mesogenic Materials. *Mol. Cryst. Liquid Cryst.* 2004, 413, 2597-2608.

266. Schmidt-Mende, L.; Watson, M.; Müllen, K.; Friend, R. H., Organic Thin Film Photovoltaic Devices from Discotic Materials. *Mol. Cryst. Liquid Cryst.* 2003, 396, 73-90.

267. Schmidt-Mende, L.; Fechtenkotter, A.; Mullen, K.; Friend, R. H.; MacKenzie, J. D., Efficient Organic Photovoltaics from Soluble Discotic Liquid Crystalline Materials. *Physica E* 2002, 14, 263-267.

268. Hesse, H. C.; Schaffer, C.; Hundschell, C.; Narita, A.; Feng, X. L.; Mullen, K.; Nickel, B.; Schmidt-Mende, L., Large Polycyclic Aromatic Hydrocarbons for Application in Donor-Acceptor Photovoltaics. *Physica Status Solidi a-Applications and Materials Science* 2012, 209, 785-789.

269. Schmidt-Mende, L.; Fechtenkötter, A.; Müllen, K.; Moons, E.; Friend, R. H.; MacKenzie, J. D., Self-Organized Discotic Liquid Crystals for High-Efficiency Organic Photovoltaics. *Science* 2001, 293, 1119-1122.

270. Hesse, H. C.; Weickert, J.; Al-Hussein, M.; Dossel, L.; Feng, X. L.; Mullen, K.; Schmidt-Mende, L., Discotic Materials for Organic Solar Cells: Effects of Chemical Structure on Assembly and Performance. *Sol. Energy Mater. Sol. Cells* 2010, 94, 560-567.

271. Zheng, Q.; Fang, G.; Bai, W.; Sun, N.; Qin, P.; Fan, X.; Cheng, F.; Yuan, L.; Zhao, X., Efficiency Improvement in Organic Solar Cells by Inserting a Discotic Liquid Crystal. *Sol. Energy Mater. Sol. Cells* 2011, 95, 2200-2205.

272. Jeong, S.; Kwon, Y.; Choi, B. D.; Ade, H.; Han, Y. S., Improved Efficiency of Bulk Heterojunction Poly(3-Hexylthiophene): 6,6 -Phenyl-C-61-Butyric Acid Methyl Ester Photovoltaic Devices Using Discotic Liquid Crystal Additives. *Appl. Phys. Lett.* 2010, 96.

273. Kumar, S.; Sagar, L. K., Cdse Quantum Dots in a Columnar Matrix. *Chemical Communications* 2011, 47, 12182-12184.

274. Kinkead, B.; Hegmann, T., Effects of Size, Capping Agent, and Concentration of Cdse and Cdte Quantum Dots Doped into a Nematic Liquid Crystal on the Optical and Electro-Optic Properties of the Final Colloidal Liquid Crystal Mixture. *J. Mater. Chem.* 2010, 20, 448-458.

275. Mirzaei, J.; Reznikov, M.; Hegmann, T., Quantum Dots as Liquid Crystal Dopants. *J. Mater. Chem.* 2012, 22, 22350-22365.

276. Mirzaei, J.; Urbanski, M.; Yu, K.; Kitzerow, H.-S.; Hegmann, T., Nanocomposites of a Nematic Liquid Crystal Doped with Magic-Sized Cdse Quantum Dots. *J. Mater. Chem.* 2011, 21, 12710-12716.

277. Shandryuk, G. A.; Matukhina, E. V.; Vasil'ev, R. B.; Rebrov, A.; Bondarenko, G. N.; Merekalov, A. S.; Gas'kov, A. M.; Talroze, R. V., Effect of H-Bonded Liquid Crystal Polymers on Cdse Quantum Dot Alignment within Nanocomposite. *Macromolecules* 2008, 41, 2178-2185.

278. Konshina, E. A.; Gavrish, E. O.; Orlova, A. O.; Artem'ev, M. V., Effect of Dispersed CdSe/ZnS Quantum Dots on Optical and Electrical Characteristics of Nematic Liquid Crystal Cells. *Tech. Phys. Lett.* 2011, 37, 1011-1014.

Chapter 2 Experimental

2.1 Materials

All materials were used as supplied unless stated otherwise.

2.1.1 Materials supplied by Sigma – Aldrich

Acetone (HPLC grade), aluminium wire, 1 mm diameter, (99.999 %); CS_2 (Carbon disulfide, 99.9 %); $CdCl_2$ (cadmium chloride, 99.99 %); CsI (Cesium iodide, 99.9 %); Chloroplatinic acid hydrate, 99.9 %; Coumarin 153 (99 %); 1,2 Dichloroethane (99.8 %, anhydrous); Ethyl cellulose (48.0-49.5% (w/w) ethoxyl basis), SnO_2 /F (Fluorine doped tin oxide) coated glass, 2.3 nm thickness, 13 Ω/sq ,lead acetate trihydrate (99.999%); LiF (lithium fluoride, 99.9 %); HTAC (hexadecyltrimethylammonium chloride); MPA (3-mercaptopropionic acid); OA (oleic acid, 90%); ODA (octadecylamine, 97%); ODE (octadecene , ≥ 97%); OLY (oleylamine, 70 %); $PbCl_2$ (lead chloride, 99.99%); PbO (lead (II) oxide, 99.99 %); KCl (99 %); KBr (99 %); KI (99 %); PVB (polyvinyl butyral); (1,4)-phenylenediamine 99 %); Rhodamine 6G (99 %); Se (99.99 %); Silver wire (diam. 1.5 mm, ≥99.99 %); NaCl (sodium chloride, 99 %); Na_2S (sodium sulphide, 97%); TBP (tributylphosphine, 90 %); Terpineol (95 %, mixture of isomers); TDPA (tetradecylphosphonic acid, 97 %); $TiCl_4$ (titanium (IV) chloride, ≥ 99 %); TMS (bis(trimethylsilyl) sulfide, ≥ 95 %); TOP (trioctylphosphine, 90 %); TOPO (trioctylphosphine oxide, 99%); $ZnCl_2$ (Zinc chloride, 99.999 %; and Zinc powder 95 %

2.1.2 Solvents supplied by Trinity College Solvent Stores

Acetone, chloroform, dichloromethane ethanol, propanol, hexane and toluene

2.1.3 Other suppliers

Brass foil, alloy 260, 0.1 mm thickness (Alfa Aesar); CdO (99.9998 %, Alfa Aesar); Dye 26 (97 %, Acros Organics); $Cd(stearate)_2$, (min 90%, Strem Chemicals); Gold pellets, (1-3 mm, 99.99%, Testbourne ltd); HPA (n-hexylphosphonic acid, 97 %, ABCR); H6TP, Hexahexyloxy-triphenylene (supplied by collaborator), IR-140 (95%)(Acros Organics); Lead Foil, (99.9%, 0.1 mm thickness, Alfa Aesar); ODPA (n-octadecylphosphonic acid, ≥ 97%, PCL Synthesis); soluble perylene diamide (PDI), (N,N9-bis(1-ethylpropyl)-3,4,9,10-perylenebis, Frontir scientific) ; RTAQ - 1,5-dihydroxy-2,3,6,7-tetrakis(3,7-dimethyloctyloxy)-9,10-anthraquinone, supplied by collaborator; S (99.999 %, Acros Organics); Silver Paint (G302, Agar); TiO_2 paste , (90-T

Transparent paste consisting of 20 nm anatase particles and WER2-O Reflector Titania Paste, Dyesol).

2.2 Experimental Details of Chapter 3

2.2.1 Preparation of oleic acid capped CdS Quantum Dots

This work was carried out using a modified method from literature.[16, 17]

2.2.1.i Preparation of 0.05 M sulphur stock solution

0.016 g (0.5 mmol) of sulphur was dissolved in 10.0 ml of degassed ODE, produced by heating the solution under argon to 200 °C for 15 minutes.

2.2.1.ii CdS QD synthesis

0.0128 g (0.997 mmol) of CdO, 0.093 g of OA (0.33 mmol) and 3.9 g of ODE were weighed into a 100 ml 3-neck round-bottom flask equipped with a condenser and thermometer. The solution was heated to 30 °C and degassed for 20 minutes under vacuum. The reaction was then switched to an argon atmosphere and then heated to 300 °C to allow formation of $Cd(oleate)_2$ which was indicated by a colour change from brown to colourless. Following this 1.0 ml of a 0.05 M solution of sulphur dissolved in ODE was injected. Growth was then allowed to proceed for 10 minutes after which the reaction was removed from the heat source and the CdS QDs were precipitated using degassed ethanol. The QD solution was cleaned using a number of dissolution and precipitation cycles with dry hexane and HPLC grade acetone.

2.2.2 Preparation of oleic acid capped CdSe

This work was carried out using a modified method from literature.[279]

2.2.2.i Se-TBP solution preparation

0.1105 g (1.399 mmol) of Se was mixed with and 3.0 ml of TBP under an argon atmosphere and sonicated until the Se become completely dissolved , indicated by a clear transparent solution.

2.2.2.ii CdSe Synthesis

0.50 g (0.0039 mol) of CdO, 4.0 g of oleic acid and 10.0 g of ODE (octadecene) were weighed into a 100 ml 3-neck round-bottom flask equipped with a condenser and thermometer. Following this, the flask was put under vacuum and degassed for 20 minutes at 30 °C. After this, the flask was switched to argon; the temperature was increased to 260 °C and allowed to stabilize. Time was then allowed for the CdO to convert to $Cd(oleate)_2$ which was indicated by a colour change from brown to colourless. At this point, the Se-TBP solution was injected. Growth was allowed to proceed for a set amount of time (10 – 220 seconds). The reaction was

then removed from the heating mantle and allowed to cool to 200 °C, following by injection of 20 ml of degassed acetone to precipitate the QDs. The resulting QD solution was cleaned using a number of dissolution and precipitation cycles with dry hexane and HPLC grade acetone.

2.2.3 *Preparation of ODPA capped CdSe QDs*

This work was carried out using a modified method from literature.[88]

2.2.3.i Preparation of Se 0.75 M stock solution

0.059 g of Se was mixed with 1.0 ml of TOP under an argon atmosphere and sonicated until the Se become completely dissolved , indicated by a clear transparent solution.

2.2.3.ii Synthesis of CdSe QDs

TOPO (3.0 g), ODPA (0.280 g) and CdO (0.060 g) were added to a 100 ml 3-neck round-bottom flask equipped with a condenser and thermometer. The solution was then heated to 150 °C and degassed under vacuum for 30 minutes. The atmospheres was then changed to argon and the solution was heated to 300 °C and held at this temperature until the solution turned optically clear and colourless, indicating formation of $Cd(ODPA)_2$. Following this 1.0 ml of TOP was injected into the flask; the solution was then heated to the required temperature. The Se-TOP solution was then injected and immediately the solution was removed from the hot plate and the reaction mixture was allowed to cool. After the solution cooled to below 150 °C, 20 ml of dried methanol was injected to precipitate the NCs and was left to cool to room temperature. The resulting QD solution was cleaned using a number of dissolution and precipitation cycles with dry toluene and methanol.

2.2.4 Preparation of Octadecylamine capped -CdSe QDs

This work was carried out using a modified method from literature.[280]

2.2.4.i Preparation of 1.5 M Se stock solution

1.184 g of Se was mixed with 10.0 ml of TOP under an argon atmosphere and sonicated until the Se become completely dissolved, indicated by a clear transparent solution.

2.2.4.ii Preparation of 0.5 M Cd stock solution

A 0.5 M solution of Cd was created by firstly degassing a solution of 1.285 g of CdO in 10.0 ml of OA and 10.0 ml ODE, which was then switched to an argon atmosphere and heated to 270.0 °C, until a clear solution was created.

2.2.4.iii SILAR stock solutions of Cd and Se

To grow the CdSe QDs further, we used a solution of 0.2 M Se stock solution and 0.2 M Cd stock solution, diluted using solvents mentioned above.

2.2.4.iv Synthesis of CdSe QDs

7.50 g of octadecylamine, 2.50 g of TOPO, 20 g of octadecene, and 2.0 ml of 0.5 M Cd-oleate were added to a 100 ml 3-neck round-bottom flask equipped with a condenser and thermometer. This solution was heated to 80.0 °C and degassed under vacuum for 20 minutes. Following this, the solution was switched to an argon atmosphere and heated to 290 °C. After which 1.0 ml of 1.5 M Se-TOP solution was injected and QD growth began. After injection of Se-TOP at 290 °C, the temperature was set at 250 °C for CdSe QD growth for 10 minutes. Following this stock solutions of Se and Cd were slowly injected in cycles to increase the size of QDs, beginning with 0.20 ml of Se, following this 0.40 ml of Cd was injected, then 0.40 ml of Se and finally 0.80 ml of Cd.

After ten minutes, the solution was cooled down to room temperature, and CdSe QDs were precipitation with acetone. The QDs were separated using centrifugation and cleaned using a number of cycle of hexane dissolution and acetone precipitation followed by centrifugation. CdSe core QDs were then re-dispersed in hexane.

2.2.5 Preparation of PbS Quantum Dots

This work was carried out using a modified method from literature.[281]

2.2.5.i Preparation of 0.1 M TMS stock solution

0.042 ml of TMS (0.2 mmol) was mixed with 2.0 ml of degassed ODE, under argon.

2.2.5.ii Oleic acid capped PbS QD synthesis

0.090 g of PbO (0.4 mmol), 0.224 g of OA and 3 g of ODE were added to a 100 ml 3-neck round-bottom flask equipped with a condenser and thermometer. The flask was put under a vacuum and degassed for 30 minutes while heating the solution to 30 °C. Following this, the atmosphere was changed to argon and the solution was heated to 120 °C and held there until the solution becomes colourless and transparent, indicating the complete conversion of PbO to Pb(oleate)$_2$. The solution then was brought to the desired injection temperature and the TMS stock solution was added. The reaction was allowed to proceed for 10 minutes after which the reaction was removed from the heat and quenched with 20 ml of HPLC grade acetone. The solution was then cleaned using a number of dissolution and precipitation cycles with dry hexane and HPLC grade acetone.

2.2.6 Preparation of CdS/CdSe Quantum Dot

This work was carried out using a modified method from literature.[17, 235]

2.2.6.i Preparation of 0.5 M sulphur stock solution

0.016 g of sulphur was dissolved in 10.0 ml of degassed ODE, produced by heating the solution under argon to 200 °C for 15 minute.

2.2.6.ii Preparation of 0.4 M Se stock solution

A 0.4 M stock solution was prepared by dissolving 0.063 g of Se in 2 ml of trioctylphosphine using sonication under argon, producing a clear solution.

2.2.6.iii Preparation of 0.4 M Cd (oleate)$_2$ stock solution

A 0.4 M solution of Cd was created by firstly degassing 0.5135 g of CdO in 10.0 ml of a 1:1 (v/v) OA :ODE solution which was then switched to an argon atmosphere and heated to 270 °C, until a clear solution was created.

2.2.6.iv CdS/CdSe QD synthesis

0.0128 g (0.00010 mol) of CdO 0.093 g of OA (0.33 mmol) and 3.9 g of ODE were added to a 100 ml 3-neck round-bottom flask equipped with a condenser and thermometer. The flask was then put under vacuum and heated to 30 °C, degassing the solution for 20 minutes. The reaction was then switched to an argon atmosphere and then heated to 300 °C to allow formation of Cd (oleate)$_2$ indicated by the solution becoming clear. Following this 1.0 ml of a 0.05 M solution of sulphur dissolved in ODE was injected (0.016 g of sulphur in 10.0 ml of degassed ODE, produced by heating the solution under argon to 200 °C for 15 minutes). Growth was then allowed to proceed for 10 minutes. After which the vessel was cooled to 215 °C and shell pre-cursor injection began.

Firstly, 0.8 mL of degassed OA was added into the reaction vessel. This was followed by injection of 0.15 ml of a Se stock solution and followed by the addition of an equimolar amount of Cd (oleate)$_2$ precursor stock solution after a 10 min interval. Following this another ten minutes was allowed for the reaction to take place. This constitutes one cycle of shell deposition. Three more cycles of Se and Cd stock solutions were injected with the same 10 min intervals between each injection, increasing the volume from 0.25 ml, to 0.4 ml to 0.6 ml for each cycle. The reaction was terminated by removing the heating source room and precipitated the QDs with degassed ethanol. The solution was then cleaned using a number of dissolution and precipitation cycles with dry hexane and HPLC grade acetone.

2.2.7 Preparation of CdSe/CdS Core-Shell Quantum Dots

This work was carried out using a modified method from literature.[280]

2.2.7.i Preparation of 0.1 M S stock solution

Sulphur stock solution was prepared by dissolving 0.032 g of sulphur in 10.0 ml of degassed ODE at 180 °C under an argon atmosphere to obtain a 0.1 M sulphur solution.

2.2.7.ii Preparation of 0.1 M Cd stock solution

A 0.1 M solution of Cd was created by firstly degassing 0.128 g of CdO in 10.0 ml of a 1:1 (v/v) OA: ODE solution, which was then switched to an argon atmosphere and heated to 270 °C, until a clear solution was created.

2.2.7.iii Synthesis of CdSe/CdS QDs

10 g of oleylamine, 20 g of ODE, and 6.75 x 10^{-7} mol of octadecylamine capped -CdSe QDs (see section 2.2.4) were added to a 100 ml 3-neck round-bottom flask equipped with a condenser and thermometer. The flask was then put under vacuum and heated to 60 °C, degassing the solution for 30 minutes. Following this, the reaction was switched to an argon atmosphere and 0.3 ml of the 0.1 M Cd stock solution was injected. This was heated to 230 °C and allowed to react for 10 minutes. This was followed by injection of 1.25 ml of a S stock solution and followed by the addition of an equimolar amount of Cd(oleate)$_2$ precursor stock solution after a 10 min interval. Following this another ten minutes was allowed for the reaction to take place. This constitutes one cycle of shell deposition. Two more cycles of shell deposition were carried out with the same 10 min intervals between each injection, increasing the volume to firstly 2.25 ml of S stock solution and 0.45 ml of Cd stock solution and then 3.25 ml of S stock solution and 0.6 ml of Cd stock solution. The reaction was terminated by removing the heating source room and precipitated the QDs with degassed ethanol. The solution was then cleaned using a number of dissolution and precipitation cycles with dry hexane and HPLC grade acetone.

2.2.8 Preparation of CdSe/CdS Core-Shell Heterostructured Quantum Rods

This work was carried out using a modified method from literature.[88]

2.2.8.i Preparation of 2.5 M S - TOP and CdSe QD stock solution

0.120 g of S was dissolved in 1.5 ml of TOP under argon; the solution was then sonicated, producing a clear transparent solution. To this was added 8 x 10^{-8} mol of ODPA capped CdSe QDs (see section 2.2.3) in TOP solution, which was prepared by mixing a set volume of CdSe QDs in hexane with TOP followed by the use of high vacuum and moderate heat to remove the hexane solvent.

2.2.8.ii Synthesis of CdSe/CdS core-shell quantum rods

0.057 g of CdO, 3 g TOPO, 0.29 g ODPA and 0.08 g HPA were added to a 3-neck flask with a condenser and thermometer. Initially the mixture was heated to 150 °C under argon, after

which the solution was placed under vacuum and degassed for 30 minutes. The flask was then flushed with argon and heated to 300 °C, holding at this temperature until the solution turned optically clear and colourless, indicating formation of the Cd complex. Following this, 1.5 g of TOP was injected into the flask and the solution was heated further to 360 °C. This was then followed by injection of the S-TOP and CdSe QDs stock solution. The QDs are then allowed to grow for 8 minutes after which the heating mantle is removed. After the solution cooled to below 150 °C, 20 ml of degassed methanol was injected to precipitate the QDs and the solution was allowed to cool to room temperature. The QDs were fully separated using centrifugation and then re-dispersed in a minimum volume of dry-toluene. This method of precipitation was repeated twice more to obtain a clean solution of QDs dispersed in toluene.

2.2.9 Preparation of CdTe/CdSe Type II Core-Shell Quantum Dots

This work was carried out using a modified method from literature.[282]

2.2.9.i 0.08 M Te Stock solution

0.0127 g (0.995 mmol) of Te, 0.20 ml of TOP (Trioctylphosphine), 0.050 g (0.15 mmol) of ODPA and 1 ml of ODE were added to a sample bottle under a strict argon atmosphere. This was heated to 120 °C and remained at this temperature until the solute became fully dissolved, producing a clear strongly yellow coloured solution, if it became opaque, oxygen contamination has taken place and the solution must be discarded and preparation must be repeated.

2.2.9.ii 0.09 M Se Stock solution

A 0.09 M solution of 0.071 g (0.0009 mol) of Se was added to 1.6 ml of TOP, in 8.4 ml of degassed ODE under argon and sonicated to produce a clear solution.

2.2.9.iii 0.1 M Cd Stock solution

A 0.1 M solution of Cd was created by firstly degassing 0.128 g (0.997 mmol) of CdO in 10.0 ml of solution containing 1.25 ml of OA and 8.75 ml of ODE, which was then switched to an argon atmosphere and heated to 270 °C, until a clear solution was achieved.

2.2.9.iv Synthesis of CdTe/CdSe Quantum Dots

0.026 g (0.20 mol) of CdO, 0.226 g (0.800 mmol) of OA (oleic acid) and 3 g of ODE was added to a 3-neck flask with a condenser and thermometer. This was degassed 30 °C using vacuum and then heated to 280 °C under argon, and time was then allowed for the Cd to coordinate with the OA, indicated by the solution becoming colourless. This was then followed by injection of the Te stock solution. This is allowed to react for 3 minutes. Following this, the reaction is cooled to 230 °C and shell precursors are added alternatively. This began by injection of 1.0 ml of Se stock solution over one minute, which was then allowed to react for ten minutes, and then

followed by 1.0 ml of Cd stock solution, added over a one-minute period, which was then allowed to react over ten minutes. This process is continued, making alternative injections of shell precursors until all of the stock solutions had been added. The reaction is then cooled and acetone is added to precipitate the QDs.

2.2.10 Preparation of PbS/CdS core-shell quantum dots

This work was carried out using a modified method from literature.[93]

2.2.10.i 0.25 M Cd Stock solution

A 0.25 M solution of Cd oleate was created by firstly degassing 0.32 g of CdO in 10.0 ml of OA, which was then switched to an argon atmosphere and heated to 270 °C, until a clear solution was achieved.

2.2.10.ii Synthesis of PbS/CdS Quantum Dots

1 x 10^{-7} mol of pre-synthesised PbS QDs (see section 2.2.5) were added to 5.0 mL of toluene under an argon atmosphere. Following this, 1.0 ml of the 0.25 M Cd-stock solution was added and the vessel was heated to 100 °C. The cation exchange was allowed to take place after which the QDs were precipitated using degassed MeOH. The solution was then cleaned using a number of dissolution and precipitation cycles with MeOH and HPLC grade toluene, eventually redispersing the QDs in toluene.[111]

2.2.11 Cation exchange of CdX quantum to Cu_2X quantum dots

This work was carried out using a modified method from literature.[112]

2.2.11.i 0.03 mM Tetrakis(acetonitrile)copper(I) hexafluorophosphate solution

0.22 g of Tetrakis(acetonitrile)copper(I) hexafluorophosphate was dissolved in 20.0 ml of MeOH

2.2.11.ii Preparation of Cu_2X quantum dots

The concentration of Cd^{2+} solution was estimated by determining the concentration of QDs in solution, then by approximating the size of the QD and the shape, and by taking using the lattice constant of the bulk material. This was then used to insure that the amount of QDs used was 0.0015 mmol of CdX produced a 1:20 ratio of Cd^{2+} to Cu^{1+} when 1.0 ml of the 0.03 mM Tetrakis (acetonitrile)copper(I) hexafluorophosphate solution was added to the QDs in 2.0 ml of toluene under rapid stirring. Upon addition of the Cu^{1+} solution, rapid colour change takes place, indicating the exchange of Cd^{2+} ions with Cu^{1+} ions. The reaction was allowed to proceed for a further 5 minutes to ensure complete exchange of the cations, after which QDs were precipitated from the reaction solution through the addition of 2.0 ml of methanol followed by

centrifugation. The resulting solid was redispersed in 5.0 ml of toluene contain 0.1 ml of OLY, to improve the stability of the colloidal solution.

2.2.12 Cation exchange of Cu_2X quantum dots to PbX quantum dots (X= Se or S)

This work was carried out using a modified method from literature.[111]

2.2.12.i Preparation of 0.15 M solution of Pb^{2+} solution

0.57 g of lead acetate trihydrate was dissolved in 1.0 ml of TBP in 10.0 ml of degassed HPLC grade methanol under an argon atmosphere.

2.2.12.ii Preparation of PbX using cation exchange (X= Se or S)

A concentration of 1.5 mmol Cu_2X QDs was dissolved in a solution of 10.0 ml of degassed toluene. This was put under an argon atmosphere and 1.0 ml of the Pb^{2+} solution was added under vigorous stirring. An immediate change in colour solution took place, gradually darkening further over time. This reaction was allowed to proceed for two hours after, after which the QDs were precipitated by the addition of 5 ml of MeOH. Following this, the PbX QDs were separated with the use of centrifugation and redispersed in toluene.

2.2.13 CdSe/CdS/Au quantum rods

This work was carried out using a modified method from literature.[283]

3.0 ml of oleylamine were degassed in vacuum at 120 °C for 1 h and subsequently cooled down to 60 °C. After purification, all of the oleylamine then injected into the three-neck flask containing 0.015 g of gold(III) chloride, and the temperature was raised to 60 °C. When the solution became yellow and clear (approximately after 5 minutes of heating), pre synthesised CdS/CdSe quantum rods (see section 2.2.8) dissolved in 0.5 ml of oleylamine were injected via syringe. The exact quantity of QRs for the synthesis of Au-QRs composites was calculated using an empirical approach, whereby the quantum rods absorption at 450 nm (band gap of CdS) multiplied by the volume of the colloidal suspension (in ml) was set to be in the range of 18-25. Upon injection of CdSe/CdS QRs into $AuCl_3$ / oleylamine mixture, the heat was brought to flask and the solution was heated to 110 °C, for 15 minutes, at a rate of 4.5 °C/min when the desired temperature was reached, the reaction was stopped by removing the heating mantle from the flask and adding 5 ml of degassed toluene. The particles were then precipitated using MeOH, and then re-dispersed in toluene.

2.2.14 Halide Oleylamine treatment

Oleylamine solutions tested were, LiF, $CdCl_2$, $ZnCl_2$, $PbCl_2$, $Cd(stearate)_2$, NaCl, KBr, KI, HTAC, TDPA, and CsI.

2.2.14.i Stock solution

A 0.1 M solution was made by dissolving 0.1 mol of the desired chemical (see list above) in 10.0 ml of oleylamine. This was carried out by adding the substance to oleylamine, which was then degassed at 50 °C for 1 hour. This was then heated to 140 °C and the salt was dissolved over a period of 2 hours under an argon atmosphere. Following this, the solution was kept under an argon atmosphere at 50 °C to avoid solidification.

2.2.14.ii Halide oleylamine solution treatment

To a solution of QDs dissolved in 1.0 ml of toluene at a concentration of 1×10^{-4} to 1×10^{-5} M of QDs, 0.1 ml of the oleylamine solution is added. The solution was then left in darkness for 24 hours to allow the solution to interact with the QDs. The solution was then diluted to the required concentrations to achieve an absorption of between 0.5 to 1 at the 1st excitonic absorption peak of the QD. Following this, the solution was diluted by a factor of ten in toluene to produce a total of 5.0 ml of QD solution. To this solution was then added an additional quantity of the halide oleylamine solution of 5 µl producing concentration 1; or 50 µl producing concentration 2. The samples Pl was then tested either immediately, or after a 3-day wait, depending on the desired data set.

2.3 Experimental Details of Chapter 4

2.3.1 Synthesis of Disodium 1,4-phenylenedicarbamodithioate (PBDT).

5.4 g (0.050 mol, 1 equivalent) p (1,4)-phenylenediamine was suspended in 100 ml of aqueous 1.25 M NaOH solution. The mixture was heated and stirred until the solution became homogeneous. After cooling down to room temperature, 50 ml of ethanol was added. Following this 7.5 ml (9.52 g, 0.125 mol, 2.5 equivalent) of carbon disulfide was added drop wise. The temperature of the mixture was maintained below 10 °C using a cold-water bath. After addition was completed, the solution was heated at 60 °C for 2 hours, then cooled to room temperature and poured into 300 ml of acetone. After 30 min, a white crystal powder precipitated and was filtered and washed thoroughly with ice-cold acetone and dried under vacuum at room temperature. A yield of 21% was achieved. 1H (400.13 MHz, D_2O) d: 7.34 (s,Harom) ; 13C (100.62 MHz, D_2O) d: 214.41 (-NH-CS_2), 139.3, 126.9 (2xCarom).[284]

2.3.2 Electrophoretic Quantum Dot Deposition

A range of different QDs were deposited upon either FTO electrodes or TiO_2 coated FTO electrodes in the experimental arrangement of Figure 2.1. A silicon spacer was used to keep the electrodes 6 mm apart or in some cases, a glass slide of 1 mm in thickness was used alternatively when a stronger driving force was needed. The nanoparticles were allowed to deposit for a set time, after which the voltage was switched off and. Two distinct approaches were developed to deposit quantum dots upon porous TiO_2 electrodes.

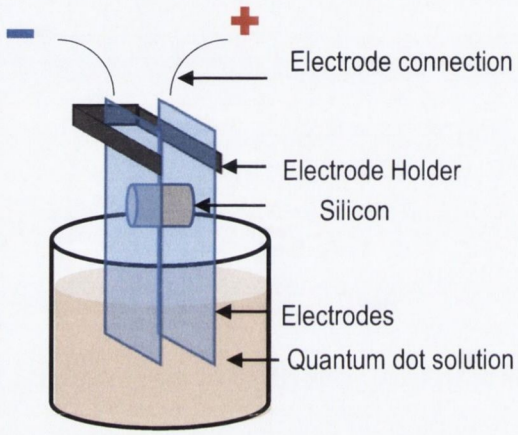

Figure 2.1 Electrophoretic deposition setup to deposit quantum dots upon electrodes

2.3.2.i Electrophoretic Deposition Method A

QDs were deposited from a solution of 1:1 v/v of acetonitrile: toluene solution. The optimum QD concentration used for this method was 1.25×10^{-6} M. Under these conditions, a 30 V potential difference was used to drive the QD deposition and the QDs were allowed to deposit for a total of 15 minutes. After this period the solution changed from a strongly coloured to clear solution, while the negative electrode becoming strongly coloured due to QD deposition.

2.3.2.ii Electrophoretic Deposition Method B

The QDs were deposited using a solution of dichloromethane and the optimum concentration of quantum, which ranged between 1×10^{-6} M to 1×10^{-5} M dependent upon the exact size of the QDs. The voltage applied was 250 V and the optimum deposition time was between 15 to 30 minutes depending upon a sample. After which quantum dots were found to have deposited upon both electrodes, producing a thicker coating upon the negative electrodes.

2.3.3 ZnS Coating of TiO_2 electrode

A ZnS layer was deposited using a dip coating technique, which was modified from literature. [235] Firstly an aqueous solution of 0.1 M $Zn(OAc)_2$ and 0.1 M Na_2S were produced. The working electrode was firstly submerged for 1 min into the Zn^{2+} solution (0.1 M $Zn(OAc)_2$) after which it is washed with deionised. Following this, it was then submerged into the S^{2-} solution (0.1 M

Na_2S) for 1 minute. This constituted a single cycle, depositing a layer of ZnS, to produce the desired thickness of ZnS; the cycle was carried out three times. The electrodes are then put through a heat treatment of 2.5 minutes at 300 °C using a small furnace for certain electrodes.

2.3.4 CdS Coating of TiO_2 electrode

A CdS layer was deposited using an aqueous solution of 0.02 M $CdCl_2$ and a solution of 0.02 M Na_2S. The TiO_2 electrode was firstly submerged into the $CdCl_2$ solution for 1 minute. Following this, the electrode was washed with deionised water. Subsequently the electrode was then submerged into the Na_2S solution for 1 minute. This electrode was then washed with deionised water. This constitutes single cycle of CdS deposition, which was carried out three times to produce the desired thickness.

2.3.5 HTAC ligand exchange of TiO_2 electrode

This was carried out by submerging the TiO_2 electrode into an MeOH based solution of HTAC at a concentration of 10 mg/ml for 1 hour under darkness. Following this, the electrode was washed in MeOH and allowed to dry in darkness, after which the electrode could be tested or incorporated into a cell.

2.3.6 MPA ligand exchange of TiO_2 electrode

This was carried out by submerging a TiO_2 electrode into a MeOH based solution of MPA (3-mercaptopropionic acid) at a concentration of 2.5% v/v for 1 minute under darkness. Following this, the electrode was washed in MeOH and allowed to dry in darkness, after which the electrode could be tested or incorporated into a cell.

2.3.7 Cation exchange of PbS QDs to PbS/CdS upon the surface of a porous TiO_2 electrode

2.3.7.i 0.025 M $CdCl_2$ solution

0.0459 g of $CdCl_2$ was dissolved in 100 ml of HPLC grade MeOH solution

2.3.7.ii Preparation of PbS/CdS sensitized TiO_2 electrode

TiO_2 electrodes were firstly sensitized with PbS Quantum dots using electrophoretic deposition approach B. These were then exchanged to CdS QDs by immersing the electrode into a solution of 0.025 molar $CdCl_2$ solution at room temperature for periods between 5 minutes and 1 week under darkness to allow the exchange to take place. Following this, electrodes were then washed using MeOH and stored in darkness.

2.3.8 Cation exchange of CdX QDs to Cu_2X upon the surface of a porous TiO_2 electrode (X= S or Se)

2.3.8.i 03 mM Tetrakis(acetonitrile)copper(I) hexafluorophosphate solution

0.55 g of Tetrakis(acetonitrile)copper(I) hexafluorophosphate was dissolved in 50 ml of MeOH

2.3.8.ii Preparation of Cu_2X sensitized TiO_2 electrode (X= S or Se)

TiO_2 electrodes were firstly sensitized with CdX Quantum dots using electrophoretic deposition approach B. Following this the electrodes were immersed in solution 0.03 mM Tetrakis(acetonitrile)copper(I) hexafluorophosphate solution in MeOH resulting in an immediate colour change of the electrode to a dark brown. The cation exchange was allowed to proceed for 30 minutes so to ensure complete conversion of the electrodes. Following this, the electrode was washed with MeOH and stored under darkness.

2.3.9 Cation exchange of Cu_2X QDs to PbX QDs upon the surface of a porous TiO_2 electrode (X= S or Se)

2.3.9.i Preparation of 0.075 M solution of Pb^{2+} solution

0.57 g of lead acetate trihydrate was dissolved in 2.0 ml of TBP in 20 ml of degassed HPLC grade methanol under an argon atmosphere.

2.3.9.ii Preparation of PbX using cation exchange (X= S or Se)

Following cation exchange to Cu_2X, from an EPD initially sensitised CdX QD TiO_2 electrode, a second cation exchange was undertaken to convert the Cu_2X to PbX. The TiO_2 electrode was placed into a sample tube and sealed using a rubber bung. Following this, the atmosphere was replaced with Argon using the Schlenk line. Following this, the 0.075 M MeOH solution of Pb^{2+} was added using syringe. An immediate change in colour solution took place, gradually darkening further over time. This reaction was allowed to proceed for two hours, in darkness. Following this, the electrode was washed with MeOH and allowed to dry in darkness.

2.4 Experimental Details of Chapter 5

2.4.1 Quantum dot Sensitised Solar Cell Fabrication

2.4.1.i Cu_2S Counter Electrode Preparation

Cu_2S counter electrodes were produced using a modified method from literature. [233] Brass foil was cut to a 3.5 cm x 2.5 cm size and was etched in concentrated hydrochloric acid (35.0 - 37.0%) at 80 C for 30 min and subsequently washed with deionized (DI) water and dried using an air gun. The electrode changed colour from a gold brass colour to a reddish brown indicative of

copper. The electrode was then immersed in a polysulfide solution composed of 1 M Na_2S and 1 M S in DI water, for 10 minutes. Immediately the surface changed to a black colour indicating formation of Cu_2S. The electrode was then washed using DI water and dried using a heat gun.

2.4.1.ii PbS Counter Electrode Preparation

PbS counter electrodes were produced using a modified method from literature. [285] Firstly, Pb metal foil was cut into 3.5 cm x 2.5 cm strips. As a pre-treatment, the foil was washed with DI water and dried. This was then immersed into a concentrated solution (~9 M) of H_2SO_4 (water: 96% H_2SO_4, ratio 1:1) for 3 hours at 60 °C temperature and afterwards washed with DI water. The pre-treatment changed the colour of the appearance of the foil from shiny metal to grey. Subsequently, the foil was inserted into a polysulfide solution (aqueous solution of 1 M Na_2S, 0.1 M sulfur, and 0.1 M NaOH) for 24 h before it was rinsed with deionized water and dried in an air stream. This treatment changed the appearance of the foil from grey to dark black indicating the formation of PbS on the surface.

2.4.1.iii Pt electrode

Pt counter electrodes were produced by using an aqueous solution of 5 mM solution of chloroplatinic acid (H_2PtCl_6), which was drop cast upon the surface of cleaned FTO coated glass. This was then placed into an oven at 80 °C to remove the solvent. Following this the film was converted to metallic Pt by heating the film in a furnace to 400 °C for 15 minutes, producing a dark grey film upon the FTO glass, ready for testing.

2.4.1.iv Electrode Cleaning

Fluorine doped tin oxide glass was cut using a glass scribe and then cleaned. The cleaning process consisted of three stages. Firstly, the glass was submerged in deionized water and detergent for 90 minutes and sonicated[214], and then washed using deionized water. This was followed by sonication in ethanol for 90 minutes, washed with acetone and finally sonication in acetone for 90 minutes. After which the glass was dried in an oven at 80 °C.

2.4.1.v Bulk TiO_2 layer deposition upon working electrode

TiO_2 electrodes were produced by firstly depositing a bulk layer of TiO_2 upon the FTO glass using a modified reported procedure. [183] This was done by producing firstly a 2 M (4.5 ml) solution of $TiCl_4$ in 20 ml of deionised water in a 3-neck round bottom at 0 °C. This was then stored in the freezer until use. As the FTO will be used as the cathode terminal, TiO_2 will be only placed on FTO. A solution of 0.006 ml of TiO_2 in 25 ml of deionised water (0.0003 M, $TiCl_4$ solution) is injected on the FTO side of the electrode. It was heated for 30 minutes at 125 °C in an oven. The electrodes were washed using deionised water and ethanol followed by drying.

2.4.1.vi Porous nanoparticulate TiO_2 layer deposition upon working electrode

Following this a porous layer of nano-particulate TiO_2 was deposited using a doctor blading approach in which a commerically sourced sol of TiO_2 (Dyesol 90-T Transparent paste consisting of 20 nm anatase particles and WER2-O Reflector Titania Paste) consisting 0f 400 nm particles nanoparticles was deposited upon the bulk TiO_2 layer described in section 2.4.1.v . This was done using a manual screen printer purchased from A.W.T. World Trade Inc. (www.awt-europe.com) using custom screens, which were purchased screens from Serigraf Ltd., were a 90T polyester mesh, and were designed to print 1 x 3 cm electrodes.

Three distinct types of electrodes were produced using the screen printer, Electrode A = 1 layer of 20 nm sized TiO_2 particles, Electrode B = 4 layers of 20 nm sized TiO_2 particles, and Electrode C = 4 layers of 20 nm sized TiO_2 particles followed by a forth layer of light-scattering 200 nm

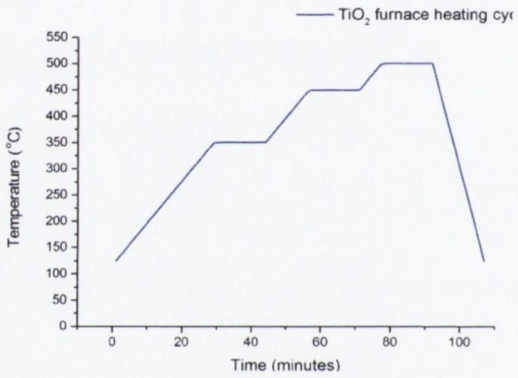

Figure 2.2 TiO_2 electrode thermal treatment cycle using a tube furnace in air

sized TiO_2 particles. Multiple layers were produced by heating the electrodes to 125 °C for 6 minutes in a furnace between depositions.

After depositing the desired layers of TiO_2 upon the electrodes, they were placed into a tube furnace and put through a pre-programmed temperature cycle (see Figure 2.2). This involved setting the furnace initially to 125 °C, and with inputting heating rate of 8 °C /min. Upon commencement, the furnace heated to 350 °C and held at this temperature for 15 minutes, after which it heated further to 450 °C held for 15 minutes and then heated to 500 °C and held for a final 15 minutes. After this, the furnace switched off and the electrodes slowly cooled to room temperature. These electrodes were then ready for sensitization.

2.4.1.vii Device Fabrication

Quantum dot sensitised solar cells were fabricated using a sensitised titanium dioxide electrode and a counter metal foil back electrode (PbS or Cu_2S). Firstly, the metal foil electrodes were drilled using a power drill to allow for filing of the cell and one side was bent upwards. Following

this the titanium dioxide electrode was sealed onto the metal foil using a 60 µm thermoplastic (Solaroinx, Meltonix 1170-60) gasket, by using a heat gun. After which the device was then filled using a syringe with a polysulphide electrolyte composed of 1 M Na_2S and 0.1 M S in a 1/9 ,v/v, degassed ethanol/H_2O solution. The device was then sealed using a glass slide.

2.4.2 DHCQD cell Fabrication

2.4.2.i FTO Etch

This method was modified from literature[286, 287] and was used to selectively etch a pattern into the FTO glass (see Figure 2.3). Firstly, the FTO glass was covered using a silicon-based tape to selectively etch the FTO from the glass. Following this, an aqueous Zn suspension (1 g of Zn powder in 100 ml of propanol) was drop cast upon the surface of the glass. This was allowed to dry on a hot plate for 10 minutes at 50 °C. Following this, the slide was submerged into a solution of 9 M HCl and the etch was allowed to take place for 3 minute, after which the glass was removed from the bath and cleaned using the procedure described in section 2.4.1.iv .

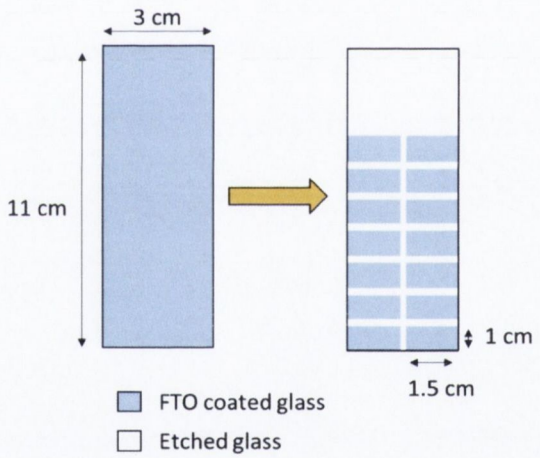

Figure 2.3 Diagram showing the FTO glass etch carried out enabling multiple DHCQD cells be produced upon the same glass

2.4.2.ii TiO_2 deposition and sintering

Firstly, a thin layer of bulk TiO_2 was deposited upon the cleaned and etched FTO electrodes and was done using the approach described in section 2.4.1.v . Following this a thin layer of porous TiO_2 layer was deposited (300 nm – 700 nm in thickness) using a commercially sourced sol consisting of 20 nm TiO_2 anatase particles (Dyesol 18-nrt), which was diluted to a concentration of 3 w/w. This was deposited using a doctor blading approach, using 3M scotch tape as a template. Following this the film was put through the same heating cycle used for TiO_2 electrodes produced for QDSSC cells see section 2.4.1.vi .

2.4.2.iii Dip coating of Colloidal Quantum Dots

Dip coating was used to deposit a thin layer of QDs upon the surface of an electrode and was done by hand using a series of solutions (see Figure 2.4). Firstly, the electrode was dipped into a solution of colloidal quantum dots capped by long alkyl ligands (i.e. oleic acid, octadecylamine or octadecylphosphonic acid) at a concentration of 10 mg/ml in hexane, and drawn out of the solution at a rate of 0.5 cm/sec. The electrode was then allowed to dry on a hot plat set to 30 °C for 2 minutes. After this, the electrode was dipped into a solution containing the desired short change ligand (PBDT or 3-mercaptoproponic acid) at a concentration of 2.5% v/v in MeOH. The electrode was kept in solution for 10 seconds and then slowly removed and allowed to dry hot plat set to 30 °C. Following this the electrode was washed by firstly dipping the electrode into a solution of MeOH, to remove excess of the short chain ligand and then followed by a dipping it into a solution hexane to remove any of the original fatty chain ligand that may be on the surface. This process constituted one cycle of deposition. This process was repeated 10 -20 times to produce a thickness of between 150 nm - 300 nm of QDs for fabrication of the DHCQD cell.

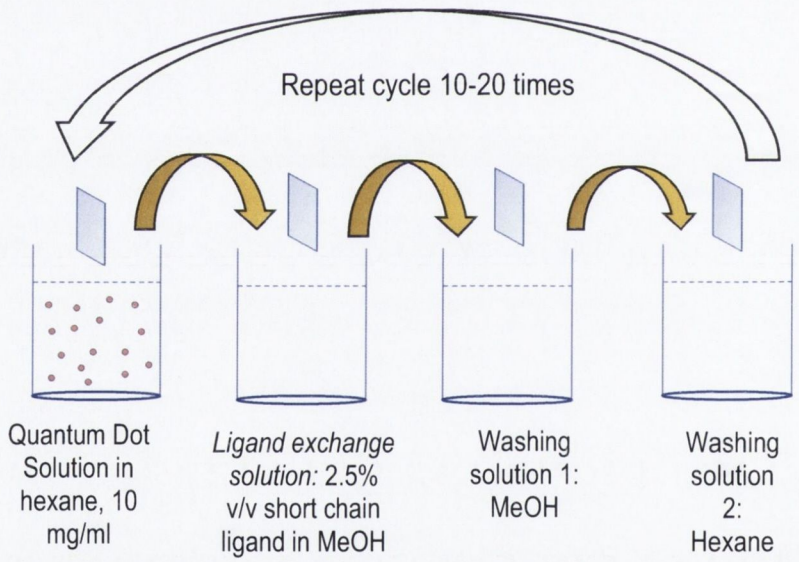

Figure 2.4 This shows the basic process used to deposit collodial quantum dots upon the TiO_2 elctrode

2.4.2.iv Metal Evaporation of Au back electrode

Metal evaporation was used to deposit the back electrode onto the deposited CQD layer. This was carried out with the use of a manual Edwards E306. This was carried out at pressures below 1×10^{-5} mbar using thermal evaporation of gold pellets, 1-3 mm, from a tungsten casket. It was not possible to monitor the deposition rate in real time, while the deposition was carried out over a period of three minutes achieving a thickness of between 50-100 nm.

2.4.3 Discotic Liquid Crystal Testing and Solar Cell Fabrication

2.4.3.i Liquid Crystal Electrical conductivity Device Fabrication

To test the DC conductivity of the QD-DLC composites, DLCs were mixed with QDs in hexane, after which the solvent was evaporated. A device fabricated from two slides of conductive glass (Fluorine Doped Tin oxide (FTO) coated glass) and a polymer spacer of 5 microns PET film (Polyethylene terephthalate) was then used to test the conductivity of the resulting films as shown in Figure 2.5. The device was filled by placing approx. 2 milligrams upon one side of the device, after which the paste was melted into the liquid phase using a heat gun, and the liquid filled the space due to capillary action. The exact size of this filled space was then recorded using a digital camera and determined using imaging software. Finally, silver paint was used to attach silver wire onto each side of the electrode. Composites were made by dissolving the constituents into hexane, followed by stirring, after which point the sample was dried, and then ready for loading into the cell.

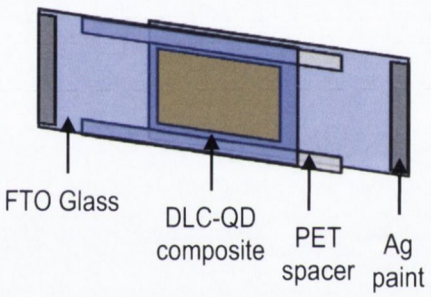

Figure 2.5 Diagram of devices fabricated to test the conductivity of DLC/QD composites

2.4.3.ii Alignment of Discotic Liquid Crystals

After loading the designed device to test the RTAQ electrical conductivity, the liquid crystal was aligned within the device, to allow testing of DLC crystal phase of the RTAQ phase. This was done by heating the device to 130 °C, after which the phase was slowly cooled to 60 °C at a rate of 0.5 °C per minute and had the effect of producing the desired aligned DLC phase of the RTAQ within the device.

2.4.3.iii Spin Coating of diluted TiO_2 paste

This method was modified from literature.[178] The paste of TiO_2 was diluted to a concentration of 1:3 w/w using terpineol. This solution was manually mixed for 15 minutes and then sonicated for an hour to produce the diluted paste. Following this, the paste was spincoated on the already retreated FTO to produce the base of the cell. The spin speed was chosen to be 3,000 rpm and the sample was spun for 1 minute. The electrodes were then placed into the tube furnace and heat-treated as described in section 2.4.1.vi .

2.4.3.iv Metal evaporation of Ag or Al back electrode

The back electrode was deposited using metal evaporation as described in section 2.4.2.iv using either 1 mm diameter Ag wire mm or 1.5 mm Al wire, depending on the desired metal.

2.5 Instrumentation

2.5.1 Microscopy

2.5.1.i Transmission Electron Microscopy (TEM)

This was performed using a Jeol 2100 TEM operating at 200 kV with a Lanthanum Hexaborise emission source, under the supervision of Mr Neal Leddy in the Centre for Microscopy and Analysis-TCD. This was utilised for general TEM imaging of samples and surveying a number of samples, especially due to the ability to load 5 samples simultaneously. Samples were diluted and dropped casted onto 400 mesh copper TEM grids coated with either a carbon film or lacy carbon film (purchased from Agar Scientific) and allowed to dry on the bench overnight.

2.5.1.ii High Resolution Transmission Electron Microscopy (HRTEM) / Scanning Transmission Electron Microscopy (STEM)

High Resolution Imaging, a FEI Titan – Transmission Electron Microscope operating at 300 kV, which was operated unsupervised in the CRANN Advanced Microscope Facility-TCD. The basic operation is this instrument is shown in *Figure 2.6*. Samples were diluted and dropped casted onto 400 mesh copper TEM grids coated with lacy carbon film (purchased from Agar Scientific) and allowed to dry on the bench overnight. The samples were then plasma cleaned for 10 seconds before imaging to remove any excess remaining fatty ligands or solvent present upon the grid.

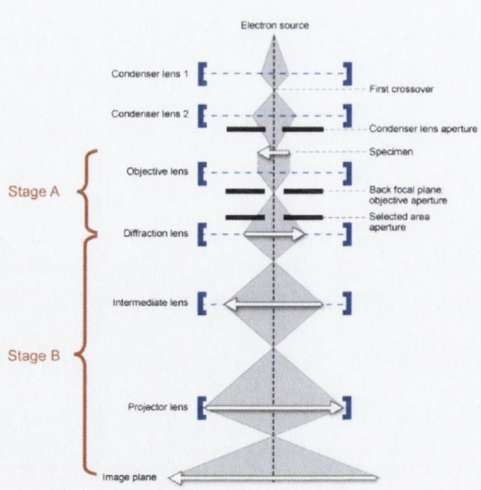

Figure 2.6 Diagram showing the basic structure of a TEM microscope. *Stage A is the scattering of an incident electron beam by a specimen. This scattered radiation passes through an objective lens, which focuses it to form the primary image. Stage B uses the primary image obtained in stage A and magnifies this image using additional lenses to form a highly magnified final image. The image was reproduced from ref 288.*

2.5.1.iii Scanning Electron Microscopy (SEM)

This was performed with the use of a Tescan Mira XMU SEM in the Centre for Microscopy and Analysis-TCD, and the Zeiss Ultra plus SEM in the CRANN Advanced Microscope Facility-TCD. Samples were coated with a gold conductive coating using a gold evaporation technique under reduced pressure before the sample was then attached to a sample stud for analysis on the Tescan SEM. While samples studied using, the Zeiss ultra were instead left uncoated and simply attached to sample studs. On both devices, working distance and acceleration voltage were varied to enable the best images possible to be produced. It should also be noted that a range of different detectors were also employed to produce the best contrast for a set of images, the basic operation of this instrument is shown in Figure 2.7.

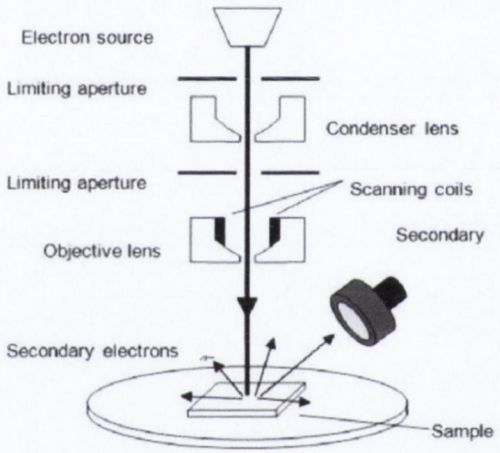

Figure 2.7 Diagram of scanning electron microscope showing the basic setup of the device. The image was reproduced from ref 288.

2.5.1.iv Incident Polarized Optical Microscopy (POM)

This was carried out using an Olympus BX51. This microscope produces contrast in an image based upon the anisotropic nature of the material being examined. This is done through modification of a microscope with the addition of linear two polarisers. The first linear polariser is placed just after the illumination source, only selectively allowing light of one polarisation to pass through. This light source is then used to illuminate the sample. After the light has passed through the sample and through the objective lens, a second liner polariser is inserted. This polariser is positioned at a 90 ° angle to the first polariser and should completely absorb any of the polarised light emitted by the light source. Therefore, if an isotropic sample is placed in a POM microscope, a black image is produced. While if a sample which has an anisotropic structure is examined, due to its interaction with the light, some of the incident light's polarization is rotated. This light now with an alternative polarization to the incident beam can now pass through the second polariser, producing an image. Therefore, the contrast in the

resulting image is based upon the materials ability to rotate the polarization of the light source. The colour produced in the image is a function of the sample thickness and the birefringent of the sample, which is the difference between the smallest and the largest refractive index present in the sample. The birefringent can also be estimated from a sample if the thickness of the film is known and a POM image with Michel-Levy Birefringence charts,[289] which can be used as a means to identify a sample.

2.5.2 Spectroscopy

2.5.2.i Ultra violet- visible –infrared (UV-Vis-NIR) absorption spectroscopy

UV-Vis absorption spectra were recorded using a Varian Cary 60 UV-Visible Spectrophotometer. UV-Vis-NIR absorption measurements were recorded using a Perkin Elmer LAMBDA 1050 UV/Vis/NIR Spectrophotometer. Samples spectra were measured in a 1 cm path length quartz cuvette cell in a range of solvents and ambient atmosphere. The basic operation of a dual beam UV-Vis spectrometer is shown in Figure 2.8. The concentration of CdSe, CdS, CdTe and PbS QD solutions were determined by measuring the absorption spectra of the solutions. From this, it was possible to calculate the concentration of quantum dots in solution by using the first exciton peak's intensity, wavelength and the hwhm of the first exciton peak, to determine the QDs concentration. The formulae used to do this has been reported in literature[49 52] and takes into account the change in the absorption coefficient of a quantum dot as the size of the QD changes.

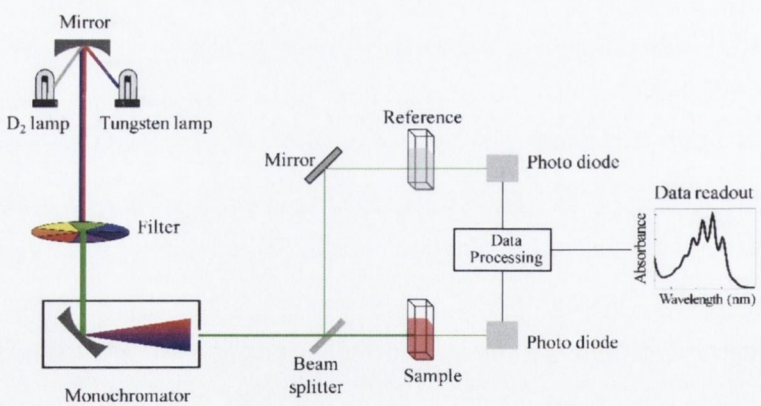

Figure 2.8 Diagram of the operation of a dual beam UV-Vis absorption spectrometer. Image reproduced from ref 290.

2.5.2.ii Photoluminescence (PL) Spectroscopy

UV-Vis photoluminescence spectra were recorded using a Varian Carly Eclipse Fluorescence Spectrometer, while NIR PL measurements were measured using a Horiba Jobin Yvon Fluorolog-3 using a Hamamastu InP/InGaAs photomultiplier (R5509-7-3) cooled to -80 ˚C using liquid nitrogen. Sample spectra were measured in a 1 cm path length quartz cuvette cell in a range of solvents with PL intensity recorded at right angles to excitation. Excitation of samples was performed at least 20 nm below the range of PL measured using a range of excitation and emission. The basic operating principle of a PL spectrometer is shown in Figure 2.9.

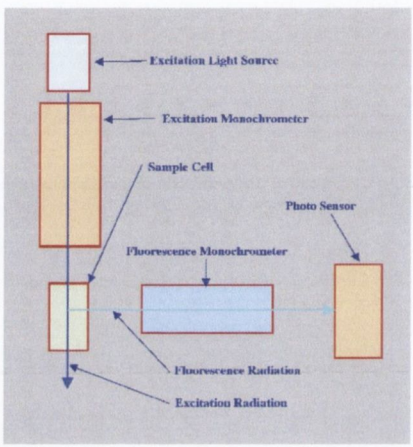

Figure 2.9 This diagram explains the operation of ta photoluminescent spectrometer. Image reproduced from ref 291.

Relative Quantum Yields were calculated by the comparison of PL intensity between a sample and a standard dye, which have well-known quantum yields and calculated using

. Four standards were used, Coumarin 153 in ethanol (QY 53%[292]) and Rhodamine 6G in ethanol (QY 95%[292]) for UV-Vis photoluminescence and IR Dye 26 in 1,2-dichloroethane (0.005%[293]) and IR Dye 140 in ethanol (16.7%[294]) for fluorescence. The specific standard used depended on the position of the QDs exciton peak relative to the dye absorption peak. Samples absorption were firstly measured to be between 0.25 and 0.5 at peak exciton value, followed by a 1:10 dilution, after which sample's PL was measured; this was done to minimize self-absorption of fluorescence

$$\Phi_x = \left(\frac{A_s}{A_x}\right)\left(\frac{F_x}{F_s}\right)\left(\frac{n_x}{n_s}\right)^2 \Phi_s$$

Equation 2.1 Used to calculate relative quantum yield of a sample. Where ϕ= quantum yield, A= absorbance, F= Integrated fluorescence, n= solvent refractive index and the subscript s is for standard and x is for sample being tested

2.5.2.iii Raman spectroscopy

Raman spectroscopy was performed using a Renishaw inVia Raman Microscope using a 785 nm Renishaw HP NIR Laser. Samples were prepared by drop casting concentrated solutions onto glass slides, followed by drying.

2.5.2.iv Energy dispersive X-ray spectroscopy (EDX/EDS)

This is an analytical technique that allows the identification of elemental composition of a sample, through the investigation of the produced X-ray, from electron beam interaction with the sample. This was performed using a Zeiss ultra SEM microscope fitted with an Oxford Instruments X-Max Silicon Drift Detector. The data was analysed using AZtecEnergy EDS software, allowing for point scans and line scans to be carried out and interpreted.

2.5.2.v Photoluminescence lifetime spectroscopy

This photoluminescence lifetime and time resolved emission spectra measurements were performed using a time correlated single photon counting (TCSPC) spectrometer (Fluorolog 3 Horiba Jobin Yvon) and a range of different semiconductor diode lasers (295 nm, 340 nm and 370 nm "Nano LED" – HORIBA jobin Yvon) with pulse duration shorter than 1 ns for excitation.

2.5.2.vi Spectrograph

An Oriel MS-125 1/8m spectrograph was coupled with an Oriel InstaSpec™ MkIV used to characterise the light produced by a number of illumination sources. The instrument allowed the measurement of illumination sources across a 500 nm window, allowing us to characterise the illumination of our Xe-arc lamp and our white light LED arrays.

2.5.3 Diffraction

2.5.3.i X-ray powder diffraction (XRD)

This was performed using a Siemens-500 X-Ray diffractometer, which used a Cu cathode Kα1 with a wavelength of 0.154056 nm under a 12-hour scan time. The samples were prepared by drop casting samples upon a glass slide and allowing the samples to dry in an oven at 80 °C for one hour.

2.6 Electrical measurements

2.6.1 Cyclic voltammetry

This was carried out using a Metrohm μAutolab type III controlled using Autolab NOVA. A three-electrode setup was used, utilising a titanium counter electrode, a saturated calomel as a reference electrode and the electrode to be tested as the working electrode. Measurements were taken in an appropriate range of voltage, generally ranging between -1 to 0 V, using a scan

rate of between 0.1 mV/sec to 0.01 mV/sec. A polysulphide-based electrolyte was utilised, of 20 mM Na_2S, 0.5 mM S, and 0.5 M KCl in deionised water.

2.6.2 DC conductivity testing

I-V curves of DLC-QD composite cells were tested using a Keithley 2400 sourcemeter, by scanning the voltage form –0.5 V to +0.5 V , from the slope of this graph the conductivity of the cell was determined. These IV curves were performed under darkness and under AM 1.5 (100 mW/cm^2) illumination using a filtered Xe-arc lamp to simulate sunlight. Films of HBC-PH12/QD were spincoated onto a film of FTO using a concentration of between 15 - 60 mg per ml in cyclo-hexane using a spin rate of 2000 rpm.

2.6.3 Photocurrent Action Response Measurement

The test was done using a three electrode arrangement made using a Metrohm μAutolab type III electrochemical impedance analyzer , using a reference, counter and working electrode in a 0.1 M aqueous solution of Na_2S using a 20 ml quartz cuvette (as shown in Figure 2.11). This was controlled using NOVA software. The reference electrode used was a saturated calomel electrode, while the counter electrode was an FTO slide. The counter electrode and working electrodes were separated using a 6 mm silicone spacer. The sample was placed 5.5 cm from the illumination source, with the working electrode illuminated through the FTO glass, which was placed parallel to the quartz glass cuvette. The working electrode was masked to produce a 1 cm^2 active area. Current readings were taken using a zero bias between the working and counter electrode and the response of the sensitised electrode was measured under darkness and illumination utilising a white light LED ring that was powered using an external voltage source, which produced on/off response of current readings when the material was photoactive (see Figure 2.10). The illumination approximated the visible region (see Figure 2.12) of the solar spectrum and allowed a determination of electrodes for the utilisation of the visible region of

the solar spectrum for photovoltaic applications, the intensity of the source measured using a calibrated power meter.

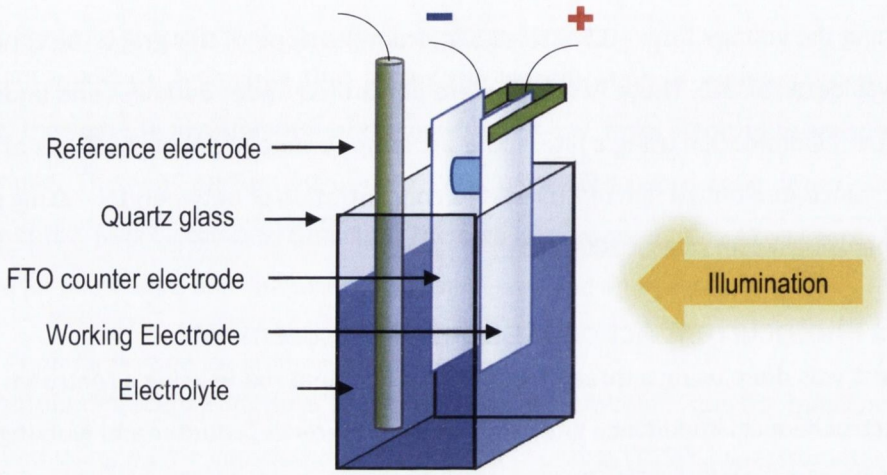

Figure 2.11 This is the experimental design used to take photocurrent action response measurements; the photoaniode illuminated is carried out using a white light LED ring.

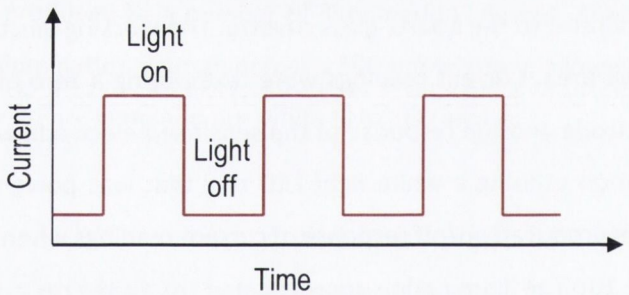

Figure 2.10 This shows the ideal current response of a photoaniode when cycled between illumination/darkness as a function of time.

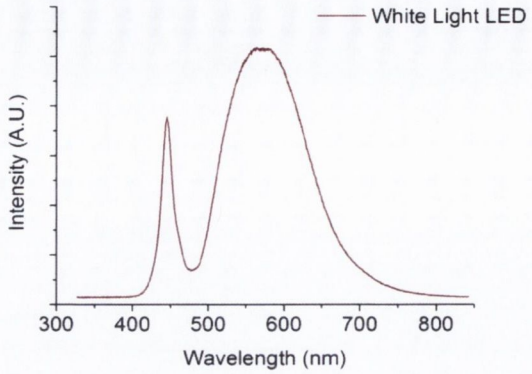

Figure 2.12 Emission spectra of white light LED used to approximate sunlight illumination for photocurrent spectra measurements

2.6.3.i Solar PCE Measurements

These measurements were performed using an in house built setup. This setup was constructed and tested by a colleague, Lorcan Brennan and myself using a modular design. This was performed using a 150 W Xe-short arc lamp with a "Ozone free" coating from Ushio(uxl-150SO), powered in a Oriel Instruments 50-500 W arc lamp housing injunction with a AM 1.5 D filter (see Figure 2.13). The resulting illumination intensity was determined using the 818-UV-L UV Enhanced Silicon Photodetector from Newport with the attachment of the OD3 Attenuator. I-V curve measurements were taken using a two-probe setup, with a Keithley 2400 sourcemeter, from which the data was recorded into a Labview-based software from Newport. The active area of the cell was determined to be 2.8 x 10^{-5} m^2 (0.28 cm^2) and cell testing was performed at room temperature under an ambient atmosphere.

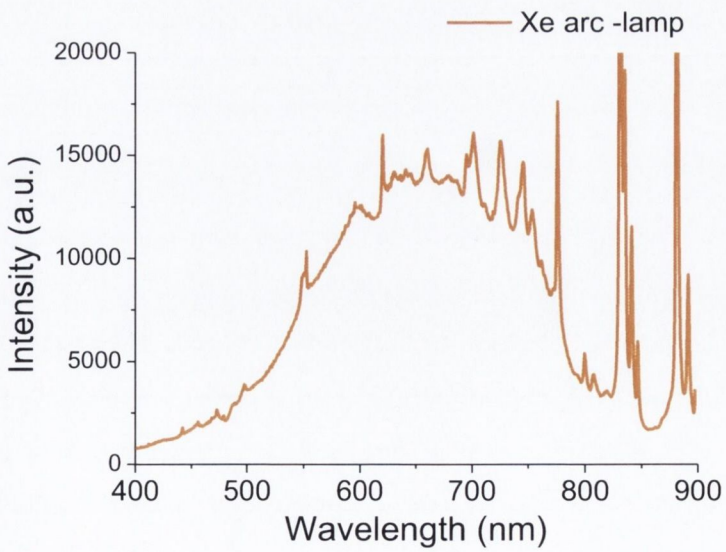

Figure 2.13 The emission spectra of the Xenon arc discharge lamp used for solar simulation.

2.6.3.ii External Quantum Efficiency (EQE) spectrum

These measurements were performed using an in house built setup, see Figure 2.14 . This was constructed and validated by myself and a fellow PhD researcher in my group, Lorcan Brennan using a modular design constructed from a number of independent devices, which were setup as shown in the diagram below. The initial illumination source used was a 150 W Xe-short arc lamp with a "Ozone free" coating from Ushio(uxl-150SO) , powered in a Oriel Instruments 50-500 W arc lamp housing injunction with a AM 1.5 D filter. This was then passed through a monochromator, using an entrance slit of 250 μm and exit slit of 50 μm. The wavelength was chosen with the use of an electronic piston purchased from Zaber, which rotated a mirror (E) in the monochromator, allowing precise control of wavelength selection.

The monochromatic light was then passed through an optical chopper, which allowed the introduction of a square wave, on/off, frequency into the monochromatic optical signal, and was set at a frequency of 200 Hz. The optical chopper was also linked as a reference into a lock in amplifier, allowing the amplifier to know the exact frequency response introduced into the light signal. After this, the light passed through a filter wheel. The filter wheel was fitted with two filters to block the second harmonic present in the light from the monochromator so glass band pass filters were used, a FSR-GG495 Coloured Glass Filter, 25.4 mm Diameter, Cut-on 495 nm and a FSR-RG715 Coloured Glass Filter, 25.4 mm Diameter, Cut-on 715 nm. The light was then split using a two way optical splitter purchased from Thor Labs, a Pellicle beam splitter (1") BP108. This allowed the use of a spectrograph, an Oriel MS-125, to be used to monitor the monochromatic lights wavelength and bandwidth. The other path of the light passed through an optical diffuser, a UV Fused Silica Ground Glass Diffuser of 120 Grit (DGUV10-120 - Ø1") purchased from Thor Labs, which was used to produce a homogeneous illumination light source relative to intensity. The resulting diffused monochromatic light intensity was measured using a calibrated photodiode.

This gave a current reading, which were then amplified using the lock in amplifier. A lock in amplifier works on the principle of filtering the incoming signal through a frequency dependent filter, and then amplifying this signal to reduce the effect of noise. The lock in amplifier uses the optical chopper as a reference frequency of the signal it should amplify. This allowed isolation of the monochromatic light signal from background noise of the photodiode and stray light, to the extent that readings could be taken if desired under ambient light conditions.

This amplified signal was then outputted to a Keithley 2400 sourcemeter and from which a simple program built using LabView software recorded the current values. These values were

converted to give the power density (P_{light}) of an illumination source, by taking into account the size and responsivity of the calibrated photodiode for a given wavelength and was calculated with the use of Equation 2.2.

$$P_{light} = \frac{Current \times Respinsivity}{Area}$$

Equation 2.2 This relates the power density of the illumination source to the current reading from a calibrated photodiode, and takes in to account the responsivity and area of the sensor for a given wavelength.

$$\eta_{EQE} = \frac{output}{input} = \frac{electrons\ out/sec}{photons\ in/sec}$$
$$= \frac{Current\ density\ (A/cm^2)/(charge\ of\ elctron)}{Power\ density\ (W/cm^2)/(energy\ of\ photon)}$$
$$= \frac{I_{cell}}{P_{light}} \times \frac{hc}{\lambda} \times \frac{1}{e}$$

Equation 2.3 This equation is used to determine the external quantum efficiency of a photovoltaic cell for a given wavelength of illumination.

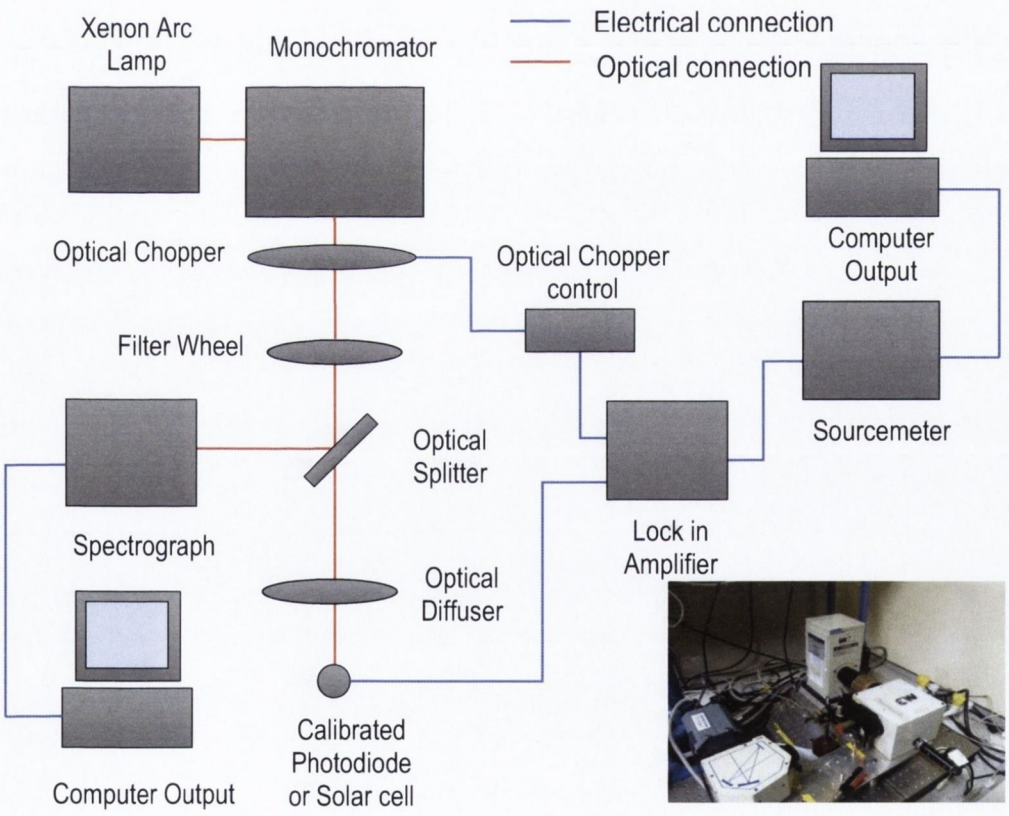

Figure 2.14 This shows the setup of the EQE device designed in house. The orange line shows the path of light from the Xenon arc lamp, through the optical chopper and filter wheel , and then being split into two different

After determining the intensity across the full wavelength range possible (400 – 950 nm), a photovoltaic cell replaced the photodiode and readings were taken of the short circuit current

(I_{sc}) response of the cell across the range of wavelengths. Then by using Equation 2.2, n_{eqe} could be determined per wavelength and graphed verses wavelength to produce a result as seen in Figure 2.15.

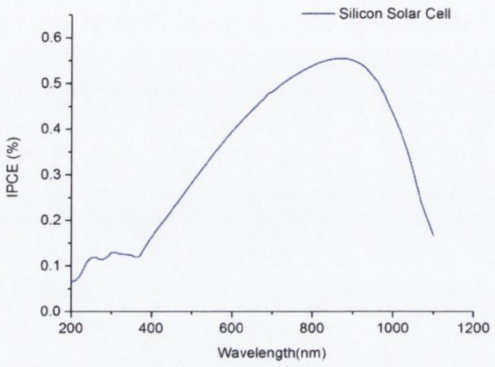

Figure 2.15 IPCE measurement of a silicon solar cell

2.6.4 Current-Voltage (IV) Curve

The standard approach to characterise a PV cell is by IV curve analysis, comparing the cells response under illumination and under darkness. Firstly, crocodile clips were attached to the positive and negative junctions of the solar cell. These junctions were then connected to a Keithley 2400 sourcemeter. The light source used was a 150 W Xe-short arc lamp with a "Ozone free" coating from Ushio(uxl-150SO) , powered in a Oriel Instruments 50-500 W arc lamp housing injunction with a AM 1.5 D filter. The resulting power of this light was determined using a calibrated photodiode, to produce an illumination of 1000 W/m^2, also called 1 sun. Then through the use of a sourcemeter, Keithley 2400 sourcemeter and which was controlled through a computer using a simple program built using LabView software, the current readings from the cells are recorded as a voltage is swept from a negative value to a positive value. This reading is taken under illumination of the light source and under darkness and produces the resulting graph, which is called an IV curve (see Figure 2.16). From this, a huge amount of information related to the cell's performance can be inferred and is explained below.

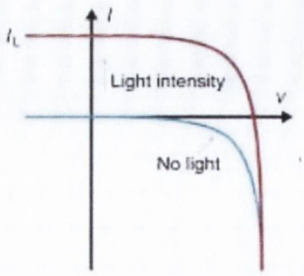

Figure 2.16. I-V curve of a solar cell under illumination and darkness, reproduced from ref 147.

2.6.4.i Power In (P_{in})

This is the total amount of solar energy applied to the cell, and so is a function of the cell size and the solar irradiance.

2.6.4.ii Short Circuit Current (I_{sc})

This is the current produced when a PV cell's cathode and anode are connected with zero resistance wire while being illuminated and corresponds to the maximum current a cell can produce. I_{sc} is related to the amount of charge carriers produced under illumination, and therefore the E_g of material. Since as Eg in a PV cell is reduced, more of the photons in the solar illumination will be able to produce charge carriers in the cell and so Isc is increased.

2.6.4.iii Open Circuit Voltage (V_{oc})

The open circuit voltage describes the voltage generated by a solar cell when it is irradiated without the two terminals of the device being connected; allowing the charge carriers to build up on each terminal and corresponds to the maximum voltage the cell can produce. If in the cell design there exists no potential drop, the Voc maximum possible out of a PV cell is related to the E_g of the material by $V_{oc}= E_g/q$ (where q is electron charge).[295] In reality, all solar cells require a potential drop to enable charge separation; therefore, the real V_{oc} is always smaller than the absorber material's E_g/q but Voc still shows a strong relation to the E_g.

2.6.4.iv Maximum Power Point (MPP), Maximum Power (P_{max}) and Theoretical power (P_t)

This refers to the voltage and current combination that delivers the maximum power from a PV cell (P_{max}) and corresponds to the knee of the cell's I-V curve. The theoretical power (P_t) is the power calculated using the V_{oc} and I_{sc}.

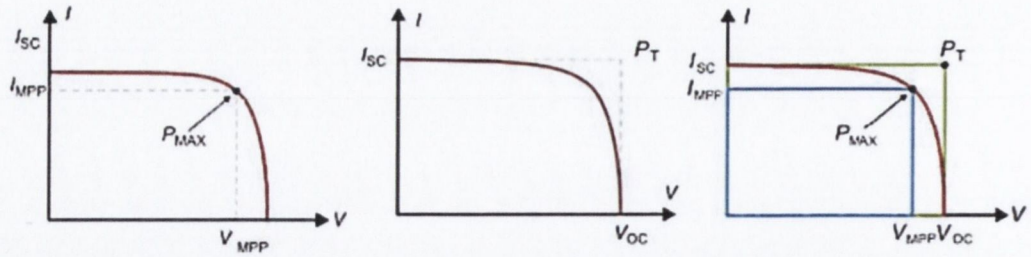

Figure 2.17.I-V curves showing P_{max}, I_{mpp}, V_{mpp} on left, I_{sc}, V_{oc} P_t in middle and FF on right, reproduced from ref 147.

2.6.4.v Fill Factor (FF)

Fill Factor (FF) describes the shape of the I-V curve of a PV cell and is given by Equation 2.4; specifically it's squareness and relates to the resistive losses of the cell. An ideal FF of 100% describes a right angle between the V_{oc} and the I_{sc} where $P_{max}=P_t$. Unfortunately, a FF of 100% is not possible in a solar since resistive losses always exist, but an efficient cell will achieve a FF over 80%.

$$FF = \left(\frac{P_{max}}{P_t}\right) = \left(\frac{V_{MPP} * I_{MPP}}{V_{oc} * I_{sc}}\right)$$

Equation 2.4 Fill factor for a cell can be calculated by relating the measured power maximum measured to the theoretical power maximum.

2.6.4.vi Series Resistance (R_s) and Shunt Resistance (R_{sh})

Series Resistance refers to the combined resistance of the cell's components that lie in the currents path including semiconductor material, metal wire and semiconductor-metal contact resistance. R_s should be as low as possible for an efficient cell (below 10 mΩ per cm^2),[295] as R_s increases the I-V curve graph changes , with current beginning to drop at a lower applied voltage. At very high R_s, the I-V curve becomes a straight line from I_{sc} to V_{oc} with I_{sc} being reduced in overall value.

The Shunt Resistance (R_{sh}) is the resistance across the junction, has its origin in current leakage across the charge separation area, and is a sign of pure rectification in the cell. R_{sh} should be as high as possible so that current travels the correct route around the circuit through the load instead of short-circuiting across the junction. The effect of low R_{sh} is that V_{oc} is decreased while the I_{sc} is maintained. In addition, the R_s and R_{sh} can be estimated by using the inverse of the IV-curve slope at I_{sc} and V_{oc} respectively.

2.6.4.vii Power Conversion Efficiency (PCE)

The PCE is (power conversion efficiency), is dependent upon the FF, Voc, Isc and the Pin and can be calculated using Equation 2.5. This is the most important figure when describing how efficient a solar cell performs under a certain set of conditions in its most basic understanding, the figure relates

$$PCE = \left(\frac{V_{oc} I_{sc} FF}{P_{in}}\right)$$

Equation 2.5. This relates the power conversion efficiency (PCE) to the open circuit voltage (V_{oc}), short circuit current (I_{sc}) , fill factor (FF) divided by the actual power in

References

16. Ouyang, J.; Kuijper, J.; Brot, S.; Kingston, D.; Wu, X.; Leek, D. M.; Hu, M. Z.; Ripmeester, J. A.; Yu, K., Photoluminescent Colloidal CdS Nanocrystals with High Quality Via Noninjection One-Pot Synthesis in 1-Octadecene. *The Journal of Physical Chemistry C* 2009, 113, 7579-7593.

17. Yu, W. W.; Peng, X., Formation of High-Quality Cds and Other Ii–Vi Semiconductor Nanocrystals in Noncoordinating Solvents: Tunable Reactivity of Monomers. *Angewandte Chemie International Edition* 2002, 41, 2368-2371.

49. Yu, W. W.; Qu, L. H.; Guo, W. Z.; Peng, X. G., Experimental Determination of the Extinction Coefficient of CdTe, CdSe and CdS Nanocrystals. *Chem. Mat.* 2004, 16, 560-560.

52. Cademartiri, L.; Montanari, E.; Calestani, G.; Migliori, A.; Guagliardi, A.; Ozin, G. A., Size-Dependent Extinction Coefficients of PbS Quantum Dots. *Journal of the American Chemical Society* 2006, 128, 10337-10346.

88. Carbone, L.; Nobile, C.; De Giorgi, M.; Sala, F. D.; Morello, G.; Pompa, P.; Hytch, M.; Snoeck, E.; Fiore, A.; Franchini, I. R.; Nadasan, M.; Silvestre, A. F.; Chiodo, L.; Kudera, S.; Cingolani, R.; Krahne, R.; Manna, L., Synthesis and Micrometer-Scale Assembly of Colloidal CdSe/CdS Nanorods Prepared by a Seeded Growth Approach. *Nano Lett* 2007, 7, 2942-2950.

93. Neo, M. S.; Venkatram, N.; Li, G. S.; Chin, W. S.; Ji, W., Synthesis of PbS/CdS Core-Shell Qds and Their Nonlinear Optical Properties. *Journal of Physical Chemistry C* 2010, 114, 18037-18044.

111. Jain, P. K.; Amirav, L.; Aloni, S.; Alivisatos, A. P., Nanoheterostructure Cation Exchange: Anionic Framework Conservation. *Journal of the American Chemical Society* 2010, 132, 9997-9999.

112. Luther, J. M.; Zheng, H. M.; Sadtler, B.; Alivisatos, A. P., Synthesis of Pbs Nanorods and Other Ionic Nanocrystals of Complex Morphology by Sequential Cation Exchange Reactions. *Journal of the American Chemical Society* 2009, 131, 16851-16857.

147. Ginley, D. S.; Cahen, D., *Fundamentals of Materials for Energy and Environmental Sustainability*. Cambridge University Press: 2011.

178. Wang, X. H.; Koleilat, G. I.; Tang, J.; Liu, H.; Kramer, I. J.; Debnath, R.; Brzozowski, L.; Barkhouse, D. A. R.; Levina, L.; Hoogland, S.; Sargent, E. H., Tandem Colloidal Quantum Dot Solar Cells Employing a Graded Recombination Layer. *Nature Photonics* 2011, 5, 480-484.

183. Pattantyus-Abraham, A. G.; Kramer, I. J.; Barkhouse, A. R.; Wang, X. H.; Konstantatos, G.; Debnath, R.; Levina, L.; Raabe, I.; Nazeeruddin, M. K.; Grätzel, M.; Sargent, E. H., Depleted-Heterojunction Colloidal Quantum Dot Solar Cells. *ACS Nano* 2010, 4, 3374-3380.

214. Adachi, M. M.; Labelle, A. J.; Thon, S. M.; Lan, X.; Hoogland, S.; Sargent, E. H., Broadband Solar Absorption Enhancement Via Periodic Nanostructuring of Electrodes. *Scientific Reports* 2013, 3, 6.

233. Lee, J.-W.; Son, D.-Y.; Ahn, T. K.; Shin, H.-W.; Kim, I. Y.; Hwang, S.-J.; Ko, M. J.; Sul, S.; Han, H.; Park, N.-G., Quantum-Dot-Sensitized Solar Cell with Unprecedentedly High Photocurrent. *Sci. Rep.* 2013, 3.

235. Pan, Z.; Zhang, H.; Cheng, K.; Hou, Y.; Hua, J.; Zhong, X., Highly Efficient Inverted Type-I Cds/Cdse Core/Shell Structure Qd-Sensitized Solar Cells. *ACS Nano* 2012, 6, 3982-3991.

279. Bullen, C. R.; Mulvaney, P., Nucleation and Growth Kinetics of CdSe Nanocrystals in Octadecene. *Nano Lett* 2004, 4, 2303-2307.

280. Mahler, B.; Spinicelli, P.; Buil, S.; Quelin, X.; Hermier, J. P.; Dubertret, B., Towards Non-Blinking Colloidal Quantum Dots. *Nat. Mater.* 2008, 7, 659-64.

281. Liu, T. Y.; Li, M. J.; Ouyang, J. Y.; Zaman, M. B.; Wang, R. B.; Wu, X. H.; Yeh, C. S.; Lin, Q.; Yang, B.; Yu, K., Non-Injection and Low-Temperature Approach to Colloidal Photoluminescent Pbs Nanocrystals with Narrow Bandwidth. *Journal of Physical Chemistry C* 2009, 113, 2301-2308.

282. Cai, X.; Mirafzal, H.; Nguyen, K.; Leppert, V.; Kelley, D. F., Spectroscopy of Cdte/Cdse Type-Ii Nanostructures: Morphology, Lattice Mismatch, and Band-Bowing Effects. *The Journal of Physical Chemistry C* 2012, 116, 8118-8127.
283. Khon, E.; Hewa-Kasakarage, N. N.; Nemitz, I.; Acharya, K.; Zamkov, M., Tuning the Morphology of Au/Cds Nanocomposites through Temperature-Controlled Reduction of Gold-Oleate Complexes. *Chem. Mat.* 2010, 22, 5929-5936.
284. Wessels, J. M.; Nothofer, H.-G.; Ford, W. E.; von Wrochem, F.; Scholz, F.; Vossmeyer, T.; Schroedter, A.; Weller, H.; Yasuda, A., Optical and Electrical Properties of Three-Dimensional Interlinked Gold Nanoparticle Assemblies. *Journal of the American Chemical Society* 2004, 126, 3349-3356.
285. Tachan, Z.; Shalom, M.; Hod, I.; Ruhle, S.; Tirosh, S.; Zaban, A., Pbs as a Highly Catalytic Counter Electrode for Polysulfide-Based Quantum Dot Solar Cells. *Journal of Physical Chemistry C* 2011, 115, 6162-6166.
286. Snaith, H. J.; Schmidt-Mende, L.; Grätzel, M.; Chiesa, M., Light Intensity, Temperature, and Thickness Dependence of the Open-Circuit Voltage in Solid-State Dye-Sensitized Solar Cells. *Phys. Rev. B* 2006, 74, 045306.
287. Hans B.Bullinger Peabody, M. Photoetching of Metal-Oxide Layers. 3615465, 1971
288. Teaching, O. f. L. a., Image Formation Basics. tem_beampath_stage_a, Ed. http://www.ammrf.org.au/myscope/tem/background/concepts/imagegeneration/detail.php, March 15, 2013.
289. Sorensen, B. E., A Revised Michel-Levy Interference Colour Chart Based on First-Principles Calculations. *European Journal of Mineralogy* 2013, 25, 5-10.
290. Sobarwiki, Ultraviolet–Visible Spectroscopy. spectrophotometer, S. o. U.-v., Ed. http://en.wikipedia.org/wiki/Ultraviolet%E2%80%93visible_spectroscopy, September 2, 2013; pp Schematic of UV- visible spectrophotometer.
291. SCOTT, R. P. W., The Constituents of a Flourescence Spectrometer. Scott, A. S. b. R. P. W., Ed. http://www.analyticalspectroscopy.net/ap2-8.htm, p The Basic Fluorescence Spectrometer.
292. Grabolle, M.; Spieles, M.; Lesnyak, V.; Gaponik, N.; Eychmuller, A.; Resch-Genger, U., Determination of the Fluorescence Quantum Yield of Quantum Dots: Suitable Procedures and Achievable Uncertainties. *Anal. Chem.* 2009, 81, 6285-6294.
293. Wehrenberg, B. L.; Wang, C. J.; Guyot-Sionnest, P., Interband and Intraband Optical Studies of PbSe Colloidal Quantum Dots. *Journal of Physical Chemistry B* 2002, 106, 10634-10640.
294. Rurack, K.; Spieles, M., Fluorescence Quantum Yields of a Series of Red and near-Infrared Dyes Emitting at 600-1000 Nm. *Analytical chemistry* 2011, 83, 1232-42.
295. Solanki, C. S., *Solar Photovoltaics: Fundamentals Technologies and Applications*. Prentice-Hall Of India Pvt. Ltd.: 2009.

Chapter 3 Hot Injection Quantum Dot Synthesis: Characterisation and Studies of the Effects of Cation and Anion Solutions

3.1 Introduction

A range of different core and core-shell colloidal quantum dots have been synthesised, since their initial discovery. The most widely studied quantum dots are binary semiconductors of group II-VI, and therefore a wide range of core and core-shell structures have been reported in the literature based upon them.[296] Cadmium based II-VI group QDs, CdS, CdSe and CdTe show absorption and emission ranging from 200 nm to 750 nm and can be produced in excellent quality with minimal size distribution, outstanding crystallinity and high luminescent quantum yields.[297] They have also been used to produce a range of core-shell QDs and other heterostructures[298] such as core-multishell QDs,[100] dot in rod,[88, 109, 113, 299] dot in tetrapod,[109] dot in platelet, therefore, these were the first category of QDs investigated.

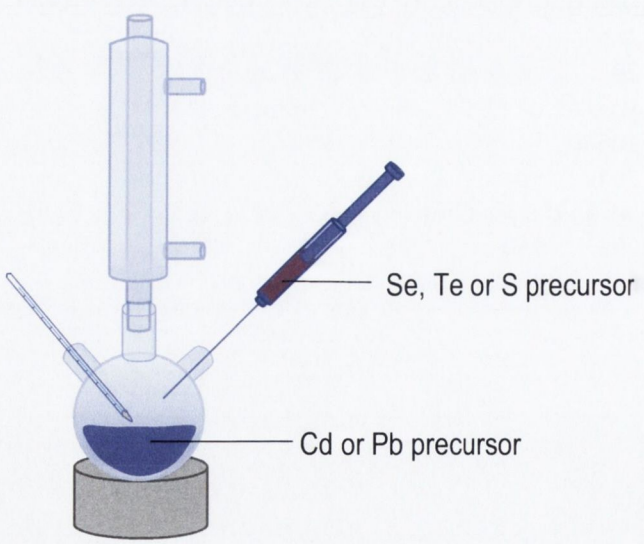

Figure 3.1 This is the basic experimental setup for hot injection colloidal quantum dot synthesis, *in which one precursor is heated to a set temperture under argon in a three neck round bottom flask*

Apart from II-VI chalcogenides, a huge range of interest has also been shown recently in NIR/IR absorbing lead based chalcogenides QDs such as PbS, PbSe and PbTe.[300] These semiconductors show large exciton Bohr radii of 23.5 nm (for PbS), 66 nm (for PbSe) and 152 nm (for PbTe),

with the electron and hole contributing nearly equally to the exciton Bohr radii , meaning both charge carriers are strongly confined in the QDs.[301] These QDs show excellent charge transfer properties when forming films[130, 132, 142] and have found application in a range of photovoltaic cells. [199, 204, 210, 233, 238] They have also been reported to display multiple exciton generation[34] under illumination and also been successfully synthesised in high quality similar to cadmium chalcogenides.[300] Therefore, these were the second category of QD investigated.

Solution based colloidal synthesis of QDs has been demonstrated in high boiling point organic solvents, within which the quantum dot crystals are rapidly formed at elevated temperatures, due to the swift introduction of the anion precursor. [85] This is termed the Hot Injection approach [85] and has been the basis for all of the quantum dots produced in this chapter using the basic experimental setup shown in *Figure 3.1*. This approach involves the production of a metal complex in a vessel under an inert atmosphere, in a solution of degassed solvent formed from the cation of the target semiconductor and the ligand in solution. Following this formation, the reaction is heated to the desired growth temperature. At this point, a syringe is used to quickly introduce a solution containing the anion precursor in a degassed solution to the reaction vessel, and rapid growth of QDs takes place. After a chosen time the reaction is removed from the heat and QDs are precipitated from solution through the addition of a non-solvent. A range of ligands are used in conjunction with a hot injection quantum dot synthesis[132] with some of the most common being long chain, fatty acids,[74] phosphonic acids[302] and amines.[303] These are used due to their high boiling points, solubility in organic solvents and polar functional groups, which coordinate to the surface of the quantum dots. Within this category of QD synthesis, a number of variables exist to control the exact size and quality of quantum dots, including injection temperature, time allotted for QD growth after precursor injection, precursor concentrations and ligand concentrations. This method therefore allows for a range of means to tailor a synthesis to produce the desired quantum dot size.

Cation exchange is a relatively recent method for quantum dot synthesis and has been demonstrated as a new approach to produce a range of structures that would prove very challenging to create using conventional synthetic techniques.[115, 116, 304] This has shown particular success when utilising cadmium and lead based chalcogenides quantum dots, allowing interconversion between lead and cadmium in a single step[93, 117, 120] or via a two-step process, involving the use of copper(I) ions to firstly displace Cd^{2+} or Pb^{2+} ions as an intermediate state.[112] When this is carried out under the appropriate conditions it has also been demonstrated that it is possible to preserve complex heterostructures; this was shown with the

interconversion between CdSe/CdS dot in rod structure to Cu_2Se/Cu_2S to PbS/PbSe,[111] while maintaining the overall anionic framework.

An extensive range of noble metal nanoparticles have been reported in the literature,[305, 306] of these the strongest plasmonic properties have been shown from gold based nanocrystals, displaying a broad plasmonic peak, with the exact peak intensity and position being strongly related to size and shape of the nanocrystals.[307, 308] Interestingly noble metal-semiconductor nano-heterostructures have also recently been reported.[309] These show a range of interesting properties, particular in regards to the unique interaction between plasmonic and excitonic optical properties.[310] The production of metal nanoparticles is most readily achieved through the thermal decomposition of a noble metal salt in a solution of binding ligands allowing controlled growth of the particles. Therefore, one of the most accessible routes to producing these unusual noble metal quantum dot heterostructures is simply by the addition of QDs to the solution of metal salts before nanoparticle formation. Due to the lower energy barrier of hetero-nucleation, this synthesis under the appropriate conditions will produce growth of metal nanoparticles or a metal shell, upon the surface of the QD particles.[298]

The effects of post treatment of QDs has been reported from a number of sources and has shown particular success with increasing quantum dot stability and luminescent quantum yields.[195, 201, 211, 311] One of the most highly successful treatments reported is the use of long chain amine ligands, such as oleylamine, sometimes in combination with cadmium halide salts [311] and has been demonstrated in lead[312, 313] chalcogenides quantum dots.[210]

3.2 Aim

The goal of this part of our work is to prepare a range of core and core-shell QDs using the hot injection approach and characterise the QDs by various instrumental techniques. We plan to optimise the synthesis of QDs with the aim of producing high quality nanocrystals. The specific quantum dots will be chosen due to their possible application for quantum dot based photovoltaic devices. Therefore, the initial work to be carried out for this project is the synthesis and characterisation of a range of group II-VI QDs; of CdS, CdSe; core-shell QDs of group II-VI CdSe/CdS, CdS/CdSe, CdTe/CdSe, heterostructured CdSe/CdS NRs; and NIR absorbing PbS QDs. Following this, the reactions are to be scaled up to allow workable amounts to be produced for incorporation into a photovoltaic device. In addition, cation exchange processes will be investigated as a means to produce alternative materials from pre-synthesised QDs. The deposition of gold upon QD heterostructures will also be investigated. The final objective of this

work is to investigate the effect of different halide salts upon the photoluminescent of core and core-shell quantum dots synthesised, with the aim to improve passivation of the QDs surface and therefore reduce recombination losses due to trap states when incorporated into photovoltaic cells.

3.3 Hot injection synthesis and characterisation of quantum nanostructures

Hot injection has been used as a means to synthesis a range of quantum dot structures detailed below, enabling the production of a range of sizes and morphologies, showing small size distributions and excellent optical properties. All of the synthesis utilised required a level of optimisation to produce the desired sizes and properties in the produced samples, and is detailed below.

3.3.1 Octadecylphosphonic acid capped CdSe Quantum Dots: Synthesis and Characterisation

Octadecylphosphonic acid capped CdSe QDs were synthesised using trioctylphosphine oxide (TOPO) as a coordinating solvent, and octadecylphosphonic acid (ODPA) as the ligand, CdO as the Cd precursor and Se dissolved in trioctylphosphine (TOP) as the Se source (see section 2.2.3 for further details). The reaction mixture of TOPO, ODPA and CdO, were degassed and then heated under an argon atmosphere to 300 °C, at which point $Cd(ODPA)_2$ was formed. After that, the reaction mixture was heated to the desired injection temperature of Se-TOP solution, ranging between 320 °C to 350 °C. The resulting CdSe QDs were then allowed to grow over a specific amount of time, before heating was removed and the CdSe QDs were precipitated from solution through the addition of a non-solvent (e.g MeOH). Control of CdSe QDs size was demonstrated by varying the injection temperature, the growth time after injection and the ratio of Cd to Se used in the reaction. A comparison of properties of the range of CdSe QDs produced is shown in Table 3.1. UV-Vis absorption spectra, photoluminescent emission spectra and TEM were used to analysis the resulting QDs.

ODPA shows a much stronger binding to the surface of CdSe QDs than other common QD ligands; in addition, TOPO acts as a coordinating solvent that also binds to the surface of the QDs. Therefore, for optimal growth of the QDs to occur after Se injection, the synthesis must be carried out at much higher temperatures than what was utilised in most of our hot injection synthesis. Also due to the large concentration of ODPA and TOPO in the synthesis relative to QDs, this process is far more costly to scale up and it required at least three to four cleaning cycles to separate the QDs from the majority of side products after the synthesis.

Table 3.1 This shows the range of phosphonic acid capped CdSe quantum dots synthesised during the experiment. *Diameters displayed are calculated from the first exciton peak position and quantum yields were determined relative to an appropriate standard Rhodamine 6G in ethanol (QY 95%[292]).*

Samples	Diameter	1st exciton absorption peak	1st Exciton FWHM	PI emission	PI FWHM	Stokes shift	Molar Ratio of Cd:Se	Temperature of Se injection	Luminescent Quantum yield	Growth time after injection
Units	nm	nm	eV	nm	eV	nm	/	°C	%	sec
CdSe I	2.64	526	0.13	535	0.094	8	1:2	320	6.5	0
CdSe II	2.81	538	0.12	547	0.091	9.0	1:2	330	11.5	0
CdSe III	4.1	588	0.2	596	0.1	8	1:2	340	8.0	0
CdSe IV	4.56	599.5	0.25	610	0.093	10.5	1:2	350	4.5	0
CdSe V	2.91	543	0.11	553	0.091	10	1:10	350	16.2	0
CdSe VI	3.17	556	0.14	564	0.089	7	1:2	330	14.0	0
CdSe VII	3.41	566	0.23	579	0.085	12	1:1	350	13.9	0
CdSe VIII	3.06	551	0.16	562	0.11	11	1:2	350	10.1	0
CdSe IX	4.15	590.5	0.28	601.5	0.11	11	1:2	350	3.1	60
CdSe X	4.72	603	0.18	613	0.13	10	1:2	350	7.5	90
CdSe XI	5.16	612	0.17	623.	0.12	11	1:2	350	8.8	120

3.3.1.i Optical analysis of ODPA capped CdSe QDs

UV-Vis absorption spectra (Figure 3.2 A) of a range of different ODPA-capped CdSe QDs showed red shifting to longer wavelengths as the diameters of the CdSe QDs increases, shifting from a first exciton peak position of 526 nm to 612 nm. This first exciton peak showed small values of FWHM of as low as 0.11 eV for some of the smaller QDs synthesised, which increases to between 0.17 eV to 0.28 eV for the larger QDs, depending on synthetic approach, noting that this is an indication of the size distribution present in the sample, with smaller values indicating a smaller size distribution. Therefore, the larger size distribution of QDs seen with larger diameters is to be expected if the growth phase is sped up through higher temperatures or the growth phase is allowed to proceed for a longer amount of time. Both of these factors naturally will have the effect of defocusing the size distribution. Even the larger FWHM values found for some of the CdSe QDs, still indicate a very small size distribution has been created in most of these QDs. This is further shown in the fine structure present in the UV-Vis absorption spectra,

which are due to other higher energy transitions within the CdSe QDs, and is found to be blurred out if the size distribution of the QD sample is large.

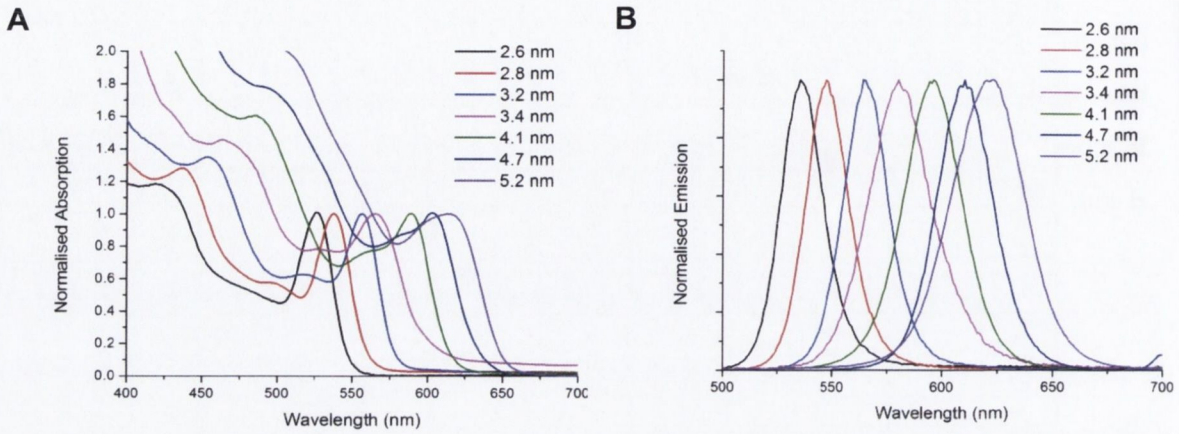

Figure 3.2 UV-Vis absorption (A) and photoluminescent emission (B) for ODPA capped CdSe quantum dots,showing a range of different diameters from 2.6 nm to 5.2 nm.

Three different parameters, growth time, inject ration temperature and Se:Cd ratio were examined during the synthesis and then analysed using UV-Vis absorption spectra with the resulting spectra shown in Figure 3.3. Increasing growth time post Se injection has the effect of producing larger QDs when tested with times up to 2 minutes of growth as shown in Figure 3.3A. Even longer times were not investigated due to a large increase in size distribution due to the onset of Ostwald ripening, which had the effect pf producing two excitonic peaks in the UV-Vis absorption spectra (for an example see Appendix C, Figure 7.2). When using two minutes of growth time, it was found that altering the injection temperature at which QD growth was carried out, also strongly effected the rate of growth and therefore the size of QDs produced, this was investigated in the range of 320 °C to 350 °C and is shown in Figure 3.3 B. While the majority of these reactions were carried out using a ratio of 2:1 Cd: Se, the effect of altering this ratio has also been investigated and is shown in Figure 3.3 C. This shows that as the excess of Cd is increased to 1:10, smaller QDs are produced under the same conditions, while when the ratio is reduced to 1:1, the CdSe synthesised in fact are increased in size. This can be explained by the effect that this change in ratio has upon the growth or nucleation step, since as the Cd excess is increased; nucleation more readily takes place, since Cd is the lower reactive precursor, producing more seeds upon injection. Exactly the opposite takes place using a 1:1 ratio, retarding the nucleation step, and therefore creating fewer seeds upon injection, which grow in the reaction mixture, and therefore have more precursor present in solution enabling them to grow to a larger size.

The same pattern of red shifting seen in the absorption spectra is reproduced in the photoluminescent spectra (Figure 3.2 B); across the range of ODPA capped CdSe QD. This displays a luminescent that can be shifted from 535 nm to 623 nm as the CdSe QD diameter increases from 2.6 nm to 5.2 nm. These QDs only show a single peak due to excitonic emission, showing a lack of defect luminescence even in some of the smaller QDs. This can be explained due to excellent passivation of the surface of the QDs due to ODPA binding.

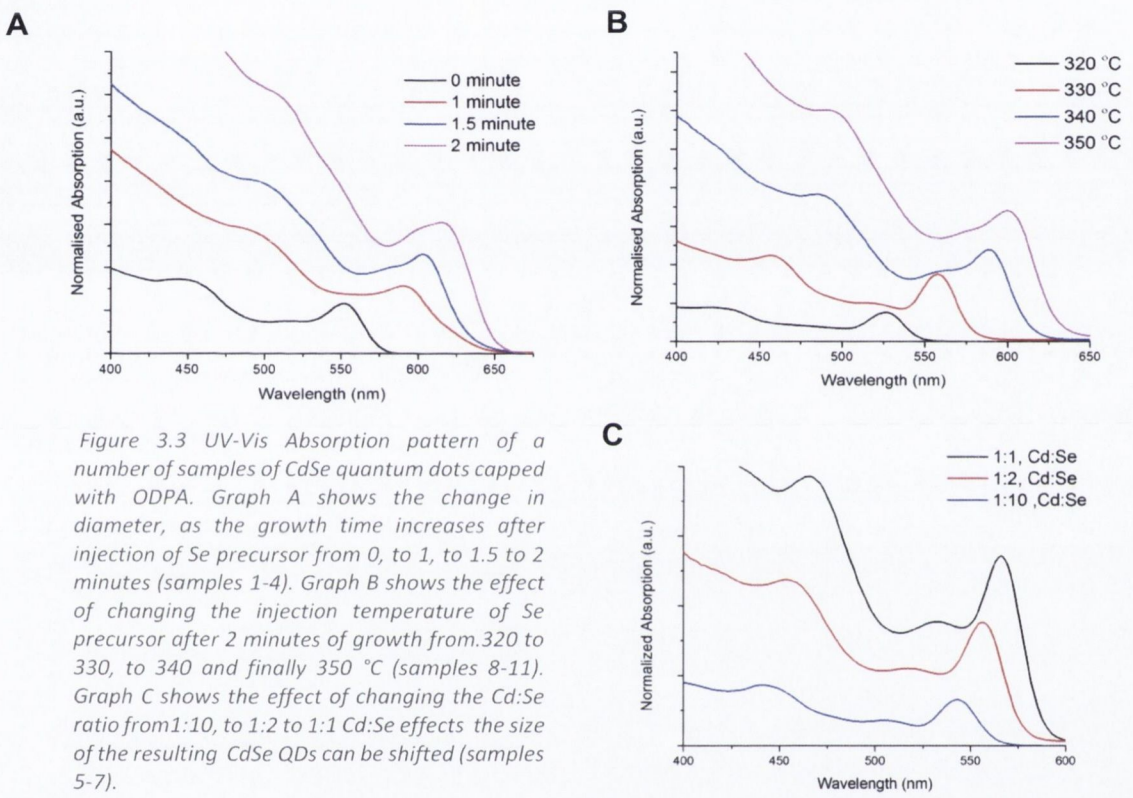

Figure 3.3 UV-Vis Absorption pattern of a number of samples of CdSe quantum dots capped with ODPA. Graph A shows the change in diameter, as the growth time increases after injection of Se precursor from 0, to 1, to 1.5 to 2 minutes (samples 1-4). Graph B shows the effect of changing the injection temperature of Se precursor after 2 minutes of growth from.320 to 330, to 340 and finally 350 °C (samples 8-11). Graph C shows the effect of changing the Cd:Se ratio from1:10, to 1:2 to 1:1 Cd:Se effects the size of the resulting CdSe QDs can be shifted (samples 5-7).

Initially after synthesis these QDs show visible luminesce, unfortunately following the cleaning steps the Pl signal is strongly reduced, giving the values shown in the table above. Luckily, this luminescence could be easily recovered through post treatment, which is discussed in section 3.5.2 .

3.3.1.ii Electron Microscopy analysis of ODPA capped CdSe QDs

TEM was used to analyse the size and shape of resulting CdSe QDs, to determine the size distribution, and to enable comparison of QD sizes calculated from the UV-Vis absorption spectra as seen in Table 3.1. The resulting image and determined distribution from these images is shown in Figure 3.4. The images show a well-defined, constant shape of these CdSe QDs, showing excellent size distribution, which after fitting the distribution gives a value of 4.7 nm in diameter with a standard deviation of 0.68 nm +/-. This is exactly identical to a calculated value

determined from the first exciton position of 4.7 nm also, showing that this method works effectively as a way to determine the QDs diameter.

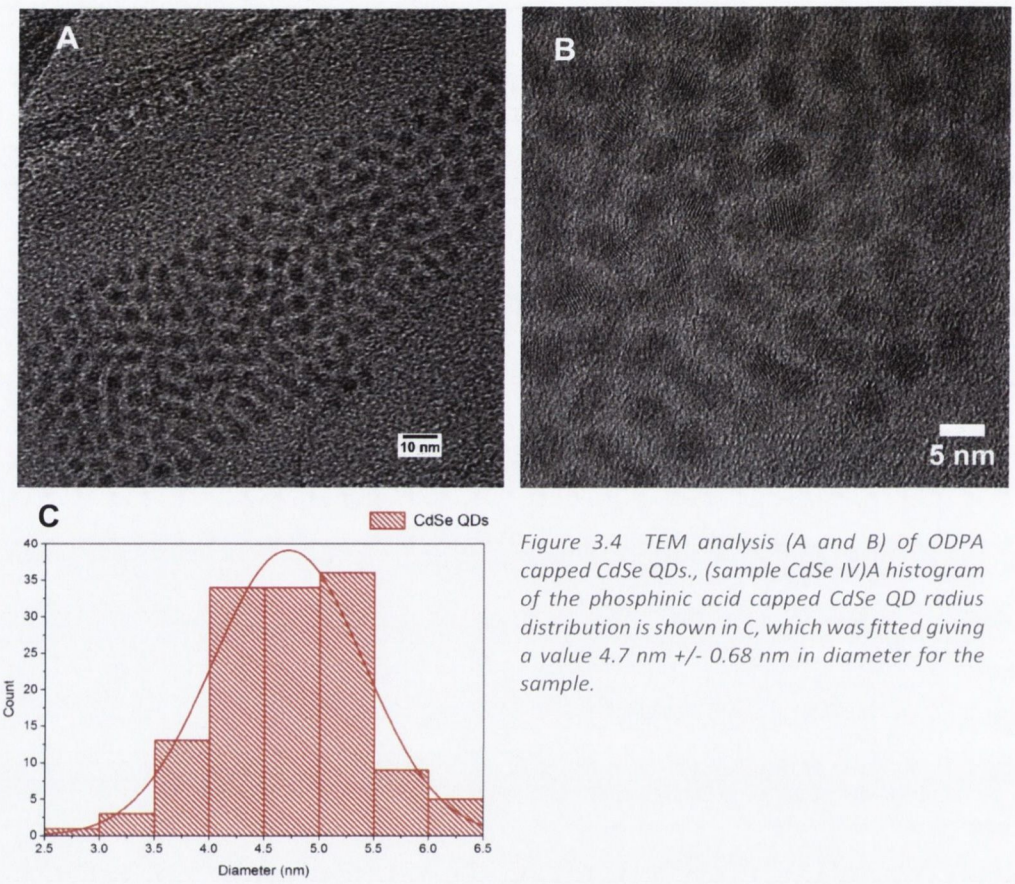

Figure 3.4 TEM analysis (A and B) of ODPA capped CdSe QDs., (sample CdSe IV)A histogram of the phosphinic acid capped CdSe QD radius distribution is shown in C, which was fitted giving a value 4.7 nm +/- 0.68 nm in diameter for the sample.

3.3.2 Octadecylamine capped CdSe Quantum Dots: Synthesis and Characterisation

A range octadecylamine (ODA) capped CdSe QDs were synthesised (see Figure 3.5) using ODA as a ligand, and a solvent mixture of octadecene, which is non-coordinating solvent and trioctylphosphine oxide (TOPO) which is a coordinating solvent using a modified method from literature.[280] In addition to ODA that acts as a ligand, oleic acid is also utilised, complicating the ligand shell structure present upon the shell of the QDs. The Cd precursor is Cd oleate formed from CdO and oleic acid, while the Se source is elemental Se dissolved in trioctylphosphine. The reaction mixture containing $Cd(oleate)_2$ is heated to between 270 °C and 310 °C followed by Se precursor injection, after which the reaction is cooled to between 230 °C and 250 °C, and QD growth is allowed to proceed for 10 minutes. Following this, a successive ion layer reaction approach is carried out (SILAR) and was used to produce CdSe nanocrystals crystals larger than 4 nm in diameter if desired, with the use of sequential injections of 0.2 M solutions of Se-TOP and $Cd(oleate)_2$.

It was found initially this reaction proved very challenging to produce QDs past the 4 nm diameter in size, which was initially attempted by modifying the ratio of Se to Cd, changing the initial injection temperature and through the use of changing the growth temperature. Unfortunately though some of these approaches did produce larger sizes, the QD's size distribution suffered severely, producing a number of different sizes indicated by the appearance of extra absorption peaks assigned to first exciton absorption peaks of newly nucleated CdSe QDs, and which when investigated using photoluminescent spectroscopy showed corresponding Pl peaks of the different sizes present. It was for this reason that SILAR was tested to produce the desired larger sizes, which when carried out appropriately, produced CdSe QDs of up to 5.5nm repeatably.

3.3.2.i Optical Characterisation

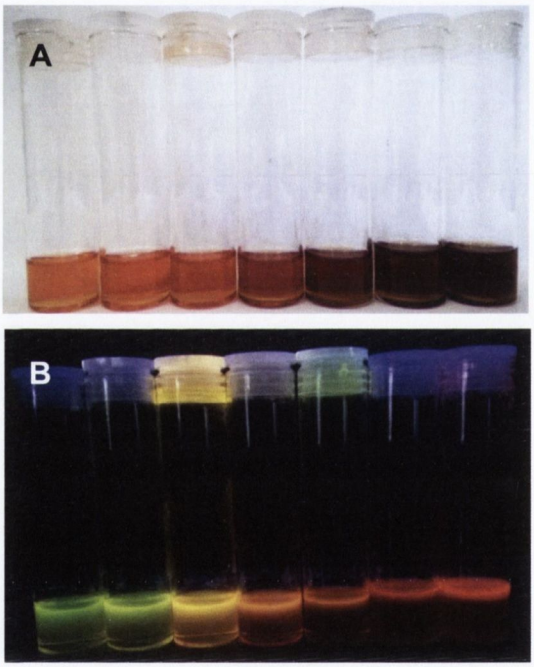

Figure 3.5 Photograph of amine capped CdSe quantum dots under visible light (A) and under UV illumination (B). This shows the change in absorption and emission as the size of the CdSe quantum dots increases from left to right.

UV-Vis absorption spectroscopy was used to analyse the initial size of CdSe QD nucleated and follow the steady growth of the QDs due to precursor injection, all of which is shown in Figure 3.6 A. This spectrum shows a strongly defined first exciton peak that shifts to longer wavelengths as the SILAR approach is used to grow larger sizes of CdSe QDs. The spectra also show much of the further fine structure of the high-energy transitions indicating a minimal size distribution. The steady growth of CdSe QDs under SILAR mediated growth was also studied using photoluminescent spectroscopy and is shown in Figure 3.6 B. As was seen in the absorption spectra red shifting of luminescence occurs due to SILAR growth of the CdSe QDs.

Also worth noting is the presence of single PL peak which is indicative of only one size population of QDs present meaning, we successfully avoided homogeneous nucleation of CdSe QDs during the SILAR mediated growth stage. These resulting QDs showed luminescent QYs which varied from 20- 30 %, decreasing with increased QD size.

3.3.3 Oleic Acid Capped CdSe Quantum Dots: Synthesis and Characterisation

A simple synthesis based on literature[279] was used to produce oleic acid capped CdSe QDs in large quantities, giving up to 1.4 mmol of CdSe per synthesis, in a range of sizes (as shown in Figure 3.7). This synthesis used Cd oleate as the Cd source dissolved in a non-coordinating solvent of octadecene, while just oleic acid was used as a ligand and the Se source was produced by dissolving Se powder in Tributylphosphine under an argon atmosphere. A Cd excess of 2.8:1 (molar ratio) was used relative to Se, and injection temperature and growth time were used to control the resulting size of the QDs produced. These dots were then investigated using UV-Vis, PL and TEM techniques.

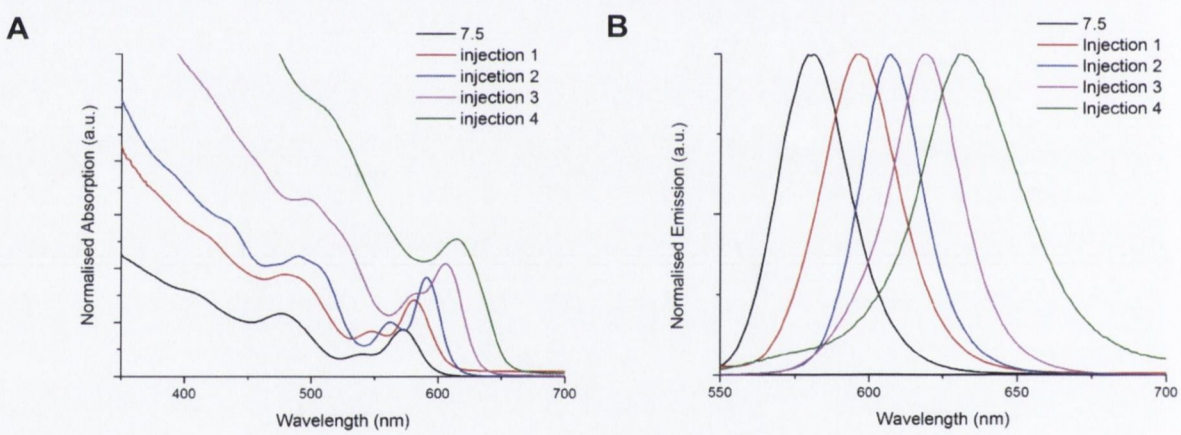

Figure 3.6 UV-Vis absorption spectroscopy (A) and photoluminescent spectroscopy (B) of Octadecylamine capped CdSe QDs showing the shifting in absorption luminescent as the size of the QD is increased sue to successive injections of Cd oleate and Se-TOP solutions after the initial nucleation of CdSe QDs

Most importantly, this synthesis could be scaled readily to produce large amounts of QDs using relatively inexpensive precursors. Also due to only one ligand being utilised, oleic acid, the ligand shell of the resulting CdSe QDs was simple and therefore these served as a model system for testing in electrophoretic deposition, as discussed in chapter 4, section 4.3 . They also served as a useful comparison with other dots coated in oleic acid such as PbS or CdS QDs.

3.3.3.i Optical characterisation of oleic acid capped CdSe

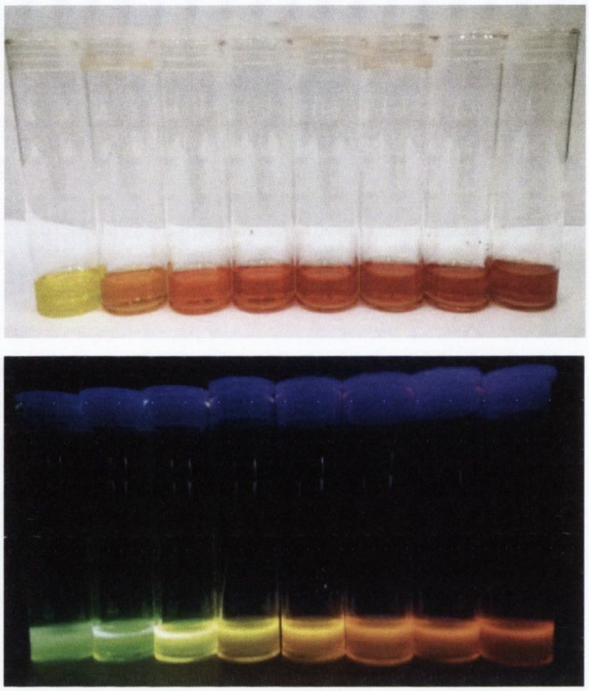

Figure 3.7 Photograph of oleic acid capped CdSe quantum dots under visible light (top) and under UV illumination (bottom). This shows the change in absorption and emission as the size of the CdSe quantum dots increases from left to right.

UV-Vis absorption spectroscopy and photoluminescence spectroscopy were used to monitor the growth of CdSe QDs following injecting of the Se precursor and is shown in Figure 3.8. The UV-Vis absorption spectra (Figure 3.8 A) shows red shifting over time as the CdSe QDs increase in size, with growth taking place very quickly during the first 10 seconds and slowing significantly up to 220 seconds. The PL spectra (Figure 3.8 B) of these QDs also show the same pattern of red shifting relative to growth time.

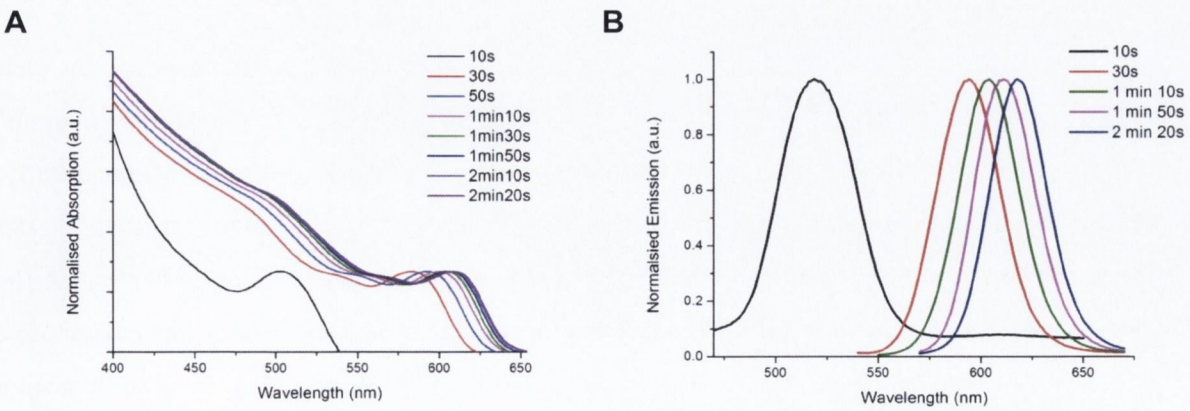

Figure 3.8 UV-Vis absorption (A) and photoluminescent emission (B) of oleic acid capped CdSe quantum dots showing a range of different sizes from 2.6 nm to 5.2 nm produced by varying the growth time following injection.

The resulting UV-Vis absorption shows a first exciton that is not very sharp in character and shows a large FWHM of 1.3 eV, indicative of a larger size distribution. When analysing the PL

spectra the same pattern can be seen, with a relatively broad emission peak, showing a FWHM of 0.1 eV, showing a range of sizes of CdSe QDs exist in these samples. These samples show poor QYs of between 2-5 % after synthesis, but could be hugely increased using post treatments discussed later on in this chapter (section 3.5.1).

3.3.3.ii Microscopic Analysis of oleic acid capped CdSe QDs

TEM was used to determine the morphology of the resulting synthesised CdSe QDs, with the resulting image shown in Figure 3.9. The QDs synthesised are of a spherical character, but also seem to show a significant size dispersity as shown by the image present, displaying noticeably larger and smaller CdSe QDs in the image.

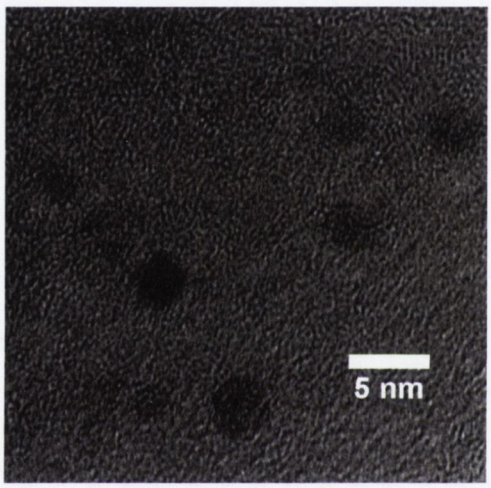

Figure 3.9 TEM of oleic acid capped CdSe QDs synthesised using a growth time of 40 seconds and an injection temperature of 260 °C..

3.3.4 CdS Quantum Dots: Synthesis and Characterisation

CdS QD particles were synthesised in a non-coordinating solvent of octadecene, using oleic acid as a ligand using a modified method from literature. [17] [16] The Cd source was cadmium oleate, which was formed under an inert atmosphere at 290 °C by reacting oleic acid and CdO. After this, the reaction mixture was heated to 300 °C and a hot injection of reagents was carried out using elemental sulphur dissolved in octadecene, with the molar ratio of S:Cd being 1:2. Heating time was used to control the size of the particles produced, by varying from 1 minute to 10 minutes. These particles were then studied using UV-Vis, PI, and TEM. Table 3.2 is a summary of the CdS QDs synthesised.

Increasing growth times after S injection were found to increase CdS QD diameters (sample CdS A and B). A small variance in QD size produced under the same conditions (sample CdS B and

C), while increasing the reaction size by a factor of 4 (sample CdS D) had the effect of producing a larger full width half max, and therefore had the effect of producing an increased size distribution.

Table 3.2 This shows the range of oleic acid capped CdS quantum dots synthesised during the experiment. Diameters displayed are calculated from the first exciton peak position and quantum yields were determined relative to an appropriate standard, Coumarin 153 in ethanol (QY= 53%[292]).

CdS QD Sample	Growth time	1st Exciton peak	Diameter	Band gap	1st Exciton FWHM	Excitonic PI Peak position	PI FWHM	Stokes shift	Scale of reaction relative to method	Luminescent Quantum yield
Units	sec	nm	nm	eV	eV	nm	eV	nm	/	%
CdS A	400	384.9	2.96	3.21	0.18	403.03	0.12	18.1	1	40%
CdS B	600	392.1	3.14	3.16	0.18	407	0.14	14.9	1	51%
CdS C	600	403	3.48	3.08	0.15	415	0.11	12	1	43%
CdS D	600	385.9	2.96	3.21	0.29	405	0.15	19.1	4	55%

3.3.4.i Optical characterisation

CdS has a bandgap of 2.42 eV, therefore QDs synthesised in this work have band gaps between 3.08 to 3.21 eV , giving a first exciton absorption peak positioned in the ultra violet, meaning a solution of CdS QDs are colourless as shown in Figure 3.10 A. The evolution of the CdS QD absorption relative to time is shown in Figure 3.11 showing the growth of the QDs in the reaction solution and the resulting redshift of the spectra, with no further change seen after 10 minutes. The lowest energy peak is described as the first exciton peak and its width is an indication of the size distribution of the CdS QDs, given by the peak's full width half max

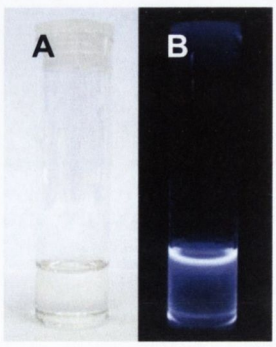

Figure 3.10 Photograph of oleic acid capped CdS QDs in toluene under visible light illumination and UV light illumination, sample C.

As the QDs grow in size it can be seen that the FWHM changes from 0.21 eV to 0.12 eV, indicating a size focusing takes place in the growth phase of the QDs. The absorption spectra also showed several other peaks at higher energies that can be attributed to other defined electronic transitions of the CdS QD; this fine structure is again only visible in QDs that have been synthesised with a small size distribution.

Figure 3.11 CdS QD UV-Vis absorption spectroscopy (A) and photoluminescent spectroscopy (B and C) of sample CdS B. Graph A depicts the change of the absorption spectra, relative to growth time after S solution injection at 300 °C. *CdS QD photoluminescent change relative to growth time after S precursor injection. A shows just the excitonic emission while the B shows the excitonic at higher energy and the defect emission at lower energies.*

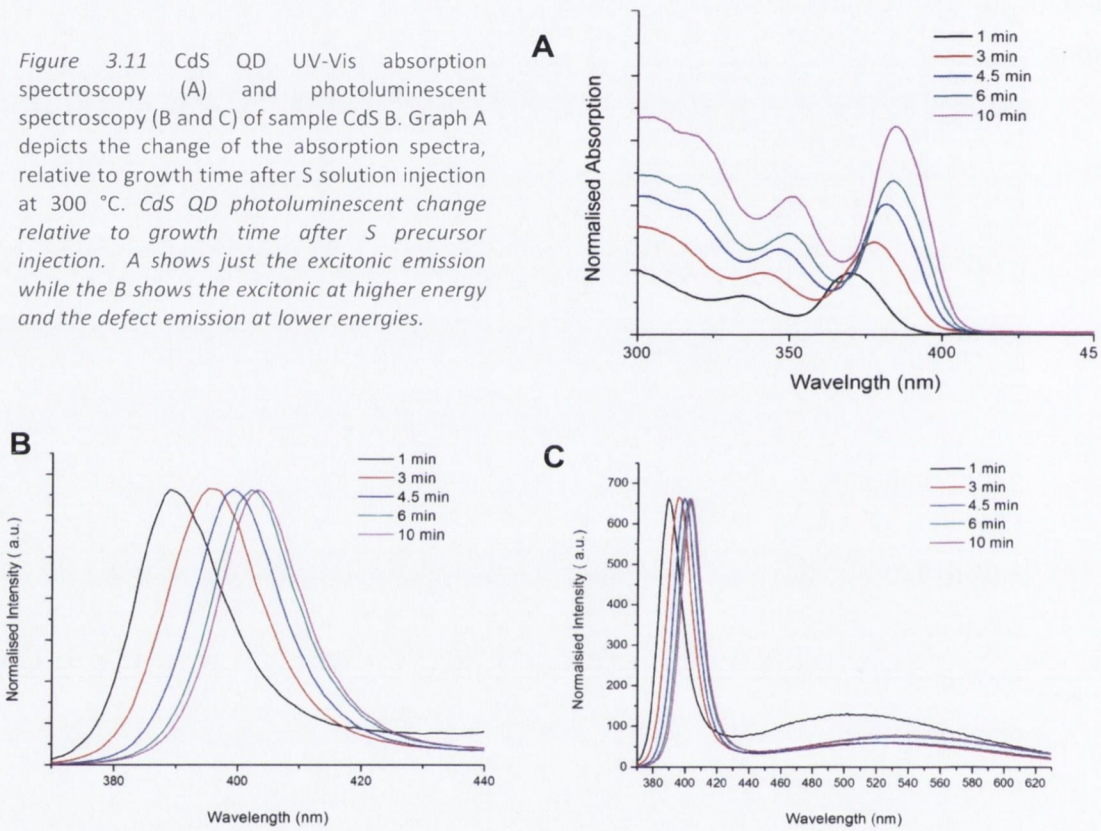

CdS QDs are strongly luminescent QDs (Figure 3.10), producing excitonic emission in the UV range, photoluminescent spectra is shown in Figure 3.11 B and C. The Bohr exciton radius of CdS is 3.6 nm, therefore CdS nanocrystals must have a smaller radius than this to show strong quantum confinement and therefore CdS QDs were synthesised with diameters of between 2.9 to 3.5 nm. Due to the small size of these nanocrystals a large proportion of the atoms that constituent the QD are surface atoms. Therefore when monitoring the luminescence of these QDs, two forms of luminescence are visible in the spectra, the first form is due to excitonic luminesce, occurring from an electron de-exciting from the lowest energy level in the conduction band to a level in the valence band and is shown in Figure 3.11. A. This luminescence produced a peak that showed a small Stokes shift relative to the first excitonic absorption peak, giving a shift of between 12 to 19 nm. The peak showed a small FWHM of between 0.12 eV to

0.15 eV and is indicative of a small size distribution in CdS diameters. As shown in the Figure 3.11 A, this peak also shows red shifting in emission position as the CdS QD size increases over the reaction time.

The emission spectra also contain a broad featureless band that is shown at longer wavelengths in Figure 3.11 C. This band is due to the surface defects that produce inter-band gap energy states within the band gap of the material. When electrons decay from these states to the valence band and emit photons, the resulting luminesce shows a strong red shift relative to absorption, therefore producing a much more pronounced Stokes shift. This form of luminescence is much more common in small QDs, with defect emission decreasing in intensity as diameter of the QD increases. This effect can be seen in Figure 3.11 C, showing clearly that a much larger defect luminescence is present for the initial QD size at 1 minute and is strongly decreased as the QD grows. Quantum yield measurements were made using coumarin 152 as a reference, and therefore the yields are only based on excitonic photoluminescence and therefore underestimate the total luminescent efficiency of the QDs. In spite of this, the total QYs were still very high for core QDs, producing yields up to 55 % and is indicative of high quality CdS QDs having been produced.

3.3.4.ii Electron Microscopy Analysis

Transmission electron microscopy (TEM) was used to analyse the produced CdS QDs and the images are shown in Figure 3.12 A and B. The CdS QDs show a circular shape with excellent crystallinity, shown by the presence of lattice fringes in image A. From these images, the size distribution of the QDs was determined and a histogram of these diameters is shown in Figure 3.12 C. The measured diameters from TEM determined by fitting a distribution curve to the histogram of diameters gives a peak centred on 2.8 nm and a standard deviation of 0.569 nm +/-. This showed excellent correlation with calculated diameters carried out by making use of the first exciton position in the UV-Vis absorption spectra of these QDs, which estimated a diameter of 2.96 nm for same sample of CdS.

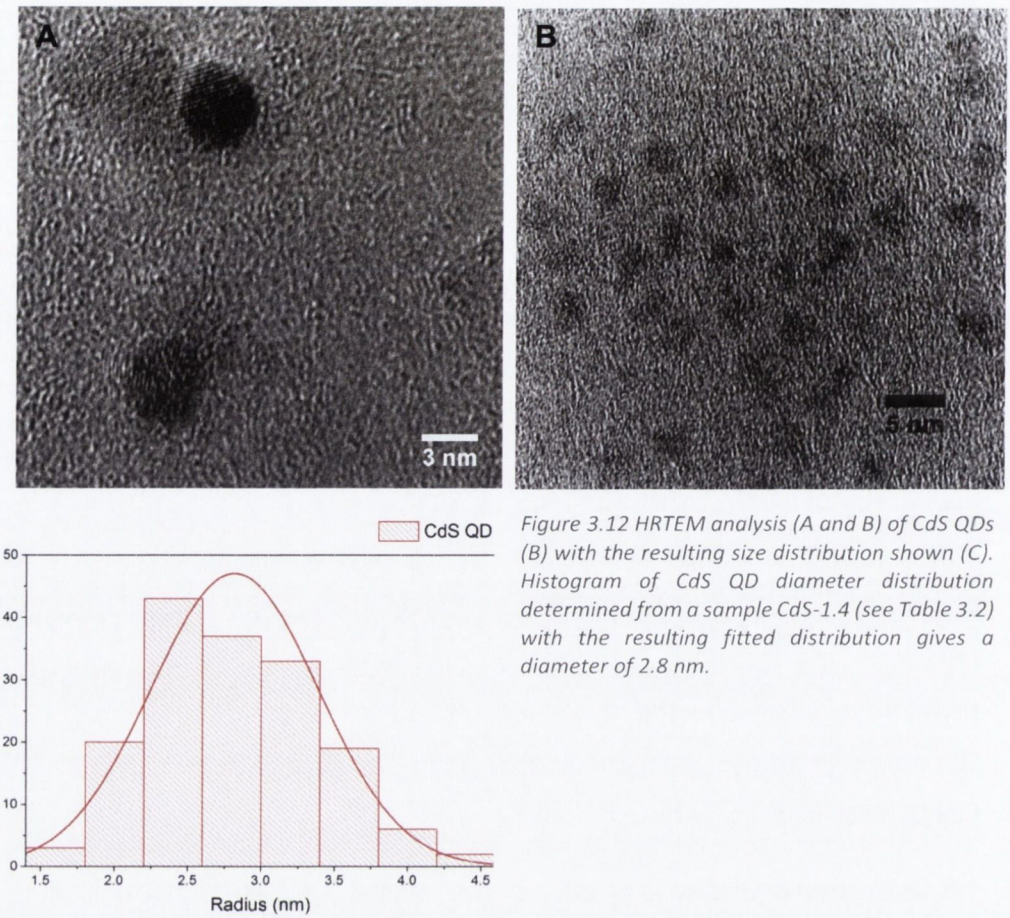

Figure 3.12 HRTEM analysis (A and B) of CdS QDs (B) with the resulting size distribution shown (C). Histogram of CdS QD diameter distribution determined from a sample CdS-1.4 (see Table 3.2) with the resulting fitted distribution gives a diameter of 2.8 nm.

3.3.5 PbS Quantum Dots: Synthesis and Characterisation

PbS QDs were synthesised using a modified method from literature,[281] using a non-coordinating solvent of ODE and oleic acid as a ligand. The Pb metal complex, $Pb(oleate)_2$, was used as the lead source, which was formed through the heating of PbO in the presence of oleic acid under an argon atmosphere to 110 °C. The sulphur source, bis(trimethylsilyl)sulfide (TMS), was then injected into this reaction at a set temperature between 80 to 140 °C, causing immediate nucleation of PbS. The growth of PbS QDs was allowed to proceed for 4 minutes after which the heating source was removed and the PbS QDs were precipitated from solution with the use of a non-solvent, acetone.

A range of PbS QDs were synthesised with their resulting properties shown in Table 3.3. These were produced by varying the temperature of TMS injection, enabling us to produce larger QD as the TMS injection temperature was increased from 60 °C to 140 °C, producing PbS QDs ranging from 2.3 nm to 4.0 nm in diameter. Injection temperatures above this are not reported due to a large increase in the size distribution. Growth time was not used to control QD size

since this was found to reach completion in an extremely short amount of time, showing no further growth in PbS QD size after 30 seconds post TMS injection. This reaction used relatively cheap material and was found to scale effectively without substantially changing the results of the reaction; this therefore meant reactions were able to produce in excess of 1 mmol of PbS.

Table 3.3 This shows the range of oleic acid capped PbS quantum dots synthesised during the experiment. Diameters displayed are calculated from the first exciton peak position and quantum yields were determined relative to an appropriate standard, IR Dye 26 in 1,2-dichloroethane(0.005%)[293] and IR Dye 140 in ethanol (16.7%)[294]

Sample name	1st exciton peak	1st exciton FWHM	Band gap	Diameter	PL emission	PI FWHM	TMS Injection Temperature	Luminescent Quantum yield
units	nm	eV	eV	nm	nm	eV	°C	%
PbS I	735	0.14	1.69	2.3	858	0.21E	60	/
PbS II	810	0.13	1.53	2.6	901	0.21	90	79
PbS III	840	0.17	1.48	2.7	943	0.16	100	/
PbS IV	896	0.11	1.38	2.9	984	0.19	110	87
PbS V	978	0.086	1.27	3.2	1048	0.15	120	/
PbS VI	1156	0.25	1.07	3.6	1223	0.16	130	/
PbS VII	1206, 1270	/	1.028,0.98	3.8, 4.0	/	/	140	/

3.3.5.i Optical measurements

PbS QDs samples were analysed using UV-Vis absorption spectroscopy and photoluminescent spectroscopy with the result shown in Figure 3.13. The absorption spectra (Figure 3.13 A) show a strong red shifting of absorption as the TMS injection temperature is increased shifting from a 1st exciton position of 735 nm to 1156 nm. The first exciton shows a FWHM of between 0.21eV to 0.11eV, indicating a relatively small PbS size distribution, with the trend across samples pointing towards better size focusing at higher temperatures up to 120 °C. Interestingly, the final sample, produced at 140 °C, shows a far less defined first exciton position, which is explained by assuming an increased size distribution, with an estimate fitting of two first exciton positions at 1206 and 1270. This is most likely caused by the onset of Ostwald ripening causing two distinct size populations to evolving; hence, results above this temperature are not reported. UV-Vis absorption was also used to demonstrate the effect of growth time upon a PbS sample and is shown in Figure 3.13 C, demonstrating that no change in first exciton position occurs after 30 s. In fact, over an extended time growth, the first exciton peak is found to broaden, indicating an increase in the size distribution and therefore reaction growth time was restricted to 4 minutes.

PbS QDs were found to show peak emission at 858 nm, which was gradually red-shifted as progressively larger PbS QD samples were produced causing emission at 1223 nm from the larger samples. The emission did not show a secondary peak due to defect emission, indicating excellent surface passivation of the PbS QDs. These samples were also found to be very efficient emitters showing excellent photoluminescent quantum yield of up to 87%. These were determined using suitable luminescent dye standards, (IR Dye 26 or IR Dye 140) as a comparison and therefore carry the usual uncertainty of at least +/- 10% of the reported value.

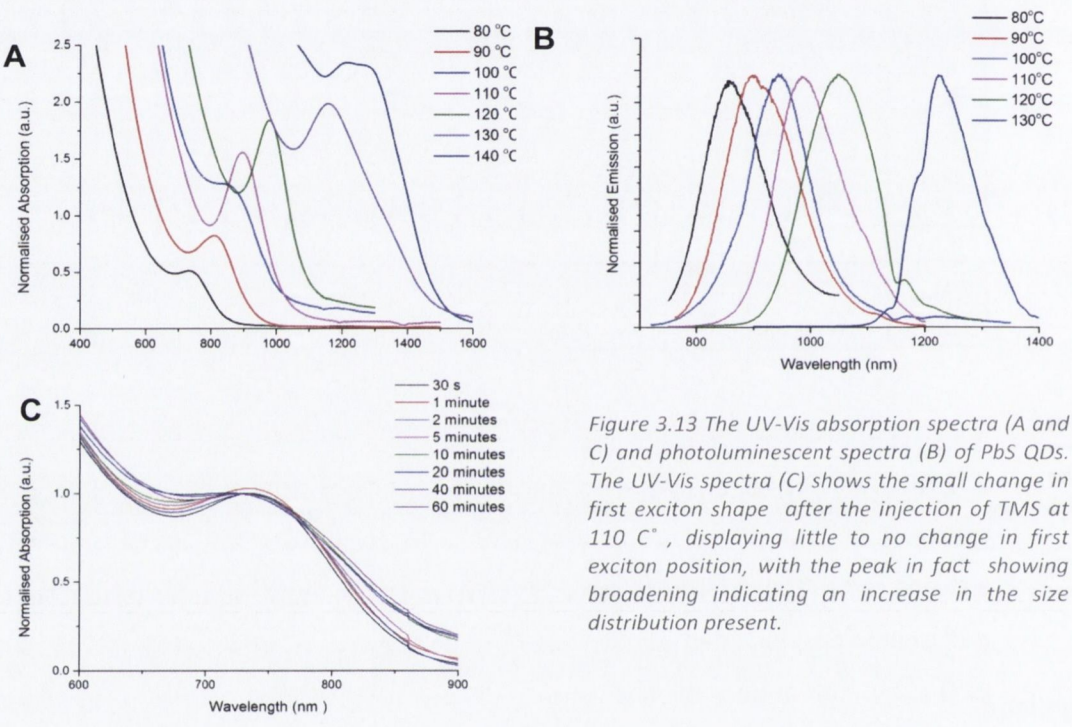

Figure 3.13 The UV-Vis absorption spectra (A and C) and photoluminescent spectra (B) of PbS QDs. The UV-Vis spectra (C) shows the small change in first exciton shape after the injection of TMS at 110 C° , displaying little to no change in first exciton position, with the peak in fact showing broadening indicating an increase in the size distribution present.

3.3.5.ii Electron Microscopy Analysis

TEM is used to investigate the morphology and the size distribution of PbS QD samples produced and is shown in Figure 3.14. The lattice fringes of a single PbS QD (sample PbS V) and can be seen in Figure 3.14 A, indicating excellent crystallinity of produced samples. The distribution of PbS QD diameters from sample PbS VI is shown in Figure 3.14 C and has been analysed and graphed (Figure 3.14 D), confirming that the diameters shows a small variance across the sample, which when fitted gave an average value of 4.7 nm and a standard deviation of 0.66 nm. To confirm, the elemental makeup of these QDs, scanning electron transmission microscopy (STEM) was carried out and is shown in Figure 3.15 A. This was used in tandem with

EDX, allowing the elemental distribution of the QDs to be measured. From this, it was confirmed that Pb and S are both present in these nanocrystals as shown in Figure 3.15 B.

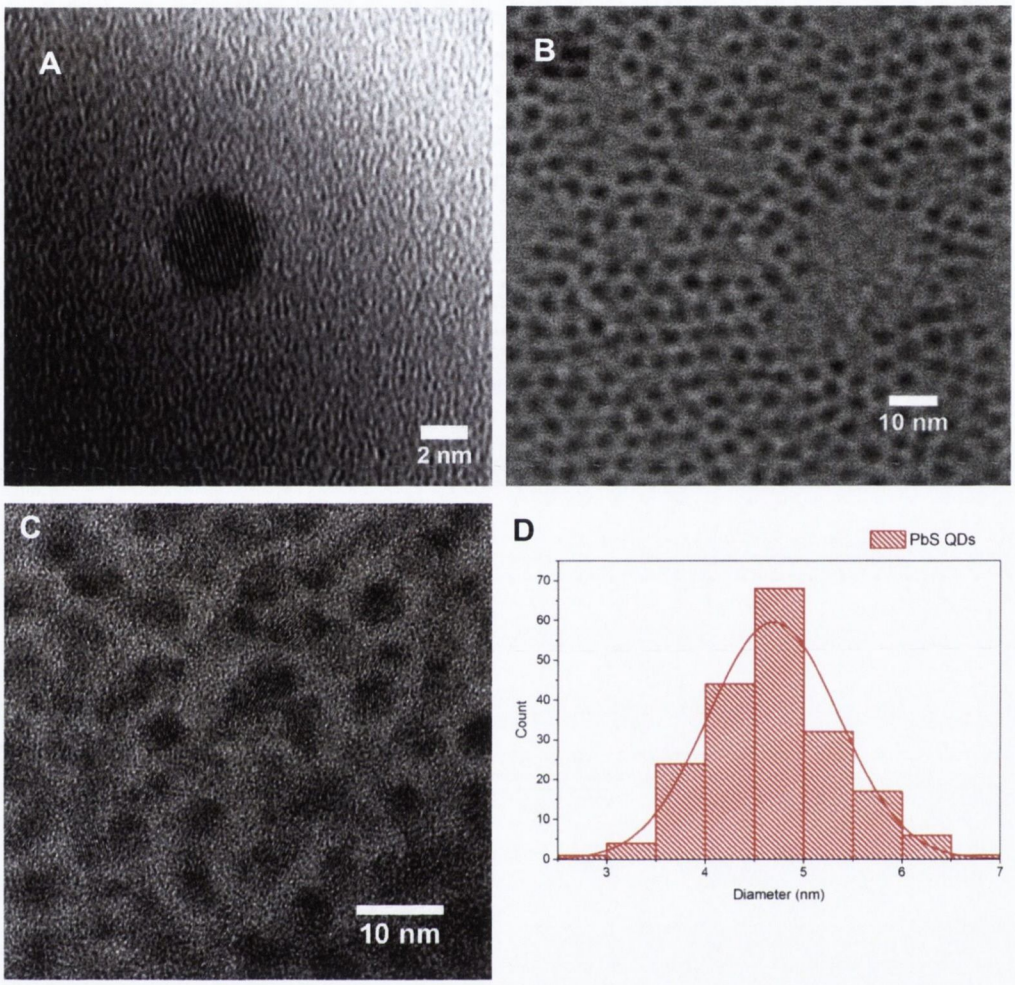

Figure 3.14 TEM images of PbS QDs. Image A (sample PbS V) is a HRTEM of a single PbS QD of 4.1 nm in diameter showing strong lattice fringes, while Image B (sample PbS IV) is a TEM image showing the distribution of size in a sample of another PbS QDs. Image C is a high resolution TEM of multiple PbS QDs,(sample PbS VI) while Image D shows the determined size distribution from this sample shown in a histogram . A fitting is made to this distribution giving an average diameter of PbS QDs in this sample of 4.7 nm.

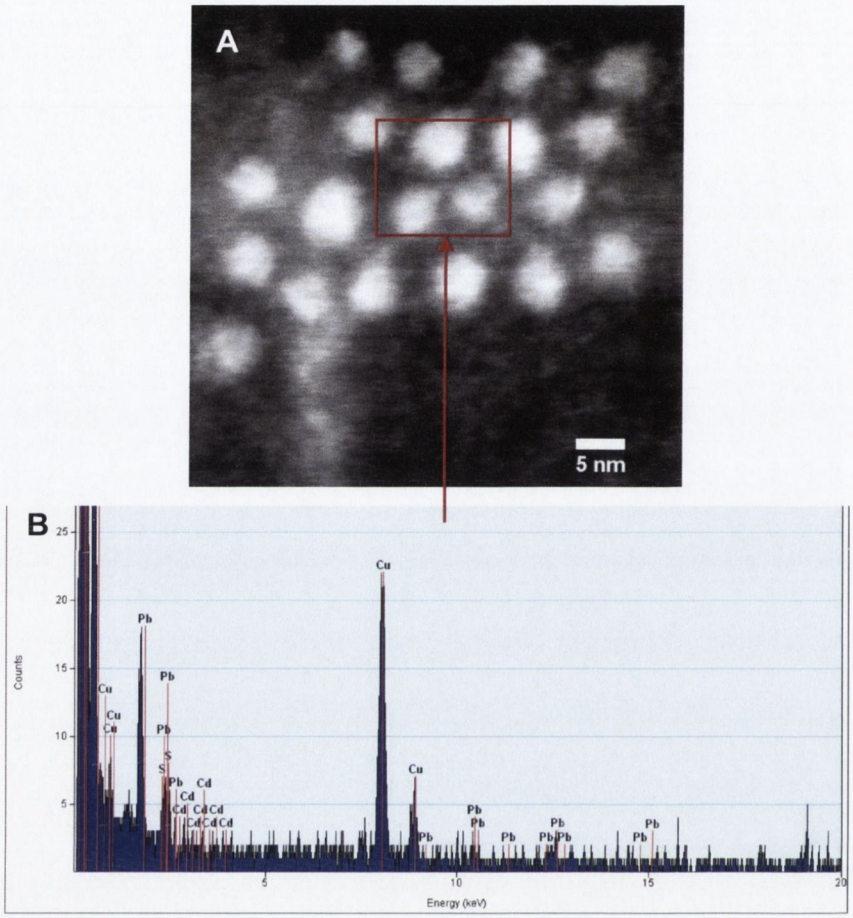

Figure 3.15 STEM (A) and EDX (B) spectra of PbS QDs (sample PbS VI). This confirms the elementental make up of the resulting QDs produced from the sythesis showing signals for Pb and S.

The X-ray powder diffraction was used to confirm the crystalline state of the synthesised PbS QDs, and to detect the specific crystal structure, which in this case is the rock salt phase. The resulting spectra is shown in Figure 3.16, with specific planes marked for clarity, and is an excellent fit to the PbS rock salt structure reported.[314]

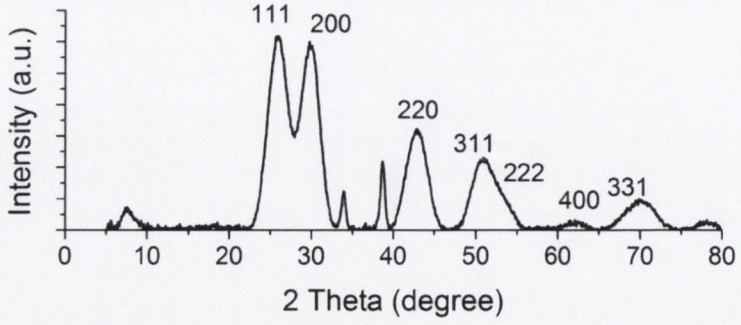

Figure 3.16 Powder x-ray crystal diffraction of PbS QDs sample, confirming the PbS rock salt crystal structure from the peak positions.

3.3.6 CdSe/CdS QD Synthesis

To synthesis more complex CdSe/CdS core/shell nanostructures, as reported in literature[88], we firstly separately produced a sample of ODA capped CdSe QDs as discussed in 3.3.2 . Following this, the CdSe QDs were used as a seeds to then grow a shell of CdS upon. This was achieved by the use of a SILAR approach in which we used successive injections of either Cd (oleate) $_2$ or elemental sulphur dissolved in ODE. This was produced by heating of a degassed solution of ODE, oleylamine and ODA capped CdSe QDs to 230 °C, after which SILAR growth was carried out. This process involved the injection of a Cd (oleate) $_2$ solution dropwise into the hot mixture, which was then allowed to react for 10 minutes, producing half monolayer of Cd^{2+} ions on the surface of the QD. Subsequently, a drop wise injection of the S precursor was then followed by a 10 minutes wait to allow the sulphur to react with the surface of the QDs, producing the first coating of CdS. For this method to be successful and avoid CdS homo nucleation, it was vital to adjust waiting times between injections and to slow the rate of injection, therefore avoiding the situation when too high a concentration of both CdS precursors were present in solution. It was also vital to make sure that the same concentration of S and Cd was added in each cycle of shell coating to ensure neither precursor was left in solution after a single cycle of shell growth. The SILAR approach allowed the exact desired thickness of CdS to be deposited upon these QDs, by controlling the number of precursor injections that were carried out. The QDs were then studies using UV-Vis spectroscopy, PL emission spectroscopy, and TEM. The basic properties of the samples produced are shown in Table 3.4 .

Table 3.4 This shows the change in spectra as a shell of CdS is grown upon a CdSe core QD producing a CdSe/CdS core/shell quantum dot.

Shell coating	1st Exciton peak of QDs	FWHM of 1st Exciton peak	Δ in 1st Absorption peak relative to core CdSe QD	Pl emission	FWHM of PL emission	Stokes shift
units	nm	eV	eV	nm	eV	nm
CdSe core	572	5.4E-02	/	575	7.1E-02	3
Shell 1	581	4.5E-02	3.4E-02	588.5	5.6E-02	7.5
Shell 2	595	5.5E-02	8.4E-02	607.5	4.4E-02	12.5
Shell 3	604	5.6E-02	1.1E-01	617	4.0E-02	13

3.3.6.i Optical Characterisation

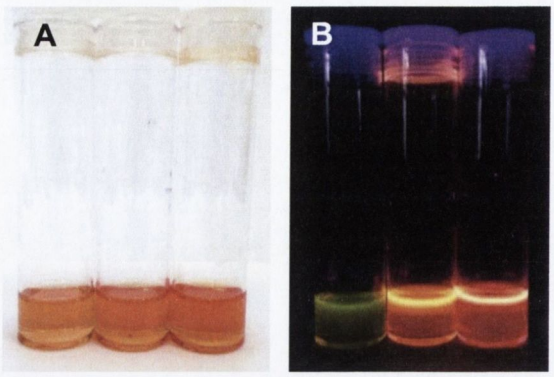

Figure 3.17 Photograph of CdSe/CdS quantum dot under visible light (A) and under UV illumination (B). This shows the change in absorption and emission as a shell of CdS is grown upon the core CdS, with shell thickness increasing from left to right.

UV-Vis absorption spectrums of the produced CdSe/CdS QDs is shown in Figure 3.18, displaying the change in spectra as a shell of CdS is grown upon the initial CdSe core, while Figure 3.17 shows a photograph of different coating thicknesses of CdSe/CdS QDs, under visible light and UV light. As CdS is deposited upon the CdSe core an overall red shifting in the first exciton position occurs, this is due to the smaller lattice constant of CdS, which causes a compression effect upon the core CdSe QD, producing a shift from 572 nm to 605 nm after the third coating.[103, 104] The coating also produces a large increase in absorption in the area of the spectrum associated with CdS absorption, which is centred on 512 nm, which corresponds to the bulk band gap of the CdS. The absorption spectrum therefore becomes a composite of CdSe absorption and CdS absorption, with the lowest energy peak corresponding to CdSe core absorption, while a large increase in absorption occurs after 550 nm due to CdS, with the ratio between these two acting as a means indication of the thickness of the CdS shell coating produced. Also importantly, the absence of CdS first excitons at wavelengths between 300 to

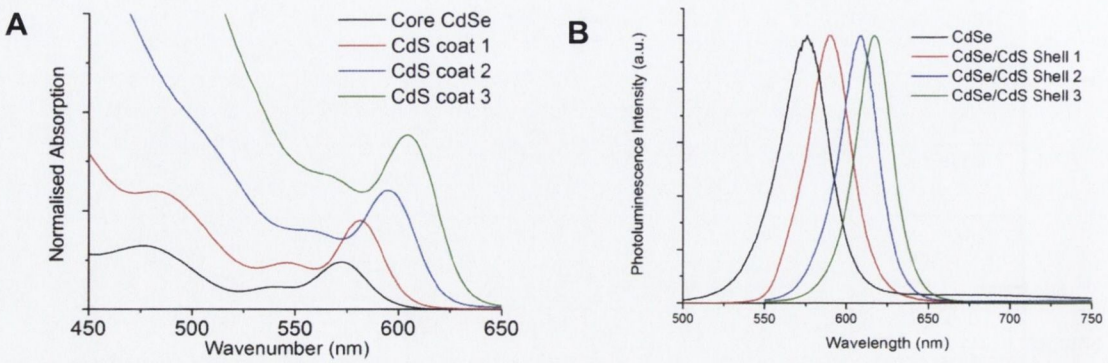

Figure 3.18 UV-Vis absorption spectroscopy (A) and photoluminescent spectroscopy (B) of CdSe/CdS core /shell quantum dots. The shift in absorption takes place as a shell of CdS is grown upon the CdSe core.

400 nm is also an indication of the absence of CdS QDs nucleating during the SILAR coating (See Appendix C, Figure 7.4 image C for an example when CdS nucleation did take place).

Photoluminescent spectra of CdSe/CdS QDs are presented in Figure 3.18 B. Interestingly, due to the smaller band gap of CdSe QDs; luminescence is only seen to be produced from the core, with excitons generated in the CdS shell, firstly de-exciting to the CdSe core before recombining. Consequently, the Pl wavelength is strongly defined by the size and electronic state of the CdSe core with the Pl spectra displaying the same red shift in peaks as shell growth takes place, as was seen with the absorption spectra. Pl spectra also serve as means to detect the homo nucleation of CdS precursors, with the absence of CdS Pl peaks in the UV range of the spectra serving to point to the absence of CdS QDs.

Due to the type I band alignment created between the CdSe core and CdS shell, a large increase in the luminescent quantum yields of the sample takes place relative to the CdSe core, producing QDs of up to 50% QYs under the test conditions. Interestingly it was found that growth past a certain level had the effect of reducing the overall QY. This is due to the lattice mismatch between the core and shell, which results in defects in the QD crystal structure as the thickness of the shell increases, causing the decrease in QY observed. [315]

3.3.6.ii Electron Microscopy Analysis

TEM was used to analyse the size and shape of a resulting sample of CdSe/CdS QDs after 3 coatings of CdS were deposited, this is shown in Figure 3.19. From this it can be seen that the particles still showed excellent size distribution, displaying similar diameters across the sample after the CdS coating, with a size distribution centred on 4.8 nm and a standard deviation of 0.56 nm +/- after measuring diameters across the sample as shown in Figure 3.19B and fitting this to a distribution. These images also showed no presence of CdS QDs, meaning that we avoided homogeneous nucleation of the shell materials (see Appendix C, Figure 7.4 A and B for an example when CdS nucleation did occur). Comparing the produced size to the original CdSe QD core coated, which had a diameter of 3.4 nm, determined from its first exciton position, we can estimate that a shell of 0.7 nm of CdS has been deposited upon the core QD, producing the core shell structure. Much larger coatings have also been produced, but also showed much larger size distributions, with QDs becoming coated unevenly in CdSe (See Appendix C, Figure 7.5).

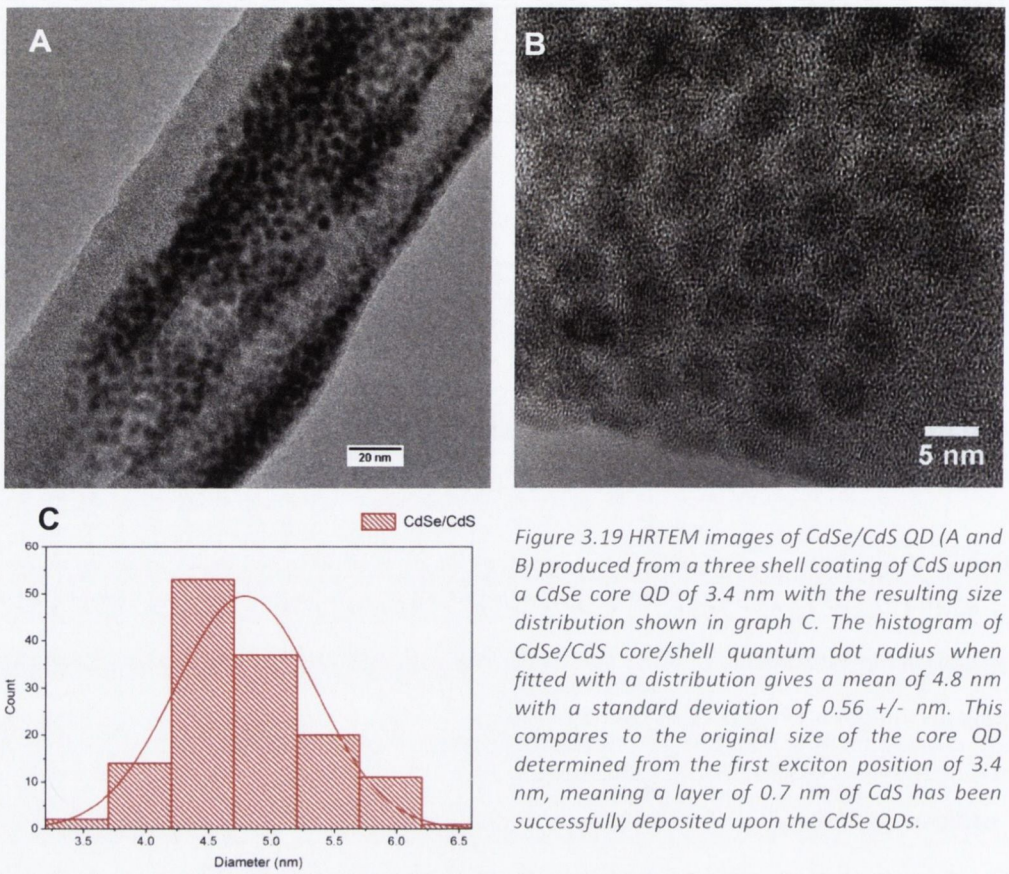

Figure 3.19 HRTEM images of CdSe/CdS QD (A and B) produced from a three shell coating of CdS upon a CdSe core QD of 3.4 nm with the resulting size distribution shown in graph C. The histogram of CdSe/CdS core/shell quantum dot radius when fitted with a distribution gives a mean of 4.8 nm with a standard deviation of 0.56 +/- nm. This compares to the original size of the core QD determined from the first exciton position of 3.4 nm, meaning a layer of 0.7 nm of CdS has been successfully deposited upon the CdSe QDs.

3.3.7 CdS/CdSe Quantum Dots: Synthesis and Characterisation

CdS/CdSe QD synthesis was carried out using a modified one-pot approach reported in literature, [17, 235] implying that CdS QDs did not need to be firstly synthesised, greatly simplifying the overall method. Therefore, firstly CdS QDs were grown using the same hot injection approach discussed previously in section 3.3.4 , noting that this synthesis used a mole ratio 1:2, S: Cd. This meant after CdS had formed and ceased growth after 10 minutes, it can be assumed no S precursor is present in the reaction solution, therefore avoiding the formation of an alloyed shell ($CdSe_{1-x}S_x$). Following this, the solution was cooled to 230 °C and CdSe shell growth was commenced. This was achieved using the SILAR method, using equal volumes of 0.4 M $Cd(olate)_2$ solution and 0.4 M Se-TOP solutions, which were injected sequentially to slowly grow the CdSe shell upon the cores. The same approach as discussed for CdSe/CdS had to be carried out, taking care to slowly add precursors, avoiding high concentrations of either precursor in solution, and therefore creating conditions favouring heterogeneous nucleation of the CdSe shell upon CdS instead of homogeneous nucleation of CdSe QDs. The resulting QDs were then studied with the

use of UV-Vis absorption spectroscopy, PL emission spectroscopy, and TEM, with the basic properties of the produced CdS/CdSe QD detailed in Table 3.5 relative to the SILAR injection.

Table 3.5 This shows the change in spectra as a shell of CdSe is grown upon a CdS core QD producing a CdS/CdSe core/shell quantum dot.

Samples	1st Exciton peak of QDs	Fwhm of 1st Exciton peak	1st Exciton peak shift due to injection	Excitonic PI emission	Defect PL emission	Stokes shift of excitonic emission
units	nm	eV	eV	nm	eV	Nm
CdS	387	0.16	/	/	451	/
CdS/CdSe injection 1 (Se)	420	0.15	0.25	/	610	/
CdS/CdSe injection 2 (Cd)	459	0.14	0.25	544	622, 664	85
CdS/CdSe injection 3 (Se)	492	0.13	0.19	544	632, 674	52
CdS/CdSe injection 4 (Cd)	528	0.12	0.16	572.5	689.5,794	44.5
CdS/CdSe injection 5 (Se)	552	0.11	0.1	599	729, 792	47
CdS/CdSe injection 6 (Cd)	574	0.11	0.086	618	802	44

3.3.7.i Optical characterisation

UV-Vis absorption spectra (Figure 3.20 A) allowed us to monitor the synthesis of CdS/CdSe in depth, by taking spectra between each CdSe injection. The spectra show the presence of the initial CdS core synthesised, which was then followed by growth of a CdSe shell upon it, producing a gradual red shifting of the absorption spectra as the shell was grown upon the core, shifting the first exciton position of the QD from 387 nm to 572 nm. This is due to the smaller band gap of CdSe, which as it's thickness increases, shifts the absorption wavelength of the QD

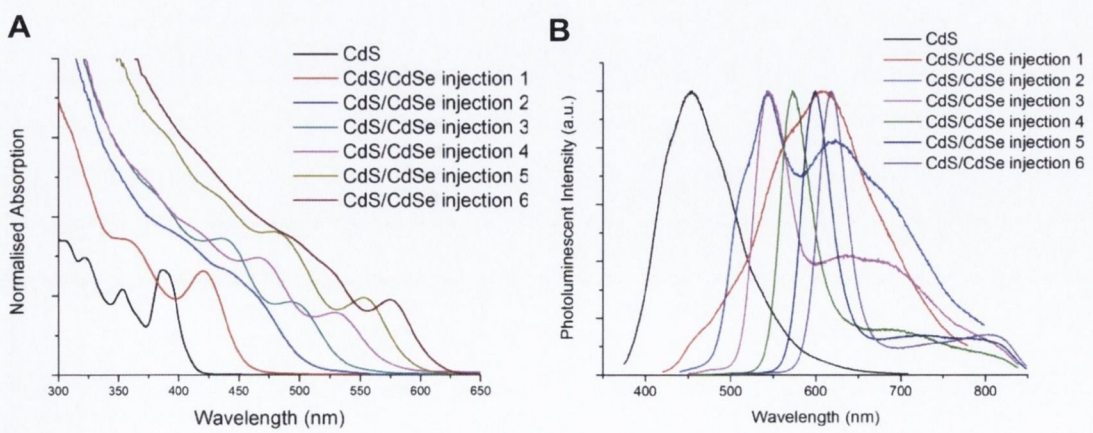

Figure 3.20 Uv-Vis absorption spectroscopy and phtoluminescent spectroscopy of CdS/CdSe QDs. This shows the change in absorption pattern as a CdSe shell is grown upon a CdS quantum dot. A SILAR approach is utilised to grow the CdSe shell and is achieved by using alternative injections of 0.4 M Cd stock solution or 0.4 M Se stock solution.

to lower energies, due to the decreasing quantum confinement of the CdSe shell, reducing its band gap.

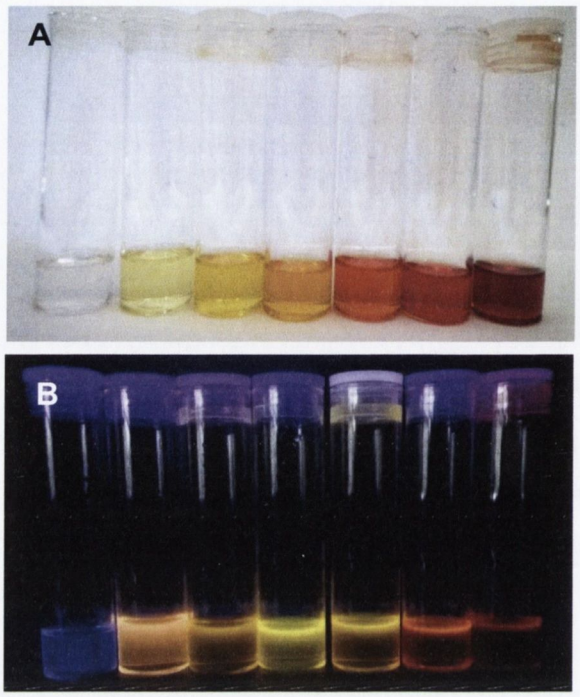

Figure 3.21 Photograph of CdS/CdSe quantum dot under visible light (A) and under UV illumination (B) This shows the change in absorption and emission as a shell of CdSe is grown upon the core CdS, with shell thickness increasing from left to right.

Photoluminescent spectroscopy is also used to study the growth of the CdSe shell upon CdS and is shown in Figure 3.20. Just as was observed for CdSe/CdS QDs; luminescence for CdS/CdSe only originates from the CdSe shell, which also shows the same pattern of red shifting as the shell of CdSe is grown upon the CdS QDs. This because of the reverse type I band alignment that is formed between the core and shell, meaning that excitons are confined to the shell of the QD. Due to this, we also see a large amount of defect emission from the QD upon initial growth of a shell, which again correlates with theory that the exciton becomes confined to the CdSe shell. This shell upon initial growth is very thin and therefore will be nearly exclusively composed of surface atoms and therefore have a much higher likely hood of producing surface defect emission due to incomplete passivation, as is seen in very small CdSe QDs such as magic sized CdSe QDs.[14, 71] This defect emission then is found to reduce as the shell of CdSe is increased, changing the majority of emission to be excitonic in nature, though interestingly the defect is not fully eliminated upon completion of CdS/CdSe QD formation.

Unfortunately, due to surface exciton confinement, this also means that the photoluminescence of these QDs show much lower efficiencies due to surface interaction causing quenching, with QYs achieved ranging between 10 to 15 %, and is highly dependent on

the level of cleaning applied to the QD, post synthesis. The Stokes shift for the QDs when observing the distance between the first exciton peak and excitonic emission is much larger than observed in CdSe QDs, with completed CdS/CdSe QDs displaying values of 44 nm.

3.3.7.ii Electron Microscopic Analysis

TEM was utilised to analyse the size and shape of completed CdS/CdSe QDs (Figure 3.22). The sample showed a relatively small size distribution in diameters, which when graphed in a histogram and fitted, gave an average diameter of 4.5 nm with a standard deviation of +/-0.65 nm. The images showed no evidence of smaller QDs formed, meaning that the CdSe was successfully heterogeneously nucleated upon the CdS QD surface. When comparing the size of these coated QDs to the original CdS QD cores synthesised, a growth in the diameter of the QDs can be seen changing from 2.95 nm (determined from first exciton position) to 4.5 nm, corresponding to the growth of the CdSe shell, producing a CdSe shell of 0.78 nm in thickness surrounding the CdS core.

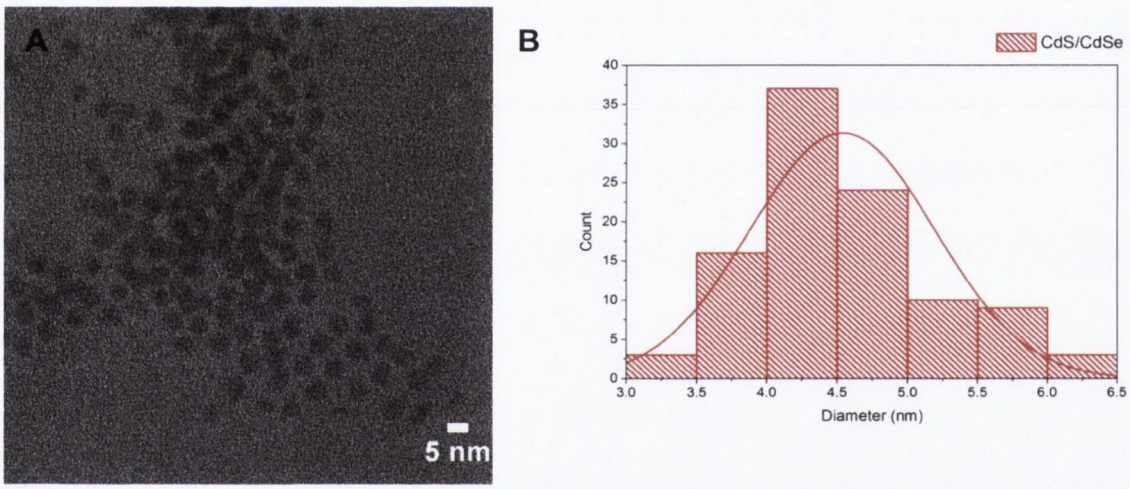

Figure 3.22. TEM and the resulting size distributions of CdS/CdSe core/shell quantum dots. Image A is the TEM image of the CdS/CdSe QDs produced, while image B is a histogram of diameters of the QDs determined from a sample, giving a diameter of 4.5 nm +/-0.65 from fitting the data.

3.3.8 CdTe/CdSe QD: Synthesis and Characterisation

CdTe/CdSe QDs were synthesised using a modified one-pot synthesis from literature.[282] This synthesis involved two distinct steps, in which firstly CdTe QDs were formed, this was then immediately followed by growth of a CdSe shell upon them and was carried out using a modified method from literature. CdTe QDs were synthesised in a non-coordinating solvent of ODE, using oleic acid and ODPA as a ligand. $Cd(oleate)_2$ was used as the Cd precursor, while Te powder was dissolved in TOP, which also contained a fraction of ODPA, another ligand . The reaction solution of $Cd(oleate)_2$, ODE and oleic acid was heated to 280 °C followed by injection of the Te /TOP/ODPA solution. QD growth was allowed to proceed for 3 minutes after which the reaction was cooled to 230 °C.

Following this, a shell of CdSe was grown upon the cores using the SILAR approach. This was carried out using successive injections of 0.1M $Cd(oleate)_2$ in ODE and 0.09 M Se/TOP solution, following the same pattern as discussed for CdSe/CdS and CdS/CdSe core shell QDs, so as to avoid homogeneous nucleation of CdSe QDs in the reaction mixture, instead favouring heterogeneous nucleation of a CdSe shell. It is also important to note that the first step of forming CdTe QDs reaction is carried out using a 2:1 molar ratio of Cd:Te. This is particular important when carrying out a one pot synthesis so as to ensure that all of the Te is reacted at the first stage of the synthesis, so as to avoid the growth of an alloyed shell consisting of $CdSe_{1-x}Te_x$. The resulting QDs were then analysed using UV-Vis absorption spectroscopy, Pl emission spectroscopy, and TEM, with the change in optical properties as the CdSe shell is grown is shown in Table 3.6.

Table 3.6 This shows the change in spectra as a shell of CdSe is grown upon a CdTe core QD producing a CdTe/CdSe core/shell quantum dot.

Shell coating	1st Exciton peak of QDs	FWHM of 1st Exciton peak	Pl emission	FWHM of PL emission	Stokes shift
units	nm	eV	nm	eV	nm
CdTe core	605	1.2E-01	615.9	0.087	10.9
Se injection 1	615.9	1.1E-01	625	0.081	9.1
Cd Injection 1	630.9	1.2E-01	641	0.084	10.1
Se injection 2	654	1.1E-01	665	0.084	11
Cd injection 2	672	1.1E-01	682	0.083	10
Se injection 3	695	1.4E-01	713	0.1	18
Cd injection 3	701	1.4E-01	720	0.1	19
Se injection 4	703	1.6E-01	729	0.1	26

3.3.8.i Optical Characterisation

UV-Vis absorption spectra and Pl spectra were used to monitor the growth of the CdTe core QDs as shown in Figure 3.23. The UV-Vis absorption (Figure 3.23 A) spectra showed the appearance of CdTe QD absorption after Te precursor solution injection, which is then gradual red shifted in absorption spectra. This produces a change in the excitonic peak, shifting it from 564 nm to 615 nm as the CdTe QDs grow in solution over 100 seconds, following this, no further

change in the spectra was observed in the experiment indicating the vast majority of Te reactive precursor reacted during the growth stage.

The Pl spectra of the CdTe core QDs shows only a sharp single excitonic peak, indicating a small distribution, which decreases as the QDs, grow in size, indicating a focusing of the size distribution of CdTe QD diameters. These spectra also showed red shifting as seen in the absorption spectra due to the growth of the dots in diameter, causing a decrease in the materials band gap.

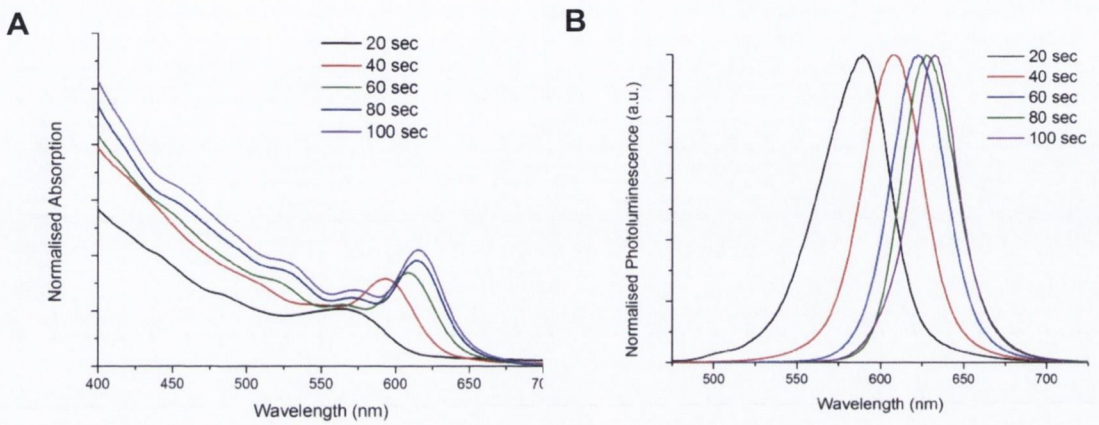

Figure 3.23 UV-Vis absorption spectra and Pl spectra chartering the growth of CdTe core quantum dots relative to time. *Graph A shows the red shifting in UV-Vis spectra as the size of the CdTe increases during the reaction while Graph B shows the red shifting in photoluminescent of the CdTe QDs as the reaction proceeded.*

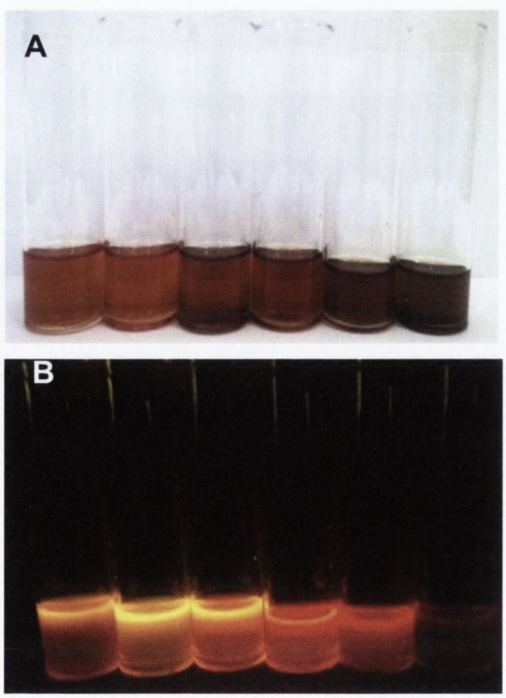

Figure 3.24 Photograph of CdTe/CdSe core/shell quantum dots under visible light (A) and under UV illumination (B). This shows the change in absorption and emission as a shell of CdSe is grown upon the core CdTe, with shell thickness increasing from left to right.

Following the synthesis of core CdTe QDs, the CdSe shell was deposited and monitored using PL and UV-Vis spectroscopy, this is shown in Figure 3.24. The UV-Vis absorption spectra (Figure 3.25 A) showed a very strong red shifting absorption band as the shell of the CdSe material is grown upon the core, shifting from the initial CdTe first exciton absorption of 605 nm to 701 nm after the 7th shell of material was deposited. This is due to the Type II band alignment that is produced between the core and shell materials, which has the effect of producing a QD that has a band gap smaller than the band gaps of either the core or the shell material, due to the staggered band alignment that occurs between CdSe and CdTe. This effect becomes more pronounced as the CdSe shell grows thicker, due to the staggered band gap becoming smaller and therefore producing the red shifting seen in the spectra.

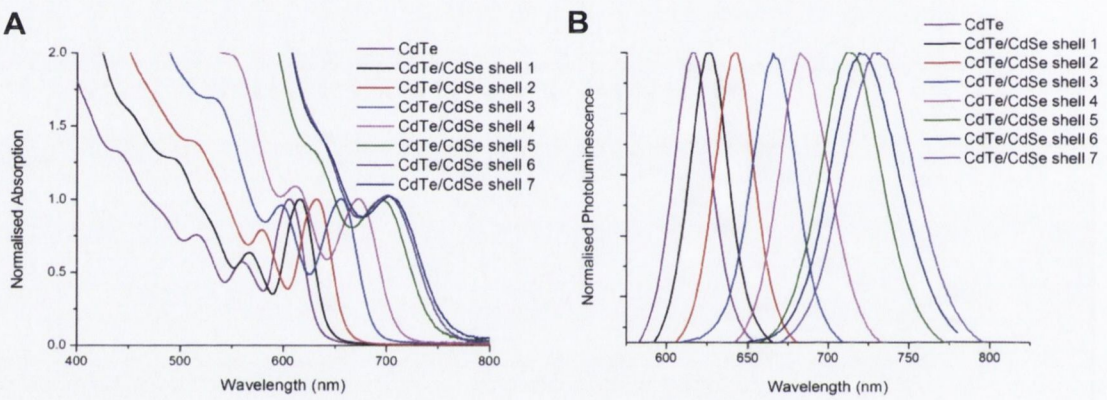

Figure 3.25 The changes in A) UV-Vis absorption spectra and B) the photoluminescence spectra of the CdTe QDs, as a shell of CdSe QDs is grown upon the surface of the QDs. *A SILAR approach is utilised to grow the CdSe shell and is achieved by using alternative injections of 1 ml of 0.1 M Cd stock solution or 0.09 M Se stock solution.*

The Pl spectra (Figure 3.25 B) show the same trend in red shifting as seen in the absorption spectra, shifting from 615 nm to 730 nm over the course of the CdSe coating of CdTe core QDs. This is again due to the staggered band alignment, with emission occurring between the recombining of a hole in the valence band of the CdTe core and an electron in the conduction band of CdSe shell. The change in width of the Pl spectra as the shell grows is in fact due to it being graphed per wavelength while looking at the FWHM of the Pl peaks it can be seen that a minimal change in this value occurs moving from the original core to the core-shell structure as seen in Table 3.6. The Stokes shift increase to 26 nm after coating, up from an original value of 11 nm for the core CdTe QD.

3.3.8.ii Electron Microscopy Analysis

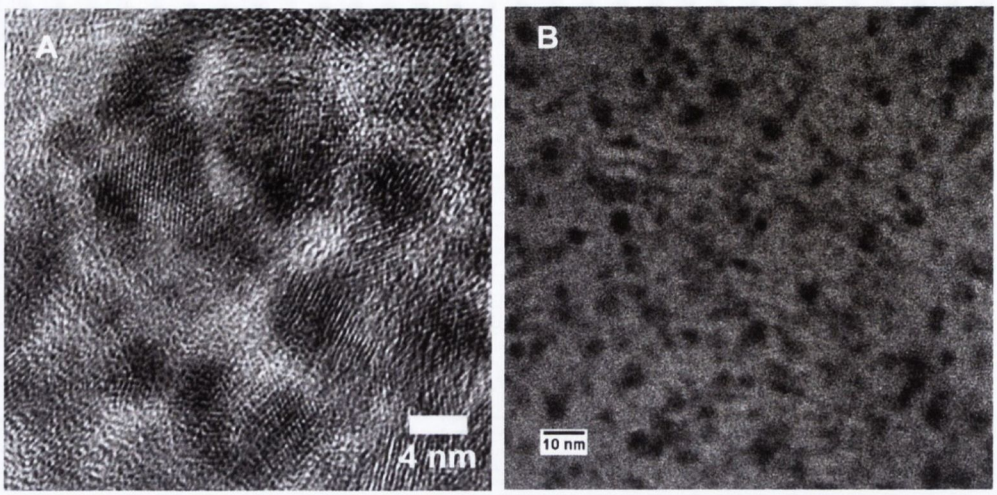

Figure 3.27 HRTEM images of CdTe QDs, showing excellent crystallinity evident by the presence of lattice fringes in image A.

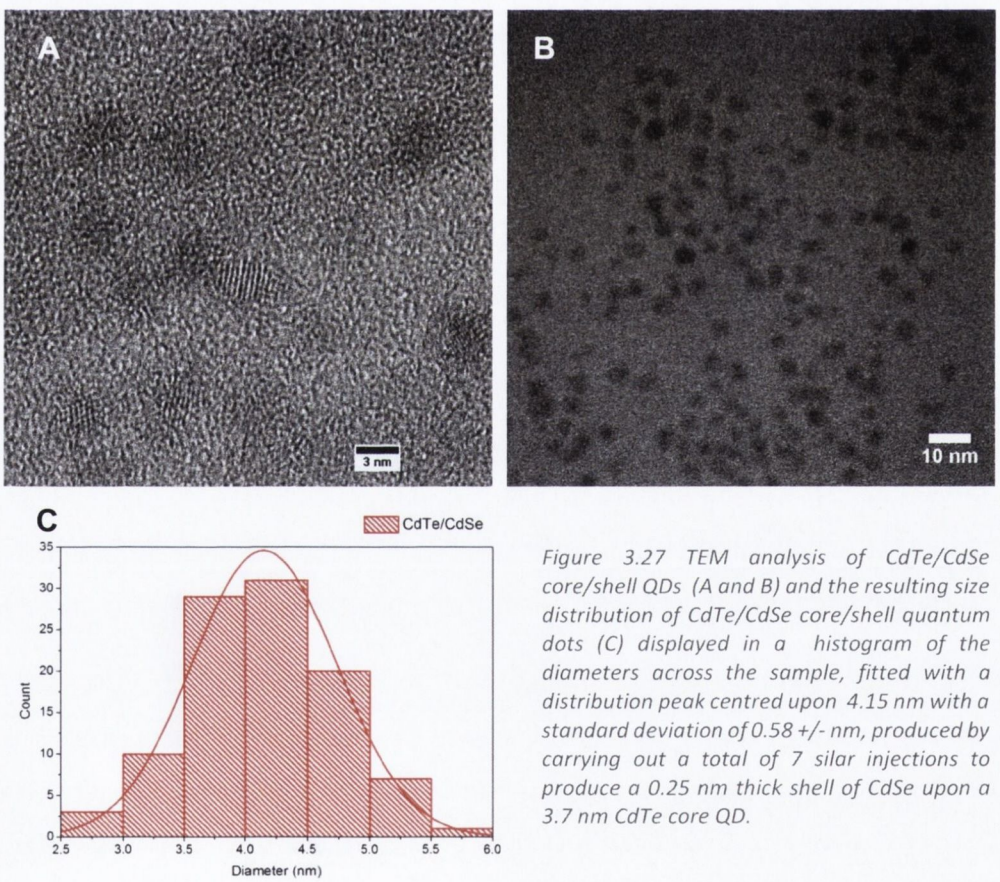

Figure 3.27 TEM analysis of CdTe/CdSe core/shell QDs (A and B) and the resulting size distribution of CdTe/CdSe core/shell quantum dots (C) displayed in a histogram of the diameters across the sample, fitted with a distribution peak centred upon 4.15 nm with a standard deviation of 0.58 +/- nm, produced by carrying out a total of 7 silar injections to produce a 0.25 nm thick shell of CdSe upon a 3.7 nm CdTe core QD.

TEM was used to firstly analyse the CdTe core QDs produced as shown in Figure 3.27. The QDs produced showed a high crystallinity as shown by the crystal planes visible in the HRTEM of the CdTe QD. TEM was then used to analyse the resulting CdTe/CdSe core shell QDs as shown in Figure 3.27. The resulting QDs retained a circular shape with no evidence of smaller QD crystal formation, which would indicate CdSe QD nucleation. The images produced, showed dots with

a small size distribution as shown in Figure 3.27 B, with the fitted size distribution centred upon 4.15 nm in diameter with a standard deviation of 0.58 +/- nm. The original diameter of the CdTe core determined from the 1st exciton position was 3.7 nm, meaning a shell of only 0.25 nm of CdSe was deposited.

3.3.9 CdSe/CdS Quantum Rods: Synthesis and Characterisation

The objective of this part of our work was to produce a CdSe QD of wurtzite crystal structure, upon which a CdS shell was then deposited, under conditions that cause a heterogeneous growth of CdS upon the QD, forming a dot in rod structure. Rod structure form due to the different surface reactivity of the CdSe QDs faces, this therefore means that CdS more readily nucleates and grows on the faces of the CdSe crystal causing the rod shape to form. This process is promoted by the use of a two different ligands during the synthesis, hexylphosphonic acid (HPA) and octadecylphosphonic acid (ODPA), which due to their different chain lengths display different binding energies, further boosting the heterogeneous growth to take place.[89]

CdSe/CdS heterostructured nanorods were synthesised using a two-step synthesis. Initially ODPA capped CdSe QDs were synthesised using the method already discussed in 3.3.1 . Following this synthesis, a CdS shell was deposited using a single hot injection previously reported method.[89] This procedure was carried out using a coordinating solvent of TOPO, and a mixture of hexylphosphonic acid (HPA) and octadecylphosphonic acid (ODPA) while the shell precursors used were $Cd(ODPA)_2$ as the Cd source, formed from the reaction between ODPA and CdO, while S dissolved in TOP was used as the S source. Cd $(ODPA)_2$ was formed in the reaction mixture at 300 °C which was then heated to the required injection temperature. At this point, the sulphur source was injected along with a solution of the core CdSe QDs dissolved in TOP. Injection took place at 360 °C, while the growth time under heating varied from zero to two minutes.

Due to the setup in this experiment, with shell precursor being introduced in a single injection, it was not possible to monitor the growth of the CdS shell. Instead, a number of reactions were carried out with a range of different size CdSe staring cores, which strongly effected the size and shape of the CdSe/CdS QRs. Properties of a range of the samples produced, are shown in the Table 3.7. The samples produced were then studied using UV-Vis absorption spectroscopy, Pl emission spectroscopy, TEM and STEM.

Table 3.7 A collection of properties of CdSe/CdS QRs synthesised.The size of CdSe cores was determine using the first exciton position of the samples in UV-Vis absorption spectra. Length and width of the resulting QRs was determined using TEM. Quantum yields were determined using a Rhodamine 6G in ethanol (QY 95%[292]).

CdSe/Cds QR Samples	1st Absorption peak of CdSe	Diameter of CdSe QD	1 st Absorption of cores	Δ in 1st Absorption peak	Pl emission	QY	Length*	Width*	Aspect Ratio
units	nm	nm	nm	eV	nm	%	nm	nm	/
CdSe/CdS 1	575	3.17	556	0.074	584	51.8	/	/	/
CdSe/CdS 2A	591	3.37	564.5	0.1	597	48.2	21.2	4.1	5.1
CdSe/CdS 2B	596	3.37	564.5	0.12	618	56.8	21.0	4.9	4.3
CdSe/CdS 3	608	3.41	566	0.15	615	40.8	35.3	4.7	7.5
CdSe/CdS 4	625	4.06	587	0.13	641	31.2	22.98	6.5	3.5

3.3.9.i Optical analysis QRs

The resulting UV-Vis absorption and PL emission spectra is shown in Figure 3.28. The UV-Vis absorption shows a very strong absorption after 512 nm, due to the onset of CdS absorption, which occurs at this wavelength. Absorption at longer wavelengths is due to the CdSe core, with the first exciton still visible in the spectra, while the position of this peak is strongly red shifted due to the CdS coating producing a shift of between 0.05 to 0.22 eV in the absorption spectra, with smaller cores displaying much stronger shifting after coating than larger CdSe QDs. This shift is caused to due to lattice mismatch between CdSe and CdS, this strain then causes a shift in the energy levels of the CdSe QD as reported in literature.[299]

These CdSe QDs showed strong luminescence as shown in Figure 3.28. The Pl emission from these QRs displayed the same features as seen in other CdSe/CdS QRs, with emission occurring from the CdSe core, and so show a strong dependence upon the diameter of the CdSe QD initially coated. In addition, since the majority of optical absorption occurs in the CdS shell, an artificially large Stokes shift occurs in these QRs. It is also interesting that due to the shell being of a rod shape, the lattice strain induced is not to the magnitude as would be observed when compared to a homogeneous shell of CdS. This enables the deposition of a thicker shell, while still producing a very high QY, with values up to 56%. A relationship has also been reported between the aspect ratio of the NR (width to length) and the luminescent quantum yield, with values showing a strong decreases with aspect ratios larger than 4, due to lattice strain and increase in surface area of theses longer NRs, which is also shown in the samples produced in this study.

Figure 3.28 Normalised UV-Vis absorption and emission of CdSe/CdS heterostructured rods , the same quantity of CdS precursor was injected in each of the reactions while a different core of CdSe was used in each case to produce the difference in spectra , the CdSe core diameter increases in size from top to bottom, from 3.15 nm (purple, sample 1) , 3.370 nm (blue, sample 2), 3.41 nm (green, sample 3) ,4.0 nm (yellow, sample 4), 4.51 nm (red, sample 5).

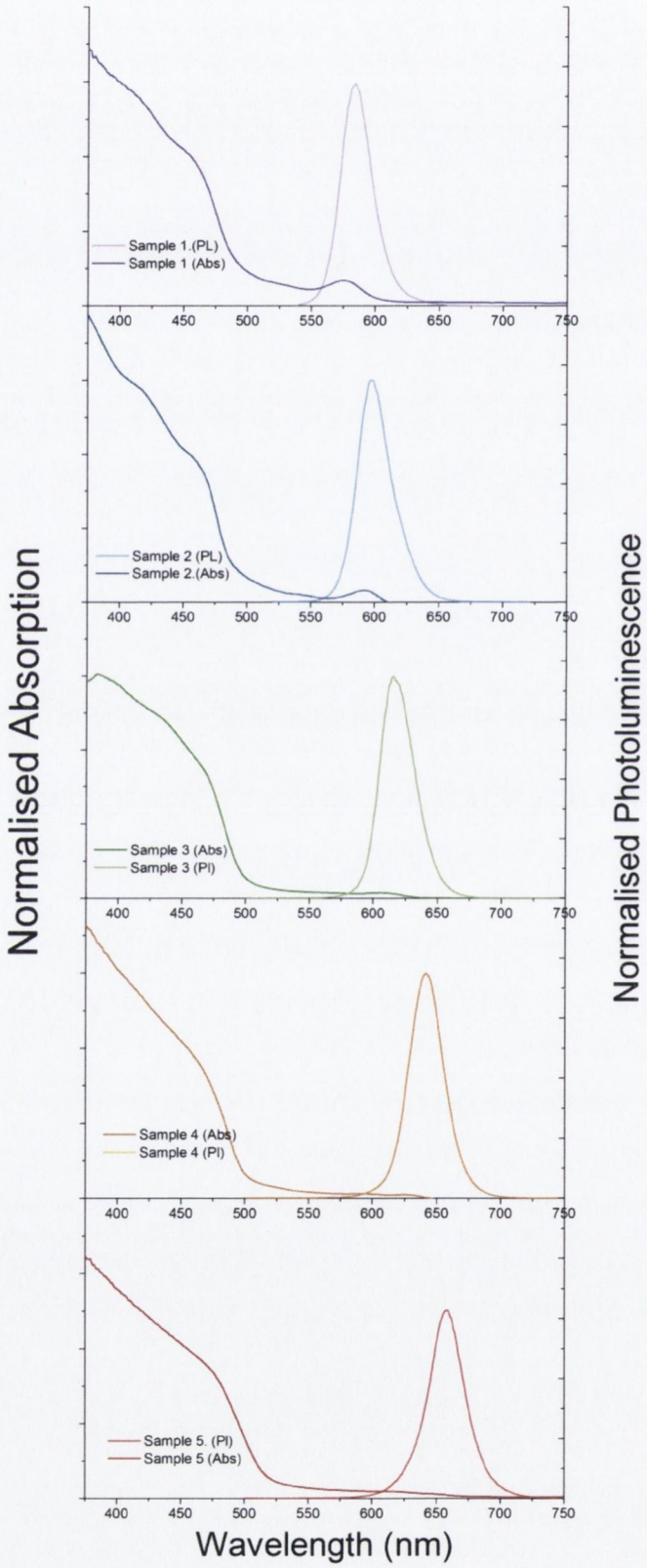

3.3.9.ii Electron Microscopy Analysis

TEM was used to characterise the morphology of the resulting QRs and is shown Figure 3.29. These images show a sample (sample CdSe/CdS 2A) produced from a 3.4 nm CdSe QD, with distributions of widths (Figure 3.29 B) and lengths (Figure 3.29 C) which were fitted to give mean values of 4.9 +/- 0.55 nm in width and 21+/- 1.66 nm in length. Therefore, this sample showed a coating of 0.75 nm CdS in the a and b direction, while in the c direction, a much thicker coating of CdS was produced, of 8.8 nm, if the CdSe QD is assumed to be found in the centre of the rod. These showed excellent size distribution and uniformity in length and width across the sample. The sample also showed a complete absence of other shapes of nano crystals present, indicating that all CdSe core QDs were coated in a CdS rod shaped shell, with no evidence in the TEM imaging of the homo nucleation of the CdS pre-cursors either. It is also worth noting that it was not possible in TEM to pinpoint the position of the CdSe core QD in the NRs, produced. A number of other CdSe/CdS NRs have also been analysed with TEM and are shown in Appendix C, Figure 7.5 and Figure 7.6.

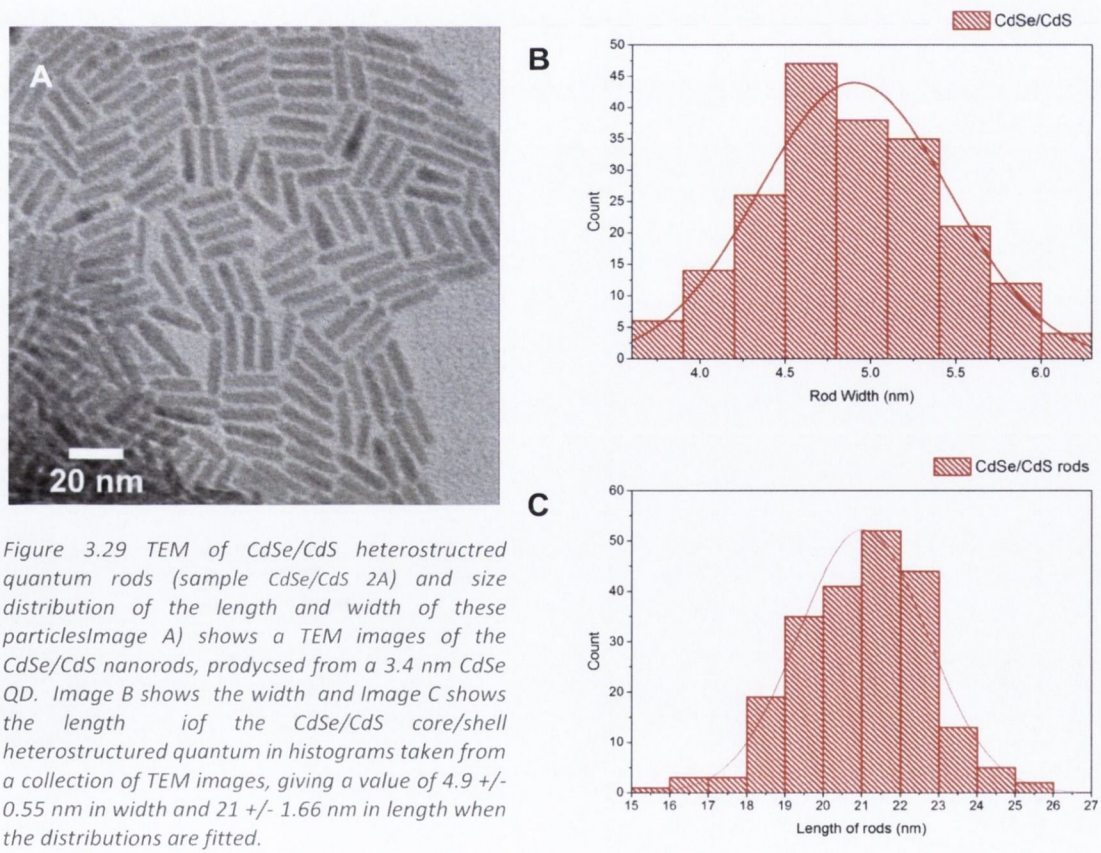

Figure 3.29 TEM of CdSe/CdS heterostructred quantum rods (sample CdSe/CdS 2A) and size distribution of the length and width of these particlesImage A) shows a TEM images of the CdSe/CdS nanorods, prodycsed from a 3.4 nm CdSe QD. Image B shows the width and Image C shows the length iof the CdSe/CdS core/shell heterostructured quantum in histograms taken from a collection of TEM images, giving a value of 4.9 +/- 0.55 nm in width and 21 +/- 1.66 nm in length when the distributions are fitted.

Following this, nanostructures have been analysed using STEM; see the images shown in Figure 3.30. STEM was very useful to examine the morphology and crystallinity of the sample, with very high quality images being obtained, displaying atomic resolution as seen in Figure 3.30 B.

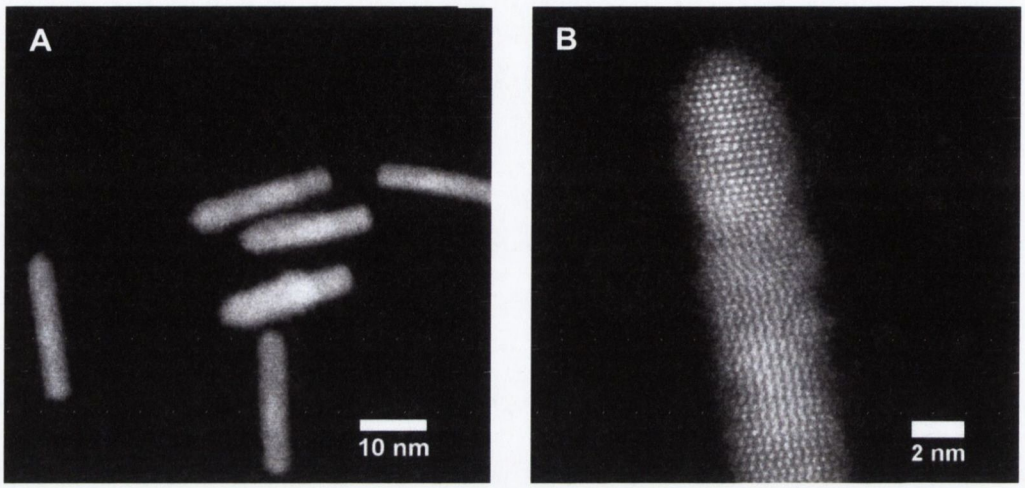

Figure 3.30 Scanning transmission electron microscopy images of CdSe/CdS core/shel heterostrucured quantum rod , displaying the highly crystaline structure of the nanoparticles, visible from the regular postions visible in image B. .

EDX (energy disperse x-ray spectroscopy) was also utilised to determine the elemental make up of another CdSe/CdS QR sample and is shown in Figure 3.31. This displays the presence of Cd, S and Se in the spectra indicative of the expected elemental makeup of the expected CdSe/CdS QRs.

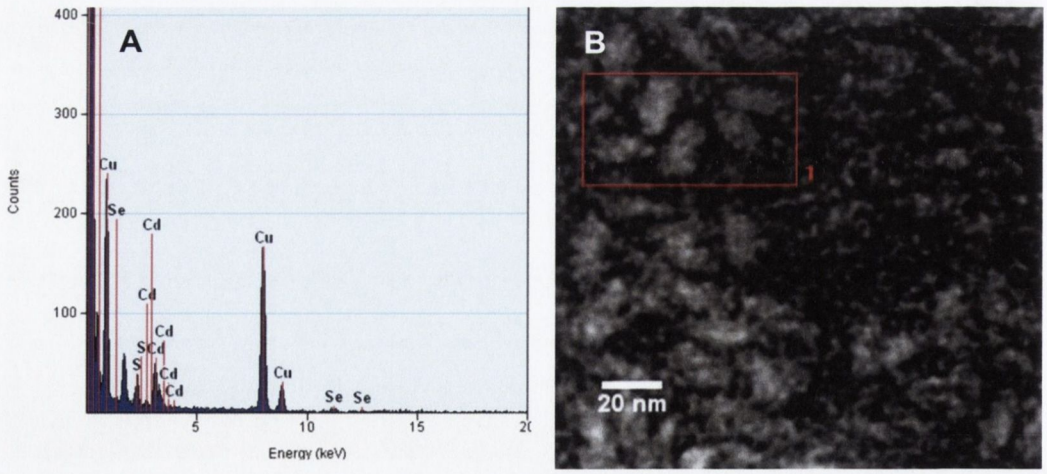

Figure 3.31 STEM and EDX analysis of CdSe/CdS rods with the sample showing the presence of Cd, S and Se as is to be expected in this QR structure

3.3.10 CdSe/CdS/Au nanocomposites Synthesis and Characterisation

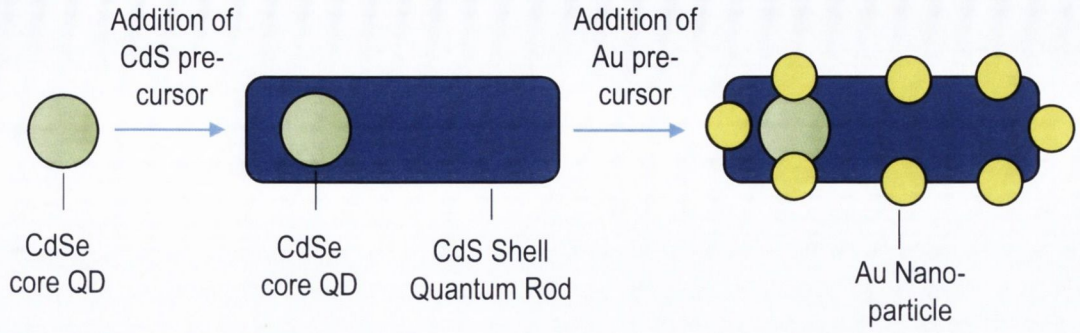

Figure 3.32 Schematic presentation of the two step process to producing a CdSe/CdS/Au nanorods, from CdSe QDs

Following the syntheis of CdSe/CdS QRs, further modifications of these structure through the depostion of Au particles was performed. This synthesis was carried out by using a sample of CdSe/CdS QDs which were added to a soltuion of gold (III) chloride in oleyamine, in which oleyamine acted both as a solvent and ligand. The reaction vessel was then heated to between 90 and 120 °C, over 10-15 minutes, from 60 °C. This heating then caused the decomposition of the gold salt, through its reduction by oleylamine, causing elemental gold to nucleate, in which case the reaction was controlled to favour homogeneous nucleation of Au particles upon the surface of the CdSe/CdS rods, instead of homogeneous nucleation of the Au as Au NPs in solution. A large differences in lattice structures exists between these materials, with gold adopting a face-centred cubic (fcc) structure with a lattice constant of 0.4079 nm, while CdS adopts a wurtzite structure with a lattice constants of a = 0.4160 nm and c= 0.6756 nm. Therefore, due to the mismatch between Au and the CdS surface of the QRs, Au heterogeneous nucleation, formed small seeds on the CdS that grew into Au NPs, instead of forming a film on the material, resulting in a raspberry-like distribution of Au on the surface of the NRs.

It was found that heating rates, higher target temperatures and longer heating times all resulted in larger Au particles being grown in solution. To favour heterogeneous nucleation, the conditions needed to be carefully controlled as shown in the table. The results were then analysed with UV-Vis spectroscopy, Pl emission spectroscopy, and TEM, with the basic properties and synthetic conditions detailed in Table 3.8.

Table 3.8 This shows a selection of CdSe/CdS/Au NRs, synthesised under varying experimental heating parameters producing samples of differing condition. All sample produced utilised a CdSe/CdS QR measuring 35.2 nm in length and 4.7 nm in width and was formed from a 3.4 nm core CdSe QD.

Sample	Time of reaction	Target Temperature	Heating rate	CdSe/CdS QR sample	Presence of Au homogeneous nucleation
units	min	°C	°C/min	/	/
CdSe/CdS/Au I	15	90	2	3	Yes , some Au NPs
CdSe/CdS/Au II	15	110	3.5	3	No, all Au NP are found on the surface of CdSe/CdS NRs
CdSe/CdS/Au III	10	120	5	3	Yes, a few Au NPs

3.3.10.i Optical Characterisation

UV-Vis absorption and Pl emission spectra of CdSe/CdS/Au QR sample 2 is shown in Figure 3.33. The UV-Vis spectra (Figure 3.33 A) display the change in absorption due to deposition of Au upon the CdSe/CdS rods, showing a large increase in absorption at wavelengths longer than 512 nm, corresponding to the cut off of CdS absorption. The increase is due to Au nanoparticles plasmon absorption and a spectrum of pure Au NPs produced in house under the similar reaction conditions has been included as a comparison (black line) (TEM images of the resulting sample can be seen in Appendix C, Figure 7.9). Au NPs show an overall absorption increasing from longer absorption to shorter wavelengths across the visible spectrum, in addition when NPs of Au are produced in certain morphologies and diameters below 500 nm, a second absorption peak is produced in the spectra due to the onset of plasmonic resonance.[307] This resulted in a broad and intense absorption with a peak value that is dependent upon on the size and morphology of the resulting AU NPs, shifting from 515 nm to 572 nm. From the UV-Vis spectra, it can be seen that a broad peak can be seen in this plasmon area, centred between 525 to 540 nm of the Au NPs and the Au coated CdSe/CdS QRs.

Pl spectroscopy was also a useful tool to investigate the interaction between CdSe/CdS NRs and Au NPs with results shown in Figure 3.33 B and C. The initial sample before coating showed a strong signal in luminescence with a QY of 40.8 %, while with following Au coating produced, this PL signal dropped to a barely detectable (within error) QY of below 0.1 %. Therefore, as expected, the Au NP demonstrated strong quenching of luminescence in these QRs, a property of gold that has been widely reported in the literature when interacting with luminescent

QDs.[309] The remaining luminescent signal could even be due to a small population of CdSe/CdS not coated in Au NPs, though none of these were observed under TEM.

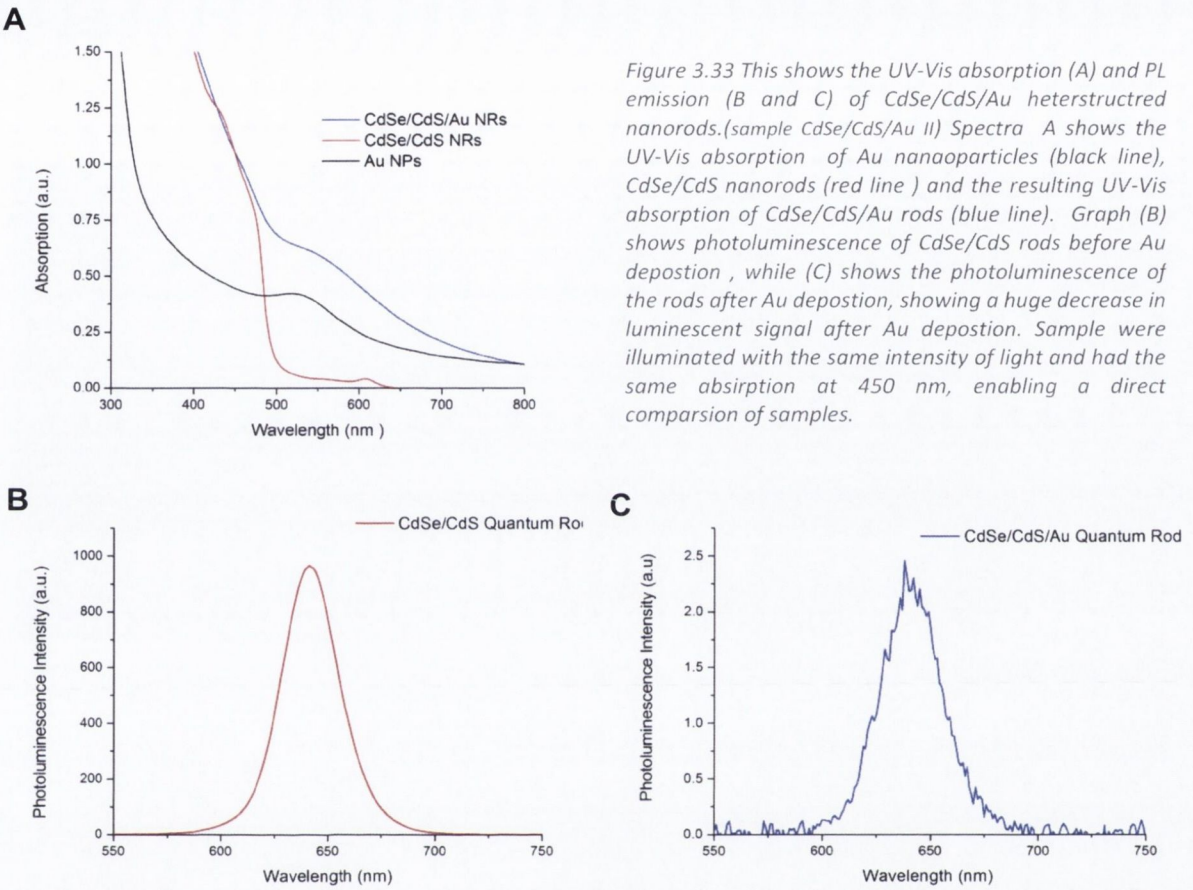

Figure 3.33 This shows the UV-Vis absorption (A) and PL emission (B and C) of CdSe/CdS/Au heterstructred nanorods.(sample CdSe/CdS/Au II) Spectra A shows the UV-Vis absorption of Au nanaoparticles (black line), CdSe/CdS nanorods (red line) and the resulting UV-Vis absorption of CdSe/CdS/Au rods (blue line). Graph (B) shows photoluminescence of CdSe/CdS rods before Au depostion , while (C) shows the photoluminescence of the rods after Au depostion, showing a huge decrease in luminescent signal after Au depostion. Sample were illuminated with the same intensity of light and had the same absirption at 450 nm, enabling a direct comparsion of samples.

3.3.10.ii Electron Microscopy Analysis

TEM was then used to analyses sample CdSe/CdS/Au II further and is shown in Figure 3.34. Firstly, it allowed us to determine the exact size of Au deposited. Interestingly, deposition produced two distinct populations of Au NP diameters, which were fitted to a distribution giving diameters of 7.6 nm +/- 1.2 nm (Figure 3.34 B) and or a smaller diameters measuring 2.93 +/- 0.61 (Figure 3.34 C) nm on the CdSe/CdS QRs. The larger Au NPs were found only to deposit once on each CdSe/CdS QR, while the smaller NPs of Au gold were found to be attached on multiple positions on each nanorod. This pattern of deposition proved true across a number samples produced and has previously been reported in literature[283] to occur due to the presence of the CdSe core QD present in the QRs, which effects the surface energy at that position in the CdS shell and therefore favours the growth of a single larger Au NP at this position. TEM also proved the success of our approach to avoiding hetero-nucleation of the Au salt, and the sample has shown the complete absence of Au NP in solution. Several other samples produced under various conditions showed the growth of Au NPs in solution, while in

the case of sample 2, this was eliminated through careful control of the synthetic conditions as described in Table 3.8. (TEM analysis of sample 1 and sample 3 is shown in Appendix C, Figure 7.7 and also includes a sample produced under an earlier approach using a different CdSe/CdS sample)

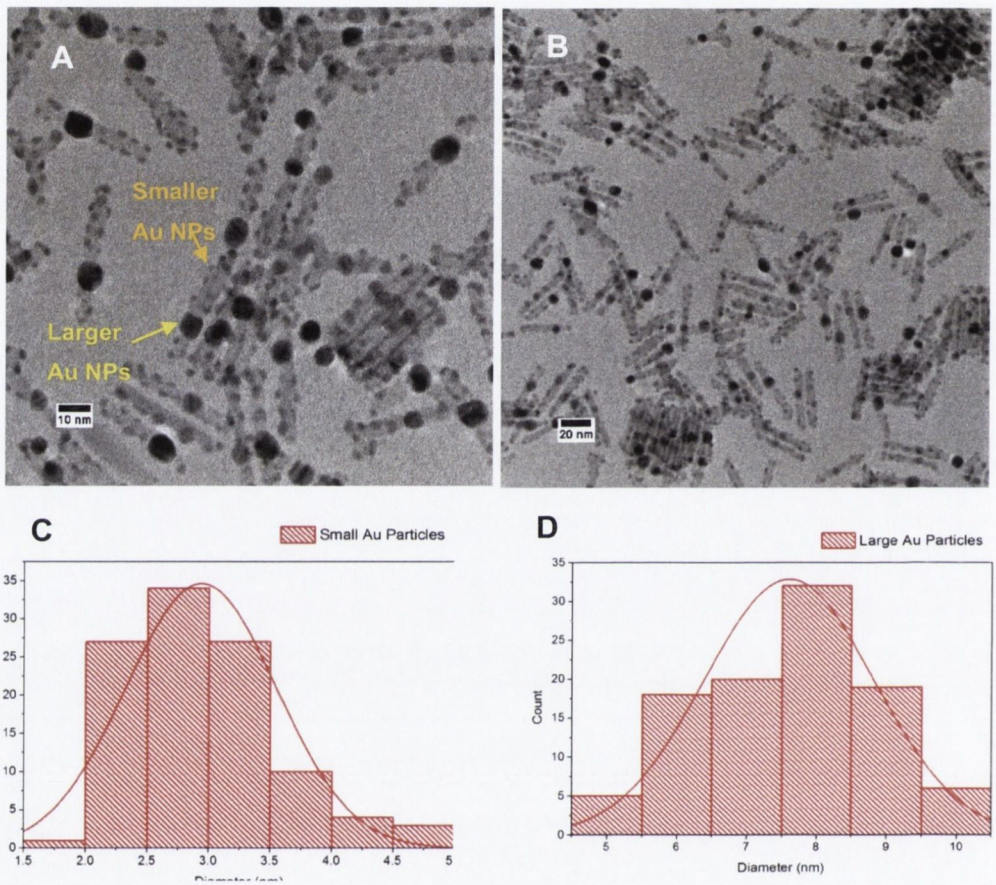

Figure 3.34 TEM images and the resulting histograms of Au NPs diameters, produced in the formation of CdSe/CdS/Au heterostructured QRs (sample CdSe/CdS/Au II) Image A and B, shows Au NPs deposited upon the CdSe/CdS rods (35.3 nm x 4.7 nm) in a raspberry structure, producing two distinct sizes. Graphs C and D shows the distributions in diameters of the two possible diameters C) shows the smaller Au NP diameters measuring 2.93 +/- 0.61 nm, while with D) showing the larger Au NP diameters of 7.6 nm +/- 1.2 nm

3.4 Cation exchange

In this section, cation exchange has been used as means to produce a range of nanocrystalline structures, by replacing cations present in QDs and QRs synthesised using hot injection in the previous section. This has allowed us to produce a range of materials not readily accessible from a more direct synthetic approach.

3.4.1 Cation exchange: PbS QDs to PbS/CdS QDs

A partial cation exchange was carried out on pre-synthesised PbS QDs in section 3.3.5 with the aim to produce a core/shell PbS/CdS QD. This was carried out by dispersing a solution of oleic

acid capped PbS QDs in a solution of toluene, oleic acid and Cd(oleate) which was heated to 100 °C under an inert atmosphere and allowed to proceed for between 10 to 80 minutes. The length of time defined the level of exchange having taken place, allowing a simple route to control the level of cation exchange. The cation exchange of Pb^{+2} to Cd^{+2} took place spontaneously due to the similar lattice constants and size of the cations, though heating needed to be applied to increase the rate of exchange.[93] The resulting samples were examined with the use of UV-Vis absorption spectroscopy, TEM, EDX and STEM.

3.4.1.i Optical characterisation

UV-Vis spectroscopy presents a simple way to monitor the progress of the cation exchange and is shown in Figure 3.35. As the Cd^{2+} ions begin to exchange with the Pb^{2+} in the QDs, the size of the resulting PbS QD shrinks, therefore this causes a blue shifting in the absorption of PbS as its band gap increases in energy. This results in a large shift initially after 5 minutes, which then slows in rate. Pl spectra of the resulting QDs after 80 minutes showed a complete absence of luminescence, completely quenching the bright luminesce measured from these PbS QDs prior to exchange.

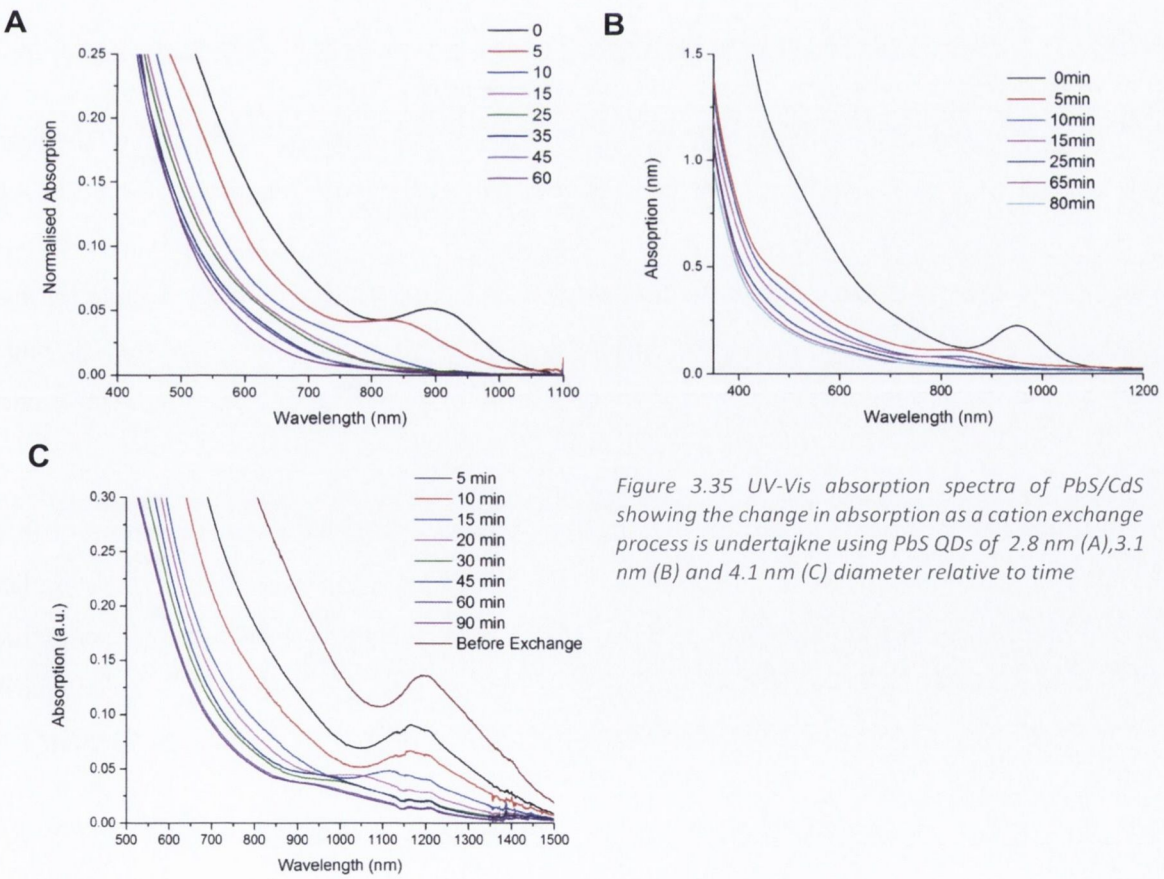

Figure 3.35 UV-Vis absorption spectra of PbS/CdS showing the change in absorption as a cation exchange process is undertajkne using PbS QDs of 2.8 nm (A),3.1 nm (B) and 4.1 nm (C) diameter relative to time

3.4.1.ii Electron Microscopy Analysis

TEM was used to analyse the size and shape of a resulting sample of PbS/CdS QDs and were compared to the original QDs before the cation exchange and is shown in Figure 3.36. Interestingly the QDs showed nearly no change in diameter before and after thr exchange well within the error recorded in the experiment. This therefore proves that the shifting seen in the UV-Vis spectra is not due to etching of the PbS QDs, instead confirming that cation exchange had taken place.

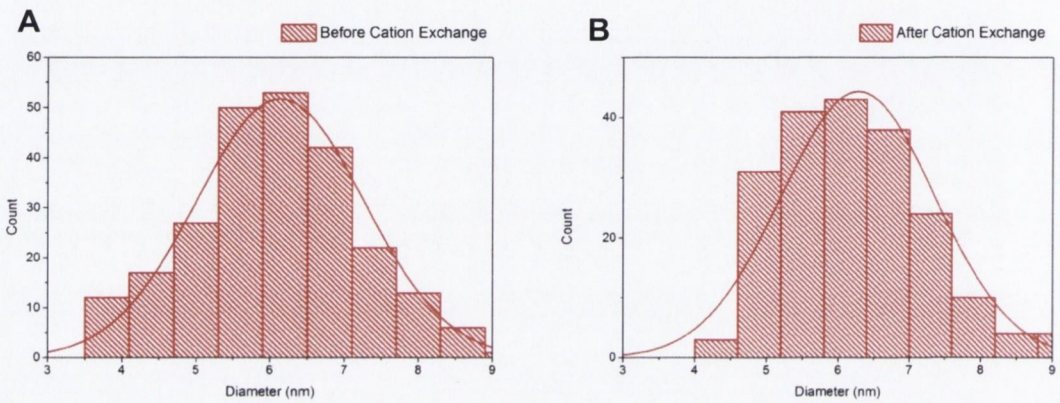

Figure 3.36 Histogram of the diameters of PbS QDs measured from TEM images before (A) and after (B) partial Cd-cation exchange, with the distribution fitting giving values of 6.1 +/- 1.12 nm before and 6.3 +/- 1.01nm after cation exchange.

STEM and EDX was then utilised to confirm the elemental composition of the QDs produced after the cation exchange and is shown in Figure 3.37. The composition of PbS/CdS QD was analysed using EDX, which showed the presence of Cd, Pb and Cu, with Cu being eliminated as a background signal due to the Cu TEM grid being utilised to mount the sample for analysis. Therefore, from this it can be confirmed that the elemental content of the QD had been converted from PbS QDs to PbS/CdS QDs, due to the presence of Cd peak in the EDX spectra.

3.4.2 Cation exchange of CdSe to $Cu_{2-x}Se$

Cation exchange was further investigated through the exchange of Cd^{2+} present in ODPA capped CdSe QDs with Cu^{1+} ions. Due to the difference in valence of the ions, the exchange in fact replaces each Cd^{2+} ions with two Cu^{1+} ions, converting CdSe to Cu_2Se nanostructure. Interestingly Cu_2Se and Cu_2S has been shown to commonly occur non-stoichiometrically, meaning that dots produced will in fact produce a QD of $Cu_{2-x}Se$ QDs after the exchange, with x equalling between 0.1-0.2.[316]

The exchange was performed using a modified method from literature[316] by firstly dispersing CdSe QDs into a solution of toluene, to which tetrakis(acetonitrile)copper(I) hexafluorophosphate (the source of Cu^{1+} ions in solution) was added. This was carried out at room temperature and the mixture was allowed to undergo reaction for 5 minutes, resulting in a complete exchange of cations. UV-Vis spectra was used for analysis of the resulting samples.

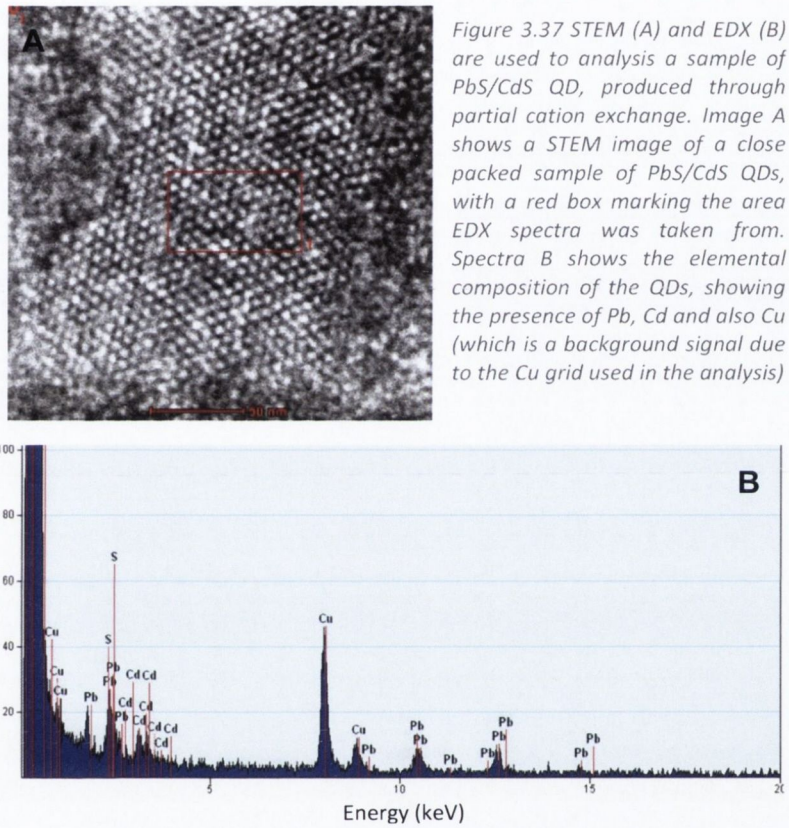

Figure 3.37 STEM (A) and EDX (B) are used to analysis a sample of PbS/CdS QD, produced through partial cation exchange. Image A shows a STEM image of a close packed sample of PbS/CdS QDs, with a red box marking the area EDX spectra was taken from. Spectra B shows the elemental composition of the QDs, showing the presence of Pb, Cd and also Cu (which is a background signal due to the Cu grid used in the analysis)

3.4.2.i Optical spectroscopy

Initially the resulting dots were analysed with UV-Vis absorption spectroscopy and is shown in Figure 3.38. A huge change in the absorption spectra takes place as a result of the cation exchange, due to a the much smaller band gap (~1 eV) of Cu_2Se causing the onset of absorption to be shifted to the infrared region. This effect is further exaggerated due to the presence of a broad absorption peak centred at 691 nm. This peak is in fact not due to excitonic absorption, but due to plasmonic absorption. This plasmon absorption occurs in $Cu_{2-x}Se$ QDs because of the non-stoichiometry, producing a heavily doped semiconductor due to intrinsic doping. This results in a large concentration of free electrons in the material, and due to the p-type intrinsic doping of the QD, which produces the observed plasmonic peak. The precise position of this plasmonic peak is a function of the stoichiometry of the QD and the diameter of the QD. It is

also worth noting that these QDs show a complete quenching of the original CdSe luminesce due to the cation exchange.

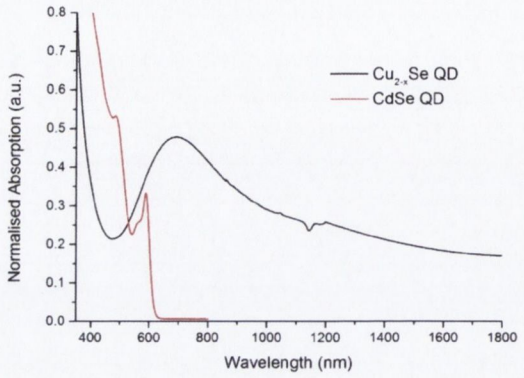

Figure 3.38 UV-Vis absorption of CdSe QD of 4.0 nm in diameter (red line) and the resulting spectra of $Cu_{2-x}Se$ QDs (black line) produced using a Cu^{+1} cation exchange.

3.4.3 Transformation of CdSe/CdS to $Cu_{2-x}Se/Cu_{2-x}CdS$ to PbSe/PbS

A final cation exchange was demonstrated using a two-step process, converting a core/shell QR of CdSe/CdS firstly to $Cu_{2-x}Se/Cu_{2-x}S$, followed by a conversion to PbSe/PbS using a modified method from literature.[316] This exchange was carried out using firstly the same method as described in section 3.4.2 . This produced a complete conversion QRs. Following this, a second exchange was carried out with the use of $Pb(acetate)_2$ dissolved in TBP as the source of Pb^{+2} ions. This process was performed under an inert atmosphere at room temperature and was allowed to proceed for 2 hours. Following this complete conversion of $Cu_{2-x}Se/Cu_{2-x}S$ to PbSe/PbS occurred; with the products studied using UV-Vis absorption spectroscopy.

3.4.3.i Optical Characterisation

UV-Vis spectroscopy was used to analyse the resulting NRs produced from the cation exchange and is shown in Figure 3.39. A large red shift occurs in the absorption spectra as result of the CdSe/CdS to $Cu_{2-x}Se/Cu_{2-x}S$ exchange; due to the smaller band gap of the Cu chalcogenides based materials. The spectra showed the presence of weak plasmon peak at 648 nm and at 1216 nm, these occur due to $Cu_{2-x}Se$ and $Cu_{2-x}S$ present, both of which are heavily intrinsically p-doped, producing plasmon absorption, with the longer energy absorption due to the shell most likely. The resulting QRs also showed a complete loss of luminesce after the Cu^{1+} cation exchange, relative to the QY of up to 55% that was measured for these structures before exchange. After the second cation exchange was undertaken, the UV-Vis absorption showed

even stronger sensitisation to the infrared region, which displayed a featureless absorption stretching out into the infrared red.

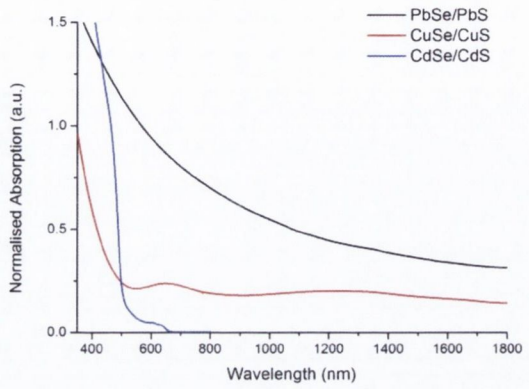

Figure 3.39 UV-Vis absorption of CdSe/CdS heterostructured nanorods (blue line) firstly converted to $Cu_{2-x}Se/Cu_{2-x}S$ (red line), followed by conversion to PbSe/PbS (black line)

3.5 Halide Oleylamine Treatment

For the final part of this work, we decided to explore the use of post treatments to improve the luminescence of QDs following the described cleaning steps. This work was carried out in an attempt to improve upon surface passivation, in the hope of improving luminescent quantum yields. A treatment reported in literature which has demonstrated the most success, utilized a solution of $CdCl_2$ or $PbCl_2$ dissolved in oleylamine, a long chain amine, and demonstrated a strong increase in PbS luminescence and therefore this has formed the basis for our work. This treatment utilised three active elements, which all could provide the enhanced surface passivation, either through oleylamine coordinating to cations on the surface, Cl^- anions that could also coordinate to the cations upon the surface, or Cd^{2+} ions that can passivate anions present on the surface of the QD. In addition, some treatments reported also included the addition of a small quantity of tetradecylphosphonic acid (TDPA), a long phosphonic acid that could also interact with the QD surface.

To investigate these effects we therefore decided to vary several of the elements present and record the resulting PL spectra. To investigate the effect of the cation present, we created solutions of $CdCl_2$, $PbCl_2$, $ZnCl_2$ and $HgCl_2$, all dissolved in oleylamine. This was further expanded to a range of other halide salts, containing other halide anions and monoatomic cations, utilising LiF, CsI, NaCl KBr and KI in oleylamine. In addition, a halide salt, hexadecyltrimethylammonium chloride (HTAC) was used which has been also reported as an effective surface passivation tool, due to the activity of just the Cl^- anion, was also tested in a solution of oleylamine. Furthermore, $Cd(stearate)_2$ dissolved in oleylamine was also tested, to determine the effect of an alternative

source of Cd^{+2}. Finally, to determine the effect of TDPA, we compared solutions of $CdCl_2$ + TDPA in oleylamine, to solutions of just $CdCl_2$ in oleylamine.

For our test conditions, all QDs were dissolved in toluene at a concentration of between 1×10^{-4} to 1×10^{-5} M of QD in a total of 1 ml; following this 0.1 ml of halide salt solution was added. The solution was then allowed to stand for one day in darkness at room temperature to allow coordination to occur. Following this, UV-Vis and Pl spectra were recorded. This study was firstly carried out upon oleic acid capped CdSe QDs that had demonstrated some of the lowest luminescent of QDs synthesised to date. Following this, the study was applied to range of other QDs synthesised.

3.5.1 Halide Oleylamine Treatment: Oleic acid capped CdSe QDs

Oleic acid (OA) capped CdSe QDs were the first QDs tested in conjunction with various oleylamine solutions described in the previous section. The oleylamine solutions were firstly added as described. After a one-day period the solutions were diluted down to an appropriate concentrations for testing and the UV-Vis spectra was recorded, producing absorption of between 0.25 and 1 at the first exciton peak position. The CdSe QDs spectra showed little to no change across the range of oleylamine solutions as shown in Appendix C, Figure 7.10.

Following this, solutions were diluted by a factor of 10 to a total volume of 5 ml (as described in section 2.5.2.ii) to avoid reabsorption loss during PL measurement. The solution was then allowed to stand for 1 day. Following this, it was found that a near complete loss of the positive effects of halide treatment took place, and was determined to be due to the large dilution that had taken place from the original solution treated. The same effect was found with CdSe QDs that were separated from the oleylamine solution through a precipitation step, following the initial treatment with the range of oleylamine solutions, indicating the positive effects were much more dependent on the concentration of the oleylamine solutions present in solution. This is a common effect found in QDs solutions, with QYs of QDs showing an inverse relationship with the number of cleaning steps applied, since as the number of cleaning cycles increase, a larger volume of ligands are removed from solution, which has the effect of decreasing surface passivation upon the QD surface.

Therefore, to investigate the effects of the halide solutions upon the CdSe QDs, an additional volume of either 5 µl, concentration 1 (Conc 1) or of 50 µl, concentration 2, (Conc 2) of oleylamine based solution was added to the QDs upon the final dilution to 5 ml for Pl measurements. Following this, Pl measurements were immediately taken and are shown in Figure 3.40 of the two different concentrations.

From this, one can see a huge increase in the PL signal of CdSe QD solutions following the range of treatments tested. With Pl signal, increasing from a QY of only 1.5% in untreated samples, to values of 31.4%, recorded in $CdCl_2$ treated solutions, which demonstrates the enormous increase in PL possible using this approach. Also interestingly, it can be seen that large increases take place for just oleylamine-based treatments, showing that oleylamine plays a very

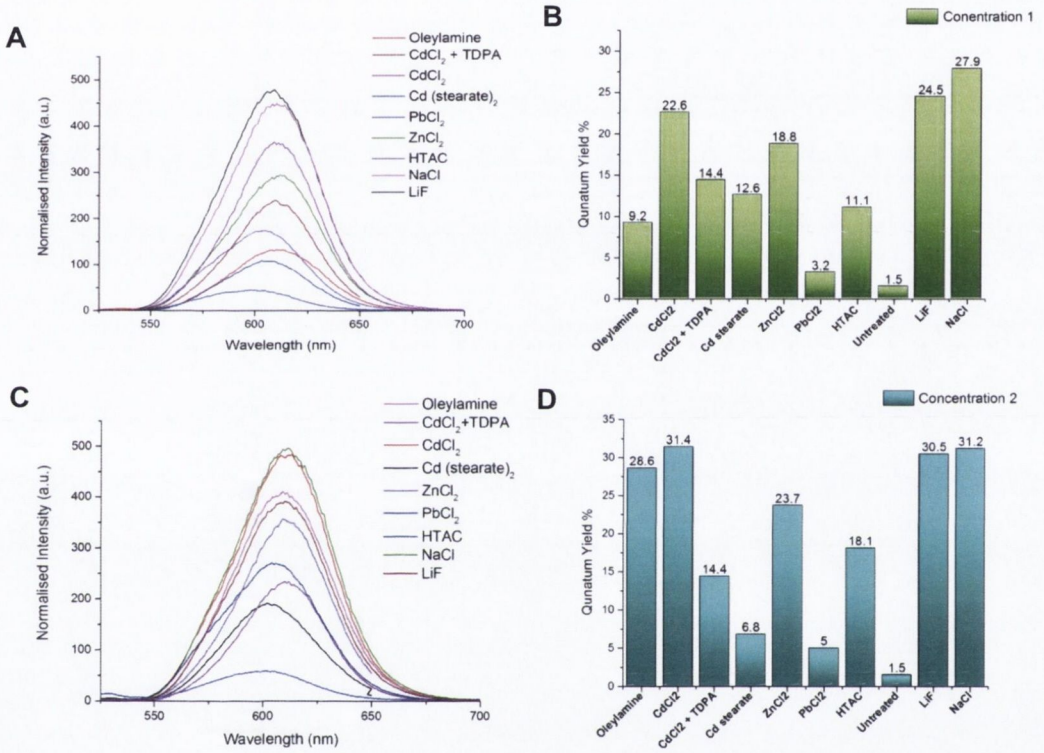

Figure 3.40 Normalised photoluminescent spectra to calculated QYs of anion treated oleic acid capped immediately following dilution. This study was carried out using two different concentrations of anion treatments , with (A) the resulting PL spectra and (B) and the resulting luminescent quantum yields of concentration 1 while (C)is the resulting PL spectra and (D) the resulting luminescent quantum yields of concentration 2.

significant part in producing the overall increase in PL recorded. It can also be seen that oleylamine shows a strong dependence on concentration, with QYs of 9.2 % for concentration 1 which increased to 28.6 % when examined at concentration 2. It should also be noted that large increases in QY took place using NaCl and LiF solutions, which demonstrated QY of 24.5 % and 27.9 % at concentration 1 increasing further to 30.5% and 31.2 % at concentration 2. Though all treatments did demonstrate an increase in PL relative to untreated CdSe QDs, a number of solutions produced values below the increase demonstrated with oleylamine, indicating that these salts in fact inhibited the total increase in PL produced. This was demonstrated with $ZnCl_2$ (13.8 % at conc 1, 23.7 % at conc 2), $PbCl_2$ (3.2 % conc 1, 5 % conc 2), HTAC (11.1 % at conc 1, 18.1 % at conc 2), $Cd(stearate)_2$ (12.6% conc 1, 6.8% conc 2) and $CdCl_2$

+TDPA (14.4 % conc 1, 14.4 % conc 2). After this treatment, the samples were left in darkness at 2 °C for 3 days, after which the PL signals were tested for a second time, with the aim to determine if this increase in PL was permanent or was in fact time sensitive , the results are shown in Figure.3.41.

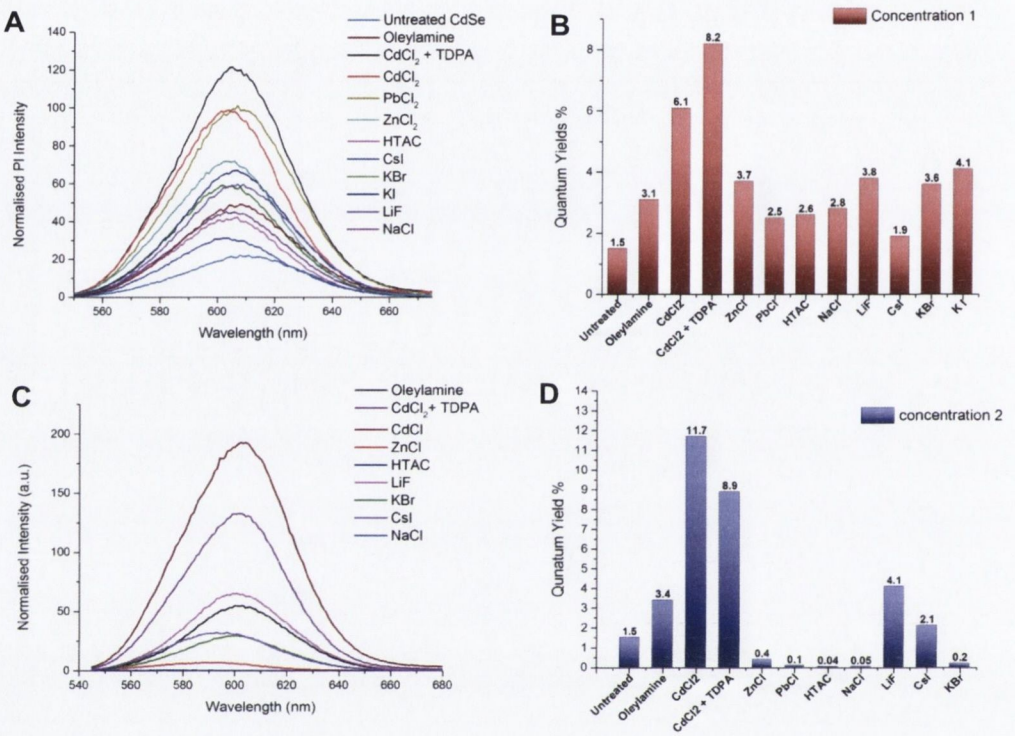

Figure.3.41 Normalised photoluminescent spectra to QYs of anion treated oleic acid capped CdSe QDs after one day of dilution. This study was carried out using two different concentrations of anion treatments , with (A) the resulting PL spectra and (B) and the resulting luminescent quantum yields of concentration 1 while (C)is the resulting PL spectra and (D) the resulting luminescent quantum yields of concentration 2.

Overall, a large decrease in PL occurred, after the three-day waiting period. The $CdCl_2$ treatments remains the most effective, but has reduced nearly threefold to a value of 6.1 % at conc 1 and 11.7 % at conc 2. Interestingly the second most effective now becomes $CdCl_2$+ TDPA, showing a value of 8.3 % at conc 1 and 8.9 %. at concentration 2. Following this the only other sample to show increased activity over a pure oleylamine treatment is LiF giving a value of 3.8 % at conc 1 and 4.1 % conc 2. The huge overall drop in intensity again demonstrates the difficulty with post treatments as effective approaches to increasing PLs, displaying that though oleylamine may prove effective at high concentrations, a huge level of the increase is lost over time. It should also be noted that some solutions after the three days wait actually caused PLs to decrease below the PL of untreated CdSe at concentration 2, including $ZnCl_2$, $PbCl_2$, HTAC, and NaCl.

3.5.2 Halide Oleylamine Treatment: ODPA capped CdSe QDs

Following these results, it was decided that concentration 2 was a more accurate indication of the overall effects of the different oleylamine solutions. We also decided only to investigate samples after giving a 3-day wait period to get the real picture of overall increase in PI achieved. Finally, the study was narrowed to a smaller set of oleylamine solutions to make for a less time intensive study. The next sample investigated were octadecylphosphonic acid (ODPA) capped CdSe QDs and the result are shown in Figure 3.42

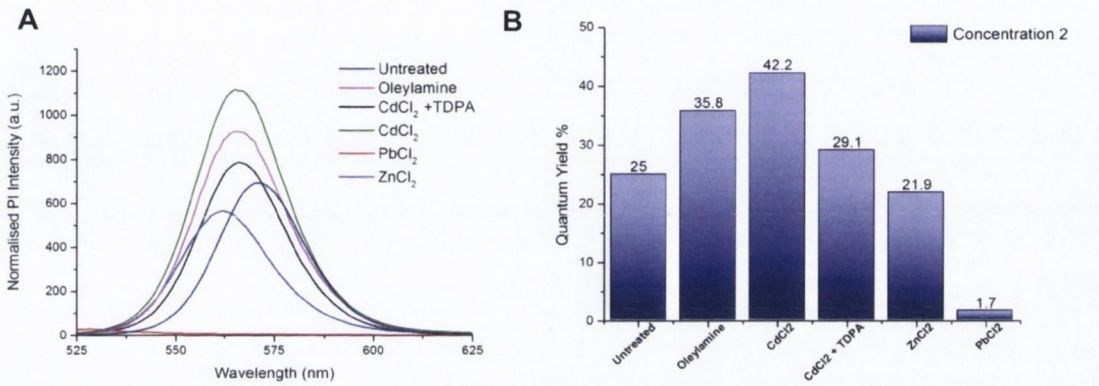

Figure 3.42 Normalised photoluminescent spectra to QYs of ODPA capped CdSe QDs (A) and the resulting luminescent QY are shown in graph B using concentration 2

These QDs already showed an adequate QY of 25%, prior to treatment, but still showed an impressive jump in luminescence to 42.2 % quantum yields after a treatment with $CdCl_2$ solutions. An increase was also noted with oleylamine, producing a luminescence of 35.8 % and a 29.1 % increase for $CdCl_2$ +TDPA. While a dramatic decrease in luminesce was noted with $PbCl_2$ to 1.7 %, while a smaller decrease was noted with $ZnCl_2$ to 21.9 %.

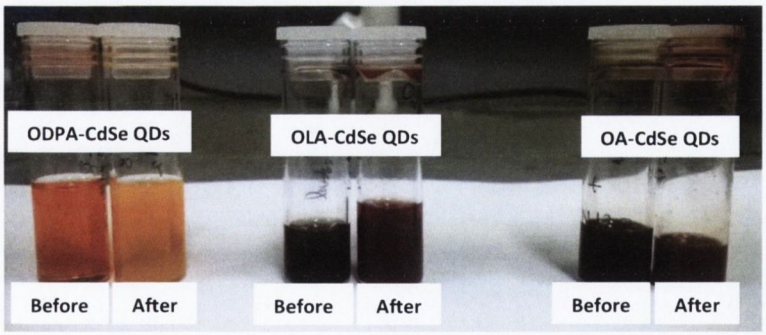

Figure.3.43 Photograph showing the effect of oleylamine/$CdCl_2$ solution treatment upon samples of CdSe capped with ODPA, OLA or OA.

3.5.3 Halide Oleylamine Treatment: ODA capped CdSe QDs

Following this we investigated ODA capped CdSe QDs with the results shown in Figure.3.45. The QDs displayed an original luminesce of 0.8 %, which showed an increase to 16.8 % under $CdCl_2$ treatment. Other samples which also showed an effective increase were $CdCl_2$ + TDPA giving an

increase to 10.8 %. It is also worth noting that only a very small increase in PL was produced from oleylamine, giving a QY of 2.4 %. This can be attributed to the ligand shell consisting of ODA, which is very similar in structure to oleylamine and must affect the ability for oleylamine to effect the surface passivation.

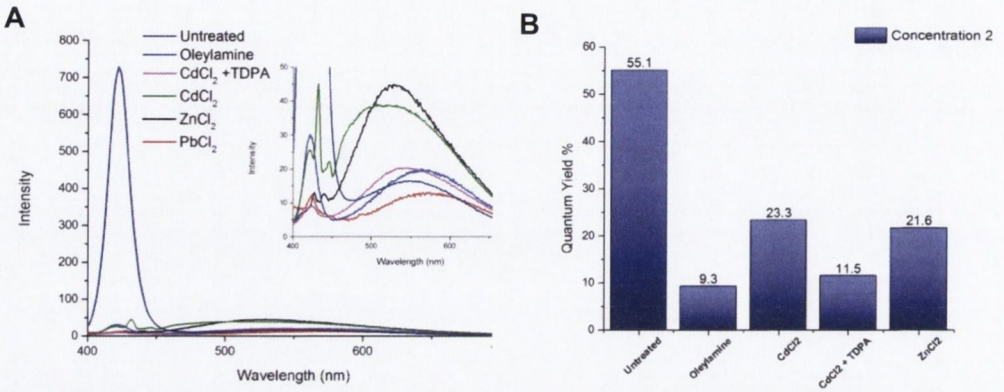

Figure.3.44 Normalised photoluminescent spectra to QYs of CdS (A) and the resulting luminescent QY are shown in graph B using concentration 2.

3.5.4 Halide Oleylamine Treatment: CdS QDs

Subsequently the study was expanded to oleic acid capped CdS QDs giving the results shown in Figure.3.44. These CdS QDs untreated showed emission which was composed of a sharp excitonic emission peak, which represented the majority of emission, with a small amount of emission occurring in the form of a broad defect emission peak which stretches to 700 nm. These QDs showed an efficient emission, giving a 55 % QY. Upon addition of oleylamine solutions, the emission of the CdS QD strongly shifted from excitonic in origin to nearly exclusively defect emission, which was accompanied with a large decrease in QY. The largest loss in luminescence occurred with the addition of oleylamine, nearly completely quenching the excitonic emission, giving a QY of 9.3 %, with the same pattern occurring for $CdCl_2$+TDPA based solutions, giving a QY of 11.5%. Interestingly a different pattern is seen in $ZnCl_2$ and $CdCl_2$ solutions, which showed strong quenching in excitonic luminescence, but was also

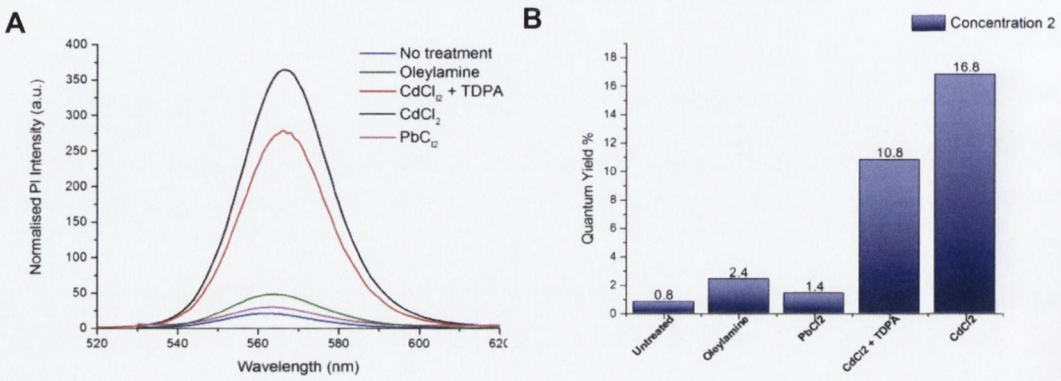

Figure.3.45 Normalised photoluminescent spectra to QYs of ODA capped CdSe QDs (A) and the resulting luminescent QY are shown in B using concentration 2.

accompanied by a noteworthy increase in defect emission, producing QYs of 23.3% for $CdCl_2$ treated and QYs of 21.6% for $ZnCl_2$.

3.5.5 Halide Oleylamine Treatment: CdSe/CdS QDs

Finally, we decided to investigate core/shell CdSe/CdS QDs, with the results shown in Figure.3.46. This sample showed a quantum yield values of 15.6% prior to treatment, and only displayed a minor increase due to oleylamine solution treatments giving a QY of 17.2 %, while an insignificant increase to 16.4 % was also noted with the use of the $CdCl_2$ solution. Interestingly $ZnCl_2$ and $PbCl_2$ solutions both produced a pronounced decrease in QY giving values of 5.4 % and 5.1 %.

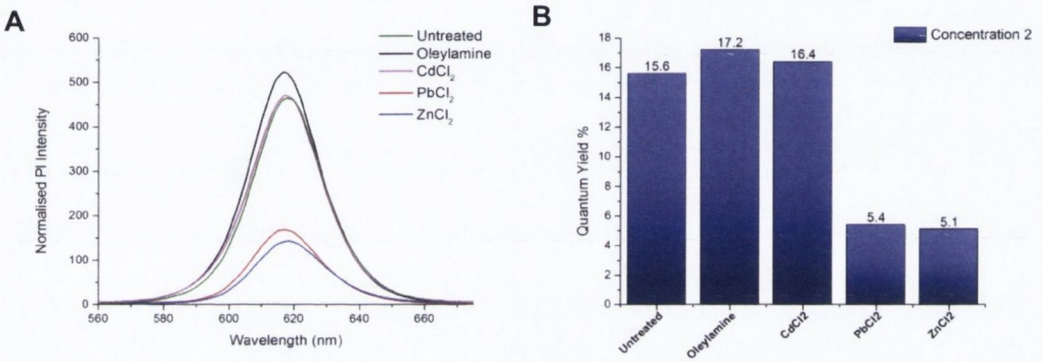

Figure.3.46 Normalised photoluminescent spectra to QYs of core/shell CdSe/CdS QDs (A) and the resulting luminescent QY are shown in graph B using concentration 2

3.6 Conclusions

In conclusion, we have demonstrated the synthesis of a range of core and core-shell quantum confined semiconductor nanostructures utilising the hot injection approach and then examined these structures' interactions with Au NPs, cations and halide/oleylamine solutions. Firstly synthesised, were three forms of CdSe QDs capped in a shell of either oleic acid, ODPA or ODA, ligands showing a range of absorption and emission properties in the visible range. Following this, two other types of core QDs were synthesised showing first exciton absorption and emission in the UV range produced using CdS, or NIR range produced using PbS. Following this, we have demonstrated the synthesis of core/shell QDs of CdSe/CdS, CdS/CdSe, and CdTe/CdSe, by making use of the SILAR approach, enabling careful control of the shell thickness produced. We have also produced heterostructured CdSe/CdS dot in rod structures in a range of aspect ratios.

Aside from hot injection synthesis of nanostructures, we have also exhibited the ability to deposit Au NPs upon CdSe/CdS NRs and shown the resulting optical properties produced. The approach of cation exchange has also been demonstrated as a means to produce other novel nanomaterials, not readily obtainable through hot injection, including PbS/CdS QDs, $Cu_{2-x}Se$ QDs, $Cu_{2-x}Se/Cu_{2-x}S$ NRs and $Pb_{2-x}Se/Pb_{2-x}S$ NRs.

For the final segment of this work, we investigated the effects of halide/oleylamine solutions upon a range of QDs. From this, we have demonstrated large increases in luminescent quantum yields observed form the addition of these solutions increasing OA capped CdSe QY from 1.5% to 32 % , ODPA capped CdSe QY from 25% to 42.2% and ODA capped CdSe QY from 0.8 to 16.8 %. We also have shown a strong quenching effect of excitonic emission in CdS QDs due to these treatments, while also demonstrating an enhancement in the defect emission present. Finally, we have displayed the lack of effect of these treatments upon CdSe/CdS QDs that we propose is due to its specific core/shell structure.

References

14. Kudera, S.; Zanella, M.; Giannini, C.; Rizzo, A.; Li, Y.; Gigli, G.; Cingolani, R.; Ciccarella, G.; Spahl, W.; Parak, W. J.; Manna, L., Sequential Growth of Magic-Size CdSe Nanocrystals. *Advanced Materials* 2007, 19, 548-552.

16. Ouyang, J.; Kuijper, J.; Brot, S.; Kingston, D.; Wu, X.; Leek, D. M.; Hu, M. Z.; Ripmeester, J. A.; Yu, K., Photoluminescent Colloidal CdS Nanocrystals with High Quality Via Noninjection One-Pot Synthesis in 1-Octadecene. *The Journal of Physical Chemistry C* 2009, 113, 7579-7593.

17. Yu, W. W.; Peng, X., Formation of High-Quality Cds and Other Ii–Vi Semiconductor Nanocrystals in Noncoordinating Solvents: Tunable Reactivity of Monomers. *Angewandte Chemie International Edition* 2002, 41, 2368-2371.

34. Ellingson, R. J.; Beard, M. C.; Johnson, J. C.; Yu, P. R.; Micic, O. I.; Nozik, A. J.; Shabaev, A.; Efros, A. L., Highly Efficient Multiple Exciton Generation in Colloidal PbSe and PbS Quantum Dots. *Nano Letters* 2005, 5, 865-871.

71. Baker, D. R.; Kamat, P. V., Tuning the Emission of CdSe Quantum Dots by Controlled Trap Enhancement. *Langmuir* 2010, 26, 11272-11276.

74. Tan, Y.; Jin, S.; Hamers, R. J., Influence of Hole-Sequestering Ligands on the Photostability of Cdse Quantum Dots. *The Journal of Physical Chemistry C* 2012, 117, 313-320.

85. Murray, C. B.; Norris, D. J.; Bawendi, M. G., Synthesis and Characterization of Nearly Monodisperse Cde (E = Sulfur, Selenium, Tellurium) Semiconductor Nanocrystallites. *Journal of the American Chemical Society* 1993, 115, 8706-8715.

88. Carbone, L.; Nobile, C.; De Giorgi, M.; Sala, F. D.; Morello, G.; Pompa, P.; Hytch, M.; Snoeck, E.; Fiore, A.; Franchini, I. R.; Nadasan, M.; Silvestre, A. F.; Chiodo, L.; Kudera, S.; Cingolani, R.; Krahne, R.; Manna, L., Synthesis and Micrometer-Scale Assembly of Colloidal CdSe/CdS Nanorods Prepared by a Seeded Growth Approach. *Nano Lett* 2007, 7, 2942-2950.

89. Talapin, D. V.; Nelson, J. H.; Shevchenko, E. V.; Aloni, S.; Sadtler, B.; Alivisatos, A. P., Seeded Growth of Highly Luminescent CdSe/CdS Nanoheterostructures with Rod and Tetrapod Morphologies. *Nano Lett* 2007, 7, 2951-2959.

93. Neo, M. S.; Venkatram, N.; Li, G. S.; Chin, W. S.; Ji, W., Synthesis of PbS/CdS Core-Shell Qds and Their Nonlinear Optical Properties. *Journal of Physical Chemistry C* 2010, 114, 18037-18044.

100. Talapin, D. V.; Mekis, I.; Gotzinger, S.; Kornowski, A.; Benson, O.; Weller, H., CdSe/CdS/ZnS and CdSe/ZnSe/ZnS Core-Shell-Shell Nanocrystals. *Journal of Physical Chemistry B* 2004, 108, 18826-18831.

103. Smith, A. M.; Mohs, A. M.; Nie, S., Tuning the Optical and Electronic Properties of Colloidal Nanocrystals by Lattice Strain. *Nature nanotechnology* 2009, 4, 56-63.

104. Al-Douri, Y.; Abid, H.; Aourag, H., Calculation of Bulk Moduli of Semiconductor Compounds. *Physica B: Condensed Matter* 2002, 322, 179-182.

109. Talapin, D. V.; Nelson, J. H.; Shevchenko, E. V.; Aloni, S.; Sadtler, B.; Alivisatos, A. P., Seeded Growth of Highly Luminescent CdSe/CdS Nanoheterostructures with Rod and Tetrapod Morphologies. *Nano Letters* 2007, 7, 2951-2959.

110. Cassette, E.; Mahler, B.; Guigner, J.-M.; Patriarche, G.; Dubertret, B.; Pons, T., Colloidal CdSe/CdS Dot-in-Plate Nanocrystals with 2d-Polarized Emission. *ACS Nano* 2012, 6, 6741-6750.

111. Jain, P. K.; Amirav, L.; Aloni, S.; Alivisatos, A. P., Nanoheterostructure Cation Exchange: Anionic Framework Conservation. *Journal of the American Chemical Society* 2010, 132, 9997-9999.

112. Luther, J. M.; Zheng, H. M.; Sadtler, B.; Alivisatos, A. P., Synthesis of PbS Nanorods and Other Ionic Nanocrystals of Complex Morphology by Sequential Cation Exchange Reactions. *Journal of the American Chemical Society* 2009, 131, 16851-16857.

113. Justo, Y.; Goris, B.; Kamal, J. S.; Geiregat, P.; Bals, S.; Hens, Z., Multiple Dot-in-Rod PbS/CdS Heterostructures with High Photoluminescence Quantum Yield in the near-Infrared. *Journal of the American Chemical Society* 2012, 134, 5484-5487.

115. Rivest, J. B.; Jain, P. K., Cation Exchange on the Nanoscale: An Emerging Technique for New Material Synthesis, Device Fabrication, and Chemical Sensing. *Chemical Society Reviews* 2013, 42, 89-96.

116. Beberwyck, B. J.; Surendranath, Y.; Alivisatos, A. P., Cation Exchange: A Versatile Tool for Nanomaterials Synthesis. *The Journal of Physical Chemistry C* 2013, 117, 19759-19770.

117. Pietryga, J. M.; Werder, D. J.; Williams, D. J.; Casson, J. L.; Schaller, R. D.; Klimov, V. I.; Hollingsworth, J. A., Utilizing the Lability of Lead Selenide to Produce Heterostructured Nanocrystals with Bright, Stable Infrared Emission. *Journal of the American Chemical Society* 2008, 130, 4879-4885.

120. Zhao, H.; Chaker, M.; Wu, N.; Ma, D., Towards Controlled Synthesis and Better Understanding of Highly Luminescent PbS/CdS Core/Shell Quantum Dots. *J. Mater. Chem.* 2011, 21.

130. Gao, Y. N.; Aerts, M.; Sandeep, C. S. S.; Talgorn, E.; Savenije, T. J.; Kinge, S.; Siebbeles, L. D. A.; Houtepen, A. J., Photoconductivity of PbSe Quantum-Dot Solids: Dependence on Ligand Anchor Group and Length. *ACS Nano* 2012, 6, 9606-9614.

132. Zhitomirsky, D.; Furukawa, M.; Tang, J.; Stadler, P.; Hoogland, S.; Voznyy, O.; Liu, H.; Sargent, E. H., N-Type Colloidal-Quantum-Dot Solids for Photovoltaics. *Advanced Materials* 2012, 24, 6181-6185.

142. Zarghami, M. H.; Liu, Y.; Gibbs, M.; Gebremichael, E.; Webster, C.; Law, M., P-Type Pbse and Pbs Quantum Dot Solids Prepared with Short-Chain Acids and Diacids. *ACS Nano* 2010, 4, 2475-2485.

195. Ning, Z.; Ren, Y.; Hoogland, S.; Voznyy, O.; Levina, L.; Stadler, P.; Lan, X.; Zhitomirsky, D.; Sargent, E. H., All-Inorganic Colloidal Quantum Dot Photovoltaics Employing Solution-Phase Halide Passivation. *Advanced Materials* 2012, 24, 6295-6299.

199. Gao, J.; Perkins, C. L.; Luther, J. M.; Hanna, M. C.; Chen, H.-Y.; Semonin, O. E.; Nozik, A. J.; Ellingson, R. J.; Beard, M. C., N-Type Transition Metal Oxide as a Hole Extraction Layer in Pbs Quantum Dot Solar Cells. *Nano Lett* 2011, 11, 3263-3266.

201. Tang, J.; Kemp, K. W.; Hoogland, S.; Jeong, K. S.; Liu, H.; Levina, L.; Furukawa, M.; Wang, X. H.; Debnath, R.; Cha, D. K.; Chou, K. W.; Fischer, A.; Amassian, A.; Asbury, J. B.; Sargent, E. H., Colloidal-Quantum-Dot Photovoltaics Using Atomic-Ligand Passivation. *Nat Mater* 2011, 10, 765-771.

204. Leschkies, K. S.; Beatty, T. J.; Kang, M. S.; Norris, D. J.; Aydil, E. S., Solar Cells Based on Junctions between Colloidal PbSe Nanocrystals and Thin Zno Films. *ACS Nano* 2009, 3, 3638-3648.

210. Luther, J. M.; Gao, J.; Lloyd, M. T.; Semonin, O. E.; Beard, M. C.; Nozik, A. J., Stability Assessment on a 3% Bilayer PbS/ZnO Quantum Dot Heterojunction Solar Cell. *Adv Mater* 2010, 22, 3704-7.

211. Ip, A. H.; Thon, S. M.; Hoogland, S.; Voznyy, O.; Zhitomirsky, D.; Debnath, R.; Levina, L.; Rollny, L. R.; Carey, G. H.; Fischer, A.; Kemp, K. W.; Kramer, I. J.; Ning, Z.; Labelle, A. J.; Chou, K. W.; Amassian, A.; Sargent, E. H., Hybrid Passivated Colloidal Quantum Dot Solids. *Nat Nano* 2012, advance online publication.

233. Lee, J.-W.; Son, D.-Y.; Ahn, T. K.; Shin, H.-W.; Kim, I. Y.; Hwang, S.-J.; Ko, M. J.; Sul, S.; Han, H.; Park, N.-G., Quantum-Dot-Sensitized Solar Cell with Unprecedentedly High Photocurrent. *Sci. Rep.* 2013, 3.

235. Pan, Z.; Zhang, H.; Cheng, K.; Hou, Y.; Hua, J.; Zhong, X., Highly Efficient Inverted Type-I CdS/CdSe Core/Shell Structure Qd-Sensitized Solar Cells. *ACS Nano* 2012, 6, 3982-3991.

238. Sung, S. D.; Lim, I.; Kang, P.; Lee, C.; Lee, W. I., Design and Development of Highly Efficient Pbs Quantum Dot-Sensitized Solar Cells Working in an Aqueous Polysulfide Electrolyte. *Chemical Communications* 2013, 49, 6054-6056.
279. Bullen, C. R.; Mulvaney, P., Nucleation and Growth Kinetics of Cdse Nanocrystals in Octadecene. *Nano Lett* 2004, 4, 2303-2307.
280. Mahler, B.; Spinicelli, P.; Buil, S.; Quelin, X.; Hermier, J. P.; Dubertret, B., Towards Non-Blinking Colloidal Quantum Dots. *Nat. Mater.* 2008, 7, 659-64.
281. Liu, T. Y.; Li, M. J.; Ouyang, J. Y.; Zaman, M. B.; Wang, R. B.; Wu, X. H.; Yeh, C. S.; Lin, Q.; Yang, B.; Yu, K., Non-Injection and Low-Temperature Approach to Colloidal Photoluminescent Pbs Nanocrystals with Narrow Bandwidth. *Journal of Physical Chemistry C* 2009, 113, 2301-2308.
282. Cai, X.; Mirafzal, H.; Nguyen, K.; Leppert, V.; Kelley, D. F., Spectroscopy of Cdte/Cdse Type-Ii Nanostructures: Morphology, Lattice Mismatch, and Band-Bowing Effects. *The Journal of Physical Chemistry C* 2012, 116, 8118-8127.
283. Khon, E.; Hewa-Kasakarage, N. N.; Nemitz, I.; Acharya, K.; Zamkov, M., Tuning the Morphology of Au/CdS Nanocomposites through Temperature-Controlled Reduction of Gold-Oleate Complexes. *Chem. Mat.* 2010, 22, 5929-5936.
292. Grabolle, M.; Spieles, M.; Lesnyak, V.; Gaponik, N.; Eychmuller, A.; Resch-Genger, U., Determination of the Fluorescence Quantum Yield of Quantum Dots: Suitable Procedures and Achievable Uncertainties. *Anal. Chem.* 2009, 81, 6285-6294.
293. Wehrenberg, B. L.; Wang, C. J.; Guyot-Sionnest, P., Interband and Intraband Optical Studies of PbSe Colloidal Quantum Dots. *Journal of Physical Chemistry B* 2002, 106, 10634-10640.
294. Rurack, K.; Spieles, M., Fluorescence Quantum Yields of a Series of Red and near-Infrared Dyes Emitting at 600-1000 Nm. *Analytical chemistry* 2011, 83, 1232-42.
296. Kumar, S.; Nann, T., Shape Control of Ii-Vi Semiconductor Nanomateriats. *Small* 2006, 2, 316-329.
297. Zhang, F.; Yi, D. M.; Sun, H. Z.; Zhang, H., Cadmium-Based Quantum Dots: Preparation, Surface Modification, and Applications. *J. Nanosci. Nanotechnol.* 2014, 14, 1409-1424.
298. Carbone, L.; Cozzoli, P. D., Colloidal Heterostructured Nanocrystals: Synthesis and Growth Mechanisms. *Nano Today* 2010, 5, 449-493.
299. Diroll, B. T.; Koschitzky, A.; Murray, C. B., Tunable Optical Anisotropy of Seeded CdSe/CdS Nanorods. *The Journal of Physical Chemistry Letters* 2013, 5, 85-91.
300. Fu, H. Y.; Tsang, S. W., Infrared Colloidal Lead Chalcogenide Nanocrystals: Synthesis, Properties, and Photovoltaic Applications. *Nanoscale* 2012, 4, 2187-2201.
301. Murphy, J. E.; Beard, M. C.; Norman, A. G.; Ahrenkiel, S. P.; Johnson, J. C.; Yu, P.; Mićić, O. I.; Ellingson, R. J.; Nozik, A. J., Pbte Colloidal Nanocrystals: Synthesis, Characterization, and Multiple Exciton Generation. *Journal of the American Chemical Society* 2006, 128, 3241-3247.
302. Gomes, R.; Hassinen, A.; Szczygiel, A.; Zhao, Q.; Vantomme, A.; Martins, J. C.; Hens, Z., Binding of Phosphonic Acids to CdSe Quantum Dots: A Solution Nmr Study. *The Journal of Physical Chemistry Letters* 2011, 2, 145-152.
303. Cooper, J. K.; Franco, A. M.; Gul, S.; Corrado, C.; Zhang, J. Z., Characterization of Primary Amine Capped CdSe, ZnSe, and ZnS Quantum Dots by Ft-Ir: Determination of Surface Bonding Interaction and Identification of Selective Desorption. *Langmuir* 2011, 27, 8486-8493.
304. Camargo, P. H. C.; Lee, Y. H.; Jeong, U.; Zou, Z.; Xia, Y., Cation Exchange: A Simple and Versatile Route to Inorganic Colloidal Spheres with the Same Size but Different Compositions and Properties. *Langmuir* 2007, 23, 2985-2992.
305. Sau, T. K.; Rogach, A. L.; Jackel, F.; Klar, T. A.; Feldmann, J., Properties and Applications of Colloidal Nonspherical Noble Metal Nanoparticles. *Advanced Materials* 2010, 22, 1805-1825.
306. Guo, S. J.; Wang, E. K., Noble Metal Nanomaterials: Controllable Synthesis and Application in Fuel Cells and Analytical Sensors. *Nano Today* 2011, 6, 240-264.

307. Eustis, S.; El-Sayed, M. A., Why Gold Nanoparticles Are More Precious Than Pretty Gold: Noble Metal Surface Plasmon Resonance and Its Enhancement of the Radiative and Nonradiative Properties of Nanocrystals of Different Shapes. *Chemical Society Reviews* 2006, 35, 209-217.

308. Pérez-Juste, J.; Pastoriza-Santos, I.; Liz-Marzán, L. M.; Mulvaney, P., Gold Nanorods: Synthesis, Characterization and Applications. *Coordination Chemistry Reviews* 2005, 249, 1870-1901.

309. Vaneski, A.; Susha, A. S.; Rodríguez-Fernández, J.; Berr, M.; Jäckel, F.; Feldmann, J.; Rogach, A. L., Hybrid Colloidal Heterostructures of Anisotropic Semiconductor Nanocrystals Decorated with Noble Metals: Synthesis and Function. *Adv. Funct. Mater.* 2011, 21, 1547-1556.

310. Khon, E.; Mereshchenko, A.; Tarnovsky, A. N.; Acharya, K.; Klinkova, A.; Hewa-Kasakarage, N. N.; Nemitz, I.; Zamkov, M., Suppression of the Plasmon Resonance in Au/CdS Colloidal Nanocomposites. *Nano Letters* 2011, 11, 1792-1799.

311. Ning, Z.; Voznyy, O.; Pan, J.; Hoogland, S.; Adinolfi, V.; Xu, J.; Li, M.; Kirmani, A. R.; Sun, J.-P.; Minor, J.; Kemp, K. W.; Dong, H.; Rollny, L.; Labelle, A.; Carey, G.; Sutherland, B.; Hill, I.; Amassian, A.; Liu, H.; Tang, J.; Bakr, O. M.; Sargent, E. H., Air-Stable N-Type Colloidal Quantum Dot Solids. *Nat. Mater.* 2014, 13, 822-828.

312. Zhang, J.; Gao, J.; Miller, E. M.; Luther, J. M.; Beard, M. C., Diffusion-Controlled Synthesis of PbS and PbSe Quantum Dots with in Situ Halide Passivation for Quantum Dot Solar Cells. *ACS Nano* 2013, 8, 614-622.

313. Thon, S. M.; Ip, A. H.; Voznyy, O.; Levina, L.; Kemp, K. W.; Carey, G. H.; Masala, S.; Sargent, E. H., Role of Bond Adaptability in the Passivation of Colloidal Quantum Dot Solids. *ACS Nano* 2013, 7, 7680-7688.

314. Sun, J.; Louis, W. U. i. S., *High-Quality Colloidal Ii-Vi and Iv-Vi Semiconductor Nanowires: Diameter-Controlled Syntheses, Quantum-Confinement-Effect Studies, and Electronic Structure*. Washington University in St. Louis: 2008.

315. Chen, Y.; Vela, J.; Htoon, H.; Casson, J. L.; Werder, D. J.; Bussian, D. A.; Klimov, V. I.; Hollingsworth, J. A., "Giant" Multishell CdSe Nanocrystal Quantum Dots with Suppressed Blinking. *Journal of the American Chemical Society* 2008, 130, 5026-+.

316. Zhao, Y.; Burda, C., Development of Plasmonic Semiconductor Nanomaterials with Copper Chalcogenides for a Future with Sustainable Energy Materials. *Energy & Environmental Science* 2012, 5, 5564-5576.

Chapter 4 Electrophoretic Deposition of CQDs to Increase Photosensitisation of TiO_2 films

4.1 Introduction

Electrophoretic deposition (EPD) is a new technique being applied to the field of nanoscience, though it is a proven technique that has been used for a number of years in other areas, such as the ceramic industry.[317, 318] Therefore EPD when applied to colloidal quantum dots solutions offers a unique relatively unexplored route to sensitise porous TiO_2 electrodes which are used as the photoanodes in QDSSCs. In this chapter, we will explore its use in this respect and then investigate a range of treatments that can affect the resulting photocurrent that is produced from these photoanodes.

A number of approaches have been reported for CQD electrophoretic deposition, either as a method to produce a monolayer upon TiO_2[249, 319] or as a route to deposit a thick film of QDs,[247, 320] up to a micron in thickness on a range of materials. The production of monolayers has been achieved generally with the application of high voltages, to QDs in non-polar solvents, (toluene, and hexane).[319, 321, 322] The exact type of surface ligands present on the CQDs, the precise stoichiometry used in the synthesis, the size of the QDs, the stability of the colloidal solution and the concentration of ligands in solution when attempting deposition all play a role in the results obtained when depositing monolayers.[252] Interestingly some approaches report deposition occurring on both the positive and negative electrode,[249] while in other cases deposition is much more strongly on one electrode than the other. Concentration used when carrying out these deposition range from 10^{-5} to 10^{-7} M of QDs, while deposition times vary hugely from 10 minutes to 4 hours with voltages ranging from between 50 – 2 kV with required force to cause deposition strongly dependent upon the size of electrode and the spacing between electrodes among other properties.

When using electrophoretic deposition as an approach to deposit CQDs as a thicker film, a different set of conditions are required.[191, 247] Normally the QDs are dispersed in a mixture of two miscible solvents, a non-polar solvent (toluene) and a certain proportion of aprotic polar solvents (acetonitrile[191]), which acts as a non-solvent to the CQDs, lowering their overall solubility in the solvent. Deposition times are usually between 5 to 20 minutes with solution concentrations ranging 10^{-5} to 10^{-6} M of CQDs. Interestingly, due to the lower stability of the QDs in solution and the much higher dielectric constant of the solvent (due to the addition of

aprotic polar solvent), the overall effect is that a much lower voltage is required to cause the deposition to take place, between 10 to 50 V depending on experimental configuration.

Only a limited range of CQDs have been deposited using the electrophoretic deposition approach, these include CdSe QDs,[248, 249] QDs CdSe nanoplatelets,[322] CdTe QDs,[191] PbS,[323] PbSeS,[323] CdSSe QDs,[321] $CuInS_2$ QDs[236] and CdSe/CdS rods.[319] These show a range of ligands including, TOPO,[249] tetradecylphosphonic acid[319] and oleic acid[320, 321, 324] all of which play an important part in the behaviour under electrophoretic deposition. Therefore, one of the focuses of our work is to demonstrate, the universality of this approach to any colloidal solution of QDs when applied under the correct circumstances.

After sensitisation of photoaniodes, it is possible to test the photo activity of these electrodes with the use of the photocurrent action response. This has been used to analyse a range of different quantum dot sensitised electrodes for photo activity,[325-329] with the approach enabling for the characterisation of the photoresponsivity of an electrode, using a simple analysis, recording the photocurrent response produced under illumination. Though unfortunately a direct efficiency of the irradiance to electric current cannot be calculated, the results obtained are indicative of the short circuit current expected when incorporated into a QDSSC design and so offer an important incite to effective QDSSC photoaniode optimisation strategies.

In addition, a range of post quantum dot deposition treatments have been reported in the literature as a means to increase the photocurrent of sensitised electrodes. The methods aim to either increase the stability of the deposited CQDs and/or reduce recombination rates of CQDs when under illumination. Relatively successful approach to this is SILAR deposition of a large band gap semiconductor such as CdS, ZnSe[330] or ZnS,[331-333] producing a type I band alignment with the QDs. Another route involves the application of a ligand exchange post deposition to better link the deposited QDs to the surface of the TiO_2 by decreasing the distance between CQDs and the TiO_2 particles.[334] This has been shown to increase charge injection through the application of bifunctional ligands such as mercaptopropionic acid. Finally, a relatively recent technique has been the utilisation of a range of halide treatments that have been shown to increase passivation of the CQD surfaces, reducing recombination due to surface trap states.[245, 334]

Lastly, it is also possible to use a post treatment to covert deposited QDs into another semiconductor, with a cation exchange. This has been shown be an effective technique to convert CQDs in solution, allowing exchange from Pb^{2+} to Cd^{2+} [93, 113, 117, 119-121] or to exchange Pb

$^{2+}$ or Cd^{2+} to Cu^{2+},[111] therefore it offers a unique way to alter chemical properties of films of QDs deposited upon electrodes.

4.2 Aim

The aim of this work is to explore the use of the novel technique of electrophoretic deposition as a means to sensitise in house fabricated nano-porous TiO_2 electrodes with quantum dots. We intend to begin the study with oleic acid capped CdSe QDs, using a range of sizes. We firstly aim to explore the effectiveness of EPD as a means to sensitize TiO_2 using two separate approaches, producing either a monolayer of CdSe or a film of up to a micron in thickness upon the TiO_2. Following this, the electrodes will be tested to determine their sensitivity to visible light using a technique termed photocurrent action spectra. The study will then be expanded to determine the effect of ligand shell upon EPD of CdSe QDs, by comparing results obtained to octadecylphosphonic acid capped and octadecylamine capped CdSe QDs of similar size. We then aim to investigate the effectiveness of a range of post deposition techniques using halide salts, short chain bifunctional ligands and semiconductor coatings with the aim to produce the measured photocurrents. Subsequently, we aim to demonstrate the flexibility of the EPD approach, by using it to sensitise TiO_2 electrodes with a range of other Cd and Pb based core and core/shell QDs. Finally, we propose to investigate the ability to convert pre-deposited QDs to new semiconductors through the application of cation exchange, and its resulting effect upon measured photocurrent.

4.3 EPD of CdSe QDs upon TiO_2 photoelectrode

For the first section of work, we will explore the use of EPD to sensitise in house fabricated TiO_2 electrodes upon FTO glass. The details of fabrication of these electrodes was covered in 5.3.2 , in which we discussed the optimisation of these electrodes. Briefly, the electrodes consist of porous TiO_2 electrode upon FTO (fluorine doped tin oxide) coated glass created from multiple depositions of 20 nm TiO_2 anatase particles which have been sintered into a porous continuous film measuring between 4 – 15 μm in thickness depending upon the number of layers deposited. These are the electrodes which we will now explore the sensitisation of with oleic acid capped CdSe QDs.

4.3.1 Quantum dots electrophoretic deposition: method A

The first approach tested to deposit QDs upon a TiO_2 electrode utilised a low voltage of between 20 – 30 V, a solution concentration of between 1×10^{-6} to 1×10^{-5} M and deposition times of up to 4 hours, based upon an approach in literature.[320, 334] The first quantum dots, selected for testing were oleic acid capped CdSe QDs, due to the simplicity of the ligand shell, and ease of large-scale synthesis. Initially, toluene was selected as a solvent to attempt deposition from, and produced a very low-level of sensitisation, which was comparable to levels obtained from soaking. Following this, the approach was altered by the use of a non-solvent / solvent mixture, (note: in this case, a non-solvent is a liquid in which oleic acid capped QDs are not soluble in). Ratios and solvents were determined experimentally to produce a solution stable (non-precipitation of CQD) and transparent, while also increasing the deposition rate of CQDs. Acetonitrile was the solvent of choice, due to its miscibility with toluene and its action as a non-solvent upon oleic acid capped CdSe QDs. It was also used due to its aprotic polar nature, giving rise to a large dielectric constant of 37.5, without the complication of solvent splitting. Acetonitrile was used at 1:1 v/v with toluene and was achieved by adding the appropriate volume of CdSe stock solution to 10 ml of toluene firstly, followed by the addition of 10 ml of acetonitrile. This was important since it was found that if the stock concentrated solution was simply added to the 1:1 v/v of toluene/acetonitrile, the solution became opaque and the deposited films showed poor adherence to the electrode, therefore for the deposition to be effective it was required for the solution to be clear. This is because as the CQD become unstable in solution, the QDs begin to aggregate, forming colloidal particles large enough to scatter light and therefore creating an opaque solution. Consequently, this causes the EPD process to change from depositing singular QDs to depositing large clusters of QDs, which has the effect of producing a film that shows poor adherence and coverage.

Deposition was performed for 15 minutes, after which the solution concentration fell by a factor of one, resulting in deposition of the majority of QDs upon the electrode surface. UV-Vis absorption spectra was used to show the solution concentration change due to EPD and is shown in Figure 4.1. The electrode produced showed a strong coloration, which displayed a significant change after multiple washings with hexane.

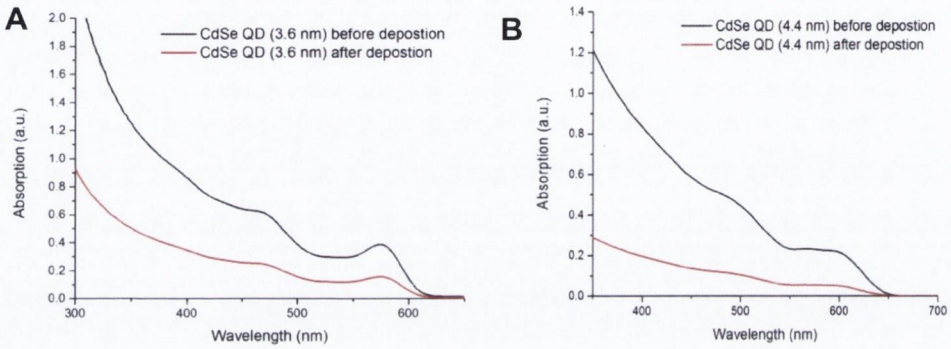

Figure 4.1 UV-Vis absorption spectrum monitoring the electrophoretic deposition of CdSe QDs upon a TiO_2 electrode using method A. The spectra show the change in QD concentration after a single deposition cycle using CdSe QDs of two different diameters A(3.6 nm), and B(4.4 nm), with the solution representing 100ul of the deposition solution diluted to 4 ml to produce the given UV-Vis spectra

SEM was used to analyse the morphology of produced electrodes and is shown in Figure 4.2. The structure of the deposited layer upon the electrode, showed a deposited film of CdSe QDs upon the surface of the TiO_2 electrode. Analysis of the film showed a fractured film structure sitting upon the upper surface of the TiO_2, and therefore the majority of QDs were found not to be penetrating into the interior of the TiO_2.

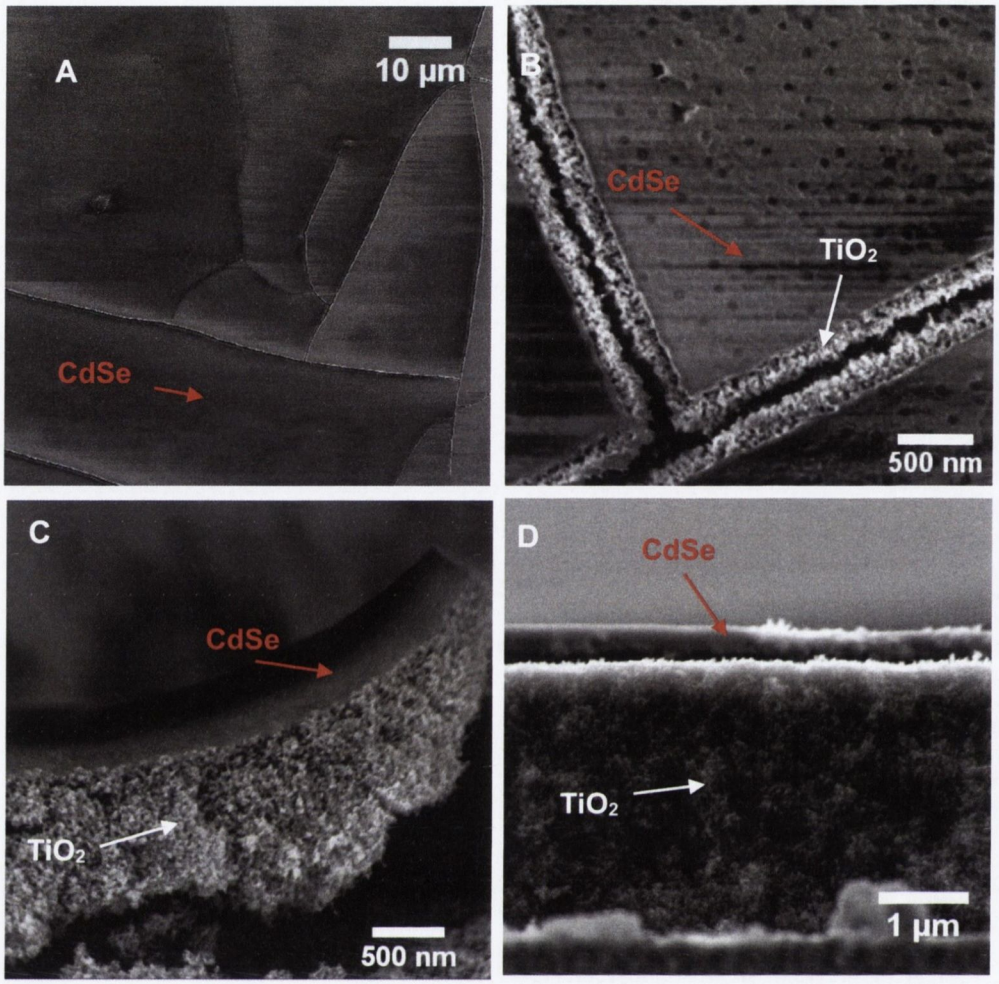

Figure 4.2 SEM of EPD CdSe quantum dots on TiO_2 using method A The layer produced sits upon the upper surface of the TiO_2 electrode as shown in the SEM profile shown in C and D. and does not permeate into the electrode. The produced film also shows wide spread cracking in the film shown in image A and D. This produces an electrode with poor photosensitisation and therefore one inappropriate for the production of a TiO_2 based photoanode for QDSSCs.

Though this approach was interesting for enabling us to produce a film upon an electrode with thicknesses up to a micron, the film acted as an insulating layer upon the TiO_2 electrode, preventing effective charge transfer to the TiO_2 electrode. This meant that under photocurrent action response, no change in signal was recorded under illuminated. The reason for this was that the film consisted of QDs coated in large long chain oleic acid molecules that are ineffective in respect to charge transport, due to the large spacing between QDs.[335] The film also acted as a physical barrier to the electrolyte preventing effective charge regeneration. Therefore, though this is a valuable approach to QD deposition, it was judged inappropriate for the use of TiO_2 sensitisation for photovoltaic applications.

4.3.2 Quantum dot Electrophoretic Deposition: Method B

Following the disappointing results of our initial approach to electrophoretic deposition, a second method was attempted .This approach used quantum dots in concentration of between 1×10^{-6} to 1×10^{-7} M in solution, and deposition times between 10 - 30 minutes. The solvent utilised was a non-polar organic solvent, one in which the QDs were fully soluble in. A voltage of 250 V was applied across two FTO glass electrodes upon which a porous TiO_2 electrode had been screen printed upon one or both. The method was firstly optimized using oleic acid capped CdSe QDs, as for EPD method A, due to the ease of large scale synthesis of this QDs, and the simplicity of the ligand coating, consisting of only oleic acid.

4.3.2.i Solvent effect

Solvent plays a key role in the EPD rate and character of produced CQD films, with studies already demonstrated in toluene,[249, 321] hexane[248] and chloroform[324] to date. Therefore, for this study we examined this effect in detail, choosing non-polar solvents in which non-polar ligand capped CQDs are fully stable. The solvents were also chosen with a range of dielectric constants to demonstrate its effect upon EPD. Therefore four common non-polar solvents were compared to examine their effectiveness, hexane, DCM, $CHCl_3$ and toluene and were investigated by examining the absorption of oleic acid capped CdSe QDs (4.4 nm) using EPD with respect to time. After deposition, electrodes were examined using UV-Vis absorption spectrometry and is shown in Figure 4.3. Maximum absorption was produced on the positive electrode, with the order of absorption across the solvents given as DCM > $CHCl_3$ >toluene >hexane, while time taken to reach maximum was toluene > $CHCl_3$ > DCM with hexane showing no change over time. DCM strongly outperformed all other solvents tested, showing maximum absorption after just 15 minutes of deposition. Therefore, DCM was chosen as the optimal solvent to carry out the rest of the electrophoretic deposition study with.

This order of EPD success can be explained by the trend in dielectric constants of these solvents, which is 8.93 - DCM, 4.8 – chloroform, 2.38 –toluene, 1.88 hexane.[336] The dielectric constant (sometimes called the 'relative permittivity') is the ratio of the permittivity of the given dielectric to the permittivity of a vacuum, so the greater the polarisation developed by a material in an applied field of given strength, the greater the dielectric constant will be. Thus as the dielectric constant increases, the applied electric potential field penetrates less into the solvent, and instead concentrates the potential drop nearer the electrode surface, increasing the ability for the electrode to pull CQDs out of solution. The increase in dielectric constant also has the effect of screening charge more effectively between QDs which has been postulated to have the effect of increasing the population of charged QDs due to thermal charging.[253]

Originally when looking at literature values other solvents were also considered for testing, specifically 1,2 dichlorobenzene and 1,2 dichloroethane, which show dielectric constants of 9.93 and 10.36 respectively, and still relatively low dipole moments($C_2H_4Cl_2$, 1.83 D and $C_6H_4Cl_2$ 2.14 D), meaning the nonpolar ligand capped QDs should show some solubility.[336] Unfortunately, we decided not to proceed with testing due to the higher viscosities of these solvents relatively to DCM (DCM = 0.44 cP, $C_2H_4Cl_2$ = 0.79 cP, and $C_6H_4Cl_2$=1.32 cP,) and lower CQD solubility, which would hinder any benefit from increased dielectric constants. This is due to the inverse relationship that electrophoretic deposition shows to reduced solution concentration, CQD instability and solution viscosity (see Appendix A, Equation 7.6). In addition, apart from EPD efficiency considerations, these solvents also show a marked increase in toxicity relative to DCM.[337-339]

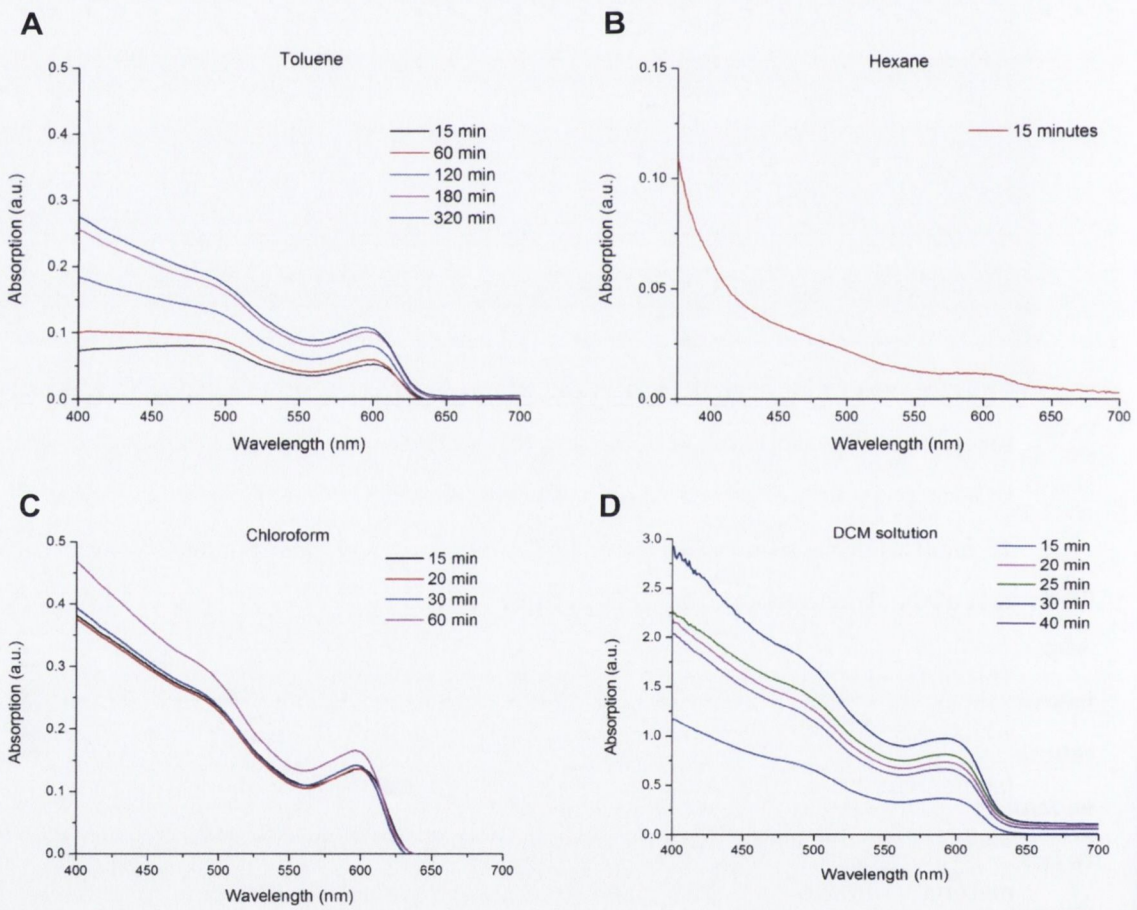

Figure 4.3 UV-Vis absorption spectroscopy was used to measure the deposition of 4.4 nm CdSe quantum dots upon a 16-μm TiO_2 electrode. Different solvents were used with the same concentration of 2.5 x 10^{-6} M and the absorption of the films was periodically measured during the deposition. The solvents tested were A) toluene, B) hexane, C) chloroform and D) dichloromethane

4.3.2.ii Time of deposition

A closer analysis of the UV-Vis absorption spectra of electrophoretic deposition in DCM (Figure 4.3 D) with respect to time also shows an unexpected loss in absorption as the deposition was allowed to proceed after 15 minutes. The reason for reduction of absorption after the maximum is proposed to be due to double layer formation at the electrode surface causing deposited QDs to dissolve over a given amount of time. To further analyse this, a more detailed study was carried out measuring absorption of the positive and negative electrode as shown in Figure 4.4. By examining both, the absorption is found to reach its peak value after 15 minutes on the negative electrode (Figure 4.4 A), with the absorption remaining near maximum from between 12.5 min to 20 min, after which a serious loss in sensitisation takes place. Interestingly, the same behaviour is not seen in the positive electrode (Figure 4.4 B) which reached maximum absorption after 10 minutes, showing no change following this. Therefore it was found that time was an important factor to reaching maximum sensitisation, with excessive time presenting as negative an effect as too little time.

4.3.2.iii Effect of potential

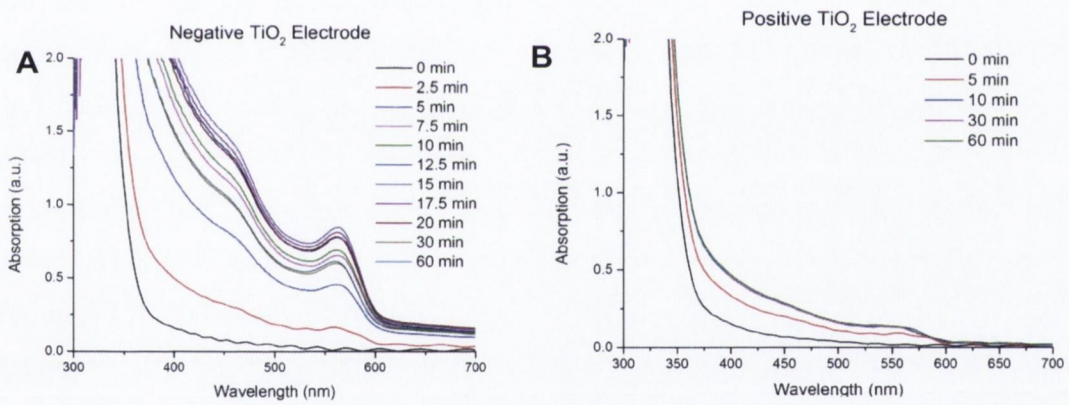

Figure 4.4 UV-Vis Absorption spectra showing the change in absorption of oleic acid capped CdSe QDs (3.3 nm) over time into a TiO_2 electrode, showing the negative electrode (A) and the positive electrode (B). The peak absorption is found to be much higher for the negative electrode than the positive electrode. Interestingly the absorption increases to a peak value for the negative electrode to a peak time of 15 minutes and actually starts to decrease after 20 minutes. The positive electrode showed a plateau of absorption after 10 minutes remaining unchanged.

A sensible route to electrophoretic optimization of QD deposition is through increasing the overall driving force being applied, therefore this can be achieved either through the use of a larger electrical potential or by concentrating this electrical potential more effectively. Since already 250 V was being utilised and voltage sources over 250 V are inherently more expensive and carry with them increased safety risks, it was decided that concentration of the electrical field was the optimal route. Hence, by reducing spacer distance between electrodes from 6 mm to a distance of 1 mm, deposition occurred far more effectively. It was also found use of a smaller counter electrode based on just FTO glass, cut to the exact width and length of the TiO_2

layer screen printed (1 cm x 3 cm) upon the FTO glass, deposition also increased. In conjunction, the FTO counter electrode needed effective cleaning after each deposition with the use of concentrated aqua regia, followed by washing with deionized water and isopropanol, to maintain the repeatability, during multiple deposition cycles.

4.3.2.iv Origin of charge and current

The precise reason for greater sensitisation of the negative electrode is not precisely known but could be due to the cadmium excess (2.75:1, Cd:Se) used in the synthesis of these CdSe QDs, which should cause an excess of cadmium cations in the QDs. This was investigated by carrying out a synthesis of oleic acid capped CdSe QDs with Se excess (1:2, Cd:Se) which were then electrophoretically deposited. Analysis of the resulting electrodes showed a near identical deposition upon the positive and negative electrode, which points towards the fact that stoichiometry plays only a part in the overall charge present upon the QDs.[252]

It should also be noted that a current can be measured while carrying out EPD, which was found on average to be between 60 $\mu A/cm^2$ to 25 $\mu A/cm^2$ at the beginning of deposition and slowly decreased by a factor of 2 or 3 over the time of deposition. This current has been reported in literature to be caused by the movements of QDs in solutions and the presence of impurities in either the CQD solution or solvents.[252] From our experiments it is clear that the electrical current we measured is due to impurities presence and was verified by the observation that currents remained the same, whether a EPD of CQDs deposited or not, which clearly indicated to us that the QDs played no part in the charge transport in solution, and therefore the current reading. It was also observed that higher current readings were achieved from CdSe QD solutions, which had been put through a fewer number of cleaning cycles, and therefore contained a higher concentration of impurities.

4.3.2.v Repeatability

During the test period of deposition, a consistent issue with repeatability took place. Several optimisations were included, which improved the reliability of this technique, though some aspects could not be completely resolved. Interestingly, it was found that solutions diluted with DCM and immediately electrophoretically deposited, produced the expected results, while solutions, left to stand for 30 minutes, produced a much lower deposition level, and after one hour of standing, no deposition took place from these solutions. It was also observed that some solutions of CdSe QDs completely lost their ability to deposit when they precipitated in storage even after the QDs were redispersed in solution. In addition, it was found that after production of the CdSe, the cleaning steps utilised were fundamentally important to producing a solution

that could be deposited. For example after oleic acid capped CdSe was synthesised, the number of cleaning cycles , which involved the addition of a non-solvent (HPLC acetone), followed by centrifugation, defined whether the solution could be electrophoretically deposited or not. With no cleaning, a large current was recorded on the power source of over 200 $\mu A/cm^2$, while no deposition of QDs occurred. After one cleaning cycle, the QDs deposited as expected, but if a second cycle of cleaning were carried out, the QDs again would not deposit, while currents recorded would be between 20 - 40 $\mu A/cm^2$. It was also found that after a single deposition, even though only a tiny loss in overall concentration of the solution occurred (~5%, see Appendix D), no further depositions could be carried out from this solution.

4.3.2.vi Adherence and comparison to controls

After deposition, electrodes were washed with DCM. Interestingly the electrodes showed only small changes in absorption after washing (~20 %, see Appendix D, Figure 7.11) indicating the majority of QDs were strongly bound to the surface. Following this, the efficiency of the optimised electrophoretic approach was compared against two other methods of sensitisation, soaking and drop casting. To test soaking, TiO_2 electrodes were immersed in a CdSe solution for 3 days in darkness with a concentration of 1×10^{-5} M CdSe QDs. These soaked electrodes were tested in hexane, DCM, $CHCl_3$ and toluene, the same nonpolar solvents tested for electrophoretic deposition. The resulting UV-Vis spectra are shown in Figure 4.5. The overall absorptions were very poor, with DCM displaying the greatest sensitisation ability among these solvents. Further measurements of electrodes was carried out after 7 days of soaking, with no increase occurring. Drop casting was also carried out using a concentrated solution (1×10^{-4} M) of CdSe QDs in DCM. After applying 1 ml of the solution to the electrode, it was left to dry in darkness. Following this the electrode was washed with DCM to remove excess QDs, from this

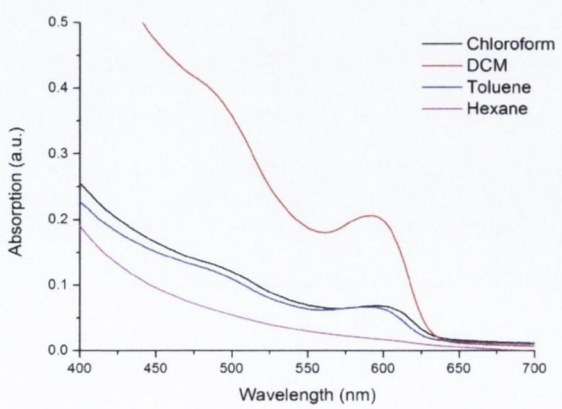

Figure 4.5 UV-Vis absorption spectrum of TiO_2 electrode after being soaked in four different solutions of oleic acid capped CdSe QDs at a concentration of 1×10^{-5} M for 3 days, using the solvents , Chloroform (black line), DCM (red line), Toluene (blue line) and Hexane (pink line).

the majority of the deposited films was removed. The remaining layer that was produced was visibly uneven and patchy, showing only barely detectable CdSe absorption.

4.3.2.vii Microscopic analysis

Judging by eye, this second approach to quantum dot deposition produced an even distribution of QDs throughout the TiO_2 electrode, while no deposition of QDs occurred upon the surrounding FTO exposed surface. To further investigate this, scanning electron microscopy (SEM) was used to analyse the resulting sensitised electrodes. The electrodes showed (Figure 4.7) little visible sign of deposition of QDs under SEM when compared to non-sensitized electrodes (see chapter 5, Figure 5.15), which is mostly due to instrument limitations.

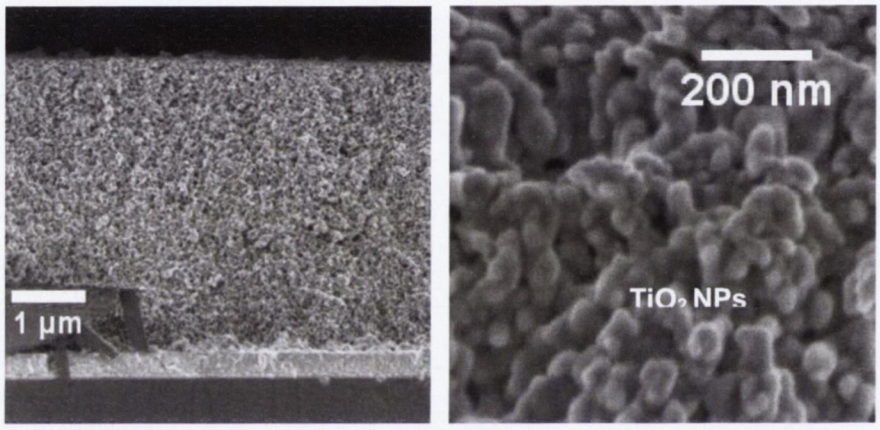

Figure 4.6 SEM of CdSe QD sensitised TiO_2 nanoparticles electrode.A) is a side profile of the electrode whiile B) shows the porous nanoparticluate structure of the electrode.

Transmission electron microscopy (TEM) was then used to analyse the sensitized TiO_2, by removing a portion of the TiO_2 film and grinding it up in a mortar and pestle. This was then dispersed in a solution of ethanol and then drop cast onto a lacey carbon TEM grid. The resulting images are shown in Figure 4.8 C and D. From these, a clear image of the TiO_2 crystals can be seen, surrounded in a large diffuse cloud of CdSe QDs of 3.2 nm in diameter. Scanning transmission electron microscopy (STEM), allowed even clearer images to be produced, due to its much stronger Z-contrast as shown in Figure 4.8 A and B. From these, the presence of individual CdSe QDs can be seen upon the TiO_2 NP surface and is marked in the image.

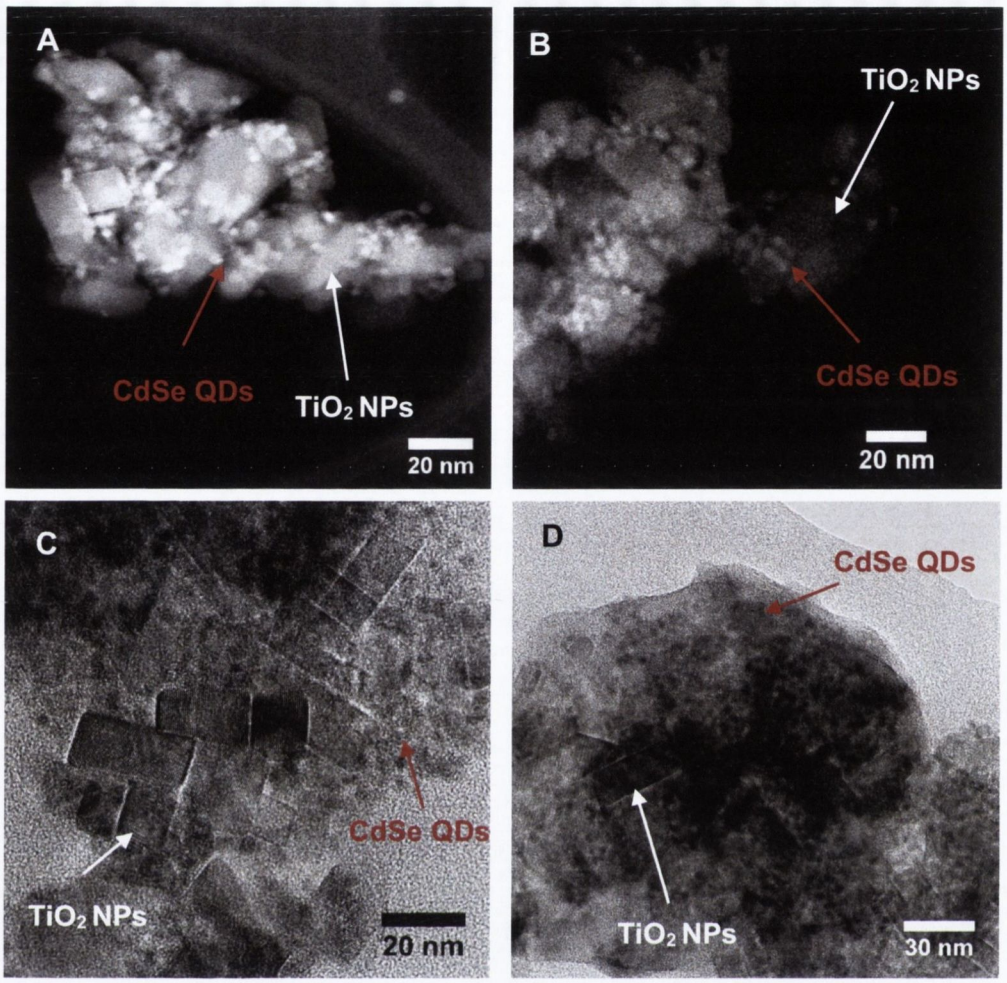

Figure 4.7 STEM images (A and B) of 3.2 nm CdSe QDs upon the surface of a 20 nm TiO_2 nanoparticles produced using electrophoretic depostion. C) and D) show the TiO_2 sensitised with 2.9 nm CdSe QDs upon the surface of 20 nm TiO_2 particles sensitised using electrophortic depostion.

4.3.2.viii EDX

Using energy disperse X-ray spectroscopy (EDX) in conjunction with SEM, it is possible to determine the elemental makeup of TiO_2 films after CQD deposition as shown in Figure 4.8. Using this it was possible to verify the success of the QD deposition and to make a determination of loading of CdSe QDs by comparing the signal of Ti to the signals of Cd and Se. This is shown in Figure 4.8 C, giving 7.3 % Cd and 5.6 % Se relative to 87.2% Ti. It also allows mapping of the elemental composition as a function of depth into the TiO_2 film, which showed that the distribution of CdSe QDs remained constant as a function of depth in the TiO_2 layer. This is the optimal distribution of sensitizers since the overall aim is to produce a near monolayer coating of QDs upon the TiO_2 particle surface to produce maximum increase in photon harvest followed by effective charge injection into the TiO_2 electrode. This is a unique advantage of electrophoretic deposition relative to the much more practised linker approach, which uses a

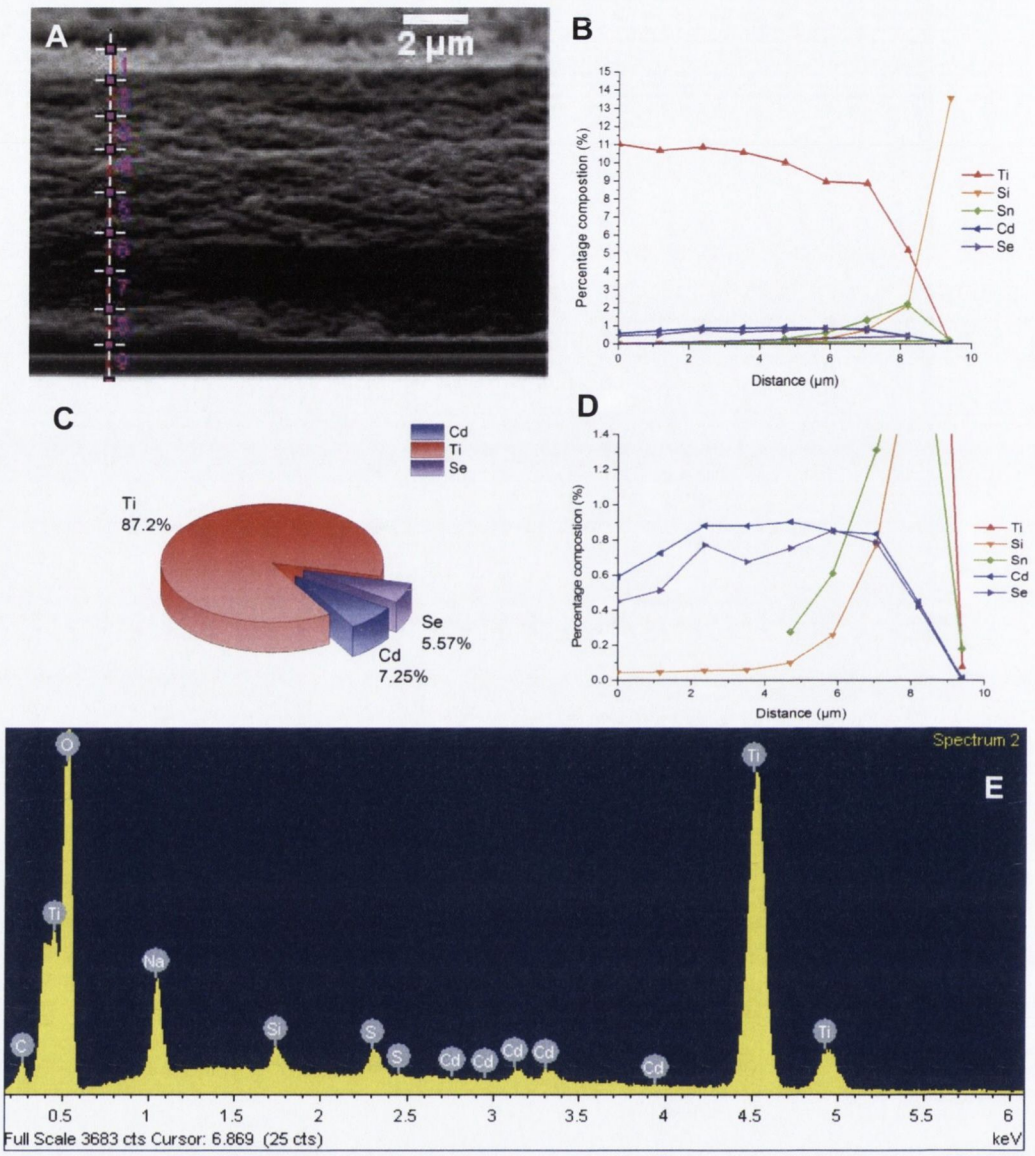

Figure 4.8 SEM and EDX of CdSe sensitised TiO_2 electrode through electrophoretic deposition. SEM of a side on profile of the electrode is shown in image A, this is marked with the positions that EDX spectra were taken. Graph B and D show the elemental composition changes across the electrode as a function of distance. While graph C and E shows the EDX spectra produced from position 5 on the SEM image, showing the elemental loading of QDs relative to Ti, to be 7.25% Cd and 5.57% Se.

short chain bifunctional ligand upon the QDs surface to cause QD deposition during a soak.[235] This linker approach instead produces a deposition that shows a reduction in CdSe concentration as the depth increases in the TiO_2 in the direction of the FTO glass. This is a far less efficient loading due to increased photon absorption occurring at an increased distance from the junction between the TiO_2 /FTO junction, meaning electrons injected, have a higher likelihood of undergoing recombination with the electrolyte before transferring to the FTO. Other elements shown in the spectra include tin, which is derived from the fluorine doped tin oxide (FTO) conductive coating, and Si, which is due to the glass substrate.

4.3.2.ix Photocurrent Action Spectra

The photoresponsivity of the produced CdSe sensitised TiO_2 was then tested using photo action spectra. This test firstly was optimised to allow effective examination of the resulting photocurrent response electrodes under illumination. Therefore two electrolytes were initially investigated, MeOH and a 0.1 M aqueous solution of Na_2S. MeOH has been shown to act as a sacrificial hole scavenger electrolyte in QDSSCs,[340] while Na_2S is used as a vital part of polysulphide based electrolytes.[221] The current generated from testing with this electrolyte is shown in Figure 4.9 A (red line), and produced a very poor response of only 0.003 mA/m^2 with our CdSe test electrode. Following this, we decided to test the response using a 0.1 M aqueous solution of Na_2S. This produced a much strong signal, giving a response of 0.035 mA/m^2 under illumination as shown in Figure 4.9 A (black line).

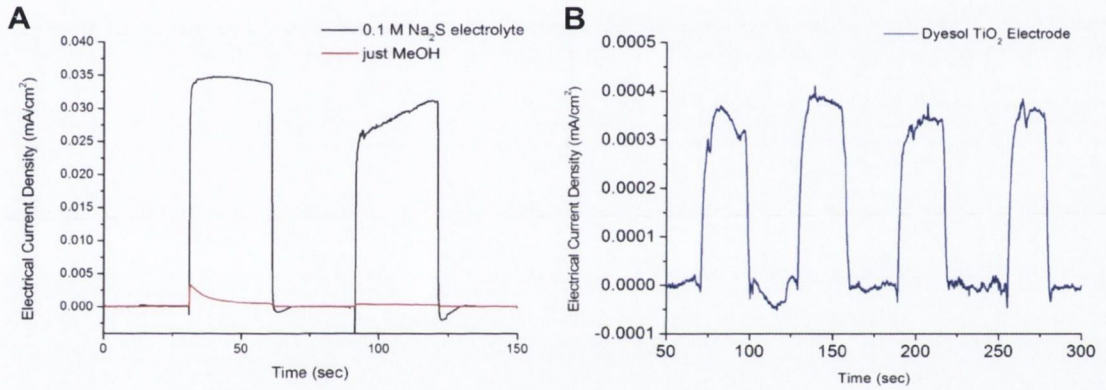

Figure 4.9 Photocurrent action response (A) of a oleic acid capped CdSe QD sensitized TiO_2 electrode using MeoH (red line) or 0.1 mol aqeouse solution of Na_2S (black line) as an electrolyte. Photocurrent response (B) of TIO_2 electrode without QD sensitization, which produced only a minimal current of 0.0031 mA/cm^2 under illumination.

Subsequent to this, a non-sensitized electrode of pure TiO_2 was used to get a baseline for the response. The electrode displayed a minimal signal, producing currents up to 0.0031 mA/cm^2 under illumination as shown in Figure 4.9 B. The minimal signal is due to the illumination source, a ring of white light LEDs, which nearly exclusively produces light in the visible range (see Figure 2.12), and since the band gap of anatase TiO_2 is 3.2 eV, most of this light will pass straight through the electrode without absorption taking place, hence the low photocurrent response.

Following this, three different sizes of oleic acid capped CdSe QDs, with diameters of 2.5 nm, 3.4 nm and 3.8 nm were deposited upon TiO_2 electrodes and the photocurrent was tested as shown in Figure 4.10. This was performed to determine the effect of QD size upon the produced photocurrent. It was found that as the size of the QDs grew, a large increase in current took place from 0.31 mA/cm^2 to 0.35 mA/cm^2 to 0.54 mA/cm^2. This can be explained by the wider absorption of larger QDs, therefore enabling them to harvest more photons from the incident light.

Following on from this initial study, we decided to investigate the deposition and performance of CdSe QDs synthesised using a more complex ligand surface, due to these QDs showing higher luminescence in solution and therefore better surface passivation, which could play an important aspect in reducing recombination when sensitising the TiO_2 electrode. The CdSe QDs investigated were, amine capped CdSe and phosphonic acid capped CdSe. These QDs also showed smaller size distributions and could be synthesised to even larger sizes to determine the optimal size of CdSe for photosensitization, which has been reported to be between 610 and 625 nm for the first exciton position.

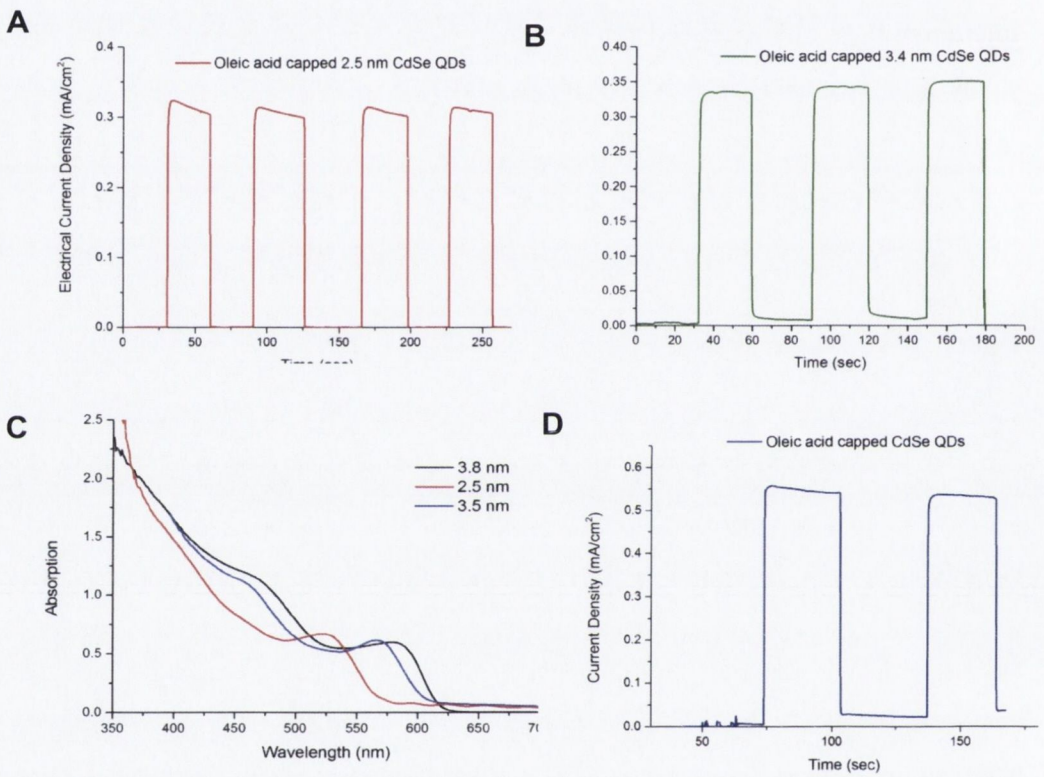

Figure 4.10 This shows the photocurrent response produced from three different TiO_2 electrodes that were sensitised using oleic acid capped CdSe QDs, the resulting photocurrent responses under illumination were , A 2.5 nm, 0.31 mA/cm², B 3.4 nm 0.35 mA/cm², and Z 3.8 nm , 0.55 mA/cm². Image C show the UV-Vis absorption of the different sized CdSe QDs deposited upon a TiO_2 electrode.

4.3.3 Octadecylamine capped CdSe QDs

QDs were synthesised in the presence of octadecylamine and oleic acid meaning the ligand shell consisted of a mix of both ligands upon the surface. Deposition was carried out under the same conditions as described for oleic acid capped CdSe QDs. Following this photocurrent response was measured and is shown in Figure 4.11. The different ligand shell and conditions of synthesis meant that the QDs had to go through three cleaning cycles before deposition was possible from the DCM solution, with deposition occurring on the negative electrode. Unfortunately, the repeatability of deposition was moderate at best especially when attempting to deposit QDs of larger sizes, which regularly precipitated from solution under the applied voltage as opposed to

sensitising the TiO_2 electrode. Therefore despite these QDs showing excellent sensitisation when deposition did occur, further use of these ODA capped CdSe QDs was discontinued.

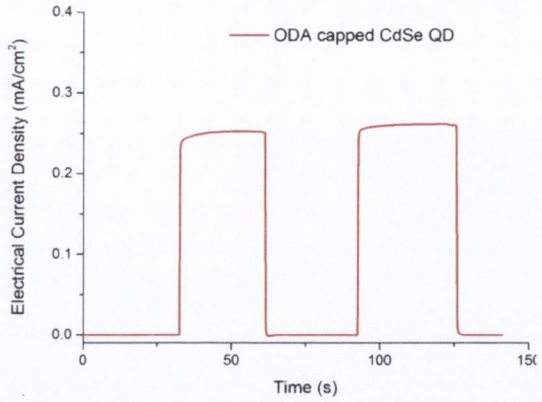

Figure 4.11 Photocurrent action response of ODA capped CdSe QDs showing a peak current of 0.25mA/cm² from 4.2 nm CdSe QDs

4.3.4 Octadecylphosphonic acid capped CdSe QDs

These CdSe QDs were synthesised in the presence of octadecylphosphonic and trioctylphosphine oxide, meaning the ligand shell consisted of a mix of both ligands upon the surface. Deposition was carried out under the same conditions as described and quantum dot loading was monitored using UV-Vis absorption, which is shown in Figure 4.12 A. Following this, photocurrent response was measured and is shown in Figure 4.12 B.

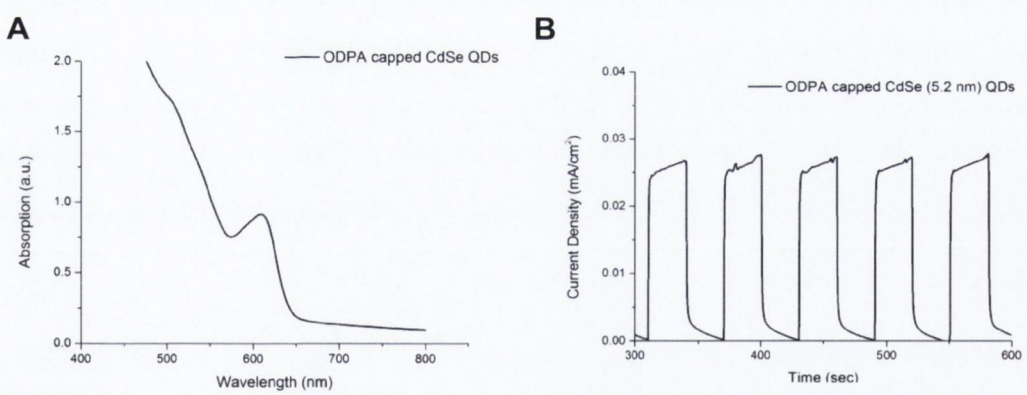

Figure 4.12 UV-Vis absorption spectroscopy (A) and the resulting photocurrent action response (B) of ODPA capped CdSe QDs (5.2 nm) EPD deposited upon a TiO_2 electrode.

The different ligand shell and conditions of synthesis meant that the even after numerous cleaning steps, involving dissolution in toluene, followed by precipitation due to addition of MeOH, an excess of ligands remained in solution with ODPA capped CdSe QDs. It was found that under these conditions the QDs could not be EPD upon a TiO_2 electrode from DCM whatsoever. Therefore an additional cleaning step was included, which involved dissolving these QDs into hexane and centrifuging at 4000 rpm for 20 minutes, producing a stable solution of QDs with a deposit of excess ligands that was then separated and discarded. After this it

became possible to deposit the QDs, but deposition time had to be increased to 20-30 minutes depending upon the exact solution being used. Interestingly after depositing, ODPA capped CdSe QDs solution from a 20 ml solution of $5x10^{-6}$ M of CdSe QDs concentration, it was found that additional cycles of between 3 - 8 depositions could be produced from the same solution, with no loss to TiO_2 deposition. In addition, it was noted that no loss of deposition ability occurred due to prolonged dilution in DCM as was seen with oleic acid capped CdSe QDs. Therefore, after comparison of repeatability, these were the CdSe QDs used for the majority of further studies.

4.4 Post EPD treatments of Electrodes

Following the deposition of CdSe QDs upon the TiO_2 electrodes, a range of approaches were applied so as to increase the photocurrent response of these electrodes, these fall under two categories, bulk semiconductor SILAR deposition and surface ligand exchange, both of which are discussed below.

4.4.1 SILAR Deposition: ZnS coating effect

ZnS is a large band gap semiconductor, and has been shown to form a type I band gap alignment with Cd chalcogenides.[91, 341] It has also been reported as a means to increase the photocurrent of QDSSCs.[331] The reason for this increase is twofold, firstly the ZnS coating produces a type I band alignment which reduces recombination loss in QDs, secondly due to the coating approach, it also coats the TiO_2 surface, acting to reduce recombination loss in the TiO_2 electrode.[342] The ZnS deposition was performed using the SILAR approach and produced using three cycles of Zn and S deposition to produce the resulting layer using 0.1 M aqueous solutions

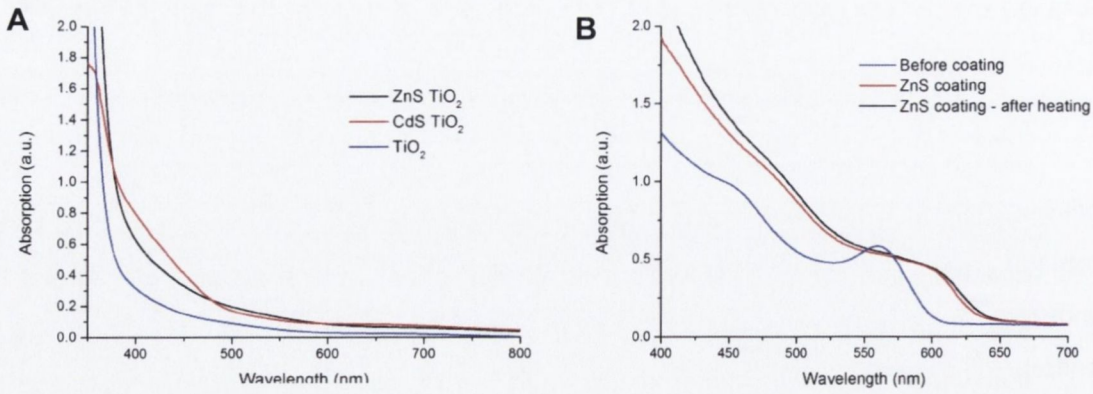

Figure 4.13 UV-Vis absorption spectroscopy, comparing the change in absorption of TiO_2 electrode (A) or a oleic acid capped CdSe QD (3.4 nm) sensitised TIO_2 electrode (B) due to ZnS coating or CdS coating (only graph A). Graph A shows the resulting increase in absorption due to 3 cycles of the SILAR deposits upon a transparent TiO_2 electrode composed of 4 layers of 20 nm TiO_2 particles. Graph B shows the large shift in absotption of a CdSe sensitiosed elctrode due to three cycles of SILAR ZnS deposition ,displaying a large red shift in the resulting UV-Vis spectroscopy.

of sodium sulphide and zinc acetate. Following this a sintering step was also tested which involved putting the produced electrode through a heat treatment of 2.5 minutes at 300 °C using a small furnace with aim of sintering the ZnS layer deposited.

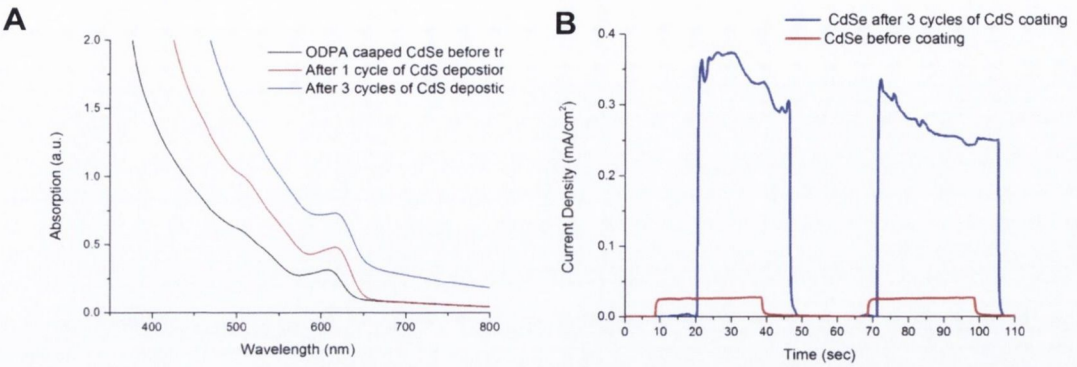

Figure 4.14 UV-Vis absorption spectroscopy (A) and the resulting photocurrent action response (B) of ODPA capped CdSe (5.2nm) sensitised TiO_2 electrode, showing the change due to SILAR deposition of CdS. Image A compares the shift in absorption due to a SILAR deposition of 1 cycle of CdS and 3 cycles relative to the untreated electrode. Image B show the change in photocurrent between electrodes due to the application of 3 cycles of CdS, from a max of 0.027mA/cm² to a max of 0.37 mA/cm².

UV-Vis absorption spectroscopy was used to show the change in absorption of a TiO_2 electrode and a CdSe sensitized TiO_2 electrode and is shown in Figure 4.13. A marginal increase in higher energy photon absorption is produced in the TiO_2 electrode (Figure 4.13 A) which coincides with the large band gap of bulk ZnS (3.54 eV). A significant increase in absorption also occurs when observing the CdSe QD sensitised TiO_2 electrode, which also produces a large red shift in the absorption of the CdSe QD also, which is due to the lattice mismatch between the materials that effects the electronic structure of the CdSe QD. Finally, photocurrent action response was used to then analyse the resulting change in photocurrent response of a CdSe sensitised TiO_2 electrode under illumination and is shown in Figure 4.15. The resulting electrodes shows an increase in photocurrent due to ZnS coating, increasing from 0.19 mA/cm^2 in the absence of ZnS , to 0.44 mA/cm^2 after ZnS coating , and finally 0.42 mA/cm^2 after ZnS coating and heat treatment. Therefore it was determined that the ZnS coating played an important part in producing efficient photoanodes based on QDs, while due to the minor decrease in efficiency due to heat treatment, this sintering step was deemed redundant.

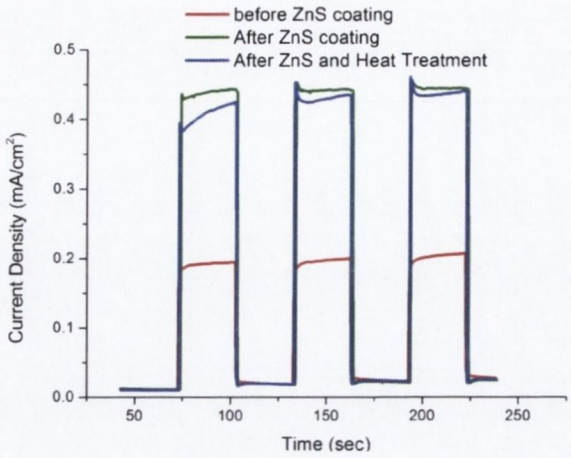

Figure 4.15 Photocurrent action response of oleic acid capped (3.4 nm) CdSe QD sensitised TiO_2 electrode, showing the change in response due to ZnS coating. The resulting maximum photocurrents produced of the electrode, before ZnS coating, 0.19 mA/cm², after ZnS coating and heat treatment 0.42 mA/cm², and after ZnS coating 0.44 mA/cm²

4.4.2 SILAR Deposition: CdS coating effect

CdS is also a larger band gap semiconductor relative to CdSe and forms a type I band alignment. Therefore, this material was used as a means to passivate the surface of the CdSe QDs and increases the absorption of the electrode, particularly at wavelengths above the band gap of bulk CdS (~ 520 nm). The CdS layer was deposited using a SILAR approach by treating the TiO_2 electrode using an aqueous solution of 0.02M $CdCl_2$ and an aqueous solution of 0.02M Na_2S solution, with the electrode alternatively dipped into each solution, washing with deionised water between dips. The change in UV-Vis absorption of a TiO_2 electrode due to CdS deposition is shown in Figure 4.13 A. The electrode shows a significant increase in absorption particularly in the higher energy area of the spectrum, matching effectively with the bulk band gap of CdS. Following this, the change in UV-Vis absorption spectroscopy of an ODPA capped CdSe sensitised electrode was analysed and is shown in Figure 4.14 A, displaying the change in absorption between a single cycle of CdS deposition and the result of a 3-cycle deposition. This shows again a very significant increase in absorption of the electrode due to the treatment, displaying significant red shifting of the CdSe 1st exciton peak position due to the treatment.

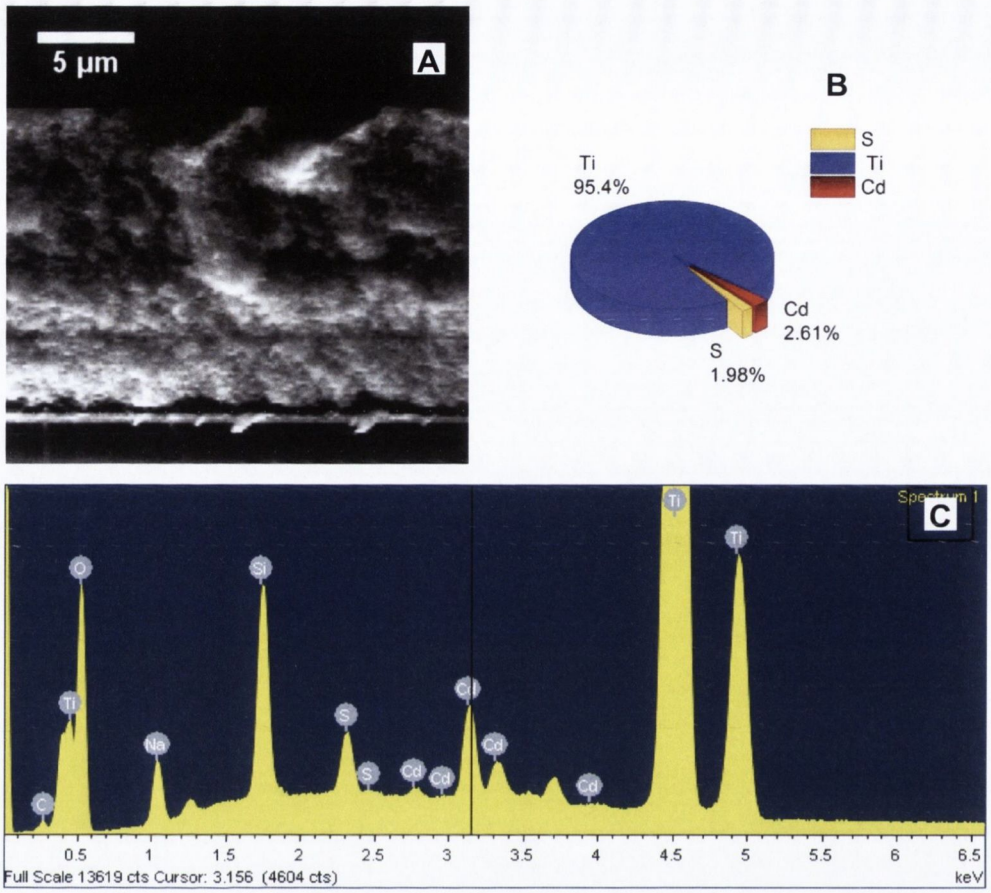

Figure 4.16 SEM (A) and EDX (B and C) of TiO_2 electrode after 3 cycles of SILAR CdS treatment. The SEM showed no significant alteration in the morphology of the electrode post CdS treatment, while EDX shows a significant incorporation of CdS into the TiO_2 electrode, showing a loading of 2.61 % of Cd and 1.98 % of S in the electrode when compared to Ti present.

After this, SEM and EDX was used to analyse the resulting electrode shown in Figure 4.16. The electrode displays no significant change in surface morphology due to the CdS deposition, while EDX shows a large loading of CdS achieved within the electrode giving concentrations (m/m) of 2.61% Cd, 1.98 % S relative to Ti and is compared in Figure 4.16 B. Following deposition of CdS upon the ODPA capped CdSe QD sensitised electrode, the resulting photocurrent response was matched to the electrode prior to the CdS deposition and is shown in Figure 4.16 B. From this, it can be seen that a large increase in photocurrent occurs due to CdS coating, producing a peak current of 0.37 mA/cm^2 from the original current of 0.027 mA/cm^2, which makes this treatment by far the most effective route to increasing photocurrent of produced photoaniodes. It must be kept in mind that the original electrode did show poor performance relative to other electrodes and therefore this treatment does need to be tested with electrodes that show larger initial photocurrent readings to determine its universal applicability.

4.4.3 Ligand exchange: HTAC

Another approach to increase charge injection is to better passivate the surface of the deposited CdSe QDs using halide anions that have already shown success in this application in DHCQD solar cells.[195, 311] Therefore ODPA capped CdSe QD sensitized TIO_2 electrodes were tested before and after a 1-hour treatment in a 10 mg /ml MeOH solution of HTAC (Hexadecyltrimethylammonium chloride). The resulting UV- Vis absorption and photocurrent response is shown in Figure 4.17. Interestingly a minor blue shift in absorption (Figure 4.17 B) is found to take place due to the HTAC treatment, accompanied with a slight overall increase in absorption, though this change in absorption is within experimental error. The photocurrent response shows a pronounced increase in current produced due to the treatment increasing the original peak current of 0.0185 mA/cm^2 to 0.039 mA/cm^2 due to HTAC treatment. Therefore, this treatment has been proven as another possible means to increase the photocurrent of produced electrodes.

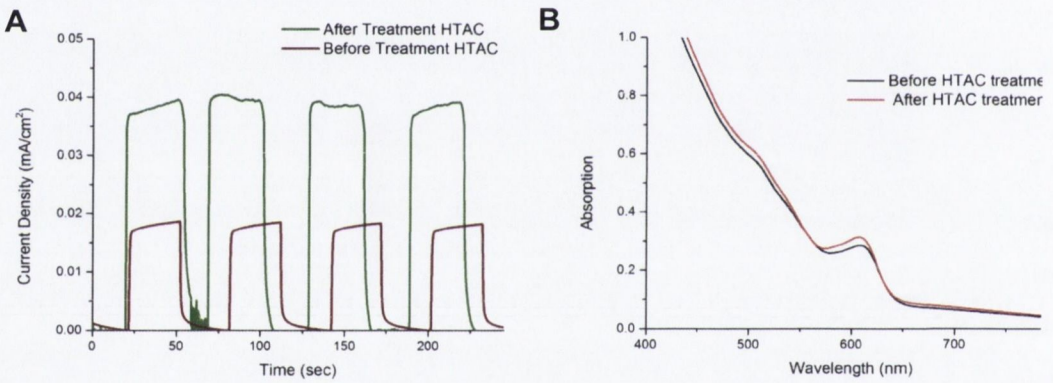

Figure 4.17 UV-Vis absorption spectroscopy and the resulting photocurrent action response of ODPA capped CdSe QDs sensitised TiO_2 electrode, showing the change due to HTAC treatment. Image A shows a large increase in photocurrent from 0.0185 mA/cm^2 to 0.039 mA/cm^2 due to HTAC treatment, while Image B only shows minor increase in absorption and blue shifting of spectra.

4.4.4 Ligand Exchange: MPA Ligand treatment

A commonly utilised ligand in the linker approach to TiO_2 sensitisation with ex situ synthesised quantum dots is 3- mercaptopropionic acid (MPA). This due to its excellent binding to TiO_2 through its carboxylic acid group and the presence of a thiol group which strongly binds to commonly tested QDs, i.e. Cd or Pb based QDs. It also is widely used due to its small size, meaning that the QD will in theory be in closer proximity to the TiO_2 surface, which should enable charge injection. We therefore tested its effect as a post treatment on ODPA capped CdSe QD sensitised TiO_2 electrodes, since the intention was to replace the bulky ODPA acid upon the QDs surface with the short chain ligand and therefore increase the resulting photocurrent of tested QDs. This was carried out by submerging the electrode into a 2.5 % v/v MeOH based solution of MPA. The electrode was firstly submerged for one minute in darkness, following

which the electrode was washed with deionised water. The photocurrent action of the resulting electrode was then tested and is shown in Figure 4.18. The original electrode showed a photocurrent of 0.012 mA/cm^2 which was reduced to 0.0016mA/cm^2 following the treatment. Subsequently a 10-minute treatment was also tested, which resulted in an electrode that showed no detectable response under illumination. Therefore, it was judged that unfortunately this treatment strongly harmed the photocurrent response of these electrodes unexpectedly.

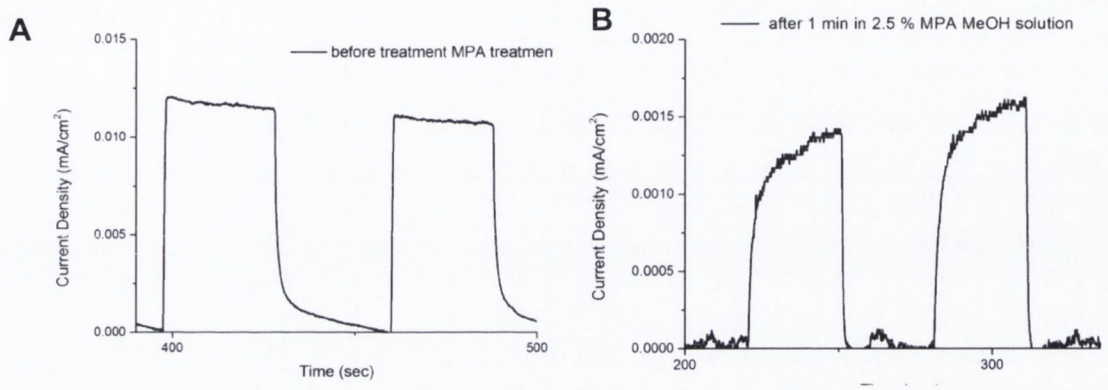

Figure 4.18 Photocurrent action response of ODPA CdSe sensitised TiO_2 electrodes showing the original electrode (A) and the resulting electrode (B) after a 1 minute treatment with 2.5% MPA MeOH solution.

After investigating the electrophoretic deposition of CdSe QDs as a means to sensitise TiO_2 electrodes, it was decided to expand the study to other types of core and core-shell QDs synthesised in chapter 3. This was carried out to firstly demonstrate the wide applications of this approach and to investigate the effects of different semiconductor and semiconductor structures upon the resulting photocurrents.

4.4.5 EPD of CdS QDs

CdS is synthesised with an oleic acid ligand surface. The resulting QDs are much smaller than CdSe, measuring between 2 to 3 nm in diameter. They were deposited using the same conditions as mentioned for CdSe, and the resulting UV-Vis spectra and photocurrent measurements are shown in Figure 4.19 A and B respectively. Deposition took place upon the positive and negative electrode with stronger absorption taking place upon the negative electrode. This deposition pattern was ascribed to the ratio of 1:2, S:Cd used in the synthesis. Unfortunately, the deposition showed the same issues regarding repeatability raised using oleic acid capped CdSe QDs.

Due to the larger band gap of CdS QDs (band gap ≥ 3eV), these QDs are exclusively UV absorbers and therefore overlap strongly with the absorption of the TiO_2 electrode. They also therefore are poor sensitizers of TiO_2 only marginally widening the range of the visible spectrum the

electrode can harvest. This is represented in the poor photocurrent responses produced of 0.0113 mA/cm^2 of the positive electrode and only 0.005 mA/cm^2 of the negative electrode.

SEM and EDX of the sensitised electrodes were then used to determine the elemental composition and the resulting loading of the TiO_2 film, shown in Figure 4.20. This confirms a linear distribution of CdS QDs throughout the electrode relative to depth (Figure 4.20 A,B and C) and produced a loading of 1.75% of cadmium and 2.93% of sulphur relative to titanium present (Figure 4.20 D and E), which compares poorly to the loading values achieved with oleic acid capped CdSe.

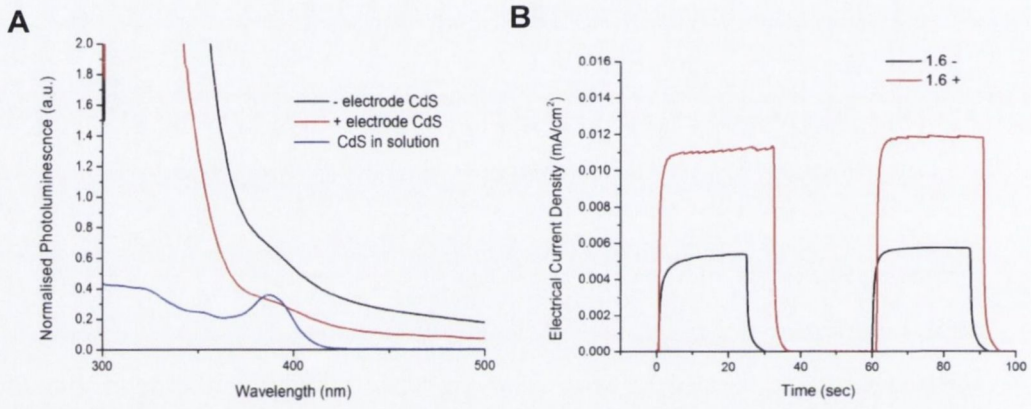

Figure 4.19 This shows the UV-vis absorption and the resulting photocurrent action response of a TiO_2-FTO electrode sensitized with 3 nm CdS QDs. A) UV-Vis absorption shows the original QD spectra in solution and then the resulting spectra of the electrodes sensitized. The positive and the negative electrode both show depostion , with higher laoding taking place upon the postive elctrode. B)Photocurrent action spectra shows a on-off response under illumination. 0.01127mA/cm^2, 0.0053mA/cm^2

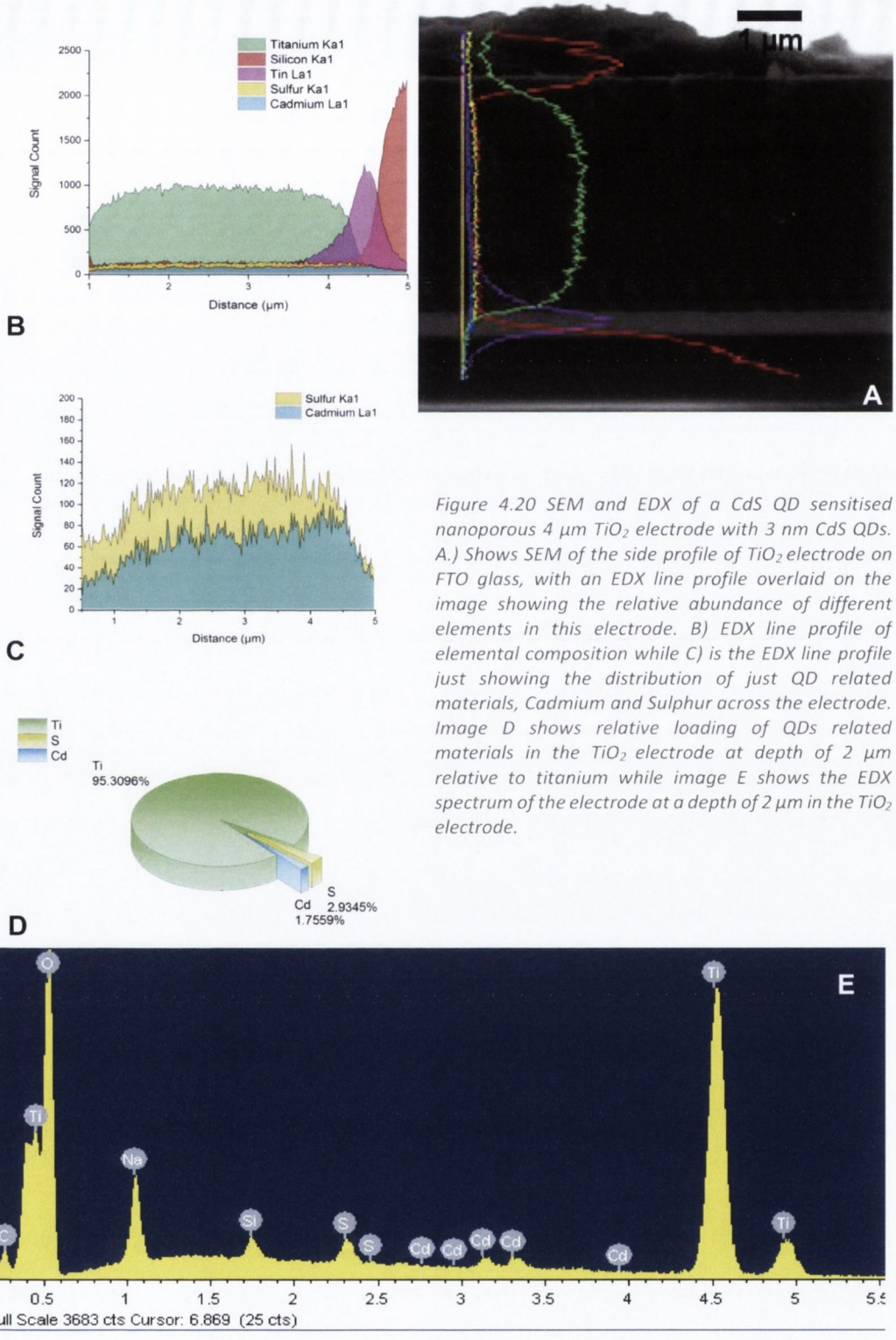

Figure 4.20 SEM and EDX of a CdS QD sensitised nanoporous 4 µm TiO_2 electrode with 3 nm CdS QDs. A.) Shows SEM of the side profile of TiO_2 electrode on FTO glass, with an EDX line profile overlaid on the image showing the relative abundance of different elements in this electrode. B) EDX line profile of elemental composition while C) is the EDX line profile just showing the distribution of just QD related materials, Cadmium and Sulphur across the electrode. Image D shows relative loading of QDs related materials in the TiO_2 electrode at depth of 2 µm relative to titanium while image E shows the EDX spectrum of the electrode at a depth of 2 µm in the TiO_2 electrode.

4.4.6 EPD of PbS QDs

PbS is a direct band gap semiconductor with a value of 0.37 eV in the bulk. Therefore, when synthesised as a QD, the bandgap can be tuned from NIR to IR values, making them a perfect candidate for producing a quantum dot with a band gap in the optimal range of the Shockley-Queisser limit, 1 eV to 1.5 eV. PbS QDs with diameters between 2.6 nm to 4.3 nm were therefore investigated.

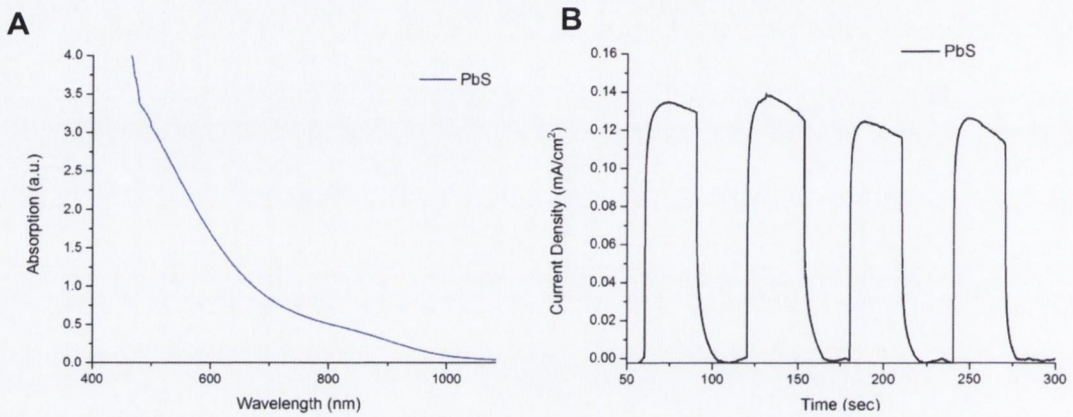

Figure 4.21 UV-Vis absorption spectra (A) and resulting photocurrent response (B) of PbS QD sensitised TiO_2 electrode. A) Shows the resulting absorption of a electrophoretically deposited PbS (2.7 nm) QD upon a TiO_2 electrode. B shows the resulting photocurrent response under illumination, producing a peak current of 0.13 mA/cm².

The same issues with deposition repeatability occurred with oleic acid capped PbS as was described with oleic acid capped CdSe QDs, presenting low repeatability, with solutions synthesised under identical conditions showing large variance with deposition rate. Instability of these solutions also contributed to this, with larger PbS QDs (diameter > 4.0 nm) showing precipitation under the applied field. The majority of deposition occurred upon the positive electrode, and is partially due to the 1:2 molar ratio of S:Pb precursors used in the PbS synthesis, producing Pb rich QDs. The resulting electrodes were analysed with UV-Vis absorption spectroscopy and photocurrent action response measurements and is shown in Figure 4.21. The electrode showed a huge increase in absorption due to PbS deposition, producing absorption into the NIR due to the small band of the 2.7 nm QDs used. The photocurrent action response of the electrode produced a peak current of 0.13 mA/cm², which though substantial, is lower than expected due to the wide absorption of the electrode. The reason for the lower response than expected can be explained due to the light source used, a white LED ring, which shows a peak emission at 570 nm (see Chapter 2, Figure 2.12), and therefore is poorly matched to the absorption of the PbS sensitised electrode.

SEM and EDX were used to further analyse the sensitisation of TiO_2 electrodes, which is shown in Figure 4.22. The distribution of QDs was found to be near constant relative to depth of the TiO_2 (Figure 4.22 A, B and C), as seen with other QDs examined previously, while the resulting loading achieved was very high, producing a loading of 7.26% Cd, 6.02 % S relative to Ti present (Figure 4.22 D and E).

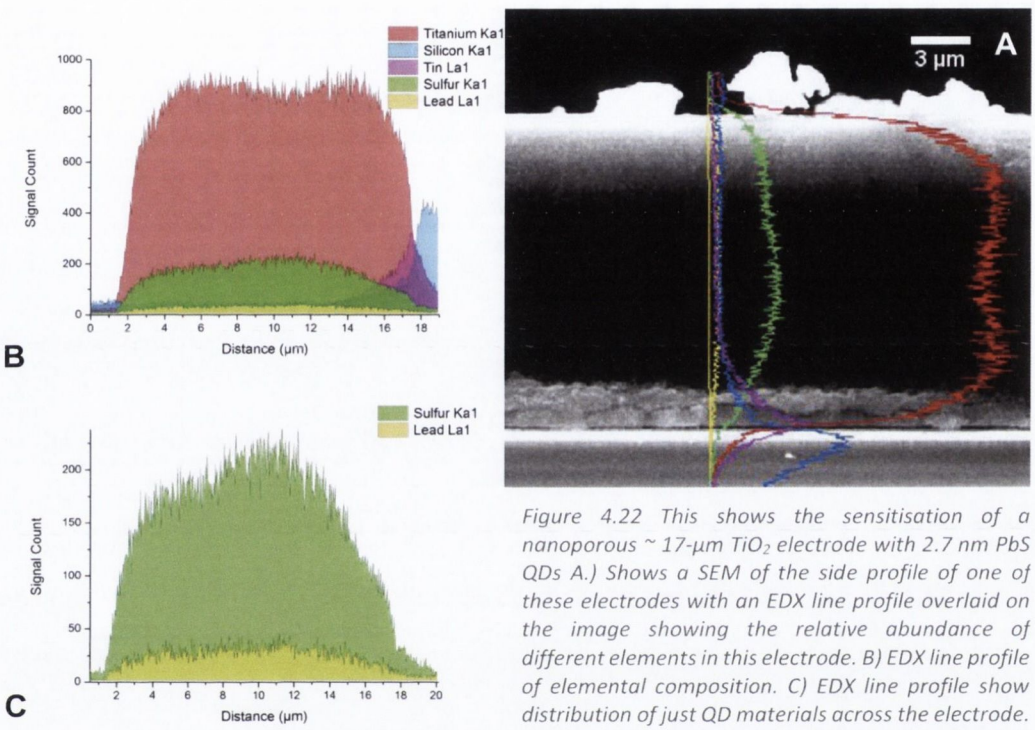

Figure 4.22 This shows the sensitisation of a nanoporous ~ 17-µm TiO_2 electrode with 2.7 nm PbS QDs A.) Shows a SEM of the side profile of one of these electrodes with an EDX line profile overlaid on the image showing the relative abundance of different elements in this electrode. B) EDX line profile of elemental composition. C) EDX line profile show distribution of just QD materials across the electrode. D) Elemental comparison of QDs in the TiO_2 electrode at depth of 7.5 µm. E.)EDX spectrum of the electrode at a depth of 7.5 µm in the TiO_2 electrode

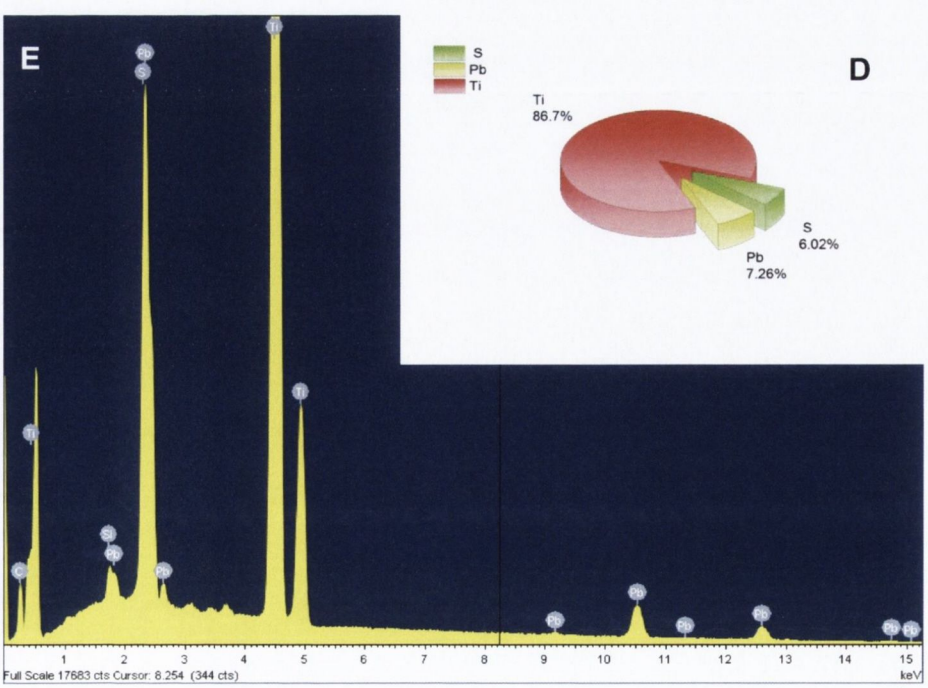

4.4.7 EPD of CdSe/CdS core-shell QDs

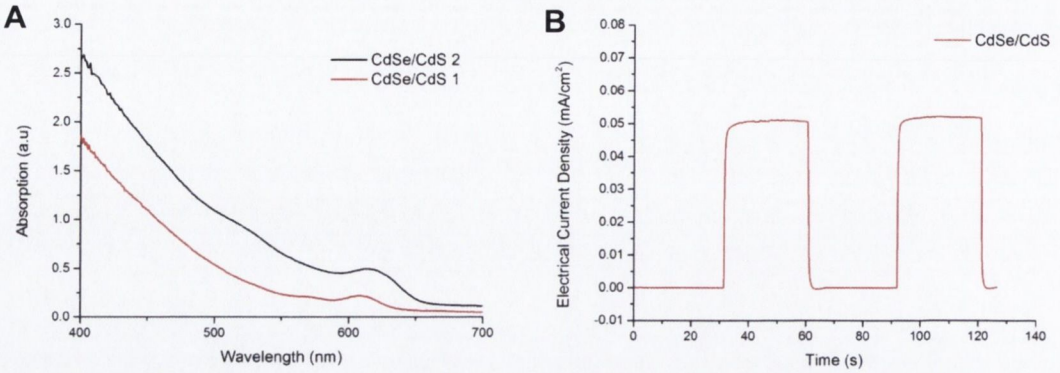

Figure 4.23 UV-Vis absorption spectra (A) and photocurrent response (B) of CdSe/CdS sensitised TiO_2 electrode. The total photocurrent produced was 0.05 mA/cm².

After testing three core QDs, it was decided to expand the study to core/shell QDs to understand the effects that these structures would have upon the photosensitisation and to deem if it was feasible to sensitise with these larger (in most cases) and more complex QD structures. Therefore, this was begun by investigating CdSe/CdS QD. This has a type I band structure meaning the exciton is confined to the inner CdSe QD core, and therefore have less interaction with surface states. This means that the exciton bears less chance of undergoing recombination through surface states or with the surrounding electrolyte, though it could also have the effect of retarding charge injection due to increased distance between the exciton and the TiO_2 surface. Two different sizes of CdSe/CdS QDs were used, the first formed from a 3.4 nm CdSe core (A), and a second formed from a 4.2 nm CdSe core (A) both of which were deposited using EPD, and their resulting UV-Vis absorption is shown in Figure 4.23A. Following this the photocurrent of 3.4 nm core CdSe, CdSe/CdS QD was tested and is shown in Figure 4.23 B. The maximum current recorded was 0.05 mA/cm², which equates to a low response, which can be attributed to the poor loading achieved from the electrophoretic deposition as shown in the UV-Vis spectra. The QDs loading was poor due to them being synthesised using a mix of oleylamine, octadecylamine and oleic acid as ligands, which strongly defined the behaviour under electrophoretic deposition, with QDs showing only partial deposition under the applied voltage, with deposition occurring only upon the negative electrode.

4.4.8 EPD of CdS/CdSe core/shell QDs

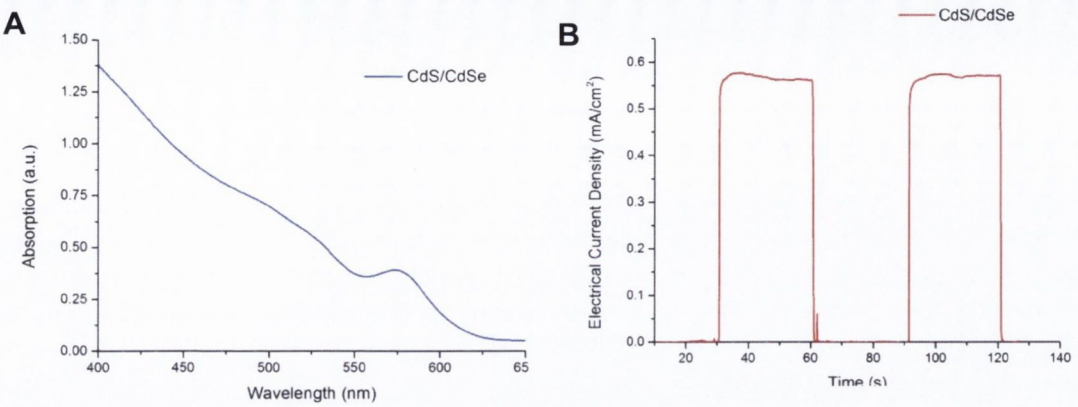

Figure 4.24 UV-Vis absorption spectra (A) and photocurrent response (A) of CdS/CdSe sensitized TiO_2 electrode showing the change in absorption before and after testing, 0.57mA/cm² and 0.515mA/cm².

The second core-shell QD that was electrodeposited was CdS/CdSe, which is a reverse type I QD, meaning the exciton is more strongly confined to the surface of the QD, which has been reported to enable charge injection to occur more readily.[235] Therefore, it is also an interesting contrast to CdSe/CdS QDs already investigated. These QDs are synthesised using oleic acid as a capping ligand and so electrophoretic deposition was similar to other oleic acid capped QDs discussed. Due to the increased size of the QDs and the inherent challenge regarding concentration determination, the loading achieved of the TiO_2 electrode was not to the level achieved using oleic acid capped CdSe QDs. The film was analysed using UV-Vis absorption spectra and photocurrent response as shown in Figure 4.24. Even though total loading was suboptimal to light harvesting, the total current produced was much higher than expected, producing a current of 0.57 mA/cm^2 under illumination, indicating the effectiveness of this core shell structure to charge injection.

4.4.9 EPD of CdTe/CdSe core/shell QDs

The last form of core-shell QD investigated was a CdTe/CdSe core-shell QD. This core/shell structure produces a staggered band alignment between CdSe and CdTe, causing the band gap of the resulting QD to be smaller than either semiconductor. This also produces the effect that the exciton is separated across the QD, with the hole confined to the core, while the election is confined to the shell. The QDs were synthesised using oleic acid and a small amount of ODPA, and produced QDs with a diameter of 5.5 nm. Electrophoretic deposition proved difficult with these QDs due to their ligand coating and larger size and therefore loading was not optimal. The resulting UV-Vis absorption achieved is shown in Figure 4.25 A while the produced photocurrents are shown Figure 4.25 B with maximum photocurrents of 0.316 mA/cm^2

recorded. Again, this electrode in fact outperformed expectations due to the pure loading of QDs achieved making it an interesting candidate for further investigation.

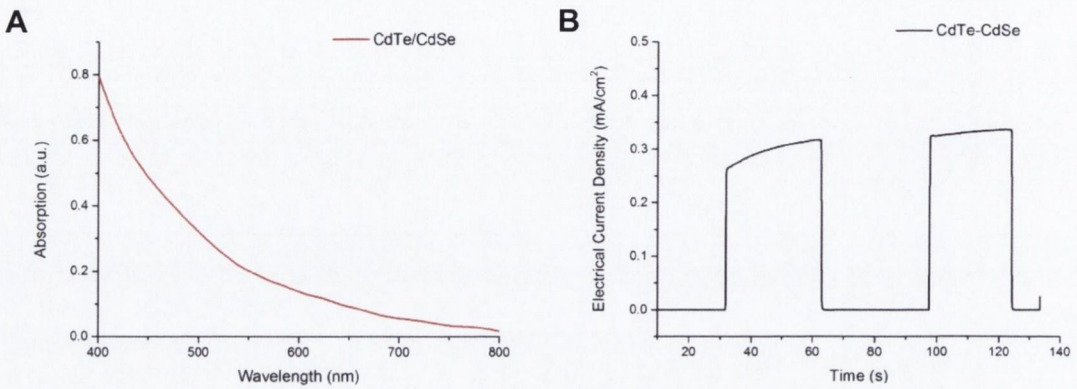

Figure 4.25 UV-Vis absorption spectra (A) of CdTe/CdSe QD sensitised TiO_2 electrode and photocurrent response (B) of the resulting electrode measured under illumination producing a current of 0.316 mA/cm²

4.4.10 EPD of CdSe/CdS heterostructured quantum rods

Finally, after analysing the three discussed Cd based core/shell QDs, it was decided that it would be interesting to look at the effect of morphology of these core/shell structures upon the overall efficiency achieved in loading and sensitisation. Therefore, CdSe/CdS dot in rod heterostructured quantum rods were electrophoretically deposited upon these TiO_2 electrodes. The CdSe/CdS NRs used were formed from 4.8 nm CdSe QDs cores, to enable increase absorption at longer wavelengths of light. These were synthesised using octadecylphosphonic acid, hexadecylphosphonic acid and trioctylphosphine oxide as ligands, which therefore due to these, just as was found regarding octadecylphosphonic acid capped CdSe QDs studies earlier (see section 4.3.4); required the inclusion of an extra cleaning step using centrifugation at 4000 rpm in hexane to remove excess ligands, before EPD deposition was effective with these particles.

The resulting UV-Vis absorption of the electrode is shown in Figure 4.26, showing a strong absorption of the CdSe/CdS NRs. Due to the high loading achieved through deposition, as was demonstrated in the UV-Vis spectra, it was decided that it would be worthwhile to investigate the distribution of QDs in the electrode with SEM and EDX, this is shown in Figure 4.28. This shows electrophoretic deposition produced a linear distribution of CdSe/CdS quantum rods throughout the electrode. It was also confirmed that a very high loading of the electrode is achieved and is shown in Figure 4.28 D, with the resulting EDX spectra shown in Figure 4.28 E. From this percentage of 9.8 % Cd, 9 % S and 0.9 % Se was determined relative to 80.3% Ti.

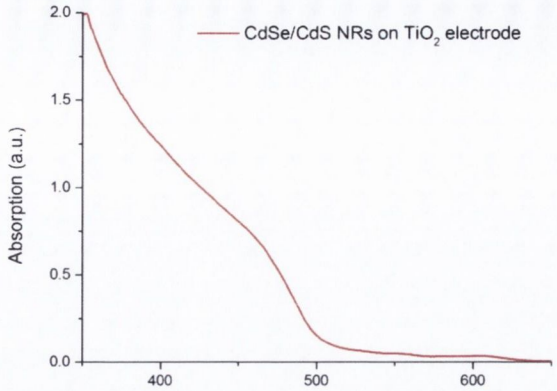

Figure 4.26 UV-Vis absorption spectra of CdSe/CdS sensitised TiO_2 electrode after a 15 min electrophoretic deposition.

Subsequently, we used STEM and EDX to confirm deposition of the QRs upon the surface of the TiO_2 surface, which is shown in Figure 4.27. From the images, the rod structures can be made out representing the CdSe/CdS NRs, while EDX confirms the presence of Cd and S indicating the presence of CdSe/CdS rods upon the surface of the TiO_2 electrodes.

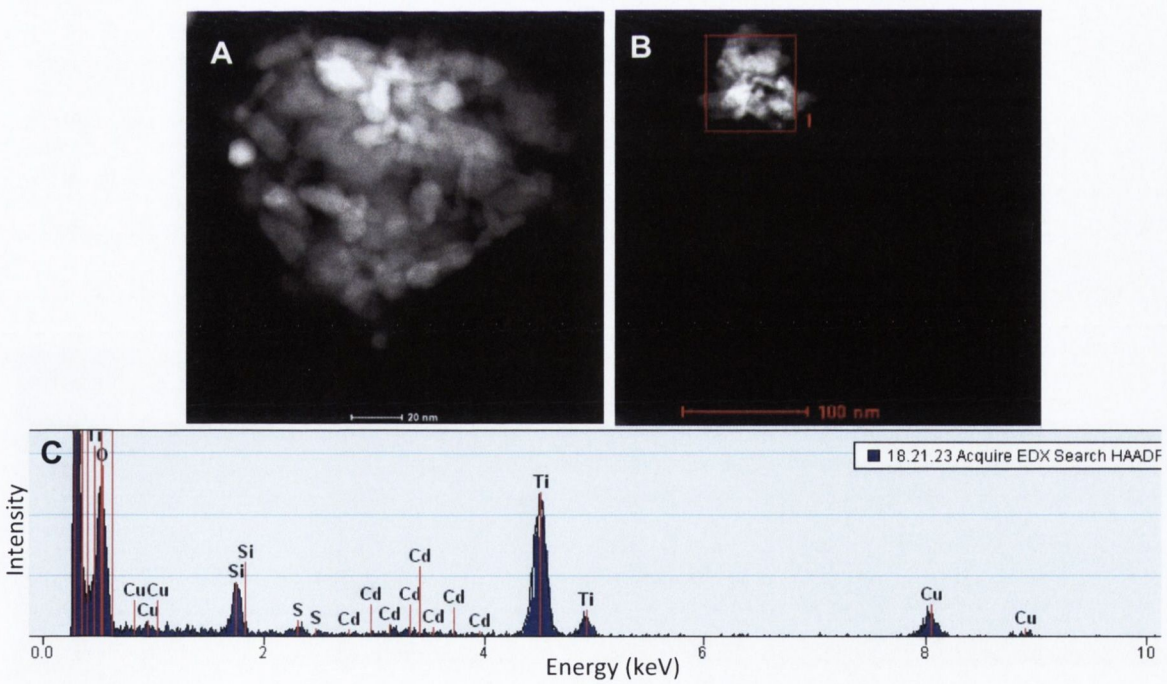

Figure 4.27 STEM and EDX of a sample of TiO_2 sensitized electrode sensitised with CdSe/CdS heterostructured nanorods. Image A and B show STEM images of CdSe/CdS sensitised TiO_2, while C shows the resulting EDX spectra obtained of the sample, showing peaks that are assigned to Cd, Ti, Cu O and S.

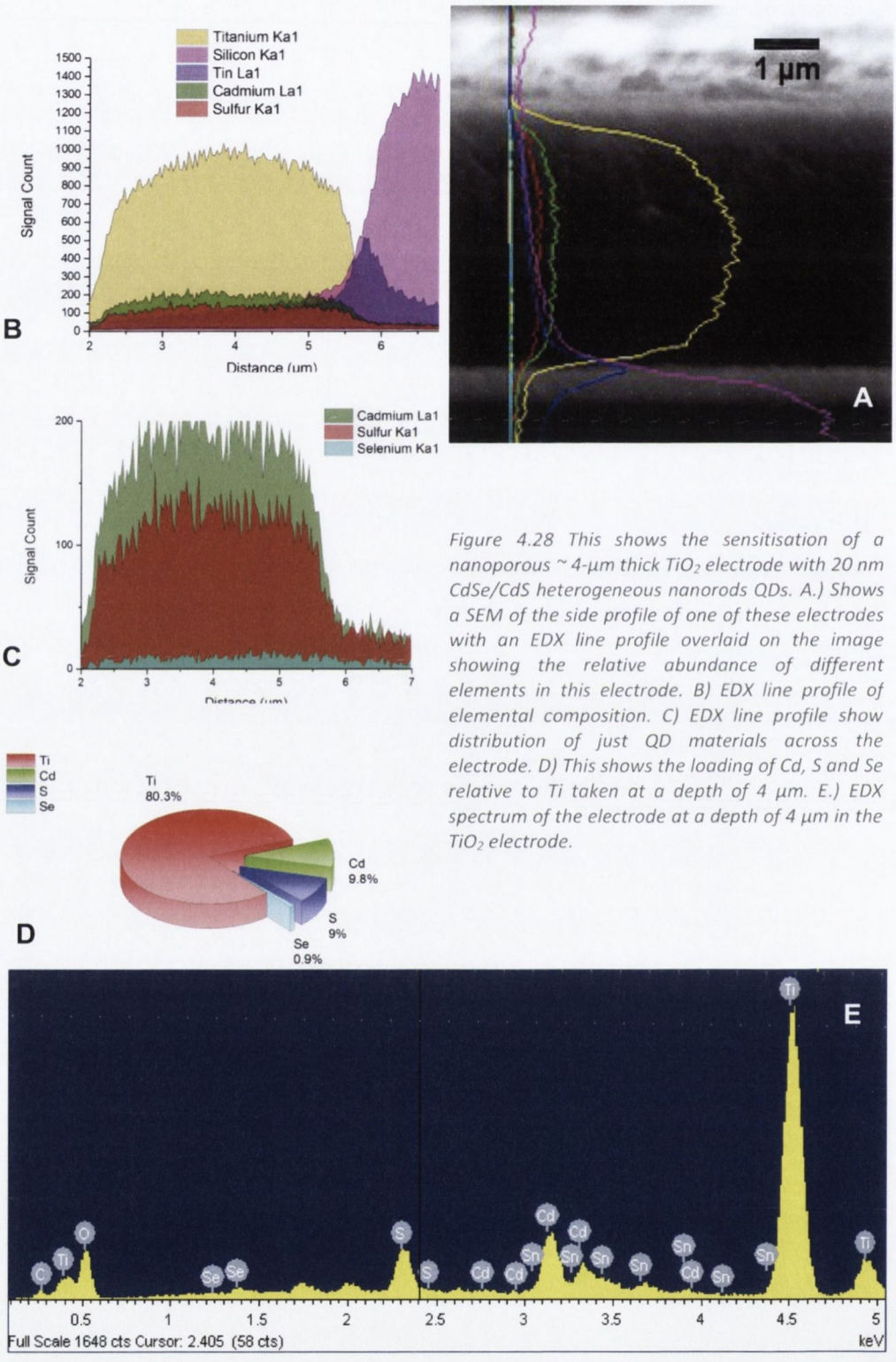

Figure 4.28 This shows the sensitisation of a nanoporous ~ 4-µm thick TiO_2 electrode with 20 nm CdSe/CdS heterogeneous nanorods QDs. A.) Shows a SEM of the side profile of one of these electrodes with an EDX line profile overlaid on the image showing the relative abundance of different elements in this electrode. B) EDX line profile of elemental composition. C) EDX line profile show distribution of just QD materials across the electrode. D) This shows the loading of Cd, S and Se relative to Ti taken at a depth of 4 µm. E.) EDX spectrum of the electrode at a depth of 4 µm in the TiO_2 electrode.

4.5 Cation Exchange of EPD QDs upon TiO_2 electrodes

Either cation exchange can be used to produce a complete exchange of cations in a host QD, or if applied under appropriate conditions, it can utilised to bring about a partial conversion. For this segment of work we demonstrate for the first time, its application to QD sensitised TiO_2 electrodes as a means to change the chemical nature of the electrode after deposition, enabling us to tailor the absorption, stability and photocurrent of the resulting electrode.

4.5.1 Cation exchange of PbS QDs to PbS/CdS QDs on TiO_2

The aim of this work was to investigate the possible beneficial effects of producing a partial exchange of Pb cations present in PbS QDs with Cd cations, with the intention of producing a PbS/CdS QD sensitised TiO_2 electrode. This could potentially impart the benefits of a type I band alignment to the PbS QDs, confining the exciton to the PbS core due to the much larger band gap of CdS, and therefore reducing recombination losses in the QD at the surface, increasing its potential as an effective photosensitizers to TiO_2. The cation conversion of PbS QDs to CdS QDs has been reported[120] and demonstrated to take place in the liquid state (see 3.4.1). Therefore, the same basic principle have been applied to this work to bring about a partial conversion in the solid state. This has been carried out by immersing a TiO_2 electrode that has been sensitised using electrophoretic-deposited PbS QDs into a MeOH solution of $CdCl_2$ in darkness. The electrode was left in solution for varying times to bring about different levels of cation exchange. A simple technique to monitor the exchange comes from changes in the resulting UV-Vis absorption spectra shown in Figure 4.29 and Figure 4.30 A. As the exchange takes place, the size of the PbS core QD begins to shrink as the outer cations exchange with Cd, producing a

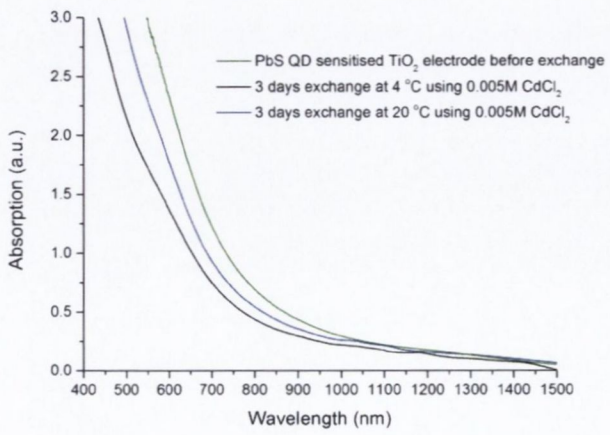

Figure 4.29 UV-Vis absorption spectroscopy of a partial cation exchange of PbS QD (6.1 nm) sensitised TiO_2 electrode to PbS/CdS, carried out at two temperatures, 4°C and 20 °C showing the change after a 3 day period

shell of CdS. This has the net result of making the UV-Vis absorption spectra of the electrode become blue shifted over time as shown in the spectra.

Using this approach, the exchange was firstly optimised by monitoring the effect of temperature upon the exchange. PbS QD sensitised TiO_2 electrodes were left in a MeOH solution of 0.005 M $CdCl_2$ at either room temperature or at 4 °C for three days and the change in the UV-Vis spectra is shown in Figure 4.29. Just as what was found in solution, the cation exchange process increases with temperature, showing a larger exchange having taken place at room temperature than at 4 °C. Since the exchange took an extended period to take place, we decided to increase further the rate of exchange by using a higher concentration of $CdCl_2$, 0.025 M, which is close to saturation. The electrode was immersed into this solution at room temperature and the rate of the exchange was then monitored every 10 minutes using a UV-Vis spectrometer, giving the results shown in Figure 4.30.

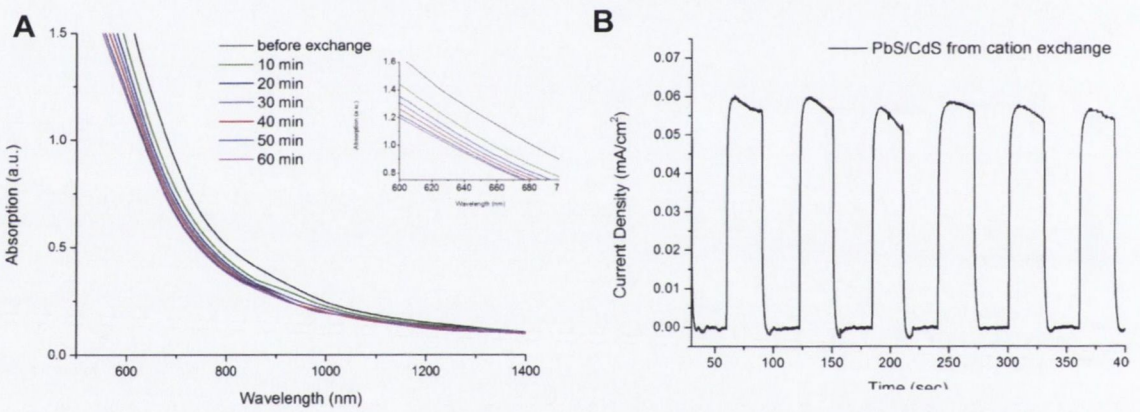

Figure 4.30 UV-Vis absorption spectroscopy (A) and photocurrent action spectra (B) of PbS/CdS QD sensitised TiO_2 electrode. Graph A shows the effect of cation exchange using 0.025 M MeOH solution of $CdCl_2$ at room temperature i, graph B shows the photocurrent response of an electrode after RT cation exchange

After allowing the exchange to take place for 1 hour, the photocurrent of the electrode was measured and is shown in Figure 4.30 B. The resulting photocurrent was much lower than what was produced prior to exchange, which is shown in Figure 4.21, this effect increased further as the exchange was allowed to take place, causing a complete loss of current. Therefore, it was judged that this exchange had the opposite effect as intended and in fact produced a significant decrease in photocurrent in the electrode.

The distribution of the exchange was then investigated using SEM and EDX techniques. This was necessary to determine if the exchange in fact had the same effect at all depths of the electrode or if exchange took place more readily at the surface than in the deeper pores of the electrode. Interestingly the signal for cadmium showed little change with depth (Figure 3.20 A,B and C) and so it could be assumed that the cadmium cation exchange took place at the same rate

throughout the electrode. The total ratio of exchange was also determined from the EDX spectra (Figure 4.31 D and E) showing a ratio of 3.7:1 , of Pb to Cd, which correlates with the target of only a partial exchange having taken place.

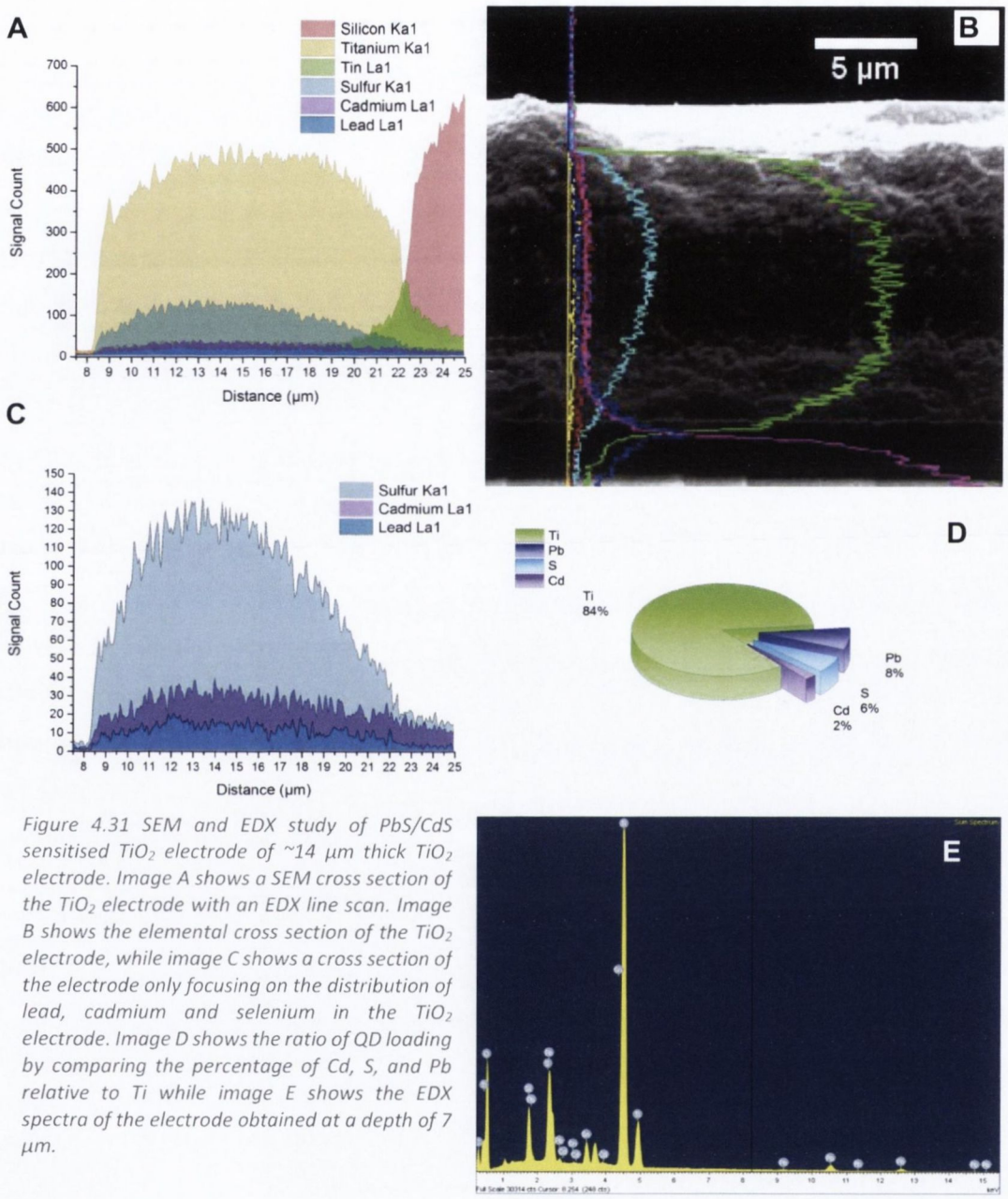

Figure 4.31 SEM and EDX study of PbS/CdS sensitised TiO_2 electrode of ~14 µm thick TiO_2 electrode. Image A shows a SEM cross section of the TiO_2 electrode with an EDX line scan. Image B shows the elemental cross section of the TiO_2 electrode, while image C shows a cross section of the electrode only focusing on the distribution of lead, cadmium and selenium in the TiO_2 electrode. Image D shows the ratio of QD loading by comparing the percentage of Cd, S, and Pb relative to Ti while image E shows the EDX spectra of the electrode obtained at a depth of 7 µm.

4.5.2 Cation exchange of CdSe to Cu_2Se to PbSe QDs on TiO_2

A second cation exchange process was undertaken using CdSe sensitised TiO_2 electrodes, firstly converting them to Cu_2Se QDs and then to PbSe QDs. To bring about the first conversion of CdSe to Cu_2S it was carried using 0.03 mM Tetrakis(acetonitrile)copper(I) hexafluorophosphate MeOH solution, which is a source of Cu^{1+}. The electrode was immersed into the solution and the conversion was allowed to take place over 5 minutes. The resulting UV-Vis spectra is shown in Figure 4.32. The blue line shows the original UV-Vis absorption spectra of the electrode before the conversion, after which the signal changes in intensity and position hugely. Firstly, the absorption shifts strongly towards the IR range, with the evolution of a broad absorption peak in the spectra, with peak position at ~ 1250 nm. This peak has been reported in literature to be due to plasmonic absorption activity in Cu_2Se. This unusual behaviour of plasmonic activity in a semiconductor is due to the large levels of intrinsic doping caused by nonstoichiometric ratio of Cu to Se present in the QDs, producing $Cu_{2-x}Se$. The peak position has been reported to be a function of the intrinsic p-doping while interestingly the plasmon also is a function of the size of the QD.[316] After carrying out the cation treatment the electrodes were then examined using SEM and EDX as shown in Figure 4.33. This was carried out to determine the elemental composition of the electrode relative to the Ti as shown in Figure 4.33 B, giving percentages of 70.2 % Ti to 9.6 % Se, 17.3 % Cu and 2.9% Cd with the produced EDX spectra shown in Figure 4.33 C. Interestingly the electrodes still showed a small percentage of Cd present after cation exchange, indicating that a complete exchange may not have taken place. It is also worth noting that the large value of Cu present is to be expected since every Cd cation is replaced by two Cu cations in the lattice.

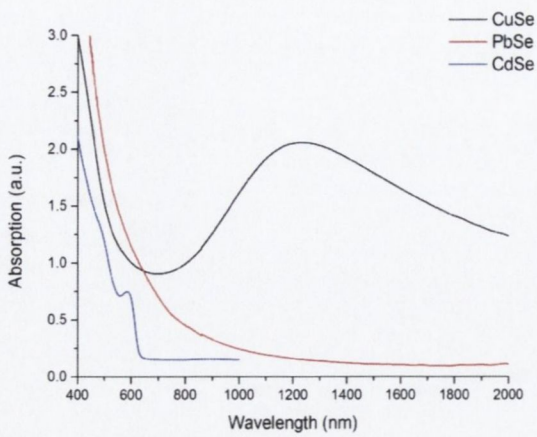

Figure 4.32 Graph of UV-Vis absorption of CdSe sensitized TiO_2 electrode ,that was firstly exchanged to become a $Cu_{2-x}Se$ electrode and then a second exchanged was carried out producing the PbSe electrode

Following this, the electrode was then converted to PbSe using a second cation exchange and was carried out by immersing the electrode into a solution of TBP (Tributylphosphine)/MeOH, (1/10, v/v) 0.075 M solution of Pb (acetate) for 2 hours in darkness. The resulting change in the UV-Vis spectra is shown in Figure 4.32. PbSe is a small band gap (bulk 0.28 eV) semiconductor and therefore absorbs in the NIR. Unfortunately, an expected peak representing the first exciton absorption is not visible in the UV-Vis and is an indication of a large size distribution in the resulting PbSe QDs produced. This must have arisen during the cation exchange, since the initial CdSe QDs show a strong first exciton peak as seen in the spectra.

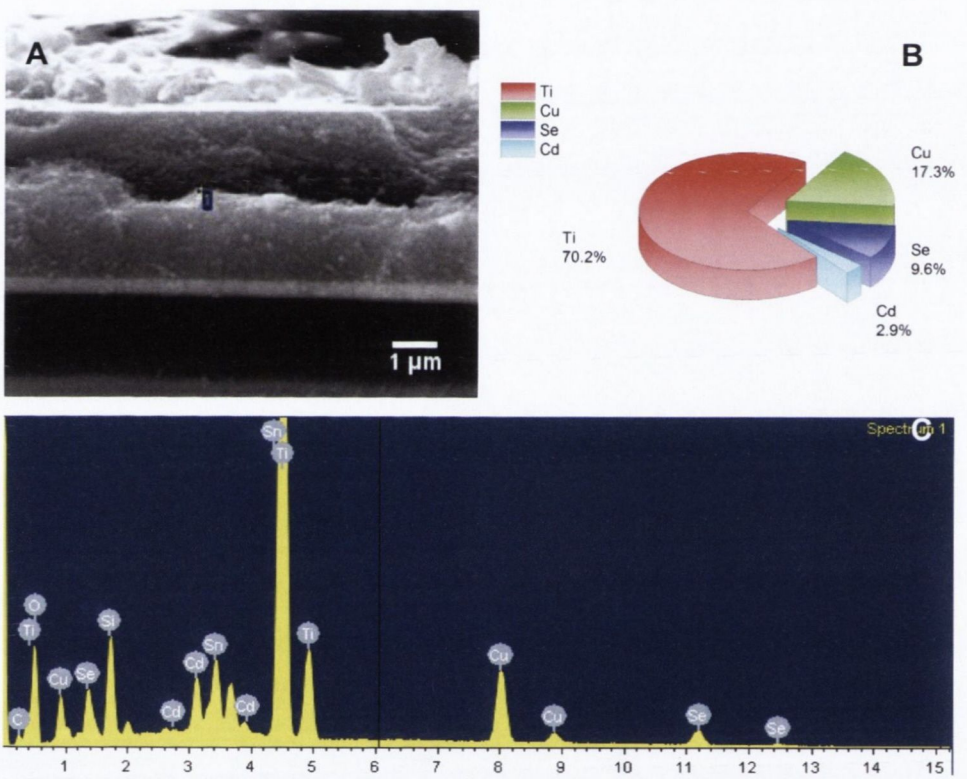

Figure 4.33 SEM and EDX of Cu_2Se QD sensitized nanoporous TiO_2 electrode. Image A shows a cross section of the 3.8 µm thick TiO_2 electrode, with a point marked showing the position of the EDX spectra. Image B shows the elemental composition of the electrodes, relating the loading of Cu, Se, and Cd to Ti present.

EDX and SEM were used to analyse the films and is shown in Figure 4.34. This was used to compare the ratio of Ti, to Cd, Cu, Se, and Pb, as shown in Figure 4.34 B giving 83.7% Ti, 9.3% Pb, 3.9% Se, Cd 1.7% and 1.4% Cu. This shows that the conversion has taken place, replacing the majority of the Cu_2Se QDs, with Pb. Unfortunately some Cu is still present, indicating that the cation conversion did not reach completion. It can also be seen that a small amount of Cd is also present; this can be explained again by assuming that the first conversion undertaken from Cd^{+2} to Cu^{+1} also did not reach completion. The EDX line spectra measured across the thickness of the electrode also shows a linear distribution of Pb relative to the TiO_2 thickness,

showing the thickness of the electrode does not retard the cation exchange process as shown in Figure 4.34 A, B and C.

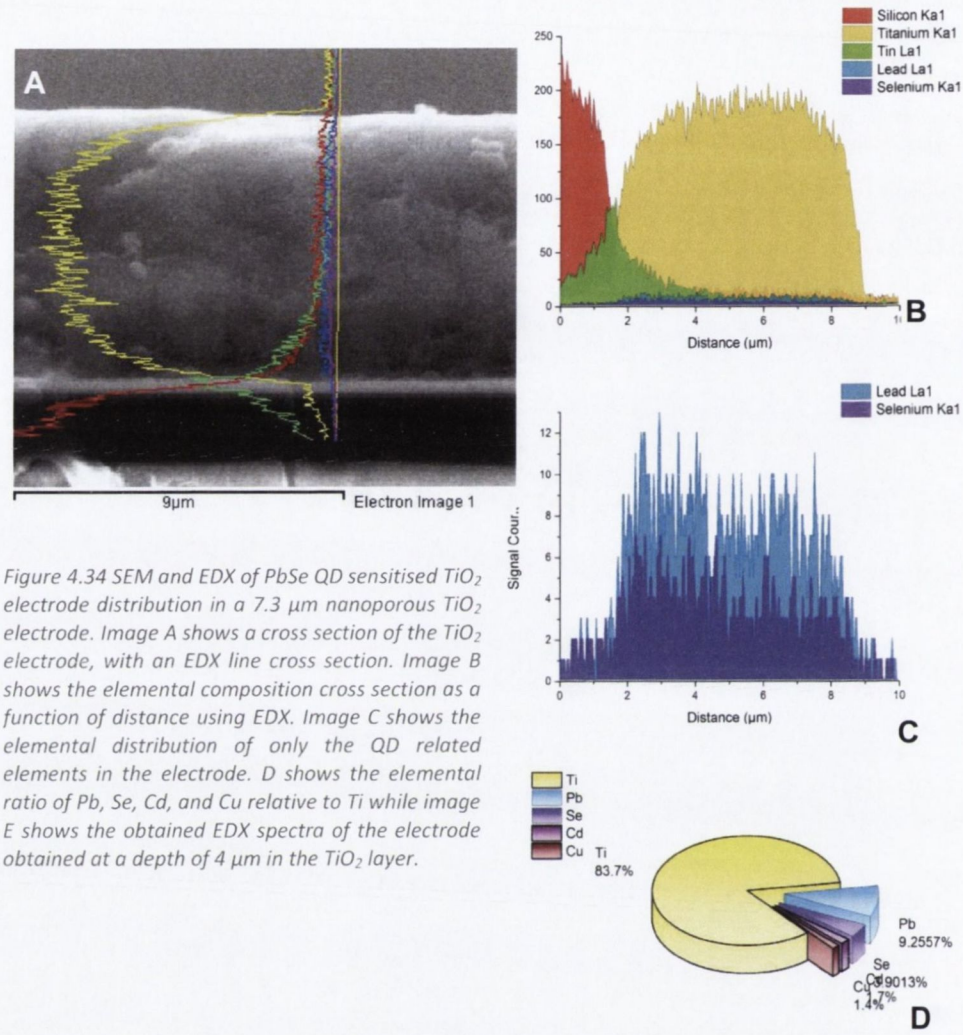

Figure 4.34 SEM and EDX of PbSe QD sensitised TiO_2 electrode distribution in a 7.3 µm nanoporous TiO_2 electrode. Image A shows a cross section of the TiO_2 electrode, with an EDX line cross section. Image B shows the elemental composition cross section as a function of distance using EDX. Image C shows the elemental distribution of only the QD related elements in the electrode. D shows the elemental ratio of Pb, Se, Cd, and Cu relative to Ti while image E shows the obtained EDX spectra of the electrode obtained at a depth of 4 µm in the TiO_2 layer.

4.6 Conclusions

In conclusion, we have demonstrated the utility of EPD as a means to sensitise porous TiO_2 electrode with a range of QDs and QRs, and the effects of a number of post treatments upon the resulting photocurrents of the electrodes tested under illumination. The study began by investigating the effects of a number of properties upon the relative success of electrophoretic deposition using oleic acid-capped CdSe QDs as the model test system. From this, we showed the novel observation that the application of DCM as a solvent for EPD has a hugely influential effect upon the total loading of electrodes achieved from deposition, increasing the success of the deposition tremendously. We have also demonstrated a unique advantage of EPD as sensation method to TiO_2 relative to other approaches, due to its ability to cause a near uniform sensitisation of the porous electrode relative to depth, allowing optimal sensitisation of the TiO_2 electrode for QDSSC applications.

Following optimisation of the deposition, we investigated the difference of QD loading when using CdSe QDs capped with other ligands, investigating the deposition of ODA capped CdSe QDs and ODPA capped CdSe QDs. From this, we determined that ODPA capped CdSe QDs showed the optimal performance under EPD, but only after an additional cleaning step to remove excess ligands present after ODPA capped CdSe QD synthesis was carried out.

Post EPD sensitisation of TiO_2 electrodes treatments were then examined with the aim to increase the resulting photocurrent of the produced electrodes. We have shown that the use of SILAR deposition of ZnS and CdS both show a large increase in the resulting photocurrents. We also investigated the effect of ligand exchange, using MPA and HTAC, with MPA showing a strong decrease in efficiency, while HTAC showed a strong increase.

We then used EPD to show its ability to produce a range of sensitised TIO_2 electrode through EPD of a range of core and core/shell QDs and QRs including CdS QDs, PbS QDs, CdSe/CdS QDs, CdS/CdSe QDs, CdTe/CdSe QDs and CdSe/CdS QRs. The photocurrent response of all electrode was also examined to determine the optimal material for photosensitisation, with CdS/CdSe and CdTe/CdSe core/shell QDs, producing photocurrents outperforming the below par loading achieved.

Finally, we have shown the novel application of cation exchange to electrophoretically sensitised TiO_2 electrodes, displaying it ability to convert already deposited CdSe QDs to $Cu_{2-x}Se$ QDs to PbSe QDs, showing a strong change in the resulting absorption spectra. We also used cation exchange as a means to produce core/shell PbS/CdS QDs from PbS sensitised TiO_2

electrodes and have investigated its effect upon the resulting photocurrent response, which surprisingly showed a decrease in current.

References

91. Reiss, P.; Bleuse, J.; Pron, A., Highly Luminescent CdSe/ZnSe Core/Shell Nanocrystals of Low Size Dispersion. *Nano Lett* 2002, 2, 781-784.

93. Neo, M. S.; Venkatram, N.; Li, G. S.; Chin, W. S.; Ji, W., Synthesis of PbS/CdS Core-Shell Qds and Their Nonlinear Optical Properties. *Journal of Physical Chemistry C* 2010, 114, 18037-18044.

111. Jain, P. K.; Amirav, L.; Aloni, S.; Alivisatos, A. P., Nanoheterostructure Cation Exchange: Anionic Framework Conservation. *Journal of the American Chemical Society* 2010, 132, 9997-9999.

113. Justo, Y.; Goris, B.; Kamal, J. S.; Geiregat, P.; Bals, S.; Hens, Z., Multiple Dot-in-Rod PbS/CdS Heterostructures with High Photoluminescence Quantum Yield in the near-Infrared. *Journal of the American Chemical Society* 2012, 134, 5484-5487.

117. Pietryga, J. M.; Werder, D. J.; Williams, D. J.; Casson, J. L.; Schaller, R. D.; Klimov, V. I.; Hollingsworth, J. A., Utilizing the Lability of Lead Selenide to Produce Heterostructured Nanocrystals with Bright, Stable Infrared Emission. *Journal of the American Chemical Society* 2008, 130, 4879-4885.

119. Justo, Y.; Sagar, L. K.; Flamee, S.; Zhao, Q.; Vantomme, A.; Hens, Z., Less Is More. Cation Exchange and the Chemistry of the Nanocrystal Surface. *ACS Nano* 2014.

120. Zhao, H.; Chaker, M.; Wu, N.; Ma, D., Towards Controlled Synthesis and Better Understanding of Highly Luminescent PbS/CdS Core/Shell Quantum Dots. *J. Mater. Chem.* 2011, 21.

121. Zhao, H.; Wang, D.; Zhang, T.; Chaker, M.; Ma, D., Two-Step Synthesis of High-Quality Water-Soluble near-Infrared Emitting Quantum Dots Via Amphiphilic Polymers. *Chemical Communications* 2010, 46.

191. Zillner, E.; Kavalakkatt, J.; Eckhardt, B.; Dittrich, T.; Ennaoui, A.; Lux-Steiner, M., Formation of a Heterojunction by Electrophoretic Deposition of CdTe/CdSe Nanoparticles from an Exhaustible Source. *Thin Solid Films* 2012, 520, 5500-5503.

195. Ning, Z.; Ren, Y.; Hoogland, S.; Voznyy, O.; Levina, L.; Stadler, P.; Lan, X.; Zhitomirsky, D.; Sargent, E. H., All-Inorganic Colloidal Quantum Dot Photovoltaics Employing Solution-Phase Halide Passivation. *Advanced Materials* 2012, 24, 6295-6299.

221. Lee, Y.-L.; Chang, C.-H., Efficient Polysulfide Electrolyte for Cds Quantum Dot-Sensitized Solar Cells. *Journal of Power Sources* 2008, 185, 584-588.

235. Pan, Z.; Zhang, H.; Cheng, K.; Hou, Y.; Hua, J.; Zhong, X., Highly Efficient Inverted Type-I Cds/Cdse Core/Shell Structure Qd-Sensitized Solar Cells. *ACS Nano* 2012, 6, 3982-3991.

236. Santra, P. K.; Nair, P. V.; George Thomas, K.; Kamat, P. V., $Cuins_2$-Sensitized Quantum Dot Solar Cell. Electrophoretic Deposition, Excited-State Dynamics, and Photovoltaic Performance. *The Journal of Physical Chemistry Letters* 2013, 4, 722-729.

245. de la Fuente, M. S.; Sánchez, R. S.; González-Pedro, V.; Boix, P. P.; Mhaisalkar, S. G.; Rincón, M. E.; Bisquert, J.; Mora-Seró, I., Effect of Organic and Inorganic Passivation in Quantum-Dot-Sensitized Solar Cells. *The Journal of Physical Chemistry Letters* 2013, 4, 1519-1525.

247. Brown, P.; Kamat, P. V., Quantum Dot Solar Cells. Electrophoretic Deposition of CdSe–C_{60} Composite Films and Capture of Photogenerated Electrons with Nc_{60} Cluster Shell. *Journal of the American Chemical Society* 2008, 130, 8890-8891.

248. Smith, N. J.; Emmett, K. J.; Rosenthal, S. J., Photovoltaic Cells Fabricated by Electrophoretic Deposition of CdSe Nanocrystals. *Appl. Phys. Lett.* 2008, 93, 3.

249. Salant, A.; Shalom, M.; Hod, I.; Faust, A.; Zaban, A.; Banin, U., Quantum Dot Sensitized Solar Cells with Improved Efficiency Prepared Using Electrophoretic Deposition. *ACS Nano* 2010, 4, 5962-5968.

252. Jia, S.; Banerjee, S.; Herman, I. P., Mechanism of the Electrophoretic Deposition of Cdse Nanocrystal Films: Influence of the Nanocrystal Surface and Charge. *Journal of Physical Chemistry C* 2008, 112, 162-171.
253. Cirillo, M.; Strubbe, F.; Neyts, K.; Hens, Z., Thermal Charging of Colloidal Quantum Dots in Apolar Solvents: A Current Transient Analysis. *ACS Nano* 2011, 5, 1345-1352.
311. Ning, Z.; Voznyy, O.; Pan, J.; Hoogland, S.; Adinolfi, V.; Xu, J.; Li, M.; Kirmani, A. R.; Sun, J.-P.; Minor, J.; Kemp, K. W.; Dong, H.; Rollny, L.; Labelle, A.; Carey, G.; Sutherland, B.; Hill, I.; Amassian, A.; Liu, H.; Tang, J.; Bakr, O. M.; Sargent, E. H., Air-Stable N-Type Colloidal Quantum Dot Solids. *Nat. Mater.* 2014, 13, 822-828.
316. Zhao, Y.; Burda, C., Development of Plasmonic Semiconductor Nanomaterials with Copper Chalcogenides for a Future with Sustainable Energy Materials. *Energy & Environmental Science* 2012, 5, 5564-5576.
317. Besra, L.; Liu, M., A Review on Fundamentals and Applications of Electrophoretic Deposition (Epd). *Progress in Materials Science* 2007, 52, 1-61.
318. Corni, I.; Ryan, M. P.; Boccaccini, A. R., Electrophoretic Deposition: From Traditional Ceramics to Nanotechnology. *Journal of the European Ceramic Society* 2008, 28, 1353-1367.
319. Salant, A.; Shalom, M.; Tachan, Z.; Buhbut, S.; Zaban, A.; Banin, U., Quantum Rod-Sensitized Solar Cell: Nanocrystal Shape Effect on the Photovoltaic Properties. *Nano Lett* 2012, 12, 2095-2100.
320. Chen, J.; Lei, W.; Li, C.; Zhang, Y.; Cui, Y.; Wang, B.; Deng, W., Flexible Quantum Dot Sensitized Solar Cell by Electrophoretic Deposition of CdSe Quantum Dots on ZnO Nanorods. *Physical Chemistry Chemical Physics* 2011, 13, 13182-13184.
321. Santra, P. K.; Kamat, P. V., Tandem-Layered Quantum Dot Solar Cells: Tuning the Photovoltaic Response with Luminescent Ternary Cadmium Chalcogenides. *Journal of the American Chemical Society* 2012, 135, 877-885.
322. Lhuillier, E.; Hease, P.; Ithurria, S.; Dubertret, B., Selective Electrophoretic Deposition of Cdse Nanoplatelets. *Chem. Mat.* 2014, 26, 4514-4520.
323. Parsi Benehkohal, N.; González-Pedro, V.; Boix, P. P.; Chavhan, S.; Tena-Zaera, R.; Demopoulos, G. P.; Mora-Seró, I., Colloidal PbS and PbSes Quantum Dot Sensitized Solar Cells Prepared by Electrophoretic Deposition. *The Journal of Physical Chemistry C* 2012, 116, 16391-16397.
324. Poulose, A. C.; Veeranarayanan, S.; Varghese, S. H.; Yoshida, Y.; Maekawa, T.; Sakthi Kumar, D., Functionalized Electrophoretic Deposition of CdSe Quantum Dots onto TiO_2 Electrode for Photovoltaic Application. *Chem. Phys. Lett.* 2012, 539–540, 197-203.
325. Wang, H.; Bai, Y.; Zhang, H.; Zhang, Z.; Li, J.; Guo, L., CdS Quantum Dots-Sensitized TiO_2 Nanorod Array on Transparent Conductive Glass Photoelectrodes. *The Journal of Physical Chemistry C* 2010, 114, 16451-16455.
326. Shalom, M.; Dor, S.; Rühle, S.; Grinis, L.; Zaban, A., Core/Cds Quantum Dot/Shell Mesoporous Solar Cells with Improved Stability and Efficiency Using an Amorphous Tio_2 Coating. *The Journal of Physical Chemistry C* 2009, 113, 3895-3898.
327. Bang, J. H.; Kamat, P. V., Quantum Dot Sensitized Solar Cells. A Tale of Two Semiconductor Nanocrystals: Cdse and Cdte. *ACS Nano* 2009, 3, 1467-1476.
328. Kongkanand, A.; Tvrdy, K.; Takechi, K.; Kuno, M.; Kamat, P. V., Quantum Dot Solar Cells. Tuning Photoresponse through Size and Shape Control of CdSe–TiO_2 Architecture. *Journal of the American Chemical Society* 2008, 130, 4007-4015.
329. Lee, H. J.; Chen, P.; Moon, S.-J.; Sauvage, F.; Sivula, K.; Bessho, T.; Gamelin, D. R.; Comte, P.; Zakeeruddin, S. M.; Seok, S. I.; Grätzel, M.; Nazeeruddin, M. K., Regenerative PbS and CdS Quantum Dot Sensitized Solar Cells with a Cobalt Complex as Hole Mediator. *Langmuir* 2009, 25, 7602-7608.

330. Jun, H. K.; Careem, M. A.; Arof, A. K., Investigation of Multilayered Quantum Dot-Sensitized Solar Cells with Different Zn Chalcogenide Passivation Layers. *J. Appl. Electrochem.* 2014, 44, 977-988.
331. Shen, Q.; Kobayashi, J.; Diguna, L. J.; Toyoda, T., Effect of Zns Coating on the Photovoltaic Properties of CdSe Quantum Dot-Sensitized Solar Cells. *Journal of Applied Physics* 2008, 103, 084304.
332. Yang, S.-m.; Huang, C.-h.; Zhai, J.; Wang, Z.-s.; Jiang, L., High Photostability and Quantum Yield of Nanoporous TiO_2 Thin Film Electrodes Co-Sensitized with Capped Sulfides. *J. Mater. Chem.* 2002, 12, 1459-1464.
333. Guijarro, N.; Campina, J. M.; Shen, Q.; Toyoda, T.; Lana-Villarreal, T.; Gomez, R., Uncovering the Role of the Zns Treatment in the Performance of Quantum Dot Sensitized Solar Cells. *Physical Chemistry Chemical Physics* 2011, 13, 12024-12032.
334. Yun, H. J.; Paik, T.; Edley, M. E.; Baxter, J. B.; Murray, C. B., Enhanced Charge Transfer Kinetics of CdSe Quantum Dot-Sensitized Solar Cell by Inorganic Ligand Exchange Treatments. *ACS Applied Materials & Interfaces* 2014, 6, 3721-3728.
335. Guyot-Sionnest, P., Electrical Transport in Colloidal Quantum Dot Films. *The Journal of Physical Chemistry Letters* 2012, 3, 1169-1175.
336. Stenutz, R., Dielectric Constants and Refractive Index. http://www.stenutz.eu/chem/solv23.php, 2013.
337. Sigma-Aldrich. *Dichloromethane Sigma-Aldrich* [Online], 2015.
338. Sigma-Aldrich. 1,2-Dichlorobenzene *Sigma - Aldrich* [Online], 2014.
339. Aldrich, S.-. 1,2-Dichloroethane *Sigma - Aldrich* [Online], 2014.
340. McDaniel, H.; Fuke, N.; Makarov, N. S.; Pietryga, J. M.; Klimov, V. I., An Integrated Approach to Realizing High-Performance Liquid-Junction Quantum Dot Sensitized Solar Cells. *Nature Communications* 2013, 4, 10.
341. Huang, G.-W.; Chen, C.-Y.; Wu, K.-C.; Ahmed, M. O.; Chou, P.-T., One-Pot Synthesis and Characterization of High-Quality Cdse/Znx (X=S, Se) Nanocrystals Via the Cdo Precursor. *J. Cryst. Growth* 2004, 265, 250-259.
342. Shankar, K.; Bandara, J.; Paulose, M.; Wietasch, H.; Varghese, O. K.; Mor, G. K.; LaTempa, T. J.; Thelakkat, M.; Grimes, C. A., Highly Efficient Solar Cells Using Tio_2 Nanotube Arrays Sensitized with a Donor-Antenna Dye. *Nano Letters* 2008, 8, 1654-1659.

Chapter 5 Quantum Dot Solar Cell Fabrication and Testing

5.1 Introduction

Over the past 10 years, a rapid development of research involving the incorporation of colloidal quantum dots into a range of third generation novel photovoltaic devices has taken place.[174, 203, 343, 344] The highest efficiencies to date have been reported from two specific designs, QDSSCs[233-235, 238] and DHCQD cells,[196, 311] which show power conversion efficiencies (PCE) of over 6 %, and have shown a steady incremental rising year on year since their appearance.[345 346] Therefore, these devices deserve a particular attention.

QDSSCs consists of two electrodes, a photoanode and a counter electrode, which are immersed in an electrolyte. In chapter 4, the focus of the work was sensitisation of TiO_2 electrodes with quantum dots. In this chapter, we would like to focus on production of the TiO_2 electrode prior to sensitisation, fabrication of the counter electrode and finally QDSSC testing.

TiO_2 films deposited upon a transparent conductive oxide (TCO) coated glass is at present the most highly efficient photoanode in use for QDSSCs,[234] though a range of other large band gap semiconductors show promising results.[347] The exact structure of these TiO_2 films is fundamentally important to the efficiency of the photoanode with films commonly being produced from either commercial sol gel pastes bought from a number of DSSC companies specialising in the production of these pastes, or can be produced in house. These pastes consist of a sol of nanoparticulate TiO_2, normally between the size ranges of 10 to 40 nm in diameter, which are deposited usually using a doctor blading approach and then put though a precise heat treatment at temperature up to 500 °C. This heat treatment is necessary to remove all other components of the paste, producing a film consisting of sintered TiO_2 nanoparticles. The film when formed correctly should consist of a nanoporous coating of TiO_2 with thicknesses of up to 20 µm. It should show excellent electrical contact to the TCO material below and mechanical robustness. The crystal phase of the TiO_2 are usually created from anatase particles, though it has also been shown that a mix of rutile and anatase TiO_2 can in fact produce the optimal electrode.[348]

In addition to the layer of 20 nm TiO_2 particles, it is optimal to also include the use of larger 200 - 400 nm particles of TiO_2 at the top most layer of the photoaniode. This is due to the light scattering properties that these much larger particles in fact produce, which has the effect of

reflecting light initially not absorbed by the photoaniode back into it, effectively increasing the absorption coefficient of the cell, and therefore increase the short circuit current of the cell.[349]

The highest efficiency QDSSCs reported utilise a polysulphide electrolyte, as opposed to the commonly utilised triiodide/iodide electrolyte found in DSSC designs.[221, 222] This is due to stability issues regarding oxidation of QDs by iodide/triiodide based electrolytes, strongly reducing cell efficiency and stability, indicated by the loss in QD absorption from exposure to this electrolyte.[221] Therefore, if a cell is to be efficient with utilising a polysulphide electrolyte, an appropriately catalytically active counter electrode must be a used. This is an important area of optimization regarding QDSSCs with a range of electrodes being tested at present including Au[226], Co_2S[229], CuS[350], Cu_2S[227, 351-353] and PbS[232, 285, 354, 355]. Sulphur based electrodes at present have shown the greatest activity, though pose issues regarding stability, due to dissolution of metal based sulphides into the electrolyte, causing loss of activity quickly over time, and complete loss of activity in some cases. A resulting fabrication strategy to combat this issue has become available using metal foils of the target metal, which has been conditioned to produce a film of the desired sulphide upon the surface. [221, 285] This therefore means that as the active area of the electrode is dissolved into the electrode it is continually regenerated from an interaction with the polysulphide electrolyte. Therefore, in this project, Pb and Cu metal foils have been utilised to produce PbS and Cu_2S counter electrodes.

DHCQD cells are fabricated very differently relative to QDSSCs but are similar in structure.[183] The cell consists of a thin film of a large band gap semiconductor of n-type, usually ZnO or TiO_2 which is deposited on the surface of the TCO coated glass, after which a thin film of CQDs (nearly exclusively PbS)are deposited upon the surface and finally a back electrode of a large work function metal, usually gold, is deposited thus producing a thin film solid state solar cell. Though ZnO has shown some excellent results, for this work,[204] TiO_2 was chosen due to its more accessible production. TiO_2 is used since it is a wide band gap semiconductor, showing high stability, simple deposition approaches and appropriate VB and CB position to allow charge collection from the CQD absorber layer (usually PbS). Also important to this application, is that anatase- TiO_2 shows intrinsic conductivity of n-type and so allows the formation of a p-n junction between the p-type PbS and n-type TiO_2. This n-type character is due to the presence of sub-stoichiometry resulting in an excess of Ti atoms and produces two crystal defects in the resulting lattice, O vacancies and Ti interstitials. [160]

The TiO_2 films of between 300 to 600 nm in thickness have been found to be optimal for DHCQD cells and in literature are produced through spin coating.[183] Specifically, commercial TiO_2 pastes

used normally for DSSC fabrication are diluted with solvents found in these pastes (Terpineol, Heptanol, etc) to concentrations of 10-20% v/v of their original concentrations.[183] These are then deposited upon the TCO glass using 1000 to 2000 rpm producing a thin film of paste upon the surface of the TCO glass. This is then put through an identical heating program used for DSSC TiO_2, producing the desired nano-porous film of TIO_2.

After deposition of the TiO_2, a layer of CQD is deposited upon the surface of the electrode. These QDs are initially coated in a layer of long chain organic ligands (e.g. oleic acid), which are then exchanged with a short chain polar ligand (e.g. 3-mercaptopronic acid). After the exchange takes place, the spacing between QDs is reduced allowing for better charge transport, due to the much shorter ligand. To produce a continuous layer of these CQDs, which show no cracks in the film, the ligand exchange process must be repeated a number of times, each time only depositing a minimal thickness of QDs (10-20 nm). This is because of film shrinkage after the ligand exchange, which causes cracks and voids in the film. Gradually over a number of cycles of deposition, a film of thicknesses of between 250 and 400 nm is deposited of the QDs, which has been found to be the optimal trade-off between maximum photon absorption and effective charge separation. The most commonly reported process to achieve this deposition is through either dip coating or spincoating.

Another type of QD based cell that has shown a level of success is the QD doped–organic solar cell.[247, 356-358] Most of these designs use CQDs as an additive to an already successful organic solar cell, as a means to improve overall PV efficiency, by increasing the light harvesting ability of the cell, though relatively recent work has become much more similar to DHCQD cells, in which a QD film is used as absorber and transportation layer.[96, 359, 360] After identifying the relatively unexplored category of discotic liquid crystal (DLC) solar cells,[268-270, 361] it was decided that it would be interesting to explore the effect of QD incorporation into these compounds to attempt to produce an effective and novel PV cell. This was due to a number of recent publications demonstrating novel interactions between liquid crystals and a range of nanomaterials such as gold NPs,[362] graphene[363] and quantum dots.[273-278]

The two discotic liquid crystals that have been studied for this project are 2,3,6,7,10,11,Hexahexyloxy-triphenylene (H6TP) (Figure 5.1 B) and 1,5-dihydroxy-2,3,6,7-tetrakis(3,7-dimethyloctyloxy)-9,10-anthraquinone (RTAQ) (Figure 5.1 A). H6TP is a member of the triphenylene family and at elevated temperature (between 55-90 °C to 120 °C) exists in a columnar liquid crystal phase while at room temperature it is in the crystalline solid phase.[257-259] It is a wide band gap semiconductor showing little visible absorption. RTAQ is a member of the anthraquinone group of liquid crystal[255, 363-365] chemical family and is a room temperature discotic liquid crystal showing a discotic liquid phase below 115.7 °C[364] above which is the isotropic phase. It shows strong absorption in the visible range and was firstly synthesised in 2008.[364] To date a QD DLC cell has never been tested, while work showing the incorporating of QDs into triphenylene DLCs has shown a positive effect upon the overall conductivity.[273]

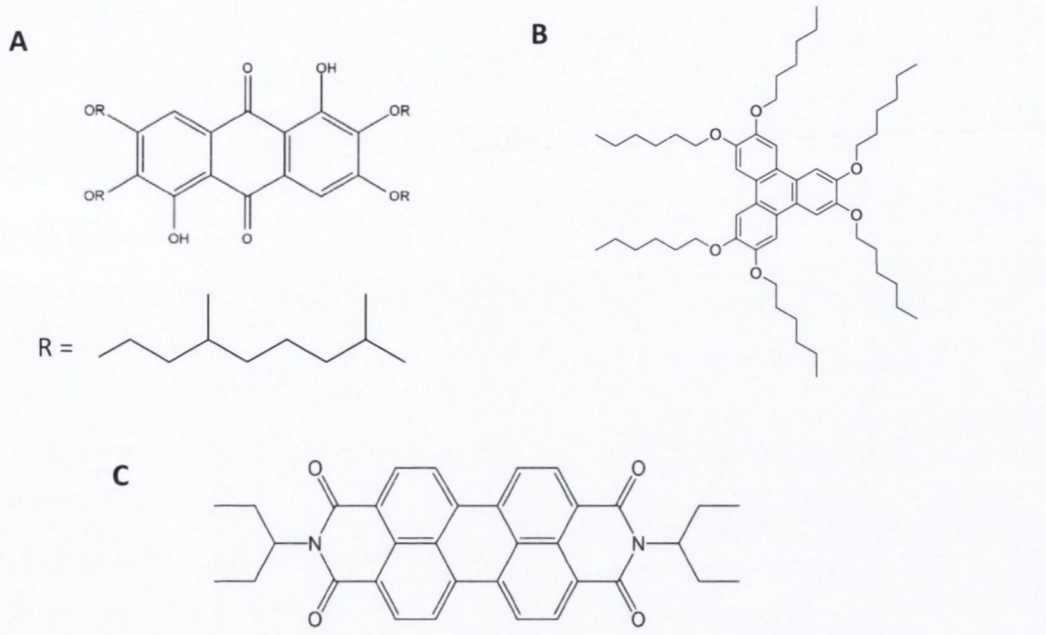

Figure 5.1 The two liquid crystals utilised in this study were RTAQ (1,5-dihydroxy-2,3,6,7-tetrakis(3,7-dimethyloctyloxy)-9,10-anthraquinone (image A), and H6TP (hexahexyloxy-triphenylene)(image B). While when constructing a DLC solar cell, PDI, a soluble perylene diamide, (N,N9-bis(1-ethylpropyl)-3,4,9,10-perylenebis) (image C) was utilised as an acceptor.

Therefore, for this part of our work we plan to investigate the electrical conductivity properties of DLCs doped with a range of QDs with different ligand shells and band gaps. Then we aim to build new PV cells incorporating QD doped DLCs. The first simple PV cell design proposed incorporate discotic liquid crystal and quantum dots, which will be spincoated upon a glass slide of fluorine, doped tin oxide coated glass. For this device, it is expected that a donor acceptor system will be set up between the QDs and the DLC, within which the electrons will migrate through one material to the aluminium back electrode, while holes will migrate towards the FTO front electrode. The second design will incorporate the use of a second organic molecule,

a soluble perylene diamide (PDI), (N,N9-bis(1-ethylpropyl)-3,4,9,10-perylenebis) (Figure 5.1 C). This has been shown to act as an acceptor for other DLC molecules such as HBC-PHC12 (dodecylphenyl-substituted hexabenzocoronene) in DLC solar cell designs and possess a high charge mobility.[269] Perylene diimides have also shown the ability to act as efficient photosensitizer to ITO in conjunction with CdSe QDs,[366] while efficient FRET processes have been demonstrated between CdSe/ZnS and other highly substituted perylene diimide.[367] [368]

5.2 Aim

The focus of this work was the design, fabrication and testing of three different designs of QD based solar cells, a quantum dot sensitised solar cell (QDSSCs), a depleted heterojunction colloidal quantum dot (DHCQD) solar cell and a novel organic solar cell design based upon DLC. Regarding QDSSCs, three different CE electrodes, Pt, PbS and Cu_2S, will be fabricated and analysed after which they will be tested in a complete QDSSC design. Multi layered films of TiO_2 will be developed and characterised as photoaniodes for the QDSSC cells also. Finally, photoaniodes incorporating a range of QDs deposited through the EPD discussed in chapter 5 approach will be tested. Concerning the DHCQD cells, we will demonstrate the use of selective etching of FTO substrates as a means to produce multiple cells upon a single FTO slide. A unique approach to TiO_2 thin film deposition will be then demonstrated using heavily diluted TiO_2 commerically sourced pastes. This will then be followed by QD deposition through the development of a novel dip coating approach involving ligand exchange, enabling the deposition of PbS, CdSe and CdSe/CdTe QDs. Subsequently, the cell will be completed through selective gold deposition to produce the completed DHCQD cell design, with efficiency characterisation of the resulting devices. Finally, regarding DLC cells, we will firstly characterise the discotic liquid crystals H6TP and RTAQ in solution and in solid phase. This will then be followed by fabrication of a range of DLC composites, created between a range of QDs, ligands and elemental Se to determine the effects upon the resulting optical, electrical properties of these films. Following this, we plan to investigate a range of possible DLC cell designs, involving the incorporation of PDI as an acceptor in some with the aim to produce a working device.

5.3 QDSSC Cells

The first type of quantum dots solar cell we will focus on is the quantum dot sensitised solar cell (QDSSC) (Chapter 1, Figure 1.13). The studies carried out have has been separated into production of the photoanode and the counter electrode, followed by investigation of the resulting QDSSCs.

5.3.1 Counter Electrodes

Three different electrodes have been fabricated and tested in QDSSC designs to determine their effectiveness upon the efficiency of the cell. The electrodes examined were Pt nanoparticle on FTO, Cu_2S and PbS. The electrodes were studied by EDX, SEM, and cyclic voltammetry techniques.

5.3.1.i PbS counter electrode

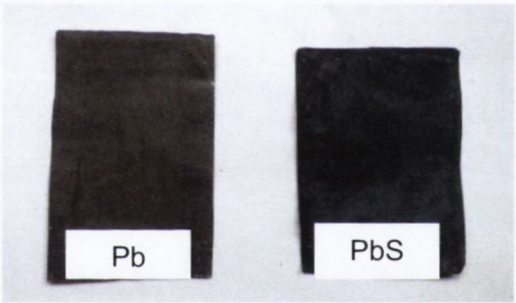

Figure 5.2 Photos of the original Pb Foil and the PbS counter electrode produced from this.

The PbS electrode is fabricated from a 0.1 mm thick Pb foil with the original foil and the produced electrode shown in Figure 5.2. The surface of the Pb foil was firstly converted from Pb foil to $PbSO_4$ through a treatment in 9 M H_2SO_4 at 60 °C for 1 hour. The electrode was then washed with deionised water and then immersed into an aqueous solution of 1 M Na_2S and 1 M S for 24 hours, producing PbS. This was then examined using SEM and EDX as shown in Figure 5.4. SEM was used to examine the change in surface morphology from the two step treatment carried out, showing the clear change in morphology going from the relative smooth surface Pb foil (Figure 5.4 A) to the roughened surface of the $PbSO_4$ (Figure 5.4 B) and then finally the strong change in morphology that occurred when converting to PbS (Figure 5.4 C). The elemental composition of the resulting PbS electrode was then examined with the use of EDX spectroscopy as shown in Figure 5.4 E, with the elemental ratio between Pb and S shown in Figure 5.4 D. The EDX showed the presence of sulphur in the spectra, while the resulting ratio determined was 20 % S to 80 % Pb ratio, indicating the formation of a PbS surface coating upon the electrode.[285]

5.3.1.ii Cu_2S counter electrode

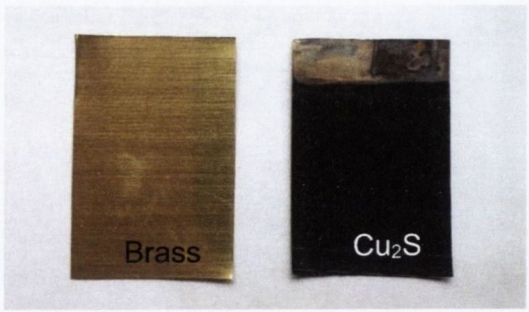

Figure 5.3 Photos of original brass foil and the produced Cu_2S coated foil produced from this.

Cu_2S electrode was produced from a 0.1 mm foil of brass (alloy 260, Cu 68.5-71.5 %, Pb 0.07 % max, Fe 0.05 % max, Zn remainder) with the brass foil and produced electrode shown in Figure 5.3. The brass foil was firstly treated in a bath of concentrated HCl solution for 30 minutes. The function of this was to etch the Zn out of the brass foil surface, leaving a purely copper surface. This produced a reactive Cu surface, which was then converted to Cu_2S. This was carried out by immersing the electrode into an aqueous solution of 1 M Na_2S and 1 M S, for 10 minutes. Following this, the electrode was analysed with the use of SEM and EDX and is shown in Figure 5.5. SEM showed a huge change in the morphology from the smooth Brass electrode (Figure 5.5 A) to Cu_2S with complex microstructure and morphology (Figure 5.5 B). EDX was then utilised to determine the elemental composition of the electrode before (Figure 5.5 C and E) and after treatment (Figure 5.5 D and F). The elemental makeup of the brass foil was determined to be Zn 31.8 % relative to Cu 68.2 % before treatment, which was then shown to convert to Cu 64 %, Zn 28.5 %, and S 7.5 % after treatment, confirming the formation of a Cu_2S surface coating. [233] Brass foil was used instead of a purely copper due to the presence Zn, which helps to form a more stable support for the Cu_2S film.

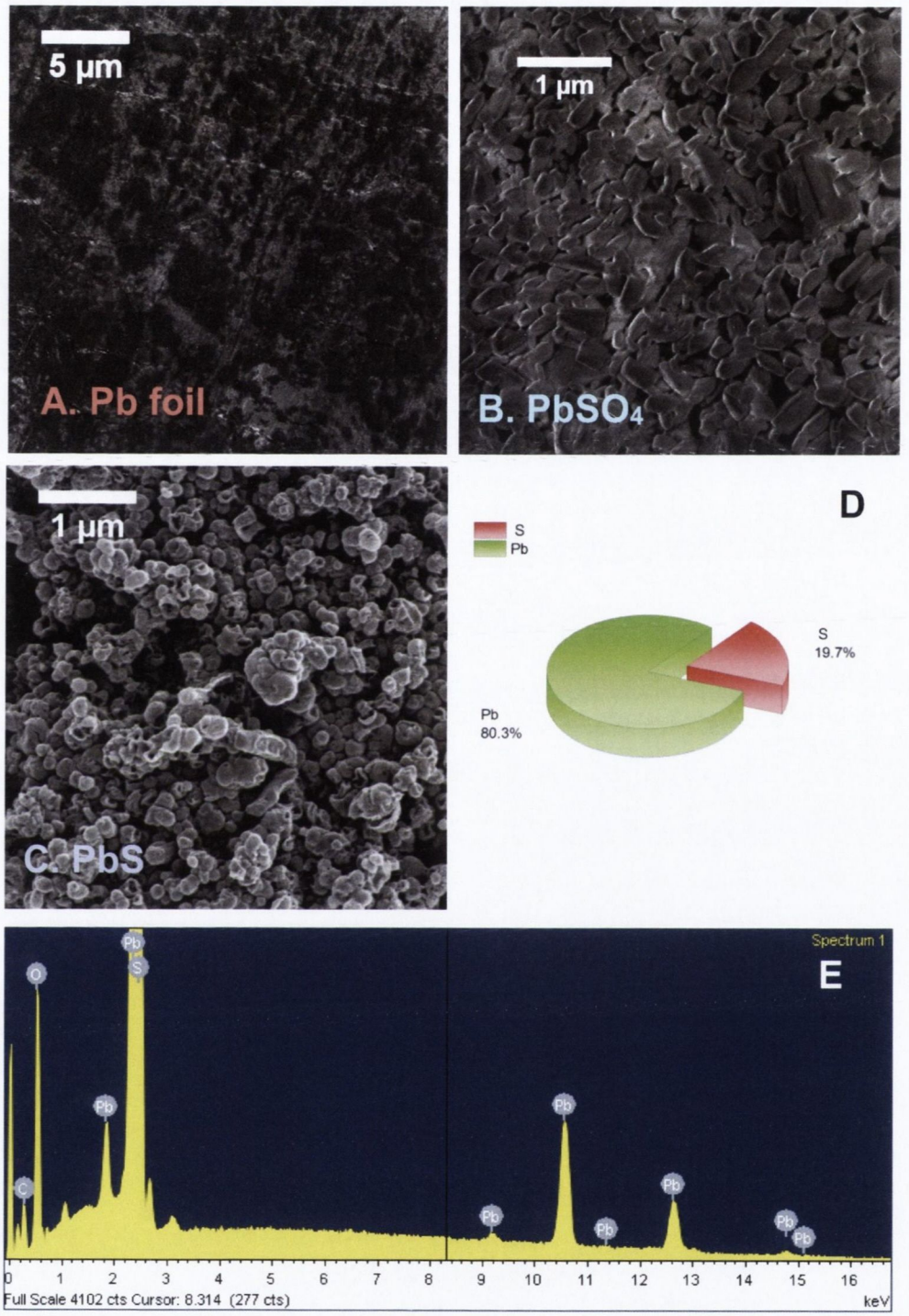

Figure 5.4 SEM images of the three stages in material as the originally purchased Pb foil (image A) is firstly converted to $PbSO_4$ (image B) and then to PbS (image C) to produce the desired PbS counter electrode. Graph D and E shows the elemental composition of the PbS film determined using EDX spectroscopy.

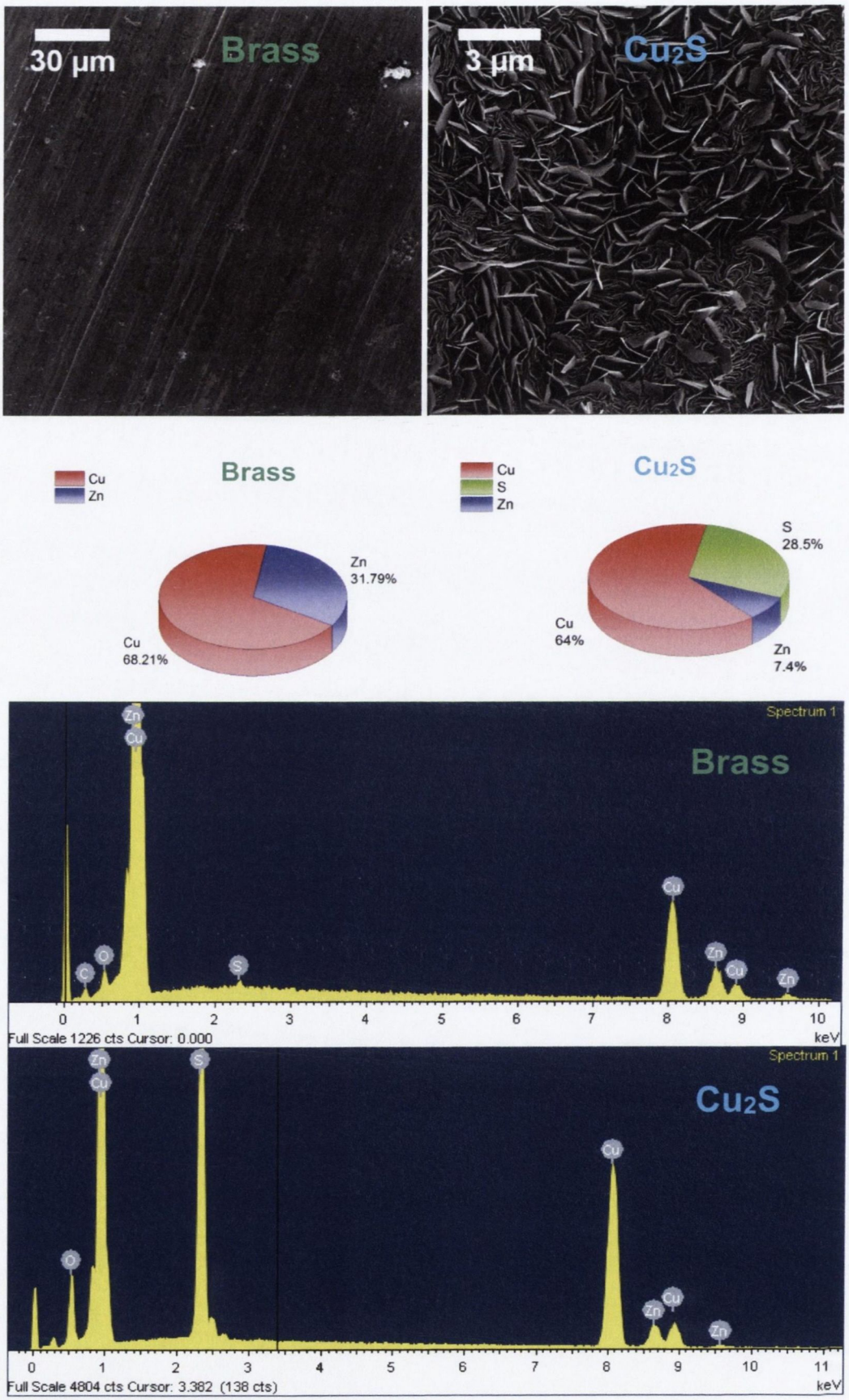

Figure 5.5 SEM images of brass foil before and after treatment to produce the Cu_2S electrode. The elemental composition of the foils was examined using EDX and compared to the original films described in the spectra and pie charts of both.

5.3.1.iii Platinum counter electrode

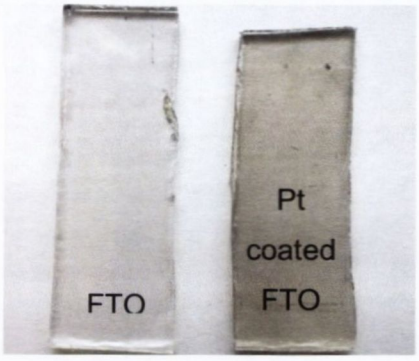

Figure 5.6 Photos showing the original FTO glass and the Pt coated FTO glass counter electrode

The Pt electrode was produced by dropcasting a solution of chloroplatinic acid upon FTO glass, which was then converted to Pt by heating to 400 °C. The resulting electrode is shown in Figure 5.6 and was characterised using SEM (Figure 5.7). We can see a thin film of Pt upon the FTO glass showing darkened areas of thicker Pt deposits and areas of lighter colour containing more dispersed Pt crystals as shown (Figure 5.7 B). The UV-Vis absorption spectra of the resulting electrode showed a featureless absorption curve, slowly increasing form longer wavelengths to shorted wavelengths.

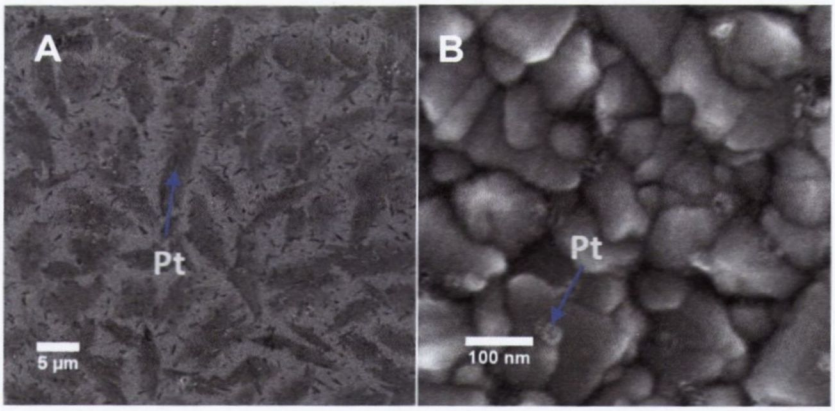

Figure 5.7 SEM of Pt coated FTO glass. Image A shows the darker distributions of the Pt on the FTO glass, with image B showing the fine details of distribution of smaller Pt crystals upon the FTO surface not fully coated.

5.3.1.iv Cyclic Voltammetry of counter electrodes

Cyclic voltammetry was then used to determine the activity of the three fabricated counter electrodes (Figure 5.8). The electrodes were tested with a scan rate of 0.05 V/s in a solution of 0.5 M KCl, 20 mM Na_2S and 5 mM S from -1 V to 0 V. The resulting graphs showed a large difference in activity between the Pt electrode and the PbS and Cu_2S electrode, with the current density being produced with Pt ranging from only - 5.22 x 10^{-4} mA/cm^2 to 1.52x 10^{-4} mA/cm^2, which when compared to Cu_2S which showed a range of to - 0.01 A/cm^2 to + 0.031 A/cm^2 ranging, while PbS showed - 0.01 mA/cm^2 to + 0.007 mA/cm^2. Thus, the metal sulphides demonstrated much higher activity than Pt, with Cu_2S showing a slightly increased activity over PbS. The reason for low activity of the Pt concerning sulphide-based electrolyte is due to sulphur poisoning of the Pt active surface, impairing the overall activity of this electrode.[369]

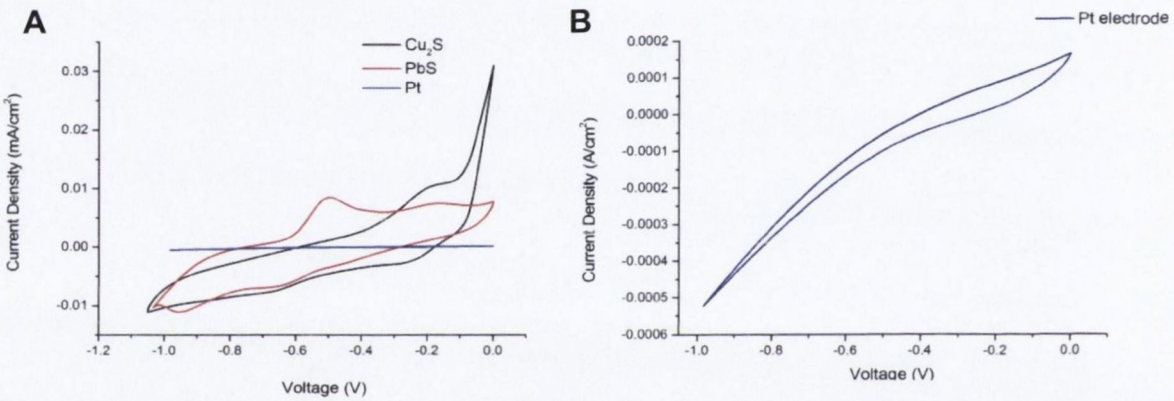

Figure 5.8 Cyclic voltammetry of three different electrodes fabricated for QDSSC cells, Cu_2S, PbS and Pt electrode. These were tested with a scan rate of 0.05 V/s in a solution of 0.5 M KCL, 20 mM Na_2S and 5 mM S. Graph A shows the combined three different electrodes, while graph B shows the Pt electrode on a reduced scale. The current ranges from 5.22 x10^{-4} mA/cm^2 to 1.52x 10^{-4} for Pt while a current of Cu_2S of + 0.031 A/cm^2 ranging to - 0.01 A/cm^2, while + 0.007 A/cm^2 to - 0.01 A/cm^{2}for PbS.

5.3.2 Photoaniode: TiO_2 Electrode

Porous TiO_2 electrodes used for QDSSCs were produced through the deposition of three distinct layers of TiO_2 on FTO coated glass and with the overall design shown in Figure 5.9. The electrode consists of an initial bulk layer of TiO_2, followed by a porous TiO_2 layer consisting of 20 mm TiO_2 anatase particles and finally a scatter layer consisting of much larger 200 nm TiO_2 particles. The fabrication of each layer is detailed below.

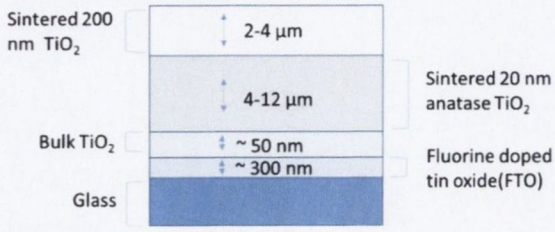

Figure 5.9 Diagram of TiO_2 electrode produced for QDSSC cells

5.3.2.i Bulk TiO_2 Layer

The first layer consisted of bulk TiO_2 layer of between 20-50 nm in thickness. This layer was deposited upon the already cleaned FTO glass surface. The function of this layer is to increase the adherence of the subsequent 20 nm TiO_2 next layer, giving an excellent electrical connection between the layers. This was deposited using an aqueous solution of 0.3 mM $TiCl_4$ that was drop cast upon the surface of the glass, and allowed to dry for 30 minutes in an oven set to 125 °C. The finished product showed a very slight change in colour, showing a minor increase in UV-Vis absorption. The resulting film thickness and distribution was then analysed with the use of SEM and is shown in Figure 5.10, determining the film thickness to be 50 nm. It was also found that the layer showed excellent adherence and near perfect surface coverage, showing no surface cracks. While this was found with the above approach, it was also established that the use of higher concentrations (~1 mM) of $TiCl_4$ solution produced a coating showing a widespread cracked surface and loss of transparency of the FTO glass and therefore a sub -optimal layer (see Appendix E, Figure 7.13). The sheet resistance of this FTO glass before coating was determined to be 25.57 Ω/m^2 using a 4-point probe setup, while after coating the sheet resistance was measured and showed an expected increase to 120.89 Ω/m^2.

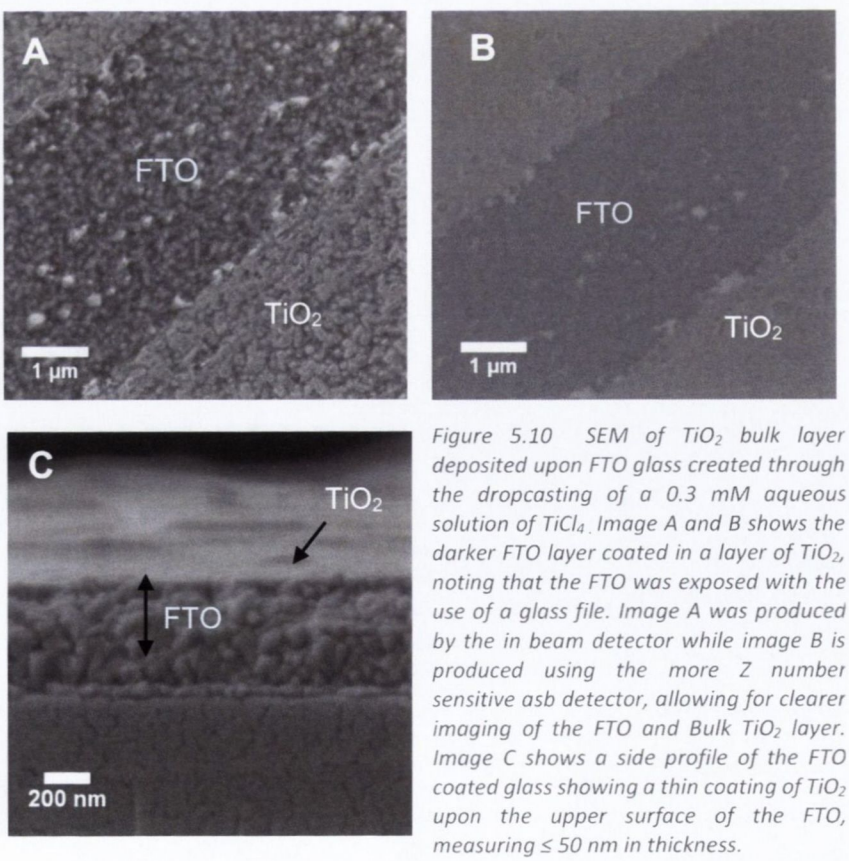

Figure 5.10 SEM of TiO_2 bulk layer deposited upon FTO glass created through the dropcasting of a 0.3 mM aqueous solution of $TiCl_4$. Image A and B shows the darker FTO layer coated in a layer of TiO_2, noting that the FTO was exposed with the use of a glass file. Image A was produced by the in beam detector while image B is produced using the more Z number sensitive asb detector, allowing for clearer imaging of the FTO and Bulk TiO_2 layer. Image C shows a side profile of the FTO coated glass showing a thin coating of TiO_2 upon the upper surface of the FTO, measuring ≤ 50 nm in thickness.

5.3.2.i Porous 20 nm TiO_2 layer

The second porous layer consisted of 20 nm anatase TiO_2 nanoparticles, which were sintering into a porous continuous film. The function of this layer is to act as the absorption layer, which can be sensitised through disposition of dye in a DSSC or in this case QDs. Therefore this layer should be relatively thick and highly porous, in order to maximize the surface area of the TiO_2 that can be sensitised, with thickness reported in literature ranging from 6-15 um.[233-235, 238]

This layer was produced using a commercial TiO_2 sol paste consisting of 20 nm nanoparticles (Dyesol, T90) which was deposited by doctor blading with the use of a screen printer, producing an electrode of 1 x 3 cm in size. After depositing this layer, the solvent was removed by heating to 125 °C, which was vital to allow the deposition of a thick layer of TiO_2, since excessive degassing can cause cracking in the film. Following this, another layer of 20 nm TiO_2 layer was deposited upon the surface of the first layer using the screen printer and was repeated a number of times, with each extra deposition increasing the thickness of the electrode. The electrode was then put through a multi-step heating process, which removed all of the organic constituents of the layer, and caused a partial fusing of the 20 nm nanoparticles into a continuous porous film.

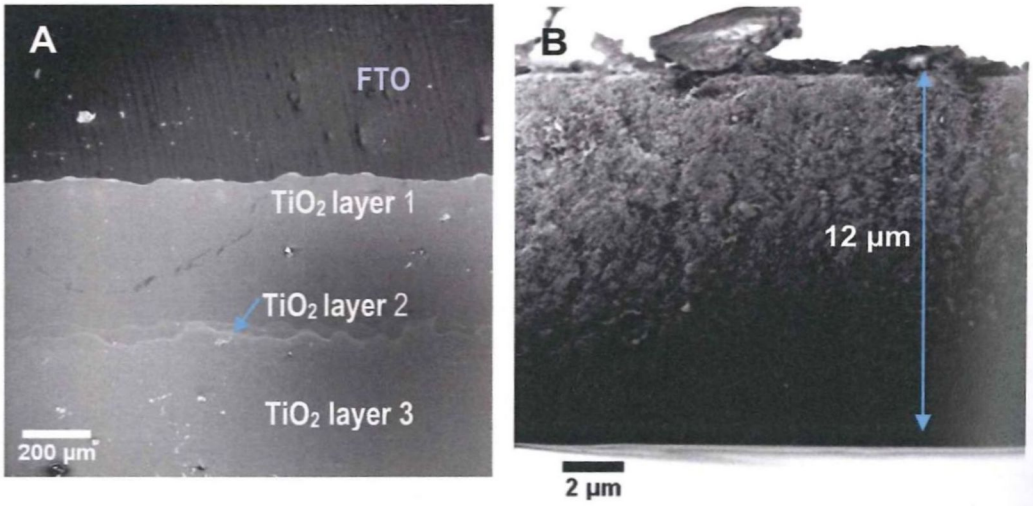

Figure 5.11 SEM images of nanoparticulate TiO_2 surface on FTO glass. Image A is looking down on the film, and shows a continuous TiO_2 coating, with no visible cracks. , this SEM also shows the overlap of three TiO_2 coatings. Image B shows a cross section of a 4 layer TiO_2 electrode which shows a continues film, measuring 12 µm in thickness.

The number of cycles of deposition was optimised since it was found that excessive deposition produced a film with numerous cracks, which crumbled off the glass surface easily or was removed under electrophoretic deposition. (Example SEMs can be seen in Appendix E, Figure 7.14) The deposited layers were examined with the use of SEM and is shown in Figure 5.11. It was found that a four layer deposition was optimal and produced a film of thickness of over 12 µm, showing a continues coverage of the glass substrate, with no visible cracks and excellent

surface adhesion. The increase in thickness as subsequent depositions were carried was also examined using UV-Vis absorption spectra and is shown in Figure 5.12. The resulting film shows a steady increase in absorption in the UV range of the spectra while still showing excellent transparency in the visible range, therefore making it ideal for light harvesting through sensitisation.

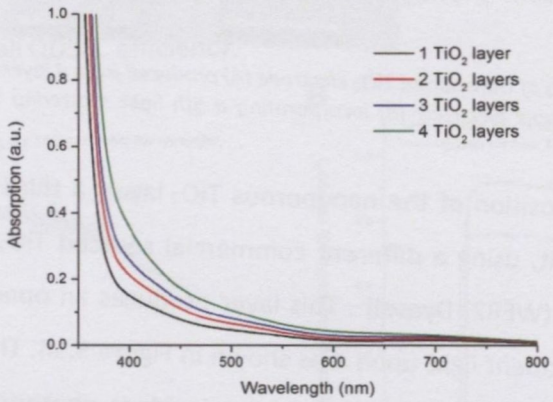

Figure 5.12 This UV-Vis absorption spectra of a FTO coated glass with a differing number of porouse TiO_2 layer deposted upon its surface. The spectra shows the change in absorption as the number of TiO_2 layers are depopsted while also expressiones the excellent transpancy of this film to visible absorption even with 4 layers which equates to a thikness of between 10-12 µm of TiO_2

TEM was also used to examine the 20 nm TiO_2 after sintering and is shown in Figure 5.13. The TiO_2 particles were confirmed to be within the 20-30 nm range (Figure 5.13 A), with particles also showing a high level of crystallinity, which was confirmed by HR TEM showing lattice fringes and which equated to a spacing of 0.165 nm which corresponds to the (211) lattice of anatase and is shown in Figure 5.11 B (Anatase phase also confirmed by Raman spectroscopy see Figure 5.24 A).

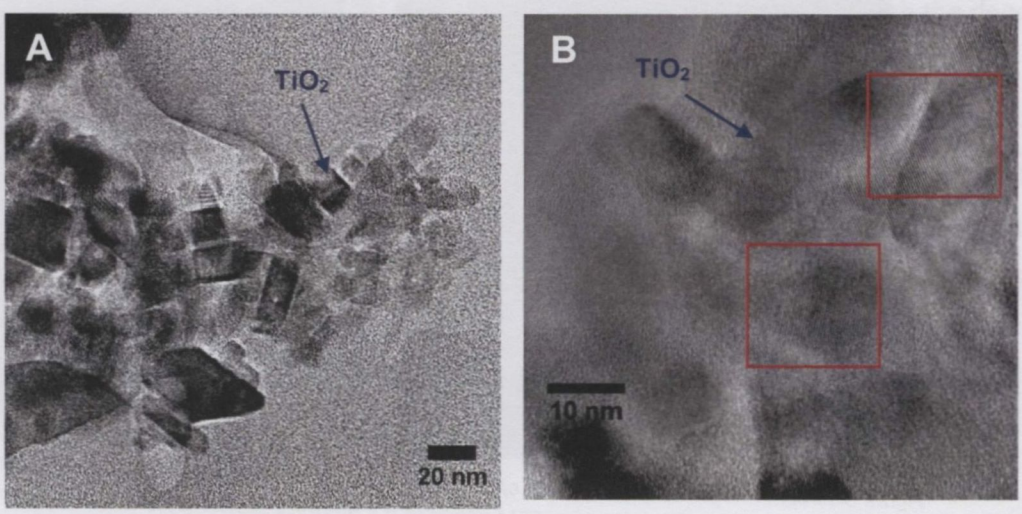

Figure 5.13 TEM images of the 20 nm TiO_2 nanoparticulate after sintering.Image A shows a number of the TiO_2 crystals, while image B shows the lattice fringes produced from these samples under HRTEM examination, showing a spacing of 0.165 nm which matches to the (211) lattice plane of anatase TiO_2.

5.3.2.ii TiO_2 Scatter Layer

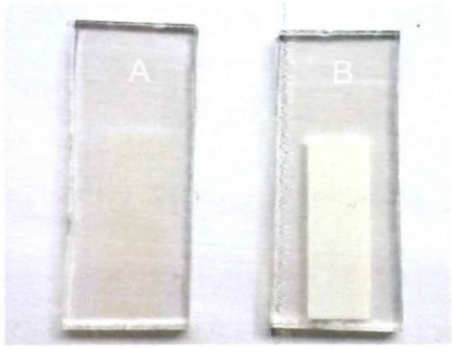

Figure 5.14 Photos of transparent TiO_2 electrode (A) produced from 4 layers of screen printed 90T Dyesol 20 nm TiO_2 paste, and the same electrode (B) incorporating a 5th light scattering layer consisting of sintered 200nm TiO_2 particles.

Following deposition of the nanoporous TiO_2 layer, a third distinct layer of TiO_2 was screen printed upon it, using a different commercial sourced TiO_2 paste consisting of 200 nm TiO_2 nanoparticles (WER2, Dyesol) . This layer produces an opaque white film, which reflects the majority of incident light upon it as shown in Figure 5.14. Therefore the function of this film is to act as a reflector/scatter layer upon incident photons which have passed through the absorber layer without absorption, scattering this light back into the absorption layer, which has the effect of increasing the light harvesting ability of the electrode. A single scatter layer was deposited upon the electrodes, and was carried out before putting the entire electrode through the already discussed heating cycle. SEM was used to image the resulting electrode and is shown in Figure 5.15. These show the scatter layer sitting on top of the porous TiO_2 film (Figure 5.15 A) , producing a layer of 3 µm in thickness , while the cubic shape of the ~ 200n m TiO_2 is shown Figure 5.15 B.

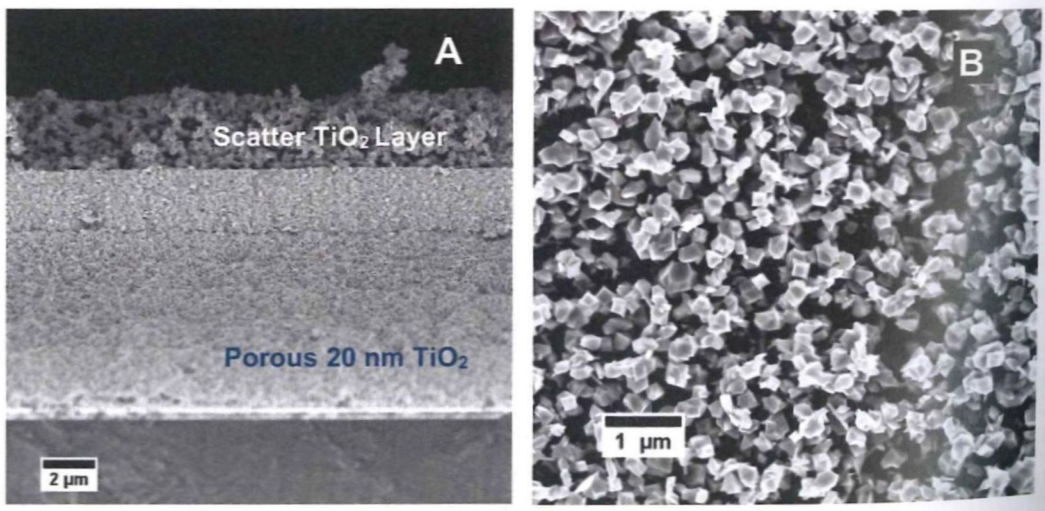

Figure 5.15 SEM image (A) of side profile of a TiO_2 electrode consisting of 10 µm thick layer, of 20 nm sintered TiO_2 nanoparticulate layers, B is a top view SEM image of a 3 µm thick scatter layer consisting of 200 nm sintered TiO_2 nanocrystals.

UV-Vis absorption spectra was used to show the resulting increase in TiO_2 electrode absorption and is shown Figure 5.16 A, displaying a huge increase across the visible spectrum. Also a demonstration of the increased photon harvesting of this electrode was carried out using photocurrent response and is shown in Figure 5.16 B. This demonstrations an impressive increase in photocurrent from 0.56 mA/cm^2 to 0.71 mA/cm^2 when comparing two TiO_2 electrodes, with and without a TiO_2 scatter layer, both of which electrodes were sensitised with CdSe QD. This equates to an increase of 27 % in photocurrent which also should result in a similar increase in overall QDSSC efficiency.

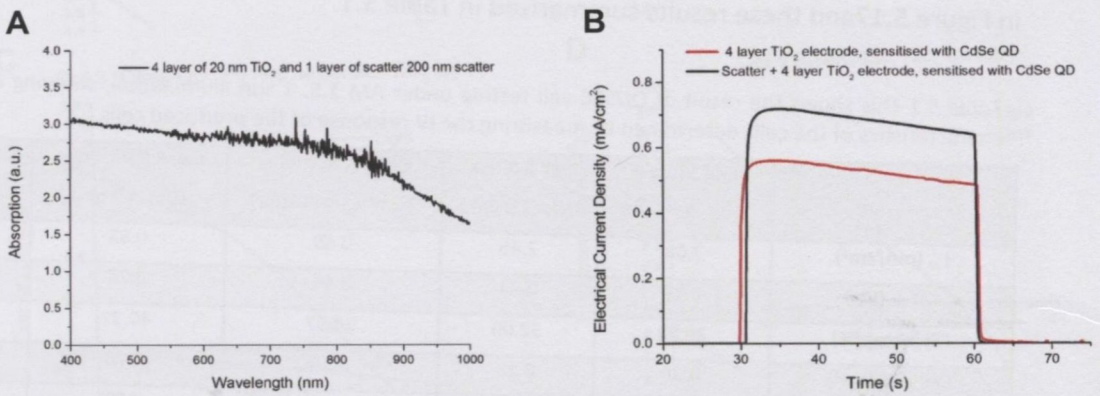

Figure 5.16 Image A shows the UV-Vis absorption spectra of TIO_2 electrode with scatter layer, demonstrating the large absorption of these electrodes. Image B shows the photocurrent response of CdSe QD (4.4 nm) sensitised TiO_2 showing the effect of the inclusion of the scatter layer producing an increase from 0.56 mA/cm^2 to 0.71 mA/cm^2producing a 27% increase in current

5.3.2.iii Post treatment

It is also commonly reported[234] that an excellent final post treatment to carry out on TiO_2 electrodes after deposition and sintering is to immersing the electrode into a solution of 20 mM $TiCl_4$ solution. This has been reported to increase the workfunction of the TiO_2 layer, and therefore increase the efficiency of the electrode when tested in cells, through the deposition of a thin film of bulk TIO_2 upon the electrode. [370] Therefore after treating an electrode in this manner by leaving it immersed in the solution for 10 minutes, sensitization of the electrode was then attempted using electrophoretic deposition. Unfortunately, it was found that a large drop in CdSe QD loading occurred. It seems due to the post treatment the electrophoretic deposition process becomes far less successful, therefore, this approach was not utilised further in TiO_2 electrode fabrication.

5.3.3 IV Testing of QDSSC Solar Cells

5.3.3.i IV testing of Closed QDSSC Cells

QDSSC cells were fabricated from counter electrodes, TiO_2 photoaniodes and a polysulphide electrolyte composed of an aqueous solution of 2 M S and 2 M Na_2S. The photoaniode and counter electrode were separated using a 60 µm thermoplastic gasket, which was heat treated to join the two electrodes at 125 °C for 10 minutes. Following this, the cell was filled with the electrolyte using a specially designed syringe and then sealed. The cells were then immediately tested under AM 1.5 illumination with the resulting IV curves of the most successful cells shown in Figure 5.17and these results summarised in Table 5.1.

Table 5.1 This shows the result of QDSSC cell testing under AM 1.5, 1 sun illumination, showing the resulting characteristics of the cells determined by measuring the IV response of the produced cells

	Cell 1 (CdSe QDs , 4.4 nm,)	Cell 2 (CdSe QDs, 3.6 nm,)	Cell 3 (CdSe QDs, 3.6 nm, no scatter)	Cell 4 (CdS/CdSe QDs, 4.5 nm)	Cell 5 (PbS QDs, 3.2 nm)
I_{sc} (mA/cm²)	2.08	2.46	0.89	0.83	0.84
V_{oc} (V)	0.28	0.24	0.46	0.28	0.25
Fill factor (%)	38.29	32.00	24.37	40.72	43.5
Cell size (cm²)	0.28	0.28	0.28	0.28	0.28
PCE (%)	0.22	0.19	0.10	0.09	0.12

The highest efficiency closed QDSSC produced to date was cell 1 and utilised EPD oleic acid capped CdSe QDs (4.4 nm) (synthesised in section 3.3.3), producing a PCE of 0.22 % under illumination. Other CdSe based cells tested included the use of oleic acid capped 3.6 nm CdSe, which brought about a drop in PCE performance to 0.19 % due to the smaller CdSe QDs applied. It was also shown that a significant drop in efficiency occurred when utilising a TiO_2 photoaniode without a scatter layer, which is shown in cell 3, producing a PCE of 0.10 % from a CdSe QD (3.6 nm) based cells. Some of the more complex core/shell QDs have also been incorporated in QDSSC cells , though only CdS/CdSe QD cells (synthesised in section 3.3.7) showed efficiency above 0.05 % , giving a PCE of 0.09 %. Apart from Cd based QDSSCs, PbS QDs (3.2 nm) (synthesised in section 3.3.5) was also tested and produced a PCE of 0.12 %.

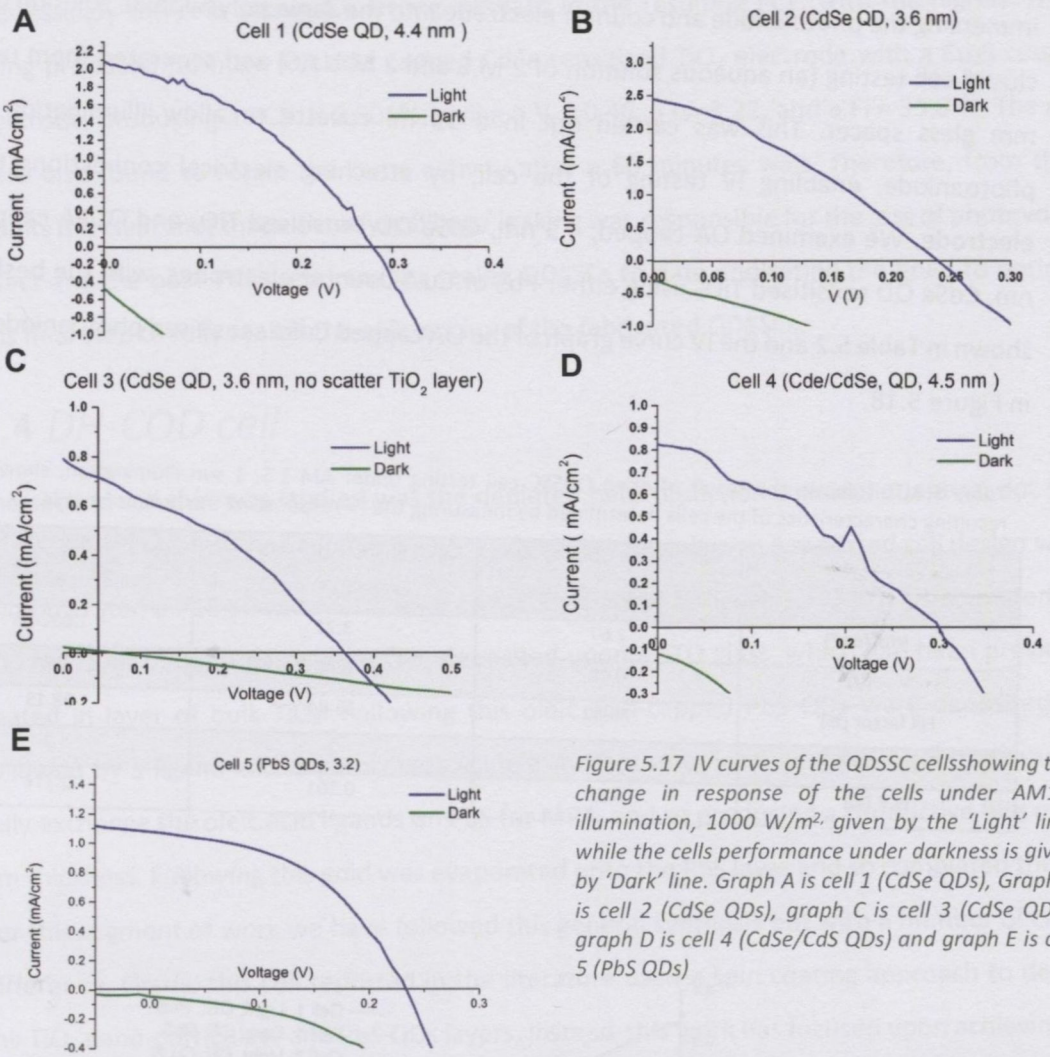

Figure 5.17 IV curves of the QDSSC cellsshowing the change in response of the cells under AM1.5 illumination, 1000 W/m², given by the 'Light' line, while the cells performance under darkness is given by 'Dark' line. Graph A is cell 1 (CdSe QDs), Graph B is cell 2 (CdSe QDs), graph C is cell 3 (CdSe QDs), graph D is cell 4 (CdSe/CdS QDs) and graph E is cell 5 (PbS QDs)

Unfortunately, only the Cu_2S counter electrode has been tested in the sealed QDSSC designs to date due to problems involving sealing of cells using the PbS counter electrode due to its fragility. All electrodes utilised a ZnS post EPD treatment of the photoaniodes to increase photocurrent. Though the novel approach of EPD to QDSSC fabrication has been demonstrated here, showing its ability to produce a wide range of QDSSC cells, the overall PCE performance achieved is below values reported in literature.

5.3.3.ii Open Cell

Aside from the lower than expected PCE achieved with closed QDSSCs, we also found that the cells lost their photovoltaic activity over the period of a few minutes after filling with polysulphide electrolyte, creating a time constraints when testing and make reproducibility challenging. This was unexpected since both the photoaniode and counter electrode had shown no loss of activity over the period of hours to days during testing, therefore we decided to investigate if it was an issue with polysulphide filling or leaking, which was causing this loss of

activity. To examine this, we decided to test the cells in an open cell design, which involved immersing the photoaniode and counter electrode into the same polysulphide solution used for closed cell testing (an aqueous solution of 2 M S and 2 M Na_2S) and separated them using a 1 mm glass spacer. This was carried out in a 15 ml cuvette to allow illumination of the photoaniode, enabling IV testing of the cell, by attaching electrical connections to each electrode. We examined OA-capped, 4.3 nm, CdSe QD sensitised TiO_2 and ODPA capped, 5.1 nm, CdSe QD sensitised TiO_2 using either PbS or Cu_2S counter electrodes, with the best results shown in Table 5.2 and the IV curve graph of the OA capped CdSe sensitised photoaniode shown in Figure 5.18.

Table 5.2 This shows the result of open QDSSC cell testing under AM 1.5, 1 sun illumination, showing the resulting characteristics of the cells determined by measuring the IV response of the produced cells

	Cell 1 (CdSe QDs , 4.3 nm, OA capped , CE: PbS)	Cell 2 (CdSe QDs, 4.3 nm, OA capped, CE: Cu_2S)	Cell 3 (CdSe QDs, 5.1 nm, ODPA capped, CE:Cu_2S)
I_{sc} (mA/cm²)	2.67	3.22	1.03E-03
V_{oc} (V)	0.48	0.46	0.44
Fill factor (%)	29.82	33.84	38.15
Cell size (cm²)	2	2	2
PCE (%)	0.38	0.501	0.172

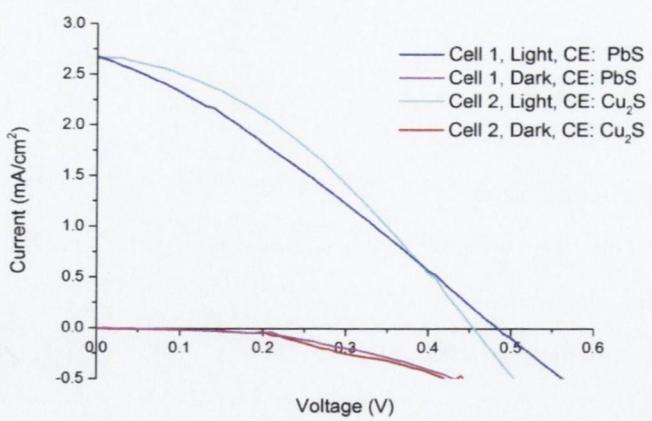

Figure 5.18 IV-curve of open cell measurement of QDSSC, using oleic acid capped, 4.3 nm, CdSe QDs, treated with 7 dip cycle of CdS following electrophoretic deposition. The open cell measurements were made using two different counter electrodes, composed of either a Cu_2S electrode on brass foil or a PbS electrode on Pb foil.

Interestingly the cells showed a strong increase in the resulting PCE, with the highest result being produced from the OA acid capped CdSe sensitised TiO_2 electrode with a Cu_2S counter electrode, producing a PCE of 0.501%, giving a V_{oc}=0.46, a I_{sc}=3.22, and a FF= 33.8 %. The cells were also found to retain the same activity after a 60 minutes wait. Therefore, from these results it is clear that that electrolyte filling / leaking was responsible for the loss of photovoltaic effect and the poor PCEs reported for sealed QDSSCs to date, indicating the need to optimise this final step to fully realise the efficiencies of the fabricated QDSSCs.

5.4 *DH-CQD cell*

The second cell that was studied was the depleted heterojunction colloidal quantum dot solar cell (DHCQD Cell). The cell produced in this project is a based upon a reported cell design which demonstrated a PCE of up to 5.1% under AM1.5 (Chapter 1, Figure 1.12).[183] This consisted of a 500 nm layer of nano-particulate TiO_2 deposited upon a FTO glass, which had been previously coated in layer of bulk TiO_2. Following this oleic acid-capped PbS QDs were deposited and followed by a ligand exchange process using 3-mecaptopropionic acid (MPA) in methanol, to fully exchange the oleic acid ligands on PbS for MPA, and so producing a conductive film of 200 nm thickness. Following this gold was evaporated onto the PbS layer and so completed the cell. For this segment of work we have followed this general synthesis but with a number of crucial difference. Firstly, this cell reported in the literature used a spin coating approach to deposit the TiO_2 nano-particulate and PbS QDs layers, instead this work has focused upon achieving the cell design with the use of more commercially viable techniques, approaches which are more easily scalable for manufacturing. Therefore, a doctor blading method was used to prepare the deposited nano-particulate layer of TiO_2 while dip coating was used to produce the desired PbS layer. We have also expanded upon the sensitisation material by also testing CdSe QDs and CdTe/CdSe QDs along with PbS QDs. Also by using doctor blading and dip coating in cell fabrication instead of spincoating, it enabled us to scale up cell fabrication allowing 14 cells to be produced upon a single piece of FTO glass. To achieve this, an intricate method of FTO glass etching was undertaken prior to TiO_2 deposition to create the desired template.

5.4.1 FTO Etch

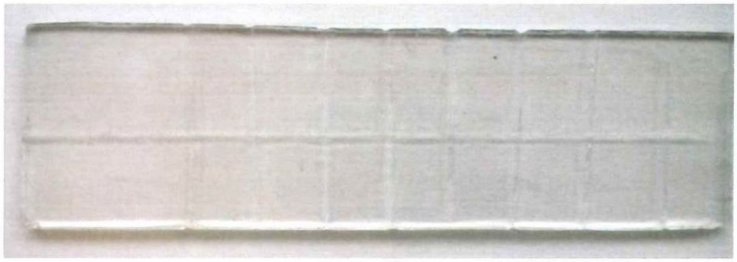

Figure 5.19 Photo of etched FTO enabling the fabrication of multiple cells upon the same glass surface

The DHCQD cell template was created through selective etching of a FTO glass (Figure 5.18). This was carried out by firstly placing a mask upon the FTO, covering sections that were desired to be left untouched. Following this an etch was carried out using Zn powder suspension in propanol, which was drop cast and allowed to dry, the electrode was then immersed into a 9 M solution of HCl for 3 minutes, resulting in removal of the FTO exposed to the solution. The etched areas showed a large increase in resistance changing from 12 Ω/sq to 2-3 KΩ/sq. Following this a glass etch pen was used to briefly treat the etched areas, producing resistance of between 200-500 KΩ/sq. The SEM was used to confirm the resulting change in FTO surface following the etch and is shown in Figure 5.20, which showed the selective removal of the conductive FTO from the glass surface due to the treatment.

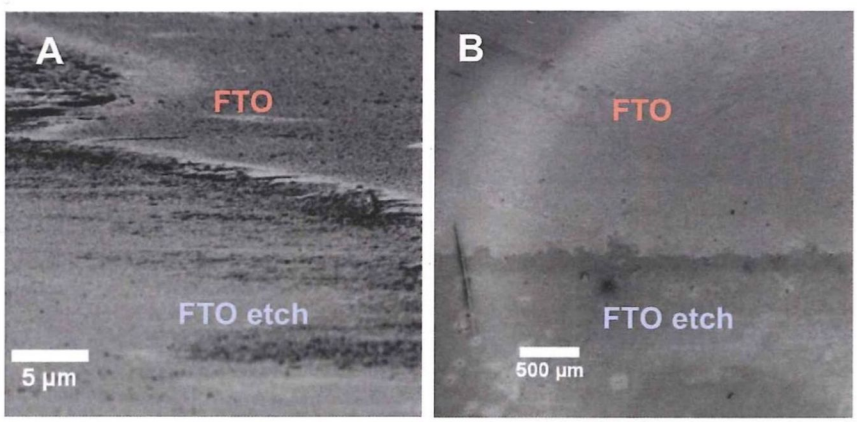

Figure 5.20 SEM images of fluorine doped tin oxide showing the change in surface structure due to the acid etch

5.4.2 TiO_2 Electrode

Following the etching of the FTO glass, TiO_2 was then deposited upon the surface. This TiO_2 film consists of two distinct layers of TiO_2. Firstly, a bulk layer of TiO_2 was deposited using the same $TiCl_4$ drop cast treatment used in the production of the TIO_2 QDSSC cell design (5.3.2.i), and bares the same primary function, to increase the adherence of the subsequent TiO_2 layer deposited. The subsequent TiO_2 layer consists of a 20 nm anatase TiO_2 particles sintered into a porous continuous layer, measure between 300 to 500 nm in thickness.

Nano particulate TiO_2 was deposited via the doctor blade approach using commercially available TiO_2 pastes with the aim to produce a well-adhered, non-cracked, transparent, uniform and sub micrometre thick film of TiO_2 on the FTO substrate. After deposition, the paste was heated to 125 °C to evaporate solvent present and put through the same heat treatment used for the QDSSC photoaniode fabrication (5.3.2.i) with the aim to sinter the TiO_2 nanoparticles into a conductive film. Three nano-particulate TiO_2 pastes were originally tested, Ethernal (20 nm anatase paste), Solaronix (8 nm anatase paste) and a Dyesol (20 nm anatase paste), though after a very brief testing period, only the Dyesol paste was further used due to its superior ability in forming the required films.

The paste was applied using a hand doctor blading approach using a simple template of 3M scotch tape of 60 μm thickness, producing films ~7-μm thickness respectively of sintered TiO_2. Following this, it was decided to dilute the concentration of TiO_2 pastes to produce a thinner film. The first approach-utilised terpineol to dilute the purchased pastes, which is a majority solvent, found in Dyesol and other commercial TiO_2 pastes and used mainly as a dispersant of the TiO_2 nanoparticles.[371] This resulted in a paste of low viscosity, which produced uneven coatings upon the FTO glass with poor glass adhesion. The next step was the utilisation of a diluent consisting of terpineol and ethyl cellulose, a commonly used ingredient that thickens the paste and increases the resulting films binding to the substrate. This resulted in films, which were transparent, uniform, and well adhered to the FTO substrate and so enabled the production of TiO_2 films of 280 nm +/- 35 nm in thickness (determined using SEM) upon FTO using pastes consisting of 3 % w/w Dyesol 90T, diluted in 23 % w/w ethyl cellulose in terpineol.

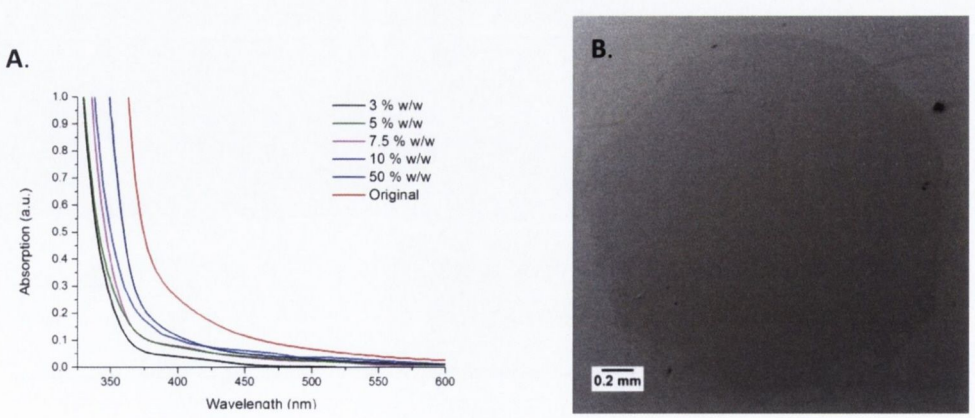

Figure 5.21 UV-Vis absorption spectra (A) of TiO_2 pastes deposited on FTO glass and SEM of the resulting diluted TiO_2 electrode (B). Graph A shows the absorption change as the TiO_2 paste used to produce the films was diluted from the original concentration to only 3 % w/w in a diluent consisting of terpineol and ethyl cellulose. Image B shows the continuous coating of TiO_2 produced from a 5 % w/w diluted TIO_2 paste upon FTO coated glass.

UV-Vis absorption (Figure 5.20) was used to demonstrate the change in transparency of TiO_2 films before and after dilution and is shown in Figure 5.21 A, showing a large decrease in absorption as the concentration of the paste used to produce the films was diluted from the original concentration to only 3 % w/w concentration.

SEM was used extensively to characterise the films deposited and is shown in Figure 5.21 B and Figure 5.22. The resulting film produced from 5 % w/w TiO_2 paste in diluent is shown in Figure 5.21 B, showing excellent coverage of the FTO glass. SEM was also used as a method to determine the thickness of the resulting films and is shown in Figure 5.22. This method only allowed a small section of TiO_2 thickness to be examined and so inherently did not give the global thickness of the film produced unless the film is uniform. It did however give a strong

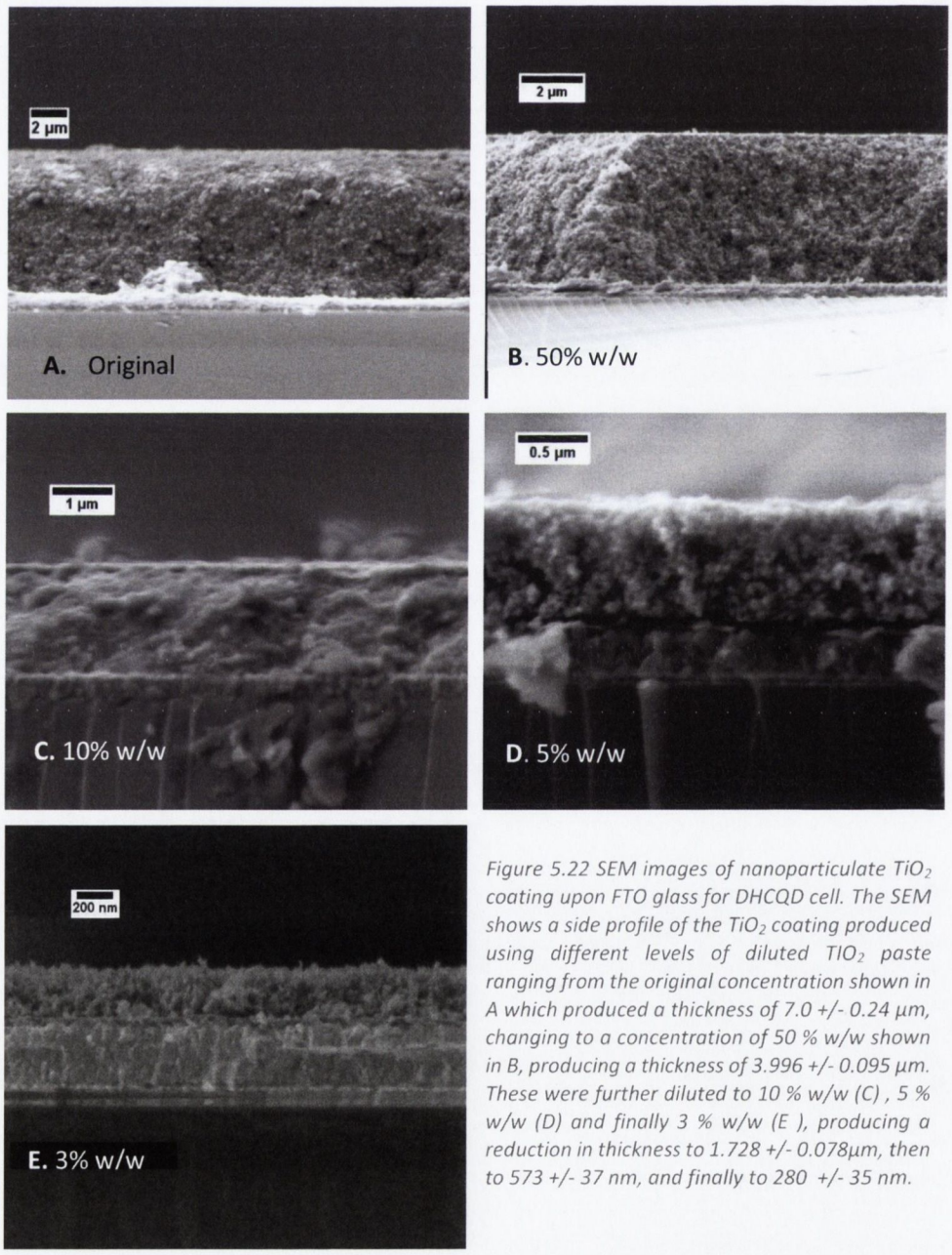

Figure 5.22 SEM images of nanoparticulate TiO_2 coating upon FTO glass for DHCQD cell. The SEM shows a side profile of the TiO_2 coating produced using different levels of diluted TIO_2 paste ranging from the original concentration shown in A which produced a thickness of 7.0 +/- 0.24 µm, changing to a concentration of 50 % w/w shown in B, producing a thickness of 3.996 +/- 0.095 µm. These were further diluted to 10 % w/w (C) , 5 % w/w (D) and finally 3 % w/w (E), producing a reduction in thickness to 1.728 +/- 0.078µm, then to 573 +/- 37 nm, and finally to 280 +/- 35 nm.

indication of sample thickness especially when results from multiple films produced under the same coating conditions were considered. The reduction in film thickness is shown as the amount of diluent (diluted in 23 %w/w ethyl cellulose in terpineol) was increased relative to TiO_2 Dyesol paste was increased from the original concentration (Figure 5.22 A, 7.0 +/- 0.24 μm) to 50 % (Figure 5.22 B, 3.996 +/- 0.095 μm), 10 % (Figure 5.22 C, 1.728 +/- 0.078μm), 5 % (Figure 5.22 D, 573 +/- 37 nm) and finally 3 % (Figure 5.22 E 280 +/- 35 nm).

Profilometery was used to examine the change in TiO_2 films due to dilution, and though time consuming allowed the entire surface of the electrode to be analysed to a 20 nm z-axis resolution and is shown in Figure 5.23 enabling the investigation of film uniformity. Figure 5.23 A and B shows the film achieved using undiluted Dyesol TiO_2 paste using a doctor blading method, resulting in a thick film (8-10 μm) upon the FTO glass. The image shows excellent film coverage and coating uniformity. Upon initial dilution of the Dyesol (33 % w/w) with just terpineol, a huge decrease in thickness is achieved (1.2-2.4 μm) but at the cost of film uniformity and is shown in Figure 5.23 C and D. Following this, ethyl cellulose was added as a diluent to thicken the paste, producing a terpineol solution containing 23% w/w ethyl cellulose. A resulting film achieved utilising this is shown in Figure 5.23 E and F, produced from a 10% w/w TiO_2 Dyesol paste. This film achieved a much reduced thickness (1.2- 1.6 μm), while still achieving an excellent uniform coverage of the FTO glass surface.

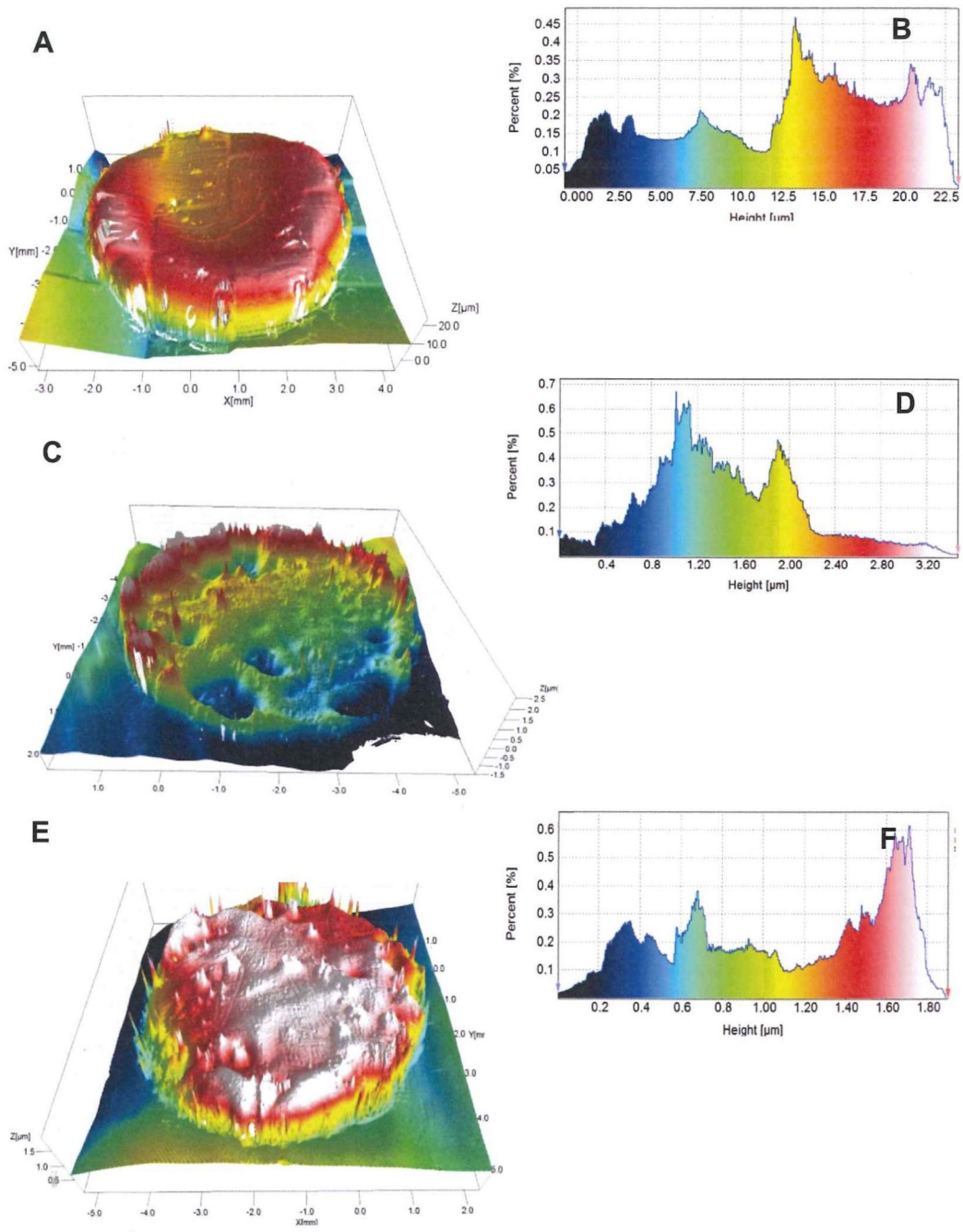

Figure 5.23. Profilometery data of Dyesol 90T TiO_2 film sintered on FTO glass, the histogram on the right shows the colour coding of the 3D image. Image A and B shows a resulting film thickness in the range of 8-10 µm and was produced using undiluted paste and a 3M scotch tape mask of 6 mm in diameter. The film shows an even coating upon the FTO glass. Image C and D shows a produced film that is very uneven showing voids of coating and also shows a wide range of thickness between 1.2-2.4 µm. It was deposited using diluted TiO_2 paste (33% w/w in Terpineol) and a 3M scotch tape mask of 6mm in diameter. Image E and F shows a film which shows an even coating, showing no voids and a thickness of between 1.2- 1.6 µm. It was deposited using diluted TiO_2 paste (10% w/w paste in solution of diluent: 23% w/w ethyl cellulose in Terpineol) and a 3M scotch tape mask of 6 mm in diameter.

Raman and FTIR spectra of the TiO_2 film are shown in Figure 5.26. The anatase form of TiO_2 has six active Raman peaks ($A1_g + 2B_{1g} + 3E_g$). The peak position are assigned to 144 cm^{-1} (E_g), 197 cm^{-1} (E_g), 399 cm^{-1} (B_{1g}), 513 cm^{-1} (A_{1g}), 519 cm^{-1} (B_{1g}), and 639 cm^{-1} (E_g). [372] Raman spectroscopy was performed to identify that the sintered pastes of TiO_2 were of the desired anatase crystal phase. Both spectra were an excellent match to anatase nano particulate TiO_2 as shown in Figure 5.24 A. FTIR spectroscopy was used to confirm that sintered films of the resulting paste did not show presence of diluents following sintering, which was feared possible due to the large dilution used to achieve the films and is shown in Figure 5.24 B. The TiO_2 films produced from a 5% w/w diluted were compared to TiO_2 films produced from non-diluted pastes, with results showing no important difference which would indicate the presence of impurities due to the large dilution, with both matching excellently with reported spectra.[373-375]

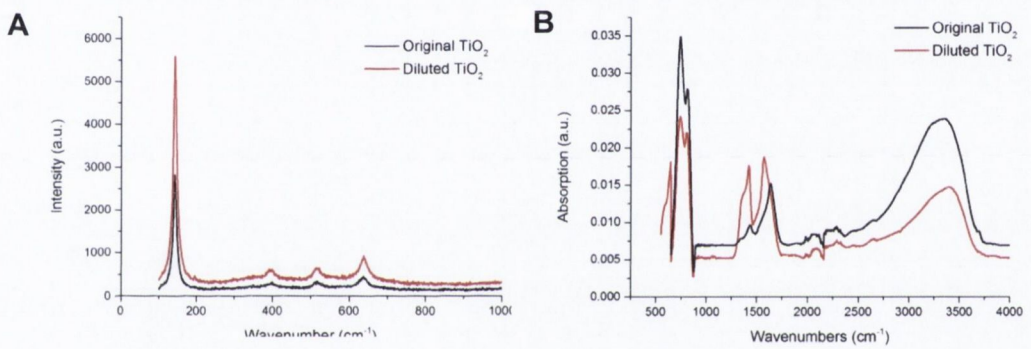

Figure 5.24 Raman (A) and FTIR (B) spectroscopy of TiO_2 sintered Dyesol diluted and ordinal pastes. Analysis of the Raman gave spectral peaks at 143 cm^{-1} (E_g),195 cm^{-1} (E_g),393 cm^{-1} (B_{1g}),510 cm^{-1} (A_{1g}),518 cm^{-1} (B_{1g}) and 636 cm^{-1}(E_g) for both diluted and undiluted pastes which correspond to anatase TiO_2, with an overall decrease in intensity for the diluted paste. FTIR spectroscopy shows a very similar spectrum between diluted (5% w/w) and undiluted pastes after sintering and matches excellently with reported spectra.

5.4.3 PbS Deposition

Following TiO_2 deposition, a novel procedure to produce a thin film coating of PbS QDs upon TiO_2 was developed using a dip coating and ligand exchange process, with the aim to produce a uniform film of 200 nm thickness. Oleic acid capped PbS QDs were used in concentrations of 10 mg/ml in hexane, with an E_g of 1.38 eV. This size of PbS was selected since PbS QDs of 1.3eV E_g are reported to show the greatest PCE performance in this cell design.[183] The TiO_2 coated FTO was then dipped into this solution and slowly removed at a rate of 0.5 cm/s, producing a thin coating of oleic acid capped PbS upon the surface. After drying, this sample was dipped into a solution of 2.5 %v/v 3-mercaptopropionic acid (MPA) in methanol. This caused the PbS to undergo spontaneous ligand exchange due to the greater binding energy of MPA. This ligand exchange caused an effective shrinking of the film volume due to the much-decreased size of the MPA molecule relative to oleic acid. MPA was used in this procedure due to its higher air

stability in comparison to other reported candidates including hydrazine[141] and ethanedithiol.[146] MPA has also been reported to form p-type conductive PbS films, with MPA acting as a bridge ligand between QDs due to its two functional groups of a carboxylic acid and thiol, both of which can bond to the PbS surface.[138]

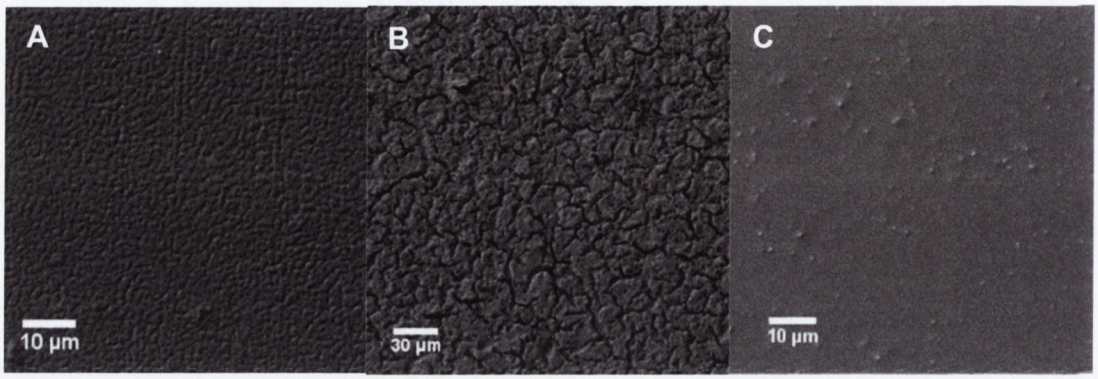

Figure 5.25 SEM images showing PbS QD deposition on TiO_2 coated FTO glass using dip coating. Image A shows oleic acid capped PbS QDs drop cast (A), image B shows PbS deposited using method 2 after 10 dip cycles and image C shows PbS deposited using method 1 after 10 dip cycles (C).

Following this two alternative methods were trialled: one in which the film was then washed in methanol to remove excess MPA , method A, while a second approach was tested in which the film was not washed of excess MPA, method B. After this, the device was then washed with hexane and allowed to dry. This completed one dip cycle, with multiple dip cycles required to produce the target thickness of 200 nm. Method 1 and 2 produced wildly different results due to the presence of excess MPA on the surface of the PbS film for method 2. This caused the deposition rate of PbS to increase hugely per dipping cycle and produced a deposition rate of 40 nm / cycle. The resulting film displayed a cracked rough morphology due to rapid deposition and visibly uneven coatings. Method 1 instead showed a deposition rate upon glass of 10 nm/cycle and produced a smooth featureless coating with no visual defects. SEM was used to

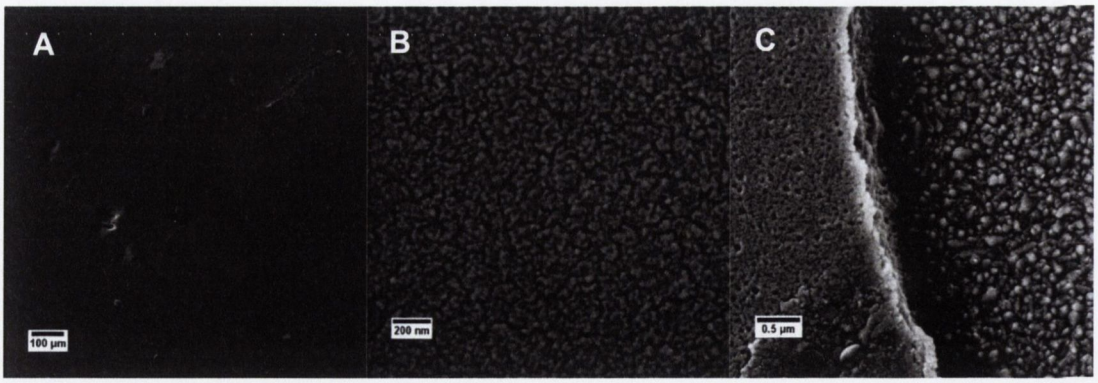

Figure.5.26 SEM of MPA-capped CdSe QDs deposited upon TiO_2 coated FTO using method 1. Image A and B shows the continuous coating achieved with image B showing the porous surface at high resolution due to shrinkage of the film from ligand exchange . Image C shows a removed segment of the film to show the FTO surface below.

characterise the surface morphology of PbS films as shown in Figure 5.25 and CdSe films shown in Figure.5.26.

Regarding Figure 5.25, image A image shows oleic acid capped PbS film, showing little surface features and/or cracks. Image B shows a MPA capped PbS film deposited using method B, showing a highly cracked surface due to rapid ligand exchange. While Image B shows a smooth deposition surface achieved using method 1. Figure.5.26 shows the deposition of CdSe QDs using dip coating method 1, which shows the fine structure of the deposited film under high magnification, showing that produced film still show a level of cracks due to ligand exchange, but too a much lesser level than produced using method 2. SEM cross section were then used to determine coating thicknesses, and is shown in Figure 5.27. Image A shows a cross section of a PbS QD film coating produced using method 1 upon glass, producing a 230 nm thick coating from a 20 dip cycle and corresponds to deposition rates reported in literature [204] Image B shows a cross section of CdSe QDs deposited upon FTO coated glass, producing a thickness of 430 nm from a 30 dip cycle.

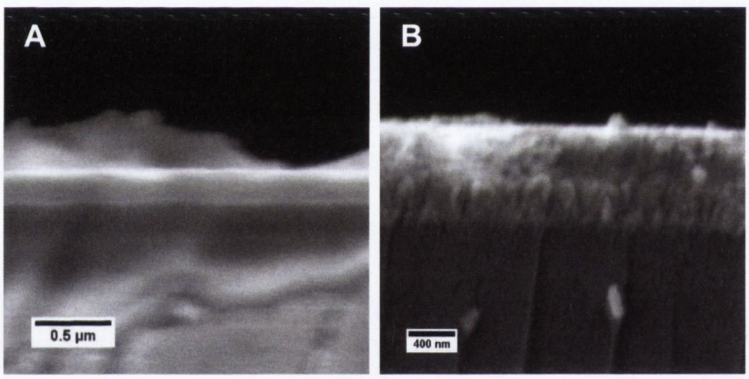

Figure 5.27 PbS QD deposition (A) upon glass and CdSe QD deposition (B) upon FTO coated glass using dip coating using deposition method 1. The PbS deposition produced a coating of 230 nm in thickness after 20 dips while the CdSe produced a coating of 430 nm in thickness from 30 dips

he deposition using method A was also monitored using UV-Vis absorption spectroscopy and is shown in Figure 5.28. This displays the steady increase in absorption of the QDs as deposited upon the electrode surface and allowed an immediate tool to monitor deposition of layers during fabrication of CdSe and PbS based DHCQD cells. One can also see these cells after 30 dips showed a significant absorption, making them suitable for photon harvesting in a solar cell device.

The deposition using method A was also monitored using UV-Vis absorption spectroscopy and is shown in Figure 5.28. This displays the steady increase in absorption of the QDs as deposited upon the electrode surface and allowed an immediate tool to monitor deposition of layers during fabrication of CdSe and PbS based DHCQD cells. One can also see these cells after 30 dips

showed a significant absorption, making them suitable for photon harvesting in a solar cell device.

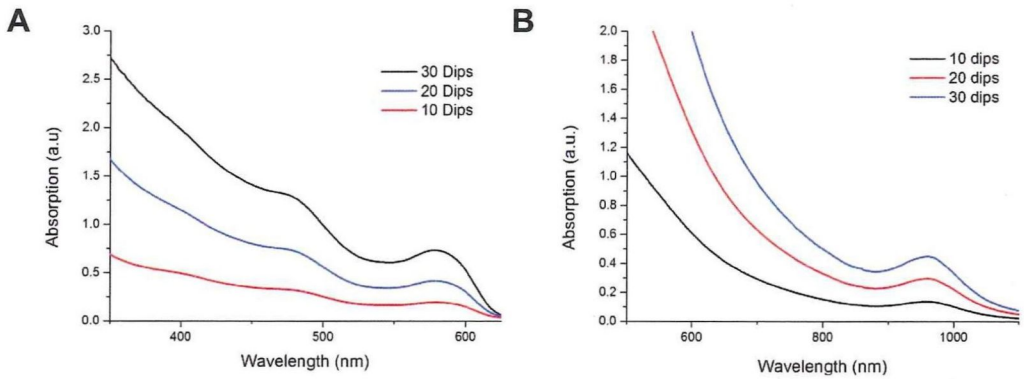

Figure 5.28 UV-Vis absorption of the deposition of CdSe QDs (A) and PbS QDs (B) upon FTO coated glass showing the increase in absorption as the number of cycles of deposition increases

5.4.4 Back electrode deposition

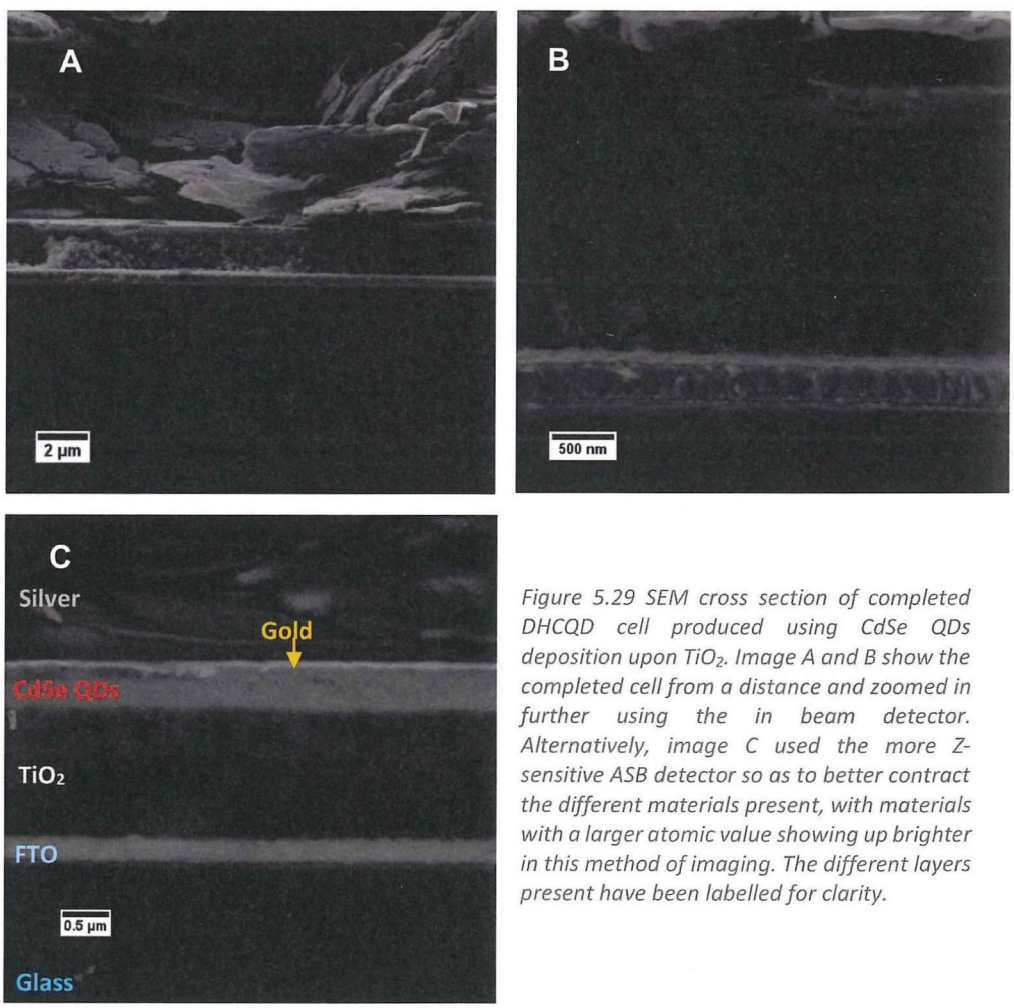

Figure 5.29 SEM cross section of completed DHCQD cell produced using CdSe QDs deposition upon TiO_2. Image A and B show the completed cell from a distance and zoomed in further using the in beam detector. Alternatively, image C used the more Z-sensitive ASB detector so as to better contract the different materials present, with materials with a larger atomic value showing up brighter in this method of imaging. The different layers present have been labelled for clarity.

After dip coating, the back electrode was deposited using metal evaporation under high vacuum, with a number of metals initially tested including Al, Ag and Au, with the best results being produced from Au deposition. Following Au deposition, silver paint was used to make a

connection to the Au contact. SEM was then used to show the resulting finished cell shown in Figure 5.29.

5.4.5 IV testing of DHCQD cells

Preliminary solar cell testing was then carried out upon three designs of DHCQD cells under 1 sun AM1.5 illumination, measuring the cell's performances using a IV curve responses with results shown in Table 5.3. Produced cells showed a definite photovoltaic effect under illumination though cell performance was shown to be far below reported values in literature with the best performing device based on PbS QDs, producing a PCE of 0.016%, with its IV curve shown in Figure 5.30. Other cells tested included CdSe based and CdTe/CdSe based cells, unfortunately these cells even showed poorer performance.

Table 5.3 This shows the result of DHCQD cell testing under AM 1.5, 1 sun illumination, showing the resulting characteristics of the cells determined by measuring the IV response of the produced cells

	CdSe QD Cell	CdTe/CdSe QD Cell	PbS QD Cell
I_{sc} (mA/cm²)	0.023	0.0034	0.0954
V_{OC} (V)	0.24	0.14	0.4
Fill factor (%)	24.4	25.3	40.8
Cell size (cm²)	0.028	0.028	0.028
Power Conversion Efficiency (%)	0.00136	0.00012	0.01556

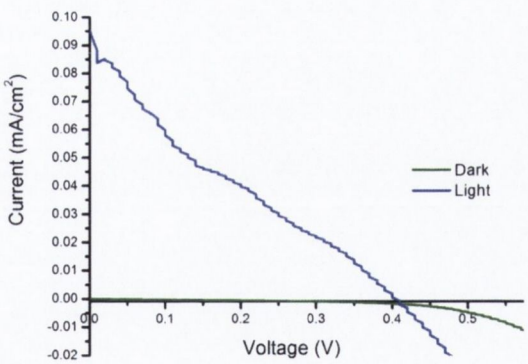

Figure 5.30 IV curve of PbS QD based DHCQD cell.Showing the change in response of the cell under illumination 1 sun AM 1.5 illumination source (light) and its reponse under darkness (dark)

The exact reason for our cells sub-par performance has not been determined but is most likely due to oxidation of the CQD films during fabrication. Only recently has it become clear in literature that for these cells to perform near optimal efficiency, the entire fabrication after inclusion of CQDs requires an oxygen free environment, including when testing the cells.[311] Unfortunately, we do not have the setup to allow us to achieve this, with all fabrication and testing presently carried out in ambient conditions.

5.5 Discotic Liquid Crystal Solar Cells

The final quantum dot based solar cell explored in this work was the discotic liquid crystal solar cell. For this work, we firstly investigated two DLCs, H6TP and RTAQ, in the solution and solid state. Following this, we examined the effective interactions between these DLCs and quantum dots as composites, investigating the resulting electrical and optical properties. Finally, a number of trial devices were investigated with the aim of producing a working solar cell.

5.5.1 Discotic Liquid Crystal Characterisation

For the first part of this work, we will briefly characterise H6TP and RTAQ which were liquid crystals supplied by a collaborator, in solution and solid, observing the materials absorption and emission propertied since these are fundamental for any material to be utilised in a photoactive device, this work is detailed below. It should also be noted the structure of H6TP and RTAQ were also confirmed with the use of 1H and 13C NMR and is shown in Appendix E, Figure 7.16 and Figure 7.17

5.5.1.i H6TP: Solution

UV-Vis absorption and emission spectroscopy was used to characterise H6TP in solution and is shown in Figure 5.31. H6TP shows absorption in the UV range of the spectrum displaying a distinct peak of absorption at 360 nm and 345 nm, followed by featureless absorption as shown in (Figure 5.31 A). The sample also showed strong luminescence in the UV/Vis range, displaying luminesce peak value at 384 nm, a smaller peak at 401 nm, followed by featureless emission stretching out to 480 nm, as shown in (Figure 5.31 B)

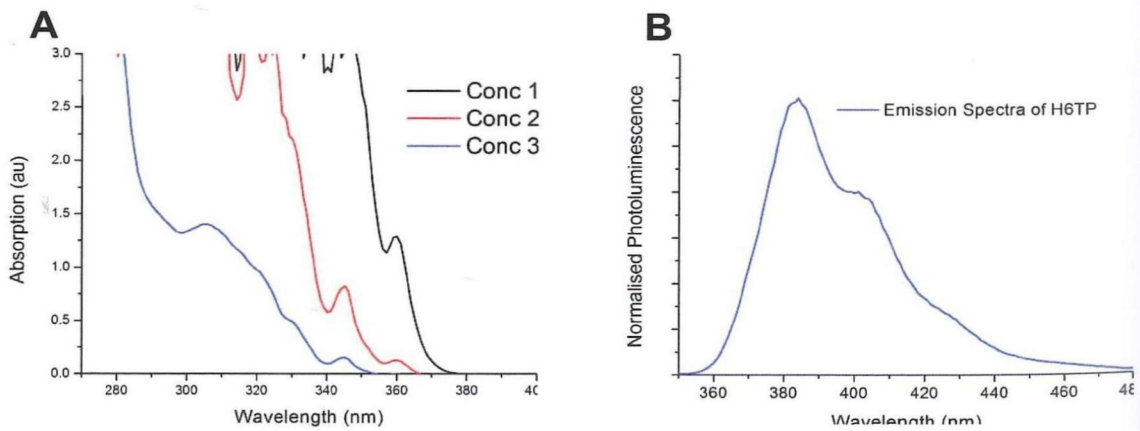

Figure 5.31 UV-Vis absorption spectra (A) and photoluminescence Emission spectra (B) of H6TP solution in hexane

5.5.1.ii H6TP: Solid State

Following optical characterisation in hexane, the pure H6TP was then characterised using UV-Vis absorption spectroscopy and Pl emission spectroscopy on a glass slide and is shown in Figure 5.32. The absorption spectra of three different states of H6TP are shown in Figure 5.32(A) and labelled as the crystalline phase, liquids phase and the liquid crystalline phase. This was carried out by placing the liquid crystal between two glass slides, heating to liquid phase transition temperature, followed by monitoring the UV-Vis absorption as the material cools, allowing the three phases to be observed. As is to be expected the scattering signal increases as the crystal cools from liquid, to liquid crystal, to solid, indicated by the increase in absorption at longer wavelengths (past 385 nm). The resulting Pl luminescence of the solid-state sample in the crystalline sample is shown in Figure 5.32B. Interestingly the sample still showed bright luminescence in the solid state with luminescence red shifted significantly, it also showed a much more defined emission spectrum with luminescence peaks found at 388 nm, 406 nm, 429 nm and 465 nm.

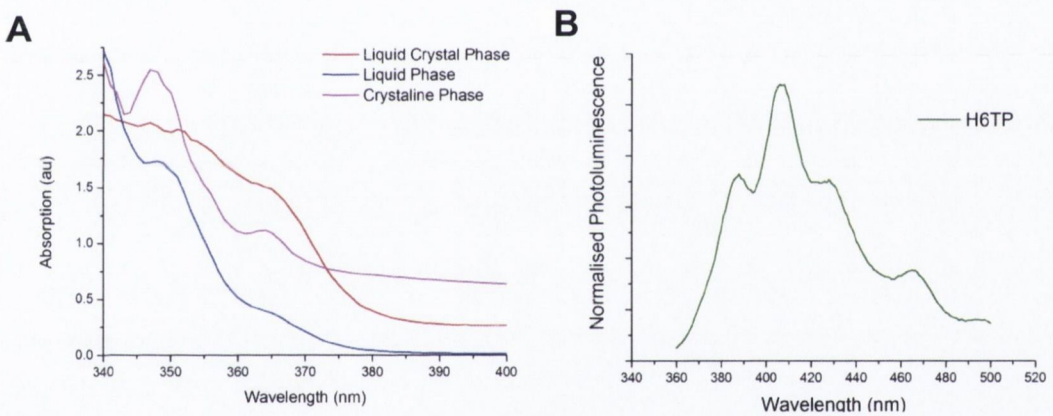

Figure 5.32 Solid-state UV-Vis absorption (A) and photoluminescence spectra (B) of H6TP liquid crystal in the solid state

5.5.1.iii H6TP/ QD solution

UV-Vis absorption and Pl emission was used to analyse solutions of oleic acid capped CdSe QDs and H6TP the results shown in Figure 5.33. The Pl emission change of the CdSe QDs shows a steady decrease in emission as H6TP was added to a solution of CdSe QDs increasing from 0.0005 g/ml to 0.008 g/ml, producing a loss in Pl emission from the original in solution and is shown in Figure 5.33 B. Interestingly a large loss in emission is seen initially upon H6TP addition, with this effect slowing as the addition of H6TP is increased.

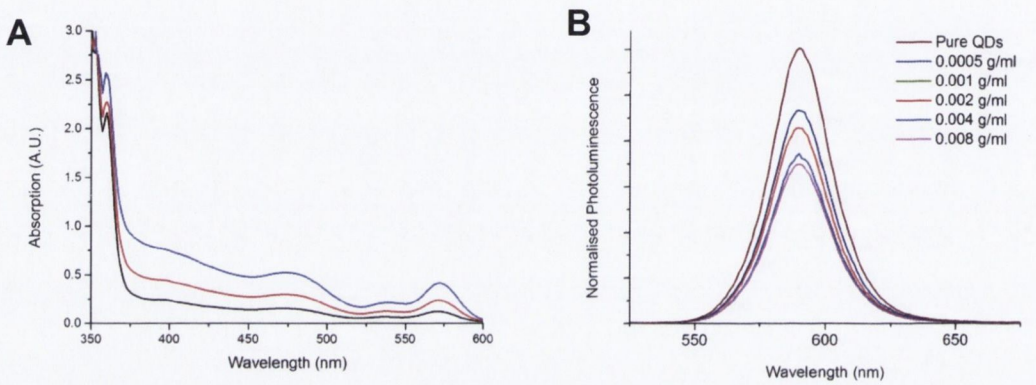

Figure 5.33 UV-Vis absorption (A) and Pl emission (B) of oleic acid capped CdSe QDS and H6TP in hexane. UV-Vis absorption shows the change in solution absorption as the CdSe QD concentration relative to H6TP increases, while the photoluminescence spectra of CdSe QD as H6TP is added to solution. The photoluminescent spectra shows an overall decrease in QD luminescent as the concentration of H6TP is added, from 0.0005 g/ml to 0.008 g/ml, producing a decrease in PL intensity relative to the QD solution to 77.7% , 70.3%, 64.3%, 60.6%, 57.6% as the concentration increases.

5.5.1.iv RTAQ : Solution

RTAQ was firstly analysed optically in hexane, with the resulting UV-Vis absorption spectra shown in Figure 5.34 A. The UV-Vis shows a broad absorption, showing three distinct areas of increased absorption at 285 nm, 344nm and 431 nm, with low levels of photon harvesting paste 500 nm. PL emission spectroscopy was also recorded of the sample but showed no detectable signal at room temperature. Following this, the solid-state absorption of RTAQ was recorded on

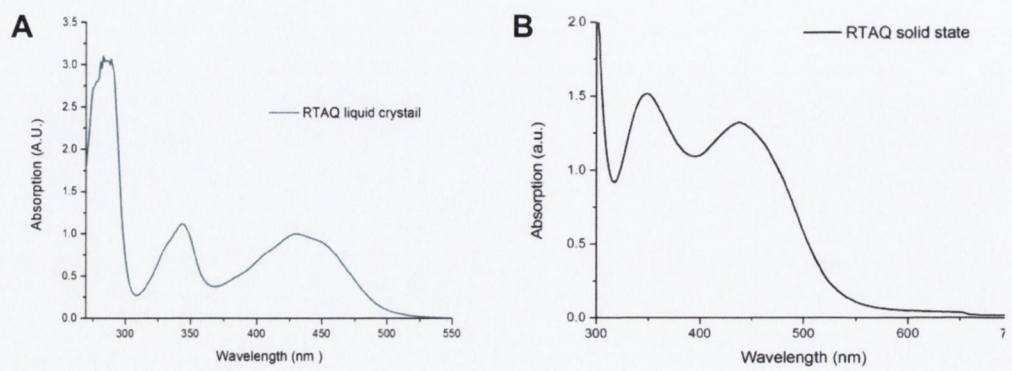

Figure 5.34 UV –Vis absorption of RTAQ liquid crystal in hexane (A) and in solid state (B) at room temperature

a glass slide and is shown in Figure 5.34 B, producing spectra showing peaks at 347 nm and 438 nm, with overall absorption red shifted from the solution UV-Vis.

5.5.2 Discotic Liquid Crystal / Quantum Dot Composite Characterisation

Following our brief characterisation of the DLCs, we then carried out work to determine the effects of quantum dot addition to H6TP and RTAQ in the solid state, through the use of polarised optical microscopy (POM) and DC electrical conductivity measurements which is detailed below.

5.5.2.i Electrical DC Conductivity of DLC-QD composites

RTAQ and H6TP composites electrical conductivity was examined with the aim to determine the effect of QD incorporation upon electrical conductivity. We decided to investigate the effects of different quantum dots; CdSe, PbS and CdS QDs addition to DLC, allowing us to contrast the effect of a UV absorber, a visible absorber and a NIR absorber to determine the total effect upon the material. The study also included the examination of Se and the incorporation of PDI. We included Se since it is used in the synthesis of CdSe QDs, and we decided it would be interesting to determine the effect of it's addition to DLC. We also investigated the addition of PDI since we planned to fabricate a DLC solar cell using a combination of QDs, PDI and RTAQ; therefore, we wanted to determine the electrical properties of a PDI/RTAQ composite. The conductivity of all cells was also examined under darkness and under illumination of AM1.5 100 W/m^2 to determine the potential application of these materials in a photovoltaic device.

H6TP was briefly investigated in this work with results shown in Table 5.4. Quantum dot doping of another DLC material of the same family, H4TP (hexabutyloxytriphenylene), by our collaborators, showed large increases in DC conductivity and was the initial reason for investigating this material. Unfortunately, after some initial studies; it was decided due to its discotic phase only being present at elevated temperatures, that it was not worthwhile exploring the results further. This was due to the clear phase separation that took place between CdSe QD /H6TP composites upon crystallisation of the H6TP at room temperature, which meant it was not possible to produce repeatable films of the materials for testing.

Our initial results showed a clear increase in conductivity after oleic acid capped CdSe QD doping of H6TP 15 % w/w, increasing the conductivity from 3.7×10^{-12} (undoped) to 3.78×10^{-9} (S/m) (doped). Both doped and undoped samples were also tested under illumination showing the undoped samples increase to 2.2×10^{-11} (S/m) while the doped sample showed an increase to 1.104×10^{-8} (S/m). Therefore, the doped sample showed a positive increase in conductivity under illumination, and a much higher overall conductivity than the undoped sample of H6TP.

Table 5.4 This table describes the conductivity measurements made on a number of H6TP composites, each reported value comes from an average of 4-6 measurements, on 2-3 devices

Sample	Contents	Composition w/w %		σ under darkness	σ under illumination	Δ in conductivity relative to RTAQ in darkness	Δ in conductivity relative to RTAQ under illumination	Δ under
		LC	QD	(S/m)	(S/m)	%	%	%
1	H6TP	100	0	3.7E-12	2.2 E-11	/	/	490
2	H6TP and Oleic acid capped CdSe QD (3.6 nm)	85	15	3.78 E-9	1.104 E-8	103 E+03	5.0 E+2	271

Both DLC when doped with QDs showed an increase in conductivity, though the magnitude of this effect was much more pronounced in the H6TP then in RTAQ. The magnitude of the doping effect does also demonstrated a general trend of increasing conductivity as the doping composition increased as seen in RTAQ (Table 5.5). Also from the data, it seems the exact type of quantum dot used did not strongly effect the change in conductivity observed for RTAQ. The effects of illumination upon the two liquid crystal shows contradicting trends, with a strong increase in conductivity found for H6TP, while for RTAQ, the conductivity was found to drop for un-doped and CdSe and CdS QDs doped samples, while it shows an increase when doped with PbS QDs. Unfortunately, in general it was very difficult to produce repeatable results with separate devices, which has introduced a consistent error, which must be taken in to account when regarding these results, the exact cause of which we have been unable to determine at present.

We have also tested briefly the effects of metallic Se powder and a non-soluble PDI upon the conductive properties of the RTAQ. Both of these materials did not dissolve into the liquid crystal effectively and so could not be properly loaded into the devices used to test conductivity effectively. In spite of this, upon testing, they both still had a noticeable effect upon the conductivity, particularly in the case of Se, increasing it significantly.

Table 5.5. This table describes the conductivity measurements made on a number of RTAQ composites each reported value comes from an average of 4-6 measurements, on 2-3 devices. Note σ is the electrical conductivity measured from - 0.5 to 0.5 V.

Cells	Contents	Composition w/w%			σ under darkness	σ under illumination	% Δ in conductivity relative to	% Δ in conductivity relative to	% Δ under illumination
		Other	LC	QD	(S/m)	(S/m)	%	%	%
1	RTAQ	0	100	0	2.05E-11	1.68E-11	/	/	-18
2	RTAQ and CdSe (3.8 nm)	0	50	50	1.65E-10	5.46E-11	7.05E+02	2.25E+02	-67
3	RTAQ and CdSe (3.8 nm)	0	85	15	5.70E-11	2.88E-11	1.78E+02	7.14E+01	-49
4	RTAQ and CdSe (3.8 nm)	0	90	10	9.82E-11	5.44E-11	3.79E+02	2.24E+02	-45
5	RTAQ and CdSe (3.8 nm)	0	99	1	9.30E-10	6.85E-10	4.44E+03	3.98E+03	-26
6	RTAQ and Se	10	90	0	7.47E-07	1.08E-06	3.64E+06	6.43E+06	44
7	RTAQ and CdS (2.1 nm)	0	50	50	1.08E-10	1.58E-10	4.27E+02	8.40E+02	47
8	RTAQ and CdS (2.1 nm)	0	90	10	2.27E-11	9.31E-12	1.07E+01	-4.46E+01	-59
9	RTAQ and CdS (2.1 nm)	0	99	1	1.33E-07	1.39E-07	6.49E+05	8.27E+05	5
11	RTAQ and PbS (3.5 nm)	0	90	10	7.99E-09	1.92E-11	3.89E+04	1.43E+01	-100
12	RTAQ and PbS (3.5 nm)	0	98	2	9.11E-09	1.87E-09	4.43E+04	1.10E+04	-79
10	RTAQ and PbS (3.5 nm)	0	99	1	4.57E-11	1.10E-10	1.23E+02	5.55E+02	141
11	RTAQ , PDI and PbS (3.5 nm)	25	74	1	2.59E-11	2.74E-11	2.63E+01	6.31E+01	6

5.5.2.ii Polarised Optical Microscopy of DLC-QD composites

Polarised optical microscopy was then used to analyse the DLC liquid crystal phase optically. H6TP is crystalline at room temperature, therefore only RTAQ was observed since it is a DLC at room temperature. This was then compared to RTAQ based composites created using QDs, common QD surface ligands and PDI. All of this was carried out by firstly filling a device designed to test DLC conductivity, consisting of two FTO coated glass slides separated by a 10-µm spacer. The device was then put through a heat treatment, involving slow cooling from the isotropic phase (above 130 °C) to insure that RTAQ was observed in its DLC phase. This device arrangement has been reported to produce the DLC phase perpendicular to the FTO glass.

Figure 5.35 shows the DLC room temperature phase of RTAQ formed after careful alignment of the isotropic phase at 130 °C cooling at a rate of 0.5 °C per minute to 60 °C. This results in an alignment of the RTAQ DLC phase perpendicular to the direction of the FTO glass, allowing use to view the phase from the top of the columns. The images shows a clear indication of the presence of a crystalline phase which is responsible for bring about the strong colours clearly visible in the images.

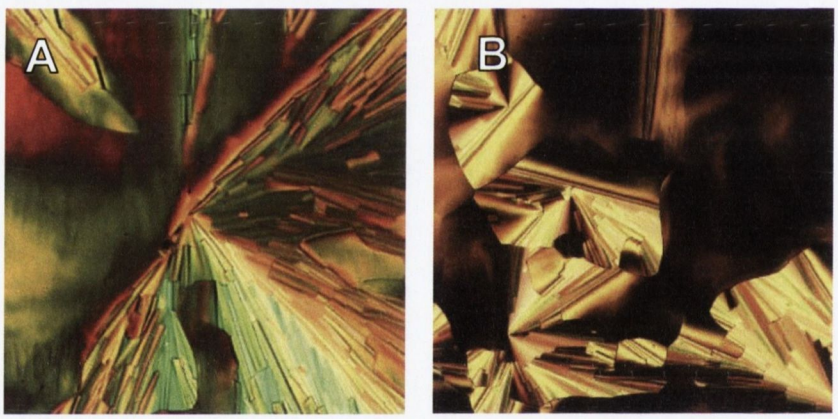

Figure 5.35 Polarused optical microscopy images of non-doped RTAQ DLC, under a 10 x zoom at room temperature showing the DLC phase.

Following this, we investigated the effects of addition of three common ligands used to cap CdSe QDs to the DLC phases of the material, octadecylamine (ODA), octadecylphosphonic acid (ODPA) and oleic acid (OA) and is shown in Figure 5.36. The first observable fact from this doping was that all three composites still produced a liquid crystal phase, but with differing levels of disruption to this phase. It can be seen from the images that disruption of the crystalline phase is most pronounced in the ODPA composite (image B), showing a much smaller crystalline individual sections and disruption of the structure around the edges. ODA doped demonstrated a lower disruption (image A) of the crystalline phase while interestingly OA doped (image C) showed the least observable disruption of the DLC phases.

Figure 5.36 Polarused optical microscopy of RTAQ DLC composite , using a 10 x zoom, mixed with 10:1, w/w, ODA (Image A), ODPA (Image B) and OA (Image C)

Subsequently three composites composed of CdSe CQDS/RTAQ, 1:10, w/w were studied. Samples coated in either OA (3.77 nm), ODA (3.66) or ODPA (3.4 nm) were analysed using POM and is shown in Figure 5.37. The three CdSe QDs investigated were similar in diameter, with ODPA capped CdSe QDs =3.4 nm, ODA capped = 3.7 nm and the OA capped = 3.8 nm, therefore the size difference could be dismissed as a cause of the differing in the composite properties. Across the three composites a definite disruption of the DLC phase can be observed, with the most pronounced taking place in ODA capped CdSe QDs (Figure 5.37 C), showing islands of the RTAQ DLC phase existing in an amorphous phase. The same effect can be seen to a lesser level in ODPA capped CdSe QDs (Figure 5.37 B) and even to a lesser extent again in OA capped CdSe QDs (Figure 5.37 A), displaying a much less pronounced disruption of the DLC phase. Due to the smaller disruption from the OA ligand found from OA QDs and OA ligand composites, only QDs coated in OA were further investigated.

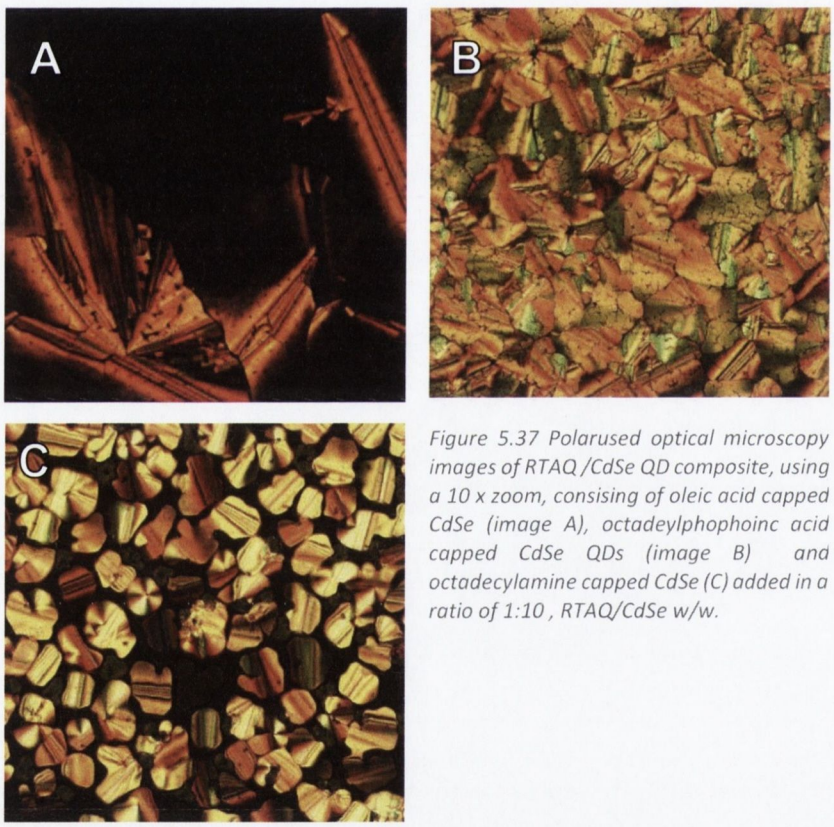

Figure 5.37 Polarused optical microscopy images of RTAQ /CdSe QD composite, using a 10 x zoom, consising of oleic acid capped CdSe (image A), octadeylphophoinc acid capped CdSe QDs (image B) and octadecylamine capped CdSe (C) added in a ratio of 1:10 , RTAQ/CdSe w/w.

POM was used to then analysis the effect of varying the concentration of oleic acid capped CdSe (3.8 nm) QDs, changing from 1:100 (A) to 1:10 (B) to 1:5 (C) to 1:1 (D) w/w and is shown in Figure 5.38. As the concentration of QDs is increased, it can be clearly seen that the DLC crystalline phase becomes more and more strongly disrupted, going from image A to D, showing smaller crystalline segments and increased darker areas indicating the presence of an isotropic phase.

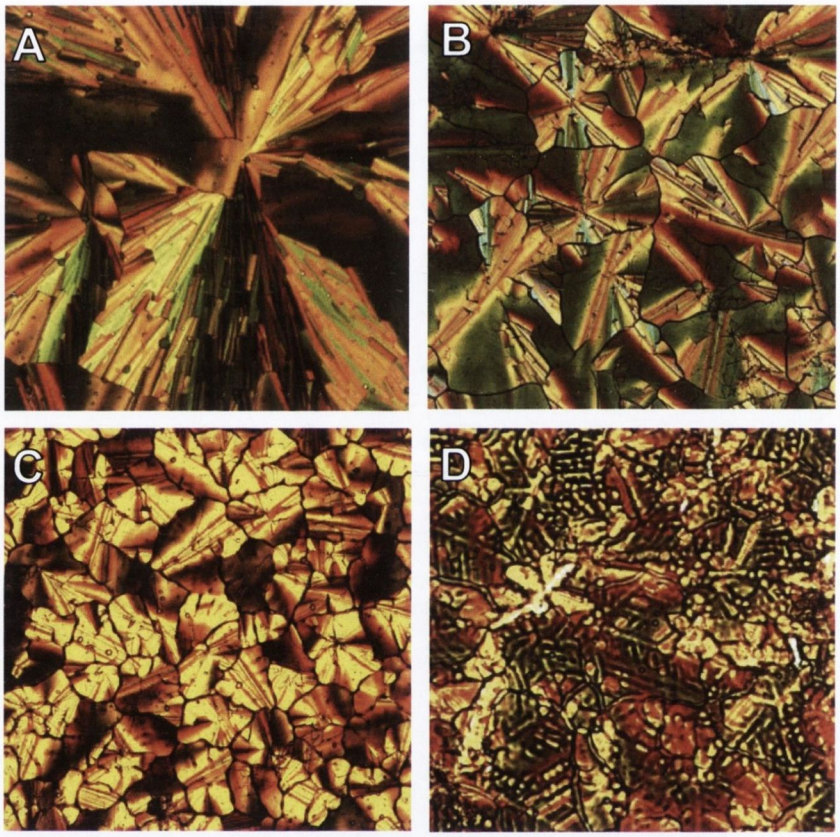

Figure 5.38 Polarised optical microscopy of RTAQ /CdSe QD composite , using a 10 x zoom, consising of oleic acid capped CdSe (3.77nm in rdiameter) added in a ratio of 1:100 (image A), 1:10 (Image B), 1:5(Image C) and 1:1 (Image D) w/w.

After observing the effects of different concentrations of oleic acid capped CdSe QDs to RTAQ, composites consisting of oleic acid capped CdS QDs or oleic acid capped PbS QDs composed were produced and studied using POM. CdS QDs composites consisting of 1:100 (A), 1:10 (B) and 1:1 (C) w/w were studied and is shown in Figure 5.39, showing the same trend of increasing disruption of the DLC phase as the concentration increased showing the formation of islands of the DLC phase in an isotropic phase.

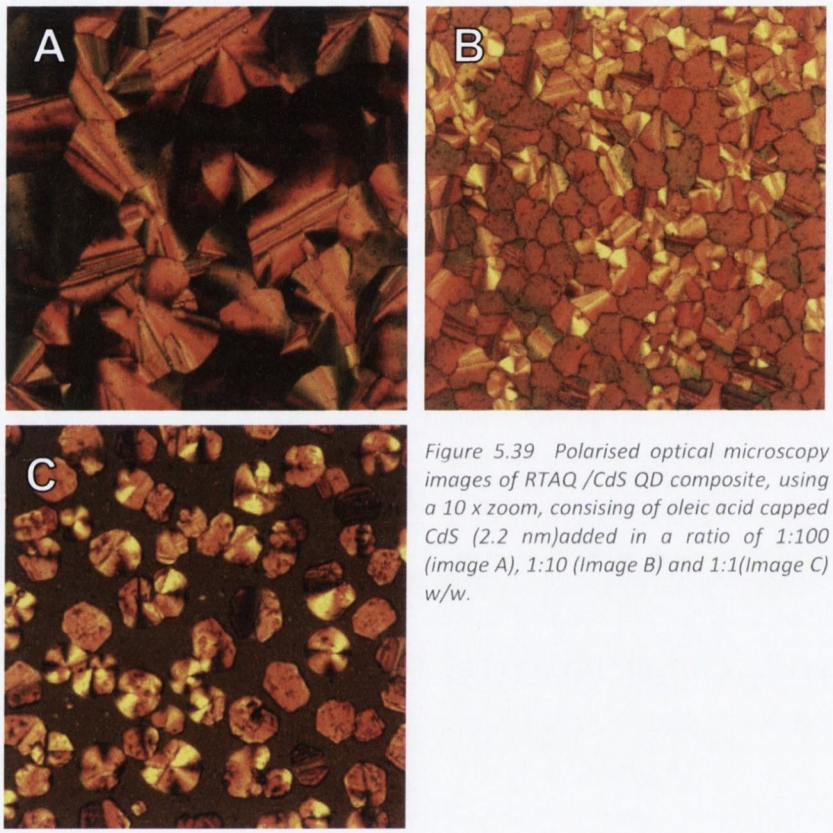

Figure 5.39 Polarised optical microscopy images of RTAQ /CdS QD composite, using a 10 x zoom, consising of oleic acid capped CdS (2.2 nm)added in a ratio of 1:100 (image A), 1:10 (Image B) and 1:1(Image C) w/w.

The addition of oleic acid capped PbS QDs to RTAQ is shown in Figure 5.40 in ratios ranging from 1:100 (image A), 1:50 (image B) and 1:10.of w/w (image C). This sample shows the same trend of crystalline phase disruption as seen in Cd/RTAQ composites. Interestingly due to the strong visible absorption of PbS QDs, the position of the PbS QDs is much more noticeable in the resulting images, showing its clear disruption of RTAQ DLC phase as seen in the black segments of the image

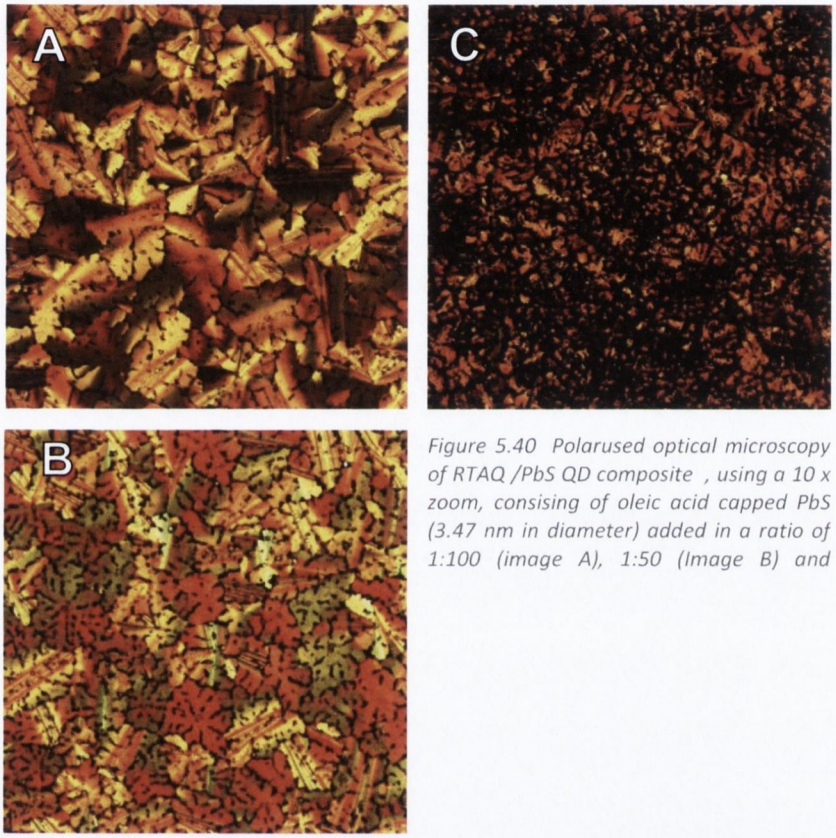

Figure 5.40 Polarused optical microscopy of RTAQ /PbS QD composite , using a 10 x zoom, consising of oleic acid capped PbS (3.47 nm in diameter) added in a ratio of 1:100 (image A), 1:50 (Image B) and

Following the study of a number of QDs/RTAQ composites, it was decided that it would be interesting to observe the effects of addition of Se to RTAQ, in a ratio 1:10 w/w and is shown in Figure 5.41. This was due to the possible presence of Se that can be found in samples of CdSe QDs if Se was used in excess during synthesis and not adequately cleaned from the QD solution afterwards. It was found that the Se did not fill easily into the device, due to its insolubility in RTAQ and therefore very little of the added Se can be observed in the image apart from the small segments displaying black deposits in certain areas of the image. This impurity was

observed did not to effect the underlying DLC phase of RTAQ, which showed excellent crystallinity under POM.

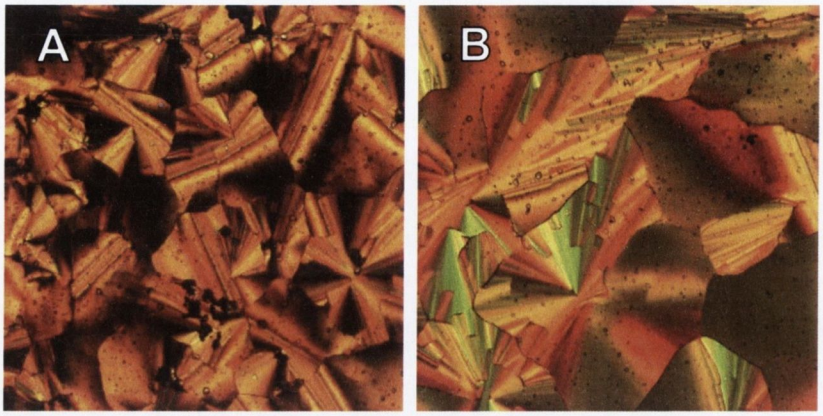

Figure 5.41 Polarused optical microscopy of RTAQ:Se composite , using a 10 x zoom, composed of 1:10 Se /RTAQ w/w .

Finally POM was used to observe the effect of addition of PDI, a soluble perylene diamide, (N,N9-bis(1-ethylpropyl)-3,4,9,10-perylenebis , to the RTAQ DLC phase and is shown in Figure 5.42 in a ratio of 1:10 PDI /RTAQ w/w. The PDI produces a very distinct structure in the RTAQ, producing needle like growths in the phase of the RTAQ. Interestingly no noticeable disruption can be seen to the overall structure of the RTAQ, which still shows a strong crystalline DLC phase, intermingled with the PDI needle phase, which is regularly distributed throughout the composite.

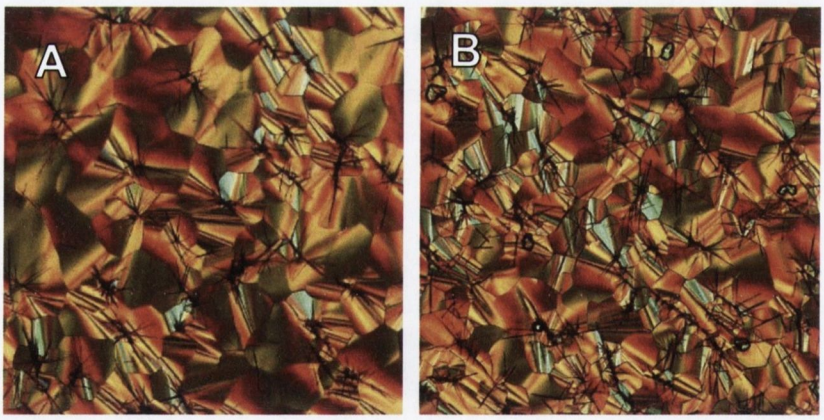

Figure 5.42 Polarused optical microscopy images of RTAQ:PDI composite , using a 10 x zoom, composed of 1:10 PDI /RTAQ w/w.

5.5.3 DLC Cell fabrication

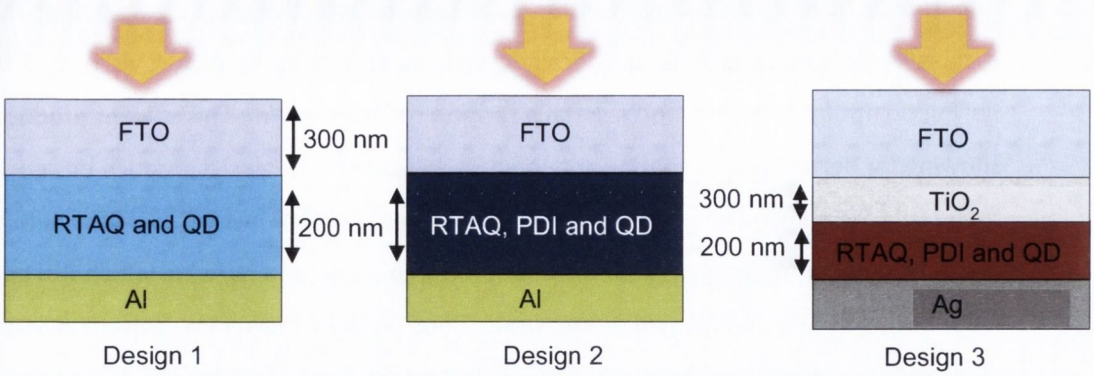

Figure.5.43. Diagram of proposed designs of DLC/QD photovoltaic cell.

Following analysis of the RTAQ composites, three designs of PV cells were fabricated and tested to see if it was possible to produce a novel photovoltaic device. The designs attempted are shown in Figure.5.43. Design 1 will simply use RTAQ and a QD, deposited upon FTO coated glass, with a low workfunction metal evaporated on as the back contact. The second design will incorporate PDI, which has been shown to work as an effective electron acceptor with other DLC designs, into the same structure as design 2. The final design incorporates the RTAQ PDI and QD layer, while also incorporating the use of a TiO_2 film upon the FTO glass. In this design, electron injection takes places into the TiO_2, and so instead of use of a low workfunction metal as seen in the two earlier designs, a larger work function metal will be used to avoid electron injection into the back electrode. Therefore, for the initial design, we have utilised Ag, but Au or Pt would also be excellent candidates. To enable the production of these three designs of DLC-QD cells describing spincoating will be used to produce the RTAQ/QD layer, while the TiO_2 layer used in design three was fabricated using the same approach used in DHCQD cell

5.5.3.i Spincoating

Spincoating has been explored as a method to deposit continuous films of RTAQ, with the aim to produce a film of between 150 nm – 200 nm in thickness. The spin coater used had a minimum setting of ramp rate 100 rpm/sec and a minimum spin speed of 1,000 rpm, therefore we were restricted in our ability to access lower ramp rates and spin speeds, which may have been more optimal for our purpose. Therefore, instead we used solvent choice and loading to control the films produced

Initially chloroform was used as the solvent, with loading of between 15 mg/ml to 30 mg/ml, unfortunately this was found to produce an uneven coating, which was also too thin. Following this, a higher viscosity solvent was investigated as a means to produce more effective surface coverage and to increase surface thickness coating. The solvent of choice also had to retain a

low boiling point and therefore would easily evaporate which is vital for spincoating and also importantly have a low surface tension so it spreads effectively during spinning .Therefore cyclic-alkenes were explored, specifically cyclohexane, due to its higher viscosity 1.02 cP, a boiling point of just 80.7 °C and a surface tension of 24.95 mN/m. This solvent produced films showing far better surface coating and increased thickness. Finally to produce design 3, it was found that PDI showed poor solubility in cyclohexane, therefore instead as a solvent mixture of (cyclo-hexane) in conjunction with the chloroform; in a 1:3 ratio (w/w) in which PDI and RTAQ were both still fully soluble within was used. Films produced using this solvent mixture were much more continues and by simply varying the weight, it was possible to produce the desired thickness, with produced films described in SEM used to determine the thickness of liquid crystal deposited and continuous surface coating with cross sections is shown in Figure 5.44.

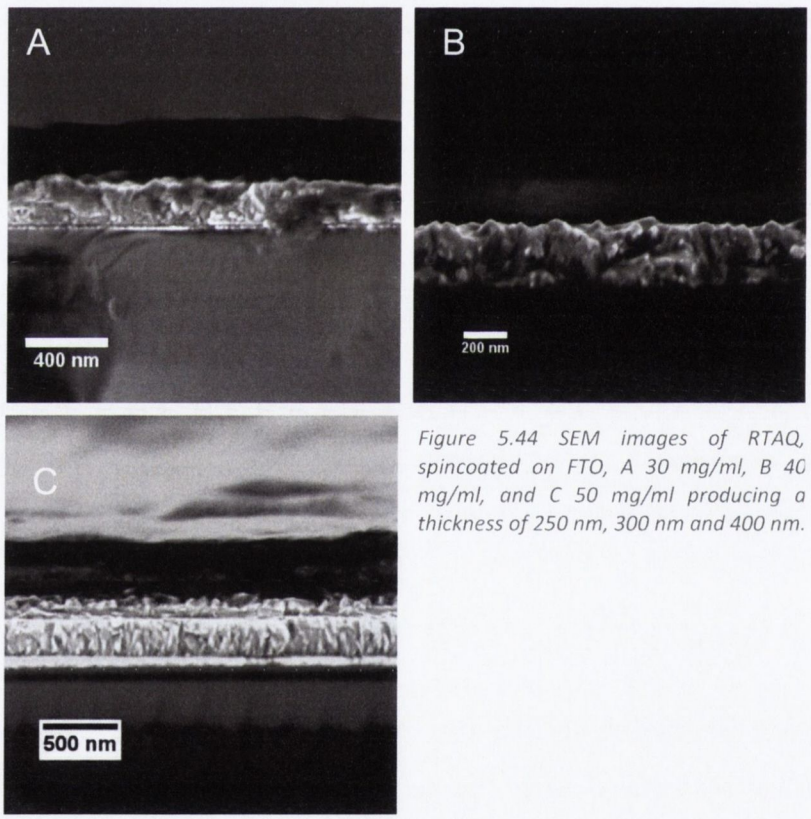

Figure 5.44 SEM images of RTAQ, spincoated on FTO, A 30 mg/ml, B 40 mg/ml, and C 50 mg/ml producing a thickness of 250 nm, 300 nm and 400 nm.

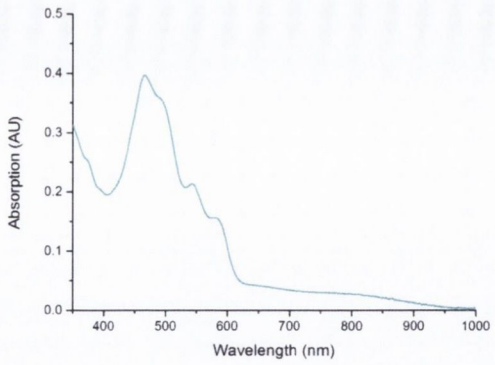

Figure 5.45 UV-Vis absorption of spincoated film of 1-1, PDI +RTAQ containing 1-10 PbS QD ,w/w, spincoated from a 40 mg per ml solution , on FTO glass

UV-Vis absorption spectroscopy was also used to analysis resulting deposited film as shown in Figure 5.45 , displaying the strong absorption of the resulting layer and its possible effectiveness at photon harvesting.

Table 5.6 Optimisation of spin coating for DLC cell fabrication showing the results obtained from a range of solutes and solvents. All spincoating was carried out at 1000 RPM, with a 200 rpm/sec ramp rate.

Contents	Composition, w/w%			Weight (mg / ml)	Solvent	Thickness	Uniformity of spincoating
	PDI	DLC	QD				
RTAQ	0	100	/	15	Chloroform	~ 30 nm	poor
RTAQ	/	100	/	30	Chloroform	~ 50 nm	poor
RTAQ	/	100	/	15	Cyclo-hexane	~ 100 nm	partial
RTAQ	/	100	/	30	Cyclo-hexane	~ 250 nm	excellent
RTAQ	/	100	/	50	Cyclo-hexane	~ 400 nm	excellent
RTAQ	/	100	/	40	Cyclo-hexane	~ 250 nm	excellent
RTAQ+PDI	66	33	/	30	1:3, w:w, Cyclo-hexane / Chloroform	~ 150 mn	excellent

5.5.3.ii Device results

To date a range of devices have been fabricated, by simply evaporating a Al or Ag based back electrode using vacuum deposition, to then produce the desired cell design. Unfortunately to date the devices have not shown a detectable electrical response under illumination, which at the moment is most likely due to improper fabrication. A range of cells produced to date is given in Table 7.5 in Appendix E.

5.6 Conclusions

In conclusion, we have demonstrated the optimisation of the separate components needed to build efficient QDSSC cells and DHCQD cells, while examining the properties of DLC/QD composites with the aim of solar cell fabrication.

Regarding QDDSCs cells, we firstly examined the fabrication of three different counter electrodes for QDDSC applications, Cu_2-S on a brass foil, PbS on a Pb foil and Pt on FTO glass. Following this, the catalytic activity of these electrodes were then analysed in a polysulphide aqueous electrolyte preferred in QDDSC designs using cyclic voltammetry, displaying the far higher response of Cu_2S and PbS relative to Pt based electrodes. Subsequently, we examined the construction of an optimal porous TiO_2 photoaniode; using three different forms of TIO_2, bulk TiO_2, 20 nm anatase TiO_2, and 200 nm TiO_2 particles, which were deposited sequentially and then put through a specific heating process to produce an electrode that was optimal for QD sensitisation. QDDSC cells were then fabricated, using a range of TiO_2 electrodes sensitised with CQDs through EPD, with the most efficient closed cell device to date shown using oleic acid capped CdSe QDs, producing a PCE of 0.22 % under AM1.5 1 sun illumination. We also demonstrated a PCE of 0.50% using oleic acid CdSe QDs in an open cell QDSSC cell design.

Concerning DHCQD cells, we have demonstrated the successful use of alternative fabrication techniques to produce the desired cells with the aim of using more commercially viable means. Therefore, firstly we have demonstrated the use of a solution based etching process to allow the production of multiple cells upon a single FTO coated glass. Next, we have shown the production of a thin film of TiO_2 for this cell through the novel use of highly diluted commercially sourced 20 nm TiO_2 pastes, producing a film of 300 nm in thickness with excellent surface coverage, adherence, chemical and crystal structure. Following this, we have shown the application of dip coating, as a novel means to produce MPA capped thin films of CdSe and PbS QDs for application in the DHCQD cell. Subsequently we demonstrated DHCQD cells using either CdSe, PbS or CdTe/CdSe QDs, from which the resulting cells showed a photovoltaic effect under illumination, though one that was below reported values to date.

Finally, we examined the effect of QD incorporation into two discotic liquid crystals, H6TP (2,3,6,7,10,11,Hexahexyloxy-triphenylene) and RTAQ (1,5-dihydroxy-2,3,6,7-tetrakis(3,7-dimethyloctyloxy)-9,10-anthraquinone). We have shown the effects of QD doping, using CdSe, PbS and CdS to these liquid crystals DC conductivity under illumination and darkness, displaying an overall increase in DC conductivity. We have also examined the effect of the same QDs

incorporation upon the resulting DLC phase of the materials using POM, showing a strong disruption of the DLC phase as QD concentration increased. Included in this study, we examined the effects of other impurities present in QD solutions, three common ligands used in QD synthesis, OA, ODA and ODPA and also elemental Se, examining their effects upon the resulting structure, with Se showing a strong increase in conductivity, while OA was shown to produce the least disruption to the DLC phase. We also examined the inclusion of a common electron acceptor, PDI, used in DLC solar cells reported and its effect upon conductivity and the DLC phase, showing little to no disrupting of the DLC phase, with a corresponding increase in conductivity of the composite. Finally we briefly carried the fabrication of novel QD/DLC solar cells using three proposed designs, though to date none of which have shown a detectable photovoltaic response.

References

96. Shen, H. B.; Yuan, H.; Niu, J. Z.; Xu, S. S.; Zhou, C. H.; Ma, L.; Li, L. S., Phosphine-Free Synthesis of High-Quality Reverse Type-I Znse/Cdse Core with Cds/$Cd_xzn_{1-x}s$/Zns Multishell Nanocrystals and Their Application for Detection of Human Hepatitis B Surface Antigen. *Nanotechnology* 2011, 22.

138. Jasieniak, J.; Mulvaney, P., From Cd-Rich to Se-Rich – the Manipulation of Cdse Nanocrystal Surface Stoichiometry. *Journal of the American Chemical Society* 2007, 129, 2841-2848.

141. Talapin, D. V.; Murray, C. B., Pbse Nanocrystal Solids for N- and P-Channel Thin Film Field-Effect Transistors. *Science* 2005, 310, 86-9.

146. Tang, J.; Wang, X. H.; Brzozowski, L.; Barkhouse, D. A. R.; Debnath, R.; Levina, L.; Sargent, E. H., Schottky Quantum Dot Solar Cells Stable in Air under Solar Illumination. *Advanced Materials* 2010, 22, 1398-+.

160. Morgan, B. J.; Watson, G. W., Intrinsic N-Type Defect Formation in Tio_2: A Comparison of Rutile and Anatase from Gga+U Calculations. *The Journal of Physical Chemistry C* 2010, 114, 2321-2328.

174. Kramer, I. J.; Sargent, E. H., Colloidal Quantum Dot Photovoltaics: A Path Forward. *ACS Nano* 2011, 5, 8506-8514.

183. Pattantyus-Abraham, A. G.; Kramer, I. J.; Barkhouse, A. R.; Wang, X. H.; Konstantatos, G.; Debnath, R.; Levina, L.; Raabe, I.; Nazeeruddin, M. K.; Grätzel, M.; Sargent, E. H., Depleted-Heterojunction Colloidal Quantum Dot Solar Cells. *ACS Nano* 2010, 4, 3374-3380.

196. Maraghechi, P.; Labelle, A. J.; Kirmani, A. R.; Lan, X. Z.; Adachi, M. M.; Thon, S. M.; Hoogland, S.; Lee, A.; Ning, Z. J.; Fischer, A.; Amassian, A.; Sargent, E. H., The Donor-Supply Electrode Enhances Performance in Colloidal Quantum Dot Solar Cells. *ACS Nano* 2013, 7, 6111-6116.

203. Ruhle, S.; Shalom, M.; Zaban, A., Quantum-Dot-Sensitized Solar Cells. *ChemPhysChem* 2010, 11, 2290-304.

204. Leschkies, K. S.; Beatty, T. J.; Kang, M. S.; Norris, D. J.; Aydil, E. S., Solar Cells Based on Junctions between Colloidal Pbse Nanocrystals and Thin Zno Films. *ACS Nano* 2009, 3, 3638-3648.

221. Lee, Y.-L.; Chang, C.-H., Efficient Polysulfide Electrolyte for Cds Quantum Dot-Sensitized Solar Cells. *Journal of Power Sources* 2008, 185, 584-588.

222. Jun, H. K.; Careem, M. A.; Arof, A. K., A Suitable Polysulfide Electrolyte for CdSe Quantum Dot-Sensitized Solar Cells. *International Journal of Photoenergy* 2013.

226. Lee, Y. L.; Lo, Y. S., Highly Efficient Quantum-Dot-Sensitized Solar Cell Based on Co-Sensitization of CdS/CdSe. *Adv. Funct. Mater.* 2009, 19, 604-609.

227. Shen, Q.; Yamada, A.; Tamura, S.; Toyoda, T., Cdse Quantum Dot-Sensitized Solar Cell Employing Tio_2 Nanotube Working-Electrode and Cu_2s Counter-Electrode. *Appl. Phys. Lett.* 2010, 97, 3.

229. Yang, Z.; Chen, C.-Y.; Liu, C.-W.; Li, C.-L.; Chang, H.-T., Quantum Dot–Sensitized Solar Cells Featuring CuS/CoS Electrodes Provide 4.1% Efficiency. *Advanced Energy Materials* 2011, 1, 259-264.

232. Lin, C. Y.; Teng, C. Y.; Li, T. L.; Lee, Y. L.; Teng, H. S., Photoactive P-Type Pbs as a Counter Electrode for Quantum Dot-Sensitized Solar Cells. *Journal of Materials Chemistry A* 2013, 1, 1155-1162.

233. Lee, J.-W.; Son, D.-Y.; Ahn, T. K.; Shin, H.-W.; Kim, I. Y.; Hwang, S.-J.; Ko, M. J.; Sul, S.; Han, H.; Park, N.-G., Quantum-Dot-Sensitized Solar Cell with Unprecedentedly High Photocurrent. *Sci. Rep.* 2013, 3.

234. Pan, Z. X.; Zhao, K.; Wang, J.; Zhang, H.; Feng, Y. Y.; Zhong, X. H., Near Infrared Absorption of $CdSe_xTe_{1-x}$, Alloyed Quantum Dot Sensitized Solar Cells with More Than 6% Efficiency and High Stability. *Acs Nano* 2013, 7, 5215-5222.

235. Pan, Z.; Zhang, H.; Cheng, K.; Hou, Y.; Hua, J.; Zhong, X., Highly Efficient Inverted Type-I CdS/CdSe Core/Shell Structure Qd-Sensitized Solar Cells. *ACS Nano* 2012, 6, 3982-3991.

238. Sung, S. D.; Lim, I.; Kang, P.; Lee, C.; Lee, W. I., Design and Development of Highly Efficient Pbs Quantum Dot-Sensitized Solar Cells Working in an Aqueous Polysulfide Electrolyte. *Chemical Communications* 2013, 49, 6054-6056.

247. Brown, P.; Kamat, P. V., Quantum Dot Solar Cells. Electrophoretic Deposition of Cdse–C_{60} Composite Films and Capture of Photogenerated Electrons with nNC_{60} Cluster Shell. *Journal of the American Chemical Society* 2008, 130, 8890-8891.

255. Murschell, A. E.; Sutherland, T. C., Anthraquinone-Based Discotic Liquid Crystals. *Langmuir* 2010, 26, 12859-12866.

257. Chiang, L. Y.; Safinya, C. R.; Clark, N. A.; Liang, K. S.; Bloch, A. N., Highly Oriented Fibres of Discotic Liquid Crystals. *Journal of the Chemical Society, Chemical Communications* 1985, 695-696.

258. Nakayama, H.; Ozaki, M.; Schmidt, W. F.; Yoshino, K., Measurements of Carrier Mobility and Quantum Yield of Carrier Generation in Discotic Liquid Crystal Hexahexyl-Oxytriphenylene by Time-of-Flight Method. *Jpn. J. Appl. Phys. Part 2 - Lett.* 1999, 38, L1038-L1041.

259. van de Craats, A. M.; Warman, J. M.; de Haas, M. P.; Adam, D.; Simmerer, J.; Haarer, D.; Schuhmacher, P., The Mobility of Charge Carriers in All Four Phases of the Columnar Discotic Material Hexakis(Hexylthio)Triphenylene: Combined Tof and Pr-Trmc Results. *Advanced Materials* 1996, 8, 823-826.

268. Hesse, H. C.; Schaffer, C.; Hundschell, C.; Narita, A.; Feng, X. L.; Mullen, K.; Nickel, B.; Schmidt-Mende, L., Large Polycyclic Aromatic Hydrocarbons for Application in Donor-Acceptor Photovoltaics. *Physica Status Solidi a-Applications and Materials Science* 2012, 209, 785-789.

269. Schmidt-Mende, L.; Fechtenkötter, A.; Müllen, K.; Moons, E.; Friend, R. H.; MacKenzie, J. D., Self-Organized Discotic Liquid Crystals for High-Efficiency Organic Photovoltaics. *Science* 2001, 293, 1119-1122.

270. Hesse, H. C.; Weickert, J.; Al-Hussein, M.; Dossel, L.; Feng, X. L.; Mullen, K.; Schmidt-Mende, L., Discotic Materials for Organic Solar Cells: Effects of Chemical Structure on Assembly and Performance. *Sol. Energy Mater. Sol. Cells* 2010, 94, 560-567.

273. Kumar, S.; Sagar, L. K., Cdse Quantum Dots in a Columnar Matrix. *Chemical Communications* 2011, 47, 12182-12184.

274. Kinkead, B.; Hegmann, T., Effects of Size, Capping Agent, and Concentration of Cdse and Cdte Quantum Dots Doped into a Nematic Liquid Crystal on the Optical and Electro-Optic Properties of the Final Colloidal Liquid Crystal Mixture. *J. Mater. Chem.* 2010, 20, 448-458.

275. Mirzaei, J.; Reznikov, M.; Hegmann, T., Quantum Dots as Liquid Crystal Dopants. *J. Mater. Chem.* 2012, 22, 22350-22365.

276. Mirzaei, J.; Urbanski, M.; Yu, K.; Kitzerow, H.-S.; Hegmann, T., Nanocomposites of a Nematic Liquid Crystal Doped with Magic-Sized Cdse Quantum Dots. *J. Mater. Chem.* 2011, 21, 12710-12716.

277. Shandryuk, G. A.; Matukhina, E. V.; Vasil'ev, R. B.; Rebrov, A.; Bondarenko, G. N.; Merekalov, A. S.; Gas'kov, A. M.; Talroze, R. V., Effect of H-Bonded Liquid Crystal Polymers on Cdse Quantum Dot Alignment within Nanocomposite. *Macromolecules* 2008, 41, 2178-2185.

278. Konshina, E. A.; Gavrish, E. O.; Orlova, A. O.; Artem'ev, M. V., Effect of Dispersed CdSe/ZnS Quantum Dots on Optical and Electrical Characteristics of Nematic Liquid Crystal Cells. *Tech. Phys. Lett.* 2011, 37, 1011-1014.

285. Tachan, Z.; Shalom, M.; Hod, I.; Ruhle, S.; Tirosh, S.; Zaban, A., Pbs as a Highly Catalytic Counter Electrode for Polysulfide-Based Quantum Dot Solar Cells. *Journal of Physical Chemistry C* 2011, 115, 6162-6166.

311. Ning, Z.; Voznyy, O.; Pan, J.; Hoogland, S.; Adinolfi, V.; Xu, J.; Li, M.; Kirmani, A. R.; Sun, J.-P.; Minor, J.; Kemp, K. W.; Dong, H.; Rollny, L.; Labelle, A.; Carey, G.; Sutherland, B.; Hill, I.; Amassian, A.; Liu, H.; Tang, J.; Bakr, O. M.; Sargent, E. H., Air-Stable N-Type Colloidal Quantum Dot Solids. *Nat. Mater.* 2014, 13, 822-828.

343. Lunt, R. R.; Osedach, T. P.; Brown, P. R.; Rowehl, J. A.; Bulovic, V., Practical Roadmap and Limits to Nanostructured Photovoltaics. *Advanced Materials* 2011, 23, 5712-5727.

344. Debnath, R.; Bakr, O.; Sargent, E. H., Solution-Processed Colloidal Quantum Dot Photovoltaics: A Perspective. *Energy & Environmental Science* 2011, 4, 4870-4881.

345. Kouhnavard, M.; Ikeda, S.; Ludin, N. A.; Ahmad Khairudin, N. B.; Ghaffari, B. V.; Mat-Teridi, M. A.; Ibrahim, M. A.; Sepeai, S.; Sopian, K., A Review of Semiconductor Materials as Sensitizers for Quantum Dot-Sensitized Solar Cells. *Renewable and Sustainable Energy Reviews* 2014, 37, 397-407.

346. Kramer, I. J.; Sargent, E. H., The Architecture of Colloidal Quantum Dot Solar Cells: Materials to Devices. *Chem. Rev.* 2013, 114, 863-882.

347. Meng, K.; Surolia, P. K.; Thampi, K. R., $Batio_3$ Photoelectrodes for Cds Quantum Dot Sensitized Solar Cells. *Journal of Materials Chemistry A* 2014, 2, 10231-10238.

348. Hurum, D. C.; Agrios, A. G.; Gray, K. A.; Rajh, T.; Thurnauer, M. C., Explaining the Enhanced Photocatalytic Activity of Degussa P25 Mixed-Phase Tio2 Using Epr. *J. Phys. Chem. B* 2003, 107, 4545-4549.

349. Hore, S.; Vetter, C.; Kern, R.; Smit, H.; Hinsch, A., Influence of Scattering Layers on Efficiency of Dye-Sensitized Solar Cells. *Sol. Energy Mater. Sol. Cells* 2006, 90, 1176-1188.

350. Xu, J.; Xiao, J.; Dong, J.; Luo, Y.; Li, D.; Meng, Q., A New in-Situ Preparation Method to Cus Electrodes for CdS/CdSe Co-Sensitized Solar Cells. *Electrochimica Acta* 2014, 127, 180-185.

351. Ke, W.; Fang, G.; Lei, H.; Qin, P.; Tao, H.; Zeng, W.; Wang, J.; Zhao, X., An Efficient and Transparent Copper Sulfide Nanosheet Film Counter Electrode for Bifacial Quantum Dot-Sensitized Solar Cells. *Journal of Power Sources* 2014, 248, 809-815.

352. Yu, X.; Zhu, J.; Liu, F.; Wei, J.; Hu, L.; Dai, S., Metal Chalcogenide Complex-Mediated Fabrication of Cu_2S Film as Counter Electrode in Quantum Dot Sensitized Solar Cells. *Sci. China Chem.* 2013, 56, 977-981.

353. Ye, M.; Chen, C.; Zhang, N.; Wen, X.; Guo, W.; Lin, C., Quantum-Dot Sensitized Solar Cells Employing Hierarchical Cu_2S Microspheres Wrapped by Reduced Graphene Oxide Nanosheets as Effective Counter Electrodes. *Advanced Energy Materials* 2014, 4, n/a-n/a.

354. Yang, Y.; Zhu, L.; Sun, H.; Huang, X.; Luo, Y.; Li, D.; Meng, Q., Composite Counter Electrode Based on Nanoparticulate PbS and Carbon Black: Towards Quantum Dot-Sensitized Solar Cells with Both High Efficiency and Stability. *ACS Applied Materials & Interfaces* 2012, 4, 6162-6168.

355. Zhang, J.; Zhao, F.; Tang, G.; Lin, Y., Influence of Highly Efficient Pbs Counter Electrode on Photovoltaic Performance of Cdse Quantum Dots-Sensitized Solar Cells. *J Solid State Electrochem* 2013, 17, 2909-2915.

356. Zhou, Y. F.; Riehle, F. S.; Yuan, Y.; Schleiermacher, H. F.; Niggemann, M.; Urban, G. A.; Kruger, M., Improved Efficiency of Hybrid Solar Cells Based on Non-Ligand-Exchanged Cdse Quantum Dots and Poly(3-Hexylthiophene). *Appl. Phys. Lett.* 2010, 96.

357. Ren, S.; Chang, L.-Y.; Lim, S.-K.; Zhao, J.; Smith, M.; Zhao, N.; Bulović, V.; Bawendi, M.; Gradečak, S., Inorganic–Organic Hybrid Solar Cell: Bridging Quantum Dots to Conjugated Polymer Nanowires. *Nano Letters* 2011, 11, 3998-4002.

358. Plass, R.; Pelet, S.; Krueger, J.; Grätzel, M.; Bach, U., Quantum Dot Sensitization of Organic–Inorganic Hybrid Solar Cells. *The Journal of Physical Chemistry B* 2002, 106, 7578-7580.

359. Choi, J. J.; Lim, Y.-F.; Santiago-Berrios, M. E. B.; Oh, M.; Hyun, B.-R.; Sun, L.; Bartnik, A. C.; Goedhart, A.; Malliaras, G. G.; Abruña, H. c. D.; Wise, F. W.; Hanrath, T., PbSe Nanocrystal Excitonic Solar Cells. *Nano Lett* 2009, 9, 3749-3755.

360. Choi, J. J.; Wenger, W. N.; Hoffman, R. S.; Lim, Y.-F.; Luria, J.; Jasieniak, J.; Marohn, J. A.; Hanrath, T., Solution-Processed Nanocrystal Quantum Dot Tandem Solar Cells. *Advanced Materials* 2011, 23, 3144-3148.

361. Feng, X. L.; Liu, M. Y.; Pisula, W.; Takase, M.; Li, J. L.; Mullen, K., Supramolecular Organization and Photovoltaics of Triangle-Shaped Discotic Graphenes with Swallow-Tailed Alkyl Substituents. *Advanced Materials* 2008, 20, 2684-+.

362. Holt, L. A.; Bushby, R. J.; Evans, S. D.; Burgess, A.; Seeley, G., A 10^6-Fold Enhancement in the Conductivity of a Discotic Liquid Crystal Doped with Only 1% (W/W) Gold Nanoparticles. *Journal of Applied Physics* 2008, 103, 063712.

363. Shivanandareddy, A. B.; Krishnamurthy, S.; Lakshminarayan, V.; Kumar, S., Mutually Ordered Self-Assembly of Discotic Liquid Crystal-Graphene Nanocomposites. *Chemical Communications* 2014, 50, 710-712.

364. Bisoyi, H. K.; Kumar, S., Carbon Nanotubes in Triphenylene and Rufigallol-Based Room Temperature Monomeric and Polymeric Discotic Liquid Crystals. *J. Mater. Chem.* 2008, 18, 3032-3039.

365. Prasad, V.; Roy, A.; Nagaveni, N. G.; Gayathri, K., Anthraquinone-Based Discotic Liquid Crystals: New Monomers and Dimers. *Liquid Crystals* 2011, 38, 1301-1314.

366. Vercelli, B.; Zotti, G.; Berlin, A., Alternate Monolayers of Cdse Nanocrystals and Perylene Tetracarboxylate: Quantum Dot Hypersensitization for Dye-Sensitized Solar Cells. *ACS Applied Materials & Interfaces* 2012, 4, 3233-3238.

367. Gerlach, F.; Täuber, D.; von Borczyskowski, C., Correlated Blinking Via Time Dependent Energy Transfer in Single CdSe Quantum Dot-Dye Nanoassemblies. *Chem. Phys. Lett.* 2013, 572, 90-95.

368. Kowerko, D.; Schuster, J.; Amecke, N.; Abdel-Mottaleb, M.; Dobrawa, R.; Wurthner, F.; von Borczyskowski, C., Fret and Ligand Related Non-Fret Processes in Single Quantum Dot-Perylene Bisimide Assemblies. *Physical Chemistry Chemical Physics* 2010, 12, 4112-4123.

369. Meng, K.; Surolia, P. K.; Byrne, O.; Thampi, K. R., Efficient Cds Quantum Dot Sensitized Solar Cells Made Using Novel Cu_2s Counter Electrode. *Journal of Power Sources* 2014, 248, 218-223.

370. Sommeling, P. M.; O'Regan, B. C.; Haswell, R. R.; Smit, H. J. P.; Bakker, N. J.; Smits, J. J. T.; Kroon, J. M.; van Roosmalen, J. A. M., Influence of a $Ticl_4$ Post-Treatment on Nanocrystalline TiO_2 Films in Dye-Sensitized Solar Cells. *The Journal of Physical Chemistry B* 2006, 110, 19191-19197.

371. Mori, R.; Ueta, T.; Sakai, K.; Niida, Y.; Koshiba, Y.; Lei, L.; Nakamae, K.; Ueda, Y., Organic Solvent Based Tio_2 Dispersion Paste for Dye-Sensitized Solar Cells Prepared by Industrial Production Level Procedure. *J. Mater. Sci.* 2011, 46, 1341-1350.

372. Choi, H.; Jung, Y.; Kim, S., Size Effects in the Raman Spectra of Tio Nanoparticles. *Vibrational Spectroscopy* 2005, 37, 33-38.

373. Li, J.-G.; Ishigaki, T.; Sun, X., Anatase, Brookite, and Rutile Nanocrystals Via Redox Reactions under Mild Hydrothermal Conditions: Phase-Selective Synthesis and Physicochemical Properties. *The Journal of Physical Chemistry C* 2007, 111, 4969-4976.

374. Rashidzadeh, M., Synthesis of High-Thermal Stable Titanium Dioxide Nanoparticles. *International Journal of Photoenergy* 2008.

375. Zhao, Y.; Li, C. Z.; Liu, X. H.; Gu, F.; Jiang, H. B.; Shao, W.; Zhang, L.; He, Y., Synthesis and Optical Properties of TiO_2 Nanoparticles. *Mater. Lett.* 2007, 61, 79-83.

Chapter 6 Conclusions and Future Work

6.1 Conclusions

In our work, we have demonstrated the utility of semiconductor nanocrystals to the application of photon harvesting for photovoltaic devices. This was achieved by firstly synthesising a range of core and core shell quantumly confined semiconductor nanostructures utilising the hot injection approaches. We therefore have synthesised a range of materials that show absorption in the UV, visible and infrared, with a range of band gap structures, with the aim to determine the optimal material for incorporation into a photovoltaic device and to explore the unmatched flexibility that the quantum dot offers in this respect.

Therefore a range of CdSe QDs were synthesised capped in a shell of either oleic acid, ODPA or ODA, displaying a range of absorption and emission properties in the visible range. Following this is, two other core QDs were synthesised showing first exciton absorption and emission in the UV range produced using CdS, or NIR range produced using PbS. Following this, we have demonstrated the synthesis of core/shell QDs of CdSe/CdS, CdS/CdSe, and CdTe/CdSe, by making use of the SILAR approach, enabling careful control of the shell thickness produced. We have also produced heterostructured CdSe/CdS dot in rod structures in a range of morphologies.

Aside from hot injection synthesis of nanostructures, we have also exhibited the ability to deposit Au NPs upon CdSe/CdS NRs and shown the resulting optical properties produced. The approach of cation exchange has also been demonstrated as a means to produce other novel nanomaterials, not readily obtainable through hot injection, including PbS/CdS QDs, $Cu_{2-x}Se$ QDs, $Cu_{2-x}Se/Cu_{2-x}S$ NRs and $Pb_{1-x}Se/Pb_{1-x}S$ NRs.

We have also shown in our investigation the effects of halide/oleylamine solutions upon a range of QDs. From this, we have demonstrated large increases in luminescent quantum yields observed form the addition of these solutions increasing OA capped CdSe QY from 1.5% to 32 %, ODPA capped CdSe QY from 25% to 42.2% and ODA capped CdSe QY from 0.8 to 16.8 %. Therefor this is an excellent method to increase surface passivation of QDs for use in photovoltaic applications, reducing efficiency loss due to recombination at the surface of the QD.

Following nanoparticles synthesis, we demonstrated the application of EPD as means to sensitise porous TiO_2 electrode with a range of QDs and QRs has been shown, and the effects of a number of post treatments upon the resulting photocurrents of the electrodes tested under illumination. The study began by investigating the effects of a number of properties upon the relative success of electrophoretic deposition using oleic acid-capped CdSe QDs as the model test system. From this, we showed the novel observation that the application of DCM as a solvent for EPD has a hugely influential effect upon the total loading of electrodes achieved from deposition, increasing the success of the deposition tremendously. We also demonstrated a specific example of EPD as sensation method to TiO_2 due to its ability to cause a near uniform sensitisation of the porous electrode relative to depth, allowing optimal sensitisation of the TiO_2 electrode for QDDSC applications.

Following optimisation of the deposition, we investigated the difference of QD loading when using CdSe QDs capped with other ligands, investigating the deposition of ODA capped CdSe QDs and ODPA capped CdSe QDs. From this, we determined that ODPA capped CdSe QDs showed the optimal performance under EPD, but only after an additional cleaning step to remove excess ligands present after ODPA capped CdSe QD synthesis was carried out.

Treatments were then examined with the aim to increase the resulting photocurrent of QD sensitised TiO_2 electrodes. We have shown that the use of SILAR deposition of ZnS and CdS both display a large increase in the resulting photocurrents. We also investigated the effect of ligand exchange, using MPA and HTAC, with MPA showing a strong decrease in efficiency, while HTAC showed a strong increase.

We then used EPD to show its ability to produce a range of sensitised TIO_2 electrode through EPD of a range of core and core/shell QDs and QRs including CdS QDs, PbS QDs, CdSe/CdS QDs, CdS/CdSe QDs, CdTe/CdSe QDs and CdSe/CdS QRs. The photocurrent response of all electrode was also examined to determine the optimal material for photosensitisation, with CdS/CdSe and CdTe/CdSe core/shell QDs, producing photocurrents outperforming the below par loading achieved.

Cation exchange was used as a novel approach to electrophoretically sensitised TiO_2 electrodes, displaying its ability to convert already deposited CdSe QDs to $Cu_{2-x}Se$ QDs to PbSe QDs, showing a dramatic change in the resulting absorption. Cation exchange was also used as a means to produce core/shell PbS/CdS QDs from PbS sensitised TiO_2 electrodes and we have investigated

its effect upon the resulting photocurrent response, which surprisingly showed a decrease in current.

Regarding QDSSCs cells, we firstly examined the fabrication of three different counter electrodes for QDSSC applications, Cu_2S on a brass foil, PbS on a Pb foil and Pt on FTO glass. Following this, the catalytic activity of these electrode were then analysed in a polysulphide aqueous electrolyte preferred in QDSSC designs. This was achieved using cyclic voltammetry, which displayed a far higher response of Cu_2S and PbS relative to Pt based electrodes. Subsequently, we examined the construction of an optimal porous TiO_2 photoaniode; using three different forms of TIO_2, bulk TiO_2, 20 nm anatase TiO_2, and 200 nm TiO_2 particles, which were deposited sequentially and then put through a specific heating process to produce an electrode that was optimal for QD sensitisation. QDDSC cells were then fabricated, using a range of TiO_2 electrodes sensitised with CQDs through EPD, with the most efficient sealed device to date shown using oleic acid capped CdSe QDs, producing a PCE of 0.22 % under AM1.5 1 sun illumination. We also demonstrated a PCE of 0.50% using an open cell QDSSC cell design using oleic acid capped CdSe QDs.

Concerning DHCQD cells, we have demonstrated the successful use of alternative fabrication techniques to produce the desired cells with the aim of using more commercially viable means. Therefore, firstly we have demonstrated the use of a solution based etching process to allow the production of multiple cells upon a single FTO coated glass. Next, we have shown the production of a thin film of TiO_2 for this cell through the novel use of highly diluted commercially sourced 20 nm TiO_2 pastes, producing a film of 300 nm in thickness with excellent surface coverage, adherence, chemical and crystal structure. Following this, we have shown the application of dip coating, as a novel means to produce MPA capped thin films of CdSe and PbS QDs for application in the DHCQD cell. Subsequently we demonstrated DHCQD cells using either CdSe, PbS or CdTe/CdSe QDs, from which resulting the cells showed a photovoltaic effect under illumination, though one that was below reported values to date.

The effect of QD incorporation into two discotic liquid crystals was also determined, H6TP and RTAQ. We have shown the effects of QD doping, using CdSe, PbS and CdS to these liquid crystals DC conductivity under illumination and darkness, displaying an overall increase in DC conductivity. We have also examined the effect of the same QDs incorporation upon the resulting DLC phase of the materials using POM, showing a strong disruption of the DLC phase as QD concentration increased. Included in this study we examined the effects of other impurities present in QD solutions, three common ligands used in QD synthesis, OA, ODA and

ODPA and also elemental Se, examining their effects upon the resulting structure, with Se showing a strong increase in conductivity, while OA was shown to produce the least disruption to their DLC phase. We also examined the inclusion of a common electron acceptor, PDI, used in DLC solar cells reported and its effect upon conductivity and the DLC phase, showing little to no disrupting of the DLC phase, with a corresponding increase in conductivity of the composite. Finally we briefly carried the fabrication of novel QD/DLC solar cells using three proposed designs, though to date none of which have shown a detectable photovoltaic response.

In conclusion, our work has explored the application of quantumly confined semiconducting materials as photon harvesters in a range of photovoltaic designs, demonstrating the great utility of these materials and the range of options open to their use in these applications. From this exploration and demonstration, we believe our work will contribute in the ongoing search for a new photovoltaic device that will allow for the efficient harvesting of the world's largest clean energy resource, the sun.

6.2 Future Work

A range of work has arisen from our research that we believe would be advantageous to explore, with the aim of furthering our aims of innovation in quantum dot based photosensitisation and photon harvesting.

1. Attempt the synthesis of a range of core-shell structure through cation exchange as a means to produce unique quantum dot materials, i.e. convert the CdTe/CdSe quantum dots to PbTe/PbSe QDs via Cu^{1+} ions exchange.
2. Synthesis and analysis of novel gold – QD structures through application of the already demonstrated Au deposition upon CdSe/CdS NRs to the range of synthesised Cd based core/shell QD to investigate the novel plasmon/plasmonic interactions.
3. Continue examination of the effects of oleylamine based post treatments effects upon QDs, by carrying out treatments with other Cd based halide salts in oleylamine to

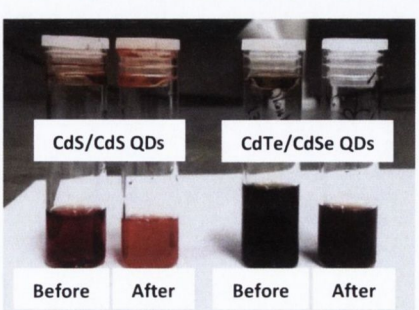

Figure 6.1 Photograph showing the effect of oleylamine/$CdCl_2$ solution treatment upon core shell QDs of CdS/CdSe and CdTe/CdSe

determine the effect of the halide anion. The study could also be expanded by the examination of the post treatments upon other core shell QDs such as CdS/CdSe and CdTe/CdSe QDs, which have shown some preliminary results indicating a strong increase in luminescence due to the addition of oleylamine solution of $CdCl_2$ as shown in Figure 6.1.

4. It has been reported that dipping an electrode into K_2S or Na_2S, S can result in exchange of the surface ligand with an elemental ligand, which therefore replaces any surface ligands prior to treatment, therefore would like to test the effect of this as an alternative ligand exchange to produce DHCQD cell.
5. Incorporate CdSe/CdS/Au NRs structures into a TiO_2 porous electrode using electrophoretic deposition and determine the change in photocurrent response due to the gold incorporation
6. Investigate the effects of shell thickness of type I, type II and reverse type I QDs upon the resulting photocurrent responses of electrophoretically sensitised TiO_2 cells and upon the resulting efficiency of QDSSC cells.
7. To further investigate the photocurrent response of QD sensitised porous TiO_2 electrodes by carrying out tests under illuminated of a AM1.5 100 W/M^2 light source using an aqueous polysulphide electrolyte (1M Na_2S, 1M S) and a CuS counter electrode, so as to better simulate the responses I should expect from electrodes incorporated into a closed QDSSC cell
8. Further characterise the quantum dot sensitised TiO_2 QDSSC electrodes through the use of a in house built incident photocurrent response efficiency , so as to determine the efficiency of the cells relative to illumination wavelength
9. Carry out further testing of QDSSC designs with PbS counter electrode using alternative means to seal the cell. In addition, carry out further testing with core/shell sensitised TiO_2 electrodes including cation exchanged QD sensitised electrodes and electrodes post treated with CdS or HTAC treatments.
10. Fabricate and test the efficiency of alternative metal foils as a means to produce novel metal sulphide counter electrodes for QDSSC cells, i.e. investigate the use of Co or Ni metal foil, since CoS and Ni nanoparticulate electrodes have been reported as an alternative effective counter electrode for QDSSC utilisation. [228-231]
11. The results obtained to date have been very disappointing concerning the DLC cells therefore it is also possible to attempt two other designs for discotic liquid based solar cells which have shown promising results with other DLCs. The new designs make us of

the incorporation of PEDOT/PSS to modify design 2 and design 3, by incorporating it between the absorber layer and the Ag back contact as seen in design 4 or between the TCO and the DLC as seen in design 5. In both cells, it serves the same function, acting as an exciton blocker layer, preventing electron injection and enabling hole transport. [271, 272].

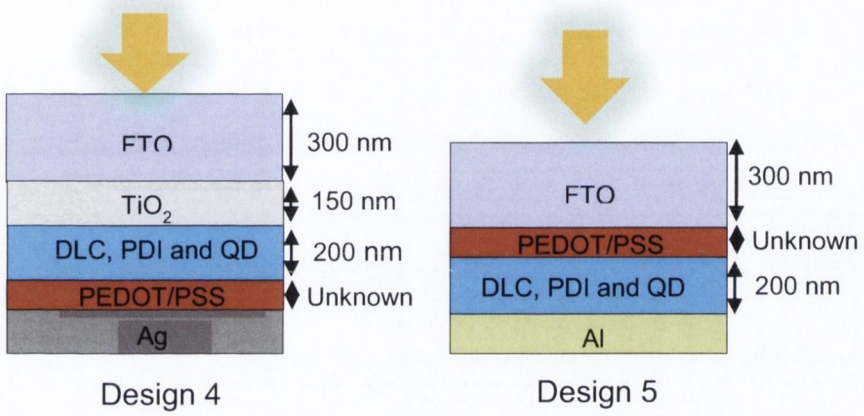

Figure 6.2 Diagram of two alternative DLC cell designs that have been reported in literature and have shown a level of success.

References

228. Yang, Z.; Chen, C.-Y.; Liu, C.-W.; Chang, H.-T., Electrocatalytic Sulfur Electrodes for CdS/CdSe Quantum Dot-Sensitized Solar Cells. *Chemical Communications* 2010, 46, 5485-5487.
229. Yang, Z.; Chen, C.-Y.; Liu, C.-W.; Li, C.-L.; Chang, H.-T., Quantum Dot–Sensitized Solar Cells Featuring CuS/CoS Electrodes Provide 4.1% Efficiency. *Advanced Energy Materials* 2011, 1, 259-264.
230. Kim, H. J.; Kim, S. W.; Gopi, C.; Kim, S. K.; Rao, S. S.; Jeong, M. S., Improved Performance of Quantum Dot-Sensitized Solar Cells Adopting a Highly Efficient Cobalt Sulfide/Nickel Sulfide Composite Thin Film Counter Electrode. *Journal of Power Sources* 2014, 268, 163-170.
231. Kim, H.-J.; Kim, D.-J.; Rao, S. S.; Savariraj, A. D.; Soo-Kyoung, K.; Son, M.-K.; Gopi, C. V. V. M.; Prabakar, K., Highly Efficient Solution Processed Nanorice Structured NiS Counter Electrode for Quantum Dot Sensitized Solar Cells. *Electrochimica Acta* 2014, 127, 427-432.
271. Zheng, Q.; Fang, G.; Bai, W.; Sun, N.; Qin, P.; Fan, X.; Cheng, F.; Yuan, L.; Zhao, X., Efficiency Improvement in Organic Solar Cells by Inserting a Discotic Liquid Crystal. *Sol. Energy Mater. Sol. Cells* 2011, 95, 2200-2205.
272. Jeong, S.; Kwon, Y.; Choi, B. D.; Ade, H.; Han, Y. S., Improved Efficiency of Bulk Heterojunction Poly(3-Hexylthiophene): 6,6 -Phenyl-C-61-Butyric Acid Methyl Ester Photovoltaic Devices Using Discotic Liquid Crystal Additives. *Appl. Phys. Lett.* 2010, 96.

Chapter 7 Appendix

7.1 Appendix A: Equations

7.1.1 Exciton Bohr radius

$$a_{ex} = a_h \, \varepsilon \, m_0/\mu$$

$$\mu = 1/(m_e^* + m_h^*)$$

Equation 7.1 Where a_{ex}= is the exciton radius, a_H is the Bohr radius of the hydrogen atom, ε is the permittivity of the material, m_o is the electron mass, m_e^* is the electron effective mass and m_h^* is the hole effective mass.

This equation can be used to calculate the Bohr exciton radius of a given semiconductor, therefore giving an insight into the desired size of nanocrystal dimensions to observe quantum confinement effects.

7.1.2 Schottky Barrier Height

$$SB = \phi_m - \chi_s \; (i) \; (n-type) \qquad SB = E_g + (\phi_m - \chi_s) \; (ii) \; (p-type)$$

Equation 7.2 This describes how to calculate the Schottky barrier height for a Schottky junction formed between an n-type semiconductor (i) or a p-type conductor (ii) and a metal, where φ_m is the workfunction of the metal, E_g is the band gap of the semiconductor and χ_s is the electron affinity of the semiconductor.

This describes the Schottky barrier height formed between a semiconductor and a metal.

7.1.3 The Marcus equation

$$k_{et} = \frac{2\pi}{\hbar} |H_{AB}|^2 \frac{1}{\sqrt{4\pi k_b T}} \exp\left(\frac{(\lambda + \Delta G^\circ)^2}{4\lambda k_b T}\right)$$

Equation 7.3 Where k_{et} is the rate of electron transfer, $|H_{AB}|$ is the electronic coupling between the initial and final states, λ is the reorganization energy (both inner and outer-sphere), and ΔG is the total Gibbs free energy change for an electron transfer reaction , k_b is the Boltzmann constant , T is temperature in Kelvin, and $\hbar$ is planks constant divided by 2π.

This equation describes the expected rate of charge transfer between different electronic states.

7.1.4 The Brus Equation

$$E = E_g + h^2/8R^2 \, [1/m_e^* + 1/m_h^*] - 1.8e^2/4\pi\varepsilon_0\varepsilon_\alpha \, R$$

Equation 7.4 Where E is the new band gap energy due to quantum confinement, E_g is the bulk band gap energy, R is the radius of the sample, , m_e^* is the electron effective mass and m_h^* is the hole effective mass, ε_0 is the permittivity of a vacuum and ε_α is the high frequency dielectric constant.

This describes the changes in the band gap of a semiconductor crystal as its radius decreases, and so demonstrated the observed effect of increased band gap energy as the crystal becomes of the order of the Bohr exciton radius.

7.1.5 Energy balance underlying Heterostructures formation

$$\Delta G_s = \gamma_1 - \gamma_2 + \gamma_{1,2}$$

Equation 7.5 This represents the Gibbs free energy surface change (ΔG_s),og a heterogeneous deposition process, while γ_1 and γ_2 represent the surface energies of the respective materials and $\gamma_{1,2}$ is the solid/solid interface energy. [298]

This equation can be used to determine the type of structure that will be formed when creating heterostructured nanocrystal.

7.1.6 Electrophoretic deposition

$$w = -\mu E S C_d \frac{\phi_s}{\phi_d - \phi_s} t$$

Equation 7.6 Where deposit yield (w), the electric field strength (E), the surface area of the electrode (S), φ_s and φ_d are the volumetric concentration of particles in suspension and deposit, respectively, C_d is the mass concentration of particles in the deposit, t is time and μ is the electrophoretic mobility and is given by

$$\mu = \varepsilon\xi/6\pi\eta$$

Equation 7.7 This describes the factors that affect the electrophoretic mobility of particles in solution, in which ε is the permittivity, ξ is the zeta potential and η is the viscosity of the solution.

This describes the factors which effect the deposition weight achieved upon a planar electrode and so accurately describes the factors to consider the deposition of QDs upon an electrode. This relationship was first derived in 1999 [317] [376] and is a modification of the Hamaker's equation.[377]

7.2 Appendix B: Tables of Material Properties

Table 7.1 Bulk modulus values for common binary semiconductors , reproduced from reference [104].

Semiconductor	Bulk Modules (GPa)
InSb	47
InAs	60
InP	71
CdTe	42
CdSe	53
CdS	62
ZnTe	61.2
ZnSe	64.7
ZnS	74.32

Table 7.2 Lattice mismatch of shell on core calculated from bulk material lattice constants of the zinc blende crystal structures of a number of common binary semiconductors.

Lattice Constants of Zinc-Blende Crystal Structure		Lattice Mismatch of Zinc Blende Crystal Structures (shell on core)													
CdTe	6.482		CdTe	CdSe	CdS	ZnO	ZnS	ZnSe	ZnTe	InP	InAs	InSb	GaP	GaAs	GaSb	GaN
CdSe	6.05	CdTe	0.0%	7.1%	11.1%	41.5%	19.6%	14.3%	6.3%	10.5%	7.0%	0.0%	18.9%	14.7%	6.3%	43.1%
CdS	5.832	CdSe	-6.7%	0.0%	3.7%	32.1%	11.6%	6.7%	-0.8%	3.1%	-0.1%	-6.6%	11.0%	7.0%	-0.8%	33.5%
ZnO *	4.58	CdS	-10.0%	-3.6%	0.0%	27.3%	7.6%	2.9%	-4.4%	-0.6%	-3.7%	-10.0%	7.0%	3.2%	-4.3%	28.7%
ZnS	5.42	ZnO	-29.3%	-24.3%	-21.5%	0.0%	-15.5%	-19.2%	-24.9%	-22.0%	-24.4%	-29.3%	-16.0%	-19.0%	-24.9%	1.1%
ZnSe	5.67	ZnS	-16.4%	-10.4%	-7.1%	18.3%	0.0%	-4.4%	-11.1%	-7.6%	-10.5%	-16.4%	-0.6%	-4.1%	-11.1%	19.6%
ZnTe	6.1	ZnSe	-12.5%	-6.3%	-2.8%	23.8%	4.6%	0.0%	-7.0%	-3.4%	-6.4%	-12.5%	4.0%	0.3%	-7.0%	25.1%
InP	5.8687	ZnTe	-5.9%	0.8%	4.6%	33.2%	12.5%	7.6%	0.0%	3.9%	0.7%	-5.9%	11.9%	7.9%	-3.7%	34.6%
InAs	6.0584	InP	-9.5%	-3.0%	0.6%	28.1%	8.3%	3.5%	-3.8%	0.0%	-3.1%	-9.4%	7.7%	3.8%	-3.7%	29.5%
InSb	6.4794	InAs	-6.5%	0.1%	3.9%	32.3%	11.8%	6.9%	-0.7%	3.2%	0.0%	-6.5%	11.1%	7.2%	-0.6%	33.7%
GaP	5.4512	InSb	0.0%	7.1%	11.1%	41.5%	19.5%	14.3%	6.2%	10.4%	6.9%	0.0%	18.9%	14.6%	6.3%	43.0%
GaAs	5.6533	GaP	-15.9%	-9.9%	-6.5%	19.0%	0.6%	-3.9%	-10.6%	-7.1%	-10.0%	-15.9%	0.0%	-3.6%	-10.6%	20.3%
GaSb	6.0959	GaAs	-12.8%	-6.6%	-3.1%	23.4%	4.3%	-0.3%	-7.3%	-3.7%	-6.7%	-12.7%	3.7%	0.0%	-7.3%	24.8%
GaN	4.531	GaSb	-6.0%	0.8%	4.5%	33.1%	12.5%	7.5%	-0.1%	3.9%	0.6%	-5.9%	11.8%	7.8%	0.0%	34.5%
		GaN	-30.1%	-25.1%	-22.3%	-1.1%	-16.4%	-20.1%	-25.7%	-22.8%	-25.2%	-30.1%	-16.9%	-19.9%	-25.7%	0.0%

Table 7.3 Lattice mismatch of shell on core calculated from bulk material lattice constants of the a and c axes of the wurtzite crystal structures of a number of common binary semiconductors.

Wurtzite Lattice Constants		
	a =	c =
CdSe	4.3	7.02
CdS	4.16	6.756
ZnTe	4.27	6.99
ZnSe	3.98	6.53
ZnS	3.82	6.26
ZnO	3.2495	5.2069
MgTe	4.53	7.405
GaN	3.19	5.189
InN	3.544	5.7034

Lattice Mismatch of Wurtzite Blende Crystal Structures (shell on core)									
	CdSe	CdS	ZnTe	ZnSe	ZnS	ZnO	MgTe	GaN	InN
CdSe	0.0%	3.4%	0.7%	8.0%	12.6%	32.3%	-5.1%	34.8%	21.3%
	0.0%	3.9%	0.4%	7.5%	12.1%	34.8%	-5.2%	35.3%	23.1%
CdS	-3.3%	0.0%	-2.6%	4.5%	8.9%	28.0%	-8.2%	30.4%	17.4%
	-3.8%	0.0%	-2.6%	3.5%	7.9%	29.8%	-8.8%	30.2%	18.5%
ZnTe	-0.7%	2.6%	0.0%	7.3%	11.8%	31.4%	-5.7%	33.9%	20.5%
	-0.4%	3.5%	0.0%	7.0%	11.7%	34.2%	-5.6%	34.7%	22.6%
ZnSe	-7.4%	-4.3%	-6.8%	0.0%	4.2%	22.5%	-12.1%	-11.8%	14.5%
	-7.0%	-3.3%	-6.6%	0.0%	4.3%	25.4%	-11.8%	25.8%	14.5%
ZnS	-11.2%	-8.2%	-10.5%	-4.0%	0.0%	17.6%	-15.7%	19.7%	7.8%
	-10.8%	-7.3%	-10.4%	-4.1%	0.0%	20.2%	-15.5%	20.6%	9.8%
ZnO	-24.4%	-21.9%	-23.9%	-18.4%	-14.9%	0.0%	-28.3%	1.9%	-8.3%
	-25.8%	-22.9%	-25.5%	-20.3%	-16.8%	0.0%	-29.7%	0.3%	-8.7%
MgTe	5.3%	8.9%	6.1%	13.8%	18.6%	39.4%	0.0%	42.0%	27.8%
	5.5%	9.6%	5.9%	13.4%	18.3%	42.2%	0.0%	42.7%	29.8%
GaN	-25.8%	-23.3%	-25.3%	-19.8%	-16.5%	-1.8%	-29.6%	0.0%	-10.0%
	-26.1%	-23.2%	-25.8%	-20.5%	-17.1%	-0.3%	-29.9%	0.0%	-9.0%
InN	-17.6%	-14.8%	-17.0%	-11.0%	-7.2%	9.1%	-21.8%	11.1%	0.0%
	-18.8%	-15.6%	-18.4%	-12.7%	-8.9%	9.5%	-23.0%	9.9%	0.0%

Table 7.4 Lattice mismatch of shell on core calculated from bulk material lattice constants of the Rock salt structure of a number of common binary semiconductors.

Rock salt Lattice Constants			Lattice Mismatch of Rock salt Structures (shell on core)								
				GeTe	SnTe	PbS	PbSe	PbTe	ZnO	MgO	MgS	MgSe
GeTe	6.012		GeTe	0.0%	-4.9%	1.1%	-1.8%	-6.9%	31.3%	43.1%	15.5%	1.8%
SnTe	6.32		SnTe	5.1%	0.0%	6.3%	3.3%	-2.2%	38.0%	50.5%	21.5%	7.0%
PbS	5.9458		PbS	-1.1%	-5.9%	0.0%	-2.8%	-8.0%	29.8%	41.6%	14.3%	0.7%
PbSe	6.12		PbSe	1.8%	-3.2%	2.9%	0.0%	-5.3%	33.6%	45.7%	17.6%	3.7%
PbTe	6.46		PbTe	7.5%	2.2%	8.6%	5.6%	0.0%	41.0%	53.8%	24.2%	9.4%
ZnO	4.58		ZnO	-23.8%	-27.5%	-23.0%	-25.2%	-29.1%	0.0%	9.0%	-12.0%	-22.4%
MgO	4.2		MgO	-30.1%	-33.5%	-29.4%	-31.4%	-35.0%	-8.3%	0.0%	-19.3%	-28.9%
MgS	5.203		MgS	-13.5%	-17.7%	-12.5%	-15.0%	-19.5%	13.6%	23.9%	0.0%	-11.9%
MgSe	5.904		MgSe	-1.8%	-6.6%	-0.7%	-3.5%	-8.6%	28.9%	40.6%	13.5%	0.0%

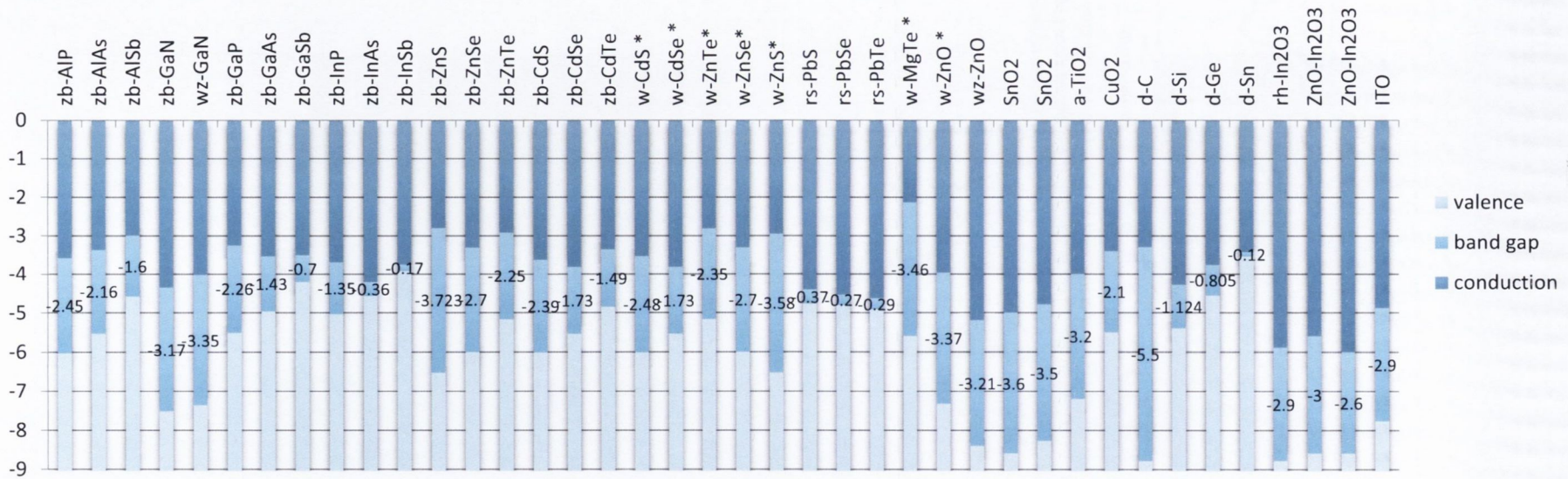

Figure 7.1 This graph shows the valence band, conduction band and band gap of a range of common elemental and binary semiconductors in eV, relative to the vacuum state For each semiconductor the exact phase of the material has also been included, zb (zinc blende), w (wurtzite) rs (rock salt) and d (diamond lattice)[378-387]

7.3 Appendix C: Extra Experimental Results of Chapter 3

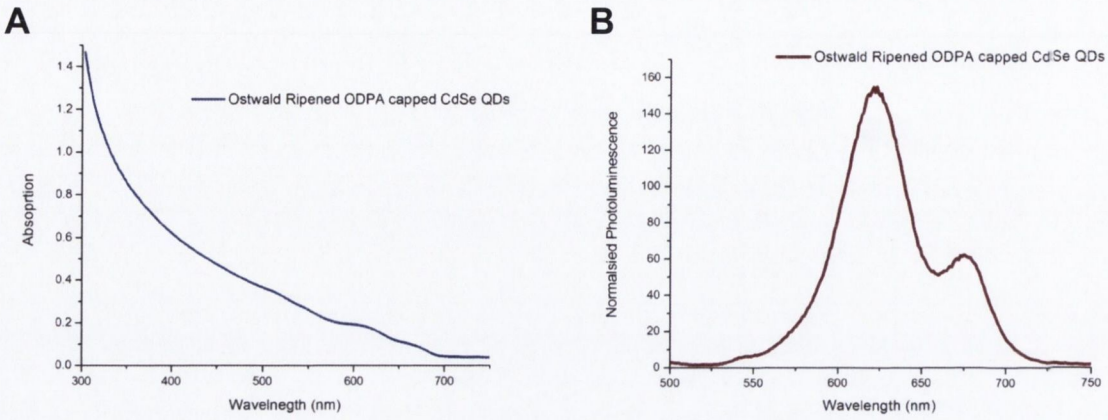

Figure 7.2 UV-Vis absorption spectroscopy and photoluminescence spectroscopy of ODPA capped CdSe QDs that have undergone excessive growth at 350 °C for 4 minutes. This had the effect of causing the onset of Ostwald ripening, causing to barely visible first exciton peaks to appear in the image A and cause to separate PL peal to appear in image B due to the presence of two distinct population sizes of CdSe QDs due to Ostwald ripening.

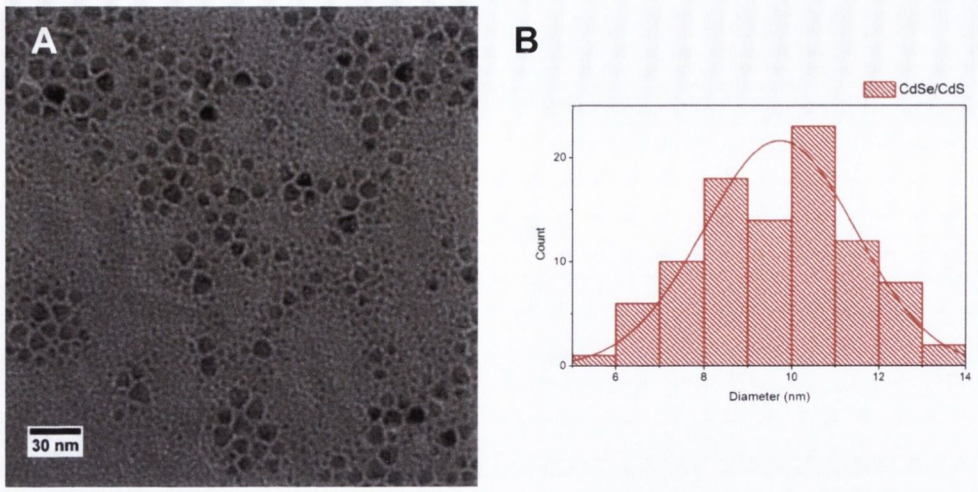

igure 7.4 TEM of CdSe/CdS QDs (A), the resulting ze distribution (B), and UV-Vis absorption spectra :) showing the evolution of the absorption spectra f as the shell was grown. The TEM shows the ucleation of large CdSe/CdS and much smaller CdS. iving a mean of 9.7 nm and a SD of 1.73 nm +/- for ıe large particles and a diameters of below 2 nm iameters. The UV-Vis absorption spectra shows the hange as the shell thickness is increased, indicating ıe homo nucleation of CdS QDs when shell 3 was rown, indicated by the absorbance of peaks which ın be assigned to the first exciton of CdS QDs, which red shifted following the next injection.

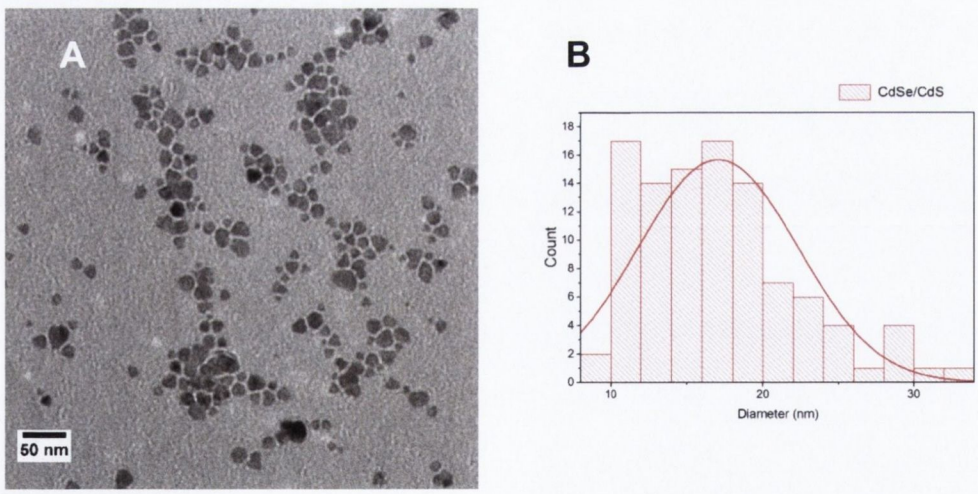

Figure 7.4 TEM (A) and the resulting size distribution (B) of a sample of CdSe/CdS core/shell quantum dot. For this sample a very large shell of CdS was grown upon the core, which producing a sample with a large size distribution giving an average of 17.6 nm in diameter as shown in B.

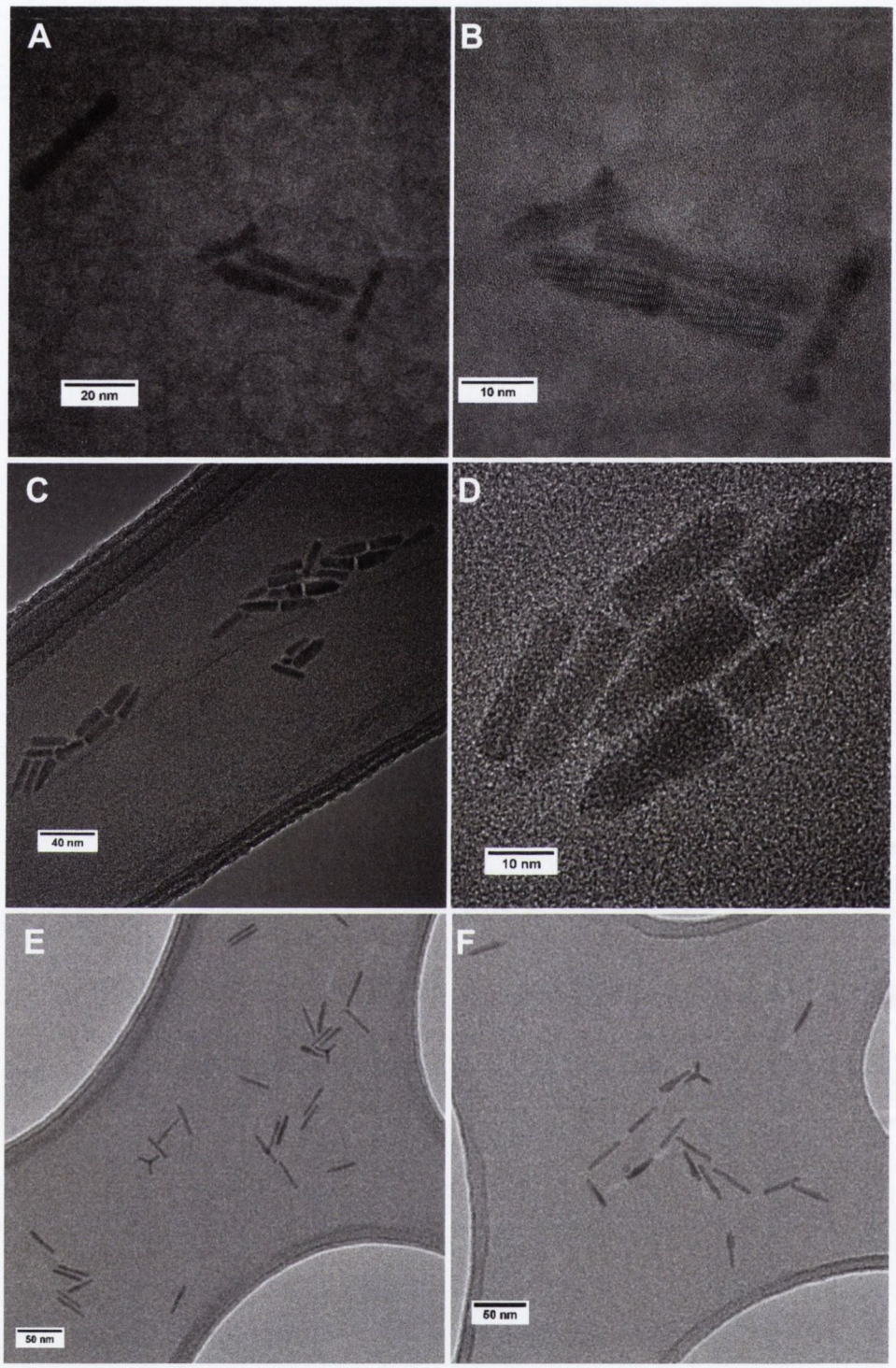

Figure 7.5 This is shows a number of other TEM images of CdSe/CdS heterostructured QRs. Image A and B were formed from 3.1 nm CdSe QDs nanorod, Image C and D were formed from CdSe of 4.05 nm QDs , while E and F were formed form 3.4 nm CdSe QDs

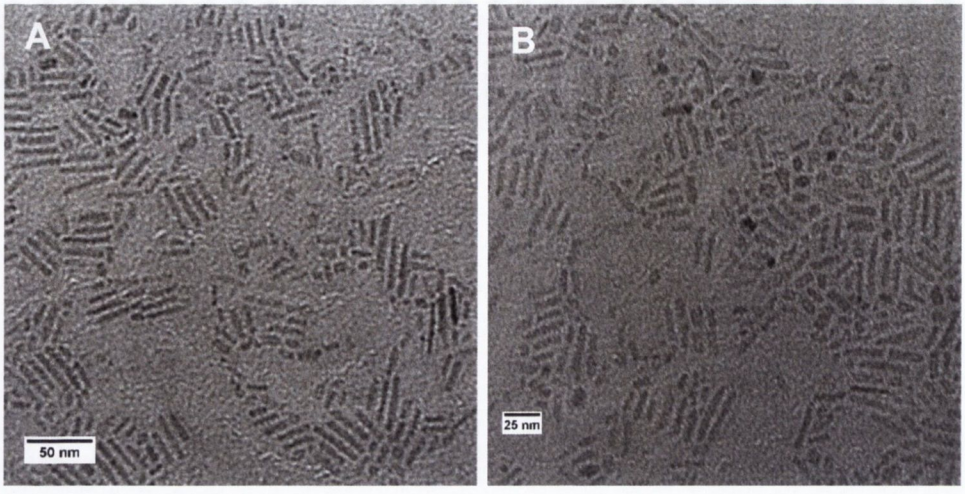

Figure 7.6 This is shows TEM images of CdSe/CdS heterostructured QRs formed from 3.2 nm ODPA capped CdSe QDs

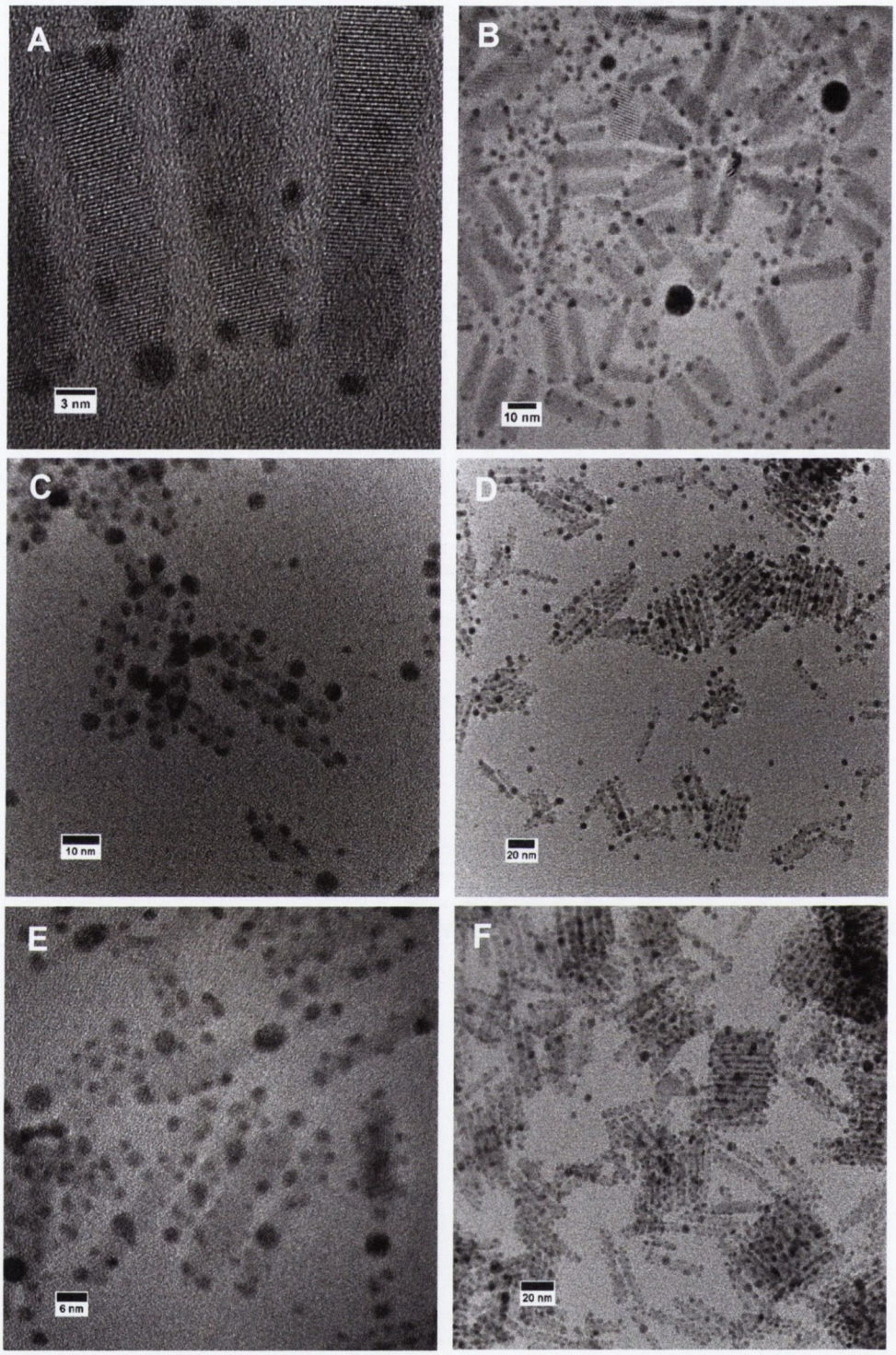

Figure 7.7 This shows the results of CdSe/CdS/Au structures showing results obtained from other sample under a range of conditions.. Image A and B sample show the results of an alternative approach, which used already formed Au NPs, which were heated in the presence of the of sample of CdSe/CdS QRs, which did showing Au coating of the nanorods. Unfortunately this also showed a large quantity of Au NPs in solution, especially large Au particles in solution, complicating analysis of the sample and therefore was deemed the not the optimal approach to CdSe/CdS/Au QR synthesis. Image C and D is samples 3, while image E and F are sample 1 in as discussed in Chapter Table 3.8.

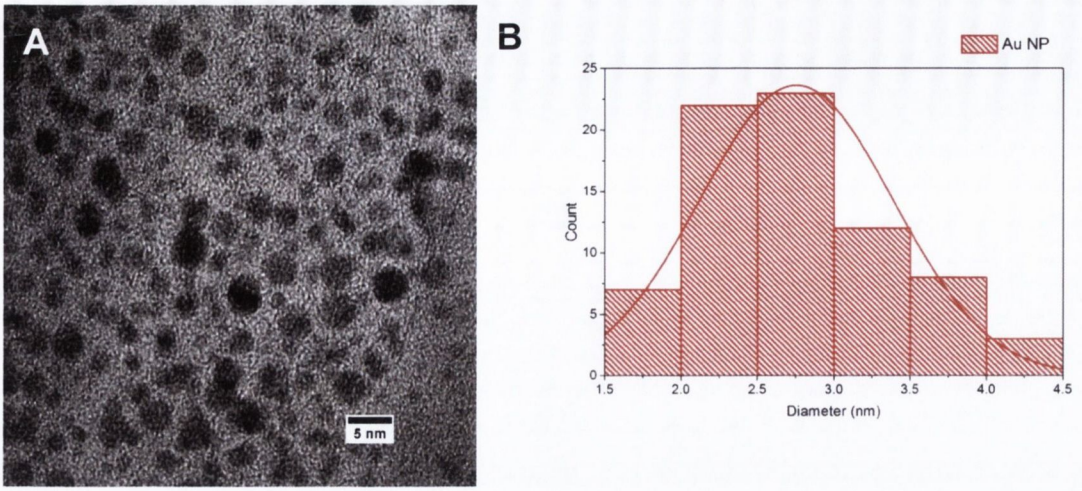

Figure 7.9 TEM of Au NP (A) and the size distribution of the resulting NPs (B). The TEM shows a large a small enough size distribution, giving an average diameter of 2.753 +/- 0.63 nm.

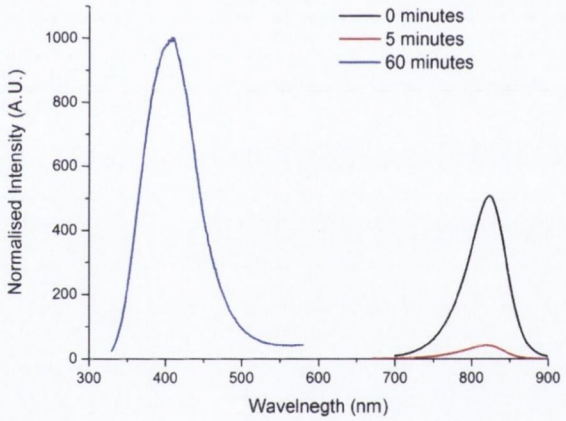

Figure 7.8 Photoluminescent spectra showing the shift in luminescence of a PbS QD as a cation exchange is carried out showing the reduction in luminescent and the eventually huge shift that took place after 60 minutes, indicating a complete exchange of the QD has taken place.

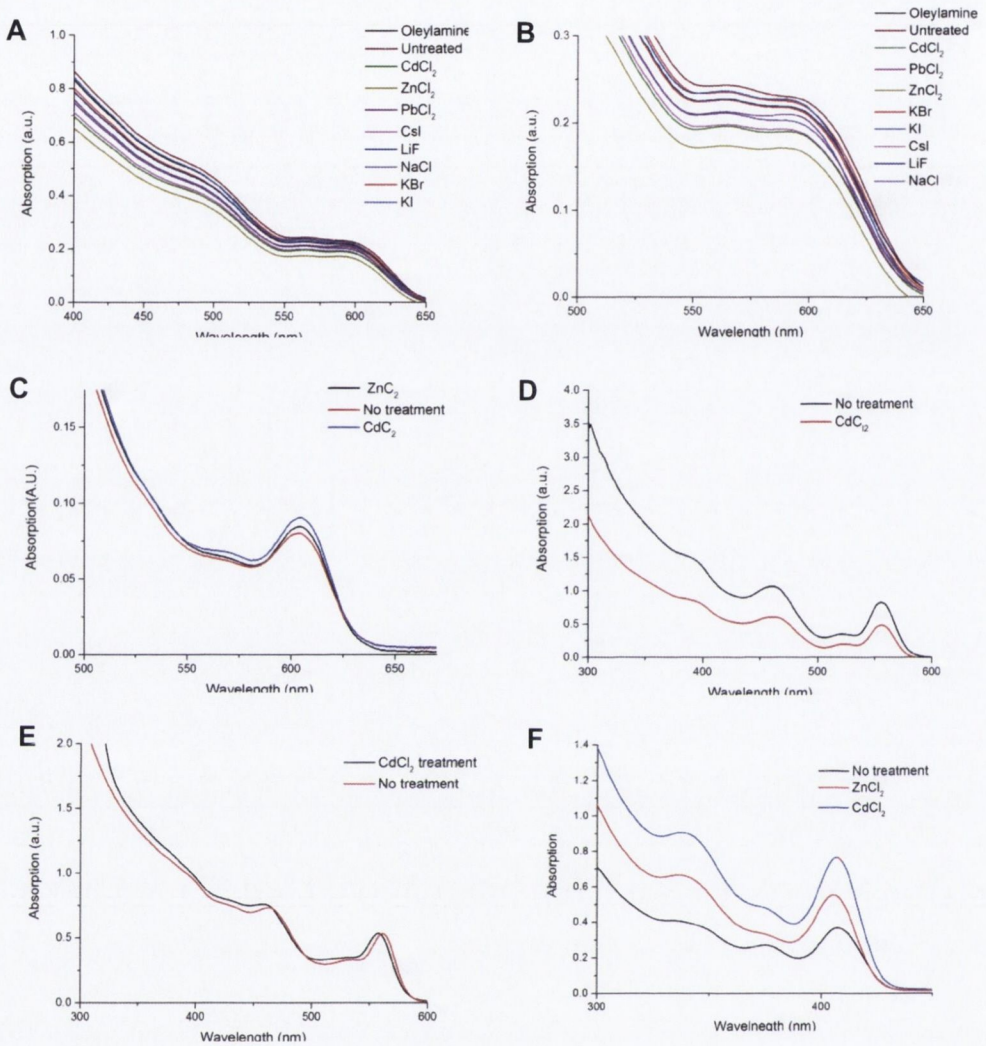

Figure 7.10 UV-Vis absorption spectra of a range of QDs treated with a variety of oleylamine based solutions. Image A and B shows Oleic acid capped CdSe QDs after anion treatments, showing little no change in the absorption peak of the QD. This same effect is seen across all samples following, with C being CdSe/CdS QD, image D is octadecylamine capped CdSe QDs, E is octadecylphosphonic acid capped CdSe and F is oleic acid capped CdS QD.

7.4 Appendix D: Extra Experimental Results of Chapter 4

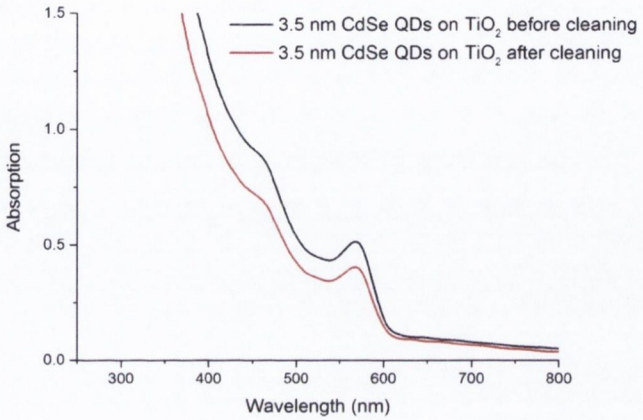

Figure 7.11 UV-Vis absorption spectroscopy of oleic acid capped CdSe (3.5 nm) sensitised TiO_2 electrode, comparing the change in loading of QDs when the electrode is washed with DCM following EPD deposition of CdSe QDs, showing a loss of 20 % of loading due to the wash.

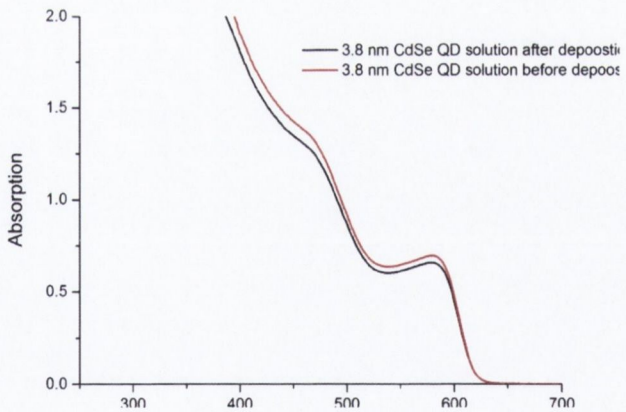

Figure 7.12 UV-Vis absorption spectroscopy of oleic acid capped CdSe (3.8 nm) in DCM showing the change in solution concentration due to deposition, which shows a loss of ~ 5.5% in concentration when comparing the concentration of before and after deposition

7.5 Appendix E: Extra Experimental Results of Chapter 5

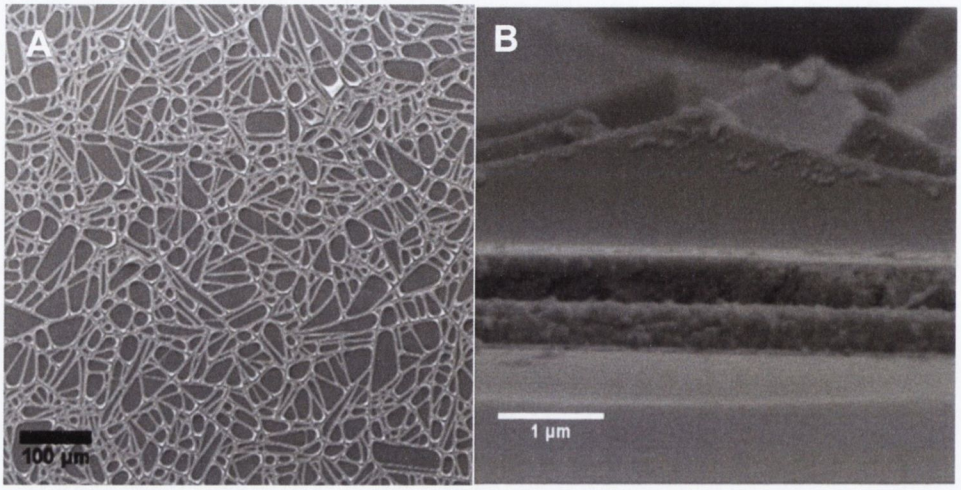

Figure 7.13 SEM of cracked bulk TiO_2 surface produced from dropcasting a solution of 10 mM $TiCl_4$ aqueous solution upon FTO glass. Image A shows the highly fractured surface, while image B shows the side profile of the film also shows a thick coating of between 300-400 nm produced o the FTO surface, with raised segments of the film visible in the background.

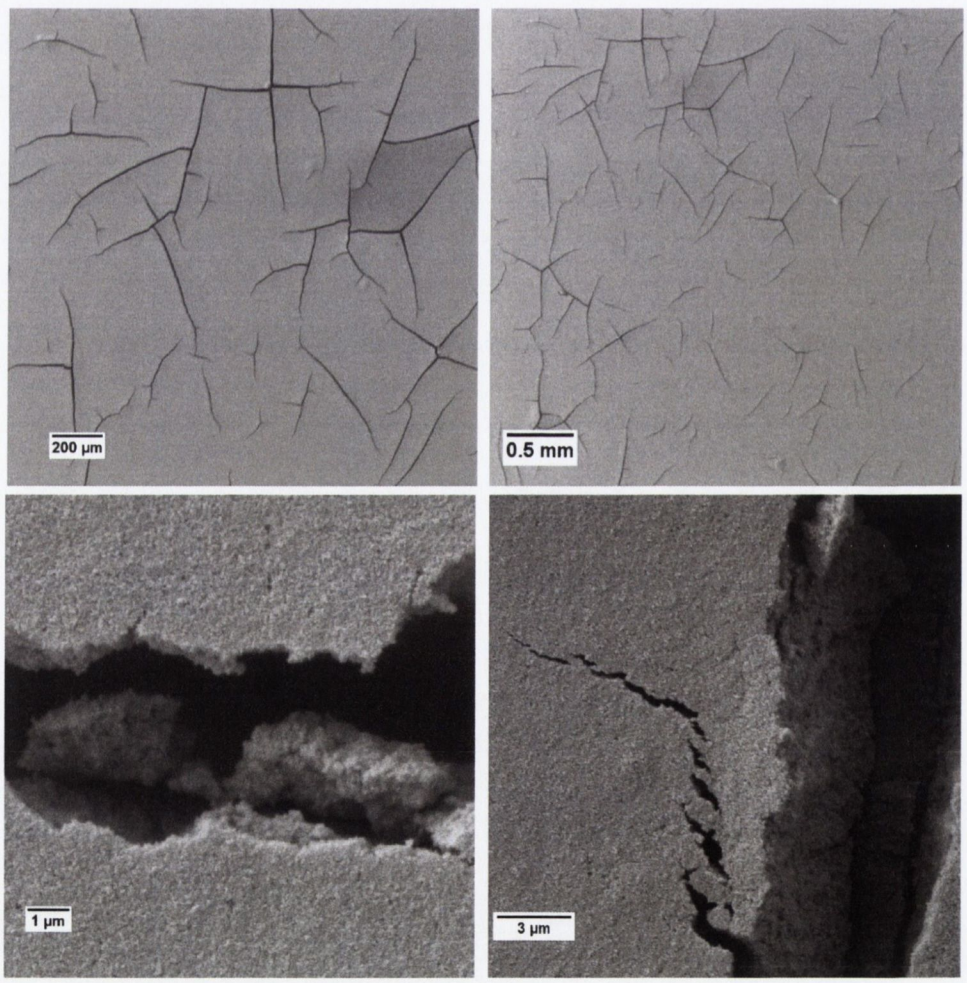

Figure 7.14 SEM images of a TiO_2 upon FTO glass that showed wide spread cracking in the surface coating due to excessive deposition of TiO_2 sol paste (Dyesol, 90T)upon the FTO glass before sintering in a furnace.

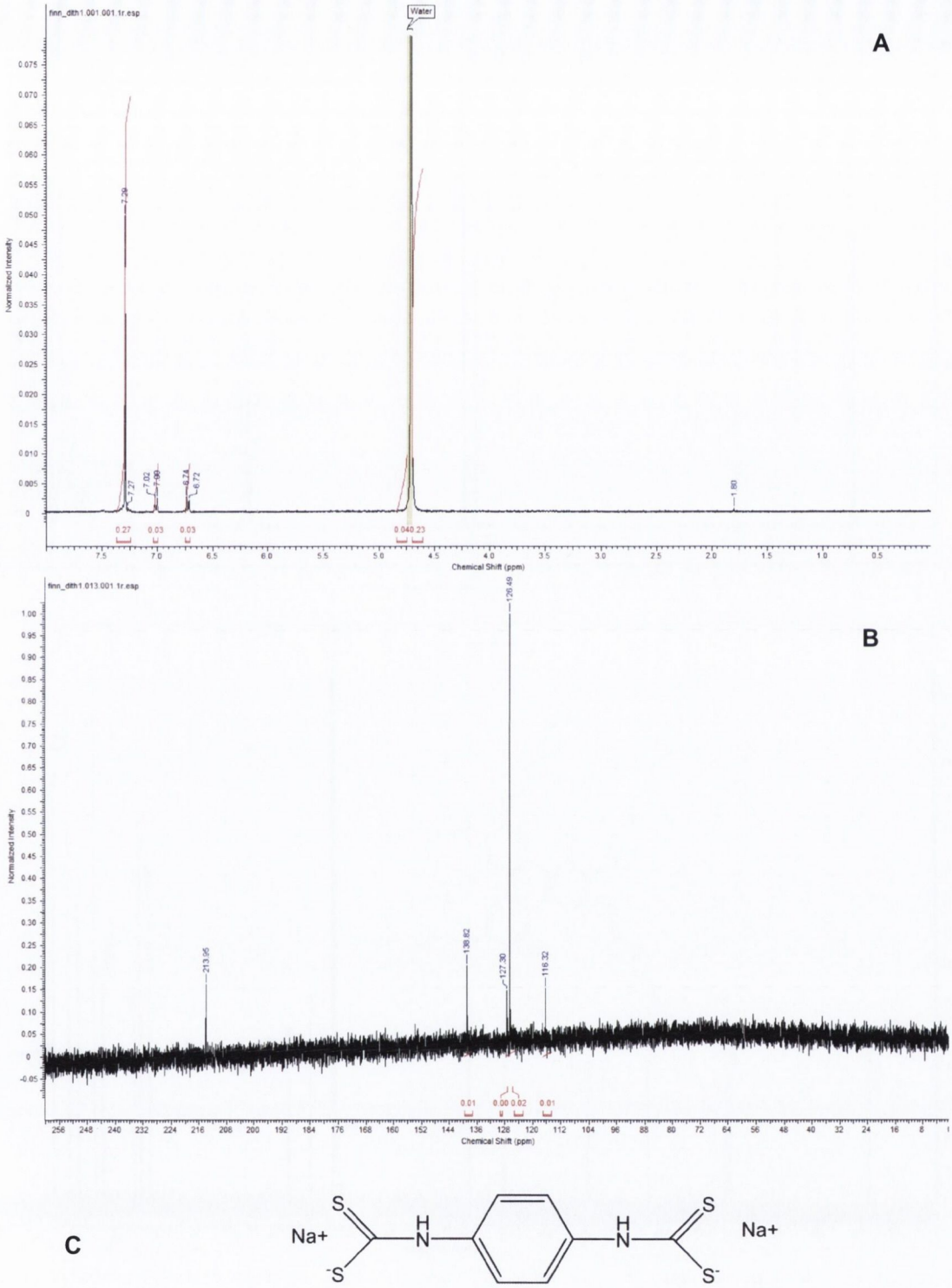

Figure 7.15 ^{1}H (Image A) and ^{13}C NMR (Image B) of Disodium 1,4-phenylenedicarbamodithioate (PBDT) (Image C). ^{1}H (400.13 MHz, D_2O) d: 7.34 (s,Harom) ; ^{13}C (100.62 MHz, D_2O) d: 214.41 (-NH-CS_2), 139.3, 126.9 (2xCarom). calcd. for $C_8H_6N_2Na_2S_4 \cdot 4\ H_2O$: C, 25.52; H, 3.75; N, 7.44; Na, 12.21; O, 17.00; S, 34.07. Found C, 25.31; H, 3.69; N, 7.68; Na, 11.94 O, 17.03; S, 34.2.

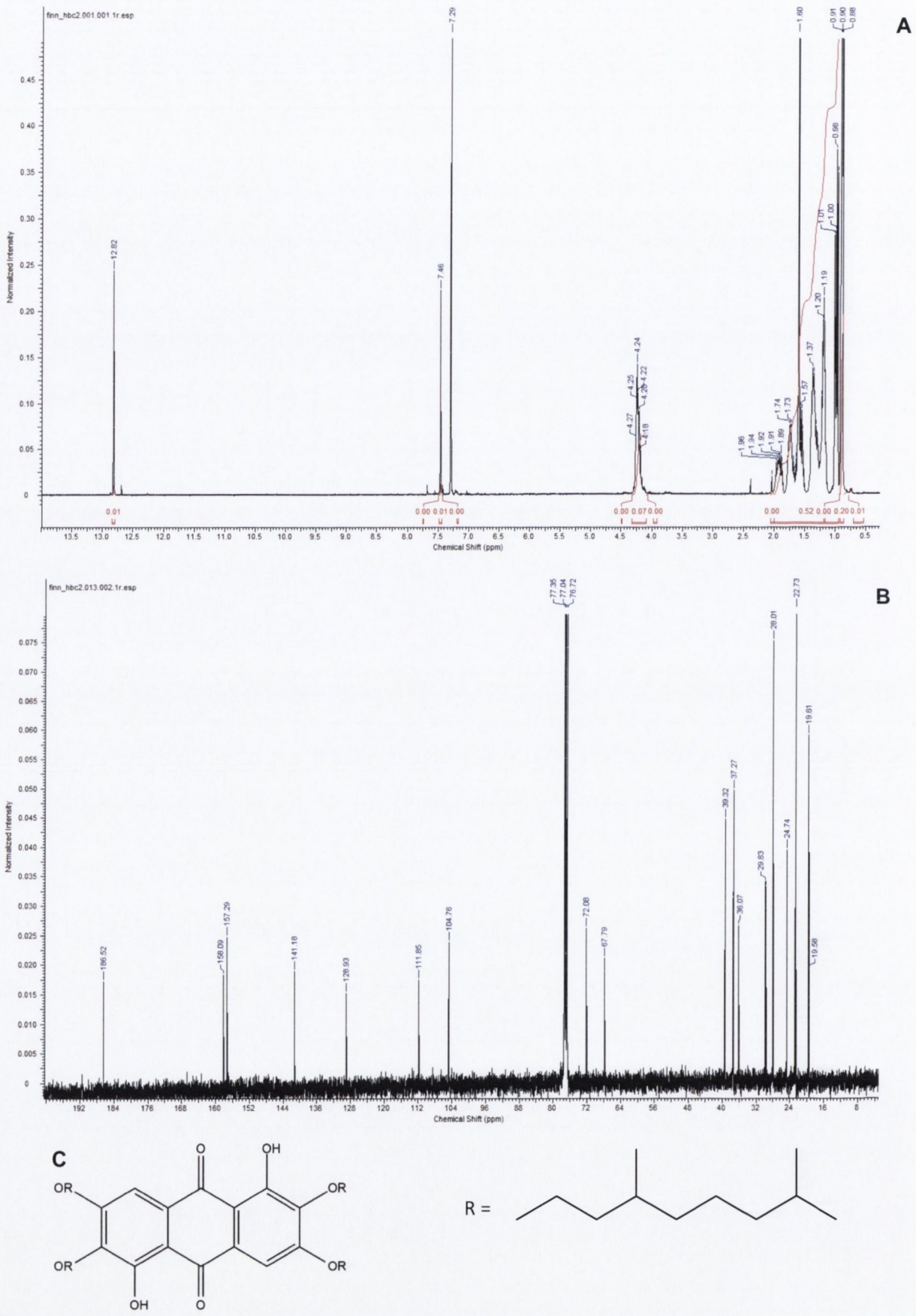

Figure 7.16 ^{1}H (Image A) and ^{13}C (Image B) NMR spectra of RTAQ (1,5-dihydroxy-2,3,6,7-tetrakis(3,7-dimethyloctyloxy)-9,10-anthraquinone) (image C).

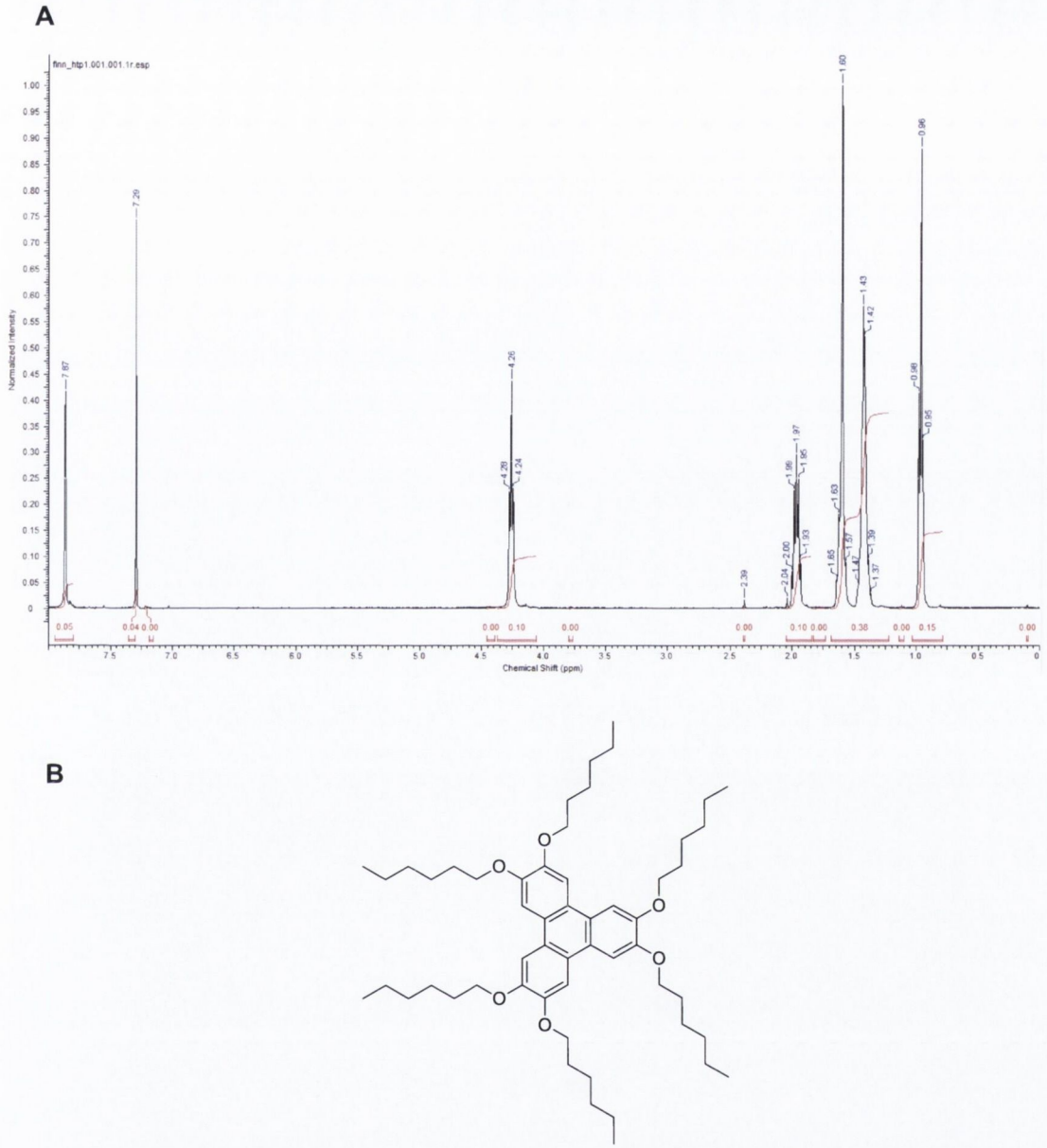

Figure 7.17 ^{1}H- NMR spectra (Image A) of High temperature liquid crystal, H6TP , (hexahexyloxy-triphenylene) (Image B).

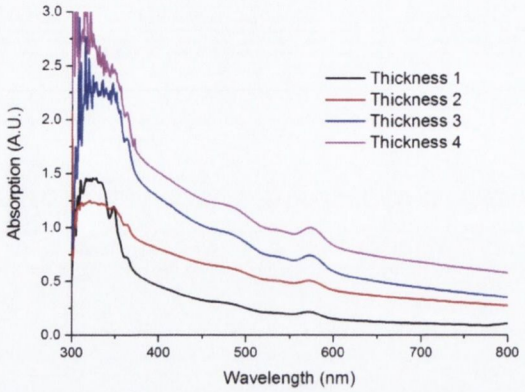

Figure 7.18 UV-Vis absorption CdSe QD doped film of H6TP.

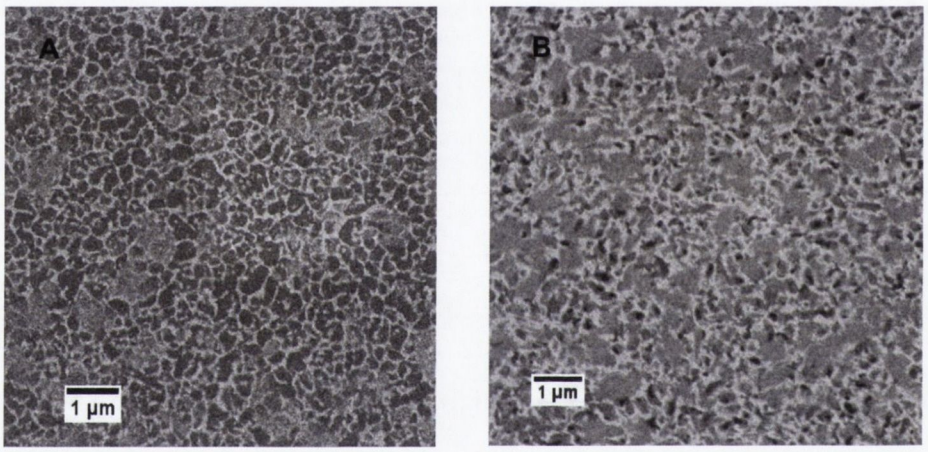

Figure 7.19 SEM image of 1:50 shown image A and PbS: RTAQ, SEM of 1:10 PbS: RTAQ is shown in image B.

Table 7.5 This shows the results of cells tested to date of DLC solar cells.

Cells	Contents	Composition w/w%			Total Weight (mg/ml) 1:3, cyclo-hexane, CHCl3)	Spin Coating Coverage of Absorber	Photovoltaic effect detected	DLC Solar Cell Design
		PDI	LC	QD				
1	Pure Lc	0	100%	0	40	Excellent	No	1
2	LC + CdSe QD	0	50%	50%	40	Good	No	1
3	LC + CdSe QD	0	91%	9%	40	Excellent	No	1
4	LC + PbS QD	0	50%	50%	40	Good	No	1
5	LC + PbS QD	0	91%	9%	40	Excellent	No	1
6	LC+PDI	33	66%	0	40	Poor	No	2
7	LC+PDI	50	50%	0	40	Okay	No	2
8	LC+PDI+PbS QD	63	30%	7	40	Good	No	2
9	LC+PDI+TiO_2	67	33	0	30	Good	No	3
10	LCI+PDI +TiO_2+PbS QD	63	30	7	30	Good	No	3

References

104. Al-Douri, Y.; Abid, H.; Aourag, H., Calculation of Bulk Moduli of Semiconductor Compounds. *Physica B: Condensed Matter* 2002, 322, 179-182.
298. Carbone, L.; Cozzoli, P. D., Colloidal Heterostructured Nanocrystals: Synthesis and Growth Mechanisms. *Nano Today* 2010, 5, 449-493.
317. Besra, L.; Liu, M., A Review on Fundamentals and Applications of Electrophoretic Deposition (Epd). *Progress in Materials Science* 2007, 52, 1-61.
376. Biesheuvel, P. M.; Verweij, H., Theory of Cast Formation in Electrophoretic Deposition. *Journal of the American Ceramic Society* 1999, 82, 1451-1455.
377. Hamaker, H. C., Formation of a Deposit by Electrophoresis. *Transactions of the Faraday Society* 1940, 35, 279-287.
378. Facchetti, A.; Marks, T., *Transparent Electronics: From Synthesis to Applications*. Wiley: 2010.
379. Li, Y.-H.; Walsh, A.; Chen, S.; Yin, W.-J.; Yang, J.-H.; Li, J.; Da Silva, J. L. F.; Gong, X. G.; Wei, S.-H., Revised Ab Initio Natural Band Offsets of All Group Iv, Ii-Vi, and Iii-V Semiconductors. *Appl. Phys. Lett.* 2009, 94.
380. Grätzel, M., Photoelectrochemical Cells. *Nature* 2001, 414, 338-344.
381. Walsh, A.; Da Silva, J. L. F.; Wei, S.-H., Multi-Component Transparent Conducting Oxides: Progress in Materials Modelling. *J. Phys.-Condes. Matter* 2011, 23.
382. Robertson, J.; Clark, S. J., Limits to Doping in Oxides. *Phys. Rev. B* 2011, 83, 075205.
383. Wei, S. H.; Zunger, A., Electronic and Structural Anomalies in Lead Chalcogenides. *Phys. Rev. B* 1997, 55, 13605-13610.
384. Wei, S. H.; Zunger, A., Calculated Natural Band Offsets of All Ii-Vi and Iii-V Semiconductors: Chemical Trends and the Role of Cation D Orbitals. *Appl. Phys. Lett.* 1998, 72, 2011-2013.
385. Schleife, A.; Fuchs, F.; Roedl, C.; Furthmueller, J.; Bechstedt, F., Branch-Point Energies and Band Discontinuities of Iii-Nitrides and Iii-/Ii-Oxides from Quasiparticle Band-Structure Calculations. *Appl. Phys. Lett.* 2009, 94.
386. Höffling, B.; Schleife, A.; Fuchs, F.; Rödl, C.; Bechstedt, F., Band Lineup between Silicon and Transparent Conducting Oxides. *Appl. Phys. Lett.* 2010, 97, -.
387. Krishnakumar, V.; Ramamurthi, K.; Klein, A.; Jaegermann, W., Band Alignment of Differently Treated TCO/CdS Interface. *Thin Solid Films* 2009, 517, 2558-2561.